Numerical, Experimental and Stochastic Modelling of Volcanic Processes and Volcanic Hazards

NEMOH

a Marie-Curie Initial Training Network for the next generation of European volcanologists

Numerical, Experimental, and Stochastic Modelling of Volcanic Processes and Volcanic Hazards

Editors

Paolo Papale, Editor-in-Chief
Istituto Nazionale di Geofisica e Vulcanologia, Via Della Faggiola 32, 56126 Pisa, Italy

Hideo Aochi
Bureau de Recherches Geologiques et Minieres, Avenue Claude Guillemin 3, 45060 Orleans, France

Christopher J. Bean
Dublin Institute for Advanced Studies, 10 Burlington Road, D04 C932 Dublin, Ireland

Costanza Bonadonna
Department of Mineralogy, University of Geneve, Rue des Maraichers 13, 1205 Geneve, Switzerland

Arnau Folch
Barcelona Supercomputing Center, Jordi Girona 29, 08034 Barcelona, Spain

Alessandro Fornaciai
Istituto Nazionale di Geofisica e Vulcanologia, Via Della Faggiola 32, 56126 Pisa, Italy

Magnus Tumi Gudmundsson
Institute of Earth Sciences, Haskoli Islands University, Sturlugata 7, 101 Reykjavik, Iceland

Stephen J. Lane
Lancaster Environment Center, University of Lancaster, LA1 4YQ Lancaster, United Kingdom

Raffaela Pignolo
Istituto Nazionale di Geofisica e Vulcanologia, Via Della Faggiola 32, 56126 Pisa, Italy

Alison Rust
Center for Environmental and Geophysical Flows, University of Bristol, Wills Memorial Building Queen's Road, BS8 1RJ Bristol, United Kingdom

Gilberto Saccorotti
Istituto Nazionale di Geofisica e Vulcanologia, Via Della Faggiola 32, 56126 Pisa, Italy

Bettina Scheu
Department of Earth and Environmental Sciences, University of Munich, Theresienstrasse 41, 80333 Munich, Germany

Editorial and Graphical Rendering:
Massimiliano Cascone, Patrizia Pantani
Istituto Nazionale di Geofisica e Vulcanologia,
Via Della Faggiola 32 - 56126 Pisa, Italy

This book has been realized in the frame of the European Union
Seventh Framework Programme (FP7/2007-2013), Project NEMOH,
Grant Agreement n. 289976.

Citation:
Book: Papale, P. et al (2018). Numerical, Experimental, and Stochastic Modelling of Volcanic Processes and Volcanic Hazards. Pacini Editore, Pisa, Italy.
Chapter: Author (2018), Chapter Title. In. Papale, P. et al. (Editors), Numerical, Experimental, and Stochastic Modelling of Volcanic Processes and Volcanic Hazards. Pacini Editore, Pisa, Italy.

Cover picture: 2001 eruption of Mount Etna.
Photo courtesy: M. Stoppato.

ISBN: 978-88-6995-428-3 •

Realizzazione editoriale
Pacini Editore
Via A. Gherardesca
56121 Ospedaletto (Pisa)

Fotolito e Stampa
IGP Industrie Grafiche Pacini

Contents

Introduction

Volcanic eruptions are among the most complex of natural processes, with physical and chemical controls occurring over spatial scales from the tens of kilometers of the magmatic system to the sub-millimeter scale of gas and crystal phase nucleation and growth. Time scales range from the multi-millennia of volcanic system evolution, through the seconds (and less) of earthquake generation and magma foam disruption into pyroclastic materials, to microsecond interactions between airborne volcanic ash particles. Volcanic systems display multi-phase, multi-component dynamics, behaviours and properties that are among the most extreme on Earth. Volcanic eruptions are also the source of large to extreme risks for human settlements and challenge engineering resilience (e.g., air traffic), and can exert severe impacts from the local to the global scale, including affecting the Earth climate. Over the last few decades disciplines such as thermodynamics, fluid dynamics, structural mechanics, advanced experiments and computation, have been incorporated within volcano science in order to properly face the great challenge of understanding volcanic processes and volcanic eruptions, and formalized treatment of uncertainties has become a prominent means of volcanic hazard evaluation. However, critically, such developments have not been accompanied by a comparable evolution in the curricula of students and young scientists undertaking a career in volcanology.

Under these circumstances a consortium formed by thirteen European partners has gathered into the FP7 Marie Curie Initial Training Network, GA 289976, "NEMOH – Numerical, Experimental and Stochastic Modelling of Volcanic Processes and Hazard", with the objective of supporting the growth of the next generation of European volcanologists, capable of extending further the knowledge and understanding of volcano dynamics and the methods and paradigms for volcanic hazard evaluation. Nine Full Network Partners plus four Associated Partners including two SMEs and one Governmental Civil Protection Department comprised the NEMOH consortium. NEMOH gave an opportunity of advanced training and research to eighteen young scientists from eight different countries, six from Europe (France, Belgium, Spain, United Kingdom, Germany, and Italy), and two from outside Europe (Mexico and India), who were recruited for a total of 528 research months.

This volume represents an overview of some of the scientific activities and results obtained by the young scientists trained under NEMOH. To date (August 2017), they have published in total nearly 70 ISI papers, a testament to the success of NEMOH and making this volume necessarily a limited description of their achievements. The original papers collected here illustrate the scientific quality of the NEMOH young scientists and the trans-disciplinary approach of the project, representing in many respects the state-of-the-art for volcanology in the second decade of the third millennium. Experimental, numerical and stochastic analysis and investigation of volcanic processes and volcanic hazards are developed to illuminate further the complexities of volcanic phenomena, from recharge of magma chambers and convection-mixing dynamics inside them, to rock dynamics, rock deformation and propagation of seismic waves, roles of aquifers and ice caps, dynamics of magma

ascent and eruption with complex behavior of melt-crystal-gas mixtures, pyroclastic flow and volcanic plume dynamics, and analysis of uncertainties in volcanic hazard forecasts; including new developments in mathematical treatments and numerical approaches, experimental volcanology, and multi-disciplinary and inter-disciplinary applications. Although interactions and cooperation between the fellows (and between their tutors) have been one major component throughout the project, this book is organized into separate chapters by individual young scientists, so to best illustrate their individual contributions. With the purpose of maximizing their exposure, each chapter is followed by a one-page self-description by the corresponding author, illustrating their background, scientific interests, and current career developments.

NEMOH has been a major opportunity of multi-disciplinary training and research for eighteen young volcano scientists in Europe and beyond. Simultaneously, NEMOH extended its training, collaboration, and exchange opportunities to nearly 300 additional young scientists who participated in training and dissemination activities, coming from all over the world and greatly extending the impact of the network. NEMOH organized six one-week long Network Schools, namely: Experimental Volcanology (Munich), Numerical Modelling and Simulations (Bristol), Volcano Monitoring and Surveillance (Stromboli), Volcano Deformation and Tectonics (Iceland), Volcanic Signal Analysis and Processing (Dublin), and Volcanic Hazard Evaluations and Forecasts (Etna). Each one delivered expert lectures, seminars and practical group activities, and included as a fundamental component training on additional skills such as poster and oral presentation, group discussion and extraction of group opinions, abstract writing, and project writing. In addition the following were also delivered: a 5-day course on parallel programming with applications in volcanology (Barcelona), a 3-days course on thermo-fluid dynamics and computational volcanology (Pisa), two NEMOH sessions and two NEMOH short courses on different aspects of quantitative volcanological research held at the EGU General Assemblies in Wien in 2014 and 2015, four NEMOH – Marie Curie Open Days aimed at introducing school students and the public to volcano research with an estimated global attendance above 500 people, and a Final Conference also attended by selected international volcano scientists and representatives from the geothermal industry.

Detailed information on NEMOH activities, and much more regarding the life of the network, is illustrated by the NEMOH website www.nemoh-itn.eu, which includes individual pages dedicated to each one of the eighteen NEMOH young scientists. Today, nearly all of them are continuing their career in science; a few of them have already attained permanent positions as scientists. But maybe the greatest success of NEMOH is that it created a community of multi-disciplinary scientists who understand each other, know what others can provide with their complementary approaches, and how their results can best fit into a multi-disciplinary approach with a global vision of volcano science and volcanic hazards forecasts. Even more significantly, they respect each other and continue to grow as a group of friends; their “NEMOH family”. This family is alive and evolving, inspiring confidence in a successful future for the science of volcanoes.

For the NEMOH Consortium: Paolo Papale, Coordinator

Chapter 1

Detecting displacement steps with seismometers: From laboratory constraints to volcano seismic applications

Johannes Thun
School of Earth Sciences, University College Dublin, Dublin, Ireland

Tutorship: Christopher J. Bean[1,2], Ivan Lokmer[1]
[1]*School of Earth Sciences, University College Dublin, Dublin, Ireland*
[2]*Geophysics Section, Dublin Institute for Advanced Studies, Dublin, Ireland*

Abstract

In seismology, seismic events are analysed and interpreted based on the waveforms recorded with seismometers at the surface. On volcanoes, the distances between sources and receivers can in some cases be as short as tens to hundreds of meters, which gives us the chance to record seismograms within the near-field of the sources, where ramp-like ground displacements or tilts can form part of the signal. Such ground motions can add valuable information to our analysis of the source process, but seismometers are not originally designed to measure these step-like signals. Our lab experiments with seismometers on step tables show that steps of the order of a few micrometres can be recovered from broadband seismograms, if we estimate and remove long-period noise using median filters. Applying this method to data recorded near the summit of Turrialba volcano, we observe a step-like ground deformation associated with long-period (LP) events, revealing a previously unobserved static component in the source time history of LP events. In a second application to data recorded above the 2014 Bárðarbunga dyke intrusion in Iceland, we discover repeating micrometre-scale deformation steps. This suggests that the rifting process happens at least partially in small, discrete steps, to our knowledge the first such observation.

Keywords: Volcano seismology, instrumental seismology, deformation, time series analysis

1. 1 - Introduction

The investigation of seismic events on volcanoes plays a major role in enhancing our understanding of volcanic systems, as they carry information on the dynamics of the volcanic edifice and its plumbing system. Different kinds of seismic events, such as long-period (LP), very-long-period (VLP) or volcano tectonic events have been observed on many volcanoes (e.g. Chouet, 2003; McNutt, 2005) and associated with various processes. However, the waveforms recorded by seismometers at the surface are strongly influenced by the medium through which the seismic waves have propagated - often a dominant effect in the heterogeneous structures of volcanic edifices. Additionally, the signals are always contaminated by varying amounts of noise of seismic (e.g. oceanic microseisms,

wind, tremor, machinery) and instrumental origin. As a consequence, the information on the source process is masked by multiple processes and thus not straightforward to recover.

While in classical earthquake seismology, the source-receiver distances are often very long, high density networks on volcanoes offer the chance to record signals very close to the source (≤ 1 – 2 km). At such short distances, near-field (NF) and intermediate-field (IF) terms can contribute significantly to recorded waveforms (e.g. Lokmer and Bean, 2010). The medium through which the seismic waves travel acts as a filter on the waveforms, altering the information sent by the source (the source-time function $M_0(t)$). For example, if there is a static deformation at the source (i.e. a step in $M_0(t)$), this will not appear as a step when observed at a distance, as the far-field (FF) terms are proportional to the time-derivative $\dot{M}_0(t)$. This kind of information is only carried directly in the NF and IF terms. If we manage to record such information, it can help to gain a better insight into the displacement history at the source and thus into the source process. However, broadband seismometers are not originally designed to record this kind of ramp signal and act as an additional filter on the waveforms. We thus carried out laboratory experiments with seismometers on step tables to expose the instrument to actual displacement steps. The recorded data were then used to design a processing routine that enables us to recover displacement steps from the seismograms.

Here we present this routine, followed by applications to two different sets of field data. The first one reveals a displacement step at the summit stations associated with LP events at Turrialba volcano, Costa Rica, not predicted by the classical resonating source models for these events (e.g. Chouet (1986), Neuberg et al., (2000)). The second dataset was recorded in direct vicinity of an active graben formation associated with an underlying dyke intrusion in Iceland. Our analysis of the local seismic events brings to light details of the deformation process in the area at the time of the experiment. The latter application shows that a careful approach to data analysis can help bridge the gap between seismology and deformation studies.

1. 2 - Methodology: Using seismometers as deformation sensors? (modified after Thun et al., 2015)

Our recent near-field observations (≤ 1 – 2 km from estimated source locations) indicate that the frequency content of small volcano seismic events (e.g. LP events) may in some cases extend all the way down to zero frequency, namely corresponding to a displacement step. However, as seismometers are not originally designed to measure such signals, here we quantify step displacement recovery from broadband seismic data using step table laboratory experiments.

In strong-motion seismology, static displacements associated with earthquakes are recovered from accelerometer data (e.g. Graizer, 2005; Chanerley et al., 2013), although it is a difficult task and displace- ments are often not entirely recoverable. The signal-to-noise ratio (SNR) in these scenarios is typically much higher than for the waveforms associated with volcanic LP events. An important difference between accelerometers and the broadband seismometers used in this study is their frequency response. While accelerometers have a finite response at zero frequency (DC), which always forms part of a step signal, broadband instruments are insensitive to DC signals - a direct technical consequence of their high sensitivity over broad frequency bands. Although for this reason seismo-

meters might not be ideal for a step recovery, they offer great sensitivity, so that potentially very small steps in the order of micrometers can be obtained.

If we seek to recover ground displacement steps from seismograms, we need to address long-period dynamic noise as well as other long-period signals (e.g. from tilt) contaminating the records. The influence of tilt motions on horizontal components of inertial seismometers has been known for a long time (e.g. Rodgers, 1968; Graizer, 2005; Pillet and Virieux, 2007). For small signals and neglecting the terms for angular acceleration and cross-axis sensitivity, the differential equation describing a horizontal pendulum is:

$$\ddot{y}_1 + 2\omega_1 D_1 \dot{y}_1 + \omega_1^2 y_1 = -\ddot{x}_1 + g\psi_2 \qquad (1)$$

where x_1 and y_1 are ground displacement and the pendulum response, respectively; ω_1 and D_1 the natural frequency and critical damping of the pendulum, respectively; g is the gravitational acceleration and Ψ_1 the ground rotation around the second horizontal axis, i.e. tilt in x_1-direction (for details see Graizer, 2005). Here we see that tilt has a first order effect on the horizontal pendulum, which can in fact become dominant at long periods (e.g. above 10 s). Currently available tilt meters on the other hand, are also susceptible to translational motion in the LP (e.g. 0.5 – 5 Hz) frequency range (Fournier et al., 2011). Hence with current instrumentation we cannot fully distinguish tilt motion from translational motion. Until real rotational sensors that can be deployed in a field setting are developed (e.g. Schreiber et al., 2006), other ways of dealing with tilt have to be adopted.

The equation for the vertical response looks similar to Equation 1, but the last (rotational) term can be neglected, which means the vertical component seismograms are not sensitive to small tilts. Wielandt and Forbriger (1999) used this difference between vertical and horizontal components to separate translational and rotational contributions on horizontal seismograms in the near-field of an assumed isotropic source. In general, this property makes a displacement step recovery from vertical recordings a lot more straightforward and less ambiguous than from horizontal components.

1. 2.1 - Laboratory experiments

As broadband seismometers measure the ground velocity, their output can be numerically integrated (e.g. with the cumulative trapezoidal method) to obtain displacement information. However, a seismometer's response filters true ground motion - by design seismometers lose sensitivity in the limit of zero frequency. Consequently, instrument noise starts to dominate for longer periods. Displacement steps (i.e. one-sided positive or negative velocity pulses) have a broad spectrum, including static (or zero) frequencies. Here we assess the degree to which displacement steps can be recovered from broadband seismometer data. We carried out laboratory experiments in which we exposed seismometers to well-defined steps, using a Lennartz CT-EW1 step table, which can achieve vertical steps as small as ~90 µm with high precision. The displacement time history varies between 0.5 s and 2.5 s, depending on table setting and load. In addition, we designed and built a simple customized step table (Figure 1C), which does not have the same precision as the calibration table, but allows for an arbitrary displacement time history. The displacement is driven by manual operation of

a micrometer screw and its value can be read directly from the screw's scale, with a resolution of 10 µm. It is directed at a 45° angle with respect to the ground, resulting in equivalent displacements in upwards and horizontal directions. Tilting of the table with angles of the order of about 10 microradians cannot be avoided in this setup and has to be kept in mind especially when analysing horizontal recordings. However, in comparison to tilt steps measured on volcanoes (typically a few orders of magnitude smaller), these signals are large and serve as an upper limit for tilt contamination of field data.

1. 2.1.1 **- Vertical component**

Figure 1A shows the integrated vertical seismograms, i.e. displacements, of a 94 µm upward step (black: ramp time 0.6 s; red: 1.8 s ramp with added noise, see below), recorded by a Guralp 3ESPCD (60 s) instrument on the Lennartz table. The uppermost plot shows unprocessed, integrated seismograms, which is approximately the instruments' impulse response, acting as a causal high-pass filter. In the second panel, the instrument response was removed without additional filters. The step is now clearly visible in the data, but amplified (very) long period noise is also present. During the deconvolution of the instrument response, high-pass filters are routinely applied in order to deal with this noise. Hence, the third plot shows the effect of an acausal high-pass filter (a zero-phase butterworth filter that conserves the waveform better; may lead to precursory signals, thus called "acausal") with the corner frequency of 0.01 Hz. Whilst it reduces long period noise, it also alters the step waveform significantly by removing its low-frequency portion. For higher filter frequencies (note that the typical lower LP filter corner of 0.3 Hz is about 5 octaves above 0.01 Hz) the step waveform is completely masked by the filter and cannot be distinguished from a dynamic motion. We assessed other filtering methods and found moving median filters suitable for the task of step recovery. Similar to moving average filters, we take the median of a window of width M around each data point x_n:

$$x_n^M = \mathrm{Median}\left(x_{n-\frac{M}{2}f_s}, \dots, x_{n+\frac{M}{2}f_s}\right) \tag{2}$$

where f_s is the sampling frequency and M is given in seconds. The filter is used to estimate the long-period noise of the velocity record and is insensitive to transient signals with durations significantly shorter than half the window length. As high frequency noise, tremor or other signal components can impede noise estimation with the (non-linear) moving median filter, a low-pass filter is applied to the instrument corrected data. A corner frequency of $f_c = 5/M$ was found suitable. The noise estimate is then subtracted from the original unfiltered, instrument corrected velocities and the result integrated to get displacements. The outcome for the previous lab example, using a moving median filter with $M = 30$ s is shown in the lowermost panel of Figure 1A, where the step waveform is successfully recovered from the seismogram. The misfit of the step estimation is:

$$\Delta_{\mathrm{step}} = \frac{u_{\mathrm{measured}} - u_{\mathrm{real}}}{u_{\mathrm{real}}} = \frac{102\ \mu\mathrm{m} - 94\ \mu\mathrm{m}}{94\ \mu\mathrm{m}} = 0.085 \tag{3}$$

i.e. the amplitude of the step is overestimated by 8.5 %. In comparison to field observations, the SNR in the experiment is very high and the rise time of the step is quite short (0.6 s). We thus used the recording of a slower step (i.e. a smaller velocity pulse) from the same table (1.8 s rise time) and added noise recorded on Turrialba summit station CIMA (red lines in Figure 1A). The noise was amplified in order to match SNRs observed on Turrialba (see Section 3). The resulting displacements show that for SNRs similar to our Turrialba field data, the step is still well recovered with a misfit of $\Delta = 0.053$, i.e. overestimated by about 5 %. Comparing different noise levels added to step table data, we estimate that the method's detection threshold for steps lies at about 1 µm for a 3ESPCD instrument. This corresponds to approximately 5 times the root-mean-square amplitude of the displacement noise below 2 Hz.

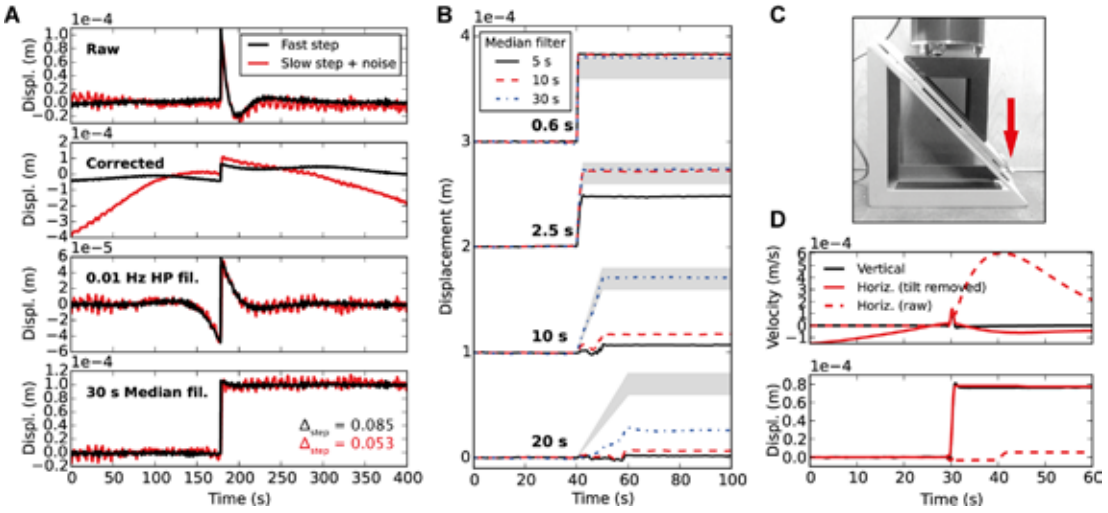

Figure 1. **A**. Recovery of a vertical 94 µm step recorded on a Lennartz step table. Black: 0.6 s ramp time; red: 1.8 s ramp time and added field data noise. The step is masked by the bandpass filter, moving median filters can reduce noise without masking the step. **B**: Recovery of vertical steps with varying ramp lengths and median filter windows, recorded on customized step table. Grey area indicates the actual displacement including errors. **C**: Customized step table, allowing for ramps of varying amplitudes and rise times; the arrow marks the micrometer screw used to control the displacement. **D**: Recovery of a horizontal step contaminated with tilt. In the upper panel, velocities are shown, exhibiting the very long period tilt response on the uncorrected horizontal component. This tilt signal can be reduced following Wielandt and Forbriger (1999). The lower panel shows the displacements after additionally applying the median filter method. Here the horizontal step aligns well with the identical vertical step (as seismometer displacements in horizontal and vertical directions are equal), meaning it is well recovered on both components (Figure modified after Thun et al., 2015).

As the Lennartz table is restricted to vertical motion and limited step rise times, we tested the performance of the processing on different ramp lengths using our customized step table. We exposed the same instrument to steps of about 100 µm (about 70 µm in vertical and north directions of the instrument), altering ramp times between 0.6 s and 20 s. We applied the processing described above, with varying median filter windows to recordings of different ramps (Figure 1B). The grey area shows the actual displacement, including an assumed error of about ±10 % (based on reading

precision at the micrometer screw). The results shown in Figure 1B confirm that stable results are achieved as long as the filter window M is chosen accordingly. We recommend a window length of about three times the ramp time. As in practice the ramp time is unknown, the signal length inferred from raw displacements can be a good starting point. If the length of the filter window is not sufficient for a given signal, it can strongly affect the recovered step. On the other hand, if the step is real, the recovered value is stable over a wide range of M (Figure 1B). Hence, we explore different windows M, starting at 3 times the signal length and gradually increasing M by 5 s each time until we achieve a robust solution with satisfactory noise removal. For now, this manual process is necessary to ensure stability and robustness of the results. There is no upper limit for the choice of M, but as filter windows get longer, less noise can be removed. Consequently, the method is limited by the SNR.

1. 2.1.2 **- Horizontal component**

Our customized table displaces the instrument horizontally to the same extent as vertically due to its 45° angle of translation with respect to the ground. During the displacements, driven by turning the micrometer screw, the table surface is tilted uncontrollably, a problem that cannot be avoided when creating horizontal displacements with this setup. This tilt leads to a long period transient dominating the horizontal seismograms (see dashed line in Figure 1D), but negligible on the vertical component. Associated with the displacements, we measure steps of about 1 to 20 $\cdot$ 10^{-6} g in instrument corrected and differentiated (i.e. acceleration) seismograms. According to the tilt term in Equation 1 this corresponds to tilt steps of about 1 to 20 µrad. Tilts this strong make it difficult to extract displacement steps from the horizontal seismograms, but do not interfere with recovery on the vertical component, as shown above. However, the tilts observed in our field experiments on volcanoes, where there are any, are several orders of magnitude smaller and thus do not create significant transients. A tilt step of the order of a few microradians would be directly visible particularly as a major waveform difference between vertical and horizontal components (see above and Figure 1D).

As the instrument in our experiment sits directly on the source and the tilt signal is negligible on the vertical component, the assumptions underlying the tilt separation method of Wielandt and Forbriger (1999) are fulfilled. We thus applied this method to the data for the fastest step (0.6 s with $u_x = u_z \approx 70$ µm), where a tilt of about 14 µrad affected the north component, while the displacement in this direction was identical to the upward motion. The horizontal raw velocity seismogram (Figure 1D, dashed red line) shows a long-period transient, the seismometer's response to a tilt/acceleration step (for details see Kinoshita, 2008). The tilt separation method was carried out between 0.005 Hz and 1 Hz, which exceeds the band suggested by Wielandt and Forbriger (1999) (0.005 Hz – 0.05 Hz), but works well here due to the high SNR. The solid line shows the resulting seismograms, in which the estimated tilt has been removed. Although the method's fit for this extreme (large tilt) example is not ideal (energy of the residual is about 8 % of the original trace), it reduces the tilt transient significantly and thus exposes the velocity pulse. The lower panel in Figure 1D shows the displacement seismograms after application of the median filter method. Whilst without

tilt reduction, the step is not retrieved on the horizontal component (dashed line), it is successfully recovered when tilt was reduced before median filter application. Both vertical and horizontal displacements show a step of about 77 μm, which is in good agreement with the known displacement (70 μm) in the presence of such large tilt contamination.

1. 2.1.3 **- Summary**

In conclusion, we demonstrate that static displacement steps can be recovered from seismometers when long-period noise is carefully addressed. Moving median filters are a suitable tool to reduce this noise adequately, although strong tilt contamination on horizontal components may have to be dealt with separately. Although we did not test this for instruments other than the aforementioned Guralp 3ESPCD (60 s; 2 x 3000 V/(m/s)) and a Guralp 6TD (30 s; 2 x 1200 V/(m/s)), in principle any broadband seismometer should be suitable for step recovery, as long as the response is well known and can be removed accurately. In our tests, the (shorter period and less sensitive) 6TD instrument showed a lower SNR at long periods than the 3ESPCD type, posing a problem for small signals. Low instrumental noise at long periods is thus desirable. In the following we apply the constraints found in this section to field observations on volcanoes.

1. 3 **- Applications to field data: Long-Period Event on Turrialba (modified after Thun et al., 2015)**

As the occurrence of Long-period (LP) seismic events is often thought to be directly associated with magmatic or hydrothermal processes (e.g. Chouet, 2003, and references therein) they can give information on the volcanic plumbing systems and changes in volcanic activity. According to the classification of LP events given by Chouet (2003) typical LP events contain frequencies between 0.5 Hz and 5 Hz, although McNutt (2005) pointed out significant changes with time and between different volcanoes. In the data recorded on Mt Etna, Sicily (Lokmer et al., 2008) and Turrialba, Costa Rica (Eyre et al., 2013), we observed additional low energy spectral content well below these typical frequencies. This observation can have significant implications for our understanding of the nature of source time functions (STFs).

STFs from LP source inversions are often explained by fluid-filled cavity models proposed e.g. by Chouet (1986) and Neuberg et al. (2000). In these models, slow waves travel at the fluid-solid interface and their interference can cause sustained resonance observed at the surface (Chouet, 1986; Ferrazzini and Aki, 1987). Full waveform inversions of LP events have been implemented in studies on several volcanoes, with results often interpreted within the scope of such models (e.g. Legrand et al., 2000; Kumagai, 2002; Nakano et al., 2003; Kumagai et al., 2005; Lokmer et al., 2007; Cusano et al., 2008; De Barros et al., 2011; Eyre et al., 2013). It is important to note that the waveforms used in these inversions were band-pass filtered. Recent observations in the summit region (e.g. Fig. 2b in Lokmer et al., 2007; Bean et al., 2014; Eyre et al., 2015) show impulsive waveforms associated with LP events. Bean et al. (2014) and Eyre et al. (2015) demonstrated that resonance observed on seismograms can be a consequence of wave propagation in poorly consolidated materials for stations more than about 1 km from the source. Consequently, Bean et al. (2014) proposed an alternative

model, where shallow LP events are a consequence of slow rupture within the volcanic edifice. Eyre et al. (2015) showed that this source model can explain LP event waveforms recorded on Turrialba volcano.

The current processing practice of filtering LP events within the most energetic frequency band prior to inversions means that most of the LP sources interpreted in the literature are band-pass filtered representations of the true source-time histories. In our unfiltered integrated field data, we recently observed small apparent displacement steps in the near-field of individual LP events. If this observation is real, it could significantly contribute to our understanding of LP sources. In the following, we show how the constraints gathered in the previous section can shed new light on the true ground motion caused by some LP events.

Figure 2B shows the vertical seismogram of an LP event recorded on Turrialba in 2009 by the summit station CIMA (map in Figure 2A), using the same instrument type that we used in the laboratory (Guralp 3ESPCD 60 s). Here we compare the classical LP band pass filtered trace to the one processed with the median filter. In both cases, a low pass filter with a corner frequency of 4 Hz was applied in advance. While the velocity seismograms do not show a significant difference, the displacements show a clear step when processed with the median filter; this displacement step cannot be seen when data are filtered with the bandpass filter, as is common practice. As the rise time of the step, starting at about 6.5 s, is no longer than about 2 s, the 20 s median filter window applied in Figure 2B is in accordance with the results from the laboratory experiments.

This step behaviour is not singular to this LP event, but can be observed for multiple events in the 2009 catalogue. Figure 2C shows seismograms of a family of 183 events (from family 2 in Eyre et al. (2013)) and a stack of these. Here the data were corrected for instrument response and trend, but no further filters were applied. The data were normalised to match the peak-to-peak amplitudes between events. Although (due to strong long-period noise) only some single events show a clear static displacement like in Figure 2B, the integrated stack of this family shows a pronounced step, even without applying a median filter. This shows that this step-like behaviour is coherent across LP events and can be detected when recorded in the near field at the summit of Turrialba. The same behaviour was observed at a second summit station CIM2 (Figure 2A), using the same instrumentation. Shorter period instrumentation and greater distances from the summit lead to sparse observation of such steps at other locations during the same field experiment.

The data demonstrate that both single event recordings and stacks of numerous repeating events show step-like displacement waveforms, which present as wave "pulses" in velocity seismograms. Low cut filtering traditionally applied prior to waveform inversion does not preserve these displacement signals, compromising our assessment of the broadband source-time history. These step-like displacement signals are only seen in the near-field region from the source, consistent with theoretical displacement fields for dislocations (e.g. Okada, 1992). The near- and intermediate-field terms, containing static deformation signals, decay much faster with the source-receiver distance than the purely dynamic far-field term (Lokmer and Bean, 2010). As a consequence, the step signal can rapidly fall under the detection threshold (around 1 μm on 3ESPCD instruments) within a distance of approximately 1–2 km from the source.

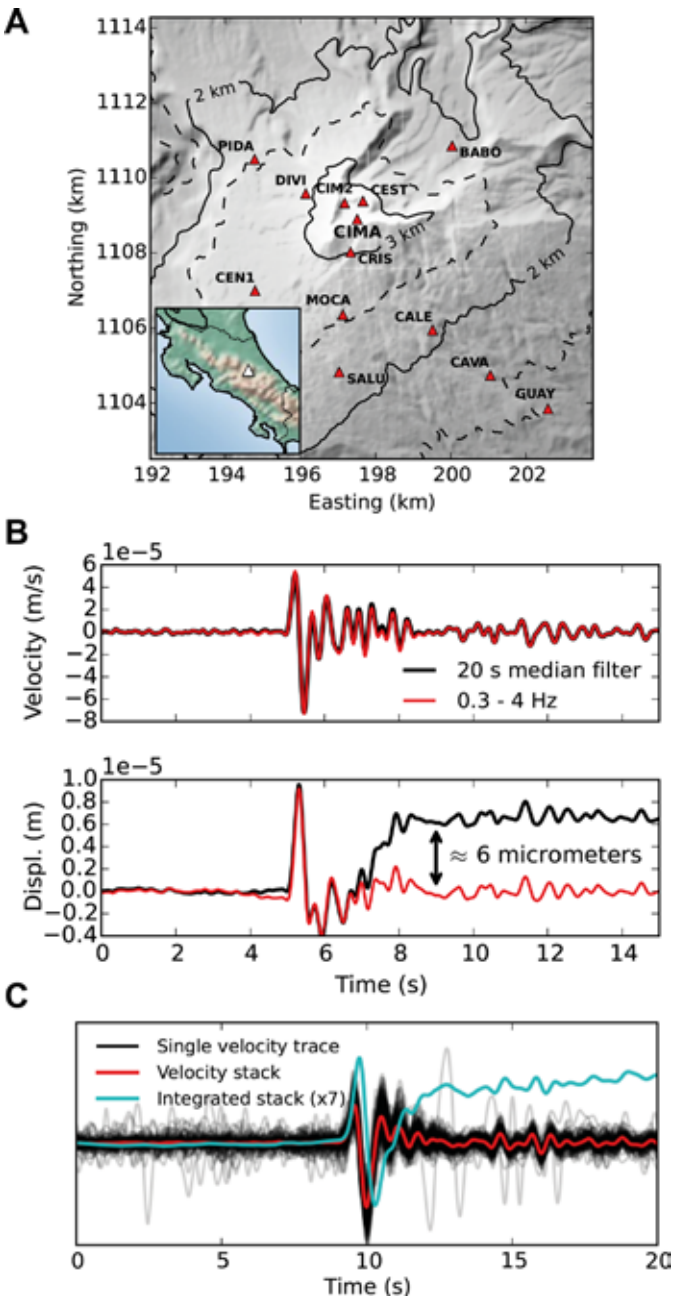

Figure 2. **A**. Station locations on Turrialba volcano in 2009. Inset shows the location of the volcano within Costa Rica. **B**: Top: Vertical LP event seismogram from Turrialba, recorded on Turrialba station CIMA in 2009, processed with median filter (20 s) or bandpass filter (0.3 – 4 Hz); Bottom: corresponding displacements; median filter processed data shows a step masked by the bandpass filter. **C**: Stack of 183 unfiltered, instrument corrected and normalised LP events from a family at station CIMA. Due to the high S/N ratio in the stack, a step similar to the single event in B is visible in the unprocessed integrated stack. (Figure reproduced from Thun et al., 2015).

A more detailed analysis of these new observations, including source inversions, is beyond the scope of this study. Hence we do not attempt to relate the surface waveforms directly to source models here. However, our results show that we are missing important information on LP sources if we analyse only the most energetic part of the recordings. These new observations pave the path for a more detailed analysis of LP sources from existing and future datasets.

1. 4 **- Applications to field data: Deformation at Bárðarbunga, Iceland (modified after Thun et al., 2016)**

Ground deformation caused by magma migration and tectonic processes can often be observed in volcanic environments with ground- and satellite-based methods such as GPS and InSAR (e.g. Ofeigsson et al., 2011; Geirsson et al., 2012; Sturkell et al., 2013; Sigmundsson et al., 2015). The technical restrictions of these methods limit the smallest observable deformations to a few millimetres at best, with actual resolutions typically in the centimetre range (Sigmundsson et al., 2015; Bürgmann et al., 2000). For InSAR, the temporal resolution is further limited to several days. As a consequence, neither method currently allows us to investigate the micrometre scale nature of near-surface deformation processes. Instead we observe accumulated deformations that smooth out the underlying details of the ground deformation process. Hence the details regarding precisely how the Earth's surface rifts at small spatio-temporal scales in volcanic environments are unclear.

An exceptional opportunity to investigate such deformation processes was posed by the 2014–2015 rifting episode and eruption at Bárðarbunga in Iceland, where we acquired data in the immediate vicinity of active surface rifting. Starting in August 2014, a lateral dyke propagated below the surface for over 45 km (Fig. 3A), indicated by the temporal and spatial evolution of seismicity and surface deformation patterns (Sigmundsson et al., 2015; Gudmundsson et al., 2016). Interestingly, despite the high level of observed seismicity below a depth of about 3 km, there was a lack of shallow (< 3km deep) earthquakes associated with such a large rifting event (Sigmundsson et al*., 2015*; Ágústsdóttir et al., 2016; Ruch et al., 2016). The dyke eventually fed an eruption at the Holuhraun eruptive fissure, the southernmost tip of which was located approximately 5 km north of the Vatnajökull glacier rim. The effusive activity lasted for 4 h on 29 August 2014 and later continued for 6 months from 31 August 2014. In the area not covered by the glacier, divergent rifting (total surface opening ~2.5m between mid-August and mid-September; Sigmundsson et al. (2015); Hjartardóttir et al. (2016)) was observed at the surface, accompanied by substantial graben subsidence (2.5 m to 5.5 m) directly above the inferred dyke (Sigmundsson et al., 2015; Hjartardóttir et al., 2016; Ruch et al., 2016). The graben formation caused large surface fractures along its borders, revealed by satellite, aerial and field observations (Hjartardóttir et al., 2016; Ruch et al., 2016) and the dip of the associated normal faults was estimated to be ~75°, based on the measured surface deformation (Hjartardóttir et al., 2016). In the northernmost region of the glacier, the graben formation caused an elongated dent in the relatively thin ice sheet (Rossi et al., 2016).

The details of the 2014–2015 Bárðarbunga volcano-tectonic episode have been addressed in numerous studies, e.g. Sigmundsson et al. (2015); Gudmundsson et al., (2016); Ágústsdóttir et al*.,* (2016); Hjartardóttir et al*.,* (2016); Rossi et al., (2016); Ruch et al., (2016); Gudmundsson et al.,

(2014). It was one of the largest rifting events and the largest effusive lava eruption in Iceland since the 1783–84 Laki eruption (Thordarson and Self, 1993) and offered an unprecedented opportunity to study rifting processes in detail.

1. 4.1 - Experiment and Data Analysis

In the afternoon of 30 August 2014, we installed a small profile of three 3-component broadband seismometers (Guralp 6TD 30 s) perpendicular to the graben and inferred dyke (Fig. 3A), with the closest station (DY3) directly at the western shoulder of one of the large graben boundary faults and the other two stations approximately 1 km (DY1) and 2 km (DY2) from DY3. The surrounding area was characterised by several metres of poorly consolidated volcanic ash and sand on top of partially fractured basaltic lava flows (Sigurgeirsson et al., 2015), a strongly scattering environment for seismic waves. As strong ground shaking could be felt during the experiment, the operation had to be aborted for safety reasons, resulting in ~26 minutes of synchronous data on all stations. On 5 September 2014, a new fissure opened approximately 600 m east of DY3 and effused lava for 2 days.

The unprocessed vertical velocity seismograms (Fig. 3B) show coherent activity on all three stations. However, the focus of this study lies in five high amplitude signals on station DY3 (red arrows in Fig. 3B), which are not registered by the other stations DY1 and DY2, suggesting that the causative events are relatively small and local to DY3. The velocity seismograms and the corresponding scalograms of these events (event number 3 shown in Fig. 4A,B) show impulsive waveforms with a main frequency peak between 3 and 8 Hz and a secondary peak above 25 Hz. As high-frequency waves are attenuated strongly when travelling through the ground, such high frequencies thus indicate a fracturing process close to the station.

In Figure 4C–E, we applied the median filter method presented in Section 2 (see also Thun et al., 2015) and observe displacement steps on all three (orthogonal) components of the instrument, i.e. the station was displaced by approximately 125 µm in a northwest, slightly upward direction. This represents a motion away from the centre of the graben and the underlying dyke. Applying this procedure to the full-length records on this station reveals similar amplitudes and ratios between different displacement components for all five events (Fig. 4F), suggesting a repetitive process with similar source locations and an apparent average inter-event time of about 4.5 minutes. As horizontal components of seismometers are also susceptible to ground rotation (Rodgers, 1968; Graizer, 2005; Pillet and Virieux, 2007), possible tilts can be estimated from the data using the tilt transfer function (Aoyama and Oshima, 2008; Genco and Ripepe, 2010; Lyons and Waite, 2011); this involves a simple integration of raw data and multiplication with a factor depending on well-known instrument properties. The resulting traces (Fig. 4G) show tilt steps of 1.3 – 4 µrad oriented in a northwest direction associated with each of the five events. The tilt step directions coincide with the direction of the displacement steps (Fig. 4H) and support a repeating source process generating the events, with roughly consistent amplitudes and locations.

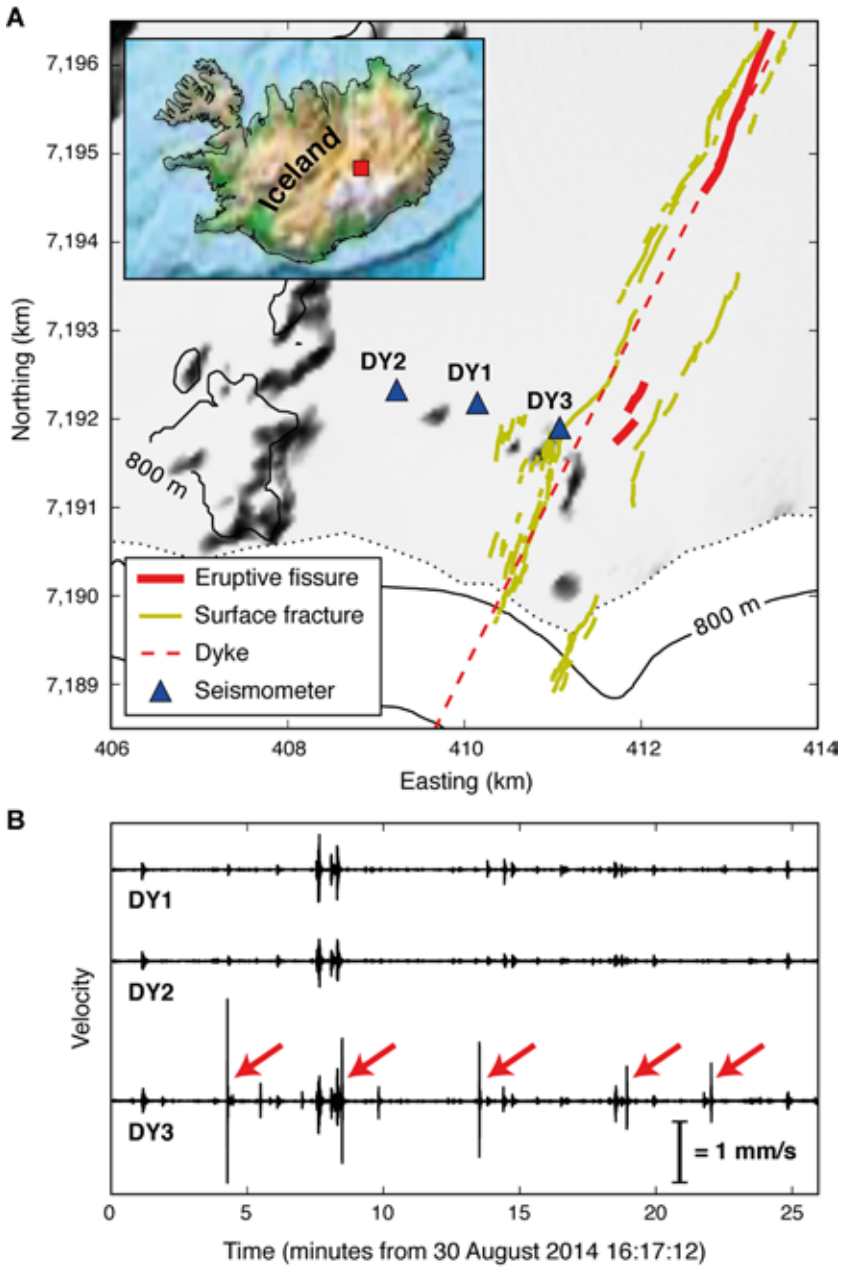

Figure 3. Overview of the seismic experiment and recorded data. **A**, Map of stations DY1, DY2 and DY3 (Guralp 6TD seismometers) installed north of the Vatnajökull glacier (white) on 30 August 2014 immediately adjacent to several large surface fractures; fractures (yellow) and eruptive fissures (red) mapped by Hjartardóttir et al. (2016); dyke location (red dashed) inferred by Sigmundsson et al. (2015); elevation data from National Land Survey of Iceland. Inset map shows the location within Iceland (plotted with Matplotlib Basemap Toolkit (Whitaker, 2014) using the ETOPO1 model (Amante and Eakins, 2009)). **B**, Unfiltered vertical recordings on all three stations. Arrows mark the step events on DY3 investigated in this study. These events are not visible on stations DY1 and DY2. (Figure modified after Thun et al., 2016).

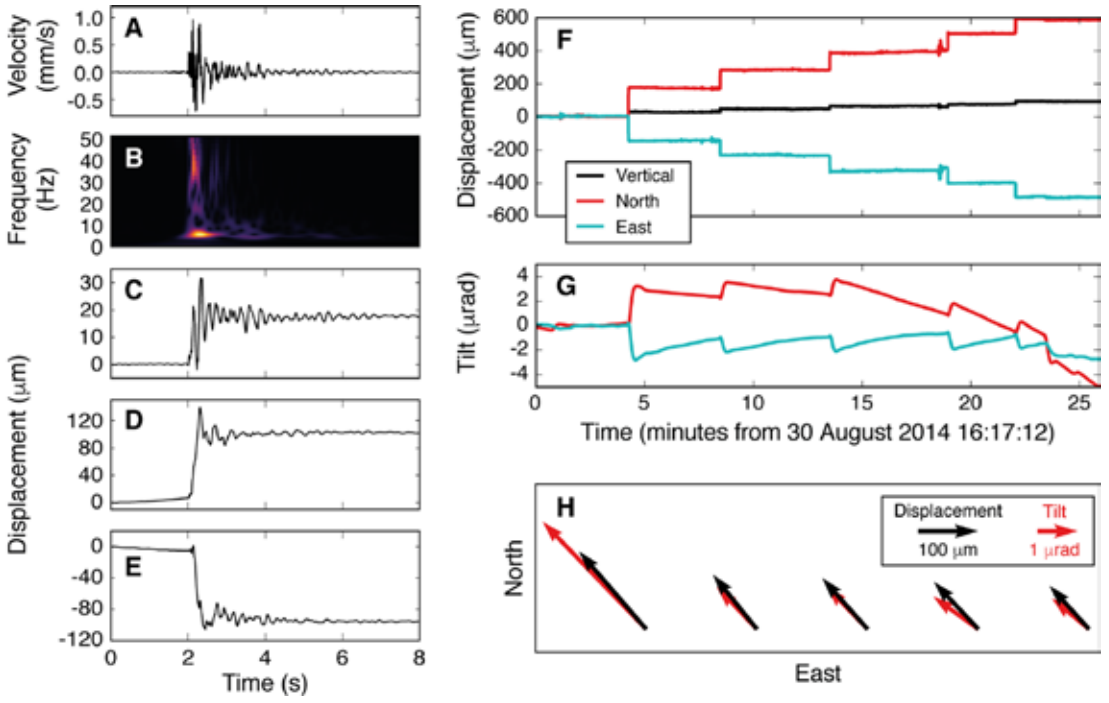

Figure 4. Individual step event (**A**-**E**) and processed full-length seismograms showing ground deformation (**F**-**H**) at station DY3. **A**, Vertical velocity waveform (instrument corrected). **B**, Scalogram illustrating relative frequency content – the main frequency peak lies between 3 Hz and 8 Hz, with an additional peak above 25 Hz. **C**-**E**, Vertical, North and East displacements, respectively; processed with the median filter method (Thun et al., 2015). The resulting displacement step is about 17 µm upward and 123 µm in a northwest direction. **F**, Median filter processed seismogram for step recovery (black: Vertical, red: North, cyan: East), showing a consistency of step direction for the individual events. Note that between events 3 and 4, a longer period event impedes the filter performance, leading to a slight artificial step. **G**, Tilt record retrieved from seismograms using the tilt transfer function (Aoyama and Oshima, 2008). While the long-period trend is not interpreted here, each of the 5 events shows a clear tilt step on both horizontal components. **H**, Directions and amplitudes of horizontal deformations of the 5 steps seen in **F** and **G**. (Figure modified after Thun et al., 2016).

1. 4.2 - Source location

Although one station is not sufficient to fully invert for source locations and mechanisms, we use the observed static deformations from DY3 to explore potential sources with a forward modelling approach. We estimate the source location and magnitude by (i) assuming a plausible source mechanism and (ii) performing a search over a 200 x 200 x 100 m^3 grid around the station (as discussed above, the source has to be a lot closer to DY3 than to DY1 at a distance of 1 km, thus we assume a distance of less than 100 m), where we match the observed ratios between different deformation components with the theoretical values for a homogeneous, elastic medium (Okada, 1992). The ratios are defined as

$$r_1 = \frac{u_Z}{u_N}, \quad r_2 = \frac{u_Z}{u_E}, \quad r_3 = \frac{u_Z}{t_N}, \quad r_4 = \frac{u_Z}{t_E} \tag{4}$$

where u_Z, u_N and u_E are displacements and t_N and t_E are tilts. Subscripts Z, N and E denote a vertical, north and east direction, respectively. These ratios are used to compute two misfits, R_d (displacements only) and R_{dt} (both displacements and tilt), defined as:

$$R_d = \left(\frac{r_{1,calc} - r_{1,obs}}{r_{1,obs}}\right)^2 + \left(\frac{r_{2,calc} - r_{2,obs}}{r_{2,obs}}\right)^2,$$
$$R_{dt} = R_d + \left(\frac{r_{3,calc} - r_{3,obs}}{r_{3,obs}}\right)^2 + \left(\frac{r_{4,calc} - r_{4,obs}}{r_{4,obs}}\right)^2. \quad (5)$$

The minimum misfits indicate the best location for the chosen source mechanism and the corresponding seismic moment M_0 can be found by a simple least squares inversion.

As the station is located in direct proximity to the faults associated with the graben formation, we suspect that the local events are part of the faulting process. Consequently, we assume a 75° dip-slip mechanism parallel to the N25°E striking boundary fault (see Hjartardóttir et al., 2016) as the source mechanism. Figure 5 shows the misfits for this normal fault mechanism, where the observed tilt and displacement values of the third step (Fig. 4F,G) are used. Here we assume a medium P-wave velocity of V_P = 500 m/s and Poisson's ratio of n = 0.3, consistent with values obtained for unconsolidated upper geological layers at various volcanoes (Ferrazzini et al., 1991; DeLuca et al., 1997; Metaxian et al., 1997; Chouet et al., 1998; Cauchie and Saccorotti, 2013) (further discussion in supplementary information). For clarity, only misfit values below 0.5 are displayed and all remaining misfits are located in the quadrant south-east of the source. As the displacement-only misfit R_d (Fig. 5A) does not converge around a single minimum, it can only indicate the approximate direction of the source with respect to DY3. When tilts are introduced (Fig. 5B), a sharp minimum misfit R_{dt} is found approximately 40 m southeast of DY3 at a depth of 8 m. The best-fitting source moment at this location is M_0 = 1.5 x 10^8 Nm (moment magnitude M_W = 0.6). When we change V_P to 1000 m/s, the source location remains unchanged, with the source moment increasing to M_0 = 7.1 x 10^8 Nm (M_W = 0.2). The same grid search with different medium parameters leads to similar source-receiver distances and source moments (Table 1). The source moments are small enough to justify the use of the point-source assumption in our forward modelling approach.

Static displacements such as those observed at DY3 are near- and intermediate-field effects and can only be observed within a fraction of a wavelength from the seismic source (Lokmer and Bean, 2010). The sources inferred above would theoretically cause total static displacements smaller than 1 µm at the next closest station, DY1. Sub-micrometre steps are not detectable with our instruments and methods (Thun et al., 2015). The fact that the events are not visible at the other stations also implies that the dynamic seismic signals, i.e. all near-, intermediate- and far-field components, fall under the noise level at these locations, likely due to strong wave attenuation in the unconsolidated surface materials (Sigurgeirsson et al., 2015).

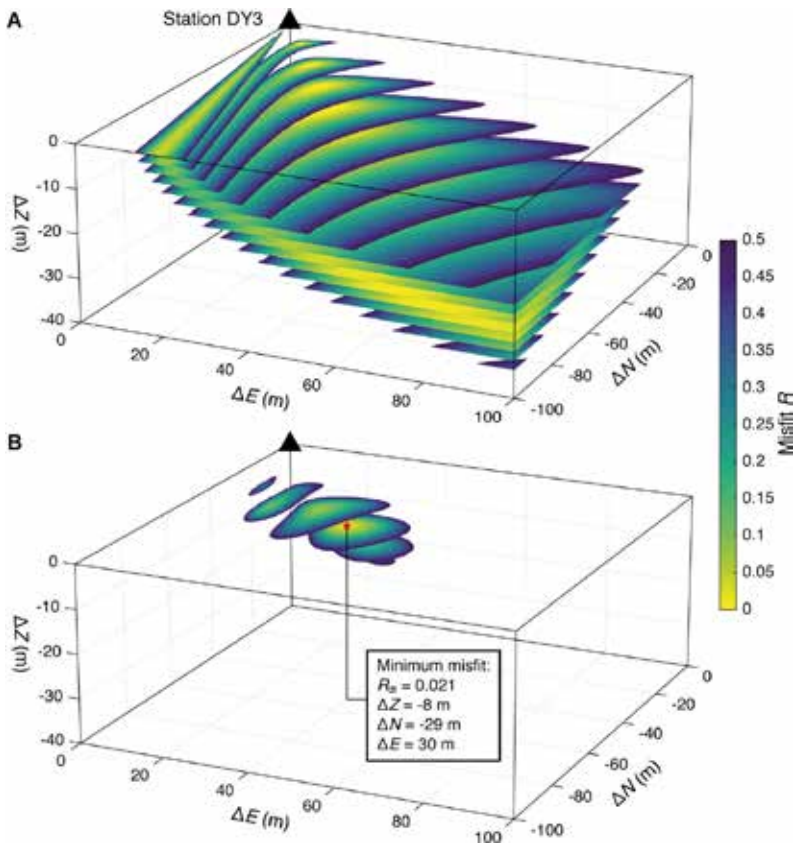

Figure 5. Misfits between field observations and displacements and tilts calculated using analytical solutions (Okada, 1992) for a 75° dip-slip (normal fault) source. **A**, Misfit R_d using only displacement ratios. **B**, Misfit R_{dt} using both displacement and tilt ratios, showing a single confined minimum at DZ = 8m, DN = 29 m, DE = 30 m. Misfits are displayed in horizontal slices of 2m spacing and values above R = 0.5 are not shown. Material parameters for both **A** and **B**: V_P = 500 m/s and n = 0.3. (Figure modified after Thun et al., 2016).

1. 4.3 - Source dimensions

For the source location found above, we determine source parameters (size and slip) by removing path effects through deconvolving modelled deformation and seismic radiation (Green's function) from the recorded seismogram shown in Figure 4C. Here we use the linear relationship between the ground displacement spectrum $U(\omega)$ and the source moment spectrum $M(\omega)$ (Lokmer and Bean, 2010):

$$U(\omega) = M(\omega) \cdot G(\omega, \boldsymbol{r}, V_P, \nu, \rho, RP, Q) \qquad (6)$$

where the Green's functions G depend on the receiver position r relative to the source, the elastic properties of the medium V_P and n, the density r, the radiation pattern RP for a specific source mechanism and the quality factor Q. This simplifies the deconvolution to a simple division $M = U / G$

for each frequency. The resulting source moment spectrum $M(w)$ is subsequently fit with a w^2 source model (Brune, 1970) in order to determine the corner frequency. We calculate $G(w)$ for the inferred normal fault source with the expressions given by Aki and Richards (2002) and modified by Lokmer and Bean (2010), using the same parameters as above (V_P = 500m/s, n = 0.3). Q is varied until we obtain the best fit to the w^2-model (Q = 20). The source-time history $M(t)$ resulting from this deconvolution is shown in Figure 6A. Its spectrum and the w^2-model fit are shown in Figure 6B, resulting in a corner frequency of 4.5 Hz.

Mechanism	n	V_P (m/s)	ΔZ (m)	ΔN (m)	ΔE(m)	M_0 (Nm)	R_{dt}
Dip-slip	0.25	500	-8	-31	26	$1.8 \cdot 10^8$	0.018
q = 25°		1000	″	″	″	$8.3 \cdot 10^8$	″
d = 75°	0.3	500	-8	-30	29	$1.5 \cdot 10^8$	0.021
		1000	″	″	″	$7.1 \cdot 10^8$	″
	0.35	500	-7	-28	28	$1.1 \cdot 10^8$	0.023
		1000	″	″	″	$5.2 \cdot 10^8$	″
Tensile	0.25	500	-7	-33	16	$8.9 \cdot 10^7$	0.006
q = 25°		1000	″	″	″	$4.2 \cdot 10^8$	″
d = 90°	0.3	500	-8	-27	24	$5.2 \cdot 10^7$	0.03
		1000	″	″	″	$2.5 \cdot 10^8$	″
	0.35	500	-7	-25	24	$3.6 \cdot 10^7$	0.036
		1000	″	″	″	$1.7 \cdot 10^8$	″

Table 1. Minimum misfit solutions from the Okada grid search for different source mechanisms and medium parameters. q indicates the strike angle (from north) and d the dip angle (from horizontal) of the crack/fault plane for the dip-slip and tensile crack mechanisms. The locations ΔZ, ΔN *and* ΔE are relative to station DY3.

This frequency is used to determine the source size (and subsequently the slip D using $M_0 = \mu AD$, with the shear modulus μ and the source area A): approximating the source as a slipping circular patch (Sato and Hirasawa, 1973; Madariaga, 1976) gives a source radius of approximately 10 m to 20 m with an average slip of 1 mm to 4 mm. As the actual source mechanism cannot be inferred from our data and a tensile component could potentially form part of the source process, we additionally performed the location grid search and source slip analysis for a tensile crack (Table 1). If a purely tensile source mechanism is considered, the slip displacement on the same patch is reduced by a factor of 2, showing the results are robust for a deviation from the pure normal faulting source.

Both results are in agreement with Liu-Zeng et al. (2005), who model the slip-to-length ratio and obtain equivalent values for small faults with rough fault surfaces.

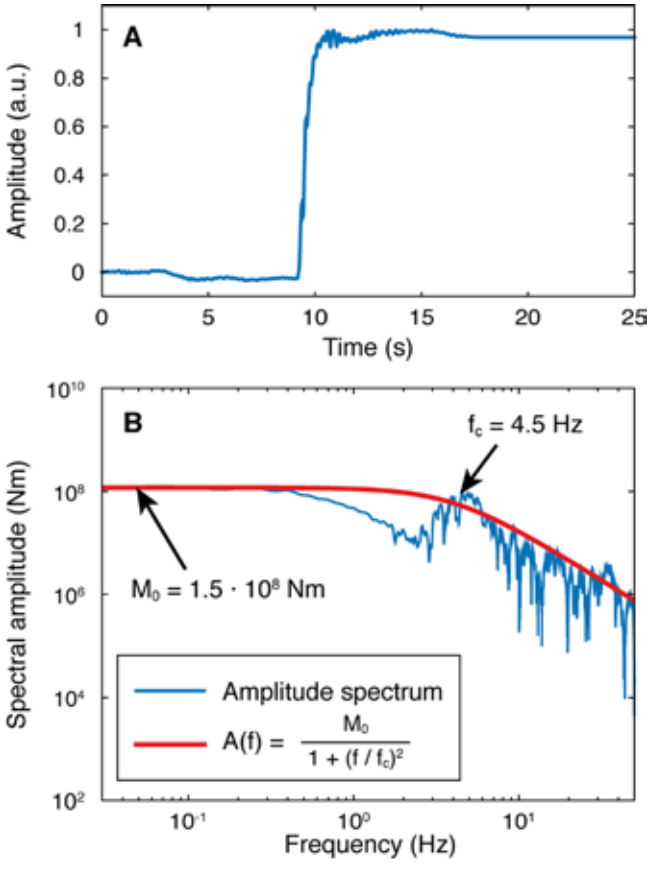

Figure 6. Source time-function and its amplitude spectrum. **A**, Normalised source-time history (slip on the fault). **B**, Moment-rate spectrum fit with a w^2-source model (Brune, 1970). The flat part of the spectrum (left arrow) corresponds to the seismic moment M_0, while the corner frequency f_c (right arrow) is related to the source size. The results shown are calculated for V_P = 500 m/s and n = 0.3 and the source location from Figure 5b. Note that varying n between 0.25 and 0.35 does not affect the corner frequency to a large extent (f_c = 4.2 – 5.6 Hz). (Figure modified after Thun et al., 2016).

We estimate stress drops of Dσ = 0.008 – 0.07 MPa using Dσ = 7 M_0 / 16 r^3 according to Eshelby (1957). These values are 2 – 3 orders of magnitude smaller than expected for tectonic seismicity (stress drops typically > 1 MPa; Kanamori and Anderson (1975)) and point to a very weak uppermost crust. They are consistent with the lack of shallow "standard" earthquakes associated with such a large rifting event. Such small stress drops are in striking agreement with the value of Dσ = 0.01 MPa obtained for shallow long period seismicity on Mt Etna, Italy (Bean et al., 2014), attributed to the presence of exceptionally weak near surface volcanic material that could not sustain high shear or tensile stresses and hence also failed at exceptionally low earthquakes magnitudes.

1. 4.4 - Discussion

Our data reveal new information about the rifting process, suggesting that it is at least partially discrete, occurring in micrometre scale steps. This raises questions about how these displacements compare to the observed long-term deformation in the area. Combining the time-history of the closest GPS stations with the total graben opening measured from satellite data (see supplementary information), the deformation rate for 30 August 2014 is estimated to be roughly 5 cm/day. Assuming a repeating process with average displacement steps of 133 μm and average inter-event times of 267 s, observed at DY3, we extrapolate our data and obtain an approximate deformation rate of 4.3 cm/day. Furthermore, accumulating normal fault slip estimates at the source of 1mm to 4mm yields a horizontal deformation rate of 7 – 27 cm/day. Although the modelled slip values are approximate, both of our displacement measures are in good agreement with the GPS estimates. The similarity suggests that the satellite and GPS-derived long-term surface deformation associated with Earth surface rifting is a consequence of displacement accumulated through very low magnitude discrete brittle failure at the millimetre scale. The detection of such steps is limited to distances within a few hundred metres from the source, highlighting the rarity of such observations. The similarity also suggests that any aseismic component is small at the spatial and temporal scales captured in this study; it also indicates that fracturing of the weak uppermost crust is limited to microseismic events, consistent with the lack of observed shallow seismicity (Sigmundsson et al., 2015; Ágústsdóttir et al., 2016).

We conclude that at its smallest temporal and spatial scales, rifting in the uppermost Earth's crust is not a steady state process but rather exhibits transient staccato-like behaviour that yields definable spreading rates only when viewed over longer time scales. Stress drop analysis on the discrete micro-events reveals that the uppermost crust is exceptionally weak in the rift zone

1. 5 - Conclusions

Our work shows that the analysis of seismic events can significantly benefit from data recorded in the near- and intermediate-field of their sources. The information contained in the waveforms at short source-receiver distances may in some cases completely change our interpretation of the source process. Furthermore, a careful analysis of broadband seismometer data can help bridge the current gap between seismology and deformation studies, as common methods of displacement detection, such as GPS or InSAR do not offer the resolution needed to resolve steps of such small magnitude (order of 1-10 μm in our experiments) and short time history. The results from our laboratory experiments show that the detection of static displacements with seismometers is possible - moving median filters can reduce long-period noise on broadband data whilst retaining displacement steps. The performance of this method is limited by the size of the step signal in relation to the long-period noise, but is applied successfully to signals comparable to real-world examples.

Applying our method to data recorded on the summit of Turrialba volcano, Costa Rica, we recovered steps associated with LP events; stacks of many events show that this is coherent across many similar events. This shows that even in relatively noisy volcanic environments we can access subtle

information, which might fundamentally change our interpretation of underlying source processes. A second application to the seismic events recorded in the immediate vicinity of the graben faults associated with the 2014 Bárðarbunga dyke in Iceland reveals their step-like nature and suggests that these signals are part of the shallow deformation process. We used these steps, together with the tilt steps also observed on the seismograms, to locate the source in a forward modelling approach and found small ($M_W < 0$), local sources approximately 30–40 m south-east of the station. The analysis shows that the uppermost crust in the rift zone is exceptionally weak, with stress drops 2 – 3 order of magnitude smaller than expected for tectonic seismicity.

Both field applications highlight how close instruments have to be to the seismic sources in order to detect possible static displacement (and in the case of Bárðarbunga, tilt) steps. As these signals can vastly improve our understanding of source processes, this fact should be taken into consideration when designing future seismic experiments on volcanoes.

Acknowledgements

The research presented in this study has received funding from the European Union's Seventh Programme under Grant No. 289976 (Project NEMOH) and Grant No. 308377 (Project FUTUREVOLC). The field work in Iceland received support from the Geological Survey of Ireland (GSI). Although this paper was compiled by J.T., I.L. and C.J.B., the work on the Bárðarbunga dyke received contributions by E.P.S. Eibl, B.H. Bergsson and A. Braiden, the co-authors of the cited manuscript to be submitted. We would like to thank F. Martini, M. Mora, J. Pacheco (field experiment on Turrialba), T. Ferreira, A. Garcia, F. Heffernan and M. Möllhoff (laboratory experiments) for their support and K. Vogfjörd for input on the Bárðarbunga experiment. We thank B. G. Ofeigsson, who helped estimate the deformation rate from the GPS data. Thanks to F. Sigmundsson for the helpful review. Data processing was aided by ObsPy toolbox (Beyreuther et al., 2010).

References

Ágústsdóttir, T. et al. (2016). Strike-slip faulting during the 2014 Bardarbunga-Holuhraun dike intrusion, central Iceland, Geophysical Research Letters 43: 1495–1503, doi: 10.1002/2014GL060519

Aki, K. and Richards, P. G. (2002). Quantitative Seismology, University Science Books.

Amante, C. and Eakins, B.W. (2009). ETOPO1 1 Arc-Minute Global Relief Model: Procedures, Data Sources and Analysis. (report). National Geophysical Data Center, NOAA.

Aoyama, H. and Oshima, H. (2008). Tilt change recorded by broadband seismometer prior to small phreatic explosion of Meakan-dake volcano, Hokkaido, Japan. Geophysical Research Letters 35: L06307, doi: 10.1029/2007GL032988.

Bean, C. J. et al. (2014). Long-period seismicity in the shallow volcanic edifice formed from slow-rupture earthquakes. Nature Geoscience 7(1): 71–75, doi: 10.1038/ngeo2027.

Brune, J. N. (1970). Tectonic stress and the spectra of seismic shear waves from earthquakes. Journal of Geophysical Research 75(26): 4997, doi: 10.1029/JB075i026p04997.

Bürgmann, R., Rosen, P. A. and Fielding, E. J. (2000). Synthetic Aperture Radar Interferometry to Measure Earth's Surface Topography and Its Deformation. Annu Rev Earth Planet Sci 28: 169–209.

Cauchie, L. and Saccorotti, G. (2013). Probabilistic inversion of Rayleigh-wave dispersion data: An application to Mt. Etna, Italy. Journal of Seismology 17(2): 335–346, doi: 10.1007/s10950-012-9323-6.

Chanerley, A. A. et al. (2013). Concerning Baseline Errors in the Form of Acceleration Transients When Recovering Displacements from Strong Motion Records Using the Undecimated Wavelet Transform. Bulletin of the Seismological Society of America 103(1): 283–295, doi: 10.1785/0120110352.

Chouet, B. (1986). Dynamics of a fluid-driven crack in three dimensions by the finite difference method. Journal of Geophysical Research 91: 13967, doi: 10.1029/JB091iB14p13967.

Chouet, B. (2003). Volcano Seismology. Pure and Applied Geophysics 160(3): 739–788, doi: 10.1007/PL00012556.

Chouet, B. et al. (1998). Shallow velocity structure of Stromboli Volcano, Italy, derived from small-aperture array measurements of Strombolian tremor. Bulletin of the Seismological Society of America 88(3): 653–666.

Cusano, P., Petrosino, S. and Saccorotti, G. (2008). Hydrothermal origin for sustained Long-Period (LP) activity at Campi Flegrei Volcanic Complex, Italy. Journal of Volcanology and Geothermal Research 177(4): 1035–1044, doi: 10.1016/j.jvolgeores.2008.07.019.

De Barros, L. et al. (2011). Source mechanism of long-period events recorded by a high-density seismic network during the 2008 eruption on Mount Etna. Journal of Geophysical Research 116(B1): B01304, doi: 10.1029/2010JB007629.

DeLuca, G. et al. (1997). Shallow structure of Mt Vesuvius volcano, Italy, from seismic array analysis. Geophysical Research Letters 24(4): 481–484, doi: 10.1029/97GL00169.

Eshelby, J. D. (1957). The Determination of the Elastic Field of an Ellipsoidal Inclusion, and Related Problems. Proceedings of the Royal Society of London A: Mathematical, Physical and Engineering Sciences 241(1226): 376–396.

Eyre, T. S. et al. (2013). Moment tensor inversion for the source location and mechanism of long period (LP) seismic events from 2009 at Turrialba volcano, Costa Rica. Journal of Volcanology and Geothermal Research 258: 215–223, doi: 10.1016/j.jvolgeores.2013.04.016.

Eyre, T. S. et al. (2015). A brittle failure model for long-period seismic events recorded at Turrialba Volcano, Costa Rica. Journal of Geophysical Research B: Solid Earth 120(3): 1452–1472, doi: 10.1002/2014JB011108.

Ferrazzini, V. and Aki, K. (1987). Slow waves trapped in a fluid-filled infinite crack: Implication for volcanic tremor. Journal of Geophysical Research 92(2): 9215, doi: 10.1029/JB092iB09p09215.

Ferrazzini, V., Aki, K. and Chouet, B. (1991). Characteristics of seismic waves composing Hawaiian volcanic tremor and gas-piston events observed by a near-source array. Journal of Geophysical Research 96(B4): 6199–6209, doi: 10.1029/90JB02781.

Fournier, N., Jolly, A. D. and Miller, C. (2011). Ghost tilt signal during transient ground surface deformation events: Insights from the September 3, 2010 Mw7.1 Darfield earthquake, New Zealand. Geophysical Research Letters 38(16): 1–5, doi: 10.1029/2011GL048136.

Geirsson, H. et al. (2012). Volcano deformation at active plate boundaries: Deep magma accumulation at Hekla volcano and plate boundary deformation in south Iceland. Journal of Geophysical Research B: Solid Earth 117(11): 1–18, doi: 10.1029/2012JB009400.

Genco, R. and Ripepe, M. (2010). Inflation-deflation cycles revealed by tilt and seismic records at Stromboli volcano. Geophysical Research Letters, 37(12): 1–5, doi: 10.1029/2010GL042925.

Graizer, V. M. (2005). Effect of tilt on strong motion data processing. Soil Dynamics and Earthquake Engineering 25(3): 197–204, doi: 10.1016/j.soildyn.2004.10.008.

Gudmundsson, A. et al. (2014). Dike emplacement at Bardarbunga, Iceland, induces unusual stress changes, caldera deformation, and earthquakes. Bulletin of Volcanology 76(10): 1–7, doi: 10.1007/s00445-014-0869-8.

Gudmundsson, M. T. et al. (2016). Gradual caldera collapse at Bárdarbunga volcano, Iceland, regulated by lateral magma outflow. Science 353(6296), doi: 10.1126/science.aaf8988.sciencemag.org.

Hjartardóttir, Á. R. et al. (2016). Fracture movements and graben subsidence during the 2014 Bárðarbunga dike intrusion in Iceland. Journal of Volcanology and Geothermal Research 310: 242–252, doi: 10.1016/j.jvolgeores.2015.12.002.

Kanamori, H. and Anderson, D. L. (1975). Theoretical basis of some empirical relations in seismology. Bulletin of the Seismological Society of America 65(5): 1073–1095.

Kinoshita, S. (2008). Tilt Measurement Using Broadband Velocity Seismograms. Bulletin of the Seismological Society of America 98(4): 1887–1897, doi: 10.1785/0120070230.

Kumagai, H. (2002). Waveform inversion of oscillatory signatures in long-period events beneath volcanoes. Journal of Geophysical Research 107: 1–13, doi: 10.1029/2001JB001704.

Kumagai, H., Chouet, B. A. and Dawson, P. B. (2005). Source process of a long-period event at Kilauea volcano, Hawaii. Geophysical Journal International 161(1): 243–254, doi: 10.1111/j.1365-246X.2005.02502.x.

Legrand, D., Kaneshima, S. and Kawakatsu, H. (2000). Moment tensor analysis of near-field broadband waveforms observed at Aso volcano, Japan. Journal of Volcanology and Geothermal Research 101: 155–169, doi: 10.1016/S0377-0273(00)00167-0.

Liu-Zeng, J., Heaton, T. and DiCaprio, C. (2005). The effect of slip variability on earthquake slip-length scaling. Geophysical Journal International 162(3): 841–849, doi: 10.1111/j.1365-246X.2005.02679.x.

Lokmer, I., Bean, C. J. (2010). Properties of the near-field term and its effect on polarisation analysis and source locations of long-period (LP) and very-long-period (VLP) seismic events at volcanoes. Journal of Volcanology and Geothermal Research 192(1–2): 35–47, doi: 10.1016/j.jvolgeores.2010.02.008.

Lokmer, I. et al. (2007). Moment-tensor inversion of LP events recorded on Etna in 2004 using constraints obtained from wave simulation tests. Geophysical Research Letters 34(22): L22316, doi: 10.1029/2007GL031902.

Lokmer, I. et al. (2008). Temporal evolution of long-period seismicity at Etna Volcano, Italy, and its relationships with the 2004-2005 eruption. Earth and Planetary Science Letters 266(1–2): 205–220, doi: 10.1016/j.epsl.2007.11.017.

Lyons, J. J. and Waite, G. P. (2011). Dynamics of explosive volcanism at Fuego volcano imaged with very long period seismicity. Journal of Geophysical Research 116(B9): B09303, doi: 10.1029/2011JB008521

Madariaga, R. (1976). Dynamics of an expanding circular fault. Bulletin of the Seismological Society of America 66(3): 639–666.

McNutt, S. R. (2005). Volcanic Seismology. Annual Review of Earth and Planetary Sciences 33(1): 461–491, doi: 10.1146/annurev.earth.33.092203.122459.

Métaxian, J. P., Lesage, P. and Dorel, J. (1997). Permanent Tremor Of Masaya Volcano, Nicaragua - Wave Field Analysis and Source Location. Journal of Geophysical Research-Solid Earth 102(97): 22529–22545, doi: 10.1029/97JB01141.

Nakano, M., Kumagai, H. and Chouet, B. A. (2003). Source mechanism of long-period events at Kusatsu-Shirane Volcano, Japan, inferred from waveform inversion of the effective excitation functions. Journal of Volcanology and Geothermal Research 122: 149–164, doi: 10.1016/S0377-0273(02)00499-7.

Neuberg, J. et al. (2000). Models of tremor and low-frequency earthquake swarms on Montserrat. Journal of Volcanology and Geothermal Research 101: 83–104, doi: 10.1016/S0377-0273(00)00169-4.

Ofeigsson, B. G. et al. (2011). Deep magma storage at Hekla volcano, Iceland, revealed by InSAR time series analysis. Journal of Geophysical Research: Solid Earth 116(5): 1–15, doi: 10.1029/2010JB007576.

Okada, Y. (1992). Internal deformation due to shear and tensile faults in a half space. Bulletin of the Seismological Society of America 82(2): 1018–1040.

Pillet, R. and Virieux, J. (2007). The effects of seismic rotations on inertial sensors. Geophysical Journal International 171(3): 1314–1323, doi: 10.1111/j.1365-246X.2007.03617.x.

Rodgers, P. W. (1968). The Response of the Horizontal Pendulum Seismometer to Rayleigh and Love Waves, Tilts and Free Oszillations of the Earth. Bulletin of the Seismological Society of America 58(5).

Rossi, C. et al. (2016). Temporal monitoring of subglacial volcanoes with TanDEM-X - Application to the 2014-2015 eruption within the Bárdarbunga volcanic system, Iceland. Remote Sensing of Environment 181: 186–197, doi: 10.1016/j.rse.2016.04.003.

Ruch, J. et al. (2016). Oblique rift opening revealed by reoccurring magma injection in central Iceland. Nature Communications 7: 12352, doi: 10.1038/ncomms12352.

Sato, T. and Hirasawa, T. (1973). Body wave spectra from propagating shear cracks. Journal of Physics of the Earth 21: 415–431, doi: 10.4294/jpe1952.21.415.

Schreiber, K. U. et al. (2006). Ring laser gyroscopes as rotation sensors for seismic wave studies. In Earthquake Source Asymmetry, Structural Media and Rotation Effects, Springer.

Sigmundsson, F. et al. (2014). Segmented lateral dyke growth in a rifting event at Bárðarbunga volcanic system, Iceland. Nature 517(7533): 15, doi: 10.1038/nature14111.

Sigurgeirsson, M. Á. et al. (2015). Geological Map of the Northern Volcanic Zone, Iceland. Southern Part. 1:100 000. Iceland GeoSurvey, Reykjavík.

Sturkell, E. et al. (2013). New insights into volcanic activity from strain and other deformation data for the Hekla 2000 eruption. Journal of Volcanology and Geothermal Research 256: 78–86, doi: 10.1016/j.jvolgeores.2013.02.001.

Thordarson, T. and Self, S. (1993). The Laki (Skaftár Fires) and Grímsvötn eruptions in 1783-1785. Bulletin of Volcanology 55(4): 233–263, doi: 10.1007/BF00624353.

Thun, J., Lokmer, I. and Bean, C. J. (2015). New observations of displacement steps associated with volcano seismic long-period events, constrained by step table experiments. Geophysical Research Letters 42(10): 3855–3862, doi: 10.1002/2015GL063924.

Thun, J. et al. (2016). Micrometre-scale deformation observations reveal fundamental controls on geological rifting. Scientific Reports 6: 36676, doi: 10.1038/srep36676.

Whitaker, J. (2014). Matplotlib Basemap Toolkit documentation. URL: http://matplotlib.org/basemap/.

Wielandt, E. and Forbriger, T. (1999). Near-field seismic displacement and tilt associated with the explosive activity of Stromboli. Annals of Geophysics 42(3): 407–416, doi: 10.4401/ag-3723.

Johannes Thun, Germany
johannes.thun@ucdconnect.ie

Affiliation under NEMOH
University College Dublin, Dublin, Ireland

Research theme under NEMOH
Constraining volcano seismic source properties using near-field observations

I graduated from Karlsruhe Institute of Technology, Germany with a *Diplom* degree in Geophysics in 2011, focusing mostly on seismology and related fields throughout my studies. During these years, I also gained my first research experience as a research assistant in engineering and seismology. While I had always been fascinated by volcanoes, my professional interest in volcanology was sparked during 5 months of voluntary work at CIIV in Colima, Mexico.

My research at UCD and DIAS (Dublin Institute for Advanced Studies), started as part of the NEMOH project, focuses on the analysis of volcano seismic events making use of near-field stations. At very short source-receiver distances (e.g. < 1-2 km), we have the opportunity to access subtle information that is too strongly attenuated to be recorded at a distance. I carried out laboratory experiments with seismometers in order to constrain how certain signals are recorded and how they can be recovered from seismograms. Some of my work can be seen as a bridge between seismology and deformation studies.

During my PhD, I was able to extend my knowledge in computing tools and programming languages such as Python and the ObsPy toolbox, Seismic Analysis Code (SAC), MATLAB and Fortran. Benefiting from the expertise in the volcano seismology group at UCD, I learned a lot about time series analysis, data processing in seismology, moment tensor inversions and working with large datasets. During my secondment at the NEMOH partner BRGM I learned how to prepare and run simulations of seismic wave propagation.

Through my NEMOH affiliation I had access to a large network of both young and well-established researchers in many areas of expertise. I received a lot of interdisciplinary training and learned how to discuss and solve problems together with people outside my fields of seismology and geophysics. Through training and activities in NEMOH and UCD and in attending many international congresses and workshops, I improved my communication skills, including conference presentations and posters, lectures and outreach activities addressing lay audiences.

In conclusion, my time in NEMOH, UCD and DIAS has provided me with a large set of skills, many of which will be beneficial for my future career. Last but not least, I've been able to spend part of my PhD time with a great bunch of people, the *NEMOH family*. We've had to master problems together and have helped each other in difficult times, such as the occasional PhD crisis. And most importantly, we had loads of fun while we were growing together as scientists and friends.

Chapter 2

Quantifying uncertainties in location and source mechanism for Long-Period events at Mt Etna, Italy.

Léna Cauchie

Istituto Nazionale di Geofisica e Vulcanologia, Sezione di Pisa, Pisa, Italy

Tutorship: Gilberto Saccorotti

Istituto Nazionale di Geofisica e Vulcanologia, Sezione di Pisa, Pisa, Italy

This work (manuscript and figures) has been partially extracted from my PhD thesis at University College of Dublin under the supervision of C. Bean.

Abstract

The manifestation of Long-Period (LP) events is documented at many volcanoes worldwide. However, the mechanism at their origin is still object of discussion. Models proposed so far involve (i) the resonance of fluid-filled cracks or conduits that are triggered by fluid instabilities or the brittle failure of high viscous magmas and (ii) the slow- rupture earthquakes in the shallow portion of volcanic edifices. Since LP activity usually precedes and accompanies volcanic eruption, the understanding of these sources is important in terms of hazard assessment and eruption early warning.

This work thus mainly aimed at the assessment of the uncertainties in the determination of LP source properties as a consequence of poor knowledge of the velocity structure and location errors.

We used data from temporary networks deployed on Mt Etna in 2005. During August 2005, about 13000 LP events were detected through a STA/LTA approach, and were classified into two families on the basis of waveform similarity. We located the most energetic source using three different approaches: (1) a single-station-location method based on the back-propagation of the polarization vector estimated from covariance analysis of three-component signals; (2) multi-channel analysis of data recorded by two seismic arrays; (3) relative locations based on inversion of differential times obtained through cross-correlation of similar waveforms.

We then defined a volume of possible source location and performed a full-waveform, moment tensor (MT) inversion for the entire catalog of events. In this manner, we obtained a MT solution for each grid node of the investigated volume. The MT solutions are parameterised through the ratio of the MT eigenvalues. The spatial changes of these ratios allow gaining a complete picture of the uncertainties in the source mechanism/geometry associated with the location errors. We observed the λ_i / λ_1 (i=2,3) ratios varying between (0.1-0.9) and (0.6-0,9), respectively. By the same token, the volumetric components of the retrieved mechanism were observed, varied by almost one order of magnitude throughout the investigated volume.

Keywords: Volcano seismicity, Long Period events, Location, Moment tensor Inversion, Source properties

2. 1 **- Introduction**

Long Period (LP) seismic activity is observed at many volcanoes worldwide preceding or accompanying volcanic eruptions; the quantitative analysis of these sources is therefore crucial in terms of hazard evaluation and eruption early warning. It is generally thought that LP signals are associated with the resonance of fluid-filled conduits and cracks in the shallowest portion of volcanic edifices (Chouet (1985), Chouet (1986)). However, any quantitative and unique model that can describe the physical mechanism triggering the resonance is still missing. Studies proposed so far include (i) the dynamics of either hydrothermal or magmatic fluids subjected to transient pressure changes (e.g.,Nakano et al., (2003), Arciniega-Ceballos et al., (2003), Chouet (1992, 1996), Kumagai et al., (2005)) and (ii) the brittle failure of highly viscous magmas (Tuffen et al., (2003), Neuberg et al., (2006)). Recently Bean et al. (2014) do not relate LP events to fluid-driven mechanisms, but interpret them in terms of low-stress-drop fracturing; under this perspective, the LP seismicity would form part of the spectrum between slow-slip earthquakes and fast dynamic rupture, thus representing a marker of deformation in the volcanic edifice.

The complexity of determining a general model for the LP source mechanism is mainly due to the severe difficulties in analysing such signals. Their emergent onsets and lack of clear P- and S-wave arrivals hinder the use of traditional location methods adopted in earthquake seismology. Moreover, the interior of volcanoes is characterised by strong heterogeneities, which heavily condition ray path trajectories. The lack of accurate definitions of the velocity structures that describe such variations at the scale of the investigated seismic wavelength leads to severe difficulties in source location, especially depth.

The quantitative estimate of LP source mechanisms can be retrieved via full-waveform moment tensor (MT) inversion. This procedure, which is generally conducted under the point-source approximation (e.g. Kanamori et al., (1993), Ohminato et al., (1998), Chouet et al., (2003), Nakano et al., (2003), Lokmer et al., (2007), Lokmer et al., (2008), Davi et al., (2010)), relies on the estimation of the best source location obtained independently prior to the MT inversion. The reliability of MT estimates, therefore, depends critically on both the accuracy of source location and the velocity model adopted for predicting the Green's Functions.

Considering these arguments, we therefore analyse different classes of volcanic signals (namely: tremor, long- period and very-long-period activity) recorded at Mt Etna in order to obtain constrained images of their respective sources. We use distinct procedures for locating the different classes of signals. For LP signals, we then calculate MT inversions for the set of most likely source locations, in order to retrieve the errors in source mechanism estimate related to uncertainties in source location. The variations of the MT solutions are described in terms of eigenvalues ratios, which provide an overview of the uncertainties in the source geometry and strength associated with location errors.

2. 2 **- Intruments and data**

2. 2.1 **- Instruments**

The data used in this study were obtained during a temporary experiment conducted on Mt Etna in 2005 comprising a sparse network and two small-aperture array deployments. The sparse network was constructed by 9 Lennartz 3-component seismometers with frequency response down to 0.05Hz; these stations are identified by ETxx in Figure 1. The two small-aperture arrays (ACPN and APCZ) were located on the southern and the northern flank of the volcano, and were comprised of 6 and 4 Lennartz 1Hz LE3D-lite seismometers, respectively. The central element of the APCZ array was equipped with a 3-component seismometer. For both the network and arrays the sampling rate was 125 samples per second. In this work, we analysed the continuous data streams collected during the month of August 2005.

Our dataset is completed with recordings from summit station ECPN of the permanent monitoring network operated at Mt Etna by the Istituto Nazionale di Geofisica e Vulcanologia (INGV). Located close to the ACPN array (Fig.1), this station is equipped with a 3D Nanometrics-Trillium seismometer with at amplitude response down to 0.025Hz and a sampling rate of 100 samples per second.

Before the analysis, all the recordings were corrected for the corresponding instrument response and converted to displacement. The locations and geometry of the overall deployment is represented in Figure 1.

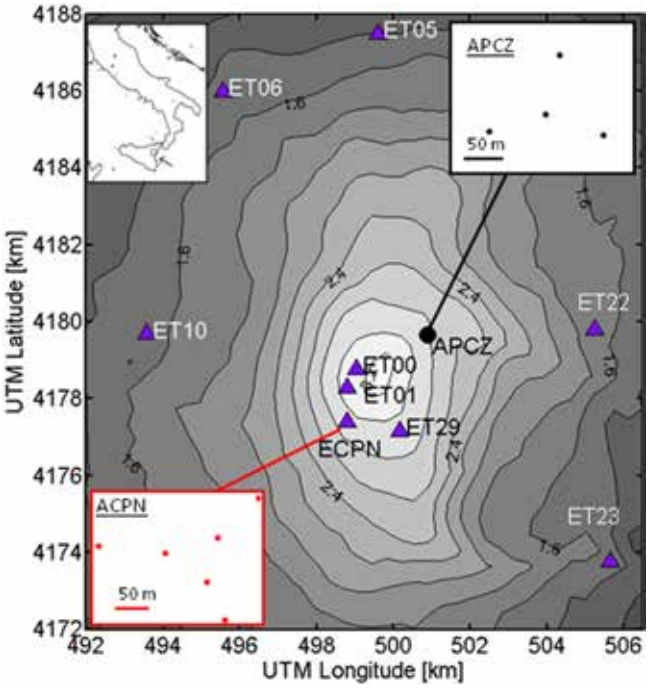

Fig.1. Location and geometry of the seismic network on Mt Etna.

2. 2.2 **- Data**

The analysed dataset spans the month of August 2005, when Mt Etna was in a quiescent stage, following the end (March 2005) of the 2004-2005 eruptive episode (Corsaro and Miraglia (2005); Burton et al., (2005); Di Grazia et al., (2006)).

Figure 2 shows a spectrogram from the vertical-component of summit station ET00.

Energy is concentrated at low frequencies, mainly below 1Hz. Several events exhibit a narrow frequency peak at frequencies between 0.3 and 1Hz. Transient signals are superimposed on the continuous background noise, extending up to 3-4 Hz. These events, which represent the most typical feature of the seismicity during the analysed time interval, are the object of the following section.

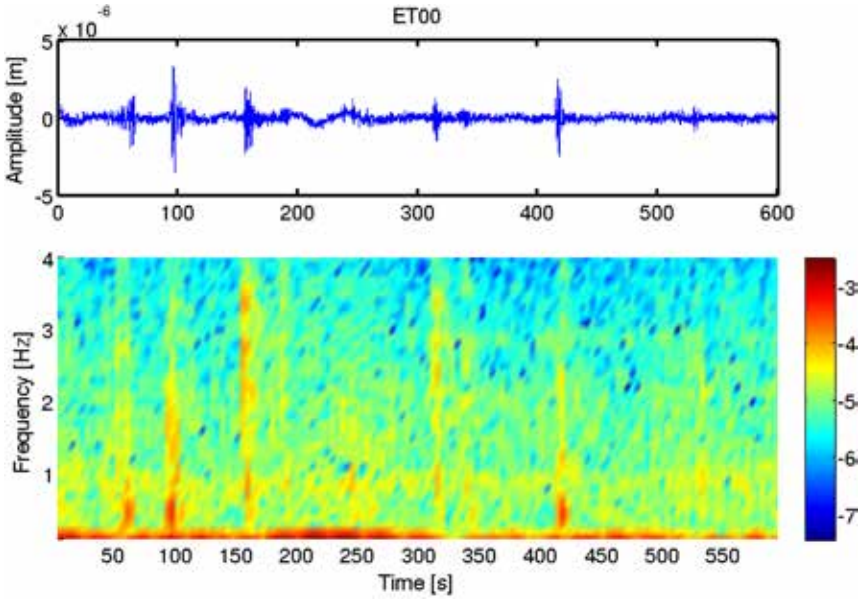

Fig. 2. Spectrogram for the vertical component of ground displacement recorded at summit station ET00.

2. 3 **- Long-Period Activity at Mt Etna**

2. 3.1 **- Event detection**

Throughout the analysed period, LP activity at Mt Etna is sustained over time, with rates of up to 5-20 events/hour. LP energy is concentrated within the 0.3 - 3Hz frequency band, with a main peak below 1Hz. Automatic detection of LP events is performed using the STA/LTA (Earle and Shearer (1994)) ratio, calculated over signals band-pass-filtered between 0.3 and 1 Hz. We thereby found 12795 events.

Figure 3a reports the amplitudes of the detected events versus time at ET00 seismic station; amplitudes are obtained by averaging the absolute value of the signal over 10 seconds around the trigger time. Figures 3b and 3c show the frequency distributions for the LP amplitudes and the

fraction of spectral amplitudes below 1.5 Hz, respectively. The distribution of delay times between stations ET00 and ETA1 derived from cross-correlation is illustrated in the histogram of Fig.3d. All the distributions reported in Figure 3 are bimodal, suggesting the presence of two distinct populations of events, characterized by different locations, spectral content and amplitude.

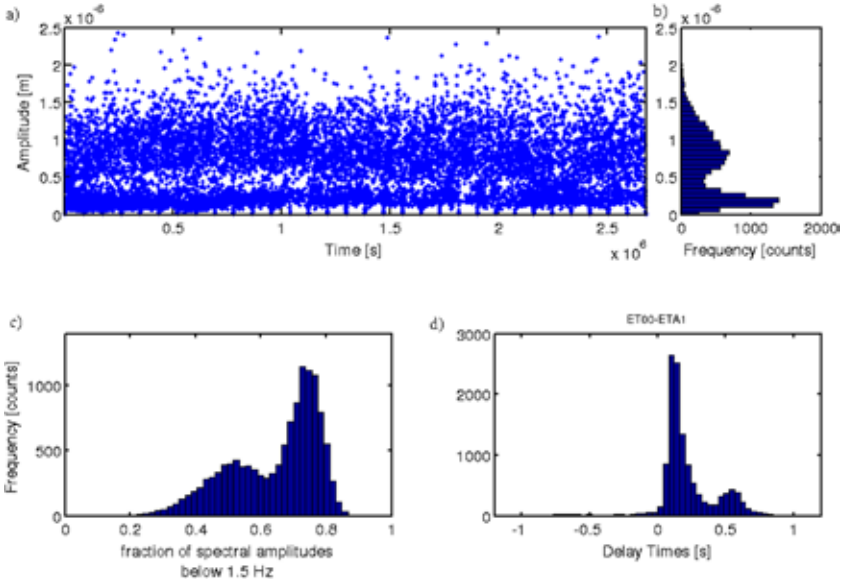

Fig. 3. Catalogue I-LP events detected by STA/LTA method: a) Amplitudes of the events over time; b) Histogram of the amplitudes; c) Spectral content expressed as the fraction of the spectral amplitudes below 1.5Hz; d) Histogram of the delay-times observed between station ET00 and ET29.

2. 3.1.1 **- Waveform classification**

LP waveforms exhibit a high degree of waveform similarity, thus providing a criterion for source classification/separation. Using the first 3000 events from the catalogue obtained through the STA/LTA approach, we calculate the cross-correlation function for all the independent event pairs, using 10-s-long windows encompassing the maximum amplitude of the 0.3-1Hz filtered signal from summit station ET00. Maxima of the cross-correlations are then arranged into a correlation matrix, which is eventually used for grouping events whose correlations were greater than a threshold of 0.8. In this procedure, once an event is extracted and assigned to a family, it is removed from the correlation matrix and thus cannot be attributed to any other cluster.

1218 out of 3000 elements are classified according to two main families. Individual family members are then aligned according to the inter-event delay times obtained from correlation analyses and stacked to derive a family-representative template waveform.

In order to improve the completeness of the catalogue, we then use these templates for a matched-filtering procedure applied to the corresponding, day-long seismograms. We retain events whose correlation with the template waveform is higher than 0.8, thus obtaining a total of 8894 and 9116 events for the first and second families, respectively (Figure 4).

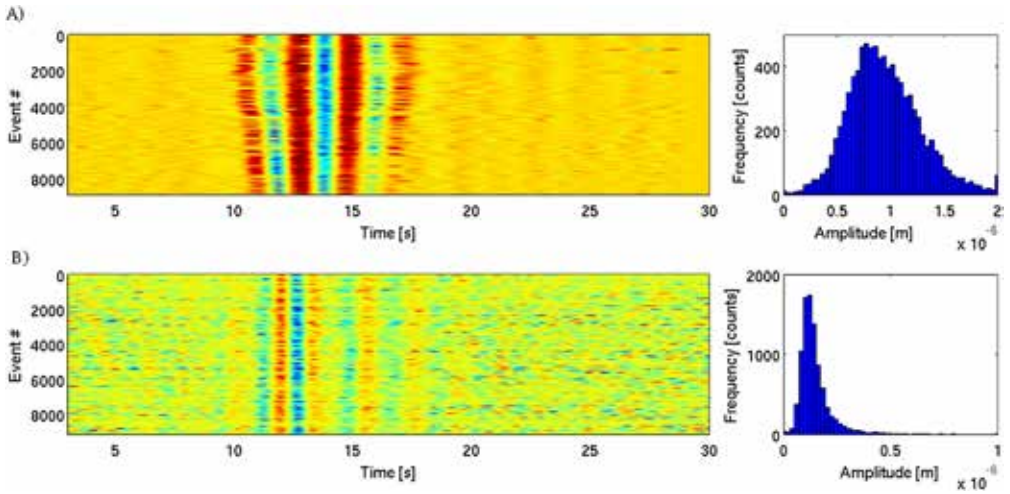

Fig. 4. Left-Representation of the Family I LP catalogue, the color represents the normalised amplitudes of the events; Right-Family I amplitude distribution; b)Left-Representation of the Family II LP waveforms; Right- Family II Amplitude distribution.

2. 3.2 **- LP Families I and II**

Associated with the first family of events are the most energetic events, with amplitude distribution peaked at 0.9×10^{-6}m. Most of the energy of these LP events is concentrated within a narrow spectral peak centered at around 0.5 Hz. Events from the second family are less energetic (lowest mode in the amplitude distribution in Fig. 3a, and the signal-to-noise ratio (SNR) is therefore poor, especially as one gets farther from the crater area. These LPs are characterised by higher frequency content, as the main spectral peak spans the 0.5Hz - 1 Hz range. Overall, these two families correspond to the two different populations of events previously identified on the base of the amplitude and spectral energy distributions. Due to the poor signal-to-noise ratio observed for family II, we pursue our analysis only considering the LP events of the family I in the following sections.

2. 4 **- Location**

2. 4.1 **- Residual Time computation**

We locate the LP events of Family I with the technique used by De Barros et al., (2009) on a dataset of LP events recorded during the 2008 eruptive crisis. This method is based on the delay-times measured between pairs of stations and involves two steps.

(i) First, we derive the location of the centroid of the cluster of events by locating a master event. We define regularly-spaced nodes of grid and for each node located at x, we compute the associated theoretical delay time $t^{th}_{ij}(x)$ between the i^{th} and the j^{th} stations. The location of the center of the cluster of events is found for x which minimises the following expression:

$$E(x) = \sum_{ij}(t_{ij}^{th}(x) - t_{ij}^{obs}(x))^2 \qquad (1)$$

(ii) the second step consists of calculating the location of the individual events, using the center of the cluster as a reference point. We thus realign the events with the delay time expected for the location of the centroid Xo. By cross-correlation, we measure the residual times: $\partial t_{ij}^{obs}(x) = t_{ij}^{obs} - t_{ij}^{th}(X_o)$.

The location is then found by minimizing the sum of the squared differences between observed and theoretical residual times for a grid of source position.

We consider the stations ET00, ET01, ET29 and the two small arrays for the location.

Other stations are not taken into account because of the waveform variations due to the path effects more pronounced for more distant stations (see Bean et al., 2014)). The master event for the first step of the procedure is obtained by stacking the aligned LP events at the chosen seismic stations. We examined grid points within a dimension of 4x4x2.2 km^3 with an inter-node distance of 100 m. We supposed a constant S-wave velocity for the computation of the travel times that minimizes the residuals, i.e. 2 km/s. We obtain the best location of the event cluster at Xo = (499.1; 4178.2; 2.45) km. For the second step of the procedure, we use gridding of a dimension of 2x2x1.4 km^3 with 20 m and 10 m spacing for the horizontal and vertical axes, respectively. For a better signal-to-noise ratio, we select the most energetic events, with an amplitude greater than 1.2 x 10^{-6} m, namely a total amount of 1477 events. An objective function is computed on the source grids for the individual events and the best location is determined by its minimum. The results are well resolved on the horizontal plane, showing a source located around 499.2 km UTM (Longitude) and 4178.2 km UTM (Latitude), as reported in figure 5. An eastward migration of the source is observed throughout the analysed time interval. The results present, along the vertical axis, a wide spreading from the surface down to approximately 1 km below the crater area, with an event clustering between 2 and 2.5 km and another one around 2.9 km of elevation a.s.l. (see Fig. 5).

2. 4.2 **- Back-propagation of the Polarisation vector**

We derive the polarisation attributes of the LP signals using the method of Kanasewich (1981), based on the computation of the covariance matrix. The matrix elements are calculated over 3s-long windows sliding by 0.5 s on the 0.3 - 3 Hz band-pass filtered signals. This is applied to stations ET00, ET01, ECPN and array APCZ. Events from Family I also exhibit a weak VLP (Very Long Period) component, which is observed only at summit station ECPN. The VLP spectral peak is centered at about 0.05Hz, with a duration of about 30 seconds. For a set of 202 available VLP events, we evaluate the covariance matrix using 20 s-long windows on the signals filtered between 0.01 and 0.1 Hz. Clear rectilinear motion for VLP events is observed only at station ECPN. Polarisation azimuths are consistent with the location inferred from travel time inversion only at station ET01, ECPN and ET29 (see Fig. 6a). The rest of the sites exhibit deviation, which suggests wavefield complexities likely related to near-field effects (e.g. Lokmer and Bean (2010)).

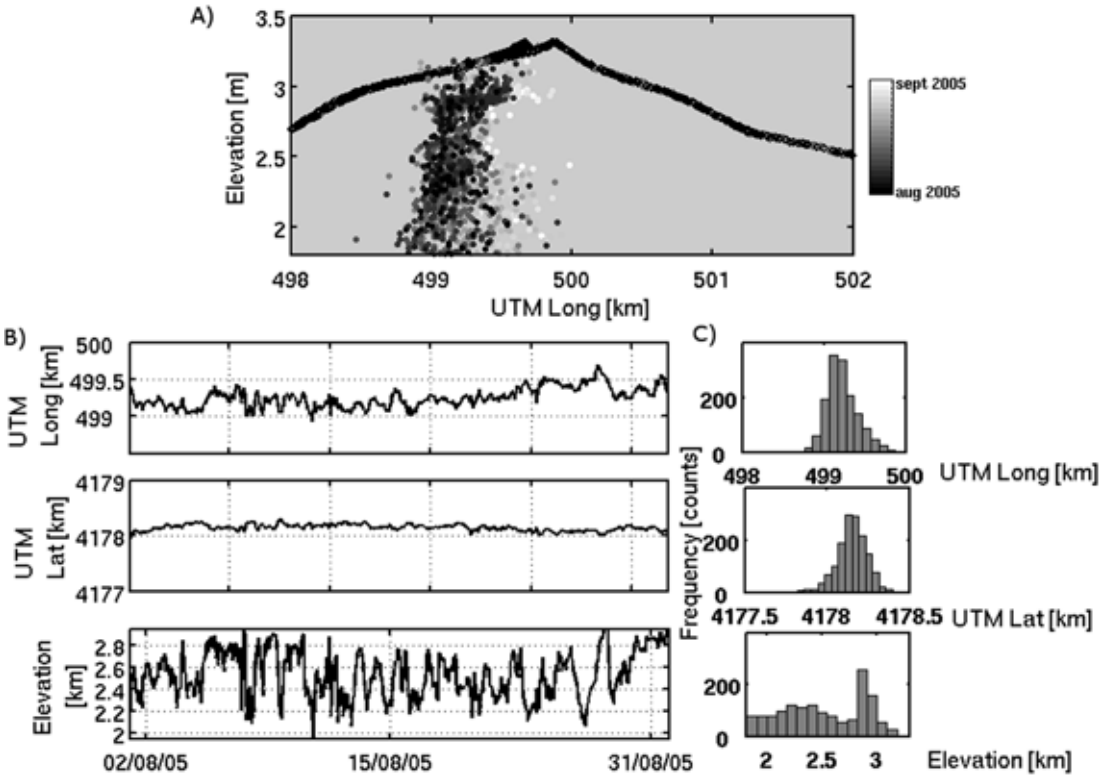

Fig. 5. Location of a set of Family I LP events at Mt Etna through the computation of the residual delay times. A) Representation of the solutions on a W-E cross-section crossing the crater area; B) Location of the events over time C) histograms of the solutions for the 3 coordinates.

To derive estimates on source depths, we projected back the polarisation parameters relative to the first impulse of the events on a vertical axis crossing the crater area. We considered the waves propagating in a homogeneous medium, thus without increase of the incidence angle with depth. Hence, we do not account for possible deviation of the ray that is reduced to a simple straight line (Fig. 6b).

2. 4.3 **- Location based on back propagation of slowness vector**

To obtain the directional properties of the long-period activity, we apply the plane wave fitting described by Del Pezzo and Giudicepietro (2002). This multi-channel technique, which is based on the plane wave approximation, computes the time delays by cross-correlation of independent pairs of signals recorded by the array. The horizontal slowness vector (Sx, Sy) is then obtained by a least squares approach. The ray parameter Rp and azimuth angle ϕ (propagation direction with respect to the geographic north) are determined by the following relationships:

$$R_p = \sqrt{\left(S_x^2 + S_y^2\right)} \qquad \phi = \tan^{-1}\left(\frac{S_x}{S_y}\right) \qquad (2)$$

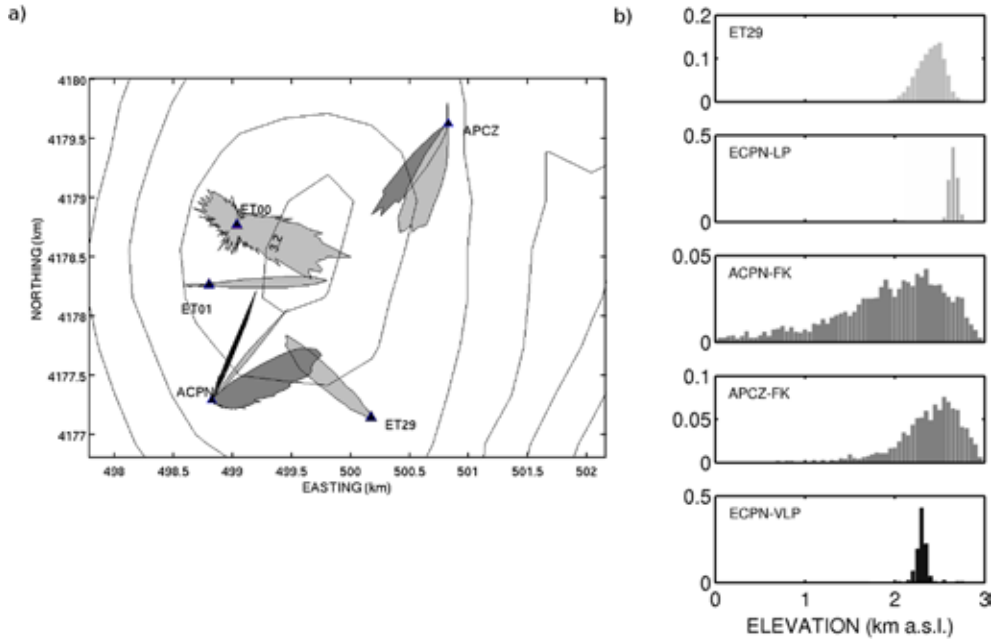

Fig. 6. a) Rose diagrams of polarisation azimuths for LP (light gray) and VLP(black) signals, and backazimuths derived from slowness analysis (dark gray); b)depths inferred from back-propagation of polarization (ET29, ECPN-LP, ECPN-VLP) and slowness vectors (ACPN-FK, APCZ-FK). The epicentral distances considered for the depth estimations are given by the distances between the stations and the averaged epicentre point obtained by the location of the LP events through the computation of the residual delay times: (499.1, 4178.2) km.

The analyses are conducted on data from the arrays ACPN and APCZ using 3-sec-long windows sliding along the LP recordings with 0.5 s increments, and for the 0.3 - 3 Hz frequency band.

Family I LP events present back-azimuth angles varying from 230 to 260° at array ACPN, thus deviating from the crater area, as inferred from the previous results. Instead, at array APCZ, back-azimuth angles span the 30-40° range, fully consistent with the central crater direction (see Fig. 6). At ACPN, the associated ray parameters are centered around 0.4 km/s. This value increases (i.e. apparent velocity decreases) after the peak amplitude of the events, suggesting the contribution of surface waves propagating in a shallower medium (observed on the entire waveforms at APCZ). We estimated the depth of the source by tracing back the seismic rays for each value of ray parameter obtained. For this procedure, we assume straight rays geometry, since the source-to-receiver distances are smaller than the wavelength of interest (~4 km). The incidence angle of the wavevector is derived from the relationship

$$\Theta = asin(R_p \times V_R) \quad (3)$$

where V_R is the average velocity throughout the ray path. By assuming V_R = 2 km/s (see section 3.1), we find Θ in the range 45-60^o, which is consistent with the incidence angles derived from polarisation estimates at station ECPN. Results indicate a source at depths spanning the 0-1 km beneath the

summit (Fig. 6). However, the aperture of the array is not wide enough to solve accurately the LP wavelengths and thus introduces uncertainties in the results as it is clearly observed by the deviation of the backazimuth angles from the crater direction.

2. 5 - Moment Tensor Inversion

The moment tensor inversion allows us to recover the seismic source properties from the signals recorded on the surface. The ground displacement is related to the system of forces acting at the source through the representation theorem (e.g. Shearer (2009)):

$$U_k(x;t) = G_{ki,j}(x,t;x_o,t_o) * M_{ij}(x_o,t) \quad (4)$$

where U_k is the k^{th} component of the displacement, M_{ij} the force couple or dipole in the ij direction acting on the source, and $G_{ki,j}$ are the derivatives along the x_j-direction of the k^{th} components of the elastodynamic Green's function G_{ki} containing the propagation effects. x_0 is the source point location and t_0 time of the source perturbation. x is the location of the receiver on the surface.

The Green's functions (GF) have been computed with the Lattice model described by O'Brien et al. (2009) with the velocity information extracted from the tomography of Patanè et al., (2002) for 7 stations located on the summit of the volcano (ET00, ET05, ET06, ET10, ET22, ET23, ET29). For the distance range spanned by the selected stations, the velocity model can be considered homogeneous. The convolution in Equation (4) is equivalent in the frequency domain to the product between the moment tensor and the partial derivatives of the Green functions. The moment tensor inversion thus consists of solving a system of linear equations expressed in matrix notation as d=Gm where d is the seismic displacement, G the matrix of the partial derivatives of the GF and m the unknown moment tensor (Auger et al., (2006)). The problem is then solved for m using the Moore and Penrose pseudo inverse (Aster et al., (2013)). Transforming the results back into the time domain, the inversion gives six Source Time Functions (STF). To determine the source mechanism and the orientation, the STFs are decomposed into their eigenvalues and eigenvectors by performing the principal component analysis described by Vasco (1989).

We then apply this moment tensor inversion to a set of grid points that encompass, as a whole, the uncertainties in location of the source inferred from the three methods presented above. The grid nodes are separated by distances of 40 m on the x and z- axes and 120 m along the y-axis. The inversion is repeated for a selection of events (144) with amplitude greater than $1.2x10^{-6}$m. The fits of the waveforms are well recovered for the four stations closest to the summit, because of the highest signal-to-noise ratio. For each grid point, we computed the residual errors between the data and the reconstructed signals through the relationship:

$$Misfit = \frac{(d-Gm)^T(d-Gm)}{d^Td} \quad (5)$$

We sum the residual errors from the three components of the signals and the seven stations for each of the grid point considered in the location volume. We obtain two clusters of minimal errors;

the first around 2.5 km of elevation and the second around 3 km. These results are consistent with the two clusters of hypocenters detected by the location through the delay residual time computation described in the previous section. In particular, the absolute minimal residual error is obtained for a source located in the point (499.2, 4178.5, 2.4) km (Fig. 7 a).
The MT solutions are parametrised through the ratio of the modulus of the MT eigenvalues.

Results are reported in figure 7b and 7c. We observe significant spatial changes for these two variables with λ_1 / λ_3 varying in between the values 0.1 and 0.9 and with λ_2 / λ_3 varying in between the values 0.6 and 0.9 for small distance variations. Consequently, errors in source location may lead to different interpretation of the source mechanism.

The results of the moment tensor inversion for the particular source point with the minimal residual errors at ~ 2.4 km a.sl. are shown in Figure 8 a). The histograms show peaks of λ_1/λ_3 and λ_2/λ_3 ratios in 0.72 and 0.85, respectively, approaching an explosion mechanism.

Similarly the results for a source situated in (499.2, 4178.25, 3) km are instead shown on Figure 8b. In this case the more likely eigenvalues ratios are both 0.63, equivalent to a system of forces of 1:1:1.7, thus approaching a crack mechanism. The trace of the moment tensor is a measure of the volume changes at the source (Shearer (2009)). We observe that such changes also vary as a function of the source position taken into account (Fig 7b). In particular, the volume changes between the two best fit LP sources (~2.4 and ~3 km a.s.l.) vary by a factor of two. This observation indicates that one has to be careful once using the MT inversion for estimating the mass budget of a volcano.

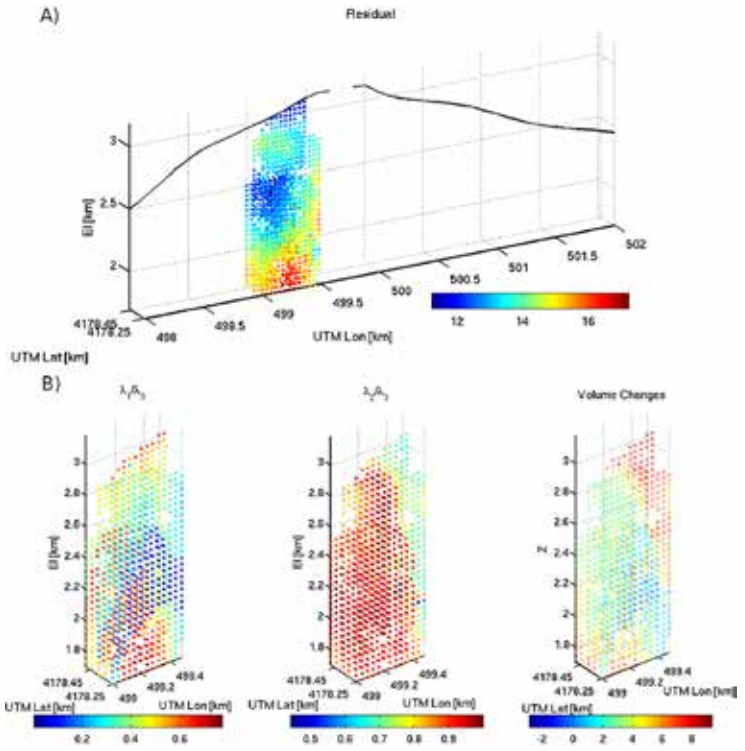

Fig. 7. A) Residual errors between the data used and the reconstructed seismograms (summed for all the events selected); B) Left and center- λ_i / λ_3 ratio averaged for all the events considered and for each location point with i = 1, 2; right- volume changes averaged on the set of LP events considered.

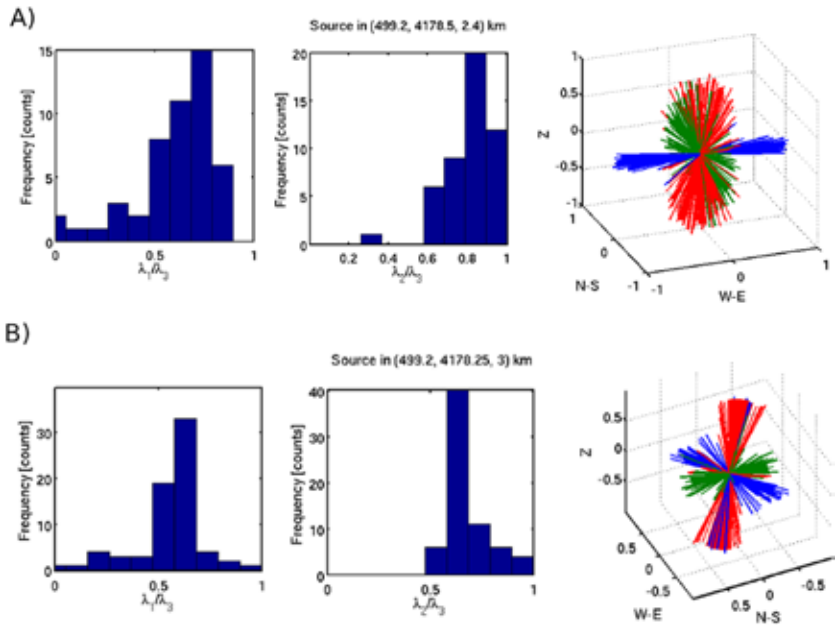

Fig. 8. Histograms of the eigenvalue ratios and direction of the forces applied on the LP source for a source (A) in (499.2, 4178.5, 2.4) km and in (B) (499.2, 4178.25, 3) km.

2. 6 - Conclusions

Despite using different location techniques, we were unable to retrieve consistent estimates for the LP source depth. This may be due to several causes, including (1) utilization of a homogeneous velocity structure, or (2) near-field effects. As for the first cause, if we assume that the true volcanic structure is characterised by a positive velocity gradient with depth, then our straight-ray approximation would lead to an over-estimate of the source depth. Mitigating this issue, however, is the fact that the dominant LP wavelengths (order of 4 km) are larger than the source-to-receiver distances accounted for herein: under this condition, ray trajectories are not significantly affected by velocity heterogeneities. Near-field effects have been thoroughly investigated by Lokmer and Bean (2010), who showed distortion in the polarisation attributes, especially when the source mechanism has weak isotropic components. At present, this interpretation is more applicable to our data. Source mechanisms determined from MT inversion are largely affected by the uncertainties in source depth, and exhibit a great variability in the estimate of both scalar moment and orientation and size of the force system acting at the source. These determinations are therefore not sufficient to put rigorous constrain on the actual physical mechanism driving LP activity.

Taken together, these points highlight the difficulties in approaching the determination of LP source mechanism at Mt Etna under a purely deterministic approach.

The lack of knowledge about the fine internal structure of the volcanic edifice hinders the accurate prediction of elastic wave propagation, thus implying large uncertainties in the estimate of source location and mechanisms.

Acknowledgements

The research leading to these results has received funding from the European Union Seventh Framework Programme (FP7/2007-2013) under the project NEMOH, grant agreement n° 289976.

I thank my supervisor G. Saccorotti for his guidance, support and encouragement along the NEMOH project and PhD. I thank my PhD supervisor C. Bean and I. Lokmer from UCD for the so many discussions and help given for my work. Thanks to H. Aochi for hosting me at BRGM for my secondment and for the long discussions on inversion. Many thanks to F. di Traglia from the University of Florence for the collaboration and interesting work achieved.

References

Arciniega-Ceballos, A., Chouet, B. and Dawson, P. (2003). Long-period events and tremor at Popocatepetl volcano (1994-2000) and their broadband characteristics. Bulletin of Volcanology 65 (2), 124-135.

Aster, R., Borchers, B., and Thurber C. H. (2013). Parameter estimation and inverse problems. Academic Press.

Auger, E., D'Auria, L., Martini, M., Chouet, B. and Dawson, P. (2006). Real-time monitoring and massive inversion of source parameters of very long period seismic signals: An application to Stromboli volcano, Italy. Geophys. Res. Lett. 33 (4).

Bean, C. J., De Barros, L., Lokmer, I., Metaxian, J.-P., O'Brien, G. and Murphy, S. (2014). Long-period seismicity in the shallow volcanic edifice formed from slow-rupture earthquakes. Nature geoscience 7 (1), 71-75.

Burton, M. R., Neri, M., Andronico, D., Branca, S., Caltabiano, T., Calvari, S., Corsaro, R., Del Carlo, P., Lanzafame G., Lodato, L., et al. (2005). Etna 2004-2005: An archetype for geodynamically-controlled effusive eruptions. Geophysical research letters 32 (9).

Chouet, B., (1985). Excitation of a buried magmatic pipe: a seismic source model for volcanic tremor. Journal of geophysical research 90 (B2), 1881-1893.

Chouet, B., (1986). Dynamics of a fluid-driven crack in three dimensions by the finite difference method. Journal of Geophysical Research: Solid Earth (1978-2012) 91 (B14),13967-13992.

Chouet, B., (1992). A seismic model for the source of long-period events and harmonic tremor. In: Volcanic seismology. Springer, pp. 133-156.

Chouet, B., (1996). New methods and future trends in seismological volcano monitoring. In: Monitoring and mitigation of volcano hazards. Springer, pp. 23-97.

Chouet, B., Dawson, P., Ohminato, T., Martini, M., Saccorotti, G., Giudicepietro, F., De Luca, G., Milana, G. and Scarpa R., (2003). Source mechanisms of explosions at Stromboli volcano, Italy, determined from moment-tensor inversions of very-long-period data. J. geophys. Res 108 (B7), 2331.

Corsaro, R. and Miraglia, L., (2005). Dynamics of 2004-2005 Mt Etna effusive eruption as inferred from petrologic monitoring. Geophysical research letters 32 (13).

Davi, R., O'Brien, G., Lokmer, I., Bean, C., Lesage, P. and Mora, M., (2010). Moment tensor inversion of explosive long period events recorded on Arenal volcano, Costa Rica, constrained by synthetic tests. Journal of volcanology and geothermal research 194 (4), 189-200.

De Barros, L., Bean, C., Lokmer, I., Saccorotti, G., Zucarello, L., O'Brien, G., Metaxian, J. and Patanè, D. (2009). Source geometry from exceptionally high resolution long period event observations at Mt Etna during the 2008 eruption. Geophys. Res. Lett., 36, L24305.

Del Pezzo, E. and Giudicepietro, F., (2002). Plane wave fitting method for a plane, small aperture, short period seismic array: a mathcad program. Computers & geosciences 28 (1), 59-64.

Di Grazia, G., Falsaperla, S. and Langer, H. (2006). Volcanic tremor location during the 2004 Mount Etna lava

effusion. Geophysical research letters 33 (4), L04304.

Earle, P. S. and Shearer, P. M. (1994). Characterization of global seismograms using an automatic-picking algorithm. Bulletin of the Seismological Society of America 84 (2), 366-376.

Kanamori, H., Ekstrom, G., Dziewonski, A., Barker, J. S. and Sipkin, S. (1993). Seismic radiation by magma injection: An anomalous seismic event near Tori Shima, Japan. Journal of Geophysical Research: Solid Earth (B4), 6511-6522.

Kanasewich, E. R. (1981). Time sequence analysis in geophysics. University of Alberta.

Kumagai, H., Chouet, B. and Dawson, P. (2005). Source process of a long-period event at Kilauea volcano, Hawaii. Geophysical Journal International 161 (1), 243-254.

Lokmer, I. and Bean, C. (2010). Properties of the near-field term and its effect on polarisation analysis and source locations of long-period (LP) and very-long-period (VLP) seismic events at volcanoes. Journal of volcanology and geothermal research 192 (1), 35-47.

Lokmer, I., Bean, C., Saccorotti, G., Patane, D., et al., (2007). Moment-tensor inversion of LP events recorded on Etna in 2004 using constraints obtained from wave simulation tests. Geophys. Res. Lett 34 (22), L22316.

Lokmer, I., Saccorotti, G., Di Lieto, B. and Bean, C. (2008). Temporal evolution of long-period seismicity at Etna Volcano, Italy, and its relationships with the 2004-2005 eruption. Earth and Planetary Science Letters 266 (1-2), 205-220.

Nakano, M., Kumagai, H. and Chouet, B. (2003). Source mechanism of long-period events at Kusatsu-Shirane Volcano, Japan, inferred from waveform inversion of the effective excitation functions. Journal of volcanology and geothermal research 122 (3-4), 149-164.

Neuberg, J., Tuffen, H., Collier, L., Green, D., Powell, T. and Dingwell, D. (2006). The trigger mechanism of low-frequency earthquakes on Montserrat. Journal of Volcanology and Geothermal Research 153 (1), 37-50.

O'Brien, G., Bean, C. and Tapamo, H. (2009). Dispersion analysis and computational efficiency of elastic lattice methods for seismic wave propagation. Computers & Geosciences 35 (9), 1768-1775.

Ohminato, T., Chouet, B. A., Dawson, P. and Kedar, S. (1998). Waveform inversion of very long period impulsive signals associated with magmatic injection beneath Kilauea volcano, Hawaii. Journal of Geophysical Research: Solid Earth 103 (B10), 23839-23862.

Patanè, D., Chiarabba, C., Cocina, O., De Gori, P., Moretti, M. and Boschi, E. (2002). Tomographic images and 3D earthquake locations of the seismic swarm preceding the 2001 Mt. Etna eruption: evidence for a dyke intrusion. Geophysical Research Letters 29 (10), 1497.

Shearer, P. M. (2009). Introduction to seismology. Cambridge University Press.

Tuffen, H., Dingwell, D. B. and Pinkerton, H. (2003). Repeated fracture and healing of silicic magma generate ow banding and earthquakes? Geology 31 (12), 1089-1092.

Vasco, D. (1989). Deriving source-time functions using principal component analysis. Bulletin of the Seismological Society of America 79 (3), 711-730.

Léna Cauchie, Belgium
cauchiecaruso@unistra.fr

Affiliation under NEMOH
Istituto Nazionale di Geofisica e Vulcanologia, Sezione di Pisa, Pisa, Italy

Research theme under NEMOH
Quantifying uncertainties in location and source mechanism for Long-Period events at Mt Etna, Italy.

I made my first steps in seismology, with immediate application to volcanology, during my MSc degree in Geophysics at the University of Pisa, Italy.

My deep interest in volcanology led me to elaborate my MSc thesis in collaboration with the Istituto Nazionale di Geofisica e Vulcanologia (INGV) on the definition of the shallow velocity structure at Mt Etna. At that time I participated to my first seismic fieldwork on Etna volcano, an experiment settled jointly with other European universities for the installation of a network of 50 seismic stations.

In 2010 I undertook a PhD at the University College of Dublin (UCD) in the Geophysics Group. I investigated the source properties of the long-period (LP) seismic events of Mt Etna through a statistical analysis. I compared the behaviour of the LP activity with the empirical laws describing earthquakes recurrence, in order to understand what kind of relationships exists between the two different earthquake classes.

I joined the NEMOH project in November 2012 at INGV-Pisa to work on the probabilistic inversion of simulated and observed geophysical data. In particular my work aimed at the assessment of the uncertainties of the LP source properties at Mt Etna as a consequence of poor knowledge of the velocity model, and was therefore in perfect line with my PhD project. Among the skills developed during the NEMOH project, I may mention seismic data processing, inversion theory, statistical analysis, coding, and interdisciplinarity.

I collaborated with several research institutions such as the University of Florence and the Bureau de Recherches Géologiques et Minières in France for part of my secondment. There, I could learn numerical codes needed in the process of inversion. I also spent my secondments in UCD where I improved my practice on the inversion of field data. The NEMOH project allowed me to participate to many workshops and to present my work at conferences such as EGU in 2013 and 2014.

After completing my PhD in 2015, I pursued my career as a post-doctoral researcher, first in collaboration with the Dublin Institute of Advanced Studies for the analysis of tremor activity at Arenal Volcano in Costa Rica and then at the University of Strasbourg on microseismicity induced by geothermal reservoirs.

My research career will definitively keep following this path: investigating (micro) seismicity to understand the mechanism at its origin. The integration of seismic data with data from other disciplines is an important aspect I intend to develop in my research career.

Chapter 3

Link between pressure variation and Moment Tensor (MT) in seismic isotropic sources: a comparison with the Mogi Problem

Claudio Trovato
BRGM, Orléans, France - ISTO, Orléans, France

Tutorship: Hideo Aochi
BRGM, Orléans, France - ISTO, Orléans, France

Abstract

Long Period (LP) and Very Long Period (VLP) seismic events recorded worldwide on volcanoes are thought to be generated by fluid and gas movements occurring in the shallow portion of the volcanic edifice. Their source process is related to tensile variation of the walls of the structure which accommodates their generation. Moment tensor inversion is the main tool used to get insight into the source mechanism of LP and VLP events, but the retrieved seismic moment may not always have a clear physical meaning. The problem comes from the fact that different approaches are proposed in literature to relate the seismic moment to the exerted pressure and the volume variation occurring at the source. In order to test different approaches, I compare an analytical solution with numerical simulations and compute the static permanent displacement recorded at the free surface resulting from an isotropic source embedded at depth. The comparison shows that the pressure variation of an isotropic source can be estimated from the retrieved moment tensor, but careful attention must be paid in defining the source geometry as errors can arise in the estimation of the pressure magnitude.

Keywords: Numerical solutions, Inverse theory, Volcano seismology, Wave propagation

3. 1 - **Introduction**

Volcano seismology is the study of earthquakes in volcanic regions. The first aim of volcano seismology is to understand the dynamics of seismic sources associated with the injection and transport of magma and related hydrothermal fluids (Chouet, 2003). The main issue is the understanding of the complex system of forces which originates in the source region. This system of forces is related to the change of stresses in the medium required to initiate the wave propagation. A unique definition of this system of forces is not present. Conventionally, this seismic source is represented by a symmetric 3x3 tensor, the so called moment tensor (Backus and Mulcahy, 1976; Gilbert, 1971; Julian et al., 1998) constituted by couple of forces with opposite direction acting on a single point (Aki and Richards, 2002; Julian et al., 1998; Madariaga, 2007). The combination of these

dipoles represents the equivalent system of forces acting in the source region. Each component is an independent function of time and can be threaded separately (Madariaga, 2007). The moment tensor is a useful tool to describe not only shear cracks but also to take in account for tensile components in the source region such as tensile cracks, pipes and explosions.

In this work I am focusing on a particular kind of seismic signals, the so called Long Period (LP) and Very Long Period (VLP) events, which are often observed in volcanic contexts and are thought to be connected to mass movements at depth and resonance occurring in the volcanic conduit (Chouet, 1996, 2003; Chouet and Matoza, 2013; De Barros et al., 2011; Gilbert and Lane, 2008; Madariaga, 2007). Recently, Bean et al., (2013) extended the observations of Harrington and Brodsky, (2007) and proposed an alternative model for explaining shallow LP seismicity. They analyzed the pulse-like nature of some LP events recorded on volcanoes and explained their origin as a slow failure of the weak shallow volcanic edifice close to the brittle-ductile transition. Their conclusions suggest that careful attention should be paid in using LP events as direct indicators of magmatic/hydortermal fluids. Here I focus on the former hypothesis which can be related to volume variation of the dikes initiated by the movement of gases or magma (e.g. De Barros et al., 2011; Chouet, 1996; Chouet and Matoza, 2013; Gilbert and Lane, 2008; Madariaga, 2007). We have to imagine a complicated interconnected system of fractures of different dimensions which are traversed by a mixture of melt rocks, crystals and gases (e.g. Kumagai and Chouet, 2000; Kumagai et al., 2005; Ohminato et al., 1998). The movement of this mixture is supposed to be triggered by pressure variations (Nakano et al., 2003). Thus, part of the displacement of the crack walls could result in a static permanent displacement The simplest case we can consider is a spherical source without deviatoric components. In this case the isotropic part of the moment tensor can be seen as the representation of an explosion/implosion. The aim of this paper is to find the connection between a real system of forces, that can be the ΔP (pressure) exercised uniformly on the wall surface of the sphere, and the equivalent moment tensor magnitude.

Mogi (1958) proposed an analytical formula to compute the static permanent displacement at the surface due to an explosion source at a certain depth. He assumed that the Earth's crust is an ideal semi-infinite elastic body and that the deformation at the surface is caused by the spherical source with hydrostatic pressure change. The analytical formulas in their compact form are:

$$\Delta d = \frac{3a^3P}{4\mu}\frac{d}{(f^2+d^2)^{3/2}} \tag{1}$$

$$\Delta h = \frac{3a^3P}{4\mu}\frac{f}{(f^2+d^2)^{3/2}} \tag{2}$$

where Δd and Δh are the radial and vertical displacement at the surface, *a* is the radius of the phere with the hydrostatic pressure, *P* is the hydrostatic pressure variation, *f* is depth of the center of the sphere, *d* is radial distance on the surface from the center and μ is a Lame's constant. Mogi

(1958) validated his formula by obtaining good correspondence between his computed values for ground deformation and field data collected on some Japanese volcanoes in the first half of 20th century. The good correspondence was obtained for *a* << f, it means a sphere of small radius embedded at a considerable depth. Even if the analytical solution has been designed for long-period deformations, I can apply the same to the sudden elastic displacement induced by a seismic source.

3. 2 - **Moment magnitude for an explosion**

The deformation of the volcanic edifice is treated like an elastic response of the volcano to an excess magmatic pressure at depth (Anderson, 1937; Battaglia et al., 2003; Bonafede et al., 1986; Delaney and McTigue, 1994; Gudmundsson, 2006; McTigue, 1987; Mogi, 1958). The parameters which control this static displacement are the ΔP, the radius of the sphere *a* and its depth *f* (Figure 1). The process producing this static permanent displacement at the free surface is directly related to the volume variation of the walls of the sphere.

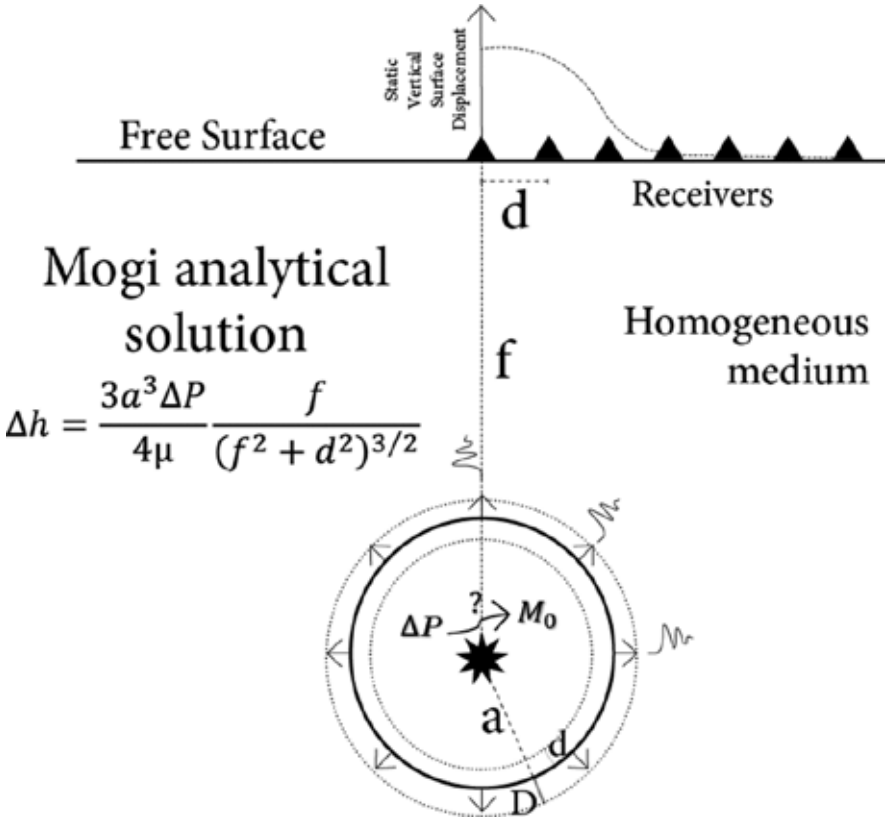

Figure 1. Schematic representation of the Mogi problem. A **ΔP** is imposed on the sphere wall at depth and a static vertical displacement is recorded at the surface. **a** is the radius of the sphere, **f** the sphere depth, **D** and **d** represent the external and internal displacement of the wall of the sphere respectively. The analytical solution of Mogi, (1958) for the static vertical displacement recorded at the surface is reported as an example. The key point is how to express the $\mathbf{M_0}$ at source in function of the **ΔP** imposed at the sphere wall.

Two main approaches are present in the literature to relate the volume expansion of a sphere and the isotropic moment of the signals recorded at the free surface: the first derived by Eshelby, (1957)

$$M_0 = \left(\lambda + \frac{2}{3}\mu\right)\Delta V \tag{3}$$

and the second proposed by Muller, (1973)

$$M_0 = (\lambda + 2\mu)\delta V \tag{4}$$

in both equations M_0 is the isotropic moment, λ and μ are the Lame's parameters of the homogenous isotropic elastic medium and ΔV and δV are the tensile expansion of the external wall of the sphere induced by the explosion. ΔV and δV are referred to the same process but I use a different notation following the work of Richards (2005) who states that their use is similar but they are referred to the computation of two slightly different volume variations. The works of Muller (2001) and Richards (2005) are complementary and both threat the issue of which of the two Equations (3) or (4) better quantify the energy released (by meaning of the volume variation) by an explosive source at depth. For Richards (2005) Equation (3) is related to the volume variation in case the source has no confining hydrostatic pressure (the so called "*unconfined volume change"*), so it's free to expand without constraints, while equation (4) should reflect the real case where the hydrostatic pressure at depth of the sphere is considered and the volume expansion is limited by the surroundings. For Muller, (2001) the two equations simply reflect two extreme cases of volume variation related to the shape of the source. Equation (3) should correspond to a crack (a volume with one dimension much smaller than the two others) while Equation (4) should correspond to a sphere. The two computed values for ΔV and δV should simply give a range of possible volume variations for different source shapes. Kumagai et al. (2014) have compared five different representations for a spherical source and their displacement fields. From the equivalence of the displacement fields, Equation (4) should be used to compute the volume variation due to a spherical or isotropic source, while Equation (3) for three tensile crack volumes or a spherical crack (Kumagai et al., 2014).

The best solution for the computation of the moment magnitude of our problem should be Equation (4) because I'm looking for the moment magnitude of a sphere (spherical source) embedded at a certain depth, so confined by a certain hydrostatic pressure. I will now compare numerically the results from both two Equations (3) and (4) in order to find the best solution.

3. 3 **- Volume Variation**

The main issue is to relate the volume variation to the ΔP imposed on the wall of the sphere. Different approaches are present in literature to relate the ΔP to the radius expansion *D* (say from *a* to *a* + *D*) (Aki and Richards, 2002; Gottsmann et al., 2006; Masterlark, 2007; Muller, 2001; Wielandt, 2001). Among all the different approaches I will focus on the solutions proposed by Aki and Richards (2002) and Muller (2001). Both equations (3) and (4) will be used to compute the isotropic moment

(M_0). I obtain the volume variation by the displacement of the sphere's wall using the formula (Aki and Richards, 2002)

$$\Delta V = 4\pi a^2 D \tag{5}$$

where *D* is the external displacement of the external wall.

Aky & Richards (2002)

The first solution comes from Aki and Richards, (2002). In chapter 3 they propose some problems connected to the quantification of the radial displacement of the external wall of a sphere. Following their equations the pressure variation can be related to the external displacement by

$$D = \frac{\Delta P\, a}{4\,\mu} \tag{6}$$

This solution applies in the case the expansion is able to attain his "*stress-free*" value, it means that the effects of the confining pressure of the medium are not taken in account. This solution corresponds to the "spherical source" in Kumagai et al. (2014). Hereafter, I refer to this solution as "*Aki & Richards I".*

A second solution from Aki and Richards, (2002) takes in account for the confinement of the source region. They propose to compute a constant of proportionality

$$A = \frac{\Delta P}{3\lambda + 2\mu} \tag{7}$$

such that the static radial displacement of the sphere wall is

$$D = Aa \tag{8}$$

Like expected the second solution leads to lower volume expansion values. This solution corresponds to the "Eshelby spherical source" with strain-free stress conditions in Kumagai et al. (2014). Hereafter, I refer to this solution as "*Aki & Richards II".*

Muller (2001)

In the approach followed by Muller, (2001) the author makes a distinction between an internal and an external displacement. He imagines a spherical tensile crack which walls, after the application of ΔP, move both outward (D) and inward (d), the sum of the two displacement is D_0=D+d (Figure 1). To compute such displacements he introduces a second constant of proportionality

$$B = \frac{\Delta P\, a^3}{4\,\mu} \tag{9}$$

then he computes the total displacement

$$D_0 = \left(\frac{B}{a^2}\right) - Aa \tag{10}$$

and the external displacement

$$D = \frac{\left(\lambda + \frac{2\mu}{3}\right) D_0}{\lambda + 2\mu} \tag{11}$$

Following the definition proposed by the author, the isotropic moment is computed by means of Equation (3) using the D_0 value for the total displacement (internal + external), and by means of Equation (4) using the D value for the external displacement. This solution corresponds to the "spherical crack source" in Kumagai et al. (2014).

3. 4 - **Comparison and results**

In this article, to calculate synthetic seismograms, I use the open-source code EFISPEC3D (http://efispec.free.fr). This computer program (under double licenses CeCILL-V2 and GNU-GPL-V3) solves the three-dimensional equations of motion using a continuous Galerkin spectral-element method. The correctness of the implementation of the spectral-element method into this code has been thoroughly verified in De Martin (2011) and Chaljub et al.(2015). EFISPEC3D is used in computational seismology to better understand the impact of lithological and topographic effects on near-surface Green's functions (Maufroy et al., 2015).

I will now show the different approaches solutions computed with EFISPEC3D and compare the numerical results with the analytical solution of Mogi in order to validate the best approximation. Geometry and model parameters are as follow. The modeled medium is a cube (x 50 km, y 50 km, z 50km). The large size becomes from the intent to avoid artificial reflections from the boundaries. I choose a homogenous medium with Vp = 3464 m/s, Vs = 2000 m/s and density ρ = 2600 Kg/m^3 in order to obtain Lame's parameters λ = μ as assumed in the Mogi (1958) assumption. The source is an isotropic source embedded at depth with three diagonal components of the moment tensor expressed as

$$m_{xx} = m_{yy} = m_{zz} = M_0 \tag{12}$$

where M_0 is computed towards Equations (3) and (4) respectively.

I choose two different cases (one with the source at 1000 m depth, the second with the source at 2000 m depth). According to the assumptions of Mogi (1958), the source radius is much smaller

compared to the source depth, hence numerical solutions are computed for two different sphere radius, *a* = 100 m and *a* = 10 m. The source time function (STF) is a hyperbolic tangent function with a final static non-zero value and a dimensionless amplitude in order to simulate the static permanent displacement (Figure 1). The frequency content of the second derivative of the STF is zero above 3 Hz in order to guarantee numerical stability in the simulations. I place 43 receivers along the *x*-axis (from x = 0 m to x = 9500 m) in order to measure the final static permanent displacement on the vertical and radial components (when the final static value is reached, I choose to take values at 5 s later than the first S-Waves arrivals).

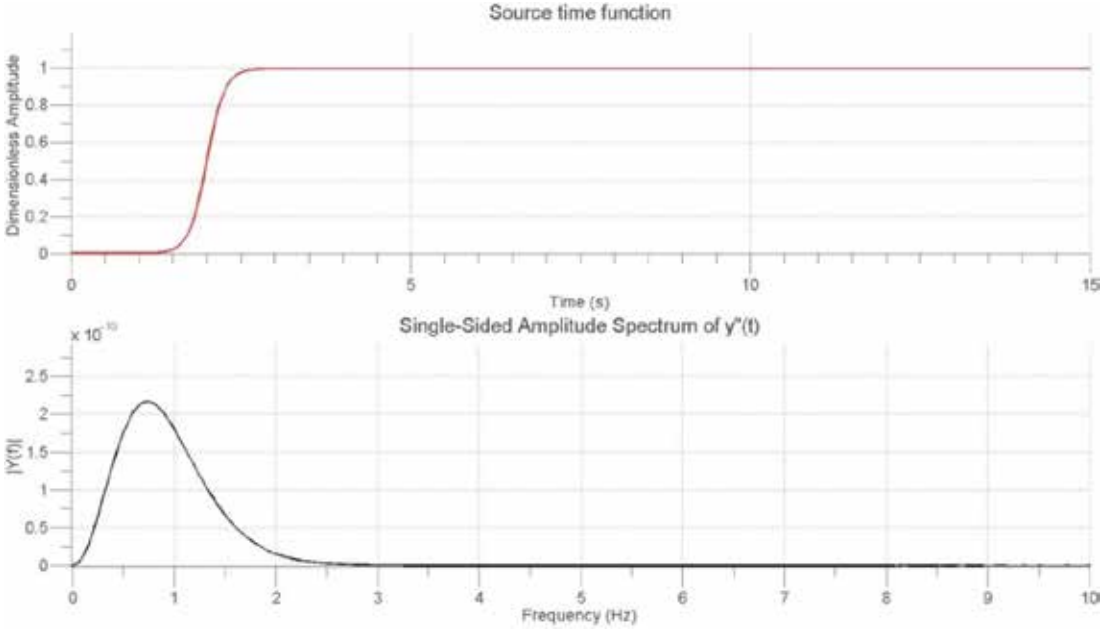

Figure 2. Step source time function used to simulate the static permanent displacement of the sphere wall numerically (top). The spectrum of the second derivative of STF (bottom) with a frequency content lower than 3 Hz.

I choose two pressure values ΔP_1 = 1 MPa and ΔP_2 = 0.1 MPa. For each pressure value and sphere radius I compute ΔV by means of equation (5) for three different D (displacement of the external wall) computed towards Equations (7), (8), and (11). The seismic moments (M_0) are then computed towards equations (3) and (4). For each geometric configuration (sphere radius and depth) listed in Table 1 I end up with five different M_0 values reported in Table 2, Table 3 and Table 4. As In the calculus for the computation of M_0 from the ΔP there is no relation to the sphere depth, the values of M_0 and ΔV computed for *configuration 4* are the same as in *configuration 1*.

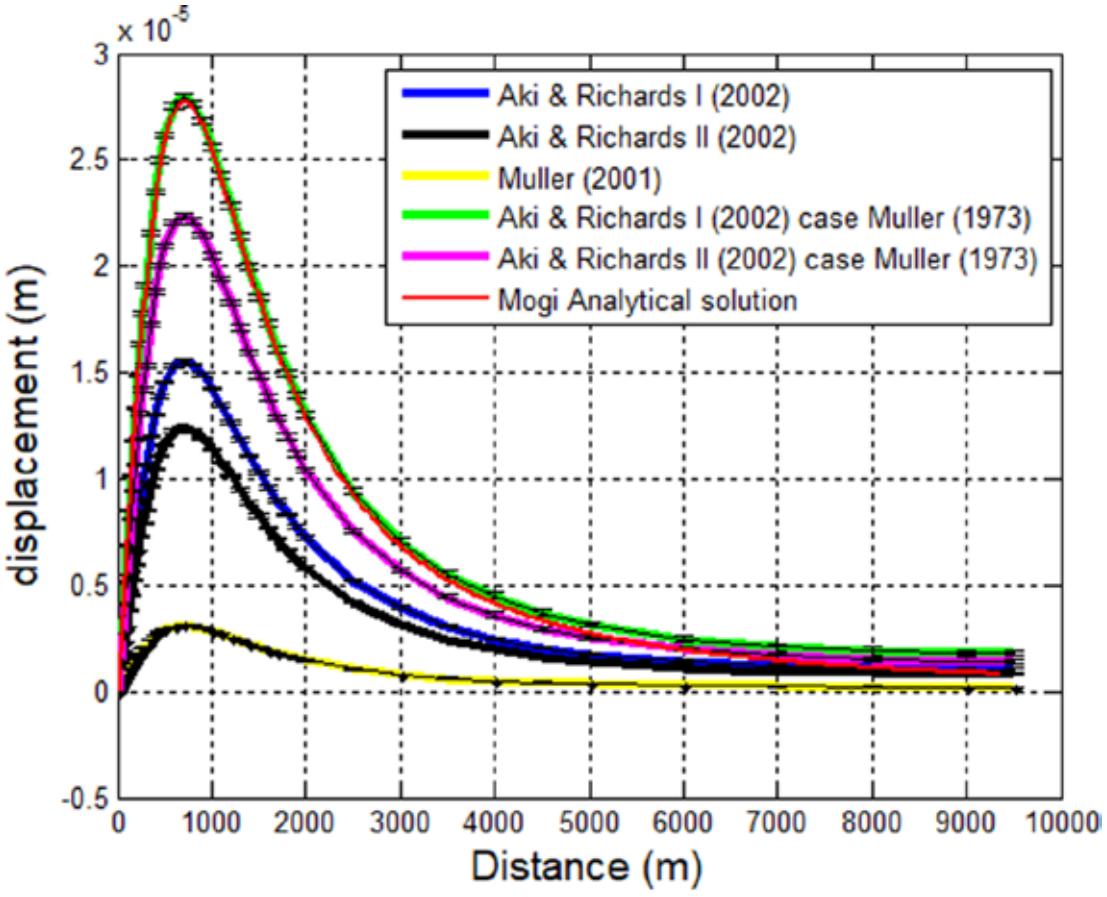

Figure 3. Horizontal static displacement recorded at the surface for the different values of M_0. The analytical solution of Mogi is the red line. Perfect correspondence is obtained with the value of ΔV computed with the "Aki & Richard I" method and the equation M_0 obtained with Equation (4) (Muller, 1973). Error bars appear on the numerical simulations.

Results for configuration 1 (Figure 3 and Figure 4) show perfect matching between the analytical and numerical solutions for the ΔV computed with the Aki & Richard I case (Equations (5) and (6)). Configuration 2, configuration 3 and configuration 4 (Table 1) solutions show analog coherent results (not showed here), hence the interpretation is conducted on configuration 1 solution. The M_0 (Aki & Richards I, case Muller 1973, in Figure 3 and Figure 4) at the source which shows perfect match with the analytical solution is computed by means of Equation (4) (Muller, 1973) which should take in account for the confining hydrostatic pressure. The ΔV variation at the source is only related to the ΔP imposed on the sphere's wall. Thus for the Aki & Richards I case the volume variation $\Delta V = \sim 300 m^3$ *(configuration 1,* Table 1*) is equivalent (Table 2) for both M_0 computed with Equation (3) or (4). In order to match the analytical solution numerically, I need a higher M_0 value to take in account for the hydrostatic pressure (Equation 4). In inverse problems, as stated by Muller (2001), the choice of Equation (3) or (4) for computing the ΔV could depend on the hypothesized source mechanism*

geometry, i.e. a spherical source for Equation (4) or a spherical crack for Equation (3). This is confirmed by Kumagai et al. (2014), perfect matching between numerical and analytical solutions is obtained for their so called "spherical source" which represents the displacement field of the Mogi model (Mogi, 1958). Conversely, if the supposed source mechanism is a spherical crack (Muller, 2001), the ΔP computed in an inverse problem would be one order of magnitude higher than the one found supposing a spherical source mechanism. Figures 3 and 4 highlight the variability when different approaches are used to compute the equivalent system of forces for different source mechanisms. These non-negligible differences must be taken in account when interpreting the retrieved moment tensor in terms of volume and pressure variation hence, careful attention should be paid in defining the source mechanism process.

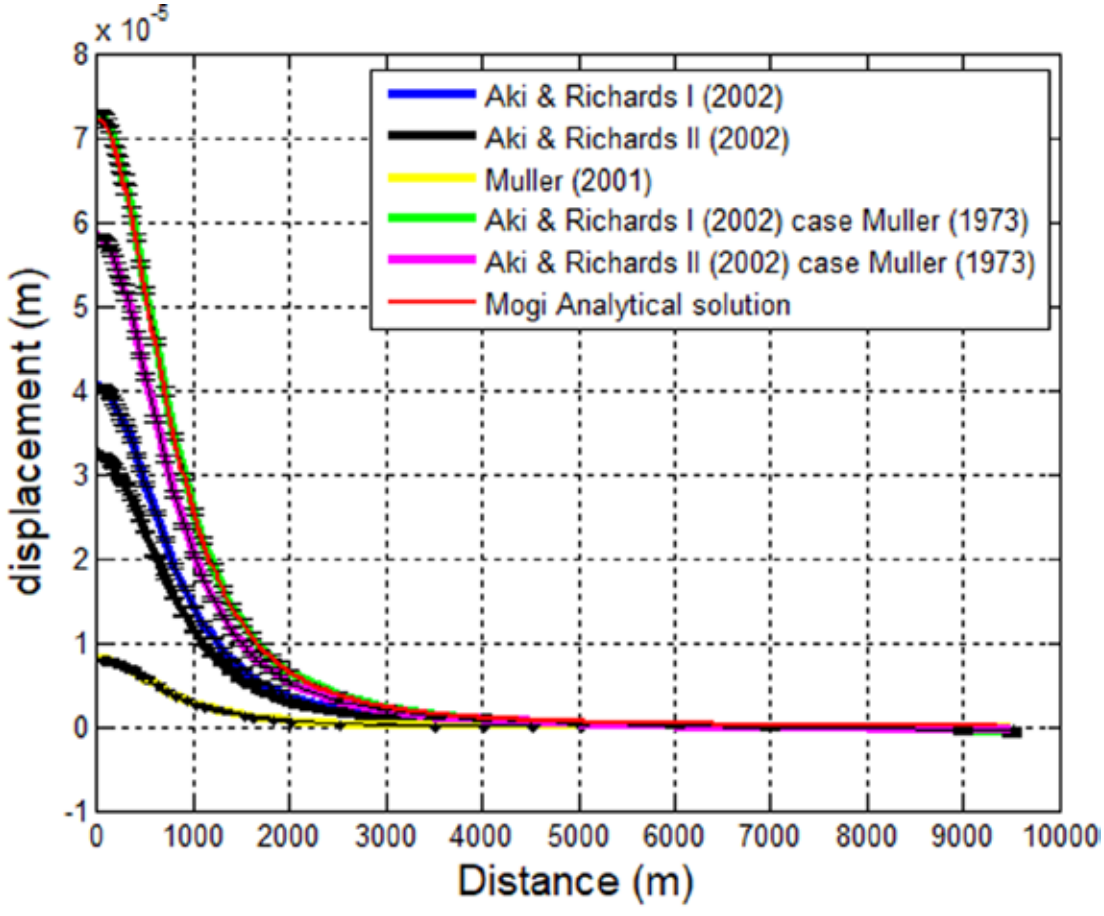

Figure 4. Same as Figure 3 but for the vertical static displacement.

Configuration	Source depth (km)	Sphere radius (m)	ΔP (MPa)
1	1	100	1
2	1	100	0.1
3	1	10	1
4	2	100	1

Table 1 – Geometric configuration for different test cases

Configuration (1)	$M_0 \times 10^{12}$ (Nm)	ΔV (m^3)
Aki & Richards I (2002)	5,23	301,9
Aki & Richards II (2002)	4,18	241,5
Muller (2001)	1,05	33 - 60
Aki & Richards I (2002) – case Muller (1973)	9,42	301,9
Aki & Richards II (2002) – case Muller (1973)	7,54	241,5

Table 2 - Values of M_0 and ΔV for the geometric configuration 1 of Table 1 for each of the considered approaches to convert the ΔP in moment magnitude (M_0). ΔV is computed from ΔP with Equations 5, 6 (*Aki & Richards I*), 8 (*Aki & Richards II*) and 11 (*Muller*). M_0 is calculated from Equation 3 for *Aki & Richards I* and *Aki & Richards II* solutions, while Equation (4) is used for *Aki & Richards I – case Muller* and *Aki & Richards II – case Muller. Muller* solution is obtained using both Equations (3) and (4) for the two different displacement of the crack sphere wall (inward/outward displacement and only outward displacement respectively).

Configuration (2)	$M_0 \times 10^{11}$ (Nm)	ΔV (m^3)
Aki & Richards I (2002)	5,23	30.2
Aki & Richards II (2002)	4,18	24.1
Muller (2001)	1,05	1.3 – 3.3
Aki & Richards I (2002) – case Muller (1973)	9,42	30.2
Aki & Richards II (2002) – case Muller (1973)	7,54	24.1

Table 3 – Same as Table 2 but for geometrical configuration 2 (Table (1).

Configuration (3)	$M_0 \times 10^9$ (Nm)	ΔV (m^3)
Aki & Richards I (2002)	5,23	0.3
Aki & Richards II (2002)	4,18	0.24
Muller (2001)	1,05	0.03 – 0.06
Aki & Richards I (2002) – case Muller (1973)	9,42	0.3
Aki & Richards II (2002) – case Muller (1973)	7,54	0.24

Table 4 - Same as Table 2but for geometrical configuration 3 (Table 1).

3. 4.1 - **Boundary conditions**

Some few remarks about the efficiency of boundary conditions implemented in EFISPEC3D code and on the decay of the vertical and horizontal permanent displacements in function of the distance from the epicenter. In EFISPEC3D absorbing boundaries are treated with Classical P1 paraxial approximation (Stacey, 1988) to prevent reflections and to guarantee stability in the numerical simulations.

The horizontal permanent displacement in Figure 3 is less attenuated with distance compared to the vertical displacement (Figure 4) which approaches a zero value at ≈3 km from the epicenter with the spherical source located 1 km deep. The boundary conditions work well for the vertical displacement while the solution for the horizontal components never converge to a zero value and show a progressive depart from the analytical solution. This influences the convergence of the horizontal displacement which never approaches a zero value. These remarks should be taken in account when using the code EFISPEC3D for computation of Green's functions or in forward problems.

3. 5 - **Conclusions**

I have investigated how the pressure exerted at the walls of a simple spherical source embedded at a certain depth can be related to the MT solution.

After defining the dimension of the sphere, the pressure value imposed on the sphere's wall has to be related to the volume variation of the sphere itself. Different approaches have been proposed in the literature to relate the volume variation and the pressure exerted at the sphere's wall (Aki and Richards, 2002; Muller, 2001). Once the volume variation computed, the moment magnitude (M_0) can be obtained by means of two different approaches (Eshelby, 1957; Muller, 1973). The retrieved moment magnitudes are used to perform some numerical simulations of the equivalent static displacement recorded at the free surface and compared to the analytical solution proposed by Mogi (1958). The results show that perfect match is obtained for the M_0 computation (Muller, 1973) which takes in account for the hydrostatic pressure at the source and

which correspond to the spherical source reviewed by Kumagai et al. (2014). The numerical simulations highlight the variability of the solutions. Remarkable differences in estimating the volume of the fluid/gas involved in the source process and the pressure variation at the source itself arise when considering different sorts of isotropic source mechanisms.
This paper aims at giving a clarified vision of the linking between the seismic moment of an isotropic source and the pressure variation exerted at the source itself.

Acknowledgements

The research leading to these results has received funding from the European Union Seventh Framework Programme (FP7/2007-2013) under the project NEMOH, grant agreement n° 289976.

References

Aki and Richards (2002). Quantitative Seismology, Second Edition, pp 700. (University Science Books.).

Anderson, E.M. (1937). IX.—The Dynamics of the Formation of Cone-sheets, Ring-dykes, and Caldron-subsidences. Proc. R. Soc. Edinb. *56*, 128–157.

Backus, M., G. and Mulcahy. (1976). Moment tensors and other phenomenological descriptions of seismic sources (Geophysical Journal of the Royal Astronomical Society).

Battaglia, M., Segall, P., Murray, J., Cervelli, P. and Langbein, J. (2003). The mechanics of unrest at Long Valley caldera, California: 1. Modeling the geometry of the source using GPS, leveling and two-color {EDM} data. J. Volcanol. Geotherm. Res. *127*, 195–217.

Bean, C.J., De Barros, L., Lokmer, I., Métaxian, J.-P., O' Brien, G. and Murphy, S. (2013). Long-period seismicity in the shallow volcanic edifice formed from slow-rupture earthquakes. Nat. Geosci. *7*, 71–75.

Bonafede, M., Dragoni, M. and Quareni, F. (1986). Displacement and stress fields produced by a centre of dilation and by a pressure source in a viscoelastic half-space: application to the study of ground deformation and seismic activity at Campi Flegrei, Italy. Geophys. J. R. Astron. Soc. *87*, 455–485.

Chaljub, E., Maufroy, E., Moczo, P., Kristek, J., Hollender, F., Bard, P.-Y., Priolo, E., Klin, P., De Martin, F., Zhang, Z., et al. (2015). 3-D numerical simulations of earthquake ground motion in sedimentary basins: testing accuracy through stringent models. Geophys. J. Int. *201*, 90–111.

Chouet, B. (1996). New methods and future trends in seismological volcano monitoring (Monitoring and mitigation of volcanic hazards Scarpa/Tilling (eds). Springer-Verlag Berlin Hieldelberg).

Chouet, B. (2003). Volcano seismology. Pure Appl. Geophys. *160*, 739–788.

Chouet, B. and Matoza, R.S. (2013). A multi-decadal view of seismic methods for detecting precursors of magma movement and eruption. J. Volcanol. Geotherm. Res. *252*, 108–175.

De Barros, L., Lokmer, I., Bean, C.J., O'Brien, G.S., Saccorotti, G., Métaxian, J.-P., Zuccarello, L. and Patanè, D. (2011). Source mechanism of long-period events recorded by a high-density seismic network during the 2008 eruption on Mount Etna. J. Geophys. Res. *116*.

Delaney, P.T. and McTigue, D.F. (1994). Volume of magma accumulation or withdrawal estimated from surface uplift or subsidence, with application to the 1960 collapse of Kilauea volcano. Bull. Volcanol. *56*, 417–424.

De Martin, F. (2011). Verification of a Spectral-Element Method Code for the Southern California Earthquake Center LOH.3 Viscoelastic Case. Bull. Seismol. Soc. Am. *101*, 2855–2865.

Eshelby, J.D. (1957). The determination of an ellipsoidal inclusion, and related problems. (Department of Physical Metallurgy, University of Birmingham).

Gilbert, F. (1971). Excitation of the normal modes of the Earth by earthquake sources. (Geophysical Journal of the Royal Astronomical Society).

Gilbert, J.S. and Lane, S.J. (2008). The consequences of fluid motion in volcanic conduits. Geol. Soc. Lond. Spec. Publ. *307*, 1–10.

Gottsmann, G. J.andRymer, H. and Berrino (2006). Unrest at the Campi Flegrei caldera (italy): a critical evaluation of source parameters from geodetic data inversion (Journal of Volcanology and Geothermal Research, 132-145).

Gudmundsson, A. (2006). How local stresses control magma-chamber ruptures, dyke injections, and eruptions in composite volcanoes. Earth-Sci. Rev. *79*, 1–31.

Harrington, R.M., and Brodsky, E.E. (2007). Volcanic hybrid earthquakes that are brittle-failure events. Geophys. Res. Lett. *34*.

Julian, B.R., Miller, A.D. and Foulger, G.R. (1998). Non-double-couple earthquakes 1. Theory. Rev. Geophys. *36*, 525–549.

Kumagai, H. and Chouet, B.A. (2000). Acoustic properties of a crack containing magmatic or hydrothermal fluids. J. Geophys. Res. Solid Earth *105*, 25493–25512.

Kumagai, H., Chouet, B.A. and Dawson, P.B. (2005). Source process of a long-period event at Kilauea volcano, Hawaii. Geophys. J. Int. *161*, 243–254.

Kumagai, H., Maeda, Y., Ichihara, M., Kame, N. and Kusakabe, T. (2014). Seismic moment and volume change of a spherical source. Earth Planets Space *66*, 7.

Madariaga, R. (2007). Seismic source theory (Elsevier), 4, chapter 4.02, 59 - 82.

Masterlark, T. (2007). magma intrusion and deformation predictions: sensitivities to the Mogi assumptions (Jour. of. Geoph. Res., B06419, doi: 10.1029/2006JB004860).

Maufroy, E., Chaljub, E., Hollender, F., Kristek, J., Moczo, P., Klin, P., Priolo, E., Iwaki, A., Iwata, T., Etienne, V., et al. (2015). Earthquake Ground Motion in the Mygdonian Basin, Greece: The E2VP Verification and Validation of 3D Numerical Simulation up to 4 Hz. Bull. Seismol. Soc. Am.

McTigue, D.F. (1987). Elastic stress and deformation near a finite spherical magma body: Resolution of the point source paradox. J. Geophys. Res. Solid Earth *92*, 12931–12940.

Mogi, K. (1958). Relations between the Eruptions of various volcanoes and the deformation of the ground surfaces around them. (Bulletin of the earthquake research institute, Vol. 36, pp. 99-134).

Muller, G. (1973). Seismic moment and long period radiation of underground nuclear explosions (Bull. Seism. Soc. Am. 63, 847-857).

Muller, G. (2001). Volume change of seismic sources from moment tensor (Bull. Seism. Soc. of America, 880-884).

Nakano, M., Kumagai, H. and Chouet, B.A. (2003). Source mechanism of long-period events at Kusatsu–Shirane Volcano, Japan, inferred from waveform inversion of the effective excitation functions. J. Volcanol. Geotherm. Res. *122*, 149–164.

Ohminato, T., Chouet, B.A., Dawson, P. and Kedar, S. (1998). Waveform inversion of very long period impulsive signals associated with magmatic injection beneath Kilauea volcano, Hawaii. J. Geophys. Res. Solid Earth *103*, 23839–23862.

Richards, P.G. (2005). Equivalent Volume Sources for Explosions at Depth: Theory and Observations. Bull. Seismol. Soc. Am. *95*, 401–407.

Stacey, R. (1988). Improved transparent boundary formulations for the elastic-wave equation. *78*.

Vavryčuk, V. (2015). Moment tensor decompositions revisited. J. Seismol. *19*, 231–252.

Wielandt, E. (2001). Basics of the volume-source model and its application in volcano seismology (Institute of Geophysics, University of Stuttgart).

Claudio Trovato, Italy
claudio.trovato@live.it

Affiliation under NEMOH
BRGM, French Geological Survey, Orlèans, France

Research theme under NEMOH
Moment tensor inversion of LP (Long Period) seismic events and quantification of uncertainties in their understanding

Since high school I was fascinated by the possibility of explaining the functioning of Earth and getting through the processes which, at all scales, interact and profoundly influence our daily life.

Deeply interested in nature and fascinated by the mountain chain of Alps I begun a career as a geologist at the University of Turin (Italy). I was introduced at all disciplines explaining the functioning of Earth from the very deep interior to surface processes. Natural risks and hazard have been a key point of my formation. I approached geotechnical and hydrogeological problems directly impacting (flows, debris) my native region (Piedmont) in Italy.

It was during my master degree which I developed a genuine interest for volcanology. A nine (9) months internship at the *Seismological and Volcanological observatory of Gwadeloupe* (Lesser Antilles) and one (1) month field trip on *Stromboli Island* (Italy) introduced me to volcanology and to the impacts which volcanic eruptions may have on inhabitants and society.

After my master dissertation on gas radon emissions on the volcanic dome of *La Soufriere* (Guadeloupe, Lesser Antilles) I moved to the field of volcano/seismology. I begun a PhD at the BRGM (French Geological Survey, Orlèans) under the European project NEMOH (*Numerical Experimental and stochastic Modelling Of volcanic processes and Hazard*). A three (3) years challenging subject on long period (LP) seismic events recorded on *Mt. Etna* (Italy) and the several opportunities offered by an international network of experts in all different fields of volcanology renewed my passion for science and volcanoes.

After completing my PhD, I am actually seeking new opportunities to couple both my field and laboratory experiences and be directly involved in the surveillance of an active volcano.

Chapter 4

Werner Wittmann, Germany

wew1@hi.is

Affiliation under NEMOH

Nordvulk, Institute of Earth Sciences, University of Iceland, *Reykjavík,* Iceland

Research theme under NEMOH

Modelling of volcano deformation and heat-flow variations at volcanoes

NOTE: due to personal reasons, Werner Wittmann could not contribute to this volume. The reader is addressed to the following paper for Werner's developments under NEMOH: Wittmann, W., Sigmundsson, F., Dumont, S., and Lavallée, Y., Post-emplacement cooling and contraction of lava flows: InSAR observation and a thermal model for lava fields at Hekla volcano, Iceland. J. Geophys. Res. Solid Earth, 2017, d.o.i. 10.1002/2016JB013444.

Having a background in physics oriented towards geophysics, I got the great opportunity to combine in NEMOH theoretical and mathematical aspects with my programming and modeling interests. I finished my studies at the University of Würzburg in a geophysical laboratory, where I measured and modeled the viscosity of lava from Gígjökull, part of Eyjafjallajökull volcano in Iceland, the eruption of which resulted in 2010 in the closure of a considerable part of the European airspace. The project included reactivation and use of the rotational viscometer. Accepting the position in NEMOH meant moving to Iceland, a country with unique possibilities for direct observation of volcanic and tectonic processes, with the perspective of working at the renowned University of Iceland. My project was part of a Ph.D. under the supervision of Freysteinn Sigmundsson. The main aspect was to understand how thermal contraction contributes to deformation measured from space by means of GPS and InSAR. The lava flows of Hekla volcano in South Iceland offered accessibility prohibited by magmas at depths, and became the primary focus of my studies. Several weeks of GPS field work there and a few other locations both in Iceland and at the Taupo Volcanic Zone, New Zealand, and two NEMOH field schools on Stromboli and in South Iceland, were enlightening. Nevertheless, most of the work required data evaluation and modeling. Training in InSAR data processing at the University, and an InSAR conference in Trieste, gave me additional background. A University course in measuring and modeling geodynamics, the NEMOH network school in Bristol in forward modeling, and the NEMOH short course in Barcelona on parallel programming, were of great help in developing a one-dimensional model that calculates subsidence. Since the end of my contract with NEMOH, I am part of the GEOthermal Research Group (GEORG) of FUTUREVOLC. During my leisure time I read books of all kinds, may it be (classical) novels, technical IT books, books about sports or politics. Solving puzzles of all kinds (e.g. projecteuler.net, cross-word puzzles etc.) is a great way to get distracted. I also like to spend a considerable time exercising, running, hiking, biking and climbing.

Chapter 5

Seismic propagation effects in the upper volcanic edifice

Beatriz Martínez Montesinos

University College Dublin, Dublin, Ireland

Tutorship: Christopher J. Bean[1,2], Ivan Lokmer[1]

[1] *University College Dublin, Dublin, Ireland*
[2] *Dublin Institute for Advanced Studies (DIAS), Dublin, Ireland*

Abstract

A seismogram contains information about the seismic source and the wave path. Understanding the path effect is important for both source inversions and geophysical investigation of the Earth's properties at depth. In volcanic environments, the correct interpretation of the signals is critical for a determination of the internal state of the volcano. My work presents an application of the adjoint methodology (Tromp et al., 2005) to investigate seismic wave propagation effects in the upper volcanic edifice. We did this by calculating sensitivity kernels, that is, by investigating the sensitivity of different portions of a seismogram to different parts of the velocity model. In particular, we examined the influence of near-surface low-velocity volcanic structure on the recorded signals. We simulated examples for Mount Etna, Italy, and calculated synthetic seismograms in a 2D heterogeneous model with topography, for sources with different dominant frequency and locations. Then, we calculated the adjoint wavefield by time-reversing the calculated seismograms and playing them back into the medium as seismic sources acting simultaneously at the original receiver positions. As a last step, we combined the forward and adjoint wavefields to calculate the travel time sensitivity kernels of Mount Etna. In order to capture a complex wave travel path, we examined the sensitivity of different portions of a seismic wavefield (i.e., different time-windows on a seismogram) to different parts of the structural models. Results show the importance of the shallowest velocity structure in shaping the recorded seismograms. This means that we cannot ignore the heterogeneity of the upper volcanic edifice by the time of interpreting the observed signals.

Keywords: Volcanic edifice, numerical simulations, near-surface, sensitivity kernels

5. 1 - Introduction

Complex stratigraphy, plumbing system filled with magmatic fluids, pronounced topography and a broad set of possible source scenarios can be found in most of volcanoes [Figure 1]. In order to obtain information about the internal state of a volcano, volcano seismology tries to understand how the above elements are reflected in the signals recorded at the seismic network. For instance, long period (LP) seismicity, which refers to seismic events with frequency in the range between 0.2 and 2 Hz, is commonly associated with magmatic and hydrothermal activity, whose occurrence at shallow depths can be interpreted as an indicator of an unrest episode (e.g., Chouet, 1996).

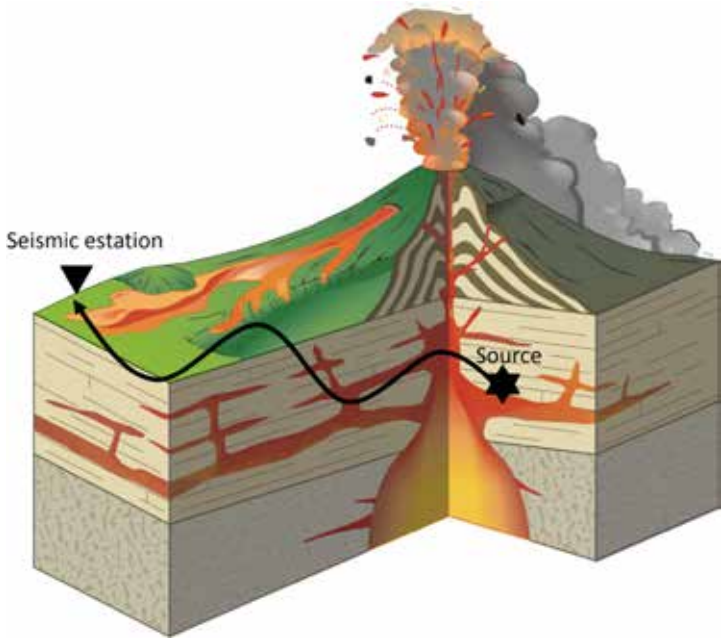

Figure 1. Cartoon of a possible volcanic scenario.

Notwithstanding the long wavelengths of LP events, the corresponding wavefield can be significantly distorted by near-surface structure and surface topography (Neuberg et al., 2000, Bean et al., 2008, O'Brien et al., 2009). Figure 2 shows an example of simulation where we observe the importance of the propagation medium in shaping the signals produced by the same source.

That is, the signals hold information about both the seismic source and the propagation path. Our objective is to improve our ability to understand path effects, in order to effectively remove their contributions and obtain seismograms that are representative of the physical processes acting within the volcano.

5. 2 **- The approach**

In a previous work, Bean et al., (2008) accounted for near-surface velocity structure in the computation of synthetic seismograms and sensitivity kernels to help with the interpretation of source inversion results for LP seismic events at Mount Etna. Here we extend the above work to make 2D numerical simulations of seismic wave propagation in the presence of topography and heterogeneous velocity structure to investigate the relationship between different parts of a seismogram and different portions of the structural model [Figure 3]. Then, we take advantage of the adjoint methodology presented in Tromp et al., (2005) to study the sensitivity of seismograms with respect to P and S wave velocities by calculating the travel time sensitivity kernels. These kernels will show the regions of the velocity model that mostly condition the wavefield impinging at the stations within the seismogram time window under investigation.

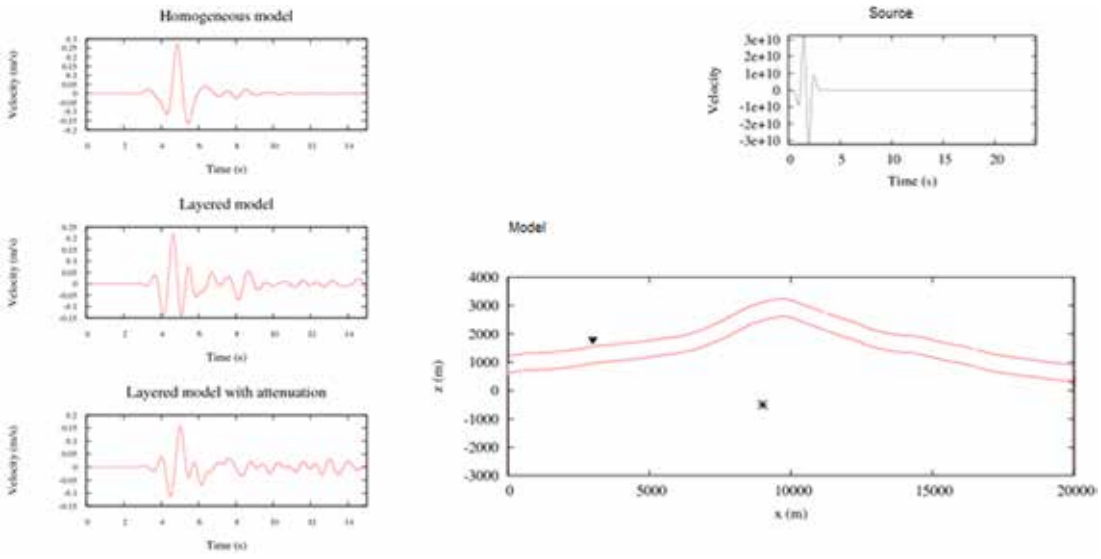

Figure 2. Example of simulation. Panels at the right indicate the source time function (top), and the source (asterisk) and receiver (triangle) locations within the 2D volcano model (bottom). The left panel shows the three different synthetics seismograms resulting from playing the same source in three different velocity models. From top to bottom, seismograms have been obtained from simulations calculated for (a) a homogeneous velocity model; (b) homogeneous velocity structure with a shallow, low-velocity layer, and (c) the same as (b), but also accounting for anelastic attenuation.

5. 3 **- The adjoint methodology**

Adjoint methodology consists of time reversing the recorded signals and using them as a seismic source located at the receiver position (adjoint source). Sensitivity kernels refer to the sensitivity of a seismogram with respect to the model parameters. This sensitivity may be obtained by means of two numerical simulations for each seismic source: one calculation for the current model (forward) and a second (adjoint) calculation that uses time-reversed signals at the receivers as fictitious sources determined by velocities obtained in the first simulation. Construction of travel time sensitivity kernels for the P-SV wave arrivals is based upon the interaction between forward and adjoint wavefield (Tromp et al., 2005).

Figure 4 shows an example from a simulation in a homogeneous half space. The source time function is a Ricker wavelet with dominant frequency of 5 Hz; the source mechanism is isotropic (i.e., an explosion). Travel time sensitivity kernels are shown with respect to density, P-wave velocity and S-wave velocity.

To run our simulations and to calculate the sensitivity kernels by means of this methodology we use the 2D-wave propagation software SPECFEM2D (Tromp et al., 2008) and run it on the Fionn Supercomputer of the Irish Centre for High-End Computing (ICHEC).

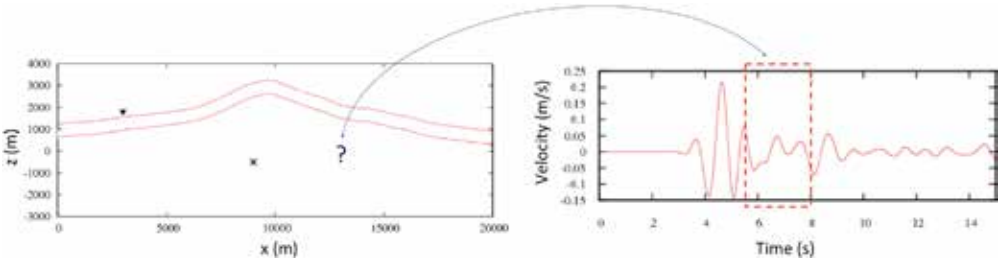

Figure 3. We want to study the relationship between different parts of the signal and different parts of the model. In other words, we would like to understand which portions of the model contribute mostly in shaping a given time window of the signal under investigation.

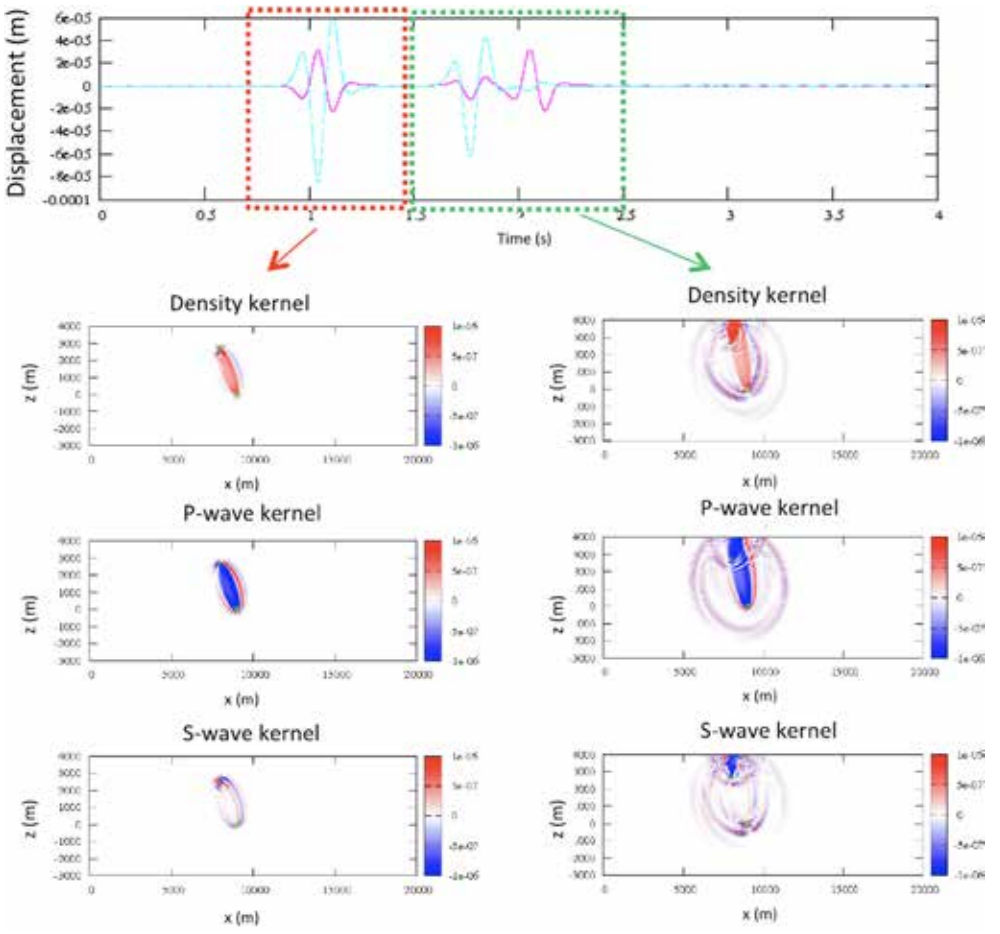

Figure 4. Example of simulation in a homogeneous half space. The upper panel shows the synthetic signal generated by an explosive source, whose source time function is a Ricker wavelet with dominant frequency of 5 Hz. Vertical and horizontal components of the displacement are plotting in blue and pink color, respectively. Source and receiver are located at coordinates (9000,0) and (8000,3000) meters, respectively. Below the signal, the sensitivity kernels corresponding to time slices [0.7-1.5] seconds and [1.5-2.5] seconds are shown at the left and right columns, respectively.

5. 4 - **Models and data**

We use a *20 km x 6,255 km* 2D model of Mount Etna, whose digital topography was obtained from http://www.cgiar-csi.org. We consider different 2D velocity models and different source mechanisms and locations. The seismic network consists of 15 recording stations distributed along the surface every *1000 m* (black triangles in Fig. 5).

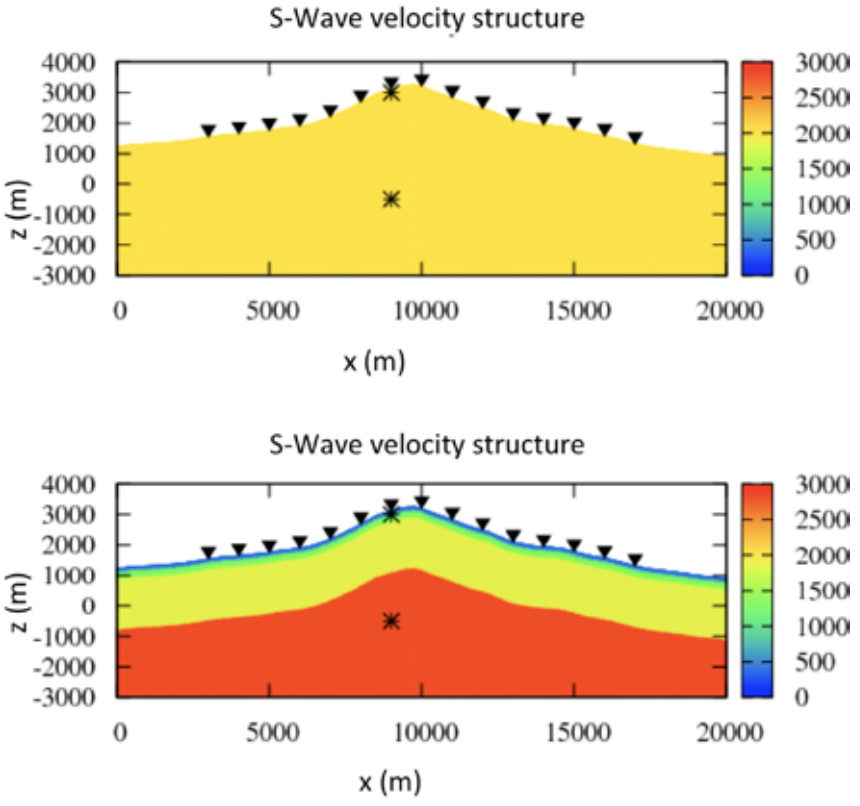

Figure 5. S-Wave velocity models considered for our simulation. Recording stations are denoted by black triangles and source positions by asterisks.

As an example, we show here simulations corresponding to two different velocity models. The first is a homogeneous one, with density $\rho = 2384\ kgm^{-3}$, P-Wave velocity $v_p = 3500\ ms^{-1}$ and S-Wave velocity $v_s = 2000\ ms^{-1}$. The second model is a heterogeneous one, and is obtained by combining the S-wave velocity structures of Cauchie et al., (2012) and Chiarabba et al., (2000) for the top *2000 m* and half space, respectively. The corresponding P-wave velocity structure is obtained using a Poisson ratio of *0.25*. From the P-wave velocity model we finally derived the density model using Gardner's relationship: $\rho = 310 v_p^{0.25}$ (Gardner et al., 1974) [Figures 5, 6].

Thickness (km)	S-wave Velocity (km/s)
H_1 = 0.06	Vs_1 = 0.43
H_2 = 0.06	Vs_2 = 0.77
H_3 = 0.06	Vs_3 = 1.13
H_4 = 0.06	Vs_4 = 1.33
H_5 = 0.06	Vs_5 = 1.33
H_6 = 0.06	Vs_6 = 1.60

S-wave velocity profile obtained from the grid search inversion procedure

Figure 6. Table from Cauchie et al., (2012), reporting the S-wave velocity structure derived from the probabilistic inversion of Rayleigh-wave dispersion data.

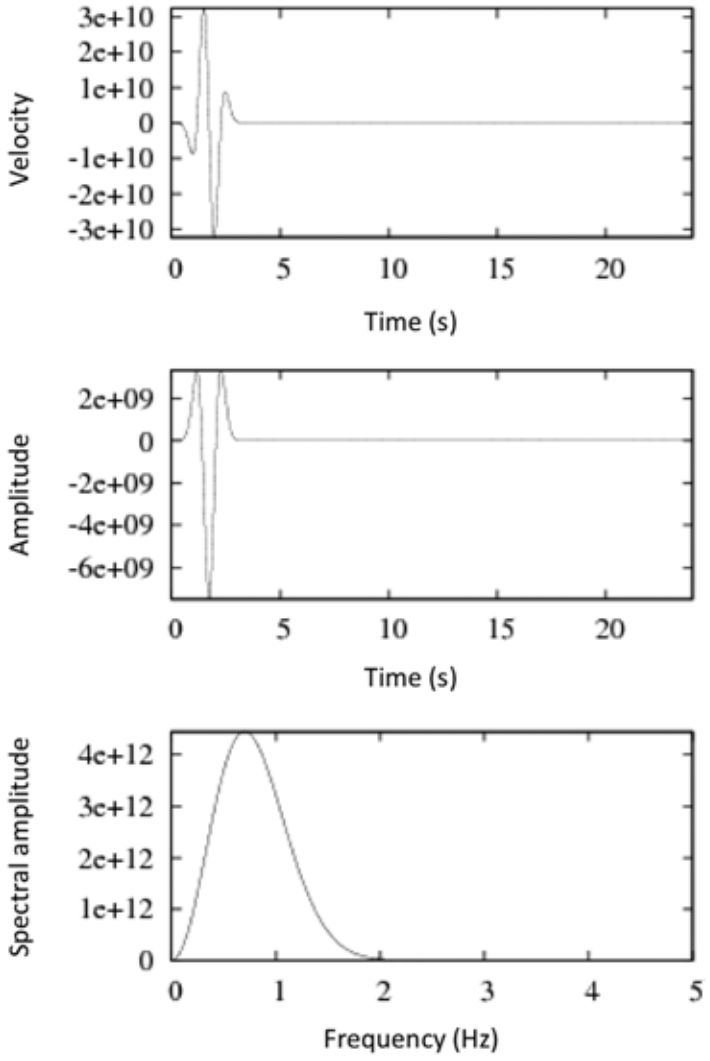

Figure 7. Vertical components of the time function (horizontal component is zero) and amplitude spectrum of the source used in our simulations (Ricker wavelet - 0.7 Hz).

The source considered here is a Ricker wavelet applied as a vertical, single force with dominant frequency of *0.7 Hz* [Figure 7]. For each model we calculated synthetic seismograms considering two different source depths close to the summit: one at *113 m* and another at *3613 m*, denoted by black stars in Figure 5. Once obtained the synthetic signals, we calculated the corresponding travel time sensitivity kernels for successive 3-seconds-long time windows sliding along our seismograms.

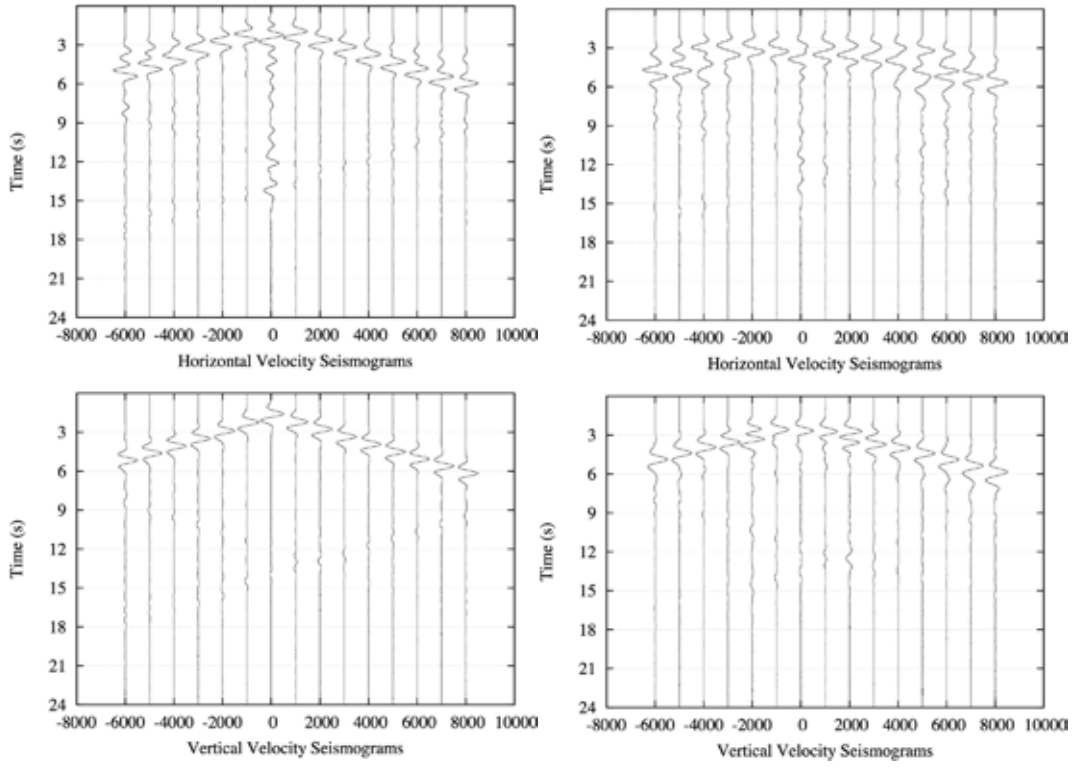

Figure 8. Velocity seismograms corresponding to a simulation in the homogeneous model for a Ricker wavelet source with dominant frequency 0.7 Hz applied as a vertical force at 113 m (left column) and 3613 m (right column) depth. Source locations are shown as black stars and station locations as black triangles in Figure 5. The x axes indicate the relative horizontal station positions from the source. Traces are individually normalized.

5. 5 **- Results**

Figures 8 and 9 show the individually-normalized velocity seismograms corresponding to simulations in the homogeneous and layered models, respectively. We note that layers have a significant influence on the recorded traces. Shallow sources in a layered model have longer duration seismograms (even for short duration sources) and this effect increases with increasing distance from the source. We observe that the source signature is highly distorted particularly for shallow sources.

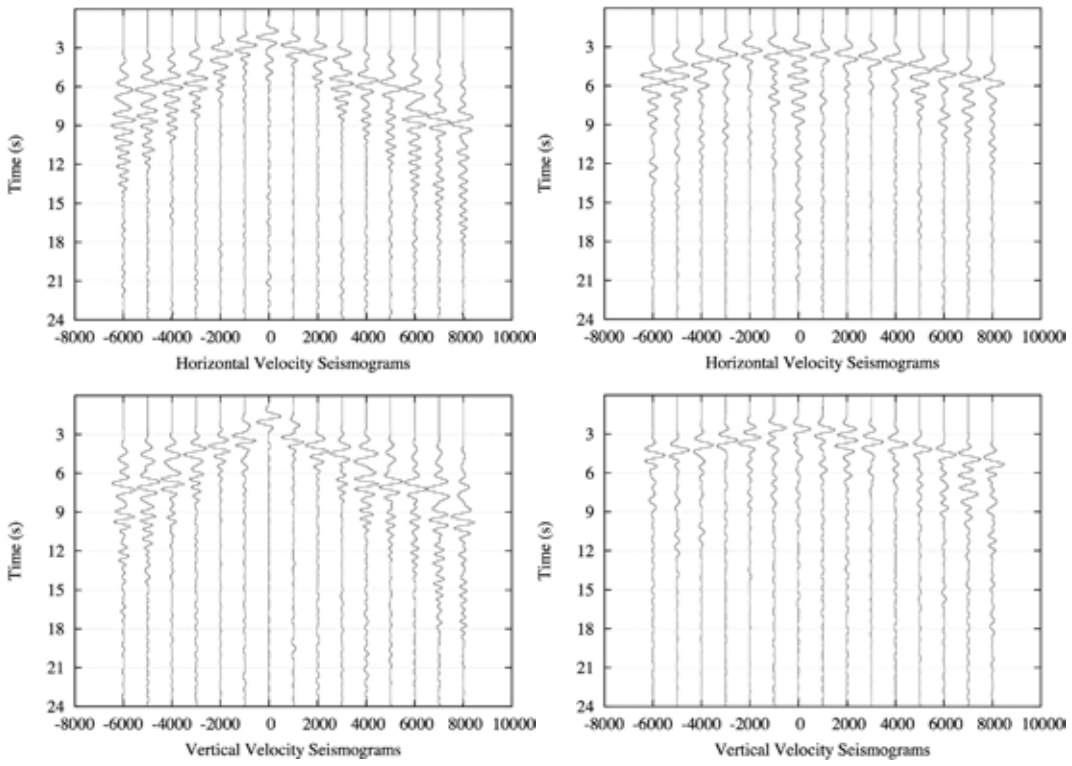

Figure 9. As in Figure 8, but for the layered model.

We then proceeded to calculating P and S wave sensitivity kernels for the above simulations. These kernels show the region of the velocity model that affects the wavefield which is arriving at a given station within a defined time window. The kernels are displayed using a colour scale which is proportional to the root mean square amplitude of the corresponding seismogram, in order to facilitate comparisons between successive intervals of time

For instance, Figure 10 shows the P-wave and S-wave velocity kernels for consecutive 3-seconds time windows of the seismogram generated by the shallow source in the homogeneous model and recorded by the station located at relative horizontal position *-6000 m*. Figure 11 shows the P- and S-wave velocity kernels for consecutive 3-seconds time windows of the seismogram generated by the deeper source in the homogeneous model and recorded by the station located at relative horizontal position *-2000 m*.

We observe that the first seconds of seismograms are mainly controlled by the area between the source and the receiver appearing with the typical banana-doughnut shapes (Tromp et al., 2005) distorted by topography effects. Figures 12 and 13 show the sensitivity kernels as in Figures 10 and 11, but for the layered model. Waves are trapped in the low velocity layers, which are the cause of the longer duration seismograms and the distortion of the signals.

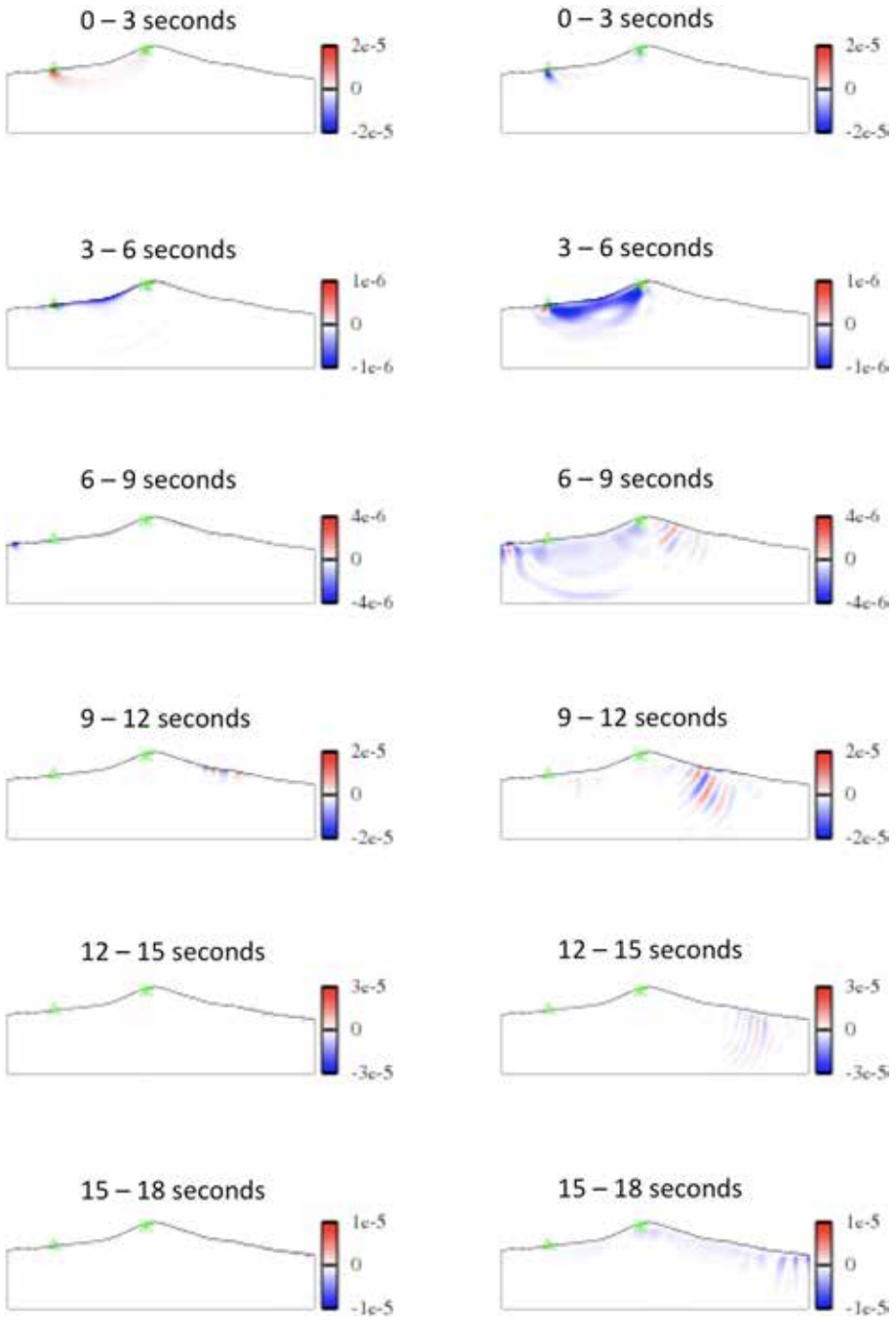

Figure 10. P wave (first column) and S wave (second column) velocity kernels for each 3 seconds time slice of the seismogram generated by the shallow source in the homogeneous model and recorded from the station located at relative horizontal position -6000 m (first station from the left).

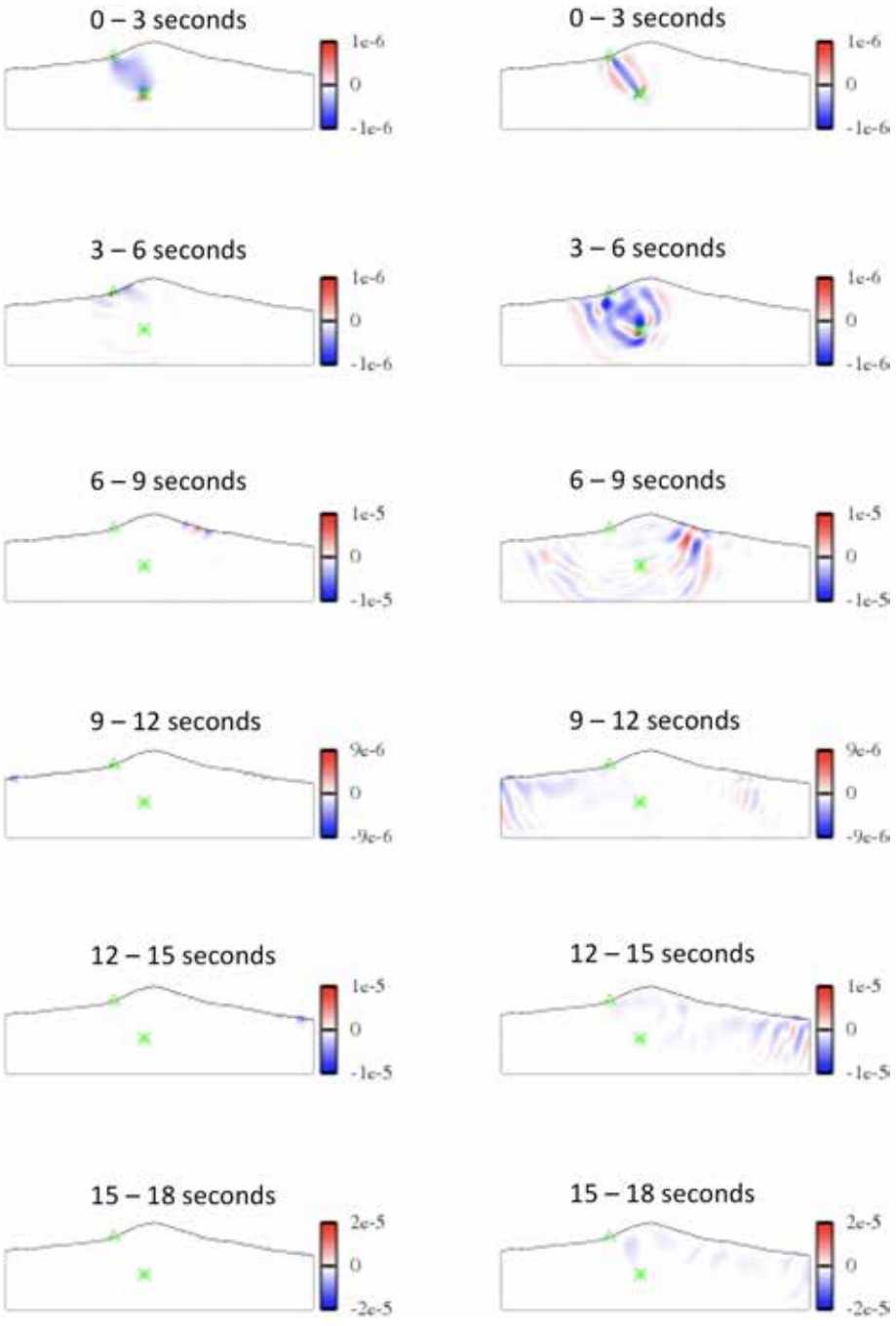

Figure 11. P wave (first column) and S wave (second column) velocity kernels for each 3 seconds time slice of the seismogram generated by the deeper source in the homogeneous model and recorded from the station located at relative horizontal position -2000 m (fifth station from the left).

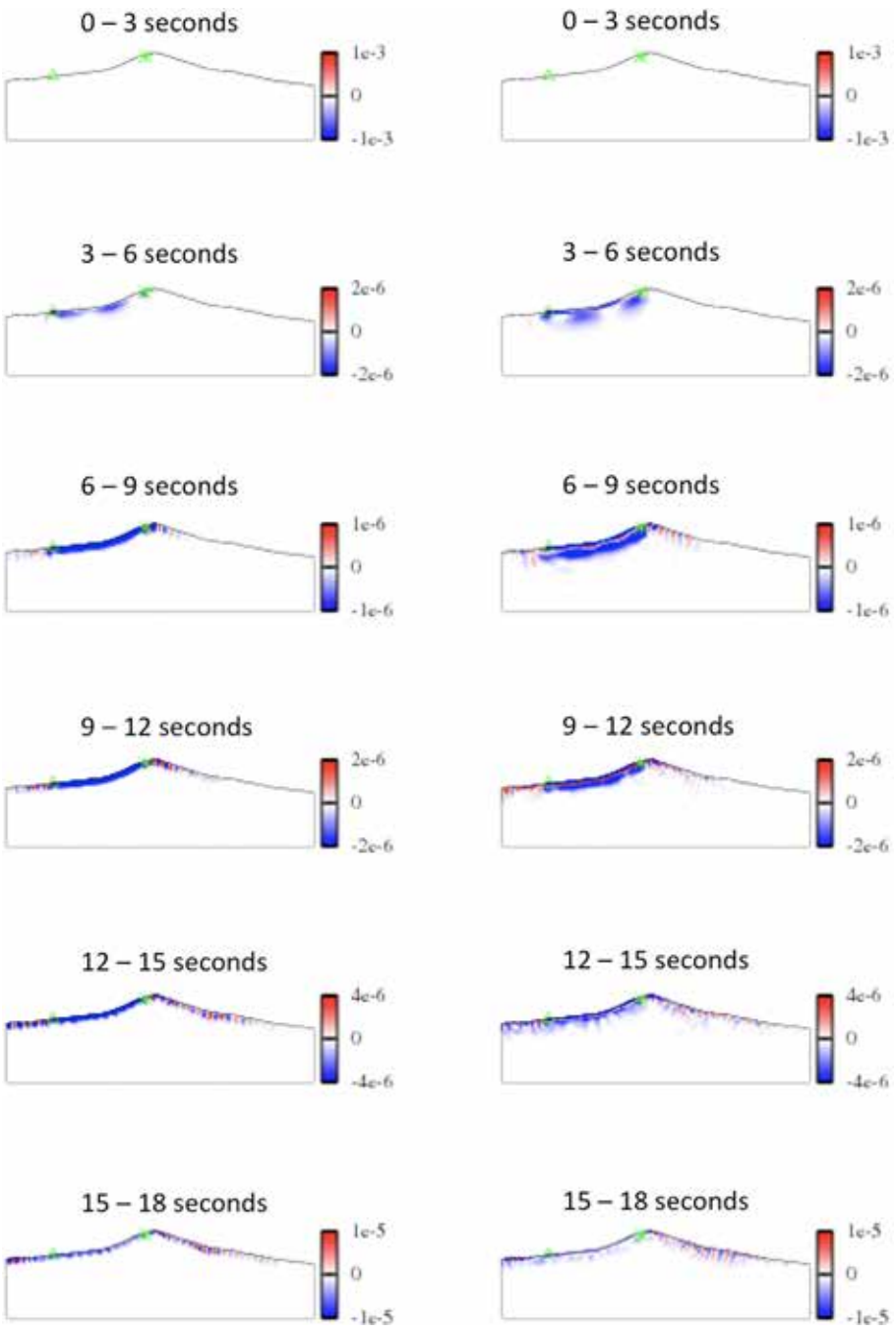

Figure 12. P wave (first column) and S wave (second column) velocity kernels for each 3 seconds time slice of the seismogram generated by the shallow source in the layered model and recorded from the station located at relative horizontal position -6000 m (first station from the left).

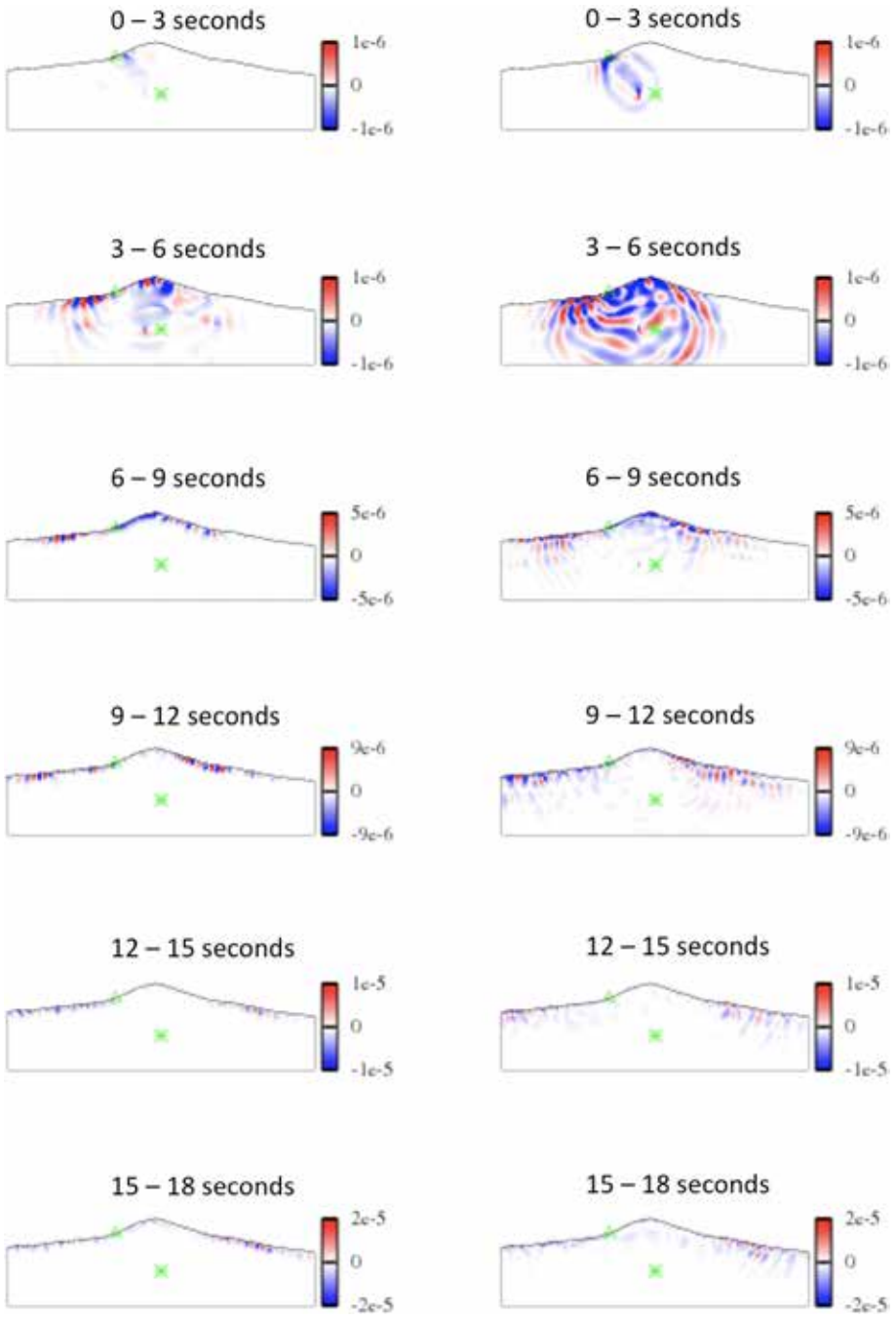

Figure 13. P wave (first column) and S wave (second column) velocity kernels for each 3 seconds time slice of the seismogram generated by the deeper source in the layered model and recorded from the station located at relative horizontal position -2000 m (fifth station from the left).

5. 6 **- Conclusions**

Results show the importance of the shallow velocity structure in shaping the recorded seismograms. This implies that we cannot ignore the heterogeneities of the upper volcanic edifice by the time of inverting the recorded ground motion for deriving the mechanism of shallow sources. Improving our knowledge of the near-surface velocity structures is thus a necessary step toward a detailed determination of the force systems acting at those shallow sources.

Acknowledgements

I thank Gilberto Saccorotti for the constructive review of this text. The research leading to these results has received funding from the European Union Seventh Framework Programme (FP7/2007 2013) under the project NEMOH, grant agreement n° 289976.

References

Bean, C., Lokmer, I. and O'Brien, G. (2008). Influence of near-surface volcanic structure on long-period seismic signals and on moment tensor inversions: Simulated examples from Mount Etna. J Geophys. Res 113: B08308, doi: 10.1029/2007JB005468.

Cauchie, L. and Saccorotti, G. (2012). Probabilistic inversion of Rayleigh-wave dispersion data: an application to Mt. Etna, Italy. Journal of Seismology. 04/2013; 17(2): 335-346. doi: 10.1007/s10950-012-9323-6.

Chiarabba, C., Amaro, A. and Boschi, E. (2000). Recent seismicity and tomographic modeling of the Mount Etna plumbing system. Geophys Res 105: NO. B5, PAGES 10,923-10,938.

Chouet, B. (1996). Long-period volcano seismicity: Its source and use in eruption forecasting. Nature, 380, 309 - 316, doi: 10.1038/380309a0.

Gardner, G. H. F., Gardner, L. W. and Gregory, A. R. (1974). Formation velocity and density – The diagnostic basics for stratigraphic traps. Geophys 39, 770-780.

Neuberg, J. and Pointer, T. (2000). Effects of volcano topography on seismic broadband waveforms. Geophys. J. Int., 143, 239 - 248, doi: 10.1046/j.1365-246x.2000.00251.x.

O'Brien, G. S. and Bean, C. J. (2009). Volcano topography, structure and intrinsic attenuation: Their relative influences on a simulated 3D visco-elastic wavefield. J. Volcanol. Geotherm. Res., doi: 10.1016 / j.jvolgeores.2009.03.004.

Tromp, J., Tape, C. and Liu, Q. (2005). Seismic tomography, adjoint methods, time reversal and banana-doughnut kernels. Geophysical Journal International, v. 160, p. 195-216.

Tromp, J., Komatitsch, D. and Liu, Q. (2008). Spectral-Element and Adjoint Methods in Seismology. COMMUNICATIONS IN COMPUTATIONAL PHYSICS, 3(1), 32.

Beatriz Martínez Montesinos, Spain
bmartinezmontesinos@hotmail.com

Affiliation under NEMOH
University College Dublin, Dublin, Ireland

Research theme under NEMOH
Improved Description of Path Effects on Volcanoes Using Numerical Modelling Tools

My name is Beatriz Martínez Montesinos. I was born in Barcelona, Spain. I worked as a computer programmer in the Information Technology sector and I gained a Bachelor Degree in Mathematics from the University of Barcelona in 2010. After several years, to pursue my interest in research, I decided to leave my job to develop my knowledge of Mathematics obtaining a Master of Science Degree in Advanced and Professional Mathematics in 2012. My goal then was to find a place where I could apply my studies in mathematics and my experience as software developer in the field of Earth Sciences.

When I heard about the NEMOH Project while in University of Barcelona I knew immediately it would offer the perfect opportunity for me to apply the experiences and skills I had acquired at that point. I joined the NEMOH Project in University College Dublin, Ireland, in September 2013.

In the Seismology Laboratory of the Geophysics Group in the School of Geological Sciences UCD I was fortunate to be with Prof. Christopher J. Bean and Dr. Ivan Lokmer who, together with the rest of the group in the lab, infected me with their enthusiasm for the physics of wave propagation. Under their supervision I developed numerical simulations for wave propagation through complex mediums with topography and calculated sensitivity kernels to examine the influence of near-surface low-velocity volcanic structure on the recorded seismic data.

During the two years I was in the project, I participated in various courses and workshops in different European institutions, in the process increasing my knowledge of volcanology. In addition, I enhanced my skills in high level programming doing my project secondments in the Barcelona Supercomputing Center, in collaboration with the Computer Applications in Science & Engineering Department of BSC. Being in Dublin of course I managed to improve my English too! I also had the opportunity to participate in and present at scientific conferences and to meet a large number of scientists from around the world.

Following my scientific interest in the field of seismology and high level programming I am now doing a PhD in the Johannes Gutenberg University of Mainz (Germany) under the Horizon 2020-Marie Skłodowska-Curie Project CREEP (Complex RhEologies in Earth dynamics and industrial Processes). My project consists of developing new 3D software to model hydrofracturing in heterogeneous viscoelastoplastic rocks using massively high-performance parallel computers. The aim is to understand how stress states and heterogeneities affect crack propagation and apply it in the field of geothermics.

Chapter 6

Methods for estimating the nature of ice-covered geothermal areas and other subglacial heat sources

Hannah Iona Reynolds

Nordvulk, Institute of Earth Sciences, University of Iceland, Reykjavík, Iceland

Tutorship: Magnús Tumi Gudmundsson[1], Freysteinn Sigmundsson[1], Gudni Axelsson[2]

[1]*Nordvulk, Institute of Earth Sciences, University of Iceland, Reykjavík, Iceland*
[2]*Iceland GeoSurvey (ÍSOR), Reykjavík, Iceland*

Abstract

Thermal signals from sub-surface magmatic sources are difficult to quantify, as the measurement of heat flux from the ground to the atmosphere is subject to large uncertainties. Iceland is home to several volcanically and geothermally active ice-covered volcanoes, e.g. Grímsvötn, Katla and Eyjafjalljökull. Depressions are observed on the glacier surface in these areas, which form due to basal melting and are known as ice cauldrons. These features are monitored using airborne radar altimeter profiling. The melting ice acts as a calorimeter, providing a unique opportunity to quantify surface heat flux to a much improved accuracy.

The heat sources responsible for the formation of ice cauldrons may either be: 1) small subglacial eruptions; or 2) increased geothermal activity induced by a shallow magmatic intrusion. Numerical modelling can be used to investigate the transfer of heat within hydrothermal systems that form around shallow magmatic intrusions, and the results compared to observed thermal data. Intrusions of various geometries and depths can be simulated, and the effect of country-rock permeabilities and initial temperature gradients explored in relation to heat flux magnitudes and the timescales and spatial extent of associated surface anomalies. Modelling results have implications for the interpretation of thermal signals observed at ice-covered volcanoes, highlighting the importance of reservoir/bedrock thermal state prior to intrusion.

Keywords: Geothermal activity, heat flux, numerical modelling, volcano-ice interaction, ice cauldrons.

6. 1 **- Introduction**

Geothermal systems generally form in areas with relatively high heat flow, and high permeability to allow for fluid circulation. Stimac et al. (2015, p. 800) list the principle categories of geothermal resources as follows: (1) igneous systems related to high permeability areas over magmatic intrusions within the shallow crust; (2) tectonic systems link to fluid circulation along fracture systems; (3) deep sedimentary aquifers and geo-pressured systems; (4) engineered geothermal systems; and (5) supercritical systems. This work principally discusses magmatic intrusion-related

geothermal systems, where cool groundwater is heated up within permeable bedrock, and a convecting system is established where rising groundwater transports heat from magma reservoirs or intrusions to the surface (e.g. Hayba and Ingebritsen, 2007; Hurwitz et al., 2003). Monitoring geothermal activity at volcanoes gives necessary insight into the associated volcanic and phreatic hazards, and the hydrothermal systems below. Fumaroles, hot springs and bubbling mud pools characterise the surface expression of many geothermal areas (e.g. Hochstein and Bromley, 2001 and 2005), however thermal signals from subsurface magmatic sources are usually difficult to quantify since the measurement of heat flux from the ground is subject to large uncertainties due to heat loss to the atmosphere. Subglacial geothermal fields present a unique opportunity to calculate the surface heat flux to a much improved accuracy, as all of the thermal energy is spent melting ice (Jarosch and Gudmundsson, 2007; Jarosch et al., 2008).

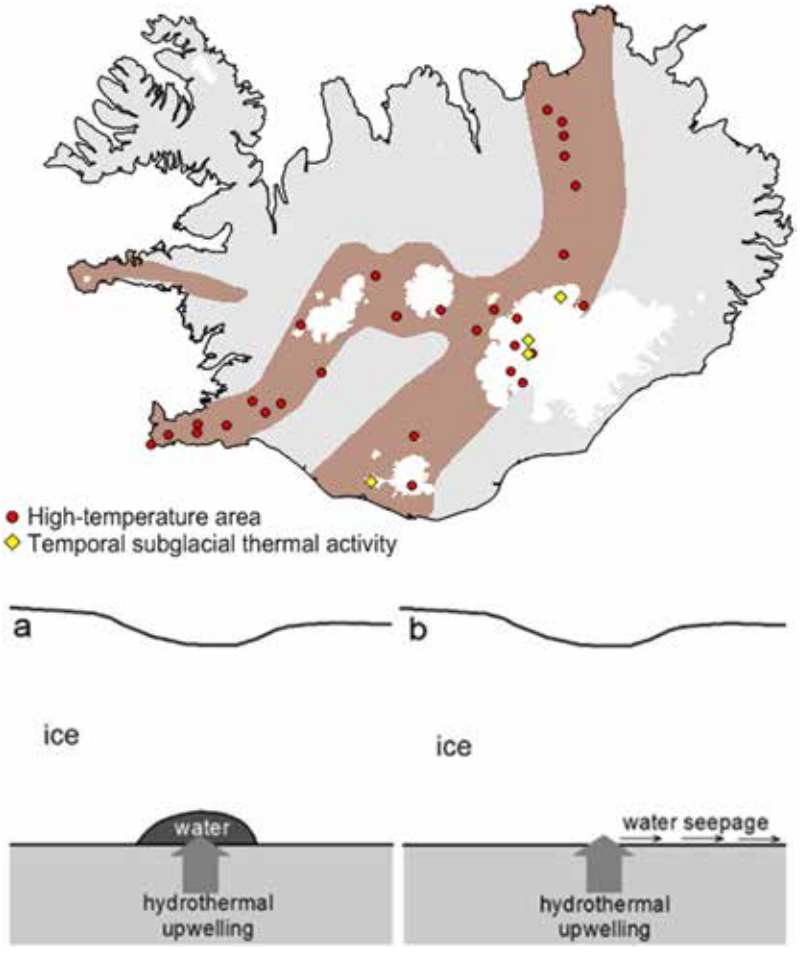

Figure 1. Map of high-temperature geothermal areas in Iceland (data from Orkustofnun, 2013), and temporal subglacial thermal activity. Schematic diagram of ice cauldron formation with (a) accumulation of meltwater and (b) continuous drainage (after Gudmundsson et al., 2007).

Thermal signals are observed at many ice covered volcanoes in Iceland (figure 1) and worldwide (Major and Newhall, 1989). Notable examples outside Iceland include the ice caves observed at Mount St. Helens and Mount Rainier in the U.S.A. (Kiver and Mumma, 1971; Anderson et al., 1998; Zimbelman et al., 2000), and at Mount Erebus in Antarctica (Giggenbach, 1976). Several thermal features evolved at Redoubt volcano, Alaska, in the build-up to the 2009 eruption, including ice surface depressions, wide-spread subsidence, and punctures created by steam (Bleick et al., 2013).

Ice cauldrons are shallow depressions which form on the glacier surface due to basal melting, as a manifestation of heat flux from below; the melting ice acts as a calorimeter, allowing estimations of heat flux magnitude to be made. The source of heat may either be a subglacial eruption or geothermal activity. Meltwater may drain continuously from below the cauldron, however if it gradually accumulates this presents a jökulhlaup risk (figure 1). Subglacial eruptions produce large volumes of meltwater in a short period due to their high rate of heat output, for example the subglacial eruption at Gjálp in 1996 produced meltwater which collected in the subglacial lake at Grímsvötn, to drain five weeks later causing a jökulhlaup (Gudmundsson et al., 1997). Several types of thermal signals are observed, with the onset time, duration, and location of the resulting cauldrons all being important factors. Geothermally generated cauldrons tend to be located above known geothermal fields, often around the edges of calderas, and produce a sustained signal over months, years or decades. Ice cauldrons resulting from subglacial eruptions have a high initial growth rate, generated by a thermal pulse as ice is in contact with magma, followed by a sharply decreasing melt rate as the eruption deposit cools. Thermal signals at ice-covered volcanoes are well-observed in Iceland (Björnsson and Guðmundsson, 1993; Jarosch and Gudmundsson, 2007). Two such examples are Grímsvötn and Bárðarbunga, two subglacial central volcanoes located beneath Vatnajökull ice cap.

Grímsvötn is a subglacial volcano which comprises three overlapping calderas; it is one of the most geothermally active calderas in the world, with sustained heat output for centuries in the Gigawatts range which is easily recognised by the many cauldrons which appear to form preferentially around the rim of the caldera (Björnsson, 1988) (figure 2). Grímsvötn has erupted three times in the past twenty years, the effects of which are visible as temporal variations in the ice surface elevation data. However, separate thermal anomalies are observed in areas unaffected by erupted products, due to increased geothermal activity (Jarosch and Gudmundsson, 2007; Reynolds et al., 2014).

The 2014-15 events at Bárdarbunga offered another display of thermal signals manifested in the surface of Vatnajökull, thus providing another opportunity to study magma-related thermal signals. Increased seismic activity was observed within the Bárdarbunga caldera on 16 August 2014. During the following two weeks, the seismic activity and deformation indicated the path of a lateral dyke for more than 45 kilometres (Sigmundsson et al., 2015). The main eruption began on 31 August at Holuhraun, north of Vatnajökull glacier, which lasted for 6 months (Gíslason et al., 2015). Ice subsidence was observed within the Bárdarbunga caldera during the course of the eruption, with no evidence of significant basal melting, representing a slow caldera collapse (Gudmundsson et al., 2016). During dyke propagation, a graben formed above the lateral flow path of magma, with

subsidence observed beneath Dyngujökull glacier and extending towards Holuhraun (Sigmundsson et al, 2015; Hjartardóttir et al., 2016). Several ice cauldrons formed above the path of the dyke on Dyngjujökull glacier (figure 2), within the graben, and the heat output of pre-existing minor subglacial geothermal areas at the caldera rim increased.

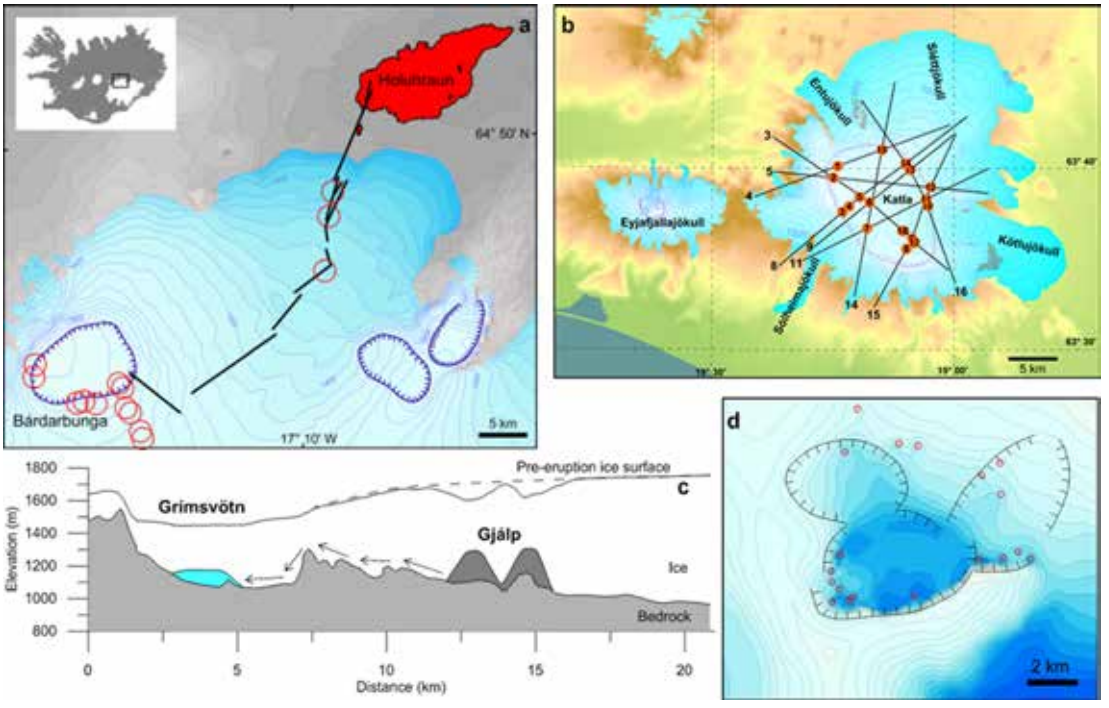

Figure 2. Examples of thermal activity at ice covered volcanoes in Iceland. (a) NW Vatnajökull, Iceland, showing Bárdarbunga caldera with several ice cauldrons (red circles) developing around the caldera edge. The black lines denote the path of the 2014 dyke (Sigmundsson et al., 2015), and several other ice cauldrons above this path (Reynolds et al., 2017). (b) Ice cauldrons on Katla with profiling lines used for airborne radar altimetry monitoring (after Futurevolc, 2016). (c) A south-north cross-section of the Grímsvötn caldera and the Gjálp eruption edifice on 1 October 1996 (mid-eruption) with arrows representing the direction of meltwater drainage. Note the depressions over the growing volcano at Gjálp. The 10-12 km wide surface depression of Grímsvötn is the result of sustained geothermal activity and meltwater drainage for centuries (modified after Gudmundsson et al., 2004). (d) Contour map of Grímsvötn with hashed lines marking the caldera, and red circles representing ice cauldrons.

The cauldrons grew to volumes in the range 2-20 million m^3. Two types of melting were observed: high initial heat flux over a period of days which gradually disappears; and slower but more sustained melting rates (Reynolds et al., 2017).

The nature of the heat source generating ice cauldrons is not always obvious, as they may result from small subglacial eruptions or increased geothermal activity induced by a magmatic intrusion. Through the evaluation and interpretation of thermal signals observed in association with magma movements and eruptions, this research can be used to advance the understanding of the behaviour of natural geothermal systems and how they interact with their environment. Conceptual, analytical

and numerical models of heat transfer through host rock, groundwater and geothermal fluids can be used to give insight into the nature of subglacial heat sources. This work outlines the methods used to estimate the heat flux at the base of glaciers, describe the heat transfer mechanisms bringing heat to the glacier base, and give an introduction to how analytical and numerical modelling can be used to understand the possible heat sources which produce the observed thermal signals.

This research impacts the understanding of both subglacial eruptions which can release significant volumes of ash into the atmosphere, and jökulhlaup hazard which poses a risk to populations, infrastructure and the environment in areas surrounding glaciers. Further to the implications for risk management, and the wider understanding and interpretation of thermal signals observed at ice-covered volcanoes, this work has relevance for the utilisation of geothermal areas by increasing understanding of the nature of subglacial heat sources.

6. 2 **- Glacier monitoring and calorimetry**

Time series data of ice cauldron evolution exist for several volcanoes in Iceland, revealing thermal fluctuations in subglacial geothermal areas during intrusive events and periods of seismic unrest. These data sets are extended routinely, with additional monitoring during and following volcanic activity.

Changes in the glacier surface are generally first identified by visual inspection during monitoring flights or using satellite images (Gudmundsson et al., 1997; 2004; 2007; 2016; Magnússon et al., 2012; Bleick et al., 2013; Sigmundsson et al., 2015). In Iceland, the evolution of these features is primarily monitored by repeated airborne radar altimetry profiling, supplemented by satellite images. Ground-based GPS profiling is also used where depressions are not crevassed, particularly for more complex features, to map the ice surface in more detail. Airborne altimetry measurements are made on board a low-flying aircraft (approximately 100 m elevation), using a C-band radar altimeter to record the aircraft elevation, and kinematic GPS to simultaneously record the precise position. Data collection is limited by weather conditions and the availability of the aircraft. An absolute accuracy of 3 m is achieved, with a relative consistency of 1-2 m. This method is outlined in detail by Gudmundsson et al., (2007).

An ice surface map can be created by interpolating the profile data to map the area and calculating the volume difference compared with a previous map. Once a surface map has been created, it can be subtracted from a previous map to reveal surface variations and allow the volume of surface features to be calculated (figure 3). The mass of ice melted can be estimated from the observed volume fluxes (Jarosch and Gudmundsson, 2007)

$$\rho_i \dot{V}_i = \dot{m}_{in} + \dot{m}_s - \dot{m}_{out} - \dot{m}_b \qquad (1)$$

with ρ_i the density of the ice, $\dot{V}_i$ the rate of change of the volume of ice, $\dot{m}_{in}$ and $\dot{m}_{out}$ respectively the mass flux of ice into and out of the study area, $\dot{m}_s$ the annual surface accumulation through precipitation, and $\dot{m}_b$ the mass loss due to basal melting.

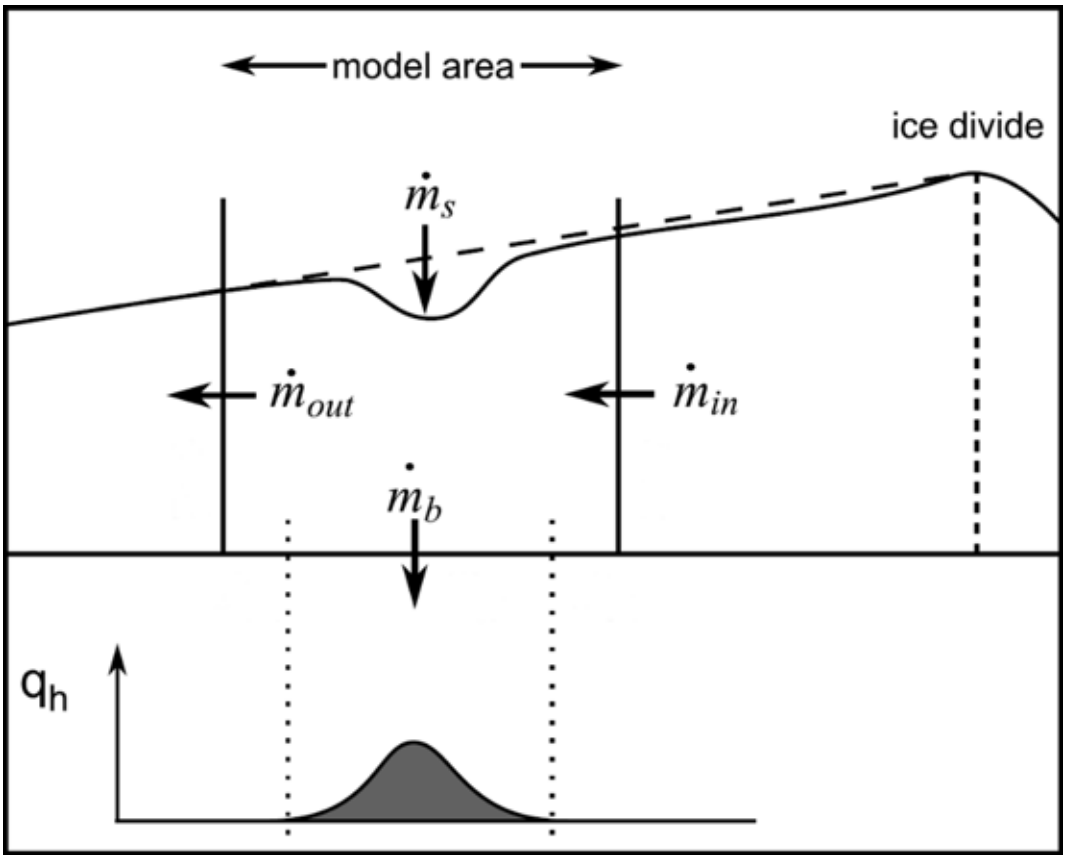

Figure 3. Schematic diagram outlining the mass flux terms used in equation 1. Modified after Jarosch and Gudmundsson, 2007.

If a map of the ice surface prior to the development of thermal features is available the total volume can be calculated, otherwise each successive map is subtracted from the previous one to show the change in volume with time (figure 4).

The resulting ice volumes represent the thermal signal at the base of the glacier, and are used to estimate the heat flux by calculating the thermal energy required to melt the volume of ice. If melting at the base is assumed to correspond exactly to the ice volume change on the surface it implies the assumption that all meltwater drains instantaneously and no significant emplacement of volcanic products in possible subglacial eruptions occurs. The glaciers in Iceland are temperate, meaning that the ice is at its melting point throughout, so only the latent heat of fusion is required to melt the ice. Therefore, the heat flux (Q) required to generate the ice cauldrons can be estimated using calorimetry, considering the volume of ice melted ($\dot{V}_i$), the density of the ice (ρ_i) and the latent heat of fusion of water (L_w).

$$Q = \rho_i \dot{V}_i L_w \qquad (2)$$

6. 3 **- Heat Transfer**

There are three mechanisms for heat transfer, which are conduction, convection, and radiation (e.g. Turcotte and Schubert, 2002). This section considers the dominant heat transfer mechanisms for three scenarios: a magmatic intrusion in the shallow crust beneath a glacier; an effusive subglacial eruption; and an explosive subglacial eruption.

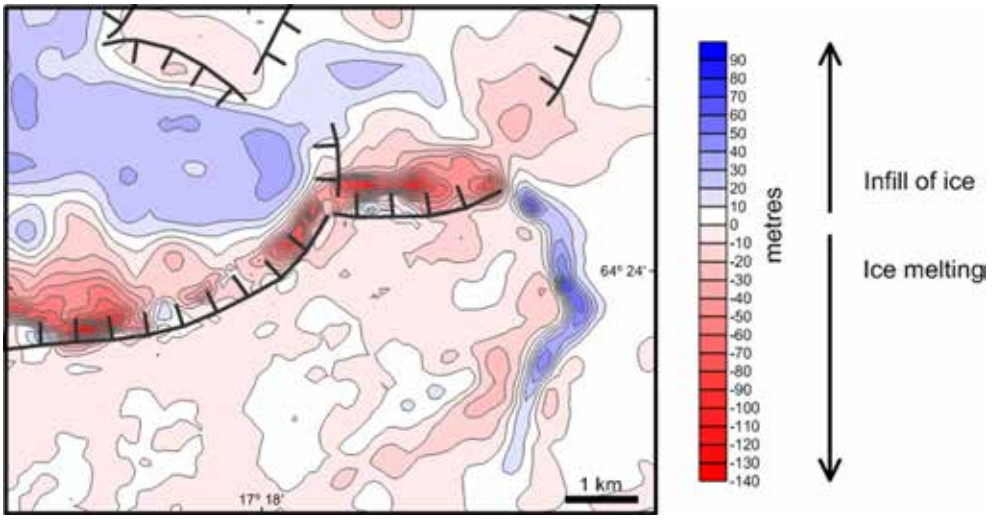

Figure 4. An example map of changes in ice surface elevation at Grímsvötn, between 1998 and 2010. Red areas represent developing ice cauldrons where ice has melted at the base of the glacier. Blue represents areas of ice infill. In the western part this is due to uplift of the ice surface caused by higher lake level, while in the area east of the caldera the increase is due to recovery of the glacier following the formation of an ice canyon over the path of the jökulhlaup of 1996 associated with the Gjálp eruption.

When a shallow magmatic intrusion is formed in the uppermost crust beneath a glacier, there is heat flux from magma from the intrusion to the country rock both by conduction and convection (figure 5). At a magma-country rock boundary, the dominant mechanism of heat transfer is dependent on the physical state of the country rock; if the country rock has very low permeability then conduction will dominate, but if the country rock is permeable then single- or two-phase hydrothermal convection will transport heat more efficiently. In the latter case heat is transported towards the country rock-ice boundary via convection, and the time scale for the thermal signal to reach the surface depends primarily on the depth of the intrusion, the permeability of the country rock, and the initial temperature of the country rock and the groundwater. Where the ice temperature is below the freezing point, some minor heat conduction will take place within the ice, but most of the heat melts the ice. If water accumulates beneath the glacier, convection transports heat within the water body.

Should the magma body reach the surface and result in a subglacial eruption, the style of eruption heavily influences which heat transfer mechanism is dominant, and the rate of heat transfer. A useful parameter to use when considering the heat transfer is the “efficiency”, defined as

the ratio of heat released from magma per unit time and the total heat content of the magma which erupted during the same time period (Gudmundsson, 2003; Gudmundsson et al., 2004). Models of subglacial effusive basaltic eruptions which form pillow lava have indicated a thermal efficiency of 10-45%, dependant on the eruption rate as the longer the lava pillows are in direct contact with the ice/meltwater, the higher the efficiency (Gudmundsson, 2003). Experiments where ice and molten lava come in to direct contact show that the heat flux was highest in the first 10 s but dropped by an order of magnitude within several minutes (Oddsson et al., 2016).

During an explosive subglacial eruption, fragmentation generates small particles, creating a large surface contact area between magma and water. The erupted products cool far more quickly than with an effusive eruption, with 70-80% of the initial heat within the erupted product transferred within the settling time (Gudmundsson, 2003; Woodcock et al., 2012).

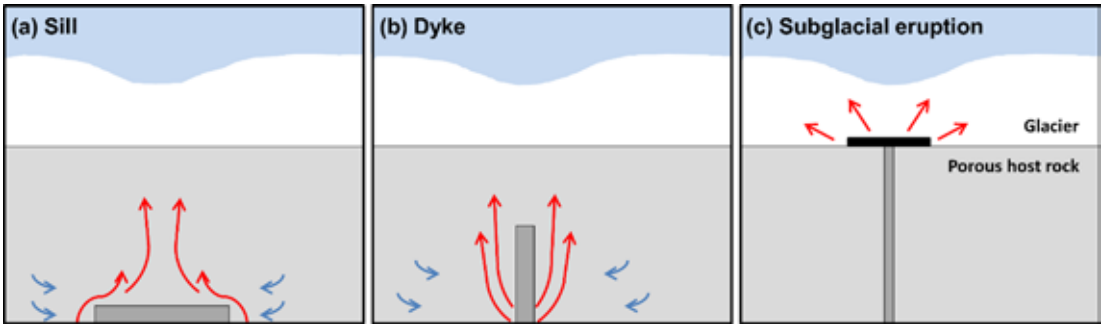

Figure 5. Conceptual model showing both sill and dyke style magmatic intrusions emplaced within a porous host-rock (a and b), where heat is transferred towards the surface by conduction and groundwater convection, generating heat flux beneath the glacier. The third image (c) shows a subglacial eruption scenario.

6. 4 - Geothermal reservoir modelling

As the groundwater is heated, convection cells develop which carry heat towards the surface. Darcy's law can be employed to estimate the fluid velocity of the groundwater, assuming that the flow remains that of a single phase liquid water, as it rises due to increased buoyancy, from a heated area around the intrusion towards the relatively cold bedrock-ice interface. The Darcy velocity (q_w) gives the volumetric flow rate per unit area (Ingebritsen and Sanford, 1999), and can be estimated as:

$$q_w = \frac{k\rho_{w,0}g\alpha_w(T_{boiling}-T_{surface})}{\mu_w} \quad (3)$$

where k is intrinsic permeability, $\rho_{w,0}$ is water density, g is the gravitational acceleration, α_w the linear coefficient of thermal expansion for water at 0 °C, and μ_w the dynamic viscosity of water. The ice-bedrock interface is considered to have a temperature $T_{surface}$ of 0 °C, the freezing point of water. $T_{boiling}$ is the boiling point of water at the depth of the intrusion, as this is the highest temperature the groundwater can reach without becoming superheated or develop into a two-phase fluid.

However, steam can play a significant role in heat transfer in hydrothermal areas, and this can be addressed using numerical models such as Hydrotherm (see below) and MUFITS (Afanasyev et al., 2015).

A two-dimensional time-dependent numerical model was produced to simulate the solidification and cooling of a dyke, into porous host rock saturated with pure water (figure 5). Simulations were produced using COMSOL Multiphysics, which is a commercial software, used to simulate physics-based problems using finite element modelling. Heat transfer through both conduction and convection are included; as the porous fluid heats up, a convection cell forms around the intrusion, transferring heat far more efficiently than by conduction alone. The thermodynamic properties of liquid water are dependent on temperature and pressure, although phase change is not considered in this model. The release of latent heat and specific heat capacity of the cooling and solidifying intrusion are simulated.

Further simulations were carried out using Hydrotherm, which is a finite difference code dedicated to simulating two-phase ground-water flow and heat transport, developed by the U. S. Geological Survey (Hayba and Ingebritsen, 1997). The COMSOL model is limited to single-phase convection, but Hydrotherm can be used to simulate the two-phase case. Otherwise, the model set-up is similar to that used in COMSOL. Numerical modelling gives the opportunity to explore different country rock permeabilities and initial temperature gradients, and different intrusion depths and geometries (figure 6). The timescale and spatial extent of the simulated surface thermal anomalies can then be compared to thermal signals observed at ice-covered volcanoes, and insight gained into the geothermal system producing the heat source at the glacier base. For simulations with temperatures below the boiling point of water, COMSOL and Hydrotherm give results for surface heat flux magnitude which are within 30% of each other. This discrepancy is due to differences in the solvers used.

The surface heat flux produced by a circular heat sources can be calculated by radially integrating the results from the two-dimensional model. For example, the cumulative total surface heat flux for a circular heat source of radius 50 m, intruded into host rock with permeability $5x10^{-14}$ m^2 and porosity of 10%, is displayed in figure 7 with the resulting volume of melted ice if this heat was released below a temperate glacier.

6. 5 **- Discussion**

Airborne radar altimetry profiling can give results very quickly, as the data can be analysed on the day they are acquired because only minimal processing is required. This makes it a very convenient tool for monitoring an ongoing event. New features on the glacier surface are generally first observed visually, as it is inefficient to collect profiles of the entire glacier surface considering that the features of interest are relatively small; for this reason, good weather with clear visibility is advantageous for monitoring flights. The penetration depth of the radar-altimeter signal varies, depending on the surface conditions. In cold and dry conditions, the signal can penetrate to several metres below the glacier surface, but in warmer conditions ice lenses form and reflect the signal close to the surface. The varying depth of penetration means that the ice profiles cannot be

considered to represent the absolute surface elevation, and instead must be used to monitor changes in volume and morphology of ice surface features relative to their surroundings.

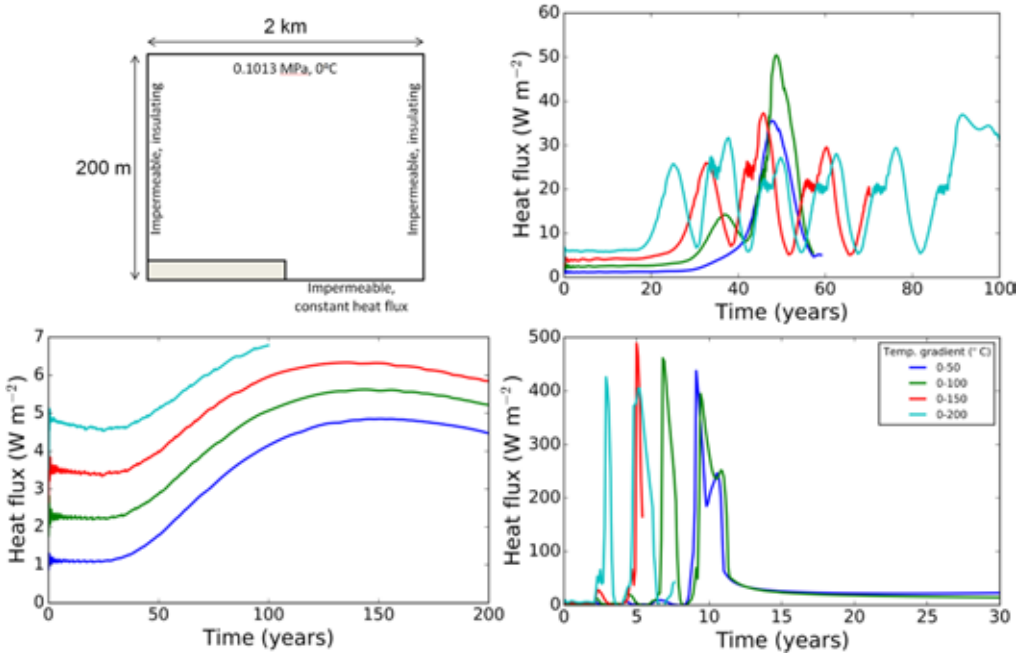

Figure 6. An example of an application of the Hydrotherm model showing results of heat fluxes for varying country rock permeability and initial temperature gradient.

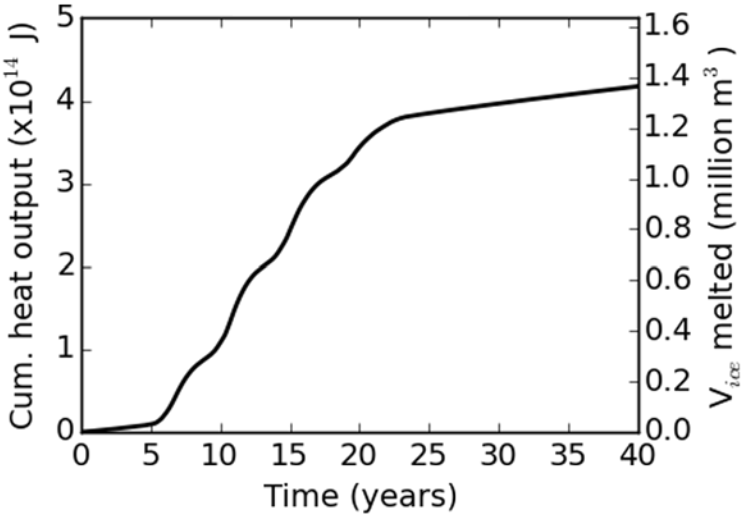

Figure 7. The cumulative total surface heat flux for a circular heat source of radius 50 m, intruded into host rock with permeability $5x10^{-14}$ m^2 and porosity of 10%, with the resulting volume of melted ice.

The calorimetry method described above to estimate the total volume basal ice melting is reliant on negligible volumes of meltwater accumulating beneath the surface depression. It is sometimes unclear whether or not meltwater is draining or accumulating, and further investigations may be required to establish this e.g. radio echo sounding to look for anomalies at the ice-rock boundary.

Both COMSOL Multiphysics and Hydrotherm can be used to investigate the surface heat flux produced by hydrothermal systems, each with advantages and disadvantages in terms of the capability to simulate the natural system and in their usability. COMSOL Multiphysics provide an easy-to-use interface, which allows for quick visualisation of data in graphs, tables and various 2- and 3-dimentional plots. The package also offers a lot of flexibility when designing the mesh nodes, which enable the discretisation of the model into small units or elements, and models are stable even with very narrow intrusion geometries. However, while single-phase convection in porous media is supported by COMSOL (version 4.3b), the two-phase case is not and cannot be simulated. Hydrotherm does simulate two-phase groundwater flow, which is particularly important when simulating higher initial country-rock temperatures characteristic of established geothermal systems. Both models explore the parameter space for host-rock heat conductivity and permeability, and the initial temperature gradient. The timescale and spatial extent of the simulated surface thermal anomalies are compared to thermal signals observed in nature.

6. 6 **- Conclusions**

Ice cauldrons are observed in several areas in Iceland (e.g. Grímsvötn, Bárdarbunga, Eyjafjalljökull, Mýrdalsjökull), both as sustained features which last for a period of years and grow slowly, and as quickly forming features which form within days or weeks.

Ice cauldron volume and morphology can be monitored aerially, and supplemented by ground-based GPS measurements and satellite images.

The frequency of cauldron monitoring should be chosen based on the activity in the area, although monitoring is subject to good weather and this can often prevent measurements from being taken for period of time, e.g. one week.

The ice acts as a large-scale calorimeter, and the power and heat flux at the rock-ice boundary can be inferred from measurements of changes to the ice surface.

Numerical and analytical modelling can be used to give insight into the possible heating scenarios which resulted in the observed ice melting.

Acknowledgements

I thank Magnús Tumi Gudmundsson and Thordís Högnadóttir for their support and guidance. The research leading to these results has received funding from the European Union Seventh Framework Programme (FP7/2007-2013) under the project NEMOH, grant agreement n° 289976., the Research Fund of the University of Iceland and the Landsvirkjun power company.

References

Afanasyev, A., Costa, A. and Chiodini, G. (2015). Investigation of hydrothermal activity at Campi Flegrei caldera using 3D numerical simulations: extension to high temperature processes. J Volcanol Geotherm Res 299: 68-77.

Anderson, C. H., Behrens, C. J., Floyd, G. A. and Vining, M. R. (1998). Crater Firn Caves of Mount St. Helens, Washington. J Caves and Karst Stud 60:44-50.

Björnsson, H. (1988). Hydrology of Ice Caps in Volcanic Regions. Soc Sci Isl, Rit 40. 139 pp.

Björnsson, H. and Guðmundsson, M. T. (1993). Variations in the thermal output of the subglacial Grímsvötn caldera, Iceland. Geophys Res Lett Vol 20, 19:2127-2130.

Blankenship, D. D., Bell, R. E., Hodge, S. M., Brozena, J. M., Behrendt, J. C. and Finn, C. A. (1993). Active volcanism beneath the West Antarctic ice sheet and implications for ice-sheet stability. Nature 361: 526-529.

Bleick, H.A., Coombs, M. L., Cervelli, P. F., Bull, K. F. and Wessels, R. L. (2013). Volcano-ice interactions precursory to the 2009 eruption of Redoubt Volcano, Alaska. J Volcanol Geotherm Res 259: 373-388.

Futurevolc (2016). D5.7 – Ice evolution Time series of elevation changes during caldera collapse and geothermal activity in Iceland.

Giggenbach, W. F. (1976). Geothermal ice caves on Mt Erebus, Ross Island, Antarctica. New Zeal J Geol Geophys 19:365–372, doi: 10.1080/00288306.1976.10423566.

Gíslason, S. R., Stefánsdóttir, G., Pfeffer, M.A., Barsotti, S., Jóhannsson, T., Galeczka, I., Bali, E., Sigmarsson, O., Stefánsson, A., Keller, N. S., Sigurdsson, Á., Bergsson, B., Galle, B., Jacobo, V. C., Arellano, S., Aiuppa, A., Jónasdóttir, E. B., Eiríksdóttir, E. S., Jakobsson, S., Guðfinnsson, G. H., Halldórsson, S. A., Gunnarsson, H., Haddadi, B., Jónsdóttir, I., Thordarson, T., Riishuus, M., Högnadóttir. Th., Dürig, T., Pedersen, G. B. M., Höskuldsson, Á. and Gudmundsson, M. T. (2015). Environmental pressure from the 2014–15 eruption of Bárðarbunga volcano, Iceland. Geochem Perspect Lett 1 (0): 84–93.

Gudmundsson, M. T., Sigmundsson, F. and Björnsson, H. (1997). Ice–volcano interaction of the 1996 Gjálp subglacial eruption, Vatnajökull, Iceland. Nature 389: 954-957.

Gudmundsson, M. T. (2003). Melting of ice by magma-ice-water interactions during subglacial eruptions as an indicator of heat transfer in subaqueous eruptions. Explosive subaqueous volcanism, 61-72.

Gudmundsson, M. T., Sigmundsson, F., Björnsson, H. and Högnadóttir, Th. (2004). The 1996 Eruption at Gjálp, Vatnajökull Ice Cap, Iceland: Efficiency of Heat Transfer, Ice Deformation and Subglacial Water Pressure. Bulletin of Volcanology 66 (1): 46–65, doi:10.1007/s00445-003-0295-9.

Gudmundsson, M. T., Högnadóttir, Th., Kristinsson, A. B. and Gudbjörnsson, S. (2007). Geothermal activity in the subglacial Katla caldera, Iceland, 1999-2005, studied with radar altimetry. Annals of Glaciology, 45: 66-72.

Gudmundsson, M. T., Jónsdóttir, K., Hooper, A., Holohan, E. P., Halldórsson, S. A., Ófeigsson, B. G., Cesca, S., Vogfjörd, K. S., Sigmundsson, F., Högnadóttir, Th., Einarsson, P., Sigmarsson, O., Jarosch, A. H., Jónasson, K., Magnússon, E., Hreinsdóttir, S., Bagnardi, M., Parks, M. M., Hjörleifsdóttir, V., Pálsson, F., Walter, T. R., Schöpfer, M. P. J., Heimann, S., Reynolds, H. I., Dumont, S., Bali, E., Gudfinnsson, G. H., Dahm, T., Roberts, M. J., Hensch, M., Belart, J. M. C., Spaans, K., Jakobsson, S., Gudmundsson, G. B., Fridriksdóttir, H. M., Drouin, V., Dürig, T., Aðalgeirsdóttir, G., Riishuus, M. S., Pedersen, G. B. M., van Boeckel, T., Oddsson, B., Pfeffer, M. A., Barsotti, S., Bergsson, B., Donovan, A., Burton, M. R. and Aiuppa, A. (2016). Gradual caldera collapse at Bárdarbunga volcano, Iceland, regulated by lateral magma outflow. Science, 353(6296): aaf8988.

Hayba, D. O. and Ingebritsen, S. E. (1997). Multiphase groundwater flow near cooling plutons. J Geophys Res, 102 (B6): 12,235-12,252.

Hjartardóttir, Á. R., Einarsson, P., Gudmundsson, M. T. and Högnadóttir, Th. (2016). Fracture movements and graben subsidence during the 2014 Bárðarbunga dike intrusion in Iceland. J Volcanol Geotherm Res 310: 242-252.

Hochstein, M. P. and Bromley, C. J. (2001). Steam cloud characteristics and heat output of fumaroles. Geothermics, 30:547-559.

Hochstein, M. P. and Bromley, C. J. (2005). Measurement of heat flux from steaming ground. Geothermics, 34:133-160.

Hurwitz, S., Kipp, K. L., Ingebritsen, S. E. and Reid M. E. (2003). Groundwater flow, heat transport, and water table position within volcanic edifices: Implications for volcanic processes in the Cascade Range. J Geophys Res Solid Earth, 108 (B12): 2557.

Jarosch, A. H. and Gudmundsson, M. T. (2007) Numerical studies of ice flow over subglacial geothermal heat sources at Grímsvötn, Iceland, using Full Stokes equations. J Geophys Res, 112: F02008, doi:10.1029/2006JF000540.

Jarosch, A. H., Gudmundsson, M. T., Högnadóttir, Th. and Axelsson, G. (2008). Progressive cooling of the hyaloclastite ridge at Gjálp, Iceland, 1996-2005. J Volcanol Geotherm Res, 170: 218-229.

Kiver, E. and Mumma, M. (1971). Summit firn caves, Mount Rainier, Washington. Science 173:320–322.

Magnusson, E., Gudmundsson, M. T., Roberts, M. J., Sigurdsson, G., Höskuldsson, F. and Oddsson, B. (2012). Ice-volcano interactions during the 2010 Eyjafjallajökull eruption, as revealed by airborne imaging radar. J Geophys Res, 117: B07405.

Major, J. J. and Newhall, C. G. (1989). Snow and ice perturbtion during historical volcanic-eruptions and the formation of lahars and floods – a global review. Bull Volc, 52: 1-27.

Oddsson, B., Gudmundsson, M. T., Sonder, I., Zimanowski, B. and Schmid A. (2016). Experimental studies of heat transfer at the dynamic magma ice/water interface: Application to subglacially emplaced lava. J Geophys Res-Sol Ea 121(5): 3261-3277.

Orkustofnun (2013). Energy Statistics in Iceland 2013. Accessed 2 August 2016. http://www.os.is/gogn/os-onnur-rit/orkutolur_2013-enska.pdf.

Reynolds, H. I. and Gudmundsson M. T. (2014). Variations in geothermal heat flux at Grímsvötn, Iceland. Geophysical Research Abstracts, 16, EGU2014-4462.

Reynolds, H.I., Gudmundsson, M. T. and Högnadóttir, Th. (2017). Subglacial volcanic activity above a lateral dyke path during the 2014-2015 Bárdarbunga-Holuhraun rifting episode, Iceland. Bull Volcanol 79(6), 38.

Sigmundsson, F., Hooper, A., Hreinsdottir, S., Vogfjord, K. S., Ofeigsson, B. G., Heimisson, E. R., Dumont S., Parks M., Spaans, K., Gudmundsson, G.B., Drouin, V., Arnadottir, T., Jonsdottir, K., Gudmundsson, M. T., Hognadottir, Th., Fridriksdottir, H. M., Hensch, M., Einarsson, P., Magnusson, E., Samsonov, S., Brandsdottir, B., White, R. S., Agustsdottir, Th., Greenfield, T., Green, R. G., Hjartardottir, A. R., Pedersen, R., Bennett, R. A., Geirsson, H., La Femina, P. C., Bjornsson, H., Palsson, F., Sturkell, E., Bean C. J., Mollhoff, M., Braiden, A. K. and Eibl, E. P. S. (2015). Segmented lateral dyke growth in a rifting event at Bardarbunga volcanic system, Iceland. Nature 517 (7533): 191–195.

Stimac, J., Goff, F. and Goff, C. J. (2015). Intrusion-Related Geothermal Systems, in The Encyclopedia of Volcanoes, edited by H. Sigurdsson et al., pp. 377–393, Elsevier, Boston.

Turcotte, D. L. and Schubert, G. (2002). Geodynamics. Cambridge University Press, 2nd edition.

Woodcock, D. C., Gilbert, J. S. and Lane, S. J. (2012). Particle-water heat transfer during explosive volcanic eruptions. J Geophys Res-Sol Ea, 117(B10).

Zimbelman, D. R., Rye, R. O. and Landis, G. P. (2000). Fumaroles in ice caves on the summit of Mount Rainier—preliminary stable isotope, gas, and geochemical studies. J Volcanol Geotherm Res 97:457–473. doi: 10.1016/S0377-0273(99)00180-8.

Hannah Iona Reynolds, United Kingdom
hir10@hi.is

Affiliation under NEMOH
Nordvulk, Institute of Earth Sciences, University of Iceland, *Reykjavík,* Iceland

Research theme under NEMOH
Understanding geophysical signals associated with magma and heat transfer

I graduated from the University of Edinburgh in 2009, with a BSc (Hons) in Astrophysics. Following this, I found that my interests lay within earth sciences and particularly natural hazards, leading to my decision to undertake an MSc Volcanology and Geological Hazards at Lancaster University, graduating in 2012. My MSc research involved an analogue experimental approach to investigate the growth rate and morphology of ice cavities, which form prior to subglacial eruptions.

My PhD research aims to advance the general understanding of heat flow in volcanoes, and how they relate to the movement and emplacement of magma, by analysing and advancing models of heat transfer from magma to the surrounding rock, groundwater and geothermal fluids. Time-dependent conceptual, analytical and numerical models of heat transfer are developed, and constrained using time-series thermal data. This research concentrates mainly on ice-covered volcanoes in Iceland, namely Grímsvötn, Katla and Bárdarbunga. Extensive ice cover provides a special situation where the ice acts as a calorimeter, allowing quantification of thermal signals from subsurface magmatic sources; this would usually be difficult due to the large uncertainties in measuring ground to atmosphere heat fluxes. I conducted numerical simulations using Hydrotherm (developed by U.S.G.S.) to investigate the cooling of magmatic intrusions, exploring the effect of intrusion geometry and bedrock parameters on the surface heat flux produced; these results were then compared to the observed thermal data.

During my PhD, I was lucky enough to witness the Bárdarbunga-Holuhraun eruption of 2014-15. I took part in the emergency scientific response and my tasks at the eruption site included: lava flow mapping and sampling for geochemical analysis, and imaging lava flow advancement and lava fountaining using high-speed and infrared cameras. My main involvement however, was in glacial monitoring, where surface observations are used to infer what is happening beneath the ice, which covers Bárdarbunga volcano. Overflights were used to take elevation profiles of the ice surface using radar altimetry, and visual observations are made of crevassing which reveal new depressions on the ice surface. This event gave me the opportunity to work on small, entirely subglacial, eruptions which complemented my research on subglacial geothermal areas.

Being part of NEMOH has led to new experiences, opportunities and collaborations which have been invaluable to my development as a scientist. My NEMOH memories will stay with me forever, and will always make me smile.

Chapter 7

Gas transport and flow regimes in crystal-bearing magmas

Julie Oppenheimer

School of Earth Sciences, University of Bristol, Bristol, United Kingdom

Tutorship: Alison Rust, Katherine Cashman

School of Earth Sciences, University of Bristol, Bristol, United Kingdom

Abstract

Gas escape from three-phase magmas modulates magma dynamics before, during, and after eruptions. Therefore, improving our understanding of outgassing in crystal-bearing magmas is critical to interpreting gas emissions from volcanoes, and constraining eruption dynamics. To this end, we performed experiments with three-phase (gas, liquid, solid) analogue materials in different container geometries (parallel horizontal plates and vertical tubes). We tracked bubble growth and migration through particle suspensions and varied bubble generation methods: in the first set of experiments, bubbles were injected directly into the suspension; in the second set of experiments, bubble growth was induced through chemical reactions; and in the third set, large bubbles were injected at the bottom of a tube, rose as gas slugs through a liquid phase, before travelling through a particle-laden layer. All experiments show that high concentrations of crystals, commonly found in natural magmas, cause significant deformation of the gas-liquid interface and increases the efficiency of gas escape from magmas. The onset of non-Newtonian behaviour marks the onset of bubble deformation at low shear. In experiments, this transition occurred at the normalised random packing (relative to random close packing, RCP): $\varphi \approx 0.63$. Significant bubble deformation at high shear began at $0.80 < \varphi < 0.86$, near the random loose packing of particles. Bubble deformation increases with increasing particle fraction until the bubble is either trapped within the particle layer, travels in fracture-like patterns, or invades the pore-space between particles. At such high particle fractions, the gas migration regime depends on other constraints such as confinement and internal bubble pressure.

Keywords: outgassing, three-phase flow, rheology, crystal-rich magma, gas migration.

7. 1 - Introduction

Crystal-rich eruption products are common. Some originate from explosive eruptions (such as the 1980 Mt St Helens eruption, or the Monte Nuovo eruption of Campi Flegrei; Cashman, 1992; Piochi et al., 2008), but many are erupted as degassed lava flows and domes (such as 'a'a and blocky lavas at Hawaii and Colima, or the Unzen lava dome; e.g. Sehlke et al., 2014; Savov et al., 2008; Shinohara, 2008; Polacci et al., 1999). The latter cases are depleted in volatiles, which raises the question: How do suspensions with such high crystallinities, thus high bulk viscosities, lose their volatiles? This question is fundamental because volatiles can also drive volcanic eruptions, and thus bubble

behaviours in crystal-rich magmas can potentially affect eruption style. This PhD, developed under NEMOH, focused on the manner in which bubbles mechanically interact with crystals in crystal-rich magmas, mainly by using analogue experiments. The following synthesis describes the results obtained from analogue experiments, and speculates on their applicability to volcanic environments.

7. 2 - The effect of particle fraction on bubble shapes and outgassing regimes: overview of analogue experiments

We observed bubble growth in analogue suspensions and tracked bubble morphology, gas migration paths, and outgassing efficiency in various environments. Here, we summarize and compare the analogue experiments, and provide an overview of their implications for particle-bearing suspensions.

7. 2.1 - Experiments and results

We used a variety of experimental set-ups to test the validity of gas migration regimes in different environments:

1) We ran several suites of experiments by continuously injecting air from a point-source into suspensions sandwiched between two horizontal glass plates. The plates were separated by a small gap (0.48 mm, not shown in Fig. 1) or a large gap (5 mm; Fig. 1 [A.1], [B.1] and [E]). The particle suspensions consisted of glass spheres of diameter ~0.1 mm in sugar syrup, typically of viscosity ~60 Pa s, but we varied the conditions to obtain syrup viscosities from 10 Pa s to >600 Pa s. These experiments are detailed in Oppenheimer et al., (2015).

2) We performed another suite of experiments with the same materials as (1) but in which bubbles were generated in-situ by chemical reactions between powders of citric acid and sodium bicarbonate. These experiments were all performed at a liquid viscosity of ~ 60 Pa s. One set of experiments was performed in small-gap parallel plates (Fig. 1 [A.2] and [B.2]), and the other in vertical cylinders of diameter 28 mm and capacity 100 mL (not shown in Fig. 1). These experiments are also described and analysed in detail in Oppenheimer et al., (2015).

3) Our final suite of experiments involved gas slugs (Taylor bubbles) that rose in a vertical cylinder filled with silicone oil (viscosity 0.1 Pa s), until they breached a layer ("cap") of silicone oil + particles overlying the pure silicone oil (Fig. 1 [A.3], [B.3], [C] and [D]). The particles were crushed polypropylene particles of diameter 0.5 – 0.7 mm. The tube was 3 m tall, filled to 1.43 m with liquid and particles, and had a diameter of 0.0257 m.
   We varied surface pressure by connecting the tube to a vacuum pump, which thus varied bubble parameters (such as bubble expansion and overpressure near the surface; Del Bello et al., 2012; James et al., 2009). These experiments are similar to those by Capponi et al., (2016), who observe slug flow through a liquid of low viscosity surmounted by a Newtonian liquid of higher viscosity. In our case, however, the upper layer has a non-Newtonian rheology at high particle fractions.

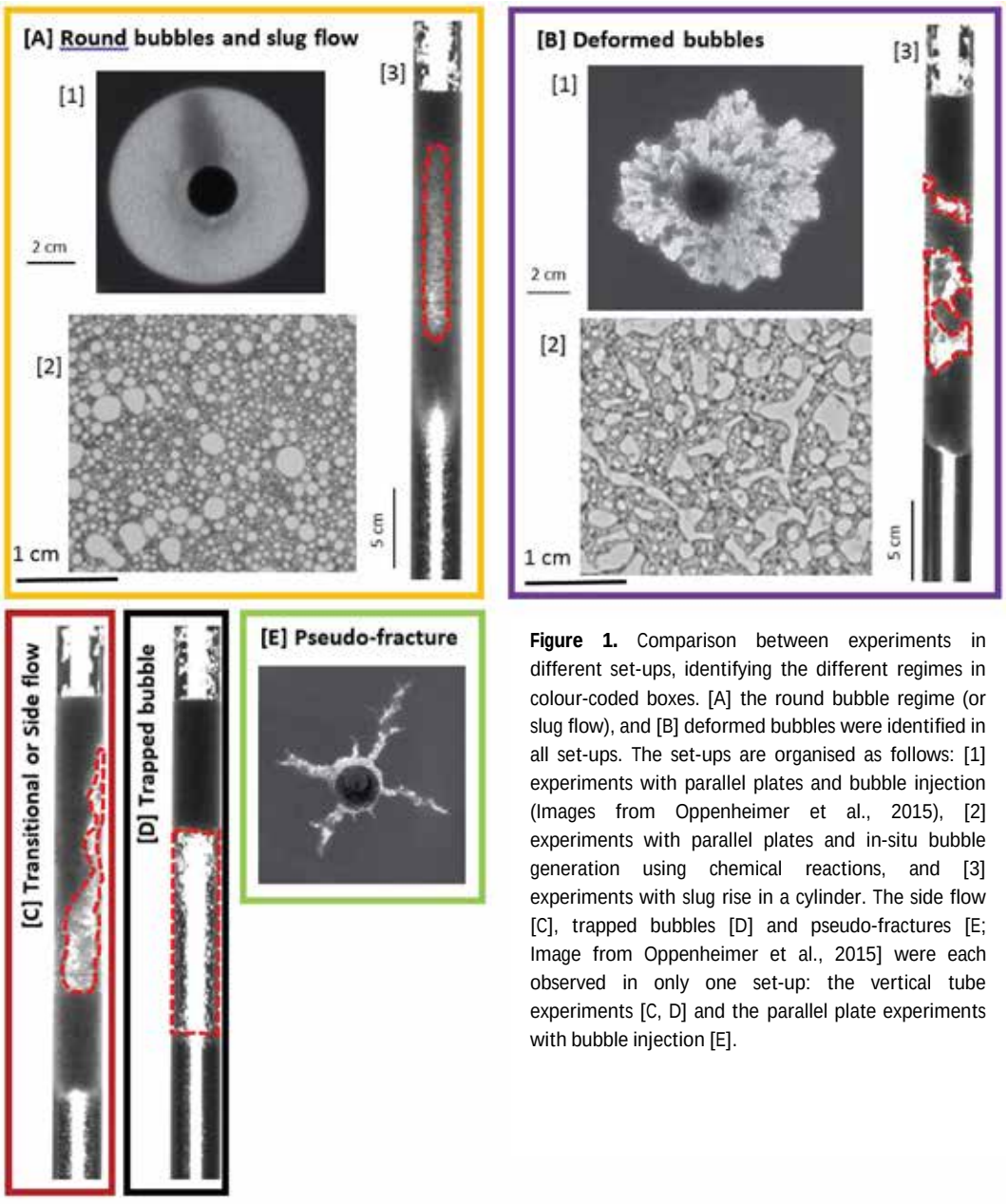

Figure 1. Comparison between experiments in different set-ups, identifying the different regimes in colour-coded boxes. [A] the round bubble regime (or slug flow), and [B] deformed bubbles were identified in all set-ups. The set-ups are organised as follows: [1] experiments with parallel plates and bubble injection (Images from Oppenheimer et al., 2015), [2] experiments with parallel plates and in-situ bubble generation using chemical reactions, and [3] experiments with slug rise in a cylinder. The side flow [C], trapped bubbles [D] and pseudo-fractures [E; Image from Oppenheimer et al., 2015] were each observed in only one set-up: the vertical tube experiments [C, D] and the parallel plate experiments with bubble injection [E].

Figure 1 shows the main bubble morphologies observed in the different experimental conditions. In dilute suspensions, growing bubbles are rounded, and slugs flowing through a particle-bearing layer retain their slug-like shape (Figure 1A). At high particle content, the bubbles deformed in all three sets of experiments (Figure 1B). The onset of more severe bubble deformation corresponded with a significant reduction in foam expansion in experiments with in-situ bubble growth (Figure 2).

Some regimes were specific to an experimental set-up. In the parallel plate set-up, we observed fracture-like gas propagation at the random close packing (RCP) which did not occur in the other set-ups. For clarity, we call these "pseudo-fractures" because they are not, in fact, brittle (Oppenheimer et al., 2015). There are also two regimes specific to the slug rise experiments: (1) side flow at intermediate particle fractions (between round bubble and deformed bubble regimes), where the bubble circumvents the particle-bearing cap by travelling up along the tube wall; and (2) trapped bubbles, at high particle fractions and high surface pressures, where the gas bubble remains indefinitely either at the base of the particle-rich cap, or within the cap.

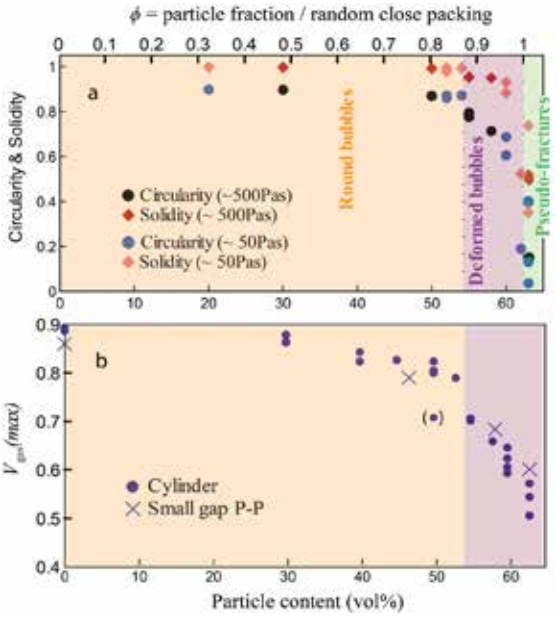

Figure 2. (a) Measurement of bubble deformation in bubble injection experiments in large-gap parallel plates (at viscosities ~50 Pa s and ~ 500 Pa s). (b) Maximum foam growth in experiments with bubbles generated through chemical reactions, expressed as a maximum gas volume fraction (relative to the bulk suspension): V_{gas}(max). The chemical concentration was kept constant, thus the amount of available chemicals decreases with increasing particle fraction, possibly causing the slight initial decrease in V_{gas}(max). The substantial decrease in maximum foam growth occurs at approximately the same particle fraction as bubble deformation in (a). Modified from Oppenheimer et al. (2015).

In order to compare the different experiments, we normalise the particle packing fraction by the random close packing (RCP), which is the maximum random packing for the particles in question (equation 1).

$$\phi = \frac{particle\ volume\ fraction}{RCP} \qquad (1)$$

φ was the main control on bubble shape (Figure 3).

In bubble injection and in-situ bubble generation experiments, the transition in bubble morphology, from round bubbles to deformed bubbles, occurred at φ ≈ 0.86 ± 0.03 (≈ 54 ± 2 vol%), at all liquid viscosities tested. This value corresponds to the random loose packing of spheres (RLP). RLP is poorly defined, but its best description to date is "the lowest possible random packing that is capable of bearing a load" (Onoda and Liniger, 1990). RLP essentially represents the onset of large-scale particle-particle interactions. This is consistent with the fact that different experimental conditions gave similar results: the particle fraction was the main control on bubble shape. Increasing particle fractions beyond RLP and up to the random close packing (RCP, the maximum random packing) caused more severe bubble deformation.

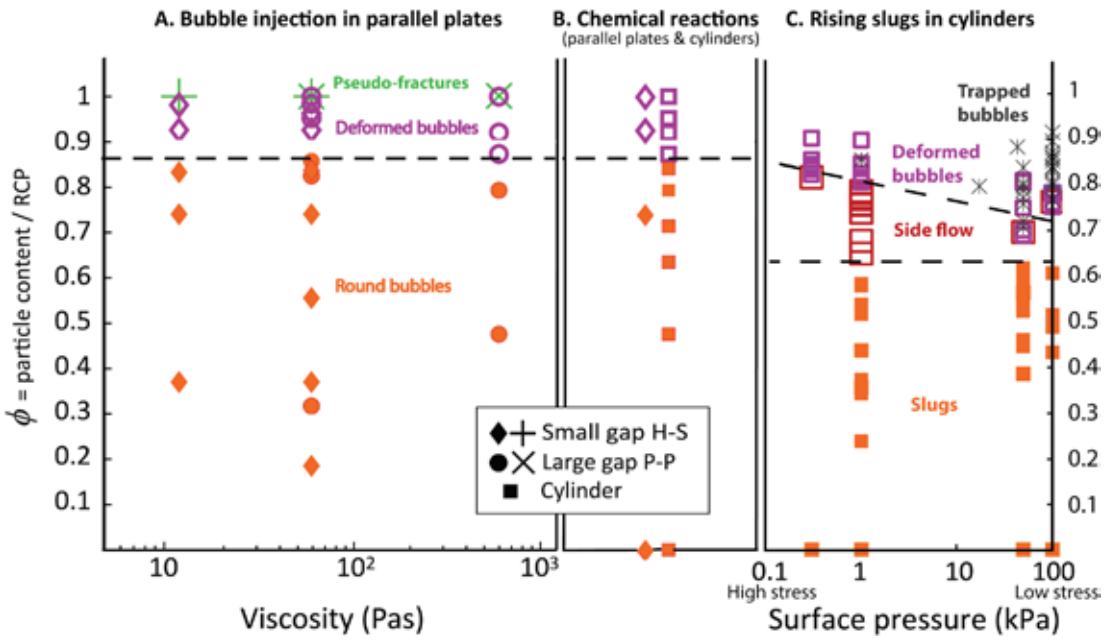

Figure 3. Regime categories for all experimental set-ups. Colours are the same as in Fig. 1. [A] shows experiments performed in parallel plates (small gap and large gap) that desmonstrate the low impact of liquid viscosity on regime transitions. [B] shows experiments with in-situ bubble growth generated by chemical reactions in small gap parallel plates and cylinders, performed at atmospheric pressure and with a liquid viscosity of ~ 60 Pa s. [C] shows experiments with rise of large bubbles in a layered cylinder, and an investigation into the effect of applied stress on regime transitions (controlled by varying surface pressure). The black dashed lines represent the position of regime transitions between round bubbles (or slugs) and deformed bubbles in [A] and [C]. The transition for chemical reaction experiments [B] was determined from the substantial decrease in foam growth (Fig. 2). Note that the particles in [B] and [C] have different shapes. [A] and [B] from Oppenheimer et al., (2015).

The experiments performed with a single large bubble flowing into a particle-rich cap provide extra constraints. These experiments were performed with finite bubbles (as opposed to continuous injection or exsolution of gas), but surface pressure was varied from one experiment to another. A low surface pressure caused more bubble expansion during rise (and thus increased the upward acceleration of the bubble nose), and increased bubble overpressure when the bubble reached the cap (Del Bello et al., 2012; James et al, 2009). Thus, by varying surface pressure in these experiments, we varied the stress applied on the cap. This shifted the regime transitions (Figure 3[C]). In experiments with higher surface pressures, the bubbles had lower overpressures and expanded less, thus the stress applied on the cap was lower and the transition to the deformed regime occurred at lower φ values. Furthermore, these experiments suggest that particles can potentially affect bubble morphology at values as low as $\varphi \approx 0.63$, where the side flow regime begins.

7. 2.2 **- Interpretation**

The transitions in bubble morphology coincide with transitions in suspension rheology and in particle-particle interactions. At low particle fractions, the suspension is ~Newtonian and bubbles in the experiments are round or slug-shaped (Figure 4[A]; Figure 2[A]). As soon as the particles begin

interacting, they form clusters and chains that cause the suspension to become shear-thinning (Figure 4[B]; e.g. Mueller et al., 2009; Soule and Cashman, 2005). The behaviour of the suspension will then depend on the applied stress. This rheological transition can explain the dependence of regime transitions on surface pressure in the slug rise experiments (Fig. 3[C]). In these experiments, an increase in surface pressure caused the bubble to expand less and be less overpressured when it interacted with the particle layer (Del Bello et al., 2012; James et al., 2009). Thus, in experiments with higher surface pressures, the gross upward force generated by the bubble "invading" the suspension is relatively low. Therefore weaker interactions between the particles suffice to affect bubble propagation and, as a result, the transition to the deformed regime occurred at lower φ. In experiments with lower surface pressures (higher bubble overpressure and nose acceleration), the interactions between particles were easily overcome, and bubbles chose the path of lowest resistance, against the tube wall where packing is inefficient. This departure from Newtonian behaviour began at $\varphi \approx 0.63$ in experiments with slug rise in a tube although, presumably, the lowest possible particle fraction at which it can occur is the percolation threshold [Saar et al., 2001], below which particles do not interact significantly.

At high stresses, the bubble deformation regime began at $0.80 < \varphi < 0.86$. This value corresponds roughly to the random loose packing of particles (RLP), as well as the onset of shear-dilation for spheres and the onset of an apparent yield strength, all of which essentially represent the onset of large-scale particle-particle interactions (Figure 4[C]; Mueller et al., 2010; Caricchi et al., 2007; Onoda and Liniger, 1990). Hence the bubble deformation regime generally occurs within the limits of RLP and RCP (as in Figure 3[A] and 3[B]). These dense suspensions dilate in response to shear, and can therefore develop a normal force against their boundaries and build force-bearing networks of particles. Therefore, in order to grow, bubbles must deform around a "backbone", preferentially displacing areas in the suspension with unconnected or weakly connected particles, where the strength opposing bubble growth is lowest. As a result, the bubble deforms into lobate or finger-like patterns ("bubble deformation regime").

The strength of the particle networks is determined by the number of particles in contact with each other (Bi et al., 2011), the friction between particles (Seto et al., 2013), and the magnitude of the forces that resist particle displacement / dilation, such as the flexibility of the boundaries against which the force chains rest (Brown et al., 2011; Brown and Jaeger, 2012), or the applied pressure (e.g., from gravitational loading; Islam et al., 2013). Therefore, since the stress that opposes bubble growth increases as particle fractions increase towards RCP, bubble deformation increases accordingly (Figure 4[D]) until it reaches the highly deformed pseudo-fracture regime (Figure 1[E]).

Furthermore, since the resistance to bubble growth increases with particle fraction, the pressure necessary for bubble growth increases with particle fraction as well. In these slug flow experiments, if the forces generated by the bubble (e.g. overpressure, buoyancy) are insufficient, the bubble may remain trapped below or within a particle-rich layer ("Trapped bubble regime"). This regime occurred strictly because the bubbles were finite: in our other experiments, the continuous injection of gas increases the pressure until it overcomes the strength of the suspension.

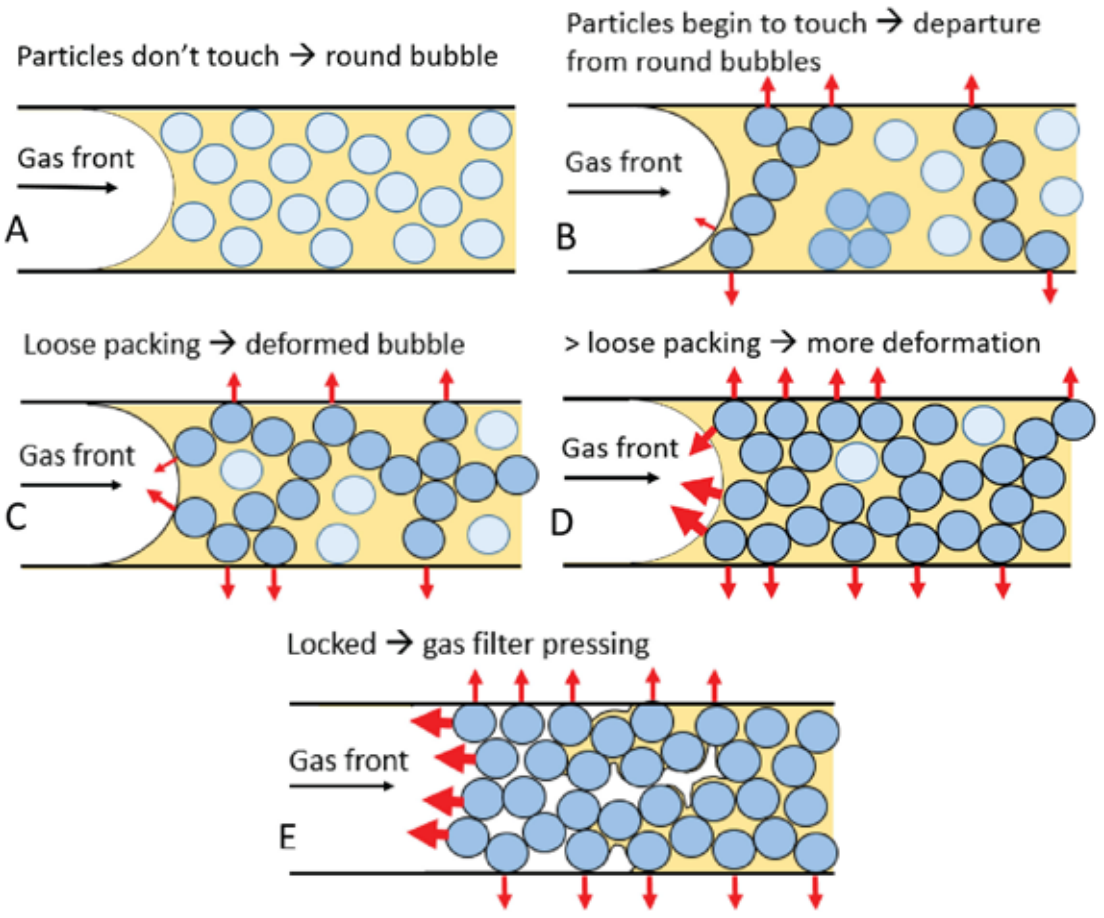

Figure 4. Cartoon representing the likely interaction of spherical particles for: dilute suspensions of unconnected particles [A], suspensions at the onset of non-Newtonian behaviour [B], at random loose packing (RLP; C), approaching random close packing [D], and locked suspensions [E]. Arrows indicate possible locations of applied normal force on experiment boundaries, and resistance to bubble growth. (Arrow size is non-proportional).

Previous research shows a more severe form of bubble deformation. If particle fraction increases beyond RCP, or if confining pressures are high at RCP, the particle network can lock. Under these conditions, the gas front cannot mobilize the particles, because the mechanical forces that resist particle displacement are stronger than those generated by bubble expansion, and the gas must advance by invading the pore-space (Figure 4[E]; Islam et al., 2013; Holtzman et al., 2010, 2012). This regime is called "pore-space invasion" by engineers, and is often referred to by volcanologists as "gas-driven filter-pressing" (Bacon, 1986; Sisson and Bacon, 1999). We also expect the onset of this regime to depend on crystal size (Jain and Juanes, 2009): as the space between crystals increases, the force necessary to mobilise the liquid becomes lower relative to the force necessary to mobilise the bulk suspension.

7. 3 **- Implications for outgassing of three-phase suspensions**

Outgassing occurs either through buoyant bubble rise or through permeable pathways created by inter-connected bubbles. In the experiments with pervasive bubble growth through chemical reaction, the significant reduction in foam expansion (Figure 2) coincided with the onset of bubble deformation, suggesting that gas was escaping these foams more effectively. This led to the conclusion that bubble deformation increased the likelihood of bubble coalescence, as demonstrated by e.g. Saar et al., (2001), and thus favoured the formation of outgassing pathways. This has implications for the vesiculation of three-phase suspensions that are sufficiently particle-rich for particle-particle interactions: at any given porosity, the bubble connectivity should be greater for greater particle fractions, up to the RCP.

The implications of our experiments for the effect of particle fraction on the development of permeable pathways are summarized in Figure 5. When particle fractions are low, bubbles remain round and there is little bubble coalescence, thus the gas percolation threshold remains high. In this "round bubble" regime, outgassing is likely to decrease with increasing particle fraction, because of the associated increase in bulk viscosity that slows bubble rise. At the non-Newtonian transition, or at random loose packing (RLP) depending on the applied stress, bubbles begin to deform and thus the gas percolation threshold decreases until the random close packing (RCP). At RCP, bubble morphology depends on parameters other than particle fraction, such as confinement and pore size [Holtzman et al., 2012; Holtzman and Juanes, 2010; Jain and Juanes, 2009]. If, for example, pore spaces are large and confinement is high, the regime is likely to switch to the pore invasion regime. In this regime, bubbles deform through Saffman-Taylor instabilities. They are less elongate than pseudo-fractures, thus the development of permeable pathways is likely reduced in the pore invasion regime relative to the pseudo- fracture regime.

7. 4 **- Application to magmas**

The gas migration regimes observed in this research could be important for crystal-rich magmas. The experiments show that variations in outgassing efficiency can be caused by crystallinity (Figure 5). In turn, outgassing efficiency is likely to affect eruption style and explosivity. Therefore, determining how these regimes might develop in crystal-rich magmas could alter our interpretations of crystal-rich eruption styles. Furthermore, a crystallising magma (or a melting magma) can have variable outgassing patterns, with implications for volcanic gas monitoring.

The experimental conditions in this research were idealised, therefore their applicability to magma must be explored. The existence of the round and deformed bubble regimes is evidenced in the textures of eruption products. In line with the analogue experiments, round bubbles are found in rocks with low crystal fractions (Figure 6a) whereas bubbles are contorted and deformed in crystal-rich rocks (Figure 6b-f). The pseudo-fracture regime, however, is unlikely to leave traces, as the pseudo-fractures sealed relatively quickly upon outgassing. Finally, gas filter-pressing is a well-established phenomenon in magmatic environments. Therefore, gas migration regimes do occur in magmas, but the transitions between regimes and the conditions in which they emerge are unclear.

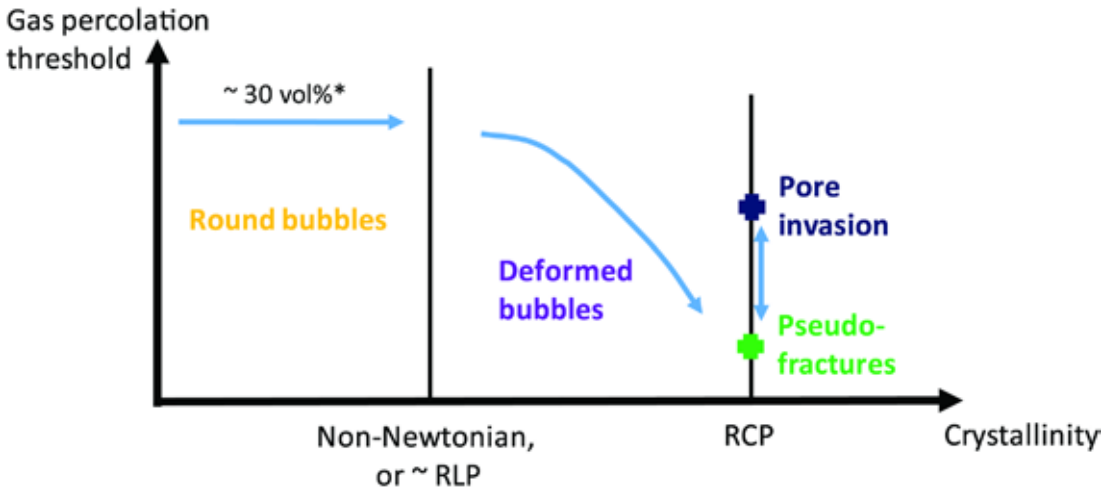

Figure 5. Idealized graph of variations in percolation threshold (bubble volume necessary for permeability development) with particle fraction, when all other parameters are constant. For volcanoes, these changes in outgassing efficiency are likely to affect eruption style and explosivity. They can also affect interpretation of volcanic gas monitoring.
* Approximate percolation threshold for round bubbles, determined through percolation theory (Saar et al., 2001).

The analogue experiments rely on several fundamental simplifications: the particles are spherical or crushed, and the bubbles are the only phase in the experiments that evolves with time. Particle shape is important because it can affect random packing values (percolation threshold, RLP and RCP), which indicate regime transitions. Crystal size and shape distributions are highly variable in magmas, and random packing values are thus poorly constrained. Furthermore, natural magmas are dynamic systems that are rarely in equilibrium. Crystals grow and resorb with changing temperature and pressure, crystals grow onto other crystals, external sources of shear are applied on the magma (e.g. during rise), and we have already suggested that stresses applied on the crystal network by the growing bubble may affect regime transitions (Fig. 3[C]). We will cover these parameters in the following sections.

7. 4.1 - Crystallinity and random packing values in magmatic environments

Variations in gas migration regimes in the experiments were due to interactions between bubbles and particles in particle-rich mushes. Here, we assess the ranges of applicability of these gas migration regimes in natural magmas, in order to determine whether these regimes can indeed affect eruption dynamics.

Our analogue experiments show an onset of bubble deformation at a similar φ value regardless of set-up geometry, liquid viscosity, and method of bubble generation. While internal bubble pressure and crystal size might shift the transition, φ remains the primary control for regime transitions. Therefore, a first step toward applying this work is to determine random packing values (percolation threshold, RLP and RCP) of crystals in magmas. Random packings, however, might vary from one magma to another, depending on crystal size and shape distributions (e.g. Baker & Kudrolli

2010; Moitra and Gonnermann, 2015), therefore investigation of random packing in natural samples can be challenging.

Modelling efforts provide estimates for the percolation threshold (Saar et al., 2001; Garboczi et al., 1995), RLP (Delaney et al., 2011) and the maximally random jammed state (MRJ) for particles of varying aspect ratio (Figure 7). MRJ is an attempt at quantitatively defining RCP as the closest packing of a suspension in its least ordered state (Torquato et al., 2000), and is useful for prolate or oblate suspensions as it ensures random orientation of the particles (Donev et al., 2003). These models can provide an estimate of the ranges of particle fractions at which particles of various aspect ratios interact.

In practice, since we suggest that shear-dilation causes bubble deformation (Oppenheimer et al., 2015), we can look for evidence of this flow behaviour in magmas. Shear-dilation was observed in experimental magmas as early as 1979 by van der Molen and Patterson, who sheared melted granites and observed that samples with higher crystallinities (65%) drew in externally available melt when sheared. More recent rheological experiments of real, synthetic, and analogue magmas have isolated an onset of "apparent yield strength" or "false yield strength" which increases significantly at high particle fractions. An apparent yield strength is a non-Newtonioan behaviour generally associated with shear dilation. For crystals with relatively high aspect ratios (e.g. plagioclase), these investigations place the rheological transition at crystallinities around 18 – 40 vol% (Picard et al., 2013 [20-40 vol%, AR 3.5 – 5]; Jerram et al., 2003 [20 – 30 vol%]; Hoover et al., 2001 [18 – 22 vol%, AR 3.4]). For more equant crystals, this rheological transition occurred around 35 – 50 vol% (Caricchi et al., 2007 [~40-50 vol%; crushed quartz]; Hoover et al., 2001 [35 – 45 vol%; AR ≈ 1.1 – 1.3]). These values are above the percolation threshold, hence the suspension rheology is likely subject to interactions between particles. However, they are also often below the model estimates for RLP: either the experimental cases haver lower RLP values than idealised models (due to experimental variability such as particle roughness, and ranges in particle size and aspect ratio), or the environmental conditions in rheological experiments are fundamentally different from ours (e.g. performed exclusively at lower stress).

There is also evidence for shear dilation in magmas from the internal and external textures of natural samples. For instance, Smith (2000) identified glassy shear zones symptomatic of shear dilation, in trachyte dykes. The expansion (i.e. dilatancy) associated with shear-dilation may also cause crystal-scale roughness of magma-gas interfaces at bubble boundaries and on the surfaces of flows or clasts (rather than smooth, ropy surfaces; Soule and Cashman, 2005; Hoover et al., 2001). Textural analysis of Hawai'ian lava flows shows that the transition from pahoehoe (smooth flows; Fig. 6a) to 'a'a (self-brecciating flows; Fig. 6b) occurs at crystallinities of 25 - 35 vol% (Katz and Cashman, 2003), consistent with the rheological transition for elongate crystals discussed above (Figure 7). Since bubble deformation is greater, and bubble content (vesicularity) is lower in 'a'a flows than in pahoehoe flows (Polacci et al., 1999; Sehlke et al., 2014), this rheological transition does seem to coincide with a transition in gas migration behaviour. Therefore, in basalts, the transition from round bubbles to deformed bubbles may occur around 25 – 35 vol% crystals.

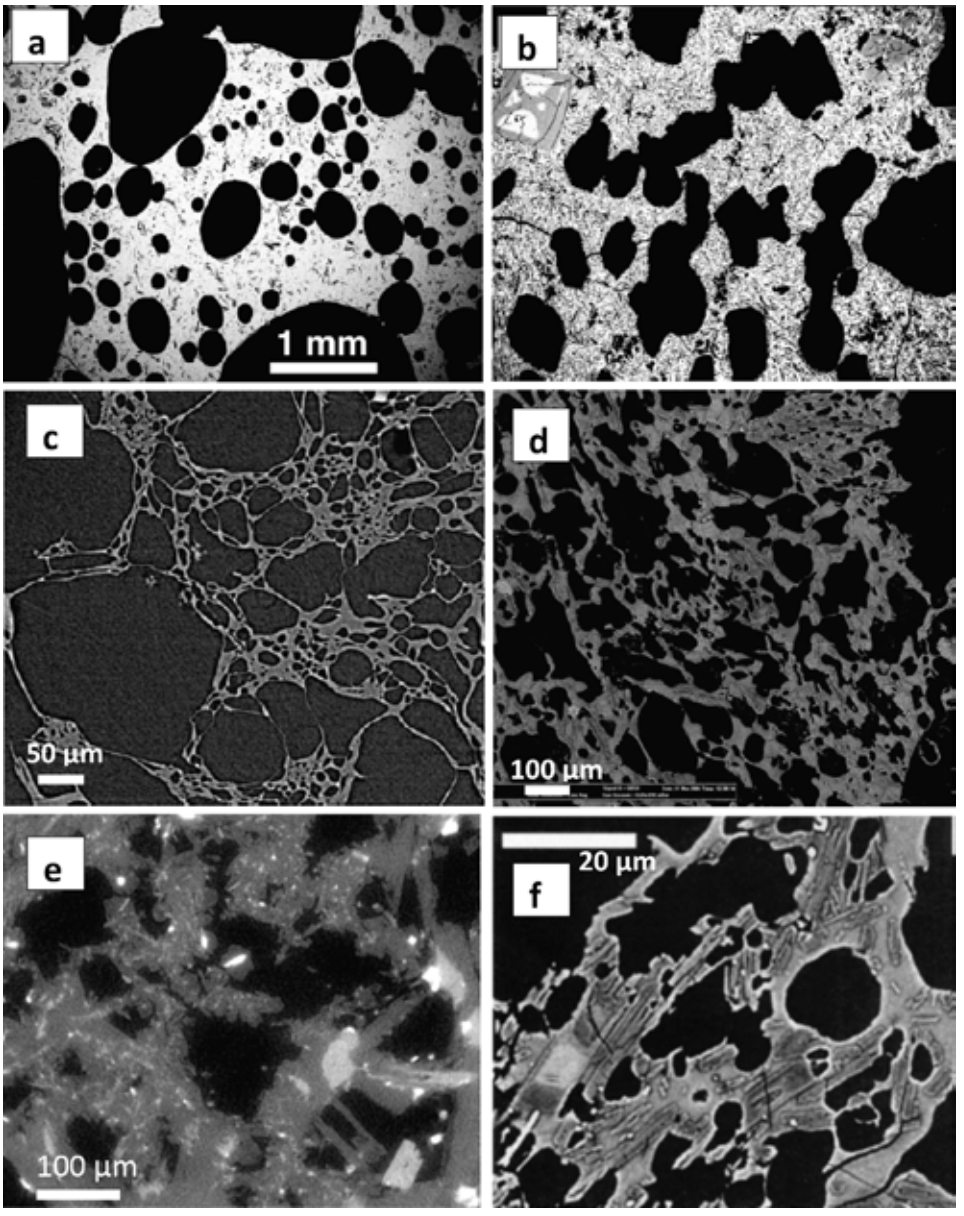

Figure 6. BackScatter Elecron microphotographs showing bubble shapes in samples from a variety of eruption styles and magma compositions. Melt and crystals are grey, bubbles are black, and all crystallinities given are bubble-free crystallinities. (a) Hawaiian pahoehoe flow with low crystallinity of 7 vol% and round bubbles (Cashman et al., 1999); and (b) Hawaiian ***basaltic***'a'a ***flow*** with crystallinity 45 vol% (Cashman et al., 1999), in which bubbles are significantly more deformed than in the pahoehoe sample. (c) ***Basaltic-andesite scoria*** from Paricutin, with crystallinity 54 vol%; (d) ***Trachytic pumice*** with crystallinity = 39 vol% from Campi Flegrei (Piochi et al., 2008); (e) ***Basaltic-andesite enclave*** from Mt Mazama, Oregon, with crystallinity > 60 vol%, showing possible pseudo-fractures (from original sample suite studied in Bacon, 1986). (f) ***Dacitic pumice*** from Mt St Helens, 1980, crystallinity ~48 vol% (Cashman and Blundy, 2000): here, straight bubble edges are visibly parallel to crystals.

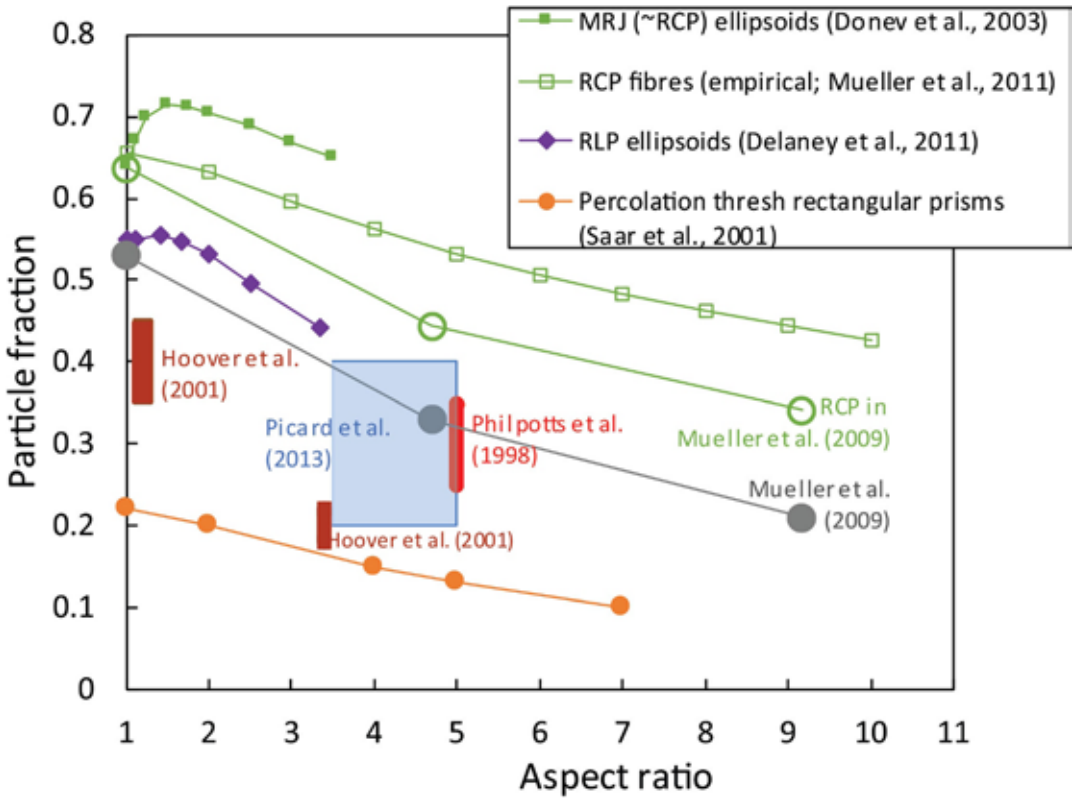

Figure 7. Rheological and packing thresholds for prolate ellipsoids and rectangular prisms from various experimental and numerical investigations. The connected data points show results from numerical models for the onset of percolation threshold (orange), random loose packing (RLP; purple), maximally random jammed state (MRJ; green, filled squares), and an empirical random close packing (RCP; green, open squares). Shaded areas represent the onset of apparent yield strengths in experimental investigations (references are indicated near the shaded areas, and referred to in the main text). Analogue experiments by Mueller (2009; grey discs) appear to have given the results closest to RCP, especially for their most "idealised" particles (glass spheres, AR = 1).

Marsh (1981) show that most erupted lavas have less than 55 vol% phenocrysts, suggesting that magmas with > 55 vol% crystals are too crystalline to erupt. To our knowledge, his value has not been challenged since, although models developed for natural cases often conservatively estimate that magmas become locked above ~50 vol% crystals (e.g. Huber et al., 2012). One might therefore assume that RCP for phenocrysts in magmas is ~55 vol%. Assuming that significant bubble deformation begins in magmas around $0.63 < \varphi < 0.86$ (depending on shear stress; Figure 3), then bubble deformation regimes begin for phenocrysts at crystallinities between 35 and 47 vol%. Microlites are generally more elongate and therefore are likely to have lower random packing values than phenocrysts (Figure 7). They are also smaller, thus less favourable for the pore invasion regime at relatively low φ (Jain and Juanes, 2009). Therefore, gas migration regimes occur at crystallinities relevant for magmas, and are particularly pertinent for groundmass textures.

In summary, the available experiments and theory on particle interactions in suspensions indicate that deformed bubbles should begin to appear in magmas between 20 and 50 vol% crystallinity

which is consistent with the textures observed in eruption products (Figure 6). Furthermore, there are strong links between the rheology of suspensions, shear dilation and gas migration regimes because they are all controlled by the interactions of particles in suspension. Therefore, critical crystal fractions can be identified through other methods (e.g. rheological tests), and used to predict gas migration regimes in different magmas.

7. 4 2 - Applicability to dynamically evolving systems

In this section, we speculate on the applicability of results from experiments with no crystallization and no external shear to dynamic natural systems, and discuss how time-dependent phenomena may affect the bubble deformation model.

Dynamic bubble growth: In the analogue experiments, the concentration of the volatile phase was the only parameter that changed with time: bubble growth was studied dynamically with either a single bubble, or with many bubbles, and the regime changes occurred at the same (bubble-free) particle concentration. Therefore, regardless of bubble number densities, once magma crystallinity reaches the critical φ, the gas migration behaviour can change dramatically from a round bubble regime to a deformed (or side flow) regime. If the suspension bears many bubbles, it can switch from a gas retention regime to a more permeable regime by forming outgassing pathways. In the case of single bubbles, a severely deformed bubble might find an outgassing pathway at lower bubble volume, through fingers (or pseudo-fractures) that reach farther into the suspension. However, gas front propagation requires higher internal bubble pressures than in particle-poor suspensions (Oppenheimer et al., 2015).

The gas migration regimes are most applicable to bubbles that are growing dynamically and are significantly larger than the crystals. Bubbles of similar size to the crystals are also affected by local force interplays at crystal boundaries (e.g. Belien et al., 2010), and bubbles smaller than the pore-space are more likely entrained in the liquid phase (e.g. Boudreau, 2016; Belien et al., 2010). The occurrence of pseudo-fractures depends on high strength of the bulk suspension, and thus is more applicable to systems with many crystals and sparse bubbles, such as evolved crystallised systems that have already lost most of their volatiles (e.g. conduit plugs and some lava domes). Finally, bubbles in our experiments mobilise the liquid-particle suspensions, and are therefore applicable when bubble pressures are high enough to compete with the mechanical forces between crystals (Holtzman et al., 2010, 2012).

Crystallisation processes: The analogue experiments did not have dynamically changing particle contents; each individual experiment had constant liquid and particle fractions. In a magma, cooling and gas exsolution cause the crystal fraction to increase. Therefore, crystallising magma can spontaneously change regime-types: it can switch from a bubble retention phase to an outgassing phase, and vice versa. When the crystallinity is at the boundary of a regime transition, a drastic change in bubble behaviour can occur with only small changes in crystallinity, causing variations in outgassing activity with time. Likewise, spatial variability can cause different vents of the same volcano to have different outgassing behaviours depending on bubble and crystal interactions near the surface (in this case, Stromboli might be a good case study; Landi et al., 2011).

Furthermore, the particles in the experiments were introduced by mixing and could not weld by growing onto each other. Thus force chains were built by contact and friction between particles. Crystals in magmas grow dynamically, and thus are likely to grow onto other crystals. On the one hand, heterogeneous nucleation can form crystal clusters, dendritic intergrowths, spherulites, or other irregular shapes which may lower the crystallinity necessary for force-bearing crystal networks to develop. On the other hand, they could form undeformable networks of particle intergrowths, as observed with plagioclase crystals by Philpotts et al., (1998, 1999) and Hoover et al., (2001). Locked (or undeformable) crystal networks can then occur at much lower crystal fractions than for unattached particles (the red area in Figure 7 shows the onset of plagioclase intergrowths by Philpotts et al., 1998). Depending on the strength of these chains, and on the behaviour of other crystals around them, bubble shapes could transition to the pore space invasion regime at substantially lower crystal fractions than suggested by the analogue experiments.

Constraints on shear: Experiments with large bubble rise in vertical tubes showed that the magnitude of the stress applied on the suspension may affect transitions in gas migration regimes. The experimental results are therefore most applicable to a magma body at rest, or flowing slowly, with crystals that are randomly oriented and in which the main source of stress is the growing bubbles. In magmas, shear stresses due to flow are higher near hard boundaries (e.g. walls of rising magmas, base of lava flows) and cause bubble elongation and coalescence (Okumura et al., 2009, 2008; Rust et al., 2003), particle re-orientation (Mueller et al., 2010; Ildefonse et al., 1992), and breakage of crystals and crystal-clusters (Mair et al., 2002; Chang and Powell, 1993). All of these parameters can affect the rheology of the suspension, as well as bubble growth, coalescence and splitting. They can therefore affect gas migration regimes.

7. 5 **- Concluding remarks**

The increase in outgassing efficiency when crystallinity approaches RCP answers our introductory question: it explains the efficient outgassing at crystal-rich volcanoes (e.g. crystal-rich and volatile-poor plutons, lava flows, and domes). However, the implications of gas migration regimes go beyond application to volatile-poor effusive eruptions. These findings also have important implications for more explosive eruptions, for eruptive processes in the conduit, and for interpretations of field samples.

The rheological changes induced by crystals in magmas can affect bubble shapes and significantly alter outgassing behaviours of crystal-bearing magmas. Bubbles that have been deformed by interaction with crystals are ubiquitous (e.g. Figure 6) and transitions in gas migration behaviour occur at crystallinities that are commonly found in magmas, but they are likely to vary with flow conditions, and with crystal size and shape distributions. The possible implications of gas migration regimes for outgassing and eruption dynamics make them worthy of further investigation. Therefore, resolving bubble-crystal interactions in dynamically changing environments may allow a more direct application to volcanic settings, as will further work into the effects of crystal shape and size distributions on gas migration regimes.

Finally, since regime transitions depend primarily on mechanical interactions between particles in the invaded suspension, our deformation regimes are also applicable to other fields in volcanology, such as liquid-mush interactions that lead to magma mixing and enclave formation, or to industrial applications of gas migration in slurries, such as for nuclear waste storage (e.g. Gauglitz et al., 2012; Rassat et al., 1998).

Acknowledgements

The research leading to these results has received funding from the European Union Seventh Framework Programme (FP7/2007-2013) under the project NEMOH, grant agreement n° 289976. I would like to extend my warmest thanks to my secondment advisors Stephen Lane, Michael James, and Antonio Capponi. Many thanks, also, to Charles Clapham for his help building the Hele-Shaw cell, and Bjornar Sandnes, Heidy Mader, Jon Blundy, Paul Jarvis, Irving Munguia, and an anonymous reviewer for conversations and comments that significantly improved this research and this manuscript.

References

Baker, J. and Kudrolli, A. (2010). Maximum and minimum stable random packings of platonic solids. Physical Reviews E, 82(6).

Belien, I.B., Cashman, K. V. and Rempel, A. W. (2010). Gas accumulation in particle-rich suspensions and implications for bubble populations in crystal-rich magma. Earth Planet. Sci. Lett. 297: 133–140. DOI: 10.1016/j.epsl.2010.06.014.

Bi, D. P., Zhang, J., Chakraborty, B. and Behringer, R. P. (2011). Jamming by shear, Nature, 480: 355-358. DOI 10.1038/nature10667.

Boudreau, A., (2016). Bubble migration in a compacting crystal-liquid mush, Contributions to Mineral Petrology, 171 (32): 17 DOI: 10.1007/s00410-016-1237-9.

Brown, E. and Jaeger, H. M. (2014). Shear thickening in concentrated suspensions: phenomenology, mechanisms, relations to jamming. Reports on Progress in Physics,77 (4): 23, DOI 10.1088/0034-4885/77/4/046602.

Brown, E., Zhang, H. J., Forman, N. A., Maynor, B. W., Betts, D. E., DeSimone, J. M. and Jaeger, H. M (2011). Shear thickening, jamming in densely packed suspensions of different particle shapes. Physical Review E, 84 (3): 11, DOI 10.1103/PhysRevE.84.031408.

Brown, E. and Jaeger, H. M. (2012). The role of dilation, confining stresses in shear thickening of dense suspensions. Journal of Rheology, 56 (4): 875-923, DOI :10.1122/1.4709423.

Capponi, A., James, M. R. and Lane, S. J. (2016). Gas slug ascent in a stratified magma: Implications of flow organisation, instability for Strombolian eruption dynamics. Earth and Planetary Science Letters, 435: 159-170, DOI: 10.1016/j.epsl.2015.12.028.

Caricchi, L., Burlini, L., Ulmer, P., Gerya, T., Vassalli, M. and Papale, P. (2007). Non-Newtonian rheology of crystal-bearing magmas, implications for magma ascent dynamics. Earth and Planetary Science Letters, 264 (3-4): 402-419, DOI: 10.1016/j.epsl.2007.09.032.

Cashman, K. V. (1992). GROUNDMASS CRYSTALLIZATION OF MOUNT ST HELENS DACITE, 1980-1986 - A TOOL FOR INTERPRETING SHALLOW MAGMATIC PROCESSES. Contributions to Mineralogy and Petrology, 109 (4): 431-449, DOI: 10.1007/bf00306547.

Cashman, K. V. and Blundy J. (2000). Degassing and Crystallization of Ascending Andesite and Dacite. Philosophical Transactions: Mathematical, Physical and Engineering Sciences, 358 (1770): 1487-1513.

Cashman, K. V., Thornber, C. and Kauahikaua, J. P. (1999). Cooling and crystallization of lava in open channels, and the transition of Pahoehoe Lava to 'A'a. Bulletin of Volcanology, 61 (5): 306-323, DOI: 10.1007/s004450050299.

Chang, C. Y. and Powell, R. L. (1993). DYNAMIC SIMULATION OF BIMODAL SUSPENSIONS OF HYDRODYNAMICALLY INTERACTING SPHERICAL-PARTICLES. Journal of Fluid Mechanics, 253: 1-25. DOI :10.1017/s0022112093001697.

Del Bello, E., Llewellin, E. W., Taddeucci, J., Scarlato, P. and Lane, S. J. (2012). An analytical model for gas overpressure in slug-driven explosions: Insights into Strombolian volcanic eruptions. Journal of Geophysical Research-Solid Earth, 117. DOI :10.1029/2011jb008747.

Delaney, G. W., Hilton, J. E. and Cleary, P. W. (2011). Defining random loose packing for nonspherical grains. Physical Review E, 83 (5). DOI: 10.1103/PhysRevE.83.051305.

Garboczi, E. J., Snyder, K. A., Douglas, J. F. and Thorpe, M. F. (1995). GEOMETRICAL PERCOLATION-THRESHOLD OF OVERLAPPING ELLIPSOIDS. Physical Review E., 52 (1): 819-828. DOI: 10.1103/PhysRevE.52.819.

Gauglitz, P.A., Buchmiller, W.C., Probert, S.G., Owen, A.T. and Brockman, F.J. (2012). Strong-Sludge Gas Retention and Release Mechanisms in Clay Simulants. Report for the U.S. Department of Energy (PNNL-21167 Rev 0).

Holtzman, R. and Juanes, R. (2010). Crossover from fingering to fracturing in deformable disordered media. Physical Review E, 82 (4): 5. DOI: 10.1103/PhysRevE.82.046305.

Holtzman, R., Szulczewski, M. L. and Juanes, R. (2012). Capillary Fracturing in Granular Media. Physical Review Letters, 108 (26): 4. DOI: 10.1103/PhysRevLett.108.264504.

Hoover, S. R., Cashman, K. V. and Manga, M. (2001). The yield strength of subliquidus basalts - experimental results. Journal of Volcanology and Geothermal Research, 107 (1-3): 1-18. DOI :10.1016/s0377-0273(00)00317-6.

Huber, C., Bachmann, O., Vigneresse, J.-L., Dufek, J. and Parmigiani, R. (2012). A physical model for metal extraction, transport in shallow magmatic systems. Geochemistry Geophysics Geosystems, 13. DOI: 10.1029/2012gc004042.

Ildefonse, B., Launeau, P., Bouchez, J. L. and Fernandez, A. (1992). EFFECT OF MECHANICAL INTERACTIONS ON THE DEVELOPMENT OF SHAPE PREFERRED ORIENTATIONS - A 2-DIMENSIONAL EXPERIMENTAL APPROACH. Journal of Structural Geology, 14 (1): 73. DOI: 10.1016/0191-8141(92)90146-n.

Islam, A., Chevalier, S. and Sassi, M. (2013). Experimental, numerical studies of CO2 injection into water-saturated porous medium: capillary to viscous to fracture fingering phenomenon. GHGT-11 Proceedings of the 11th International Conference on Greenhouse Gas Control Technologies, 37: 5511-5519. DOI: 10.1016/j.egypro.2013.06.471.

Jain, A. K. and Juanes, R. (2009). Preferential Mode of gas invasion in sediments: Grain-scale mechanistic model of coupled multiphase fluid flow, sediment mechanics. Journal of Geophysical Research-Solid Earth, 114. DOI: 10.1029/2008jb006002.

James, M. R., Lane, S. J., Wilson, L. and Corder, S. B. (2009). Degassing at low magma-viscosity volcanoes: Quantifying the transition between passive bubble-burst and Strombolian eruption. Journal of Volcanology and Geothermal Research, 180 (2–4): 81–88. DOI: 10.1016/j.jvolgeores.2008.09.002.

Jerram, D. A., Cheadle, M. J. and Philpotts, A. R. (2003). Quantifying the building blocks of igneous rocks: Are clustered crystal frameworks the foundation? Journal of Petrology, 44 (11): 2033-2051. DOI: 10.1093/petrology/egg069.

Katz, M. G. and Cashman, K. V. (2003). Hawaiian lava flows in the third dimension: Identification, interpretation of pahoehoe, 'a'a distribution in the KP-1, SOH-4 cores. Geochemistry Geophysics Geosystems, 4. DOI: 10.1029/2001gc000209.

Landi, P., Marchetti, E., La Felice, S., Ripepe, M. and Rosi, M. (2011). Integrated petrochemical, geophysical data reveals thermal distribution of the feeding conduits at Stromboli volcano, Italy. Geophysical Research Letters, 38. DOI: 10.1029/2010gl046296.

Mair, K., Frye, K. M. and Marone, C. (2002). Influence of grain characteristics on the friction of granular shear zones. Journal of Geophysical Research-Solid Earth, 107 (B10). DOI: 10.1029/2001jb000516.

Marsh, B. D. (1981). On the crystallinity, probability of occurrence, and rheology of lava and magma. Contributions to Mineralogy and Petrology, 78 (1): 85-98. DOI: 10.1007/bf00371146.

Moitra, P. and Gonnermann, H.M. (2015). Effects of crystal shape- and size-modality on magma rheology. Geochemistry Geophysics Geosystems, 16(1): 1-26.

Mueller, S., Llewellin, E. W. and Mader, H. M. (2010). The rheology of suspensions of solid particles. Proceedings of the Royal Society a-Mathematical Physical, Engineering Sciences, 466 (2116): 1201-1228. DOI: 10.1098/rspa.2009.0445.

Mueller, S., Llewellin, E. W. and Mader, H. M. (2011). The effect of particle shape on suspension viscosity, implications for magmatic flows. Geophysical Research Letters, 38 (13): 5. DOI: 10.1029/2011gl047167.

Okumura, S., Nakamura, M., Takeuchi, S., Tsuchiyama, A., Nakano, T. and Uesugi, K. (2009). Magma deformation may induce non-explosive volcanism via degassing through bubble networks. Earth and Planetary Science Letters, 281 (3-4): 267-274. DOI: 10.1016/j.epsl.2009.02.036.

Okumura, S., Nakamura, M., Tsuchiyama, A., Nakano, T. and Uesugi, K. (2008). Evolution of bubble microstructure in sheared rhyolite: Formation of a channel-like bubble network. Journal of Geophysical Research-Solid Earth, 113 (B7). DOI: 10.1029/2007jb005362.

Onoda, G. Y. and Liniger, E. G. (1990). RANDOM LOOSE PACKINGS OF UNIFORM SPHERES, THE DILATANCY ONSET. Physical Review Letters, 64 (22): 2727-2730. DOI: 10.1103/PhysRevLett.64.2727.

Oppenheimer, J., Rust, A.C, Cashman, K. V. and Bjornar, S. (2015). Gas migration regimes and outgassing in particle-rich suspensions. Frontiers in Physics, 3 (60): 13.

Philpotts, A. R., Brustman, C. M., Shi, J. Y., Carlson, W. D. and Denison, C. (1999). Plagioclase-chain networks in slowly cooled basaltic magma. American Mineralogist, 84 (11-12): 1819-1829.

Philpotts, A. R., Shi, J. Y. and Brustman, C. (1998). Role of plagioclase crystal chains in the differentiation of partly crystallized basaltic magma. Nature, 395 (6700): 343-346. DOI: 10.1038/26404.

Picard, D., Arbaret, L., Pichavant, M., Champallier, R. and Launeau, P. (2013). The rheological transition in plagioclase-bearing magmas. Journal of Geophysical Research-Solid Earth, 118 (4): 1363-1377. DOI: 10.1002/jgrb.50091.

Piochi, M., Polacci, M., De Astis, G., Zanetti, A., Mangiacapra, A., Vannucci, R. and Giordano, D. (2008). Texture, composition of pumices, scoriae from the Campi Flegrei caldera (Italy): Implications on the dynamics of explosive eruptions. Geochemistry Geophysics Geosystems, 9. DOI: 10.1029/2007gc001746.

Polacci, M., de Maisonneuve, C. Bouvet, Giordano, D., Piochi, M., Mancini, L., Degruyter, W. and Bachmann, O. (2014). Permeability measurements of Campi Flegrei pyroclastic products: An example from the Campanian Ignimbrite, Monte Nuovo eruptions. Journal of Volcanology and Geothermal Research, 272: 16-22. DOI: 10.1016/j.jvolgeores.2013.12.002.

Rassat S.D., Claey, S.M., Bredt, P.R., Gauglitz, P.A., Rinehart D.E. and Forbes, S.V. (1998). Mechanisms of Gas Retention and Release: Experimental Results for Hanford Single-Shell Waste Tanks 241-A-101, 241-S-106, and 241-U-103. Report for the U.S. Department of Energy (PNNL-11981).

Rust, A. C., Manga, M. and Cashman, K. V. (2003). Determining flow type, shear rate, shear stress in magmas from bubble shapes, orientations. Journal of Volcanology and Geothermal Research, 122 (1-2): 111-132. DOI: 10.1016/s0377-0273(02)00487-0.

Saar, M. O., Manga, M., Cashman, K. V. and Fremouw, S. (2001). Numerical models of the onset of yield strength in crystal-melt suspensions. Earth and Planetary Science Letters, 187 (3-4): 367-379. DOI: 10.1016/s0012-821x(01)00289-8.

Savov, I. P., Luhr, J. F. and Navarro-Ochoa, C. (2008). Petrology, geochemistry of lava, ash erupted from Volcan Colima, Mexico, during 1998-2005. Journal of Volcanology and Geothermal Research, 174 (4): 241-256. DOI: 10.1016/j.jvolgeores.2008.02.007.

Shinohara, H., (2008). Excess degassing from volcanoes and its role on eruptive and intrusive activity. Reviews of Geophysics, 46 (4), RG4005. DOI: 2007RG000244

Sehlke, A., Whittington, A., Robert, B., Harris, A., Gurioli, L. and Medard, E. (2014). Pahoehoe to 'a' a transition of Hawaiian lavas: an experimental study. Bulletin of Volcanology, 76 (11). DOI: 10.1007/s00445-014-0876-9.

Seto, R., Mari, R., Morris, J. F. and Denn, M. M. (2013). Discontinuous Shear Thickening of Frictional Hard-Sphere Suspensions. Physical Review Letters, 111 (21): 5. DOI: 10.1103/PhysRevLett.111.218301.

Sisson, T. W. and Bacon, C. R. (1999). Gas-driven filter pressing in magmas. Geology, 27 (7): 613-616. DOI: 10.1130/0091-7613(1999)027<0613:gdfpim>2.3.co;2.

Smith, J. V. (2000). Textural evidence for dilatant (shear thickening) rheology of magma at high crystal concentrations. Journal of Volcanology and Geothermal Research, 99 (1-4): 1-7. DOI: 10.1016/s0377-0273(99)00191-2.

Soule, S. A. and Cashman, K. V. (2005). Shear rate dependence of the pahoehoe-to-'a'a transition: Analog experiments. Geology, 33 (5): 361-364. DOI: 10.1130/g21269.1.

Torquato, S., Truskett, T. M. and Debenedetti, P. G. (2000). Is random close packing of spheres well defined? Physical Review Letters, 84 (10): 2064-2067. DOI: 10.1103/PhysRevLett.84.2064.

Julie Oppenheimer, France
jo0231@my.bristol.ac.uk

Affiliation under NEMOH
University of Bristol, Bristol, United Kingdom

Research theme under NEMOH
Gas migration regimes in crystal-bearing magmas

I have a fairly eclectic background in geoscience: During my undergraduate degree, I specialized in physical geography and glaciology, then chose to study a Masters in Science of Natural Hazards. For my Masters thesis, I ran batch reaction models of chemical reactions and reactive transport in a magmatic hydrothermal system (using the program PHREEQC). It was during my PhD with NEMOH that I became fascinated with experimental work, and specifically with how bubbles and crystals affect eruption behaviour. I used three-phase analogues to simulate magma and observed the manners in which bubble morphology and gas migration pathways respond to interaction with particles. I then matched some of the experimentally determined flow regimes to textures in field samples from Mt Mazama (Crater Lake, Oregon), by tracking the morphology and volume fraction of bubbles and crystals in 2D (microscope and SEM) and 3D (X-ray tomography). During my NEMOH secondment in the Lancaster Environment Centre, I collaborated with NEMOH fellow Antonio Capponi: we ran analogue experiments to better constrain eruption behaviours of Stromboli Volcano (Italy). Through that collaboration, and through the NEMOH schools, I was introduced to acoustic and seismic signals at volcanoes, their use for interpretation of volcanic activity, and the manners in which they can be matched to experimental signals.

NEMOH has taught us, among many other lessons, the necessity for multi-disciplinary approaches to monitor and interpret volcanic eruptions. The multifaceted aspect of volcanology is what attracted me to the field in the first place. Hence, while I aspire to continue working in experimental volcanology, I also hope to develop my skills in other areas, specifically in analysis of field samples and geophysical signals to better link my experimental results with field data. In March 2017, I started a postdoctoral research position at Columbia University (NY, USA), further developing the research I started with NEMOH.

Chapter 8

Explosivity of steam-driven eruptions in volcanic systems

Cristian Montanaro

Department of Earth and Environmental Sciences, Ludwig-Maximilians-Universität München, Munich, Germany

Tutorship: Bettina Scheu

Department of Earth and Environmental Sciences, Ludwig-Maximilians-Universität München, Munich, Germany

Abstract

Steam-driven eruptions (e.g. phreatic and hydrothermal) represent a large percentage of explosive events, perhaps the majority, in volcanic systems. These eruptions only expel fragments of non-juvenile rocks disintegrated by the expansion of water as liquid or gas phase. The conditions that cause steam-driven eruptions arise through a rapid increase in temperature or decrease in pressure. Thus, these eruptions may occur with different degrees of explosivity, as their violence is related to the magnitude of the decompression work that can be performed by expansion of fluids. Steam-driven eruption deposits, though generally hardly recognized or badly preserved, yield information on the dynamics and energy of these explosive events.

In this chapter results from a study of two recent eruptive events, and a further experimental study are discussed. In particular these studies investigate the role played by i) the pressure, temperature and liquid fraction within a system before an eruption, and ii) the nature of the rock hosting the hydrothermal system. These parameters control the rate at which energy is released and in turns the violence of such explosive events.

Overall, the energy surplus in the presence of steam-flashing leads to 1) a faster fragmentation with respect to a gas-driven process, 2) a significant reduction of the average grainsize of produced material, as well as an increase in amount of very fine material, and 3) higher ejection velocities of fragmented particles. The lithologies investigated in this work (from loose sediments, to very heterogeneous tuff breccias and agglutinates, and fine-grained tuffs) cover large spectra of porosity, permeability and rock strength. The presence of low permeability layer or rocks may 1) lead to overpressurized condition during vaporization of water within loose sediment, or 2) reduce the pressure dissipation during the fragmentation process. Additionally, low strength rock can produce higher amount of fine particles than firmly cemented rocks. Finally the homogeneous or heterogeneous nature of rocks plays another important role, since the mixed presence of fine-grained matrix and dense clast can contribute to create both a large amount of very fine material (feeding pyroclastic density currents), together with larger fragments (analogous to ballistics formation).

Keywords: Steam-driven eruptions, explosive energy, experimental, fragmentation, hydrothermal eruptions.

8. 1 **- Introduction**

In this work I investigate the explosivity of steam-driven eruptions in volcanic systems by using several approaches, which involved field based studies, together with laboratory and theoretical studies.

Steam-driven eruptions are a very complex type of explosive event, and despite their frequent occurrence many questions remain open, particularly concerning the parameters controlling their violence (or explosive power). The violence depends largely on the different explosivity of fluids (liquid or gaseous) driving them, as well as on the rate of mechanical energy release. Both factors are in turn controlled by 1) the pore liquid fraction and its physical condition (pressure-temperature) before an explosive event, and 2) the lithology and the petrophysical properties (mainly porosity, permeability and strength) of the host medium. A wide range of initial temperature, pressure and liquid fraction, as well as a variety of lithotypes characterize the volcanic environments affected by steam-driven eruptions, and consequently they show a wide range of eruptive styles.

A combined field and experimental approach as a tool to characterize the explosivity of steam-driven eruptions may provide many estimates of the controlling parameters. Field data (e.g. deposit volume, thickness, area, etc.) are a solid basis for defining the boundary conditions for the application of both experimental and theoretical methods. Natural samples used for decompression experiments under controlled conditions (pressure, temperature, liquid fraction, etc.) permit further estimation of the energetic parameters of steam-flashing processes. Finally the energy associated with steam flashing can be assessed via thermodynamic modelling based on an isenthalpic (irreversible) approach. This method results in a more realistic estimation of explosive energy than the reversible approach. A comparison of these estimated energies with those obtained from independent methods (craterization energy, seismic energy, etc.) could help to define the energy portioning.

8. 2 **- Steam-driven eruptions**

Eruptions in magmatic and hydrothermal systems are violent phenomena that result in an explosive release of energy generated by the mechanical work of expanding fluids (Mastin, 1995; Zhang, 2000; Thiéry and Mercury, 2008, 2009; Thiéry et al., 2010). The best known and studied eruptions involve the expulsion of magma and magmatic gases from a vent (Gilbert and Sparks, 1998, Sigurdsson et al., 2015 and references therein). Yet a large percentage of eruptions, perhaps the majority, only expel fragments of non-juvenile rocks disintegrated by the expansion of flashed steam, gas or supercritical fluids (Mastin 1995; Browne and Lawless 2001; Morgan et al., 2009). Many partially exotic names have been introduced for these type of events, and referred to specific eruption mechanisms (Barberi et al. 1992; Mastin 1995; Browne and Lawless 2001), such as “hydro-explosions”, “hydrothermal eruption”, “steam-blast eruptions”, “phreatic eruption”, “boiling-point eruptions”, “gas-driven eruptions” and “mixing eruptions”, often creating ambiguity. Nevertheless the main cause of all of these types of explosive events is the presence of near-surface water, in liquid or gas form, whose expansion as steam drives the eruptions. Thus the more general term of *“steam-driven* eruption” can be used to include many of the above-described mechanisms.

The most common steam-driven eruptive events are represented by both phreatic and hydrothermal eruptions (following the terminology presented in Browne and Lawless, 2001). Heated ground or surficial water is the driving fluid behind phreatic eruptions (Stearns and McDonald 1949), but the input of mass (fluids) and energy deriving from magma is thought to be the trigger (Figure 1-3; Browne and Lawless, 2001). Hydrothermal eruptions instead specifically involve water close to its boiling temperature ("boiling-point" eruption of Mastin, 1995). This eruption type is generated in the near-surface, and result from the (rapid) formation of steam following a (sudden) pressure decrease (Browne and Lawless 2001; McKibbin et al., 2009). Generally hydrothermal eruptions do not result from any input of mass or energy directly derived from magma (Figure 2 and 4).

Steam-driven eruptions can last from seconds to hours (Browne and Lawless 2001; Jolly et al., 2014), and produce craters spanning from a few meters up to more than 2 km in diameter (Muffler et al., 1971; Browne and Lawless 2001). Typical ejection velocities vary between few tens of m/s up to more than 200 m/s (Mastin 1995; Kilgour et al., 2010; Breard et al., 2014). Deposits are generally of low volume ($<10^5$ m^3); they are typically very-poorly sorted, matrix-supported, and may contain hydrothermally altered clasts if they occur in geothermal reservoirs (Nelson and Giles 1985; Browne and Lawless 2001; Morgan et al., 2009). Although the deposits are often badly preserved and generally not recognized or described, they do provide important insights to quantify the dynamics and energy of the explosive events that generated them. The rock properties of the groundwater and hydrothermal systems reservoir, in particular, control the efficiency in the energy release during an eruption, directly affecting the craterization and ejection behavior (Browne and Lawless 2001; Thiéry et al., 2010; Breard et al., 2014; Lube et al., 2014; Mayer et al., 2015; Montanaro et al., 2016).

Steam-driven eruptions are common in many volcanic terrains as well as other areas of high heat flow where abundant hydrothermal or magmatic activity favors conditions for (rapid) generation of steam and pressure build-up (Figure 2). Active crater lakes also represent an increased potential for such events as they favor condensing of fluids that rise into the lake from below. This condition makes these lakes very sensitive to sudden pressure changes (fluid injections), increasing the likelihood of steam-driven eruptions (Manville et al., 2015).

Steam-driven eruptions affect a limited area surrounding the explosive vent(s). Still, they can be highly dangerous in densely populated zones, or in geothermal areas, which often host power plants, as well as visitor parks. Major hazards are produced by:

1) ejected ballistic blocks (Etna in Italy, 1979 and 1987: 9 and 2 deaths; Agua Shuca in El Salvador, 1990: 26 deaths; Mayon in Philippines, 2013: 5 deaths);

2) discharge of clouds of toxic or paralyzing gases (Larderello in Italy, 1282: uncertain number of deaths; Dieng in Indonesia, 1979: 149 casualties; Nyos in Cameroon, 1986: over 1700 casualties; Asa in Japan, 1997, 2 casualties);

3) production of base surges, lahars and directional blasts, sometimes accompanied by debris avalanches (Bandai in Japan, 1888: 461 victims; Karkar in Papua New Guinea, 1979: 2 victims; Ontake in Japan, 2014: 57 victims).

Figure 1. Phreatic eruption at Laguna Caliente on Poas Volcano, February 25, 2014 (on the left; source OVSICORI), and at White Island in New Zealand, on the August 19, 2013 (on the right; GeoNet webcam). Both the areas touristic site.

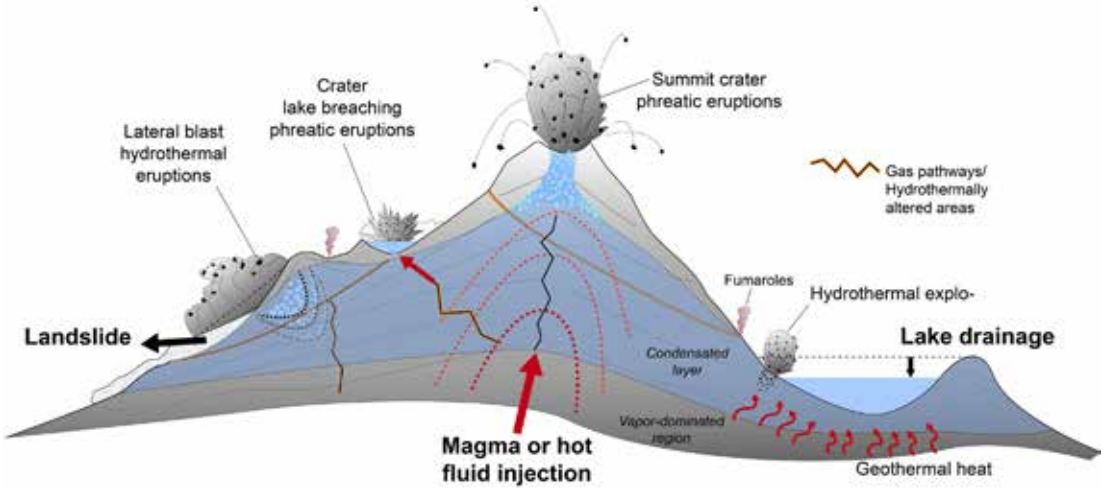

Figure 2. Schematic model of the main type of steam-driven eruptions and triggering mechanisms within a volcanic system.

The recent hydrothermal eruptions at Mt. Ontake in Japan (Yamamoto, 2014; Kato et al., 2015), as well as Ruapehu and Te Maari, in New Zealand (Figure 3; Kilgour et al., 2010; Breard et al., 2014), further highlighted the major proximal hazards of these events. Moreover they occurred with little or no pre-eruptive monitoring signals (Hurst et al., 2014). Indeed a part of their hazard potential is due to the fact that the timing and magnitude of hydrothermal eruptions are difficult to predict as they have manifold triggers (variances in groundwater and heat systems, earthquakes, material fatigue, water level failure, etc.; Barberi et al., 1992; Browne and Lawless, 2001). Consequently there are many problems concerning their detection in volcano monitoring systems; even though steam-driven eruptions have precursor phenomena, it is very difficult to single out the specific precursors (Barberi et al., 1992; Browne and Lawless 2001).

The conditions that cause steam-driven eruptions arise through a (rapid) increase in temperature or decrease in pressure. The contained fluids may flash to steam, resulting in significant volume increase and fragmentation of the enclosing rocks (McKibbin et al., 2009). The heating is the result of an increase in reservoir energy, (e.g. by injection of magma or magmatic gases), as in the recent Mt. Ontake eruption (Kato et al., 2015). Pressure reduction can arise due to removal of fluid from a geothermal area, for instance by exploitation, or a reduction in confining pressure by a landslide (e.g. Te Maari eruption; Breard et al., 2014), erosion processes, lowering of groundwater, or rapid draining of an overlying lake (e.g. Gengissig lake in Figure 4; Montanaro et al., 2016; Morgan et al., 2009; Muffler et al., 1971).

The response of a groundwater or geothermal system either to (rapid) increase in temperature or (sudden) decompression depends mostly on its permeability. Highly permeable rock systems are likely to efficiently release any steam generated, thus largely preventing pressure build-up and eruption. However, if such a system is capped by low-permeability layers, steam generated may not escape and pressurization of the groundwater or geothermal system is likely; sufficient pressurization may cause rupture of the capping layers and thus initiate rapid depressurization and thus eruptions (Browne and Lawless 2001; Seki et al., 2015; Montanaro et al., 2016).

8. 3 **- Explosivity of steam-driven eruptions**

An explosion is the violent response of a system to a physico-chemical perturbation, and the resulting energetic metastable state. Fast thermodynamic processes, such as the heating of water by magma, or rapid depressurization of a liquid produce highly transient metastable states, which tend to reach equilibrium in a very rapid and explosive way [*Thiéry and Mercury*, 2009]. Thus, rapid physical transformations of water are the causes of strong instabilities, which lead to explosive manifestations such as steam-driven eruptions. Particularly for hydrothermal systems, the (sudden) decompression of hot pressurized water is the main cause of such events [*Browne and Lawless*, 2001]. The (rapid) release of water stored at a temperature above its atmospheric-pressure boiling-point results in instantaneous vaporization (steam flashing). Steam-driven eruptions thus occur with different degrees of explosivity, as their violence is related to the magnitude of the decompression work that can be performed by the steam flashing [*Mastin*, 1995; *Thiéry and Mercury*, 2008, 2009; *Thiéry et al.*, 2010].

Figure 3. View of the western fissure from the ballistic field at Upper Te Maari, on Tongariro Volcanic complex, New Zealand. The eruptive fissure (red line) and delimitation of amphitheatre (dark brown line) created by the landslide are reported on the background. In front, the ballistic field impacted during the 2012 eruptions.

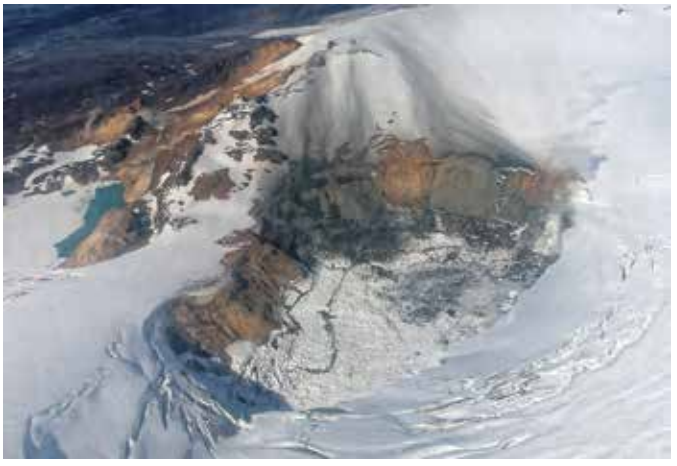

Figure 4. Aerial photo of Gengissig ice dammed on the 16th of August 2013; several small fans of ejecta are visible north of the lake to a distance of about 1 km. Hydrothermal explosions were triggered by the sudden lake drainage (photo of Hannah I. Reynolds).

The explosive energy released by the expansion work of the fluids (gas or liquid) in the rock pore space, from the breaking pressure in the pore up to the atmospheric pressure, is given by:

$$E_{Expl} = m \times DU \quad (1)$$

where E_{Expl} is the available explosive energy which can be released in the expansion of the fluids (J), m is the mass of fluid already existing in the pores at the moment of the failure (g), DU is the difference in internal energy of the fluid under the conditions before and immediately after the expansion (J/g). The estimated E_{Expl} gives the amount of energy which can be converted into fragmentation, kinetic and all other forms of energies such as inelastic deformation, shock waves, etc.. The maximum amount of work that can be extracted from an expansion, and thus the associated explosive energy, depends upon the thermodynamic path (Mastin, 1995; Thiéry and Mercury, 2009).

By assuming a fluid expansion which is adiabatic and reversible (isentropic), the produced work must be equal to the variation in internal energy of the fluid DU:

$$DU = -P_{atm} \times DV \quad (2)$$

where P_{atm} is the atmospheric pressure (1 bar), and DV is the volume increase (m^3). This assumption implies that the fluid expands isentropically as an ideal gas, and ignores any energy consumption through internal friction. Planas-Cuchi et al., (2004) modified this approach by equating the internal energy change of a fluid (water) to the irreversible work performed as the expanding vapor pushes against the surrounding medium. They also assumed that immediately after the expansion, there is liquid-vapor equilibrium at atmospheric pressure and at the corresponding saturation temperature. This assumption is much closer to the real situation and allows less conservative estimations of overpressure by taking irreversibility factors into account such as: friction, heat loss, unrestrained expansion of a gas, and others. The analytical solution of equation [2] applied to a mass of liquid which vaporizes, enables calculation of the flashed steam fraction accounting for irreversibility (Planas-Cuchi et al., 2004; Thiéry and Mercury, 2009) as:

$$x = 1\text{-}f = 1 - ([P_{atm} \times (v_{initial} - v_{vap}) - U_{vap} + U_{initial}]/[U_{liq} - U_{vap} + P_{atm} \times (v_{liq} - v_{vap})]) \quad (3)$$

where x and f represent the steam and liquid fraction respectively, v is the molar volume, and U the internal energy. $U_{initial}$ (J/mol) and $v_{initial}$ (m^3/mol) are calculated at the initial condition of the system. U_{liq} (J/mol), v_{liq} (m^3/mol), U_{vap} (J/mol) and v_{vap} (m^3/mol) are all calculated at 100°C and 1 bar (atmospheric-pressure boiling-point). Thiéry and Mercury (2009) demonstrated that an isenthalpic hypothesis yields a good approximation of the irreversible case. Under this assumption the irreversible energy of an expanding saturated liquid can be calculated as:

$$E_{Expl\text{-}I} = m_w \times (P_{atm} \times [(1\text{-}f) \times v_{vap} + f \times v_{liq} - v_{initial})]) \quad (4)$$

where E_{Expl-I} is the irreversible explosive energy released (in J), and m_w is the mass of water (g) in the pore space (Figure 5).

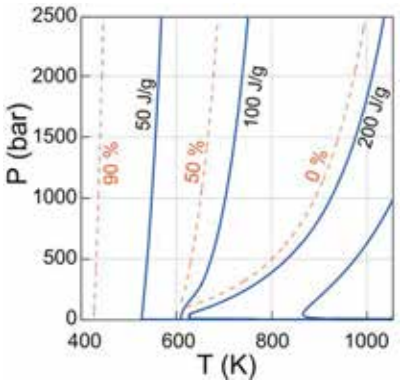

Figure 5. P-T diagram showing the mechanical work (full solid lines, in J/g of water) released by the irreversible adiabatic expansion of hot and pressurized steam as a function of the initial P-T conditions. Dashed lines indicate the liquid fraction (in mass percentage) of the gas-liquid mixture at a final state of 1 bar and 100°C. Modified from Thiéry and Mercury (2009).

8. 4 **- Experimental investigation of steam-driven eruptions**

An experimental approach, based on a rapid decompression experiments, has been used to investigate diverse scenarios likely for steam-driven eruptions in various types of volcanic setting. The decompression experiments were performed in the fragmentation bomb at LMU, described in detail by Alidibirov and Dingwell (1996) and developed further by e.g. Alatorre-Ibargüengoitia et al., (2010), Rager et al., (2014), and Mayer et al., (2015).

In these experiments fragmentation can be triggered by decompression of 1) argon gas, 2) steam, or 3) water flashing to steam within the connected pore space of the samples. The device permits the accurate control of temperature, gas overpressure and decompression rate in order to best represent variable magmatic and hydrothermal conditions. It consists of a large upper stainless steel low-pressure tank (l =3.0 m; d =0.4 m) at ambient pressure and temperature conditions, and a lower high-pressure chamber (autoclave) containing the sample, which is heated and pressurized by either argon gas or steam. The autoclave is separated from the upper chamber by a series of diaphragms (Figure 6).

The controlled rupturing of the diaphragms initiates the rapid decompression of the autoclave. Following the diaphragm failure, a shock wave travels upwards into the low-pressure collector tank, and a rarefaction wave propagates downwards into the autoclave, traveling through the sample. Under argon and steam expansion, a brittle fragmentation of the sample is expected to occur in a layer-by-layer way (Alidibirov and Dingwell 2000; Fowler et al., 2010; McGuinness et al., 2012), and the particles are ejected into the upper chamber. In the case of water flashing to steam the fracturing may be less dependent on the decompression front, but more on the orientation of pore space and eventually pre-existing fractures (Rager et al., 2014). For each sample the fragmentation speed (Spieler et al., 2004) is calculated by using the time delay Δt of the pressure drop over the

entire sample, as recorded by the transducers above and below the sample, and the sample length (Scheu et al., 2006).

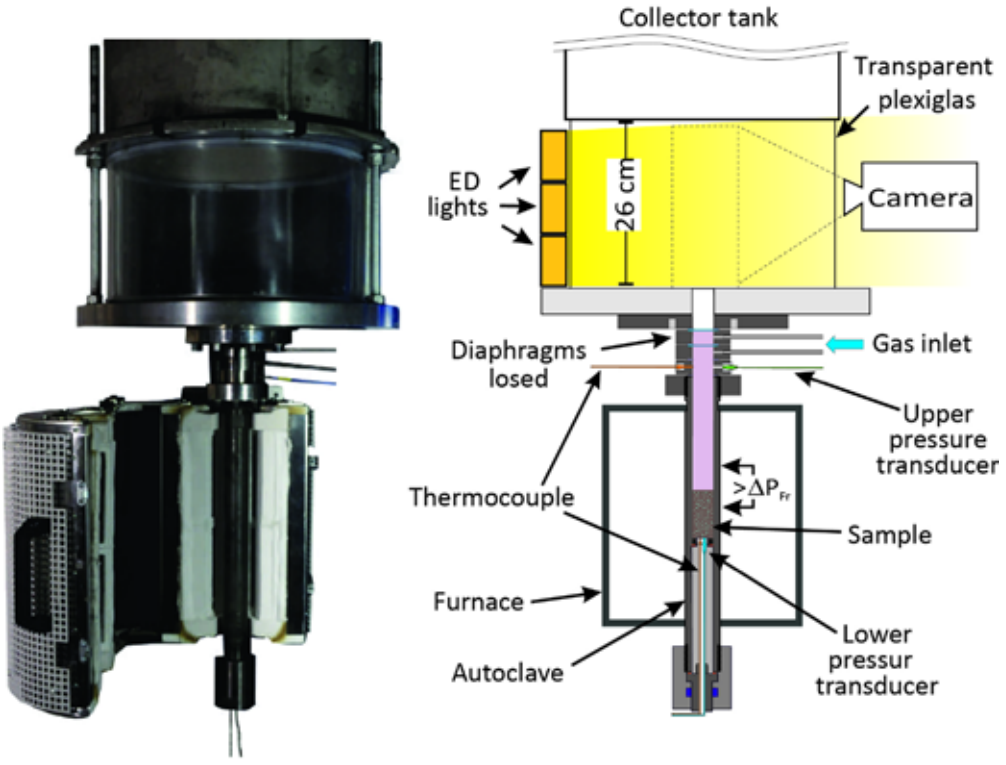

Figure 6. Fragmentation bomb setup: frontal (camera) view of experimental setup (left) and schematic drawing (right) of the fragmentation bomb used during this study (Mayer et al., 2015).

Prior to the experiment, each rock sample is mounted into a cylindrical steel crucible. For the argon-dry decompression experiments, samples were mounted into the crucible and directly placed inside the autoclave ready for fragmentation experiments. For the experiments with steam, the mounted sample is placed within the autoclave together with a specific amount of distilled water. The amount of water is calculated by means of steam tables in order to achieve the desired pressurization within the connected pore space of the sample, and in the remaining autoclave chamber above the sample, solely by steam pressure. Temperature rise up to the boiling point, and gases generated upon vaporization increase the pressure in the autoclave until the targeted dwell conditions are reached. The system is generally left to equilibrate for 10 minutes before triggering the fragmentation. For experiments in the presence of steam-flashing, mounted samples are submerged in water and placed under a vacuum for at least 72 h to facilitate the water absorption within the connected porosity, assuring maximum water saturation. During the decompression of the system, the phase transition from liquid water to water vapor is crossed. The ejection of the sample is filmed by a high-speed camera (Phantom V710®347, Vision Research, USA) at 10,000

frames per second through a transparent Plexiglas inlet at the bottom of the large chamber. This allows the tracking of fragmented particles and an estimation of their ejection velocities.

The fragmented material is collected from the large chamber and its grain size distribution is analyzed using dry sieving at half-phi steps of particles >63 μm in size. Due to the sealing between the Plexiglas cylinder and the collector tank, as well as the adhesion of very fine particles on the lid and along the rim of the tank, a complete recovery of the very finest fraction is not possible; however, a minimum weight yield of 90-95% is generally achieved.

8. 5 **- Case studies and main findings**

To unravel the parameters controlling the energetics of the steam-driven eruptions a combined field and experimental approach, together with other methodology when possible, have been used to investigate two recent hydrothermal explosive events. These represented two end-member cases for steam-driven eruptions. Their characteristics as well as the findings of the studies are summarized below:

i) Small hydrothermal explosions: consist of jetting of hydrothermal fluids (steam, water) and substantial amounts of solid material (mud and rock fragments). Such events can last a few seconds to minutes, and produce craters spanning from a few meters up to hundreds of meters in diameter. The crater depths range from a few meters to several hundred meters and strongly depend on host rock composition. Ejected debris may reach velocities of a few tens of m/s, and usually produce low volume deposits. These are generally very poorly sorted, and matrix-supported.

Our case study of small hydrothermal explosions is the Gengissig hydrothermal explosions (Figure 7; Montanaro et al., 2016) that occurred within an active geothermal area at Kverkfjöll, a central volcano at the northern edge of Vatnajökull. On August 15th 2013, a small jökulhlaup occurred when the Gengissig ice dammed lake drained at Kverkfjöll. The lake level dropped by approximately 30 m, decreasing pressure on the lake bed and triggering several hydrothermal explosions on the 16th. Detailed fieldwork, laboratory studies, and models of the energetics of explosions with information on duration and amplitudes of seismic signals, have been used to analyse the mechanisms and characteristics of these hydrothermal explosions. Field and laboratory studies were also carried out to help constrain the sedimentary sequence involved in the event. The explosions lasted for 40-50 seconds and involved the surficial part of an unconsolidated and hydrothermally altered glacio-lacustrine deposit composed of pyroclasts, lavas, scoriaceous fragments, and fine-grained welded or loosely consolidated aggregates, interbedded with clay-rich layers. Several small fans of ejecta were formed, reaching a distance of 1 km north of the lake and covering an area of approximately 0.3 km^2, with a maximum thickness of 40 cm at the crater walls. The material (volume of approximately 10^4 m^3) has been ejected by the expanding boiling fluid, generated by the pressure failure affecting the surficial geothermal reservoir.

The maximum thermal, craterization and ejection energies, calculated for the explosion areas, are on the order of 10^{11}, 10^{10} and 10^9 J, respectively. These are in good agreement with estimates from the volume of the ejecta and the crater sizes. According to our estimates, approximately 30% of the available thermal energy was converted into mechanical energy during this event. The residual

energy was largely dissipated as heat, while only a small portion was converted into seismic energy. Estimation of the amount of freshly-fragmented clasts in the ejected material obtained from SEM morphological analyses, reveals that there was a low but significant energy consumption by fragmentation.

Decompression experiments were performed in the laboratory mimicking the conditions due to the drainage of the lake. Experimental results confirm that only a minor amount of energy is consumed by the creation of new surfaces in fragmentation, whereas most of the fresh fragments derive from the disaggregation of aggregates. Furthermore, ejection velocities of the particles (40-50 m/s), measured via high-speed videos, are consistent with those estimated from the field. The multidisciplinary approach used here to investigate hydrothermal explosions has proven to be a valuable tool that can provide robust constraints on energy release and partitioning for such small-size yet hazardous, steam-explosion events.

ii) Large hydrothermal eruptions: similar to those at Mt. Ontake in Japan (Yamamoto, 2014), and Ruapehu, in New Zealand (Kilgour et al., 2010) involve different mechanisms (magma fluid injection, hydrothermal sealing, etc.) and also larger volumes (~105 m^3), durations, products and types of confining rock. Another example of large hydrothermal eruptions is the Upper Te Maari eruption, representing the more violent end-member case studied in this work (Figure 8). The eruption was triggered by a landslide on the western flank that unroofed the hydrothermal system and produced west- and east-ward directed blasts and a vertical ash plume. All explosions were accompanied by ballistic ejection, some of which impacted NZ's most popular hiking trail and a mountain lodge 1.4 km from the source. The mapping and characterization of ballistics from the western, and most impacted strewn-field, allowed identification of the main lithology groups. These could be traced back to specific explosion-source locations in the vent region.

The main lithology types were used for rapid decompression experiments mimicking hydrothermal explosions under controlled laboratory conditions. A special set-up was built to reduce the influence of large lithic enclaves (up to 30 mm in diameter) within the samples. The experiments were conducted in a temperature range from 250°C – 300°C and applied pressure between 4 MPa – 6.5 MPa in order to span the range of expected conditions below the Te Maari crater. Within this range the rapid decompression of pre-saturated samples from both the liquid-dominated field and the vapor-dominated field were tested. Additionally dry samples at the same PT-conditions were used. Clasts were ejected with velocities of up to 160 m/s as recorded with a high-speed camera. The resulting fragments were analyzed for their grain size distribution and lithology. Besides a few larger clasts (in analogy to ballistics), a large amount of fine and very fine (<63 µm) ash was produced in all experiments. Using the westward (and most energetic) directed blast as a comparison, our results suggest that the liquid-to-vapor (flashing) expansion is significantly more energetic (one order of magnitude higher) than steam expansion, and far more likely to explain the eruption occurred at the Te Maari. We estimate a minimum explosive energy for the western blast of 7×10^{10} to 2×10^{12} J. The host rock lithology appears to control the explosion dynamics, and the energy partitioning. For the investigated samples the ratio of fragmentation to explosive energy is 9.5 to 15.2%, whereas the conversion ratio to kinetic energy is on the order of 0.02% up to 0.1%.

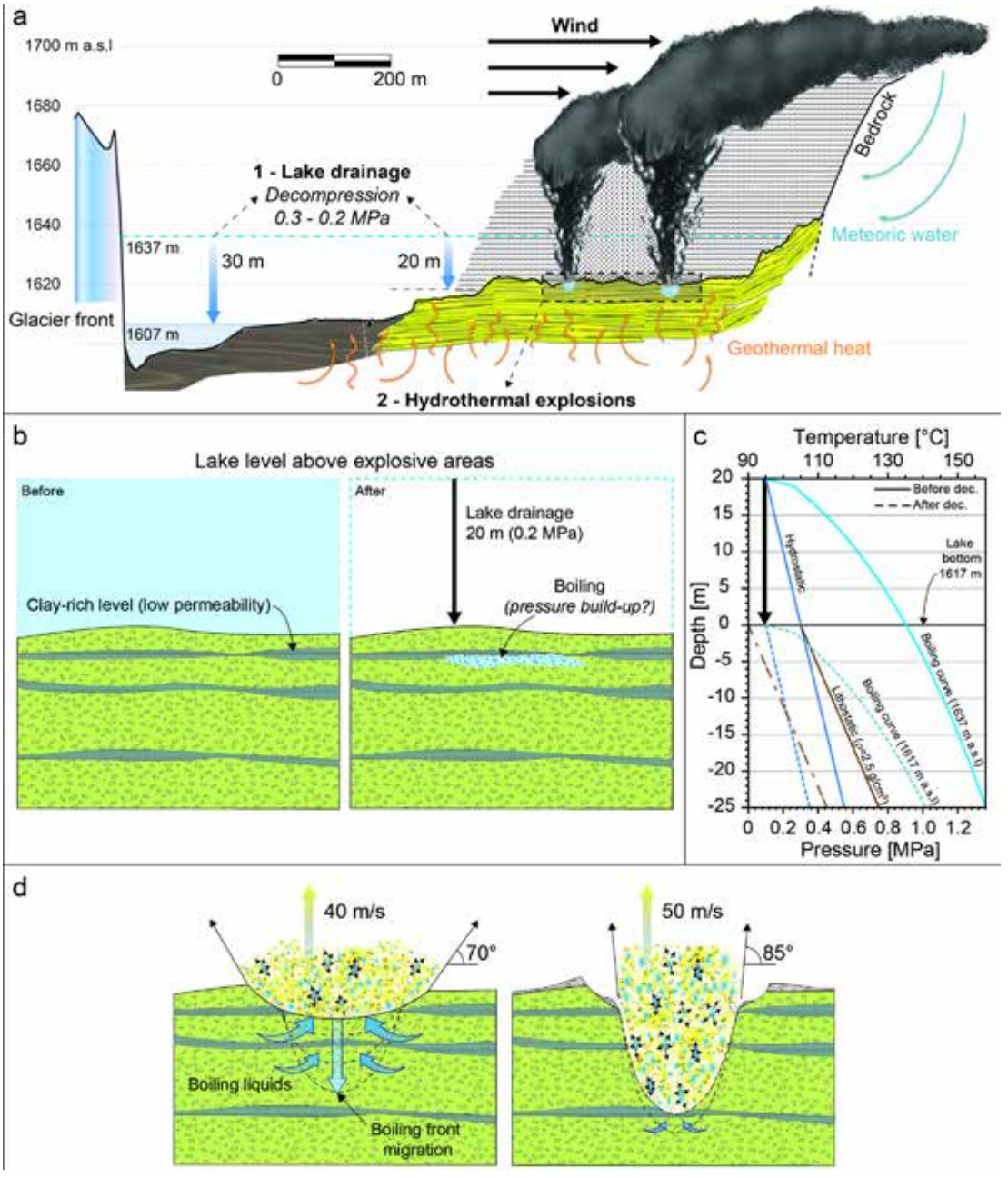

Figure 7. Sketch showing the setting before and after the lake drainage (Montanaro et al., 2016). Profile across Gengissig, based on kinematic GPS collected 12 days after the explosions (A). (B-D) Conceptual model of the hydrothermal explosions evolution: lake drainage (pressure failure) and boiling initiation (B); hydrostatic, lithostatic and boiling point temperature before and after lake drainage (C); explosion caused by clay layer failure and subsequent pressure release and progressive downwards propagation of boiling front. See text for more explanation (D).

In addition to the two case studies, an experimentally-based investigation of the influence of liquid fraction and rock petrophysical properties on the steam-driven explosive energy was conducted. For this study, a series of fine-grained heterogeneous tuffs from the Campi Flegrei caldera were investigated for their petrophysical properties. Decompression experiments simulate a scenario likely for a steam-driven eruption involving the shallow part of the hydrothermal system. The rapid depressurization of various amount of liquid water within the rock pore space produced a different fragmentation and ejection behavior for the investigated tuffs. Porosity and permeability of the tuffs strongly affect the amount of available energy, whereas the rock strength has only shown a secondary effect on the fragmentation behavior.

8. 6 **- Conclusions**

The findings of this study suggest that the pore liquid fraction and its physical conditions (pressure-temperature) control the stored explosive energy: an increasing liquid fraction within the pore space increases the explosive energy. Overall, the energy released by steam-flashing is estimated to be one order of magnitude higher than for the solely (Argon) gas or steam expansion. Additionally the decompression of liquids at an initial pressure and temperature close to their boiling-point may result in a higher production of fine material already under partial saturation conditions.

The lithologies investigated in this work (from loose sediments, to very heterogeneous tuff breccias and agglutinates, and fine-grained tuffs) cover large spectra of porosity, permeability and rock strength. These parameters control the energy storage, as well as its partitioning in the form of fragmentation and particle ejection. Flashing of water in loose saturated sediments can produce violent explosion even for small decompression events (e.g. lake drainage). Consequently craters of tens-of-meter size can be generated and debris launched at significant distance (>100m). Interbedded low permeability, clay-rich levels may account for the over-pressurization and failure of the system, while the loose material can allow an efficient conversion of the explosive energy into other forms. In the case of consolidated rock, the connected porosity relates to the amount of stored energy, with higher porosities accounting for higher energies. The energy surplus in the presence of steam-flashing leads to a faster fragmentation with respect to a solely gas-driven process. As a result, higher ejection velocity may be reached by the fragmented particles. Low permeability rocks, which do not allow pressure dissipation during the fragmentation process, maximises the amount of produced fine. Additionally, at constant porosity weaker rocks generated more fine particles than firmly cemented rocks. The fragmentation of very heterogeneous rocks, including low porosity clasts, can create both a large amount of very fine material, together with larger fragments (analogous to ballistics formation). Destabilization of a hydrothermal system with pressurized fluids hosted in such a heterogeneous lithology, may produce extended ash plumes and (dilute) pyroclastic density currents as well as widespread ballistic events.

The multidisciplinary approach (field, laboratory, theoretical, and seismic studies) has unravelled the energetics of steam-driven eruptions and provided many estimates of parameters controlling

their explosivity. These finding should be considered for both modeling and evaluation of the associated hazard of steam-driven eruptions.

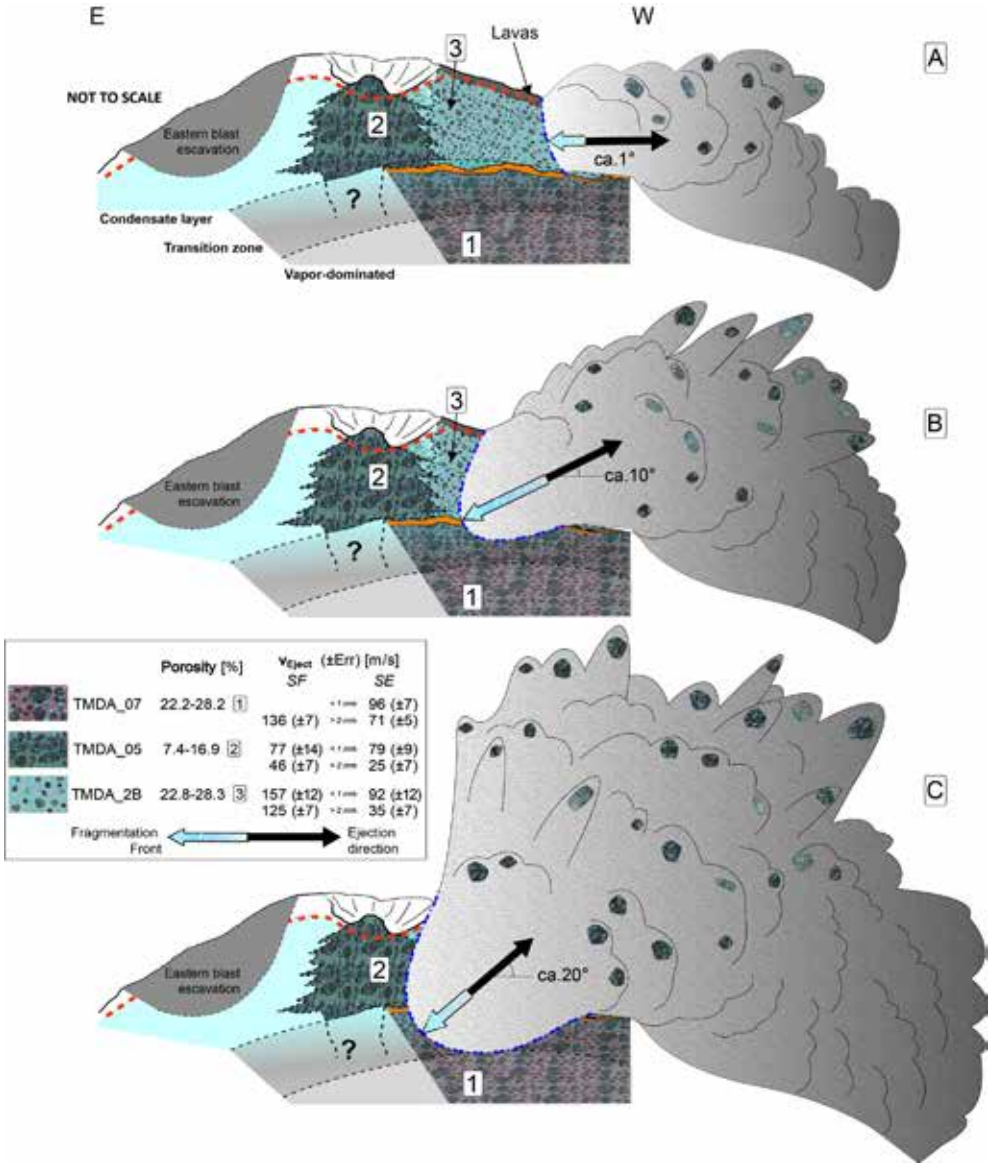

Figure 8. Te Maari hydrothermal eruption: conceptual model of the fragmentation and ejection process during the westward directed blast evolution (Montanaro et al., 2016). In the legend the ejection velocities refer to particles larger than 2 mm. In this simplified model it is assumed that the tuff breccia and agglutinate (which differ in porosity and lithologic texture) used as sample material for the decompression experiments are representative of the source rock. Type 4 refers to a block type described in Breard et al., 2014, and originated from the fragmentation of the 1528 lava flow (an part of smaller recent lavas). The length of the "Fragmentation Front" arrow gives an idea of the fragmentation speed in the different lithologies.

Acknowledgements

The research leading to these results has received funding from the European Union Seventh Framework Programme (FP7/2007-2013) under the project NEMOH, grant agreement n° 289976. Most of this work has been realized with the support of many people who collaborated, taught and helped me during the years of Nemoh and after. First of all thanks to Bettina Scheu for being a friend first and a great supervisor after, and to Klaus Mayer for being a friend and a solid-rock colleague. Thanks to Don Dingwell and the LMU people for their support, friendship and fruitful discussions through the years.

I also would like to thank: Magnus Tumi Gudmundsson, Hannah Iona Reynolds, Tobias Dürig, Karen Strehlow, Stefanie Rott, Thierry Reuschlé, Kristín Vogfjörd, and to all the people from the Vatnajökull 2014 spring expedition, in particular to Herdís Schopka, Baldur Bergsson, Melissa Pfeiffer, Katerina Mistal and Ísleifur Friðriksson (for their support in the field), and Tinna Jónsdóttir for the support and friendship during the time spent in Iceland until the writing of the manuscript. Thanks to Shane Cronin, Eric Breard, and Gert Lube for the great adventure at the mystical Te Maari, and the magic days spent on the Mt.Tongariro. Thanks to: Giovanni Orsi, Roberto Moretti, Roberto Isaia, Antonio Carandente and many other people from Naples for the numerous discussions on the Campi Flegrei and their restless help during the field activity, and the writing of the manuscript.

Note of the Author

Most of the content of this chapter has been published in scientific journals, is in the state of a submitted manuscript in review, or in preparation for submission to a scientific journal. Detailed references are listed below. Only slight modifications have been made, mainly in terms of formatting and style for incorporation into a consistent overall chapter design.

Montanaro, C., Scheu, B., Cronin, S. J., Breard, E. C. P., Lube, G., & Dingwell, D. B. (2016). Experimental estimates of the energy budget of hydrothermal eruptions; application to 2012 Upper Te Maari eruption, New Zealand. Earth and Planetary Science Letters, 452, 281–294. https://doi.org/10.1016/j.epsl.2016.07.052.

Montanaro, C., Scheu, B., Gudmundsson, M. T., Vogfjörd, K., Reynolds, H. I., Dürig, T., … Dingwell, D. B. (2016). Multidisciplinary constraints of hydrothermal explosions based on the 2013 Gengissig lake events, Kverkfjöll volcano, Iceland. Earth and Planetary Science Letters, 434, 308–319. https://doi.org/10.1016/j.epsl.2015.11.043.

Montanaro, C., Scheu, B., Mayer, K., Orsi, G., Moretti, R., Isaia, R., & Dingwell, D. B. (2016). Experimental investigations on the explosivity of steam-driven eruptions: a case study of Solfatara volcano (Campi Flegrei). Journal of Geophysical Research: Solid Earth, 121(11), 7996–8014. https://doi.org/10.1002/2016JB013273.

References

Alatorre-Ibargüengoitia, M. A., Scheu, B., Dingwell, D. B., Delgado-Granados, H. and Taddeucci, J., (2010). Energy consumption by magmatic fragmentation and pyroclast ejection during Vulcanian eruptions. Earth Planet. Sci. Lett. 291, 60–69. doi:10.1016/j.epsl.2009.12.051.

Alidibirov, M., and Dingwell, D. B. (2000). Three fragmentation mechanisms for highly viscous magma under rapid decompression. J. Volcanol. Geotherm. Res. 100, 413–421. doi:10.1016/S0377-0273(00)00149-9.

Alidibirov, M. and Dingwell, D. B. (1996). An experimental facility for the investigation of magma fragmentation by rapid decompression. Bull. Volcanol. 58, 411–416.

Barberi, F., Bertagnini, A., Landi, P. and Principe, C. (1992). A review on phreatic eruptions and their precursors. J. Volcanol. Geotherm. Res. 52, 231–246. doi:10.1016/0377-0273(92)90046-G.

Breard, E. C. P., Lube, G., Cronin, S. J., Fitzgerald, R., Kennedy, B., Scheu, B., Montanaro, C., White, J.D.L., Tost, M., Procter, J.N. and Moebis, A. (2014). Using the spatial distribution and lithology of ballistic blocks to interpret eruption sequence and dynamics: August 6 2012 Upper Te Maari eruption, New Zealand. J. Volcanol. Geotherm. Res. doi:10.1016/j.jvolgeores.2014.03.006.

Browne, P. R. L. and Lawless, J. V. (2001). Characteristics of hydrothermal eruptions, with examples from New Zealand and elsewhere. Earth Sci. Rev. 52, 299–331. doi:10.1016/S0012-8252(00)00030-1.

Fowler, A. C., Scheu, B., Lee, W. T. and McGuinness, M.J. (2010). A theoretical model of the explosive fragmentation of vesicular magma. Proc. R. Soc. A Math. Phys. Eng. Sci. 466, 731–752. doi:10.1098/rspa.2009.0382.

Galland, O., Gisler, G. R. and Haug, O. T. (2014). Morphology and dynamics of explosive vents through cohesive rock formations. J. Geophys. Res. Solid Earth 119, 4708–4728. doi:10.1002/2014JB011050.

Gilbert, J. S. and Sparks, R. S. J. (1998). The Physics of Explosive Volcanic Eruptions, Geological Society - Special Publication 145. doi:10.1144/GSL.SP.1996.145.01.01.

Haug, O. T., Galland, O. and Gisler, G. R. (2013). Experimental modelling of fragmentation applied to volcanic explosions. Earth Planet. Sci. Lett. 384, 188–197. doi:10.1016/j.epsl.2013.10.004.

Hurst, T., Jolly, A. D. and Sherburn, S. (2014). Precursory characteristics of the seismicity before the 6 August 2012 eruption of Tongariro volcano, North Island, New Zealand. J. Volcanol. Geotherm. Res. doi:10.1016/j.jvolgeores.2014.03.004.

Jolly, A. D., Jousset, P., Lyons, J. J., Carniel, R., Fournier, N., Fry, B. and Miller, C. (2014). Seismo-acoustic evidence for an avalanche driven phreatic eruption through a beheaded hydrothermal system: An example from the 2012 Tongariro eruption. J. Volcanol. Geotherm. Res. 286, 317–330. doi:10.1016/j.jvolgeores.2014.04.007.

Kato, A., Terakawa, T., Yamanaka, Y., Maeda, Y., Horikawa, S., Matsuhiro, K. and Okuda, T. (2015). Preparatory and precursory processes leading up to the 2014 phreatic eruption of Mount Ontake, Japan. Earth, Planets Sp. 67, 111. doi:10.1186/s40623-015-0288-x.

Kilgour, G., Manville V., Pasqua, F. D., Graettinger A., Hodgson, K. A. and Jolly, G. E. (2010). The 25 September 2007 eruption of Mount Ruapehu, New Zealand: Directed ballistics, surtseyan jets, and ice-slurry lahars. J. Volcanol. Geotherm. Res. 191, 1–14. doi:10.1016/j.jvolgeores.2009.10.015.

Lube, G., Breard, E. C. P., Cronin, S. J., Procter, J. N., Brenna, M., Moebis, A., Pardo, N., Stewart, R. B., Jolly, A. and Fournier, N. (2014). Dynamics of surges generated by hydrothermal blasts during the 6 August 2012 Te Maari eruption, Mt. Tongariro, New Zealand. J. Volcanol. Geotherm. Res. doi:10.1016/j.jvolgeores.2014.05.010.

Manville, V., Rouwet, D. and Morrissey, M. M. (2015). Mechanisms of Crater Lake Breaching Eruptions, in: Volcanic Lakes. pp. 73–91. doi:10.1007/978-3-642-36833-2.

Mastin, L. G. (1995). Thermodynamics of gas and steam-blast eruptions. Bull. Volcanol. 57, 85–98. doi:10.1007/BF00301399

Mayer, K., Scheu, B., Gilg, H.A., Heap, M.J., Kennedy, B.M., Lavallée, Y., Letham-Brake, M. and Dingwell, D.B. (2015). Experimental constraints on phreatic eruption processes at Whakaari (White Island volcano). J. Volcanol. Geotherm. Res. 302, 150–162. doi:10.1016/j.jvolgeores.2015.06.014.

McGuinness, M. J., Scheu, B. and Fowler, A. C. (2012). Explosive fragmentation criteria and velocities for vesicular magma. J. Volcanol. Geotherm. Res. 237-238, 81–96. doi:10.1016/j.jvolgeores.2012.05.019.

McKibbin, R., Smith, T. A. and Fullard, L. (2009). Components and Phases: Modelling Progressive Hydrothermal Eruptions. ANZIAM J. 50, 365. doi:10.1017/S144618110900011X.

Montanaro, C., Scheu, B., Gudmundsson, M. T., Vogfjörd, K., Reynolds, H. I., Dürig, T., Strehlow, K., Rott, S., Reuschlé, T. and Dingwell, D. B. (2016). Multidisciplinary constraints of hydrothermal explosions based on the 2013 Gengissig lake events, Kverkfjöll volcano, Iceland. Earth Planet. Sci. Lett. 434, 308–319. doi:10.1016/j.epsl.2015.11.043.

Montanaro, C., Scheu, B., Cronin, S. J., Breard, E. C. P., Lube, G. and Dingwell, D. B. (2016). Experimental estimates of the energy budget of hydrothermal eruptions; application to 2012 Upper Te Maari eruption, New Zealand. Earth and Planetary Science Letters, Volume 452, 15 October 2016, Pages 281-294, ISSN 0012-821X, http://dx.doi.org/10.1016/j.epsl.2016.07.052.

Morgan, L. A., Shanks, W. C. P. and Pierce, K. L. (2009). Hydrothermal processes above the Yellowstone magma chamber: Large hydrothermal systems and large hydrothermal explosions, Geological Society of America Special Paper.

Muffler, L. J. P., White, D. E. and Truesdell, A. H. (1971). Hydrothermal explosion craters in Yellowstone National Park. Bull. Geol. Soc. Am. 82, 723–740. doi:10.1130/0016-7606(1971)82[723:HECIYN]2.0.CO;2.

Nelson, C.E. and Giles, D.L. (1985). Hydrothermal Eruption Mechanisms and Hot Springs Gold Deposits. Econ. Geol. 80, 1633–1639.

Prugh, R.W., 1991. Quantitative Evaluation of "Bleve" Hazards. J. Fire Prot. Eng. 3, 9–24. doi:10.1177/104239159100300102.

Rager, A. H., Smith, E. I., Scheu, B. and Dingwell, D. B. (2014). The effects of water vaporization on rock fragmentation during rapid decompression: Implications for the formation of fluidized ejecta on Mars. Earth Planet. Sci. Lett. 385, 68–78. doi:10.1016/j.epsl.2013.10.029.

Seki, K., Kanda, W., Ogawa, Y., Tanbo, T., Kobayashi, T. and Hino, Y. (2015). Imaging the hydrothermal system beneath the Jigokudani valley , Tateyama volcano , Japan : implications for structures controlling repeated phreatic eruptions from an audio-frequency magnetotelluric survey 0–8. doi:10.1186/s40623-014-0169-8.

Spieler, O., Dingwell, D.B. and Alidibirov, M. (2004). Magma fragmentation speed: An experimental determination. J. Volcanol. Geotherm. Res. 129, 109–123. doi:10.1016/S0377-0273(03)00235-X.

Stearns, H.A. and McDonald, G.A. (1949). Geology and groundwater resources of the island of Hawaii. Hawaii Div Hydrogr Bull 9, 1–363.

Thiéry, R., Loock, S. and Mercury, L. (2010). Explosive properties of superheated aqueous solutions in volcanic and hydrothermal systems., in: Metastable Systems under Pressure. pp. 293–310.

Thiéry, R. and Mercury, L. (2009). Explosive properties of water in volcanic and hydrothermal systems. J. Geophys. Res. Solid Earth 114, 1–19. doi:10.1029/2008JB005742.

Thiéry, R. and Mercury, L. (2008). Explosive properties of water in volcanic and hydrothermal systems, in: ICPWS XV. p. 7. doi:10.1029/2008JB005742.

Wohletz, K. H. (1986). Explosive magma water interactions Thermodynamics, explosion mechanisms, and field studies. Bull. Volcanol. 48, 245–264.

Yamamoto, T. (2014). The pyroclastic density currents generated by the September 27, 2014 phreatic eruption of Ontake Volcano, Japan. Bull. Geol. Surv. Japan Vol.65 (9/, 117–127.

Zhang, Y. (2000). Energetics of gas-driven limnic and volcanic eruptions. J. Volcanol. Geotherm. Res. 97, 215–231. doi:10.1016/S0377-0273(99)00164-X.

Cristian Montanaro, Italy

cristian.montanaro@min.uni-muenchen.de

Affiliation under NEMOH
Department of Earth and Environmental Sciences Ludwig-Maximilians-Universität, Munich, Germany

Research theme under NEMOH
Dynamics of steam-driven eruptions in volcanic systems

Driven by curiosity and passion I started to open a few doors on what is a very complex world of volcanoes... I graduated in Geophysical and Structural Geology at the University of Rome "La Sapienza" with a thesis focused on the stratigraphic reconstruction of pyroclastic products from hydromagmatic eruptions. This work also included the study of the spatial and temporal evolution of the hydromagmatic centers through morphological analysis, as well as the energetic parameterization of these explosive events via quantitative analyses of ejected ballistics.

After my graduation I started working as a marine geophysicist within the framework of MAGIC (MArine Geohazards Along the Italian Coasts) project. Here I developed knowledge on the processing, analysis and interpretation of geophysical data. One key task was the identification of potential geo-hazards for human settlements and infrastructures in the offshore and along coastal zones, with particular focus on the Aeolian Islands.

In parallel I started collaborations with the “Istituto Nazionale di Geofisica e Vulcanologia” (INGV) of Rome dealing with the innovative technique of high-speed imaging applied to volcanic phenomena. In this I initially developed methods for the analyses of high-speed imaging which allowed definition of the complex dynamics of the strombolian eruptions. I also studied ashfall settling, in particular the investigation and definition of the physical features of ash aggregates by combining high-speed video analysis and laboratory experiments.

In between these experiences I spent six months in Alaska where I carried out a research project on volcanic island edifice instabilities along the western part of Aleutian island arc. The main results included the recognition and mapping of new landslide deposits, insight into their origin as well as the estimation of their tsunamigenic potential.

In August 2012 I got a position as Early Stage Researcher (PhD) within the framework of the Nemoh Marie Curie Initial Training Network. I have been employed at the Department of Earth and Environmental Sciences, Ludwig-Maximilians-Universität (LMU) in Munich where I finally obtained my PhD in July 2016. My PhD studies focused on the understanding of the physical processes of steam-driven eruptions in volcanic systems. Throughout the PhD I developed knowledge in the field of experimental volcanology, and gained field-based skills from involvement in several field campaigns to volcanic sites such as the Tongariro volcano (New Zealand), the Solfatara in Campi Flegrei (Naples), and the geothermal area of Kverkfjöll (Iceland). I further participated in several schools, conferences within and outside the Nemoh network. For the final part of the PhD I have been involved in the MED-SUV (MEDiterranean SUpersite Volcanoes) project focusing on the effect of rock permeability on the outgassing behaviour within hydrothermal systems.

Chapter 9

Investigation on the degassing behaviour of analogue volatile- and crystal-bearing magmas upon slow decompression and implications for basaltic system

Laura Spina

Department für Geo- und Umweltwissenschaften, Ludwig-Maximilians-Universität München, Munich, *Germany*

Tutorship: Bettina Scheu

Department für Geo- und Umweltwissenschaften, Ludwig-Maximilians-Universität München, Munich, *Germany*

Abstract

A series of decompression experiments were performed on analogue basaltic magmas, aimed to define the effects of physical properties and decompression rate on degassing in basaltic eruptive systems, and the related timescales of outgassing. As a proxy for volatile- and crystal-bearing magmas, we used Ar-saturated silicone oils with different viscosities (1-1000 Pa s), loaded with different percentages of micro spherical glass beads (aspect ratio ca. 1) or glass fibres (aspect ratio ca. 10). The rheology of both spherical- and elongated-particle-bearing suspensions were characterized by concentric cylinder rotational rheometry. The flow dynamics of the bubbly fluid, from nucleation up to the development of a permeable bubble network, were monitored through a system of pressure sensors located at the top and at the bottom of the autoclave, and a video camera recording at 25 fps. Different degassing regimes were identified and characterized as a function of the physical properties. The experimental observations were related to the natural volcanic system through detailed a-dimensional analysis.

Keywords: analogue, bubble dynamics, timescales, crystals, decompression

9. 1 **- Introduction**

The exsolution of volatiles is a key-process in the lifetime of volcanic systems. Indeed, the gas phase provides both the buoyancy force that drives magma ascent and the expansion force for explosive activity, and therefore plays a major role in determining the eruptive style. The kinetics of degassing might promote crystallization, modifying the rheology of magmatic fluids ascending toward the surface. It is therefore not surprising the great amount of different techniques applied to investigate the history of the gas phase in the conduit and determine the reciprocal role of the most relevant parameters (i.e. P-T state, physical properties, ascent history) on the behaviour of volatile-bearing magmas.

Since the pioneering work of Sparks (1978), numerical studies (e.g. Proussevitch et al., 1993; Barclay et al., 1995) provided important constrain on the dynamics of bubble nucleation and growth. An important milestone in linking volcanic products at the surface with the system thermodynamic state at depth was made by Toramaru (2006), who related bubble number density of the volcanic samples to their decompression rate. Additionally, numerical models assessed the striking importance of disequilibrium degassing in dynamically vigorous systems, and its effects on the estimation of the fragmentation depth (Massol and Koyaguchi, 2005).

However, a wide knowledge on the relationship between the thermodynamic properties of the volcanic system and the behaviour of volatiles derives from experimental studies, both on natural melts and analogue materials. For instance, experiments performed on high-silica melts demonstrated the fundamental role of decompression rate in determining the departure from equilibrium degassing (e.g. Gardner et al., 2000; Mourtada-Bonnefoi and Laporte, 2004). On the opposite side of the melt composition-spectrum, the evolution of bubbles in a synthetic volatile-bearing basaltic glass was investigated by Bai et al. (2008) as a function of temperature at ambient pressure.

The great advantage of analogue experiments is the possibility of a deeper control in the physical properties and thermodynamic state of the system, allowing to draw a map of the reciprocal relationships among different investigated parameters. Accordingly, a flourishing branch of experimental studies is devoted to analogue volatile bearing fluids, in which nucleation takes place during the experiment either by fluid decompression (e.g. Rivalta et al., 2013) or by chemical reaction (e.g. Oppenheimer et al. 2015), or-alternatively- a pre-existing well-known bubble distribution is present at the initiation of the experiments (e.g. Namiki and Manga, 2006).

In this report, we will summarize the results of a series of decompression experiments, listed in Table 1**,** performed on analogue materials, aimed to characterize the role of physical properties on degassing behaviour of analogue basaltic samples.

The results of the experiments was published in Spina et al., (2016a, b), where additional information can be found.

9. 2 **- Experimental setup**

9. 2.1 **- Device for slow decompression of analogue samples**

In order to perform slow decompression experiments under controlled conditions we developed a dedicated shock tube setup (Spina et al., 2016a,b), composed by two units: i) a high-pressure autoclave; ii) a low-pressure tank (Fig. 1). The former consists of a 20 cm transparent Plexiglas tube, with an internal diameter of 2.0 cm. A cross-sectional variation in the diameter allows for the insertion of the sample holder - a small Plexiglas cylinder, mounted over a steel platform and filled with the investigated analogue mixture (silicone oil + crystals) up to 6.5 cm of height.

We monitored the pressure state of the system through two pressure sensors, located respectively at the top of the autoclave, along the cylinder wall, and at the base, below the sample holder and coaxially with the autoclave itself.

The low-pressure unit is a cylindrical voluminous ambient pressure tank that allows for collection of diaphragms fragments if rapid decompression is performed.

Exp. name	Liquid Viscosity (Pa s)	Particle content -shape (% vol)	Saturation time (hours)	Saturation Pressure/ Initial pressure (MPa)	Exp. name	Viscosity (Pa s)	Particle content -shape (% vol)	Saturation time (hours)	Saturation Pressure/ Initial pressure (MPa)
1	1	0	72	10	15	100	3-elongated	72	10
2	10	0	72	10	16	100	7-elongated	72	10
3	100	0	72	9,5	17	100	10 - elongated	72	10
4	100	0	72	10	18	100	16-elongated	72	10
5	1000	0	72	10	19	100	20-elongated	72	10
6	1000	0	72	10	20	100	30-elongated	72	10
7	100	1 - spherical	72	10	21	100	0	24	10
8	100	1-spherical	72	10	22	100	0	24	9
9	100	10 - spherical	72	10	23	100	0	24	8
10	100	20 - spherical	72	10	24	100	0	24	7
11	100	30 - spherical	72	10	25	100	0	24	7/10
12	100	40 - spherical	72	10	26	1000	0	72	10
13	10	5 - spherical	72	10	27	1000	0	72	10
14	100	0.3 - elongated	72	10	Modified from Spina et al., 2016a,b				

Table 1. Overview of the experimental conditions. The light azure and azure colours indicate experiments performed in diluted and semi-diluted regimes, respectively, whereas the dark blue colour stands for experiments performed in the concentrated regime.

9. 2.2 - **Saturation state of the system**

In order to obtain fully saturated volatile-bearing analogue samples, Argon gas was injected in the autoclave through a system of capillary tubes, under the control of a manometer, with a maximum loading pressure of 10 MPa. Then, we sealed the system and kept it under control for 72 hours. Experiments #21 to #25 were saturated for a shorter amount of time (24 hours) at different final pressure (from 7 up to 10 MPa) to determine the effect of saturation state.

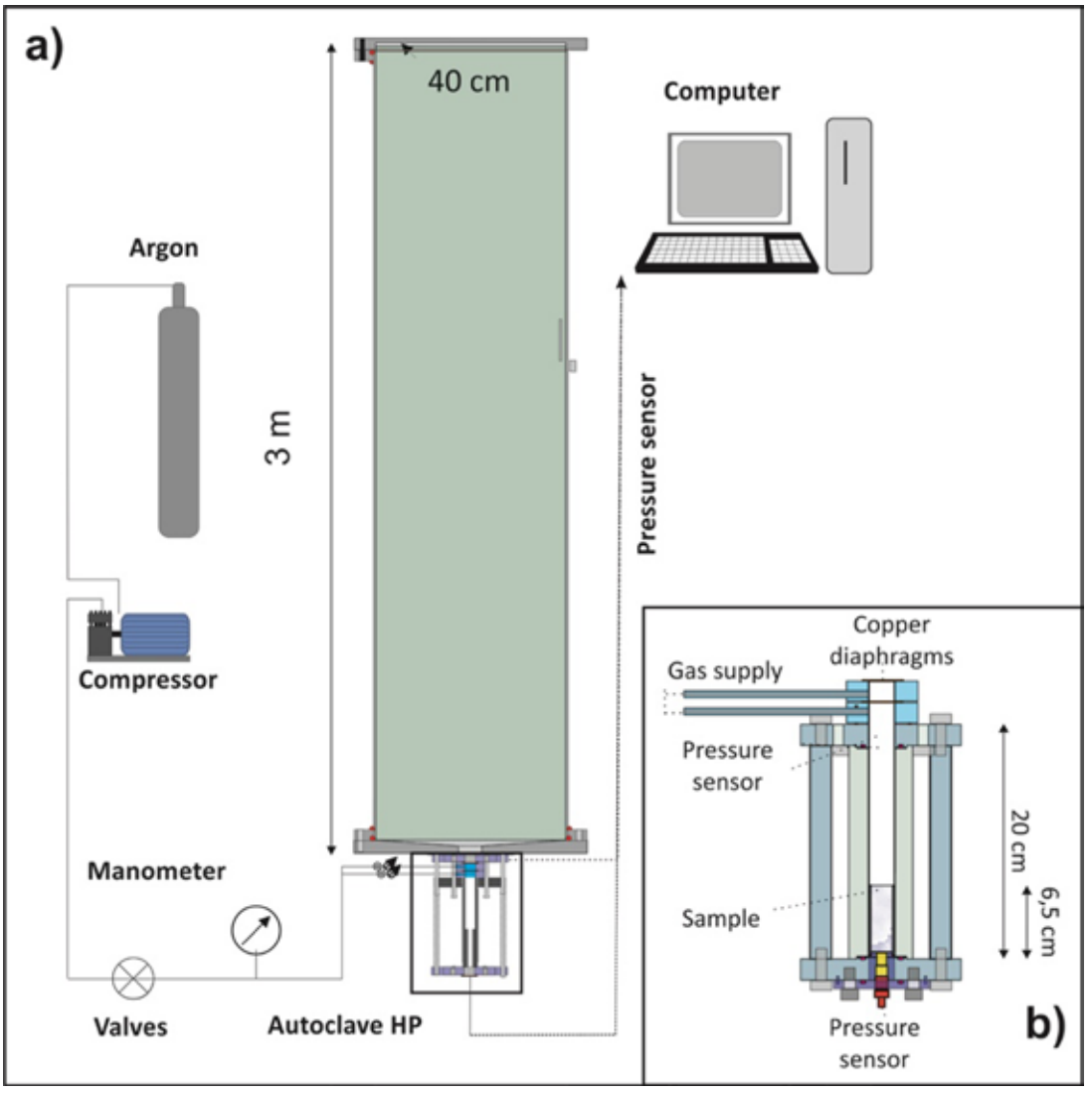

Figure 1. a) Sketch of the experimental setup, showing the high-pressure autoclave fastened below the low-pressure tank and connected to the argon supply through a capillary system. **b)** Detail of the high-pressure autoclave (modified from Spina et al., 2016a).

Fig. 2 shows the pressure state within the autoclave, measured via manometers after the sealing of the system; laboratory conditions (i.e. temperature and humidity) were monitored simultaneously. In order to define the amount of gas diluted into the sample we applied the *single-chamber sorption method* (e.g. Lundberg, 1962).

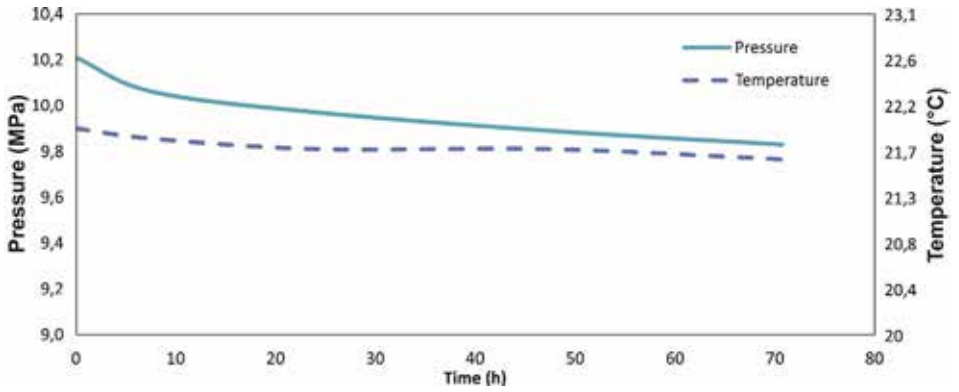

Figure 2. Pressure state of the experimental setup during saturation phase (e.g. #6). The solid line represents the decay in pressure within the autoclave measured by manometers; the dotted line indicates the variation of the temperature in the laboratory.

This technique is based on the evidence that the decrease in pressure -measured in a close system during saturation- depends on the amount of gas moles diluted into the fluid. By using Wan Der Waals'equation for Ar, we estimated a total amount of 0.0095 moles of Argon diluted in the samples after 72 hours, corresponding to a mass fraction equal to 1.8 wt % (Spina et al., 2016a). No relevant differences were observed in experiments with saturation time bigger than 72 hours, therefore we assume this amount of time to be sufficient for allowing complete sample saturation.

9. 2.3 - **Decompression of the system**

A system of copper diaphragms (2-3 rupture discs) allows instantaneous decompression to be performed under repeatable pressure conditions, whereas a dedicated valve system is used for slow (ca. 0.025 $MPas^{-1}$) decompression rate. In the latter case, the decompression process lasts roughly 1000-1200 seconds (Fig. 3).

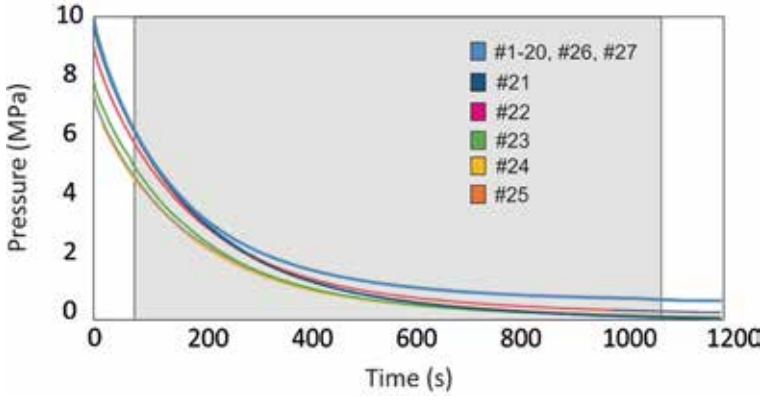

Figure 3. Decompression curve of experiments performed after 72 hours of saturation at 10 MPa (#1-20 and #26, #27) and 24 hours of saturation at 10, 9, 8 and 7 MPa (experiments #21, #22, #23 and #24, #25, respectively). The grey area represents the interval of video recordings (modified from Spina et al., 2016a).

The dynamics of bubbly analogue fluid in response to the decompression is monitored through the above-mentioned pressure sensors -recorded with a DAQ system from Yokogawa (WE7000)- and by using an high-speed camera at frame rates of 25 fps. Low frames rate is justified from the timescale of the observed phenomena. The recording of high-speed videos and pressure signals at high frame rate is synchronized.

9. 2.4 - **Analogue mixture and their properties**

In order to reproduce the behaviour of volatile-bearing magmas we used silicone oil (polydimethylsiloxane) as a proxy for basaltic melts. Two different types of particles were used to mimic crystals with different shape (Fig. 4): glass beads (diameter=83 mm; density=0.794 g/cm^3; aspect ratio=1) and glass fibres (length= 149 mm; diameter=14 mm; density=2.55 g/cm^3; aspect ratio=10). For both spherical- and elongated- particle bearing samples, different volume percentages were used to investigate the diluted, semi-diluted and concentrated regimes (see colour code in Table 1). Indeed, according to Mueller et al. (2010 and references therein), for spherical particles the diluted and semi-diluted regimes are restricted to $f \leq 0.02$ and $f \leq 0.25$, respectively. Conversely, for a spheroidal particle with an aspect ratio of 10, the regimes are confined to $f \leq 0.005$ and $f \leq 0.05$, respectively.

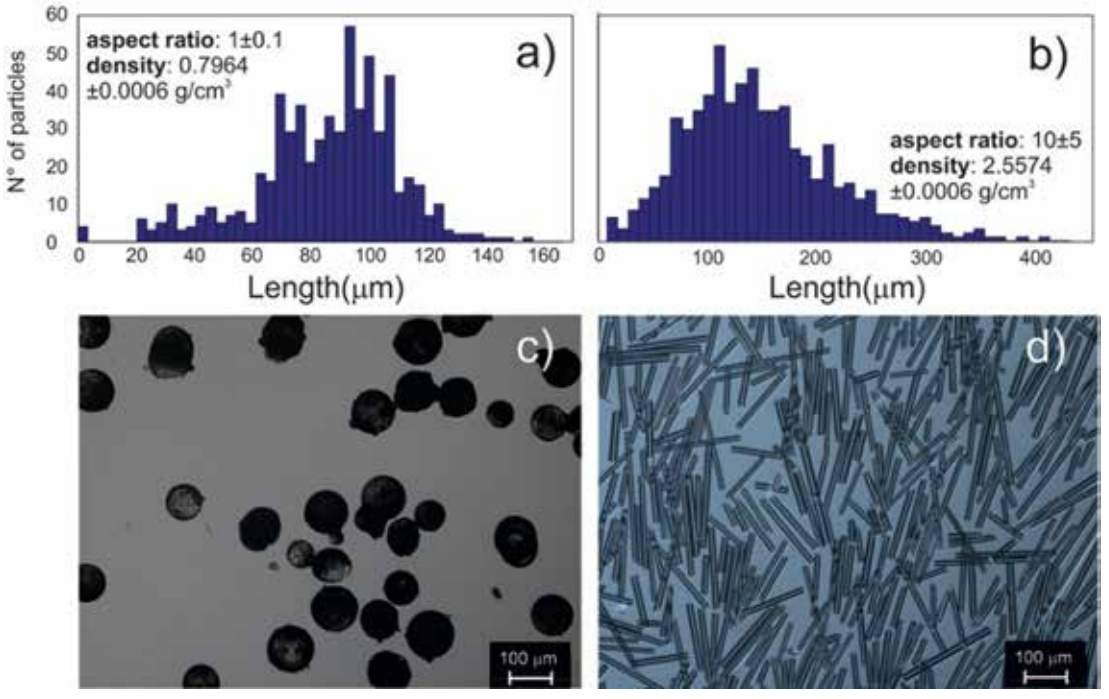

Figure 4. a, b Histograms of spherical and elongated particle length, respectively, measured on a population of more than 500 particles; c,d) Microscopic image of spherical and elongated particles.

9. 3 - **Rheological investigation of particle-bearing samples**

The influence of solid loading on the viscosity of the mixture has been widely demonstrated by several studies (e.g. Mueller et al., 2010; Mader et al., 2013). Therefore, we characterized the rheology of our particle-bearing samples, by using a concentric-cylinder narrow-gap viscometer (MCR502 from Anton Paar). The measurements were performed at temperatures of 21, 25 and 30 °C and strain rates of 1, 5 and 10 s^{-1}. In the high concentrated regime (f equal to 0.40 and 0.33 for spherical and elongated particle, respectively), measurements were performed at the additional values of strain rates equal to 0.01 and 0.001 s^{-1} to remove transient effects and avoid slippage along the walls. The results of viscosity measurements are shown in Fig. 5, where we also report the best fit curve obtained by using the model defined in Costa et al., (2009; for more information on the model and on the best fit parameters see Spina et al., 2016a).

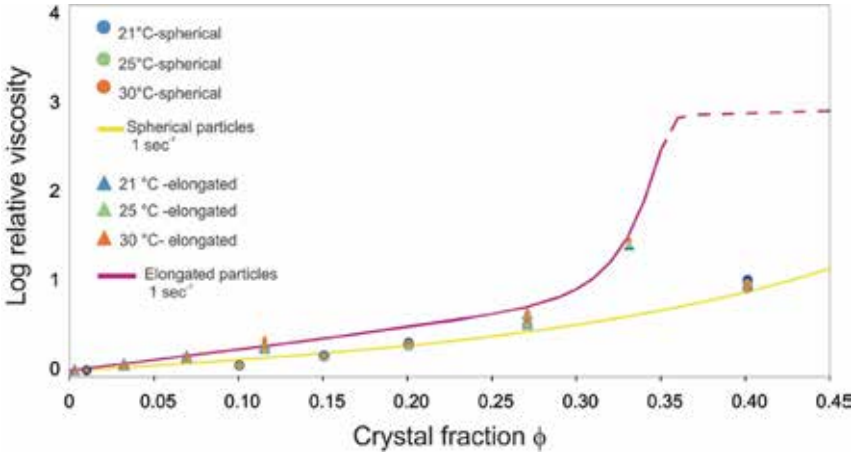

Figure 5. Rheological characterization of particle-bearing samples. Blue, green and orange triangles and dots represent the elongated and spherical particle-bearing measurements, respectively, performed at temperatures of 21, 25 and 30◦C. The best-fit curve obtained by applying the equation of Costa et al., (2009), using strain rates of $1s^{-1}$ is shown (pink and yellow lines for elongated and spherical particles, respectively; modified from Spina et al., 2016a).

The maximum packing fraction was experimentally determined after Cimarelli et al., (2011). We added an excess volume of particles to the liquid; then centrifuged the samples and weighted the remaining fraction of non-wet particle, from which we derived the amount of particles within the fluid. The maximum packing fraction f_m in our experiments is equal to 0.70 and 0.33 for elongated and spherical particles, respectively (Spina et al., 2016a). Concerning spherical particle-baring mixtures, the measured values are coherent with previous estimates f_m =0.64, 0.68 reported for sheared suspension (Mueller et al., 2010 and references therein) and predicted for a mono-disperse population of spherical particles (Mader et al., 2013). The values of maximum packing fraction obtained for elongated particle-bearing mixtures is coherent with the results of Cimarelli et al., (2011) but slightly lower than expected in Mader et al., (2013) for a mono-disperse population of particles with aspect ratio of 10. We assume that such discrepancy is related to particle

polydispersity or alternatively to sample inhomogeneity and/or sample preparation reproducibility limits (Spina et al., 2016a).

9. 4 - **Results**

The evolution of the samples upon decompression was tracked by measuring the increase in the height of the mixture, expressed as percentage of the original sample height at the beginning of the experiments (Fig. 6). The following discussion summarize the result described in Spina et al., 2016a,b where additional information can be found.

The decompressional response of the analogue mixture was characterized by three different regimes that will be described in detail in sections 4.1, 4.2, 4.3, respectively.

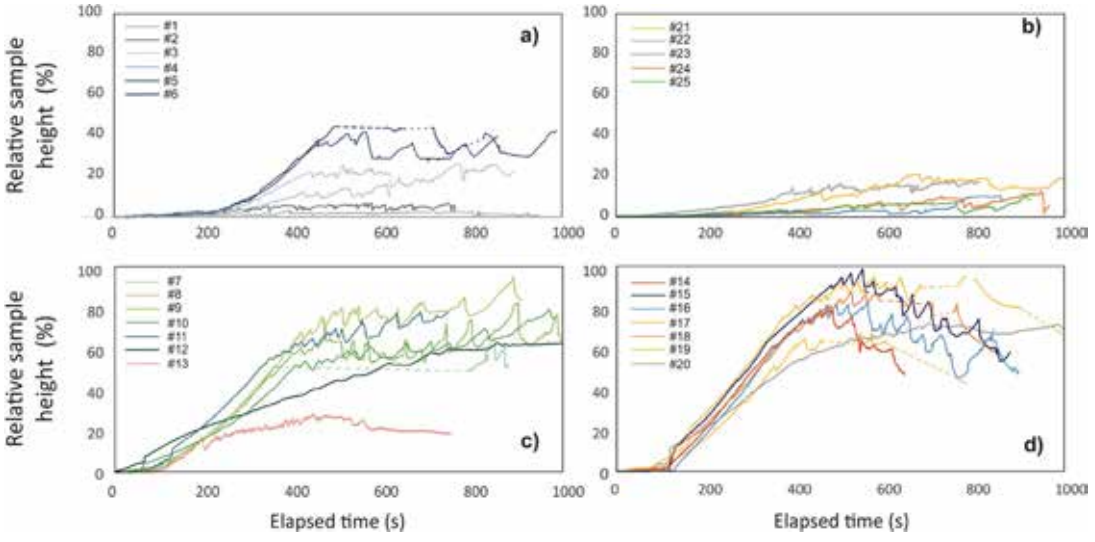

Figure 6. Comparison among degassing behaviour of experiments #1 to #25. The percentage increase in height of the mixture is plotted against time. The zero-time correspond to the initiation of video recordings (ca. 70 s after the start of the decompression; modified from Spina et al., 2016a).

9. 4.1 - **Nucleation**

Isolated bubbles are nucleated first at the outermost part of the sample. Indeed, nucleation is favoured at the free-surface, inducing the development of a vertical gas profile in its wake. The foaming at the top of the sample further steepens the concentration gradient, enhancing bubble nucleation immediately below the foam layer. The pressure values correspondent to the appearance of the smallest visible bubble (ca. 0.05 mm radius) for the 24 and 72 h experiments is in the range 3–5 MPa and 4.4 to 6 MPa, respectively (i.e. slight tendency of nucleation pressure to increase with saturation pressure and time). Upon decompression, the nucleation level migrates downwards.

Nucleated bubbles soon begin their ascent toward the surface, while growing radially (e.g. Fig. 7). The growth rate increases during the decompression, ranging from 10^{-3} mm/s up to 10^{-1} mm/s for bubbles nucleated at later stage. Lower values of ascent rate were measured in lower viscosity fluid

(up to 10^{-1} -1 mm/s, for experiments #2, #1, respectively). On the contrary, ascent rates of less than 10^{-2} mm/s were measured in higher viscosity fluids (#4 to #6). The intrinsic opacity of the particle-bearing mixtures at high solid loading prevented observations on bubble nucleation. However, in experiments performed in the diluted regime, it was still possible to notice a more pervasive distribution of smaller bubbles nucleating at a pressure of roughly 6 MPa, and a deepening of the nucleation level through time. The observed change in the bubble size distribution, here only qualitatively assessed, is linked to the heterogeneous bubble nucleation (e.g., Hurwitz and Navon, 1994) favoured by particles loaded in the sample.

9. 4.2 - **Foam build-up**

Once several bubbles nucleate at the top of the sample, the ascent speed of the mixture increases abruptly (Fig. 6, Fig. 7). We consider this stage to mark the beginning of foam build-up phase. No foams developed in experiments #2 and #1, due to the ability of bubbles to escape quickly from the mixtures and therefore no foam build-up was observed. For particle-free experiments we measured the vesicularity (γ) observed in video images at the initiation of foam build-up (ca. 200 seconds). γ was computed by the ratio between the surfaces of bubbles versus the total area interested by nucleation; the values of γ are equal to 0.19-0.27 for #3 and #4 and 0.23-0.21 for #5 and #6, respectively. The obtained values of vesicularities are in accordance with the results of Bai et al., (2008), where a value of 0.18 was defined to mark the initiation of an expansion-dominated phase. We infer that such value of vesicularity marks the threshold above which bubble nuclei are affected by the decrease in confining pressure related to the surrounding bubble swarm, and consequently expand faster. The occurrence of an enhanced growth rate for bubble swarms rather than for individual bubbles is coherent with numerical data (e.g. Proussevitch et al., 1993; Barclay et al., 1995). It is noteworthy that similar relatively low values of vesicularity can be observed also at very shallow level within the infill of basaltic conduits (Peck, 1978).

The starting time of foam build-up ranges from 200-250 s in pure liquid experiments to 60-130 s in particle-bearing mixtures. The anticipation of the expansive ascent of the bubbly mixture in particle bearing samples is likely to be a consequence of heterogeneous nucleation, that allows for a higher gas volume fraction at earlier times. We additionally observed that the maximum gas volume fraction depends strongly on the properties of the investigated materials (mainly on liquid viscosity and particle content). This result is shown in Fig. 8, where sample viscosity is plotted against gas volume fraction at the end of foam build-up (except for #1, #2, #12 and #20 were this value was taken right at the end of the initial liquid expansion).

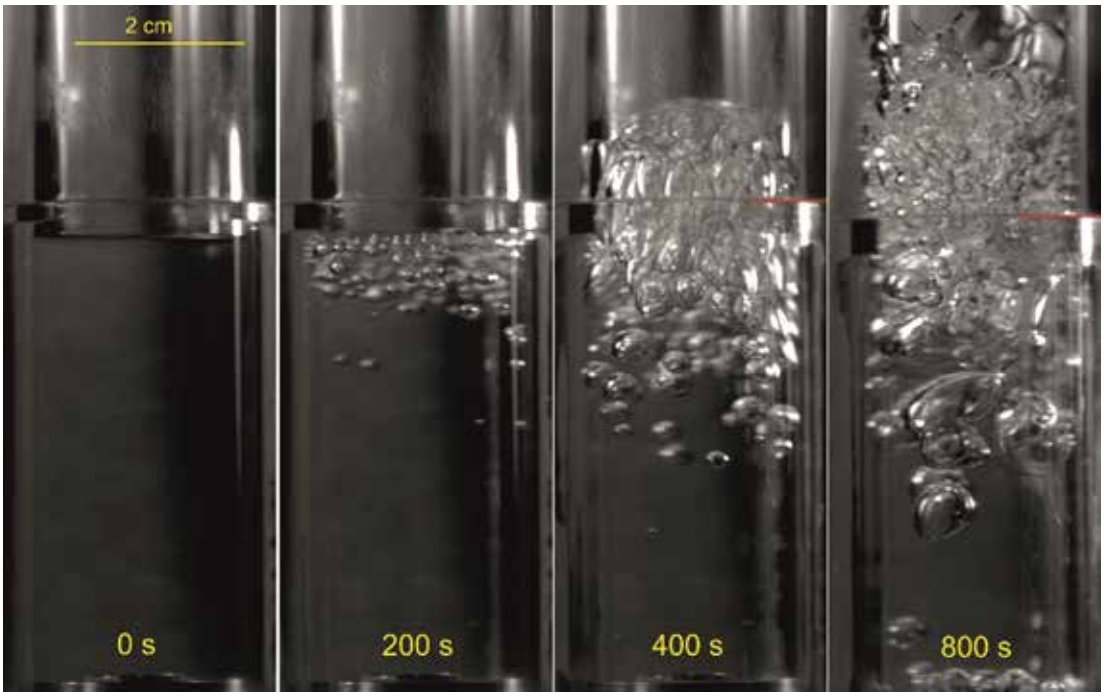

Figure 7. Snapshots of # 6 picturing different stages during decompression of 1000 Pa s silicone oil. The zero time refers to the initiation of video recordings (ca. 70 s after the start of decompression).

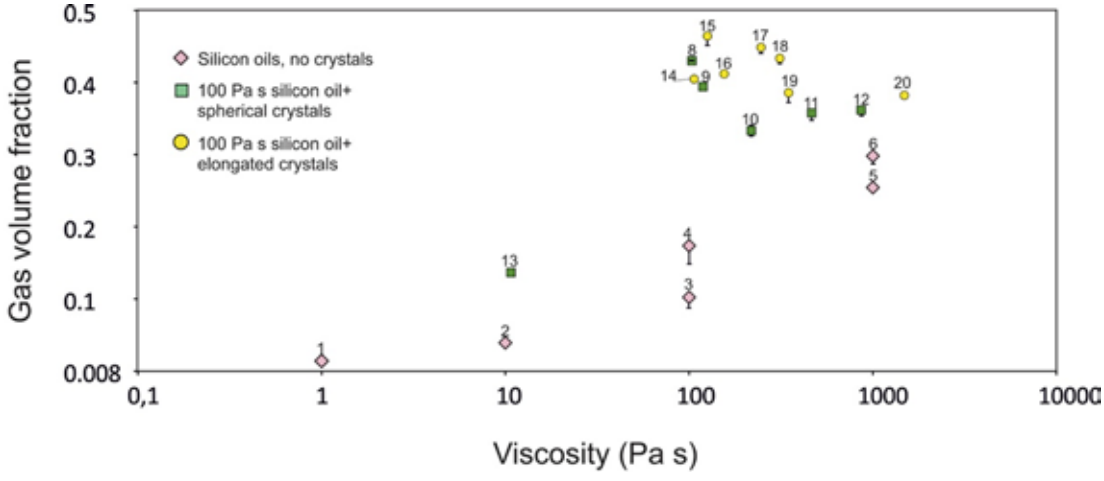

Figure 8. Gas volume ratio of pure silicone oils (pink diamonds) and spherical (green square) and elongated (yellow dots) particle-bearing samples versus sample viscosity at the beginning of the experiment. The error bars show the maximum error on the computation of volume related to the convex shape of the fluid column (when not present, the error lies within the data point; modified from Spina et al., 2016a).

Gas volume fraction increases remarkably with the addition of particles (Fig. 8, Fig. 9). For spherical particle-bearing experiments, we observe first an increase (up to f £10%) and then a decrease of the gas volume fraction with viscosity (i.e. solid content). This dual role of particle loading is coherent with studies performed in "bubble column reactors" (i.e. cylindrical vessels with a gas distributor at the base), where a similar trend with local maxima at 0.20–0.30 (Mena et al., 2005) and less than 0.10 (Bukur et al., 1990) have been found, respectively. Banisi et al., (1995) suggested that small amount of fine particles, as well as large number of big particles tend to decrease coalescence and therefore increase gas volume fraction. For elongated particle-bearing experiments, this effect is still evident thought the dataset is relatively sparser, probably due to the settling of denser particles during saturation phase. Finally, elongated-particle bearing experiments show a decaying trend of the fluid level after reaching the maximum growth (except #20), that can be described as an increased efficiency in degassing. This is likely related to the re-orientation of the axis of elongated particle along the direction of the fluid, similarly to what observed in the field (Ventura et al., 1996). Alternatively, particle flocculation (i.e. growth and segregation of fibre-network) can produce the development of preferential path for gas escape. Indeed, when fibre mass fraction is high the breakup of large bubbles and the formation of different gas–escape pathways - active on a timescale of seconds to minutes- is expected (e.g. Tang and Heindel, 2005).

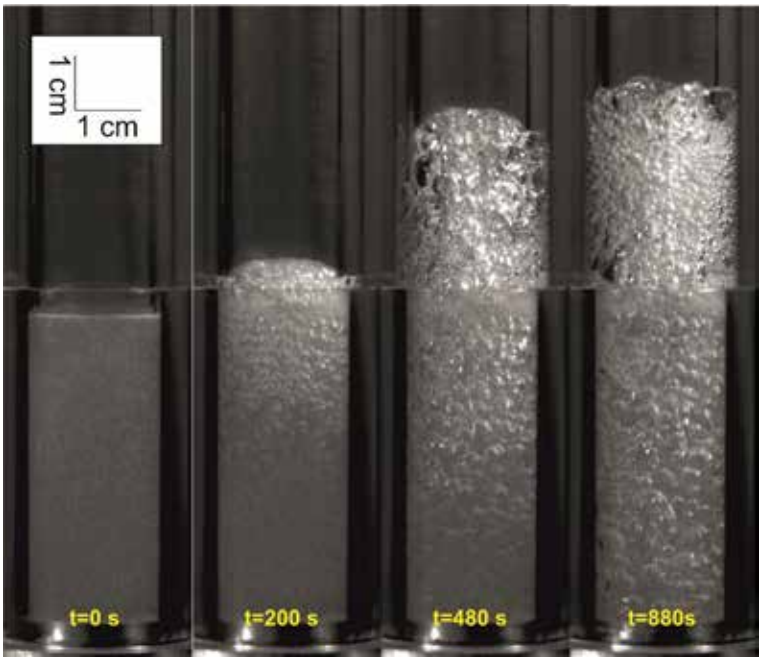

Figure 9. Snapshots of # 7 picturing different stages during decompression of 100 Pa s silicone oil bearing 1 vol % of spherical particles. The zero time refers to the initiation of video recordings (ca. 70 s after the start of decompression; modified from Spina et al., 2016a).

9. 4.3 - **Foam oscillation**

Soon after the expansion of the mixture, the foam becomes dominated by coalescence, and starts to oscillate cyclically around an equilibrium level in response to the balance between outgassing and foam-renewal. In pure silicone oils, the outgassing takes often place through individual large bubbles that rise to the surface and burst (e.g. Fig. 10). The duration of a complete growth-and-fall cycle ranges between 10 and 150 seconds. The cyclical upraise of the sample front was previously observed on a different range of timescales in other analogue systems upon decompression (e.g. Taddeucci et al., 2006). Average shorter time-scales were measured for particle-bearing experiments in the semi-diluted regime, likely in response to the increased bubble breakup-coalescence due to the solid network. The relatively broad-distribution of cycle duration is in agreement with the complex nature of foams (e.g. Neethling et al., 2005). In particle-bearing experiments, we additionally observed an increase in the oscillation time-scale with elapsed time, likely related to the hindering role of particles in redistributing the liquid involved in the precedent bursting phases.

In both particle-bearing mixtures at high solid content (#12 and #20), the curves in Fig. 6 reveal low ascent velocities and resemble a “stick-slip” behaviour, related to the damping effect of the dense solid network. Stix and Phillips (2012) drew similar curves for high viscosity Gum Rosin Acetone (GRA) samples.

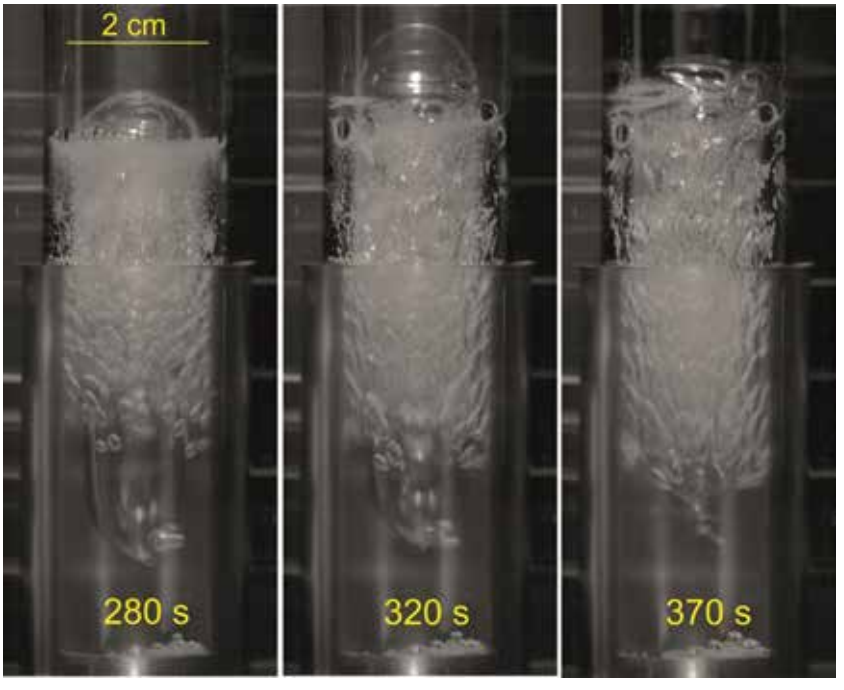

Figure 10. Bursting of a slug-type of bubble at the surface of the foam.

9. 5 - **Scaling and application to natural systems**

A fundamental step of the experimental investigations is defining the range of applicability of experimental results to the fluid dynamics of the targeted system, and the eventual limitations of the applied techniques in mimicking the investigated physics processes.

Given that in the shallow conduit the growth of bubbles is dominated by decompression rather than by diffusion (Sparks, 1978), laboratory experiments where decompression prevails, as here, are required to target the shallow feeding system. Depending on the eruptive style, decompression rate <0.02 $MPas^{-1}$ are expected for natural system (Fiege et al., 2014 and references therein). In particular, according to Namiki and Manga (2006) for decompression rates of the bubbly column equal to 20–200 Pas^{-1}, 2 $\times 10^4$ $Pas^{-1}$and >10^6 Pas^{-1}, effusive eruptions, explosive eruptions and fragmentation are expected, respectively. Therefore, the decompression rate here investigated is suited to reproduce the dynamic of effusive and explosive basaltic eruptions.

Nonetheless, it is important to remark that in our experiments we do not take into account the effect of degassing-driven crystallization, but rather mimic a condition where the magma is aphyric (in the case of the pure silicone oil) or a crystalline phase is present prior degassing (in the case of particle-bearing experiments).

In order to quantify the extent of similarity of our experiment to the fluid dynamics of basaltic volcanoes, we evaluated a set of non-dimensional numbers, accounting for the balance of forces (i.e. inertial, viscous, surface tension, buoyancy and capillary forces) acting on each fluid volume (Table 2: modified from Spina et al., 2016a). Reynold numbers were estimated for all the experiments and found to be <<1 in accordance with the observation that the initial flow expansion below the fragmentation level is laminar (Massol and Jaupart, 1999). Reynold, Eötvos, Morton bubble numbers and Capillary number were evaluated for each experiment performed in the dilute regime during bubble nucleation (phase I) and part of foam build-up (phase II). Indeed, for volume fraction f <0.45 and Ca<0.3 the role of bubble on rheology is assumed to be weak to negligible (e.g. Manga et al. 1998; Lane et al., 2001). The comparison with natural estimates (e.g. Manga and Stone, 1994, Belien et al., 2010, Del Bello et al., 2012, Moitra et al., 2013 and Nguyen et al., 2013) confirms the analogy between the investigated laboratory system and basaltic volcanoes. The opacity of the mixture at high solid content prevent to extend the scaling analysis to such experiments.

For higher gas volume fraction, few additional considerations are necessary. In fact, foams are metastable time-varying system, with short-scale longitudinal and radial variation and for which no rheological models are defined (e.g. Mader et al., 2013; LLewellin and Manga, 2005). Therefore, we will not extend the non-dimensional analysis to the last phase, although given that the properties of the natural and analogue bubbly fluid are evolving in the same direction during degassing, we expected dynamic similarity to be valid also during phase III (e.g. Lane et al., 2001).

Adimensional parameter	Experimental Value	Volcano-scale condition
$R_e = {D\rho U}/{\eta}$	10^{-7}-10^{-5}	$<10^{3}$
$Re_b = {\rho D_b U_b}/{\eta}$	10^{-10}-10^{-3}	<<1
$E_0 = {g\Delta\rho {D_b}^2}/{\sigma}$	10^{-3}-10^{1}	$10^{-3}< 10^{6}$
$M_0 = {g\eta^4\Delta\rho}/{\rho^2\sigma^3}$	10^{2}-10^{14}	10^{2}-10^{15}
$C_a = {\eta u_e}/{\sigma}$	10^{-5}-10^{-1}	<<1

Parameters list:

D=Conduit diameter, U= fluid velocity, h=fluid viscosity, r =fluid density, U_b=bubble velocity, D_b= bubble diameter, Dr = absolute value of density difference between bubbles and fluid phase, s =surface tension, u_e=expansion velocity.

Modified from Spina et al., 2016a.

Table 2. Comparison of experimental and natural fluid-dynamic conditions via non-dimensional numbers. The references for volcano-scale condition are given in paragraph 5. The non-dimensional numbers were computed for pure silicone oils and diluted particle-bearing experiments during phase I and initiation of phase II.

9. 6 - **A taste of further implications: Integrating numerical and experimental approaches**

In order to investigate numerically complex physical variables, near-to-exact input parameters are required. Nonetheless, it is part of the intrinsic nature of volcanic feeding systems to be not accessible to direct observations. Therefore, experimental studies represent a unique opportunity to validate numerical models of the plumbing systems, given the high degree of control on the physical properties allowed by laboratory approach. At the lights of such considerations, we took advantage of our set of decompression experiments to validate a complex multiphase, multicomponent numerical code in the ©*Openfoam* framework, developed from the *twoPhaseEulerFoam* solver. In order to reproduce the experimental conditions, the autoclave was represented by a bi-dimensional rectangular grid with $9.3*10^4$ cells containing: (i) a liquid mixture composed by silicone oil plus 1.8 wt % of diluted Argon (up to 6.5 cm) and (ii) Argon gas in equilibrium with the fluid below.

At the top of the modelled autoclave, we fixed outlet boundary condition for pressure, and we used the decompression curve recorded by the upper sensor to describe the pressure history at the outlet. Finally, a relaxation time-scale, namely t, for gas exsolution was derived from:

$$\Gamma_{2,1} = \frac{x_{2,1} - x_{2,1}^{eq}}{\tau_{2,1}} \qquad (1)$$

where $G_{2,1}$ represents the mass fraction per unit volume and time of Argon gas passing from liquid phase to gas phase, whereas $x_{2,1}$, $x^{eq}_{2,1}$ are the mass fraction excess and mass fraction at equilibrium of gas in the liquid phase, respectively. Two sets of simulations have been performed using 100 Pa s and 1000 Pa s silicone oil fluid as references, and by varying systematically the value of $t_{2,1}$. Our results show that experimental decompression are far from the equilibrium degassing for both fluids.

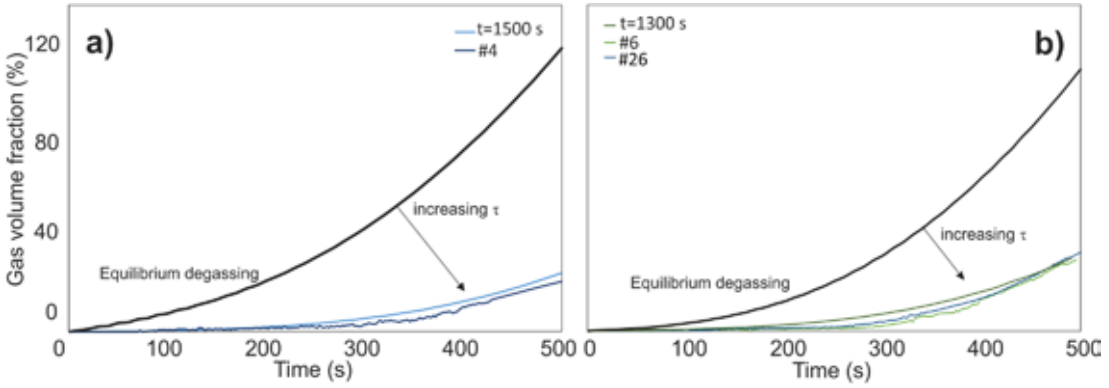

Figure 11. a) Numerical results of simulations performed at 100 Pa s, showing the curve for equilibrium degassing (black solid line; tau <10), the experimental curve (blue line, # 4) and the best fit curve (azure line; tau 1500 s); b) Numerical results of simulations performed at 1000 Pa s, showing the curve for equilibrium degassing (black solid line; tau <10), the experimental curves (dark and light green lines, #6 and #26, respectively) and the best fit curve (grey line; tau 1300 s).

This evidence is strikingly important, given that in most cases it is assumed that the effect of higher diffusivity and lower surface energy of mafic melts allows for an efficient exsolution (i.e. Mangan et al., 2004), thus preventing disequilibrium effects.

9. 7 - **Concluding remarks**

Decompression experiments performed on analogue basaltic samples (Argon-saturated silicone oil plus particles) allowed to quantitatively constraining the effect of physical properties on degassing in shallow basaltic systems.

i. Upon decompression, different regimes were characterized: (i) bubble nucleation, (i.e. the appearance of isolated bubbles at the top of the sample); (ii) foam build-up, (the abrupt fast expansion of bubbles as they approach to develop a foam); (iii) foam oscillation (cyclic repetition of foam outgassing and renewal).

ii. The presence of particles, even at volume percentages as low as 0.3-1 %, affect strongly the degassing behaviour by inducing heterogeneous nucleation. In particle-bearing mixtures, we observed halved time for foam-build up, whereas the maximum gas volume fraction is more than doubled in comparison to pure silicone oils samples at the same viscosity.

iii. The amount of solid content plays a dual role: at low volume percentage (<10 %), the maximum gas volume ratio increases with solid content, due to the increase in available nucleation sites. Above this threshold, we observed a relative decrease in the maximum gas volume ratio, possibly linked to the bubble coalescence and break-up favoured by solid network.

iv. The shape of particles affects the dynamics of degassing on a long-term basis. Indeed, provided enough time for rearrangement of the particle network (e.g. through particles re-orientation and/or flocculation), elongated particles increase the efficiency of degassing.

v. Experimental results were used to validate a complex multiphase multicomponent numerical code developed in *Openfoam* framework. The results of the numerical simulation show that the assumption of equilibrium degassing might be oversimplifying, also when modelling low viscosity fluid (<1000 Pa s) and relatively low decompression rates (0.025 MPa s^{-1}).

Acknowledgements

The research leading to these results has received funding from the European Union Seventh Framework Programme (FP7/2007-2013) under the project NEMOH, grant agreement n° 289976.

References

Bai, L., Baker, D. R. and Rivers, M. (2008). Experimental study of bubble growth in Stromboli basalt melts at 1 atm. Earth Planet. Sci. Lett. 267 (3–4), 533–547.

Banisi, S., Finch, J. A., Laplante, A. R. and Weber, M. E. (1995). Effect of solid particles on gas holdup in flotation columns—I. Measurement. Chem. Eng. Sci. 50, 2329–2334.

Barclay, J., Riley, D. S. and Sparks, R. S. J. (1995). Analytical models for bubble growth during decompression of high viscosity magmas. Bull. Volcanol. 57, 422–431.

Belien, I. B., Cashman, K. V. and Rempel, A. V. (2010). Gas accumulation in particle- rich suspensions and implications for bubble populations in crystal-rich magma. Earth Planet. Sci. Lett. 297 (1–2), 133–140. http://dx.doi.org/10.1016/ j.epsl.2010.06.014.

Bukur, D. B., Patel, S. A. and Daly, J. G. (1990). Gas holdup and solids dispersion in a three- phase slurry bubble column. AIChE J. 36, 1731–1735.

Cimarelli, C., Costa, A., Mueller, S. and Mader, H. M. (2011). Rheology of magmas with bimodal crystal size and shape distributions: insights from analog experiments. Geochem. Geophys. Geosyst. 12, Q07024. http://dx.doi.org/10.1029/ 2011GC003606.

Costa, A., Caricchi, L. and Bagdassarov, N. (2009). A model for the rheology of particle- bearing suspensions and Partially molten rocks. Geochem. Geophys. Geosyst. 10, Q03010. http:// dx.doi.org/10.1029/2008GC002138.

Del Bello, E., Llewellin, E. W., Taddeucci, J., Scarlato, P. and Lane, S. J. (2012). An analytical model for gas overpressure in slug-driven explosions: insights into Strombolian volcanic eruptions. J. Geophys. Res. 117, B02206. http://dx.doi.org/10.1029/ 2011JB008747.

Fiege, A., Holtz, F. and Sarah, B. C. (2014). Bubble formation during decompression of andesitic melts. Am. Mineral.99, 1052–1062. http://dx.doi.org/10.2138/am.2014.4719.

Gardner, J. E., Hilton, M. and Carroll, M. R. (2000). Bubble growth in highly viscous silicate melts during continuous decompression from high pressure. Geochim. Cosmochim. Acta., 64(8), 1473-1483.

Hurwitz, S. and Navon, O. (1994). Bubble nucleation in rhyolitic melts: experiments at high pressure, temperature, and water content. Earth Planet. Sci. Lett. 122, 267–280.

Lane, S. J., Chouet, B. A., Phillips, J. C., Dawson, P., Ryan, G. A. and Hurst, E. (2001). Exper- imental observations of pressure oscillations and flow regimes in an analogue volcanic system. J. Geophys. Res. 106, 6461–6476.

Llewellin, E. W. and Manga, M. (2005). Bubble suspension rheology and implications for conduit flow. J. Volcanol. Geotherm. Res. 143, 205–217.

Lundberg, J. L., Wilk, M. B. and Huyett, M. J. (1962). Estimation of Diffusivities and Solubilities from Sorption Studies, J. Polym. Sci., Vol. 57, pp 275-299.

Mader, H. M., Llewellin, E. W. and Mueller, S. P. (2013). The rheology of two-phase magmas: a review and analysis. J. Volcanol. Geotherm. Res. 257, 135–158. http:// dx.doi.org/10.1016/j.jvolgeores.2013.02.014.

Manga, M. and Stone, H. A. (1994). Interactions between bubbles in magmas and lavas: effects of bubble deformation. J. Volcanol. Geotherm. Res. 63 (3–4), 267–279. http://dx.doi.org/10.1016/0377-0273(94)90079-5.

Manga, M., Castro, J., Cashman, K. V. and Loewenberg, M. (1998). Rheology of bubble- bearing magmas. J. Volcanol. Geotherm. Res. 87, 15–28.

Mangan, M., Sisson, T. and Hankins, W. B. (2004). Decompression experiments identify kinetic controls on explosive silicic eruptions, Geophys. Res. Lett., 31, L08605,doi :10.1029/2004GL019509.

Massol, H. and Jaupart, C. (1999). The generation of gas overpressure in volcanic erup- tions. Earth Planet. Sci. Lett. 166, 57–70.

Massol, H. and Koyaguchi, T. (2005). The effect of magma flow on nucleation of gas bubbles in a volcanic conduit. J. Volcanol. Geotherm. Res., 143.1, 69-88.

Mena, P. C., Ruzicka, M. C., Rocha, F. A., Teixeira, J. A. and Drahoš, J. (2005). Effect of solids on homogeneous–heterogeneous flow regime transition in bubble columns. Chem. Eng. Sci. 60, 6013–6026.

Moitra, P., Gonnermann, H. M., Houghton, B. F. and Giachetti, T. (2013). Relating vesicle shapes in pyroclasts to eruption styles. Bull. Volcanol. 75, 691. http://dx.doi.org/10.1007/s00445-013-0691-8.

Mourtada-Bonnefoi, C. C. and Laporte, D. (2004). Kinetics of bubble nucleation in a rhyolitic melt: an experimental study of the effect of ascent rate. Earth Planet. Sci. Lett. 218 (3–4), 521–537.

Mueller, S., Llewellin, E. W. and Mader, H. M. (2010). The rheology of suspensions of solid particles. Proc. R. Soc. A 466, 1201–1228. http://dx.doi.org/10.1098/ rspa.2009.0445.

Namiki, A. and Manga, M. (2006). Influence of decompression rate on the expansion velocity and expansion style of bubbly fluids. J. Geophys. Res.111, B11208. http://dx.doi.org/10.1029/2005JB004132.

Nguyen, C. T., Gonnermann, H. M., Chen, Y., Huber, C., Maiorano, A. A., Gouldstone, A. and Dufek, J. (2013). Film drainage and the lifetime of bubbles. Geochem. Geophys. Geosyst. 14, 3616–3631. http://dx.doi.org/10.1002/ggge.20198.

Neethling, S. J., Lee H.T. and Grassia, P. (2005). The growth, drainage and breakdown of foams, Colloids and Surfaces A: Physicochemical and Engineering Aspects, 263 (1-3), 184-196. http://dx.doi.org/10.1016/j.colsurfa.2004.12.014.

Oppenheimer, J., Rust, A. C., Cashman, K. V. and Sandnes, B. (2015). Gas migration regimes and outgassing in particle-rich suspensions. Front. Phys. 3: 60. doi: 10.3389/fphy.

Peck, D. (1978). Cooling and Vesiculation of Alae Lava Lake, Hawaii. U. S. Geol. Surv. Prof. Pap., vol. 935-B. 59 pp.

Proussevitch, A. A., Sahagian, D. L. and Anderson, A. T. (1993). Dynamics of diffusive bubble growth in magmas: isothermal case. J. Geophys. Res. 98 (B12), 22283–22307.

Rivalta, E., Pascal, K., Phillips, J. and Bonaccorso, A. (2013). Explosive expansion of a slowly decompressed magma analogue: evidence for a delayed bubble nucleation. Geochem. Geophys. Geosyst. 14 (8), 3067–3084.

Sparks**,** R. S. J. (1978). The dynamics of bubble formation and growth in magmas: a review and analysis. J. Volcanol. Geotherm. Res. 3, 1–37.

Spina, L., Cimarelli, C., Scheu, B., Di Genova, D. and Dingwell, D. B. (2016a). On the slow decompressive response of volatile-and crystal-bearing magmas: An analogue experimental investigation. Earth Planet. Sci. Lett, 433, 44-53.

Spina L., Scheu, B., Cimarelli, C., Arciniega‐Ceballos, A. and Dingwell, D. B. (2016b). Time scales of foam stability in shallow conduits: Insights from analogue experiments. Geochemistry, Geophysics, Geosystems, 17(10), 4179-4194.

Stix, J. and Phillips, J.C. (2012). An analog investigation of magma fragmentation and degassing: effects of pressure, volatile content, and decompression rate. J. Volcanol. Geotherm. Res.211–212, 12–23.

Taddeucci, J., Spieler, O., Ichihara, M., Dingwell, D. B. and Scarlato, P. (2006). Flow and fracturing of viscoelastic media under diffusion-driven bubble growth: An analogue experiment for eruptive volcanic conduits. Earth Plan. Sci. Lett., 243(3), 771-785.

Tang, C. and Heindel, T. J. (2005). Effect of fiber type on gas holdup in a cocurrent air– water–fiber bubble column. Chem. Eng. J. 111, 21–30.

Toramaru, A. (2006). BND (bubble number density) decompression rate meter for explosive volcanic eruptions. J. Volcanol. Geotherm. Res. 154, 303–316.

Ventura, G., De Rosa, R., Colletta, E. and Mazzuoli, R. (1996). Deformation patterns in a high-viscosity lava flow inferred from the crystal preferred orientation and imbrication structures: an example from Salina (Aeolian Islands, southern Tyrrhe- nian Sea, Italy). Bull. Volcanol. 57, 555–562.

Laura Spina, Italy
laura.spina@unipg.it

Affiliation under NEMOH
Department für Geo- und Umweltwissenschaften, Ludwig-Maximilians-Universität München, Munich, Germany

Research theme under NEMOH
Influence of decompression path and physical properties on the eruption behaviour: A Lab approach with analogue material

My current research focuses on the mobility of volatiles in the shallow conduit through a twofold approach, based on: 1) Laboratory experiments on analogue magmatic samples. 2) Investigation of seismic and acoustic signals related to volcanic degassing.

I accomplished the Bachelor Degree in Geological Science in October 2008 (110/110 cum laude) and, successively, the Master Degree in Geophysical Science in October 2010 (110/110 cum laude) at *University of Catania*. In December 2010, I was enrolled in a PhD course on Earth Science at *University of Catania*, in cooperation with *Istituto Nazionale di Geofisica e Vulcanologia (INGV), Sezione di Catania*. My PhD project aimed to unveil the long-term dynamics of different branches of the feeding system at Mt. Etna (Italy) through seismic and acoustic signals. The investigation of the eruptive processes at basaltic volcanoes was additionally enriched by a dataset of acoustic events from Mt. Yasur (Vanuatu). On February 2014, I obtained my PhD in Earth Science.

From October 2012 to March 2015 I was enrolled in NEMOH at *Ludwig Maximilians Universität München* (LMU München; Munich, Germany), under the supervision of Dr. Scheu. NEMOH offered me the chance to build-up a novel project focused on the effect of physical properties and decompression rates on volatiles behaviour. With this aim, I performed shock-tube decompression experiments on analogue basalts (argon-saturated silicone oils+glass beads/fibres). In NEMOH, I carried out two secondments held at: 1) *Department of Civil Protection* (Rome, Italy), in collaboration with Dr. C. Cardaci, where I learnt about the Italian Civil Protection System and the development of hazard maps for volcanic areas; 2) *INGV, Sezione di Pisa* (Pisa, Italy) were I implemented a numerical code for multi-phase multi-component fluids in the shallow conduit in collaboration with Dr. De' Michieli Vitturi and Dr. Colucci.

From April 2015 to October 2016 I was post-doctoral researcher at LMU München in the frame of the Europeans Projects EVOKES (Explosive volcanism in Earth System, n° 247076) and MED-SUV (MEDiterranean SUpersite Volcanoes, n°308665). Since November 2016, I have a research grant at *Università di Perugia* (Perugia, Italy), where I aim to derive empirical laws through the application of geophysical methods to magma mixing experiments.

Chapter 10

Rheological heterogeneity in basaltic volcanism

Antonio Capponi

Lancaster Environment Centre, Lancaster University, Lancaster, United Kingdom

Tutorship: Stephen J. Lane , Michael R. James

Lancaster Environment Centre, Lancaster University, Lancaster, United Kingdom

Abstract

Strombolian volcanic activity, one of the most common on Earth, results from the burst of large gas pockets (*slugs*) following ascent through relatively low-viscosity magma within the volcanic conduit. However, this paradigm was forged when the complex rheology of the magma at Stromboli, the model-type volcano for this activity, was still poorly constrained. Textural and petrological evidence has recently suggested the presence of viscous, degassed magma layers in the upper portion of the conduit at Stromboli. This layer acts as a plug, through which slugs burst, controlling the eruptive dynamics. To date, little has been done to integrate this scenario into current models of volcanic eruptions and interpretation of geophysical signals. This study investigates slug ascent through a rheologically stratified magma column using analogue laboratory experiments, numerical modelling and 3D computational fluid dynamic simulations. The results illustrate (1) the range of slug flow configurations that develops in a rheologically stratified column, (2) the relevance of such configurations to Strombolian-type volcanoes, and (3) the key parameters controlling the transition in flow configurations. Each identified configuration encompasses processes affecting slug expansion and burst: for example, dynamic narrowing and widening of the conduit, instabilities along the falling liquid film and slug break-up. These complexities lead to variations in eruption magnitude and style; furthermore, the presence of a plug seems to be a pre-requisite for the generation of eruptive pulses observed in single explosions at Stromboli.

Keywords: Slug flow, Strombolian eruptions, eruption dynamics, analogue experiments, Taylor bubble.

10. 1 **- Introduction**

Strombolian eruptions are relatively mild, impulsive releases of gas and pyroclasts, typically lasting a few to tens of seconds and ejecting a gas-particle mixture to several tens to hundreds of metres in height (e.g. Houghton and Gonnermann, 2008; Cashman and Sparks, 2013; Taddeucci et al., 2015). It is now generally accepted that the explosions result from the arrival and burst of large gas pockets (*slugs*) at the surface of a relatively low-viscosity magma (Houghton and Gonnermann, 2008; Vergniolle and Gaudemer, 2015). This paradigm is supported by a large body of literature concerning the general mechanism behind Strombolian explosions and the parameters determining

the changes in eruptive dynamics (e.g., Vergniolle and Brandeis, 1996; Houghton and Gonnermann, 2008; James et al., 2009; Del Bello et al., 2012; Lane et al., 2013). Most work investigating the ascent, expansion and burst of slugs in rheologically uniform media and only very few studies investigated these processes in a rheologically stratified magma (Del Bello et al., 2015). However, the model of ascent and burst of unimpeded slugs cannot explain recent field observations and textural data. Petrological studies have established that the magma in the shallower part of the conduit is degassed, crystalline and more viscous, and that mingling between magmas may occur within the conduit (e.g., Lautze and Houghton, 2005, 2006; Colò et al., 2011; Gurioli et al., 2014). Imaging studies showed a clear pulsatory behaviour in a single Strombolian explosion, likely related to successive pressure release pulses and sub-pulses (e.g., Taddeucci et al., 2012; Gaudin et al., 2014). The instabilities that may be responsible for this kind of pulsatory behaviour, however, are also difficult to explain with the canonical Strombolian paradigm. These evidence shed doubts on the fluid-dynamical view of the conduit dynamics.

This study challenges the assumption of a rheological uniform magma column, providing insights into the role played by an upper viscous layer at the top of the conduit (a "plug") on the eruption dynamics. We investigated the scenario of a gas slug ascending through a rheologically stratified magma column using first-order analogue laboratory experiments, numerical modelling and 3D computational fluid dynamic simulations. Through laboratory experiments, we identified the different flow configurations that can develop in association with slug flow in a rheologically stratified conduit. Then we developed an experimentally-validated 1D model, supported by 3D computational fluid-dynamics simulations, to illustrate the relevance of the identified configurations to Strombolian-type volcanoes. Finally, we explored the possible role of the identified flow configurations on Strombolian eruptive processes (Capponi et al., 2016).

10. 2 - **Methods**

We investigated the processes of gas ascent, expansion and burst in a layered system with an experimental apparatus comprising a 3-m-high tube filled with a column of Newtonian oil (silicone oil *AS 100*, viscosity μ = 0.1 Pa s, density ρ = 990 kg/m^3) overlain by a variable thickness layer of higher viscosity oil (castor oil, μ = 1 Pa s, ρ = 961 kg/m^3; Fig 1). Layer thickness was non-dimentionalised as a function of the tube diameter, *D*: ~2.5 (1*D*), ~5 (2*D*), ~12.5 (5*D*), ~25 (10*D*) and ~50 (20*D*) cm. We carried out the experiments under reduced ambient pressure P_a (3 ± 0.1 kPa, 1 ± 0.1 kPa and 300 ± 0.1 Pa) to scale for gas expansion (James et al., 2008) and injecting volumes of air (V_0) of 2, 4, 6, 8, 10, 17, 24, 32 and 49 ± 0.1 ml at the base of the tube. Each experiment was imaged with a Basler acA2000-340km high-speed camera at a frame rate of 300 ± 0.1 fps (Capponi et al., 2016).

To extend our 1D numerical model to volcanic-scale, we considered an idealised volcanic system with a 200-m-high magma column filling a conduit of radius 1.5, 2 or 2.5 m, covering the range of values appropriate to Stromboli (Taddeucci et al., 2012; Gaudin et al., 2014). Magma viscosities ranged between 10–50 kPa s and 50–500 Pa s, and densities of 1300 kg/m^3 and 900 kg/m^3(Gurioli et al., 2014), for the plug and the underlying magma respectively (Capponi et al., 2016).

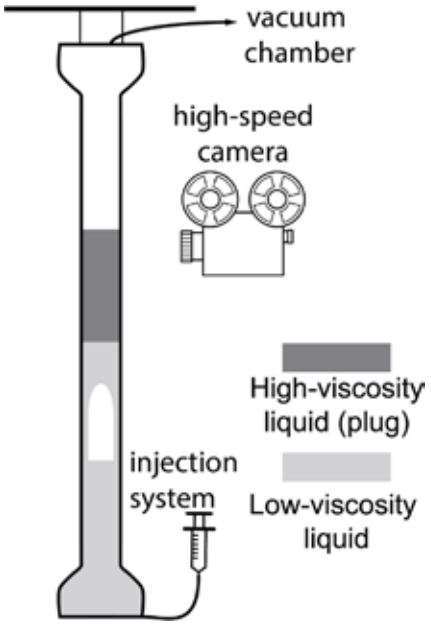

Figure 1. The experimental apparatus comprised a 3-m-high vertical tube, with a diameter D of 0.025 m, connected to a vacuum chamber and a gas injection system. Each experiment was imaged with a high-speed camera at 300 fps.

10. 2.1 - **Scaling considerations**

A well-established parametrization exists for describing the behaviour of an ascending, constant-length slug in a tube filled with a liquid, through a series of dimensionless numbers (e.g., White and Beardmore, 1962; Wallis, 1969; Seyfried and Freundt, 2000).

The Morton number, $Mo = \frac{g\mu^4}{\rho\sigma^3}$, where g is the gravitational acceleration, μ and ρ the viscosity and density of the liquid, and σ the surface tension, represents the ratio between the viscous and surface tension forces. The Eötvös number, $Eo = \frac{\rho g D^2}{\sigma}$, where D is the internal diameter of the conduit, represents the ratio between buoyancy and surface tension forces. For $Mo > 10^{-6}$ (Seyfried and Freundt, 2000) and $Eo > 40$ (Viana et al., 2003), surface tension plays a negligible role (e.g., Seyfried and Freund, 2000; Llewellin et al., 2012), and the ascent of a slug is controlled by the inverse viscosity N_f. Thus, Morton and Eötvös numbers can be combined to eliminate σ and derive N_f:

$$N_f = \left[\frac{Eo^3}{Mo}\right]^{\frac{1}{4}} = \frac{\rho}{\mu}\sqrt{8gr_c^3} \quad (1)$$

where r_c is the pipe radius.

For the idealised volcanic scenario, fluid properties and conduit geometries give N_f ~0.42 to ~4.55 for the plug and ~29 to ~630 for the magma beneath the plug (Table 1). These values lie in regions of

the flow regime where the slug behaviour is controlled by viscosity in the plug, and by inertia with viscous contributions in the fresh magma (e.g., N_f = ~1.6 for a magma μ = 20 kPa s, ρ = 1300 kg/m^3 and N_f = 150 for a magma μ = 150 Pa s, ρ = 900 kg/m^3, with a conduit radius r_c = 2 m; Table 1). For the experimental tube diameter D = 0.025 m, we obtain N_f values of ~12 and ~122 for the castor oil and silicone oil respectively. These values give slug ascent under dominant viscous control in the plug, but with a significant degree of inertial contribution within the liquid beneath the plug (e.g., White and Beardmore, 1962). Thus, both system lies in the same regimes during the active flow processes (Capponi et al., 2016).

Dimensionless parameters	Silicone oil	Castor oil	Fresh magma	Plug
Viscosity (Pa s)	0.1	1	150	20000
Density (kg/m^3)	990	961	900	1300
Conduit diameter (m)	0.025		2	
Inverse viscosity, N_f	122.57	11.89	150.34	1.62
Froude number, *Fr*	0.31	0.108	0.317	0.016
Film cross section A'	0.41	0.52	0.39	0.55
Dimensionless film thickness, λ'	0.41	0.527	0.394	0.544
Slug radius (m)	0.0096	0.0085	1.55	1.35

Table 1. Comparison between experimental and volcano-scale parameters

For the *1D* model, slug base ascent velocity, v_s, is evaluated using the dimensionless relationship from Wallis (1969), where v_s is expressed as $v_s = Fr\sqrt{gD}$, where *Fr* is the dimensionless Froude number, given by (Viana et al., 2003; Llewellin et al., 2012): $Fr = 0.34\left[1 - \left(\frac{31.08}{N_f}\right)^{1.45}\right]^{-0.71}$.

The experimental injected volumes are non-dimentionalised to give the dimensionless gas slug volume through the number $V_a^{'}$ (Del Bello et al., 2012), expressed as $V_a' = V_a \frac{\rho g}{\pi r_c^2 P_a}$, where V_a is the volume that the slug would have at ambient pressure. Finally, the dimensionless thickness of the falling film λ' ($\lambda' = \lambda/r_c$) is determined from N_f (Llewellin et al., 2012):

$$\lambda' = \left(0.204 + 0.123\tanh\left(2.66 - 1.15\log_{10} N_f\right)\right)r_c \qquad (2)$$

10. 3 - **Flow configurations**

For the liquids properties and tube geometry, experiments have shown that the flow can be organized in three main flow configurations, bracketed by end-member scenarios of a tube filled with either high- or low-viscosity liquid: Configuration 1 – Thick Plug, Configuration 2 – Medium plug

and Configuration 3 – Thin Plug (Fig. 2; from now on referred as Configuration 1, Configuration 2 and Configuration 3; Capponi et al., 2016).

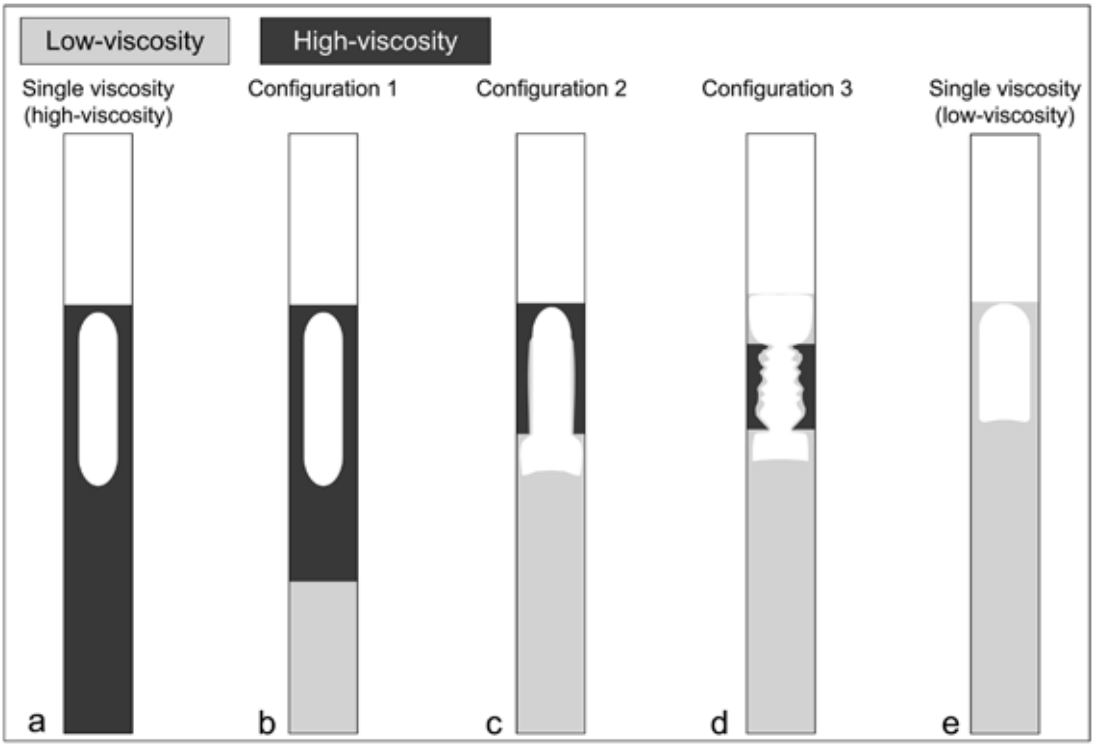

Figure 2. Conceptual sketches of a conduit filled with (**a**) high-viscosity and (**e**) low-viscosity liquid representing the configuration end-members bracketing three main flow configurations: (**b**) Configuration 1 – Thick Plug, (**c**) Configuration 2 – Medium plug and (**d**) Configuration 3 – Thin Plug, where a thin layer of low-viscosity fluid is formed on top of the high-viscosity one (reproduced from Capponi et al., 2016).

10. 3.1 - **Single-viscosity**

The two single-viscosity end-member scenarios can be interpreted as an infinitely tick (i.e., conduit fully filled with the high-viscosity liquid) or thin (i.e., conduit fully filled with the low-viscosity liquid) plugs (Fig. 2a, e). Here, a slug rose, expanded and elongated surrounded by a falling liquid film (James et al., 2008; Lane et al., 2013; Del Bello et al., 2015; Capponi et al., 2016). The slug burst when all the liquid head above it has flowed into the falling film, except for a thin layer forming a meniscus. When ascending in a low-viscosity liquid (Fig. 2e), the slug occupied almost all the cross sectional area of the tube, surrounded by a thin falling film of liquid. At burst, the meniscus ruptured, and its remnants were dragged upward by the released gas. For a high-viscosity liquid, the slug ascended with a lower velocity, surrounded by a thicker falling film, thus the area of the tube occupied by the slug decreased, while its length increased. The rate of gas expansion was slower, leading to a slower

acceleration of the liquid surface. At burst, the meniscus rupture was slow, without the ejection of any droplets (Capponi et al., 2016).

10. 3.2 **- Configuration 1 – Thick Plug**

In a layered system in which the plug volume was greater than the slug volume, a steady slug flow was established in both the low- and high-viscosity liquids (Fig. 2b), with a transitional period as the slug moved between the fluids. As the slug ascended in the low-viscosity oil, gas expansion drove an intrusion of low-viscosity liquid into the plug. The intrusion displaced and spread the high viscosity liquid along the tube wall, forming a viscous annulus around it, which thickness was thinnest at the plug base; thus the annulus acted effectively as a diameter reduction (Fig. 3a). As the slug nose reached the plug base and entered the annulus, first it used the intrusion as pathway through the plug and then, at some point, it moved from within the low-viscosity intrusion to within the plug liquid. As soon as the slug base was in the plug, the entire slug volume was fully accommodated by the plug (Fig. 3a). As result of the higher viscosity, the falling liquid film around the slug thickened and the slug ascent velocity was drastically reduced. At burst the rupture of the viscous meniscus was slow with very few droplets ejected along the tube (Capponi et al., 2016).

10. 3.3 **- Configuration 2 – Medium Plug**

If the plug volume cannot accommodate both the intrusion and the slug volumes, then the slug will burst with its nose within the plug, whilst its base is still in the low-viscosity liquid. Gas expansion drove a greater amount of liquid into the plug compared to Configuration 1, and again the slug used it to ascend through the plug, with only the nose moving from the intrusion to the plug liquid before burst (Fig. 3b). The area of the tube occupied by the slug further decreased because, once ascending through the plug, the slug was surrounded by both a low- and high-viscosity liquid film (Fig. 3b). At burst, the rupture of the meniscus was fast with droplets ejected along the tube (Fig. 3b; Capponi et al., 2016).

10. 3.4 **- Configuration 3 – Thick Plug**

Gas expansion is sufficiently large to drive the intrusion right through the plug, emplacing a layer of low-viscosity liquid above the plug. The base of annulus represents then a dynamic restriction of the conduit diameter, while its top creates a widening (Fig. 3c). As the slug nose passed through the widening, it accelerated causing a rapid drainage of the liquid head above the slug that accumulated at the top of the plug. Instabilities started to propagate around the falling film along all the slug length, mixing with the annulus. At the top of the plug, if liquid accumulation was excessive, a liquid neck formed around the slug, generating partial blockages of the slug path. When the neck closed completely, it led to slug break-up. This resulted in a pulsatory release of the gas (Fig. 3c; Capponi et al., 2016).

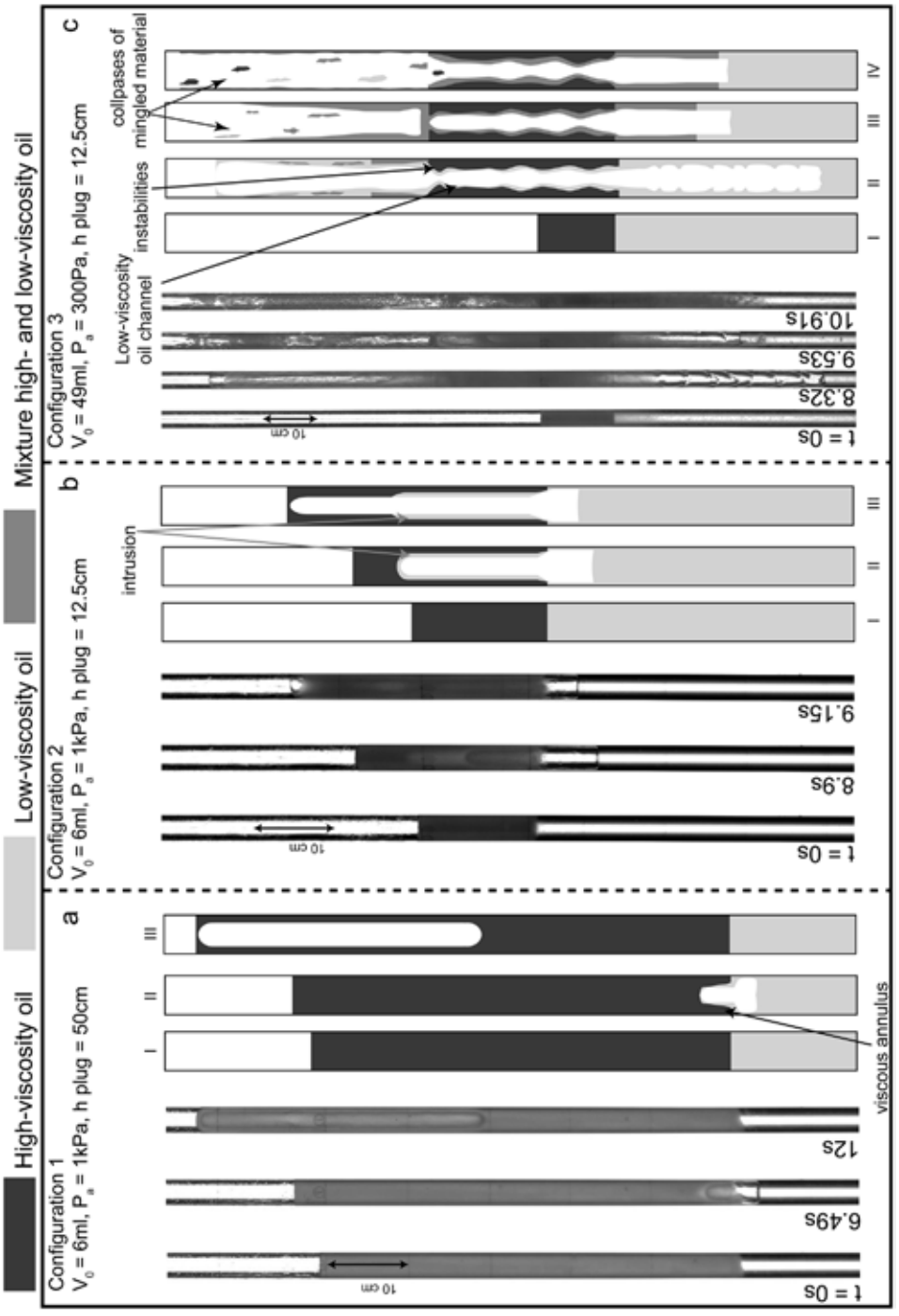

Figure 3. Still frames and interpretative sketches from selected experiments representative of (**a**) Configuration 1, (**b**) Configuration 2, and (**c**) Configuration 3 are shown (reproduced from Capponi et al., 2016).

10. 4 **- 1D model**

To define the observed configurations at volcano-scale, a new 1D model has been developed. The conduit geometry is simplified as a cylindrical tube filled with two liquids with different properties, and an ascending cylindrical slug (Fig. 4; e.g. Vergniolle, 1998; James et al., 2008; James et al., 2009; Del Bello et al., 2012; Capponi et al., 2016). A second assumption is that inertial forces are neglected. These are important when large rates of gas expansion are involved but expansion rates will be reduced by the presence of the plug and the model stops as soon as the slug nose arrives at the plug base. So expansion will be slightly overestimated but for a model aimed only to the definition of the configurations this is a suitable simplification (Capponi et al., 2016).

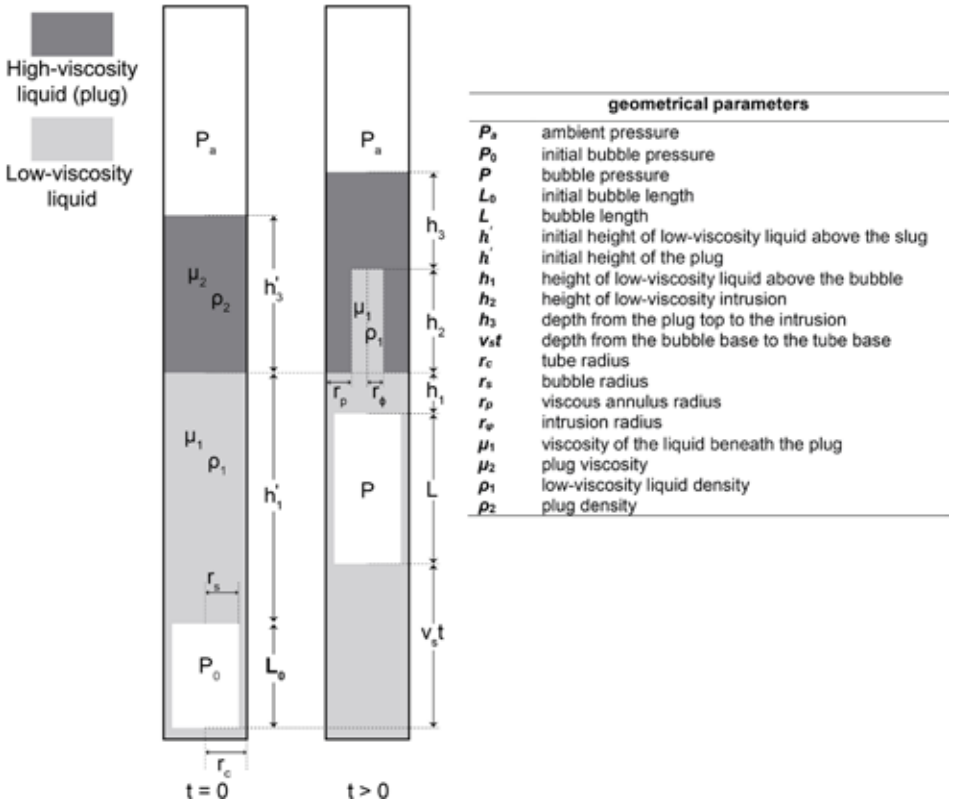

Figure 4. The 1D model geometry (reproduced from Capponi et al., 2016).

The slug is represented as a cylinder of length L and constant radius r_s, ascending in a vertical tube of radius r_c (*Fig. 4*). Above the slug, we consider a column of low-viscosity liquid (viscosity μ_1, density ρ_1, height h_1) overlain by an uppermost section of more viscous liquid, representing the viscous plug (viscosity μ_2, density ρ_2, radius r_c and height h_3). Between the low-viscosity liquid and the plug we consider the intrusion of low-viscosity liquid into the high-viscosity plug to form the annulus (viscosity μ_1, density ρ_1, length h_2 and radius $r_\phi = r_c - r_p$, where r_p is the thickness of the high-viscosity layer against the tube wall which forms the high-viscosity annulus). Due to the evolving

nature of the annulus, r_p will vary in space and time. Consequently, in order to provide a characteristic first-order estimate in our straightforward model we assume a thickness as for a falling film surrounding a slug, which can be given as a function of the inverse viscosity, N_f (equation 1; Llewellin et al., 2012; Capponi et al., 2016).

As initial conditions we impose the height of the low-viscosity liquid above the slug nose, h_1', the height of the plug, h_3', the initial (magmastatic) bubble pressure, $P_0 = \rho g(h_1' + h_3') + P_a$, the slug length, L_0, and radius, $r_s = r_c - \lambda$, calculating λ, the thickness of the low-viscosity falling liquid film, by using equation (2) for the low-viscosity liquid (Capponi et al., 2016).
For constant velocity of the slug base, v_s, at any time, t, h_1 is given by:

$$h_1 = (L_0 - L) - v_s t + h_1' \tag{3}$$

The intrusion volume can be equated to the gas expansion, thus we express h_2 as:

$$h_2 = -A(L_0 - L) \tag{4}$$

where $A = \frac{r_s^2}{r_\phi^2}$. Conservation of volume for the plug liquid yields:

$$\pi r_c^2(h_3 + h_2) - \pi r_\phi^2 h_2 = \pi r_c^2 h_3' \tag{5}$$

Simplifying and substituting for h_2, h_3 can be expressed as:

$$h_3 = h_3' + (L_0 - L)(A - B) \tag{6}$$

where $B = \frac{r_s^2}{r_c^2}$.

The gravitational force and the force on the liquid column above the slug due to the pressure difference between the slug and the surface is given by $F_g = -\pi r_s^2 \rho h g$ and $F_p = \pi r_s^2 (P - P_a)$ respectively, where ρ and h are respectively the density and the height of the involved liquid, and g is the acceleration due to gravity. If the slug behaves like a perfect gas and adiabatic expansion, then $PV^\gamma = constant$ (where γ is the ratio of specific heat), and F_p, with constant radius and pressure P_0 at t = 0, can be expressed as:

$$F_p = \pi r_s^2 \left(P_0 L_0^\gamma L^{-\gamma} - P_a\right) \tag{7}$$

Finally, assuming no-slip conditions at the wall, and that the liquid flow is equal to the volume flux controlled by the gas expansion, Poiseuille law gives the viscous force for a laminar flow in a cylindrical pipe:

$$F_v = -8\pi\mu h \dot{L} B \tag{8}$$

Equating the pressure force with the sum of the gravitational and viscous forces for the low-viscosity liquid column above the slug, the low-viscosity liquid intrusion, and the plug, and simplifying and substituting for both h_2 and h_3, we obtain:

$$\dot{L} = \{-g[\rho_1(h_1 - A(L_0 - L))] - g[\rho_2(h_3' + (L_0 - L)(A - B))] + (P_0 L_0^{\gamma} L^{-\gamma} - P_a)\} / \{8r_c^{-2}[\mu_1 h_1 + \mu_2 [h_3' + (L_0 - L)(A - B)]] + 8r_\phi^2 \frac{r_c^{-2}}{r_s^2} \mu_1 [-A(L_0 - L)]\} \quad (9)$$

Equation (9) is solved in Matlab using a Runge-Kutta formula and the model stops when either the intrusion breaches the plug surface, h_3 = 0 (i.e., Configuration 3) or when the slug reaches the plug base, h_1 = 0. In this latter case it will define the flow configuration occurring in the conduit calculating and comparing the volumes of plug, slug and liquid intrusion, determining if there is sufficient plug material to fully accommodate the slug volume (i.e., Configuration 1), or not (i.e., Configuration 2; Capponi et al., 2016).

When applied to the idealised volcanic scenario, the model illustrates the relevance of the identified configurations to Strombolian-type volcanoes. Which configuration operates is a function of gas mass, plug thickness, viscosity and conduit radius. The configuration diagrams (Fig. 5) do not change within the range of viscosity 50-500 Pa s for the magma beneath the plug, suggesting that the underlying magma acts simply as a mean to deliver the slug into the plug. In contrast, plug viscosity and conduit radius matter: increasing either plug viscosity or conduit radius, the size of the Configuration 3 domain (dashed lines for plug viscosity of 10 kPa s) decreases. Also, the same gas volume can lead to the different configurations, implying that vents of different radius or characterized by plugs with different properties (or both) could erupt with different styles (Capponi et al., 2016).

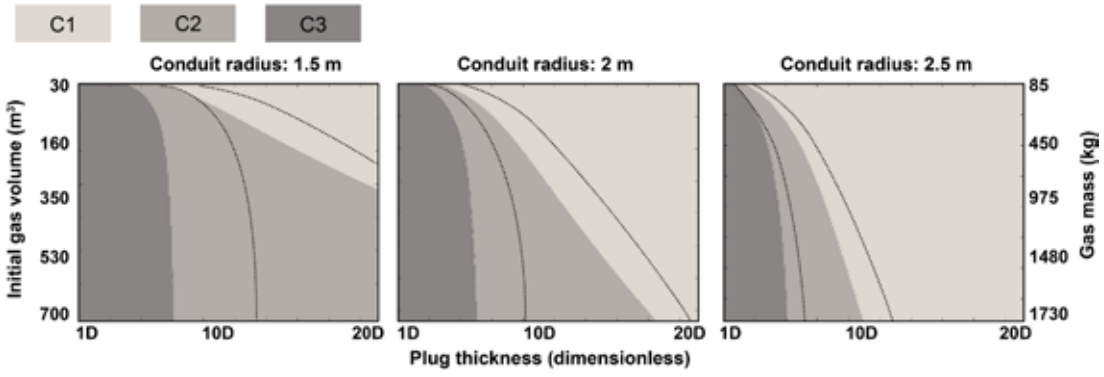

Figure 5 Flow configurations forecast by the 1D model for an idealized volcanic scenario are shown, for a plug viscosity of 10 kPa s (dashed lines) and 50 kPa s, and as function of initial gas volume/mass (m^3; kg), plug thickness (dimensionless), magma viscosity (50-500 Pa s) and volcanic conduit radii of 1.5 (left), 2 (middle) and 2.5 (right) m; the configuration distribution is insensitive to the viscosity of magma beneath the plug within the limit 50-500 Pa s (modified from Capponi et al., 2016).

10. 5 - **3D computational fluid dynamics simulations**

To support the applicability of the 1D model to a volcanic-scale scenario, 3D computational fluid-dynamics (CFD) simulations have been carried out using the commercial software package Flow3D (James et al., 2008; Chouet et al., 2010; Del Bello et al., 2015; Capponi et al., 2016).

Simulations were carried out both at laboratory-scale, to validate the CFD model with experimental data, and at volcano-scale, to explore the applicability of the fluid-dynamics observed in the laboratory to a volcanic scenario. In both cases, above the liquid surface there was no gas, and the gas slug was modelled as a continuous void region (i.e., contains no mass) governed by the equation PV^{γ} = constant. We modelled the experimental tube and the volcanic conduit as vertical, rigid (no elastic deformation) cylinders, closed at their base. The low-viscosity liquid and the high-viscosity layer (either magmas or silicon/castor oil) were modelled as incompressible Newtonian liquids with a temperature-dependent viscosity. The liquid column was divided in two distinct temperature regions. A high-temperature region covered either the silicone oil or the low viscosity magma, from the base of the cylinder up to the base of the high-viscosity layer; the second region, defined the high-viscosity layer, covering all its height. To reduce the effect of heat transfer across the magma column that could lead to a gradual variation in the viscosity, we imposed a thermal conductivity of 10^{-8} W m^{-1} K^{-1} (Capponi et al., 2016).

Selected laboratory experiments were modelled, covering the range of experimental pressures and gas volumes. The same experimental conditions (apparatus geometry, injected slug volumes, experimental ambient pressures and thickness of the plug) were recreated. Simulations at volcano-scale represented a 300-m-high volcanic conduit, of diameter 3 m, filled with a 200-m-high column of magma. Viscosity values ranged between 20 and 1000 Pa s for the magma beneath the high-viscosity layer and between 1 and 20 kPa s for the viscous layer. The selected ranges give N_f = ~732-~14 for the low-viscosity magma, and N_f = ~2.1-~1.05 for the viscous layer (Capponi et al., 2016). The simulations were initiated considering a slug, represented as a cylinder of length L_0 and radius r_s, at the bottom of the conduit (or pipe). When modelling experimental volumes, L_0 and r_s were derived from the mass of gas injected in the apparatus. For volcanic slugs the initial volume of the slug was scaled for the volcanic case through the dimensionless parameter V_a' (Del Bello et al., 2012, 2015; Capponi et al., 2016).

The results of 3D CFD simulations at laboratory-scale compare well with the experimental observations in terms of burst dynamics, generation of flow instabilities and slug disruption (Fig. 6 upper panel). At volcanic scale, simulations reproduced the observed phenomena in terms of burst dynamics, slug disruption and flow instabilities (Fig. 6 lower panel). Furthermore, simulations showed that the same gas slug expanding and bursting in each flow configuration at volcanic scale led to differences in burst dynamics. Configuration 1 was characterized by a slow fragmentation of the viscous meniscus above the slug, and almost no pyroclasts ejection. A faster fragmentation of the magma meniscus atop the slug, ejecting particles up to tens of meters above the burst point, was observed in Configuration 2. In contrast, Configuration 3 showed a range of styles depending on slug volumes and plug properties, with the burst process characterized by dynamics common to both Configuration 1 and 2: ejection of material above the burst point but at heights inferior to

Configuration 2 that collapsed back in the conduit, creating partial blockages and causing the disruption of the slug into smaller pockets of gas (Capponi et al., 2016).

Simulations also corroborate the role of the viscosity of magma beneath the plug, apparently not important for the determination of the pre-burst configurations; however, it seems to have an important role in controlling the burst and post burst processes. Indeed a lower viscosity magma, compared to a higher viscosity one, drained faster after burst on the conduit walls and the annulus, creating dynamic partial or complete blockages of the slug path. These blockages led to a pulsatory release of the gas, and, when the slug was disrupted, to formation of offspring bubbles that burst sequentially. So, the viscosity of the magma beneath the plug seems unimportant during slug ascent, but can promote the pulsatory behaviour at burst (Capponi et al., 2016).

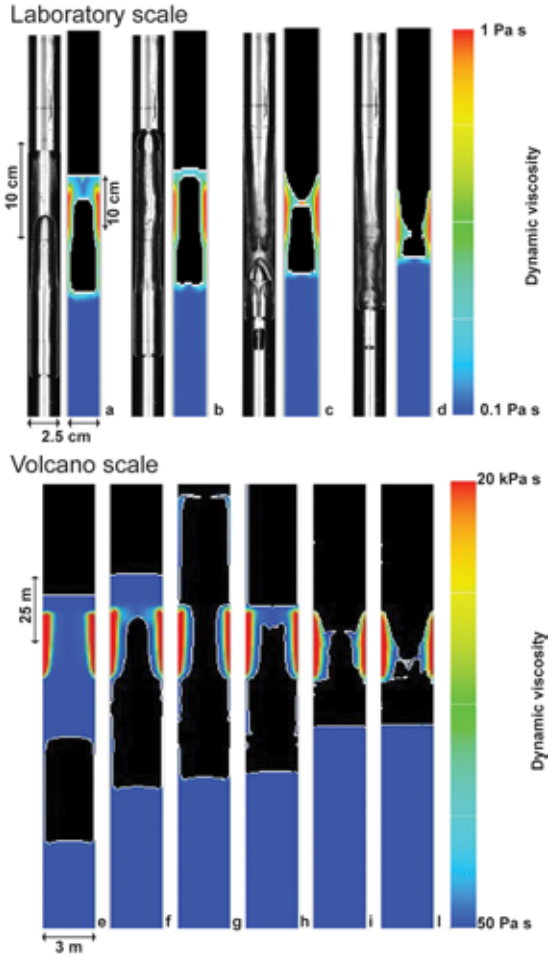

Figure 6. Still frames comparing a laboratory experiment and 3D CFD simulation for a 10 ml slug (**Upper panel**; P_a=3 kPa, plug h = 12.5cm). Note how the CFD simulation reproduced experimental observation well. (**Lower panel**) Still frames from a 3D CFD simulation at volcanic-scale (V_0=140 m^3, P_a=10^5Pa, μ magma=50 Pa s, μ plug=20 kPa s, r_c=1.5 m, column h = 200m, conduit radius r_c=1.5 m, conduit h =300m, plug h =15 m; reproduced from Capponi et al., 2016).

10. 6 **- Implications for Strombolian eruptions**

This study challenges one of the main simplifications in current modelling of Strombolian eruptions, the assumption of a rheologically uniform magma column. The experimental and numerical approaches presented here allowed identification of (1) a plausible spectrum of slug flow configurations possible within a rheologically stratified column, (2) configuration relevance to Strombolian-type volcanoes, with an emphasis on Stromboli volcano, and (3) constraints on the parameters controlling configuration transition.

For a particular conduit radius, which configuration operates is a function of gas mass, plug thickness and viscosity. Configuration seems insensitive to the viscosity of the underlying magma that can be considered mainly as a means of delivering the slug into the plug. In contrast, decreasing plug viscosity increases the size of the C3 domain (Fig. 5, dashed lines). Also, conduit radius has a strong influence on configuration transitions, with the Configuration 1 domain increased with increasing radius (Fig. 5; Capponi et al., 2016).

Both experimentally and numerically, it seems that the presence of a plug always leads to a more vigorous burst compared to an unplugged scenario. Previous models of single-viscosity systems demonstrated how slug overpressure varies with the thickness of the falling film, λ, controlled in turn by magma viscosity (James et al., 2009; Del Bello et al., 2012). Film thickness plays an important role in a plugged conduit as well, where it strongly depends on which flow configuration operates in the conduit. Furthermore, the presence of the plug itself modifies gas overpressure during slug ascent in the lower viscosity liquid, by hindering gas expansion. Therefore, the final overpressure at burst will depend on how much the plug hinders slug expansion during ascent and how thick is the film surrounding the slug at burst. The same initial gas volume in a low-viscosity liquid (thin film) will burst with a lower overpressure compared to in Configuration 1, where 1) the slug is surrounded by a thicker film, and 2) the slug overpressure increased while ascending in a low-viscosity liquid due to pressurisation of the conduit below the plug: the greater the plug thickness and viscosity, the more pressure can be retained, leading to a more vigorous when released at burst (Capponi et al., 2016).

Within Configuration 2, gas expansion drove a greater volume of low-viscosity liquid into the plug, generating a low-viscosity channel enclosed within the viscous annulus used by the slug to ascend within the plug. Therefore, the slug is surrounded by a complex and thicker “double” falling film, resulting in increased slug lengthening to accommodate gas expansion, opposed by the presence of the un-intruded plug above, and enhancing the generation of overpressure (Capponi et al., 2016). In Configuration 3, gas expansion is sufficiently large to intrude the low-viscosity liquid through and above the plug, removing its capping effect and allowing the slug to expand freely, consequentially reducing slug overpressure compared to Configuration 1 and 2. Furthermore, the partial constriction of the tube and the gas slug break-up into smaller pockets produced multiple bursts and modulation of the gas release within Configuration 3 (Capponi et al., 2016). For Configuration 1 and 3, the differences in the associated acoustic amplitudes identified by Del Bello et al. (2015) corroborate the role of different flow configurations on slug overpressure. Indeed, for the same initial gas volumes, all their plugged experiments, that now we can categorize as Configuration 1 or 3, showed a greater acoustic amplitude and an increase in slug overpressure with respect to the

unplugged (single-viscosity) experiments, with slugs bursting in Configuration 1 characterized by a greater increase in acoustic amplitude compared to slug bursts in Configuration 3 (Del Bello et al., 2015; Capponi et al., 2016).

Models of Strombolian eruptions based on single-viscosity systems give correlations between initial slug volume, burst pressure and magma viscosity, and have been used to parameterise theoretical transitions between passive, transitional or explosive regimes at Stromboli (James et al., 2009; Del Bello et al., 2012; Lane et al., 2013). At Stromboli, trends in infrasonic and seismic signals have been associated with the varying eruptive activity and different vents (e.g., Ripepe and Marchetti, 2002; McGreger and Lees, 2004; Chouet et al., 2008), with acoustic measurements used to infer erupted gas volumes at atmospheric pressure of 2–2 × 104 m^3 (0.5–3000 kg) for normal Strombolian activity, and 50–190 m^3 (10–30 kg) for gas puffers (Harris and Ripepe, 2007). If a dual-viscosity system is in place, such relationships will need to be reassessed due to the different and potentially varying pre-burst flow configurations associated with the same range of gas masses (Fig. 5), and linking field results to fluid dynamic models will be further complicated (Capponi et al., 2016).

10. 6.1 **- Pulsatory behaviour**

At Stromboli, Gaudin et al., (2014) related individual pyroclast ejection pulses to successive pressure release pulses and sub-pulses of duration between 0.05–2 s and an average pulse rate of 7 pulses per second, with a minimum of 3 up to 120 pulses per eruption. As a general trend, the greater the number of pulses and sub pulses, the longer the explosions, with greater gas masses involved (Gaudin et al., 2014). Although no formal scaling exists for this process at laboratory scale, it correlates with the trend observed first in our experiments, then in the CFD simulations at volcanic scale. Experimental observations show that the greater number of secondary bursts (pulses), followed by sub-pulses generated by the burst of secondary gas pockets created by transient partial blockages of the gas path due to instabilities in the falling film, was achieved only in Configuration 3 when large gas volumes (24–49 ml) were involved. Smaller volumes (8–17 ml) led to the generation of offspring bubbles, without any sub-pulse, and shorter burst times (Capponi et al., 2016). With these volumes scaled to the volcanic-case (Del Bello et al., 2015; Capponi et al., 2016), 3D CFD simulations showed a similar trend at volcanic scale, with secondary pulses and sub-pulses generated only in Configuration 3, implying that the presence of a plug is a pre-requisite for the pulsatory behaviour (Capponi et al., 2016). Secondary bursts from offspring bubbles and sub-pulses generated by partial blockages of the conduit were favoured by greater initial volume of gas and lower viscosity of the underlying magma, while a higher viscosity led mainly to sub-pulses (restriction of gas escape pathway), with the generation of fewer, or no, secondary bubbles (blockage of gas escape pathway). Hence, while not measurably affecting the pre-burst processes, the viscosity of the underlying magma can noticeably influence sin-and post-burst dynamics and therefore any measured geophysical signals (Capponi et al., 2016).

10. 7 **- Conclusions**

We define a framework to describe the possible spectrum of flow configurations that develops for the ascent, expansion and burst of slugs in a rheologically stratified conduit. Conduits that are fully filled with either high- or low-viscosity magma represent end-member scenarios. In between, three main fundamental flow configurations exist: 1) in Configuration 1, the plug volume is sufficiently large to fully accommodate the ascending slug. 2) In Configuration 2, the plug volume can accommodate the intrusion of low-viscosity liquid, but not the entire slug volume. The slug will burst with its nose in the plug and part of the body in the low-viscosity liquid. 3) In Configuration 3, the intrusion extrudes a low-viscosity layer above the plug, in which the slug burst. The annulus generates two regions of diameter changes, leading to instabilities in the falling liquid film as the slug passes through them and slug disruption with multiple bursts.

A new 1D model and 3D CFD simulations explore the configuration parameter space for Strombolian-type volcanoes, showing gas mass, conduit radius, plug thickness and viscosity as the main controls on which configuration style operates; transitions were much less sensitive to properties of the underlying magma. Each configuration led to distinct burst processes and encompassed a variety of processes: narrowing and widening of the conduit, generation of instabilities along the falling liquid film, transient blockages of the slug path and slug break-up. These complexities influenced the slug ascent dynamics and gas overpressure at burst, and thus also the resulting eruptive style and, potentially, geophysical signals.

In Configuration 3, flow instabilities cause a narrowing of the gas escape pathway causing sub-pulses within the eruption process. The flow instabilities can be sufficient to seal the gas escape pathway and cause slug break-up through the creation of transient blockages, resulting in a pulsatory, multi-bubble burst process. A widening of the conduit was needed for the slug break-up and falling film collapses, and both the viscosity of the underlying magma and the gas volume seemed to determine the frequency of pulses and sub pluses.

Our results showed how these flow configurations can influence eruption vigour and style, however more needs to be done in order to fully understand how this configuration framework may potentially affect, e.g., the slug-burst related geophysical signals. Therefore, future works should investigate how to better understand the link between flow processes and pressure variations in a stratified conduit, and how a viscous plug can influence geophysical signals within liquid and gaseous phases during Strombolian eruptions. Also, the increasing use of high-speed, thermal and SO_2 cameras is allowing new insights into explosion dynamics and measurements of gas emissions, providing robust datasets of key parameters controlling the eruptions (e.g., gas mass, pyroclasts ejection velocities, mass and size distribution), and strengthening the link between field observations and conduit dynamics. Indeed, in light of the new framework of flow configurations for rheologically stratified conduits presented here, detailed observations of the pre- and syn-eruptive processes would help in better understand how a plug leads to the observed dynamics. Thus, now more than ever, integration of experimental and numerical methods with field observation is needed to better link the eruptive dynamics to the source process, eventually producing a more detail picture of the physical conditions in the shallower volcanic conduit.

Acknowledgements

The research leading to these results has received funding from the European Union Seventh Framework Programme (FP7/2007-2013) under the project NEMOH, grant agreement n° 289976. I am grateful to Steve Lane and Mike James for all the insightful discussions and support during my PhD at Lancaster University. Thank you to B. Scheu for the review of this manuscript. Last but not least, I must thank the big NEMOH family. Thanks to Paolo Papale, Raffaela Pignolo and Alessandro Fornaciai for the creation and support of an amazing group of crazy people and for believing in us. And thanks to all the NEMOHs: I had the most amazing time with you guys: I doubt I could have had better years during my PhD. Looking forward to see you again, doing science while having great time!

References

Capponi, A., James, M.R. and Lane, S.J. (2016). Gas slug ascent in a stratified magma: Implications of flow organisation and instability for Strombolian eruption dynamics. Earth Planet Sci Lett, http://dx.doi.org/10.1016/j.epsl.2015.12.028.

Cashman, K.V. and Sparks, R.S.J. (2013). How volcanoes work: a 25 year perspective. Geol Soc Am Bull, 125:664–690.

Chouet, B.A., Dawson, P.B., James, M.R. and Lane S.J. (2010). Seismic source mechanism of degassing bursts at Kilauea Volcano, Hawaii: Results from waveform inversion in the 10–50 s band. J Geophys Res, doi:10.1029/2009JB006661.

Chouet, B., Dawson, P. and Martini, M. (2008). Shallow-conduit dynamics at Stromboli Volcano, Italy, imaged from waveform inversions. In: Lane SJ, Gilbert JS (Eds.), Fluid Motions in Volcanic Conduits: A Source of Seismic and Acoustic Signals: Geol Soc, London, Special Publications, 307, pp. 57–84.

Colò, L., Ripepe, M., Baker, D.R. and Polacci, M. (2010). Magma vesiculation and infrasonic activity at Stromboli open conduit volcano. Earth Planet Sci Lett, doi: 10.1016/j.epsl.2010.01.018.

Del Bello, E., Llewellin, E.W., Taddeucci, J., Scarlato, P. and Lane, S.J. (2012). An analytical model for gas overpressure in slug-driven explosions: Insights into Strombolian volcanic eruptions. J Geophys Res doi: 10.1029/2011JB008747.

Del Bello, E., Lane, S.J., James, M.R., Llewellin, E.W., Taddeucci, J., Scarlato, P. and Capponi, A. (2015). Viscous plugging can enhance and modulate explosivity of strombolian eruptions. Earth Planet Sci Lett, v. 423, http://dx.doi.org/10.1016/j.epsl.2015.04.034.

Gaudin, D., Taddeucci, J., Scarlato, P., Moroni, M., Freda, C., Gaeta, M. and Palladino, D.M. (2014). Pyroclast Tracking Velocimetry illuminates bomb ejection and explosion dynamics at Stromboli (Italy) and Yasur (Vanuatu) volcanoes. J Geophys Res, doi: 10.1002/2014JB011096.

Gurioli, L., Colò, L., Bollasina, A.J., Harris, A.J.L., Whittington, A. and Ripepe, M. (2014). Dynamics of strombolian explosions: inferences from field and laboratory studies of erupted bombs from Stromboli volcano. J Geophys Res, doi:10.1002/2013JB010355.

Harris, A. and Ripepe, M. (2007). Temperature and dynamics of degassing at Stromboli. J Geophys Res, 112, B03205, doi:10.1029/2006JB004393.

Houghton, B.F. and Gonnermann, H.M. (2008). Basaltic explosive volcanism: Constraints from deposits and models. Chemr Erde Geochem, http://dx.doi.org/10.1016/j.chemer.2008.04.002.

James, M.R., Lane, S.J. and Corder, S.B. (2008). Modelling the rapid near-surface expansion of gas slugs in low viscosity magmas. Geological Society, London, Special Publications, v. 307, doi: 10.1144/SP307.9.

James, M.R., Lane, S.J., Wilson, L. and Corder, S.B. (2009). Degassing at low magma-viscosity volcanoes: Quantifying the transition between passive bubble-burst and Strombolian eruption. J Volcanol Geotherm Res, doi: 10.1016/j.jvolgeores.2008.09.002.

Lane, S.J., James, M.R. and Corder, S.B. (2013). Volcano infrasonic signals and magma degassing: First-order experimental insights and application to Stromboli. Earth Planet Sci Lett, doi: 10.1016/j.epsl.2013.06.048.

Lautze, N.C. and Houghton, B.F. (2005). Physical mingling of magma and complex eruption dynamics in the shallow conduit at Stromboli volcano, Italy. Geology, doi: 10.1130/G21325.1.

Lautze, N.C. and Houghton, B.F. (2006). Linking variable explosion style and magma textures during 2002 at Stromboli volcano, Italy. Bull Volcanol, doi: 10.1007/s00445-006-0086-1.

Llewellin, E.W., Del Bello, E., Taddeucci, J., Scarlato, P. and Lane, S.J. (2012). The thickness of the falling film of liquid around a Taylor bubble. Proc R Soc, Math Phys Eng Sci, doi: 10.1098/rspa.2011.0476.

McGreger, A.D. and Lees, J.M. (2004). Vent discrimination at Stromboli volcano, Italy. J Volcanol Geotherm Res, doi: http://dx.doi.org/10.1016/j.jvolgeores.2004.05.007.

Ripepe, M. and Marchetti, E. (2002). Array tracking of infrasonic sources at Stromboli volcano. Geophys Res Lett, doi: 10.1029/2002GL015452.

Seyfried, R. and Freundt, A. (2000). Experiments on conduit flow and eruption behaviour of basaltic volcanic eruptions. J Geophys Res, doi: 10.1029/2000JB900096.

Taddeucci, J., Scarlato, P., Capponi, A., Del Bello, E., Cimarelli, C., Palladino, D.M. and Kueppers, U. (2012). High-speed imaging of Strombolian explosions: The ejection velocity of pyroclasts. Geophys Res Lett, doi: 10.1029/2011GL050404.

Vergniolle, S. and Brandeis, G. (1996). Strombolian explosions 1. A large bubble breaking at the surface of a lava column as a source of sound. J Geophys Res, 101(B9):433–447.

Vergniolle, S. (1998). Modelling two-phase flow in a volcano. In Proc. 13th Australasian Fluid Mech Conf Aristoc Offset, Monash University, Melbourne, 647-650.

Vergniolle, S. and Gaudemer, Y. (2015). From Reservoirs and Conduits to the Surface: Review of Role of Bubbles in Driving Basaltic Eruptions. Hawaiian Volcanoes: From Source to Surface, 208, p.289.

Viana, F., Pardo, R., Yanez, R., Trallero, J.L. and Joseph, D.D. (2003). Universal correlation for the rise velocity of long gas bubbles in round pipes. J Fluid Mech, doi:10.1017/S0022112003006165.

Wallis, G.B. (1969). One-dimensional two-phase flow (Vol. 1). New York: McGraw-Hill.

White, E.T. and Beardmore, R.H. (1962). The velocity of rise of single cylindrical air bubbles through liquids contained in vertical tubes. Chem Eng Sci, v. 17, p. 351–361.

Antonio Capponi, Italy

antonio.capponi@durham.ac.uk

Affiliation under NEMOH
Lancaster Environment Centre, Lancaster University, Lancaster, United Kingdom

Research theme under NEMOH
Dynamics of magma degassing in rheologically stratified magma columns

I started to work on basaltic volcanism during my MSc. Studies at the Earth Sciences department of Sapienza, University of Rome. These focussed on the dynamics of Strombolian eruptions, investigating their complexities through image processing and interpretation of visible and thermal high-speed videos of Strombolian activity. After graduation, I continued this work thanks to a research grant at Sapienza/INGV, and then as PhD project, also developing an experimental set-up for analogue laboratory experiments at INGV, aimed to investigate the pulsatory behaviour observed at Stromboli during my imaging studies.

At the end of the second year, I was awarded with the Marie Curie Fellowship in Lancaster, United Kingdom, within the project NEMOH, so I moved abroad and started in parallel a new PhD under the supervision of Steve Lane and Mike James. I successfully defended my PhD on June 6th, 2016. Here I investigated the range of slug flow configurations that develop in a rheologically stratified column and how the fluid dynamics involved in these flows modify the associated geophysical signals, using analogue laboratory experiments, numerical modelling and 3D computational fluid dynamic simulations. While working in Lancaster, I also maintained my collaboration with INGV, continuing to investigate conduit dynamics through processing and interpretation of high-speed and thermal videos. Furthermore, NEMOH allowed me to have a great amount of extra training. Indeed, each year I attended several training courses and field schools, international conferences, and participated to annual field campaigns at Stromboli in collaboration with other international research groups (INGV, LMU, LMV, and University of Hawaii). In 2015 I was also co-convener in one of the session at EGU. This involvement gave me the chance, already during my PhD, to gain experience on how to organize a scientific session, interact with other conveners, the authors and the conference organizers.

With my PhD project at Lancaster and the intense training offered by NEMOH, I developed a strong background in experimental volcanology, and an in-depth knowledge of conduit dynamics, in particular for basaltic volcanic systems, and in processing and interpretation of field and experimental data. As next step, on November 1st, 2016, I started a 3-years PDRA position in the Department of Earth Sciences at Durham University, funded by the UK NERC as part of the Large Grant project: 'Quantifying disequilibrium processes in basaltic volcanism (DisEqm)'. My role is to design and commission a large-scale apparatus for multiphase fluid dynamic experiments and conduct scaled analogue experiments to investigate the processes associated with the flow of multiphase magma in fissure geometries.

Chapter 11

The variety of Strombolian activity observed and interpreted by high-speed imaging

Damien Gaudin

Istituto Nazionale di Geofisica e Volcanologia, Sezione di Roma, Roma, Italy

Tutorship: Jacopo Taddeucci

Istituto Nazionale di Geofisica e Volcanologia, Sezione di Roma, Roma, Italy

Abstract

Strombolian eruptions are the most common, and often observed, explosive volcanic activity worldwide. However, descriptions include a comparatively large range of variations that, despite arising from the same basic process, are not yet integrated in a general, interpretative scheme. In that context, this study focuses on the ejection of gas and particles from Stromboli volcano (Italy), Etna (Italy), Yasur (Vanuatu) and Batu Tara (Indonesia). 22 vents were filmed by both visible-light and thermal infrared high-speed infrared videos. Videos are processed by original algorithms in order to quantify the size and the trajectories of bomb-size pyroclasts as well as the dimensions and the ejection velocity of the gas and ash clouds, enabling objective comparisons between all vent activities. This database demonstrates that a continuous spectrum of activity exists, from puffing to Strombolian explosions, and from gas rich through bomb-rich to ash rich explosions. These variations in Strombolian activity can be explained by the combination of two well-established controls: 1) the length of the bursting gas pocket with respect to the vent diameter, and 2) the presence and thickness of a high-viscosity layer in the uppermost part of the volcanic conduit. The interaction of these two factors determines, at first order, the main explosion parameters, including its duration, the evolution of the ejection velocity with time, its products and its pulsatile behaviour.

Keywords: Strombolian activity, high speed imaging, pyroclast trajectories, gas pockets, database analysis.

11. 1 **- Introduction**

Stromboli volcano, on the northernmost Aeolian island, is well known for its frequent explosions (in the order of 10 per hour) throwing incandescent pyroclasts at heights of several hundred metres, which earned it the nickname of “Lighthouse of the Mediterranean”. Such activity has been continuously observed for more than 200 years [*Washington*, 1917], but probably started 1500 years ago [*Rosi et al.*, 2000], being only interrupted by paroxysmal episodes occurring a few times per decades [*Barberi et al.*, 1993]. This so-called “Strombolian” activity is not only limited to Stromboli volcano but it has been reported during periods of variable duration in numerous volcanoes worldwide, the most famous being Parícutin (Mexico), Villarica (Chile), Erebus (Antarctica), Etna (Italie) and Yasur (Vanuatu).

Strombolian activity is defined as the "weak, discrete, short-lived explosions that are the surface manifestation of the impulsive release of pressurized pockets of gas" [*Taddeucci et al.*, 2015]. However, this simple definition gathers a wide variety of cases. First, the relative amount of each class of pyroclasts –ash (<2mm), lapilli (2-64 mm) and bombs (>64mm) – is highly variable, not only from a volcano to another but also within the different vents of a volcano. Second, the intensity of the explosions, represented by the total mass erupted and the launch velocity, ranges over several orders of magnitude from metre-sized bubble puffing with velocities smaller of a few metres per second [*Harris and Ripepe*, 2007] to normal and paroxysmal Strombolian explosions with supersonic velocities [*Ripepe and Harris*, 2008; *Taddeucci et al.*, 2012].

This large variety raises the question of the definition of Strombolian activity. In other words, what are the invariants in the Strombolian explosive mechanism, and what are the main factors underlying its variability?

In order to answer this question, the volcanology group of the Rome section of the Istituto Nazionale di Geofisica e Vulcanologia (INGV) has developed a portable multi-parametric instrument, named FAMoUS (Fast MUltiparametric Setup), including high speed thermal and visible-light cameras, to monitor volcanic explosions worldwide. Currently, the INGV database includes high speed videos from 8 volcanoes, from bubble bursts from the Halema'uma'u lava lake at Kilauea volcano (Hawaii), through Strombolian episodes at Etna (Italy) to Vulcanian explosions at Sakurajima (Japan). The interpretation and comparison of this large dataset require objective and quantitative methods, but opens new perspectives for the interpretation of Strombolian activity.

This paper aims to give a comprehensive summary of the studies I achieved during my NEMOH fellowship at INGV Roma on the quantification of Strombolian activity through dedicated image processing methods, and propose an integrated perspective of Strombolian activity from the high speed imaging point of view. Most of the results are presented, in a more expanded way, in articles published. The reader is referred to these papers for more details.

11. 2 **- The INGV database of Strombolian activity: acquisition and processing**

11. 2.1 **- Targeted volcanoes**

The INGV database includes high speed thermal and visible-light videos from 8 basaltic to andesitic volcanoes from 4 continents (Figure 1). It is mainly focused on Strombolian activity (Stromboli, Italy; Yasur, Vanuatu; Batu Tara, Indonesia; a parasitic cone at Etna, Italy). However, in order to better understand the phenomena, examples from other related types of activity have been observed: spattering in Halema'uma'u lava lake in Kilauea (Hawaii), where the gas pocket is not confined in a conduit; and Vulcanian activity (Fuego, Guatelama; Santiaguito, Guatemala; Sakurajima, Japan) where higher explosion intensities lead to frequent reshaping of the conduit.

In all cases, field campaigns lasted between 1 and 10 days, focusing on all visible active areas. Observations were achieved at a distance ranging from 200 m for some vents of Stromboli to 3500 m for Sakurajima, where the intensity of the explosion was the highest.

Herein, vents are denoted using source volcano, vent area, eruption year and specific vent (e.g., S-NE14c marks the activity of vent 'c' at the North-East vent area of Stromboli in 2014).

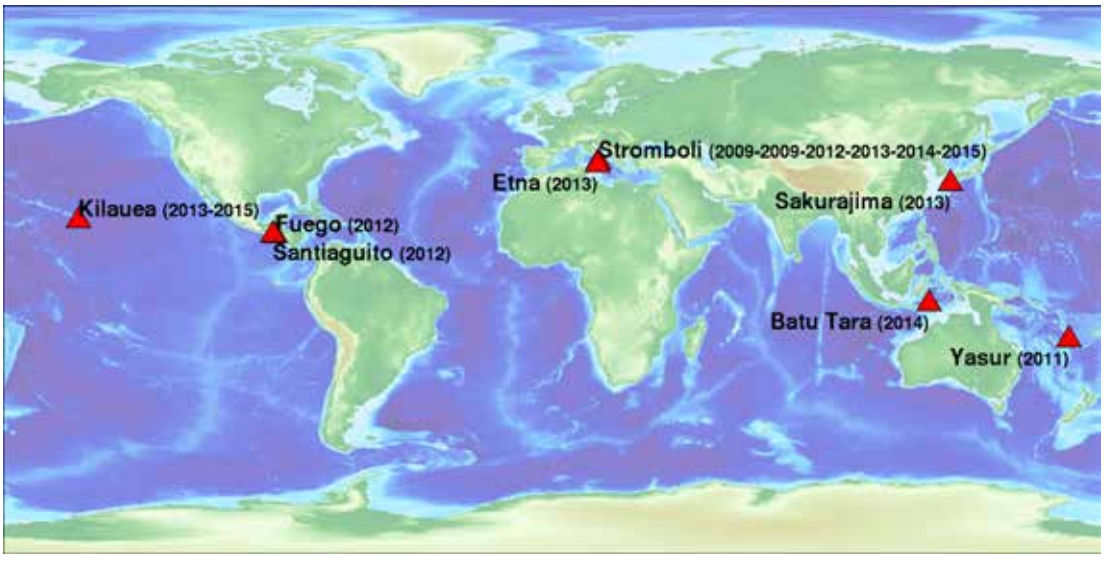

Figure 1. Location and date of the field campaigns of the INGV Roma1 database, achieved with the FAMoUS (Fast MUltiparametric Setup) developed at the institute. Note that all these volcanoes, with the exception of Kilauea, are located in a subduction context.

11. 2.2 **- Cameras**

The INGV database was made using various high-speed cameras, both in visible and in thermal infrared wavelengths. Visible-light high speed cameras include NAC HotShot 512 (512×512 pixels definition at 500 frames per second) for field campaigns in 2009, Optronis CR600x2 (1280×1024 pixels at 500 fps) for field campaigns since 2011 except Kilauea in 2015, and NAC Memrecam HX-6 (2560×1920 pixels at 1000 fps). We used tele lenses, usually 300 or 400 mm and up to 800 mm to reach centimetre resolutions at a distance of hundreds of metres. For instance, at Stromboli where the typical distance crater-camera is about 300 m, a 300 mm tele lens achieves a resolution of 2.0 cm per pixel. At these frame rates and resolutions, recordings are limited to a few seconds up to a minute. Thus, visible light cameras were mainly used to track the fastest and smallest pyroclasts during the explosions.

Since 2011, the setup also includes a FLIR SC655 high speed thermal camera, recording at up to 200 frames per second, and at 50 frames per second in full resolution (640×480 pixels). The 41 mm lens allows reaching 12 cm per pixel at a distance of 300 m. The lower definition and time-resolution of the thermal camera allows continuous recording over several minutes. In addition, thermal infrared wavelengths are more sensitive to gas. Consequently, the thermal camera was mainly used to observe the general activity of the vents.

The high speed thermal and visible-light cameras are powered and synchronized through a common infrastructure called FAMoUS (FAst, MUltiparametric Set-up for real-time observation of explosive eruptions).

11. 2.3 **- Processing methods**

11. 2.3.1 **- Activity diagrams**

In order to objectively describe and compare volcanic activities at the different volcanoes and vents, I developed an original algorithm to generate activity diagrams from thermal infrared images independently from observation conditions (distance, framerate, etc.). First, frames are cropped into a vertical rectangle with the vent centred near the base. Considering the typical size of the vents hosting Stromboli activity, we used a 25 × 10 metre window. Second, in order to minimize the effects of slow changes due to, e.g., clouds and rock falls, we remove the background, computed as the minimum value of each pixel in a moving window of 2 seconds preceding each frame. Finally the evolution of the maximum temperature in each row is plotted in a time/height diagram, hereafter referred as "rise history diagram". These diagrams allow tracking the vertical motion and velocity of ejecta, parabolic tracks and blurred streaks representing ballistics and ash/gas clouds, respectively. Similarly, by plotting the temperature on a horizontal line just above the vent, we also visualized the lateral extent of ejection over time ("lateral extent diagram").

In the case of pulsating activity, the lateral extent diagrams can be used to isolate the release of single gas pockets. To this purpose, I developed an original algorithm to count these events [see details in *Gaudin et al.*, 2017b]. The rise velocity of the ash/gas cloud and the ejecta correspond to the slope of the tracks and streaks in the rise velocity diagrams. The width and duration of the released gas pockets can be measured directly on the lateral extent diagram. Combining these two estimations, one can derive the total volume of the gas cloud at the exit of the vent [*Gaudin et al.*, 2017b].

11. 2.3.2 **- Tracking of the bombs**

In addition to the activity diagram, I used specific to track and quantify the ejection of bombs. Indeed, their relatively high masses prevent them from being significantly slowed down in the first metres of their travel in the atmosphere, and thus, their ejection velocity can be directly linked to the processes occurring in the vent.

Bombs can be tracked from high-speed visible-light imaging, using the MTrackJ plugin [*Abramoff*, 2004] of the ImageJ software. However, this technique is operationally limited by its slow speed and consequently is restricted to use on relatively few pyroclasts (order of thousands).

In order to maximize the number of bombs tracked, I developed a tracking algorithm based on Particle Tracking Velocimetry techniques [*Gaudin et al.*, 2014a]. This class of algorithms was initially designed to spot and track automatically solid markers set in transparent fluid to obtain a complete velocity field. In our case, the relatively low quality of the videos, and above all the large numbers of particles to track make the traditional techniques less efficient. In order to optimize the number of bombs tracked, we use a specific algorithm providing first estimate of pyroclast displacement between two successive frames based on the identification of image features and the solution of the optical flow equation [*Moroni and Cenedese*, 2005], jointly with preprocessing and post-processing techniques to improve image quality. The whole processing chain is referred as "Pyroclast Tracking

Velocimetry" (PyTV), is described in details in *Gaudin et al.*, [2014a]. We estimate that PyTV efficiently tracks 50 to 90% of the potential bombs candidates visible in the videos, i.e. 100 to 1000 times more than for the manual tracking.

As for the manual tracking, the databases built from PyTV only allows the reconstruction of bomb trajectories in a plan perpendicular to the line of sight, neglecting the motion of the particles towards or away from the camera, which may lead to underestimation of bomb velocities and does not allow the directionality of the ejections to be studied. To overcome this limitation, I used two or three synchronized high speed camera to obtain a stereoscopic view of the explosions. I adapted photogrammetry techniques in order to reconstruct the bomb trajectories in 3D [*Gaudin et al.*, 2015, 2016]. Since the same bombs must be recognized in different videos, it is not currently possible to use the PyTV to automatically track the bombs. Therefore, I limited the analysis to a few representative examples.

11. 3 **- Results: a bestiary of Strombolian activity**

11. 3.1 **- Overview of Strombolian activities**

In this section, I focus only on Strombolian activity observed at Stromboli, Etna, Batu Tara and Yasur. Field observations show a large range of Strombolian activity, which can be classified on the basis of (i) their intensity and recurrence time, and (ii) their products (Figure 2).

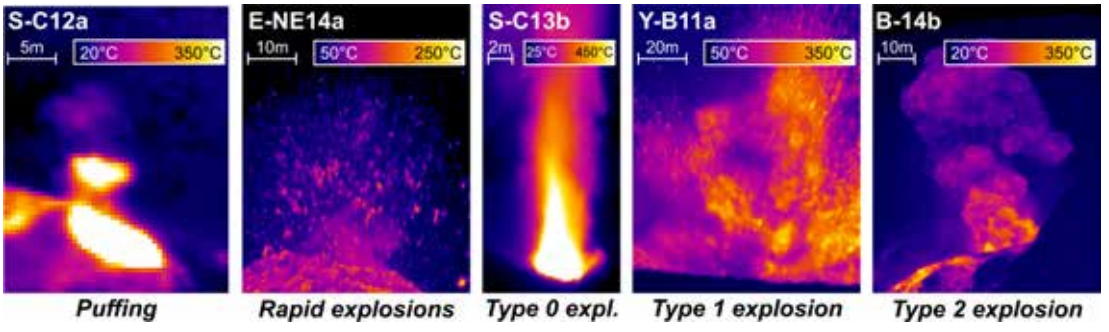

Figure 2. Still frames of videos of the INGV database, showing the different types of Strombolian activity. S-, E-, Y-, and B- refers to Stromboli, Etna Yasur, and Batu Tara volcanoes, respectively, numbers refer to year (from 2011 to 2015), capital letters marks vent areas and small letters marks individual vents.

The manifestation with the smallest intensity is called puffing, defined by Ripepe et al., [1996] and Landi et al., [2011] as the release of "*discrete overpressurized puffs of gas/vapour that occur at a few seconds interval, radiating excess pressure in the atmosphere and eventually ejecting small amount of incandescent lava fragments*" (Figure 2). We note that puffing is never associated with the ejection of ash.

At the other end of the spectrum, normal explosions "*typically involves <20-s-long explosions, which eject centimetre- to metre-sized pyroclasts to heights of 50–400 m*" [*Rosi et al.*, 2013; *Houghton et al.*, 2016]. Based on the relative amount of erupted pyroclasts, normal explosions can be classified into Type 0 (gas-rich and pyroclast-poor, sometimes denoted Type 3), Type 1 (bomb-

rich), Type 2a (ash- and bombs-rich) and Type 2b (ash-rich and bombs-poor) [*Patrick et al.*, 2007; *Goto et al.*, 2014; *Leduc et al.*, 2015]. While Type 0 is rare (about 5% of the observed activity), Types 1, 2a and 2b are equally frequent at Stromboli. We note that, unlike Type 0, 1 and 2a explosions where the beginning of the explosion is impulsive, Type 2b explosions tend to be emergent [*Spina et al.*, 2015].

Between these two end-members, a rarer type of activity has been observed, both at Etna and at Stromboli, consisting of frequent (each few seconds), short (<1 s) explosions associated with the ejection of thousands of bombs, but never with ash. Houghton et al., [2016] named this activity "rapid explosions", defined as "*very closely spaced and, generally, very weak explosions, with a periodicity at least two orders of magnitude higher than that of normal explosions at Stromboli*".

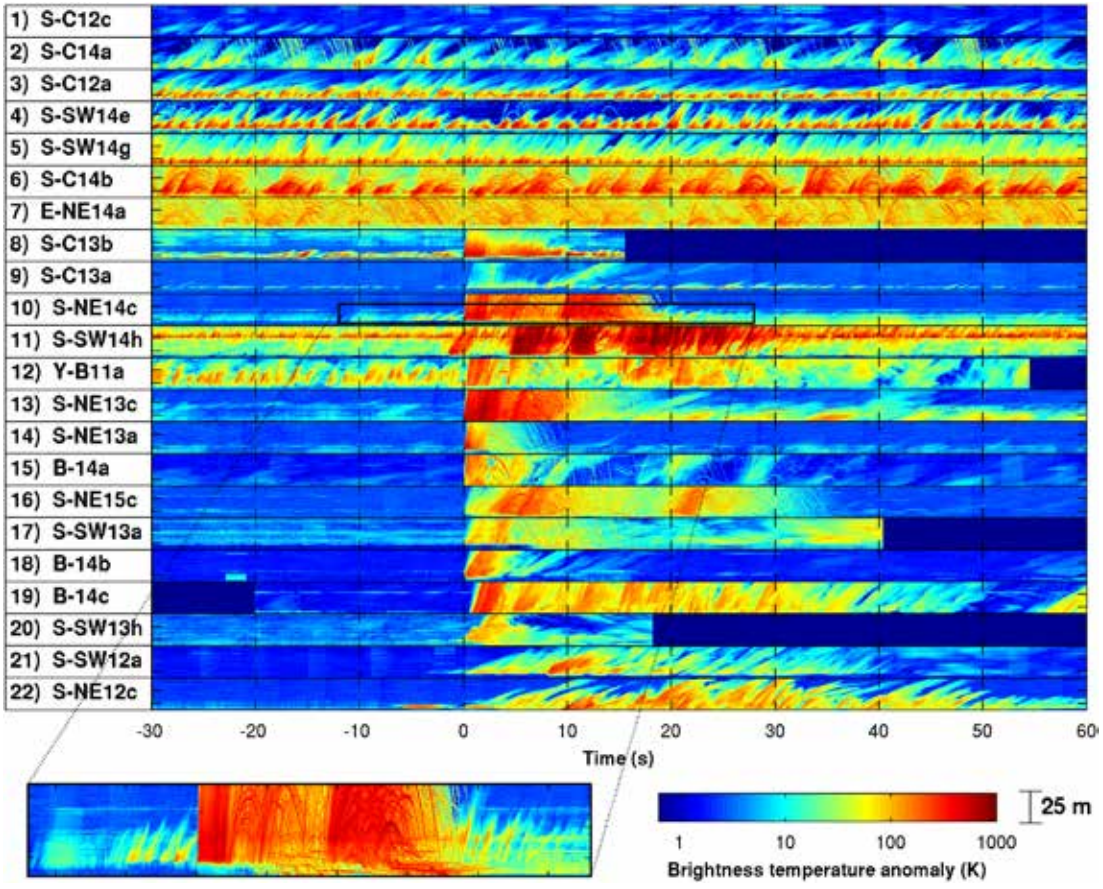

Figure 3. Rise history diagrams showing the activity of 22 representative vents of Stromboli, Yasur, Etna and Batu Tara. Parabolic tracks and blurred streaks represent bombs and ash/gas clouds, respectively. The zoom highlights the increase of puffing activity before and after the explosions.

Figure 3 shows 90 s snapshots of the 22 activities of Stromboli, Yasur, Etna and Batu Tara. The pulsating behaviour of puffing and rapid explosions is immediately recognizable, while normal explosions are transient. The ejection of bombs is also visible, in particular for rapid explosions and normal explosions of Type 1 and 2a.

11. 3.2 **- Ejection velocities**

The ejection velocities of bombs in four Type 1 and Type 2a explosions are represented in *Figure 4*. PyTV detects 100 to 1000 more bombs than manual tracking. Both techniques show the same internal features, but with a much higher time-resolution for the PyTV. Conversely, PyTV is not able to catch the smallest, blurred bombs that usually have higher velocities, in particular for cases Y-A11a and Y-A11b. However, we note that the velocities measured by the PyTV are well aligned with the manual ones (and even overlap them in the three first cases), pointing out the reliability of both methods. The two techniques are consequently complementary and must be used together.

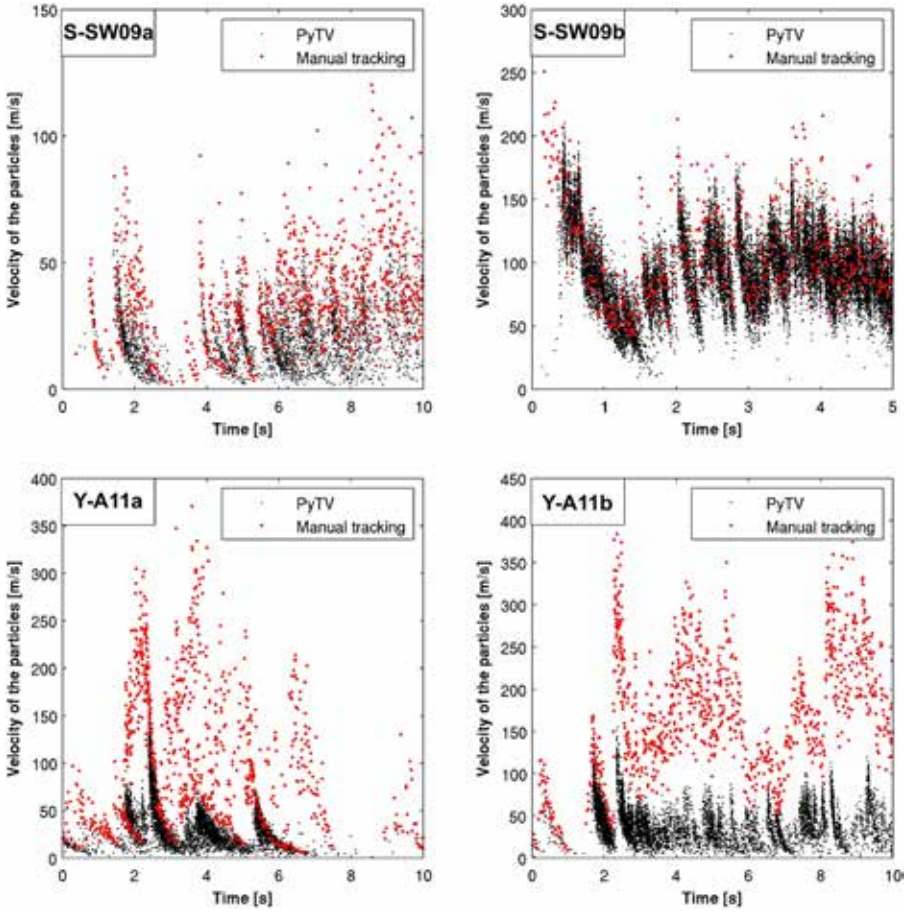

Figure 4. Ejection velocity of bombs in 4 normal explosions from Stromboli (top) and Yasur (bottom) [modified after Gaudin et al., 2014a].

The ejection velocity of the bombs during normal explosions can reach 405 m/s [*Taddeucci et al.*, 2012]. These supersonic velocities are confirmed by the occurrence of jet noise that can be either measured by microphone or even observed on some high speed videos [*Taddeucci et al.*, 2014]. In rapid explosions and puffing, due to the technical impossibility to record continuous high speed records, we use the maximum height reached by the bombs to deduce their initial velocity, v_e, using the ballistic equations and neglecting the drag force:

$$v_e = 2\sqrt{(gz)} \qquad (1)$$

where z is the height of the summit of the parabola with respect to the vent and g is the acceleration due to gravity. From Figure 3, we deduce that velocities observed in rapid explosions are about 30 m/s while velocities during puffing never exceed 20 m/s.

The stereoscopic observations (*Figure 5*) demonstrate that all the particles seem to originate from a narrow region (corresponding to the vent exit) and that the highest velocities are reached for the particles going vertically.

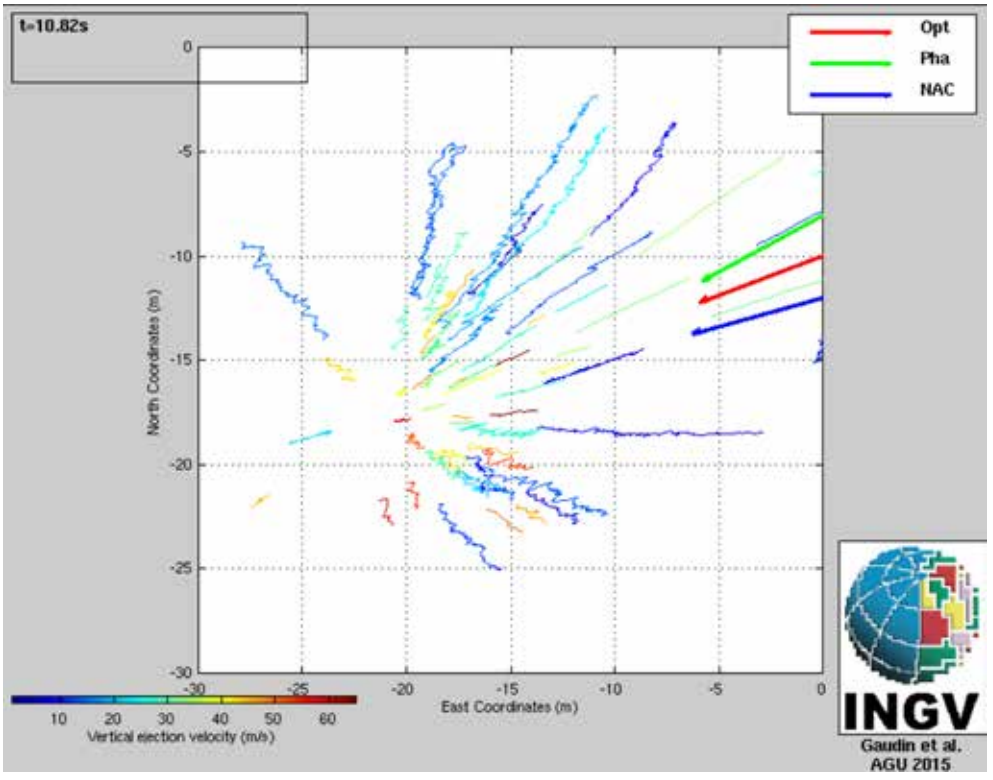

Figure 5. "Bird eye view" of the trajectories of bombs erupted during a normal explosion of vent S-NE14c of Stromboli, reconstructed by stereoscopic techniques [Gaudin et al., 2015]. Opt, Pha and NAC represents the direction from the Optronis, Phantom and NAC cameras to the vent, while t stands for the total duration of the explosion.

The very high temporal resolution enabled by the use of PyTV allows "ejection pulses" to be detected in all the studied explosions. Pulses have been defined as *"a cluster of fast bombs arriving in a short time interval and displaying a non-linear decay of the vent ejection velocity over time"* [Gaudin et al., 2014b]. The average duration of the pulses is about 1s, but some of them can last down to 0.1 seconds. During a pulse, the evolution of v_e can be modeled as (Figure 6):

$$1/v_e = (t-t_0) / h \qquad (2)$$

where t_0 is a time representing the start of the pulse and h a characteristic length. The shock tube theory [Alatorre-Ibargüengoitia et al., 2010; Taddeucci et al., 2012; Gaudin et al., 2014b] suggest that this length corresponds to the distance between the height of the line where the velocities are measured and the depth of the bubble burst. Superimposed on these pulses, variations of ejection velocity might occur in the timescale of a few seconds within a normal explosion (see case S-SW09b in Figure 4). However, being themselves constituted of multiple pulses, I will not consider them as proper pulses but as trends.

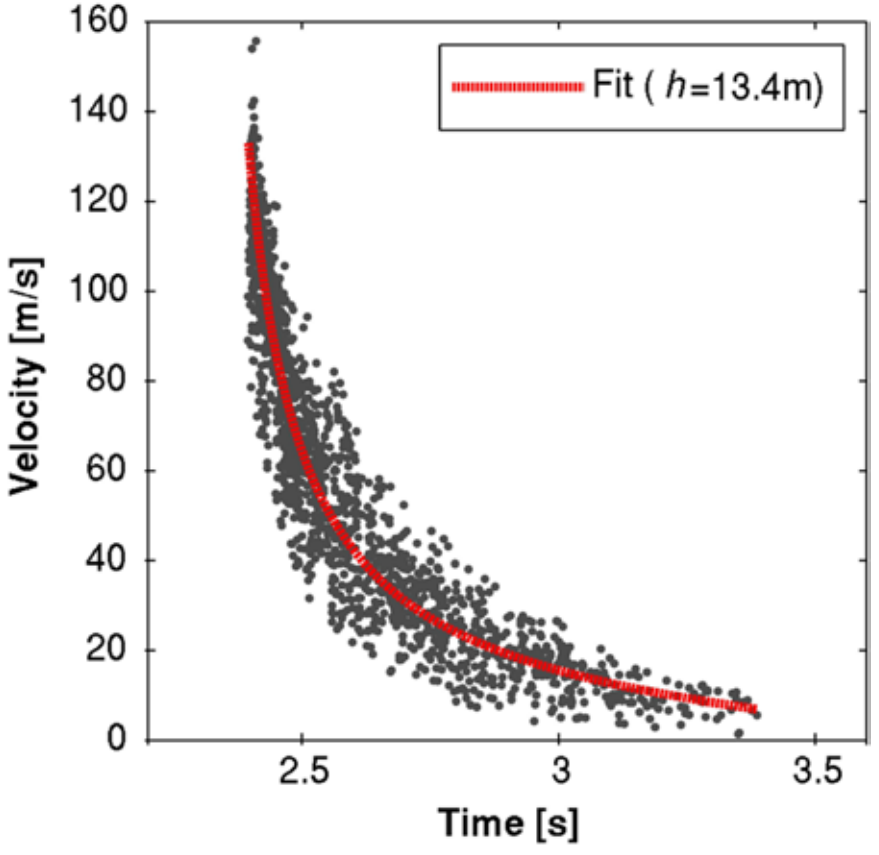

Figure 6. Example of an ejection pulse on vent S-NE09a. In this case, velocities are measured 4m above the vent, thus h suggest a burst depth of 9.4 meters below the surface [modified after Gaudin et al., 2014a].

Up to 100 pulses have been observed in normal explosions at Stromboli with a linear relation between pulse frequencies and ejection velocities (Figure 7). This relation is less obvious in the case of Yasur volcano, where the pulse frequencies for a given mean velocity are lower (Figure 7).

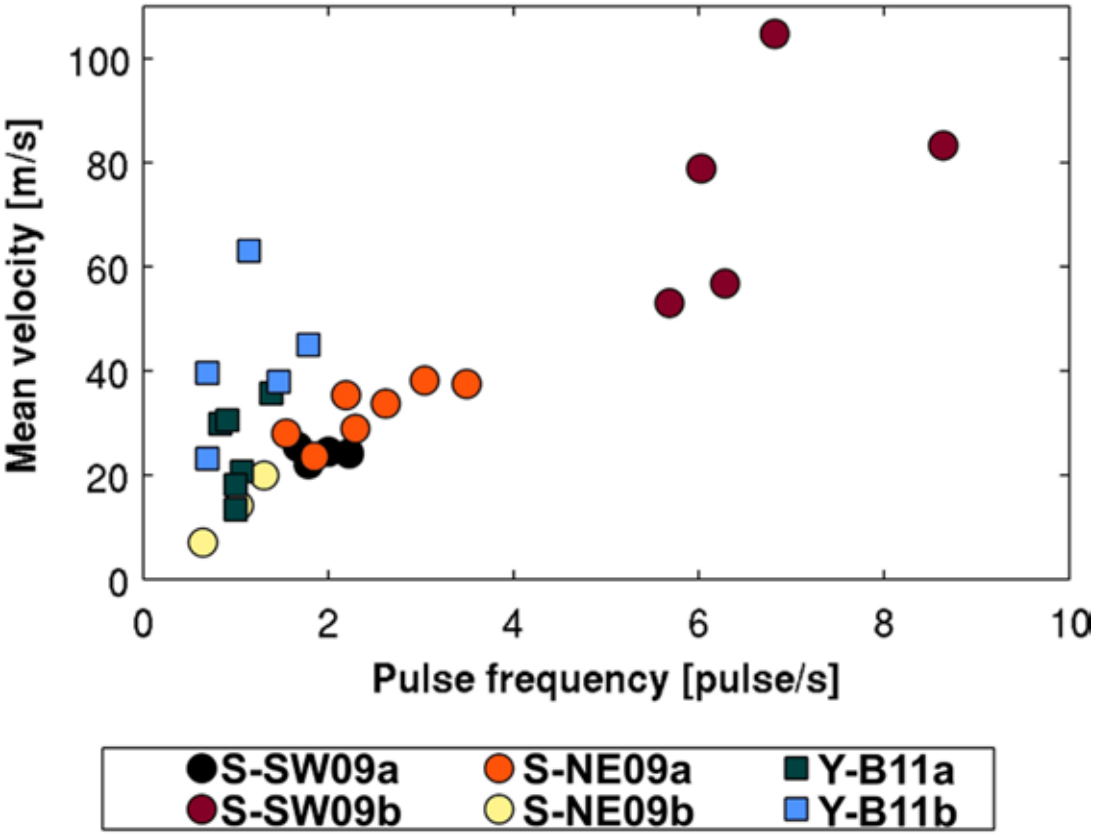

Figure 7. Relationship between mean pulse frequency and mean velocity in 30 normal explosions at Yasur and Stromboli [modified after Gaudin et al., 2014a].

In the case of rapid explosions, a few pulses may be observed (Figure 3), which is never the case for puffing activity.

11. 3.3 **- Sizes and volumes**

Figure 8 shows the evolution of the thermal anomaly on a horizontal line just above the vent. All the thermal anomalies of a vent generated by puffing and explosions are located in the same, narrow band, corresponding to the width of the vent. In some cases, (e.g. C12a, SW14e), the width of the puffs are smaller than the vent diameter, which is never the case for rapid and normal explosions.

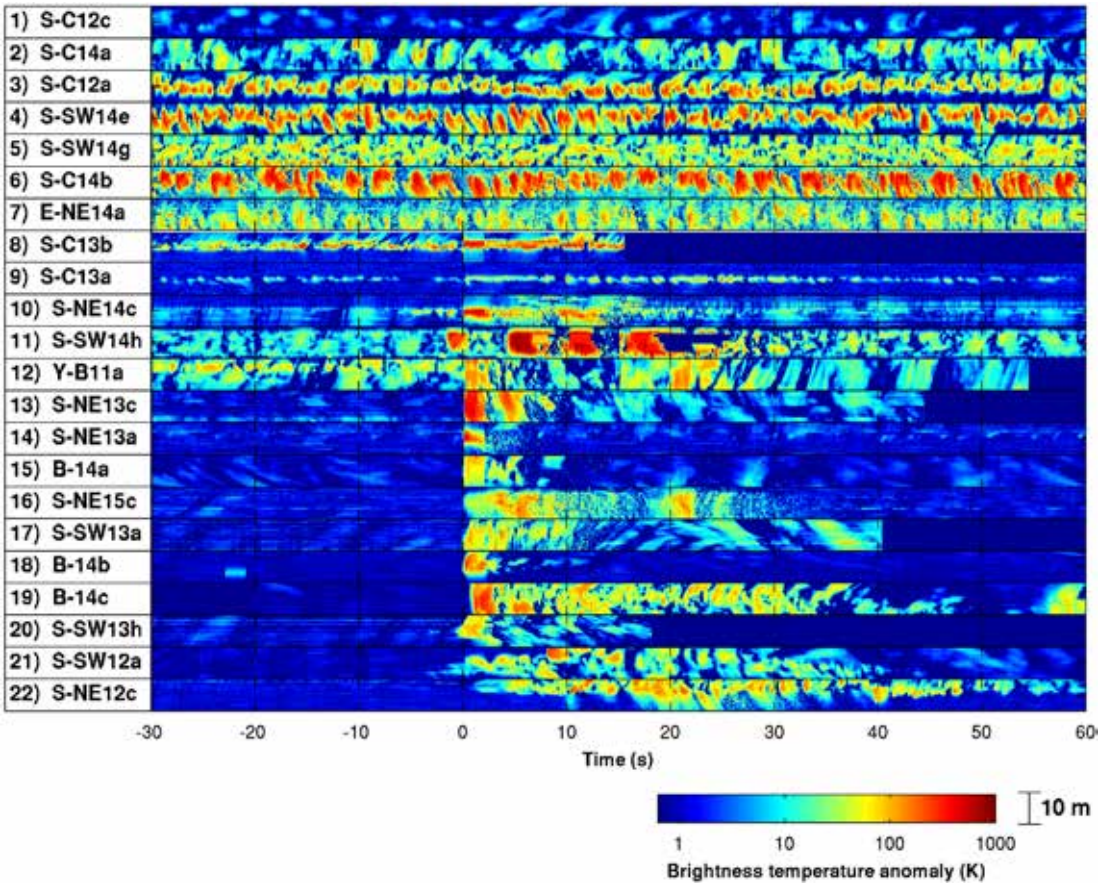

Figure 8. Evolution of the lateral extent the thermal anomaly on the same 22 representative active vents as Figure 3. [modified after Gaudin et al., 2017a].

The volume of the explosions V can be directly derived from these diagrams as [Gaudin et al., 2017b]:

$$V=\int_t S\, v(t)\, \mathrm{d}t$$

S being the section of the vent and $v(t)$ the exit velocity as a function of the time t. Table 1 shows that volumes of normal explosions are about 1000 times higher than those of puffing, while their frequency is typically 1000 times lower. For all estimates, rapid explosions appear as an intermediate term between the two endmembers.

	Puffing	Rapid explosions	Normal explosions
Repetition time	0.5-3 s	2-5 s	100-5000 s
Duration	0.1-1 s	0.5-2 s	10-90 s
Exit velocity	3-20 m/s	20-35 m/s	30-400 m/s
Width of the gas pocket	0.5m to slightly less than vent diameter	Slightly less than vent diameter	Slightly less than vent diameter
Number of pulses per event	1	1-5	Up to 100
Products			
Gas	0.02-30 m^3	70-500m^3	1 000-40 000 m^3
Bombs	None to <1 kg	1-100 kg	Up to 50 000 kg
Ash	None	None	Possible

Table 1. Characteristics of the three main types of Strombolian activity described in this study. Volumes of gas are estimated at ambient pressure.

11. 3.4 **- Activity interactions**

The three types of Strombolian activity can coexist at the same volcano. At Stromboli (Figure 9), puffing is preferentially located at the center of the crater terrace (Center vents and north-east of the SW crater), while normal explosions are preferentially in the SW and the NE craters. The only occurrence of rapid explosions (in May 2014) was located at the close vicinity of the puffing activity. [Gaudin et al., 2017a].

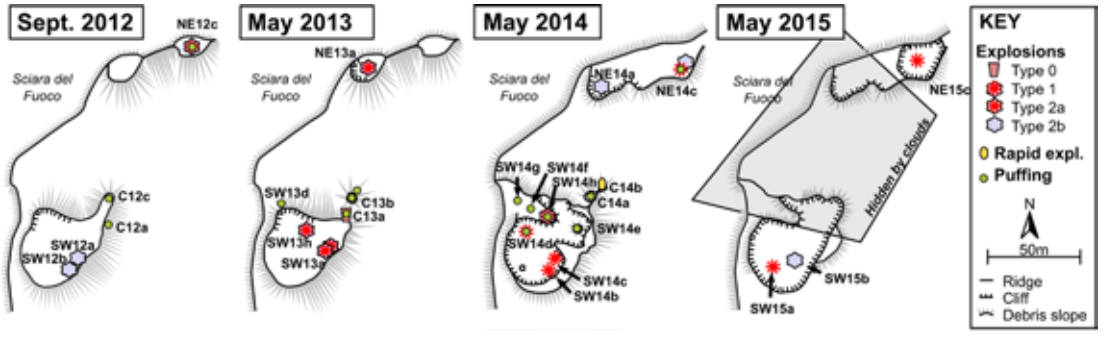

Figure 9. Location of vent activities at Stromboli terrace, during the four field campaigns from 2012 to 2015.

At Yasur and Stromboli, some vents were hosting both puffing and normal explosions (Figure 3). This is the case for vent S-C13a, hosting the only example of Type 0 explosion and for about one third of the vents hosting Type 1 and Type 2a explosions. In some of the cases, an increase of the puffing activity was observed before and after the explosions Figure 3). In Figure 10, the focus is on the increase of degassing before the explosion for the vent NE14c of Stromboli. In the first case, a clear increase of puffing is visible in the 4 seconds before the explosion. In the second example, the gas escapes from a 5m ring around the explosion point. We hypothesize that this ring corresponds to the border of the conduit that is hindered by debris.

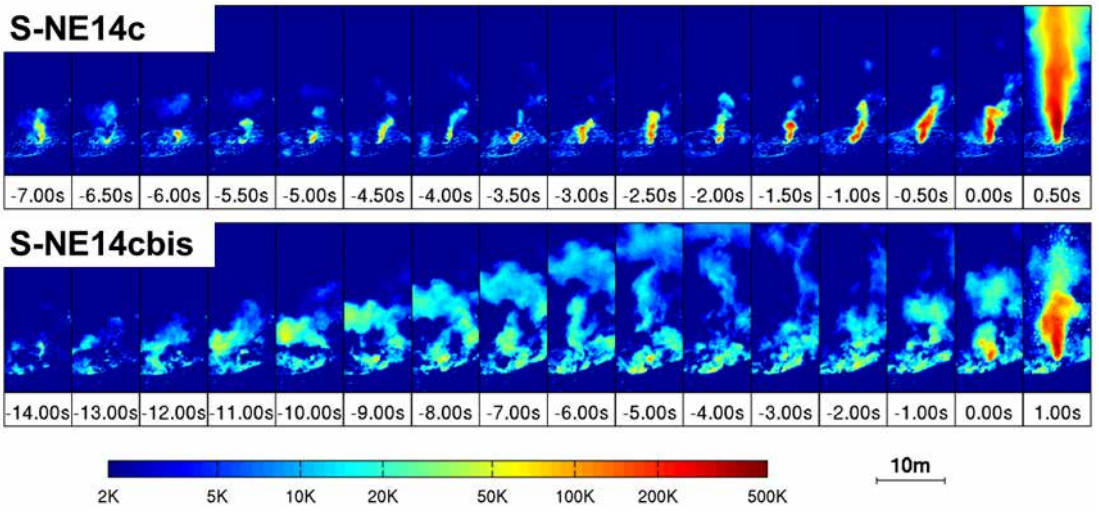

Figure 10. Processed still images showing the increase of puffing activity before two normal explosions on the vent S-NE14c. t=0s refers to the beginning of the explosions (ejection of the first pyroclasts).

11. 4 **- Discussion: the shallow modulation of Strombolian activity**

Strombolian activity is generally thought to be driven by the release of decoupled pressurized gas pockets that ascent through the shallow system magma [Blackburn et al., 1976; Vergniolle and Brandeis, 1996; Ripepe and Gordeev, 1999; Ripepe et al., 2002; James et al., 2004; Del Bello et al., 2012, 2015, Taddeucci et al., 2012, 2014; Capponi et al., 2016a]. Here, rather than discussing the source mechanisms of the gas pockets, I focus on their release process, and propose two factors whose interaction may explain the observed variety of Strombolian activity.

11. 4.1 **- The length of gas pocket/conduit diameter ratio**

The most striking difference between puffing, rapid explosions and normal explosions is the volume of gas released (Table 1). In the case of puffing, volumes are of the order of a cubic metre. These volumes may not be sufficient to fill the whole section of the conduit, as evidenced in Figure 8. Conversely, for normal explosions, the very large volumes of released gas imply the existence of elongated gas pockets in the conduit, or slugs.

Larger volumes are associated to higher ejection velocities. In fact, it has been shown by experimental studies that the pressure of the slugs at burst is first determined by the length of the slug [James et al., 2009; Del Bello et al., 2012], and to a lesser extent, the magma viscosity and the conduit diameter.

Together with the increase of volume from puffing through rapid explosions to normal explosions, the number of pulses increases from 1 to up to 100. Neither numerical modeling [Capponi et al., 2016a] nor experimental studies from shock tube experiments [Alatorre-Ibargüengoitia et al., 2010], buried explosives [Gaudin et al., 2014c] or pressurized rise slug in liquids [Taddeucci et al., 2013; Gaudin et al., 2014c; Capponi et al., 2016a] could satisfactorily model this

pulsating behavior. Among the hypotheses that have not been considered in these previous studies the non-linear behavior of the crystal rich magmas that may favour the splitting of large gas pockets in smaller ones [Oppenheimer et al., 2015] and the elastic response of the conduit walls that might act as a valve are possible candidates. This last hypothesis is supported by observations at Erebus [Dibble et al., 2008] and Halema‘uma‘u [*this study*] lava lakes (that can be seen as very large conduits) where explosions are made of only one pulse.

The ejection pulses are characterized by the non-linear decay of the vent ejection velocity over time (Equation (2)), allowing a characteristic depth of 0-20 m to be defined both for normal explosions [Gaudin et al., 2014b] and rapid explosions [Gaudin et al., 2017b]. This decay is very similar to that observed during shock tube experiments [Alatorre-Ibargüengoitia et al., 2010; Gaudin et al., 2014c] and suggests that the computed parameter *h* scales with the depth from which the particles originate. This supports once again the fact that the long slugs are split close to the surface.

11. 4.2 **- Thickness and viscosity of the cap layer**

The second striking feature of Strombolian activity is the variety of the erupted products (e.g. Figure 2), even at a single volcano (Figure 9). While puffing produce mostly gas with rare bombs, rapid explosions erupt a significant amount of bombs with the gas, and Strombolian explosion may erupt either ash, bombs, both or none of them, defining the 4 types of explosions [Patrick et al., 2007; Goto et al., 2014; Leduc et al., 2015] : ash- and bomb- free (Type 0), ash-free and bomb-rich (Type 1), ash- and bomb- rich (Type 2a), ash-rich and bomb-free (Type 2b).

The characteristics of explosions tend to follow a general trend. On one side, Type 0 explosions are the shortest, with the highest pulse rate and ejection velocities. Type 1 and Type 2a represent intermediate terms, while Type 2b explosions are usually the longest, with low ejection velocities and few ejection pulses. While the highest velocities are usually reached at the beginning of the explosions for Types 0 to 2a, Type 2b explosions tend to be emergent.

This behavior has been linked to the presence of a high viscosity layer on top of the conduit by [Leduc et al., 2015; Capponi et al., 2016b]. Such a cap may reduce the rise velocity of the gas pockets, allowing more time for the pressure to decrease, thus leading to fewer pulses and lower velocities. In the end-member case of Type 2b explosions, gas must make its way through the cap. The first release of gas may increase the permeability of the cap, thus allowing more gas to flow through. The increase of puffing activity prior to Type 1 and 2a explosions can also be explained by the increase of permeability of the cap, probably due its deformation due to the expansion of the gas pocket. We note that vents hosting Type 2b explosions never host puffing, because the presence of a thick cap preventing the release of small gas pockets, not buoyant enough to reach the surface with enough pressure to generate a burst.

11. 5 **- Conclusions - perspectives**

From these observations, we proposed an interpretative scheme of Strombolian explosions based on the interaction between the two controlling factors mentioned above (Figure 11). While the length of the gas pocket over conduit diameter ratio controls the size of the explosion (puffing,

rapid or normal), the thickness and the viscosity of the cap control the relative amount of erupted ash and bombs.

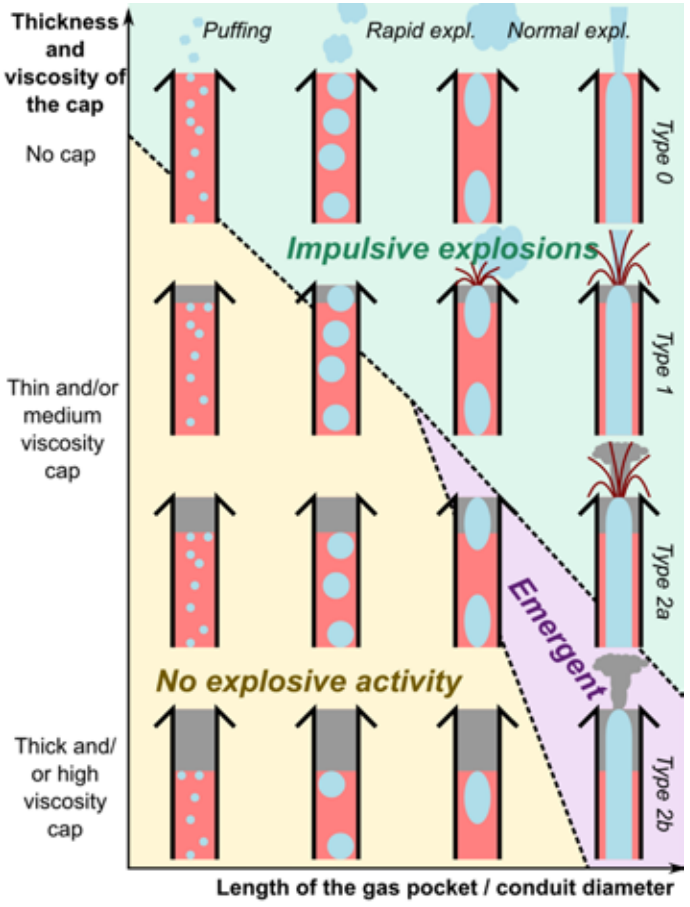

Figure 11. Interpretative scheme of vent dynamics for Strombolian activity. (This scheme is purely qualitative and does not intend to consider the origin or the release frequency of the gas pockets).

Our study demonstrates that these two factors strongly interact together. For instance, pressure inside the gas pocket which control the exit velocity of the gas and particles is determined both by the size of the gas pocket and its rise velocity. The latter is determined by the viscosity of the upper section of the magma column. Thus, higher velocities are observed in the top right corner of the diagram (Figure 11), while in the bottom left corner, the pressure is not sufficient to provoke any explosive activity. The number of pulses within the explosions follows the same trend (Figure 7).

We note that the relationship between the thickness of the viscosity cap and the ejection velocity of the pyroclasts is opposite to what is suggested by laboratory experiments [Del Bello et al., 2015; Capponi et al., 2016a] where it has been demonstrated that the presence of a plug maintains a higher pressure inside the slug compared to a mono-viscosity scenario. The differences may be

associated to the fragmentation processes which are not taken into account in the experiments, but may consume a major part of the energy associated to the slug overpressure for thick cap cases.

Figure 11 also depicts what associations of activities are possible. Indeed, while gas pockets of different length can rise in a single conduit, the thickness and viscosity of the cap is a parametre of the vent. As a consequence, only horizontal associations are possible in this diagram, explaining why puffing is never observed together with Type 2b explosions. Changes in the properties of the cap can be achieved in timescales of hours. It has been hypothesized that more frequent explosions allows the cleaning of the conduit [Capponi et al., 2015, 2016b; Llewellin et al., 2015], leading in turn to more powerful explosions in a retroactive loop. This hypothesis is supported at Stromboli by the location of the most active vents in the center of the crater of the system (Figure 9) where the heat and gas flux may be the highest [Landi et al., 2011], leading to enhanced activity.

The diagram of Figure 11 is currently limited to Strombolian activity. A possible next step would be to determine to which extent other types of activities (e.g. lava fountains, Vulcanian explosions, spattering in lava lakes) could be integrated in this diagram.

Acknowledgements

This work has been supported by project FP7/MC-ITN 289976 NEMOH. At the end of this project, I would like to say an "enorme grazie" to the INGV team that supported me during these four years. First of all, Jacopo Taddeucci who treated my "playing with Matlab instead of writing paper" disease (Sorry, it looks like I infected you) and who helped me so much, both for my professional and my family life. I would also like to thank Piergiorgio Scarlato for his benevolence and support, Elisabetta del Bello and Tullio Ricci for all the scientific discussions and the field trips, and Pierre-Yves Tournigand for all the work and the fun in the office.

NEMOH was an amazing experience, thanks to Paolo Papale, Alessandro Fornaciai, Raffaela Pignolo (grazie, grazie, grazie !) but also all the people, students and professors I met in various European cities. I cannot cite all of them, but I want to thank in particular Ulrich Küppers, Bettina Scheu, Mike James, Stephen Lane, Antonio Capponi, Cristian Montanaro and Laura Spina. Thank you Mike and Steve for the review of this paper and for the constructive remarks you provided!

In the scope of this work, I had the chance to work also with Bruce Houghton, Tim Orr and Andrew Harris that I would like to thank also.

References

Abramoff, M. (2004). Image processing with ImageJ. Biophotonics Int 11, 36–42.

Alatorre-Ibargüengoitia, M.A., Scheu, B., Dingwell, D.B., Delgado-Granados, H. and Taddeucci, J. (2010). Energy consumption by magmatic fragmentation and pyroclast ejection during Vulcanian eruptions. Earth Planet. Sci. Lett. 291, 60–69. doi:10.1016/j.epsl.2009.12.051.

Barberi, F., Rosi, M. and Sodi, A. (1993). Volcanic hazard assessment at Stromboli based on review of historical data. Acta Vulcanol. 3, 173–187.

Blackburn, E.A., Wilson, L. and Sparks, R.S.J. (1976). Mechanisms and dynamics of strombolian activity. J. Geol. Soc. 132, 429–440. doi:10.1144/gsjgs.132.4.0429.

Capponi, A., James, M.R. and Lane, S.J. (2016a). Gas slug ascent in a stratified magma: Implications of flow organisation and instability for Strombolian eruption dynamics. Earth Planet. Sci. Lett. 435, 159–170. doi:10.1016/j.epsl.2015.12.028.

Capponi, A., Taddeucci, J., Scarlato, P. and Palladino, D.M. (2015). A Mouthful of Dirt: Feedbacks Between the Presence and Nature of In-Vent Debris and the Dynamics of Strombolian Explosions, in: 2015 AGU Fall Meeting. Agu.

Capponi, A., Taddeucci, J., Scarlato, P. and Palladino, D.M. (2016b). Recycled ejecta modulating Strombolian explosions. Bull. Volcanol. 78, 1–13. doi:10.1007/s00445-016-1001-z.

Del Bello, E., Lane, S.J., James, M.R., Llewellin, E.W., Taddeucci, J., Scarlato, P. and Capponi, A. (2015). Viscous plugging can enhance and modulate explosivity of strombolian eruptions. Earth Planet. Sci. Lett. 423, 210–218. doi:10.1016/j.epsl.2015.04.034.

Del Bello, E., Llewellin, E.W., Taddeucci, J., Scarlato, P. and Lane, S.J. (2012). An analytical model for gas overpressure in slug-driven explosions: Insights into Strombolian volcanic eruptions. J. Geophys. Res. Solid Earth 1978–2012 117, B02206. doi:10.1029/2011JB008747.

Dibble, R.R., Kyle, P.R. and Rowe, C.A. (2008). Video and seismic observations of Strombolian eruptions at Erebus volcano, Antarctica. J. Volcanol. Geotherm. Res., Volcanology of Erebus volcano, Antarctica 177, 619–634. doi:10.1016/j.jvolgeores.2008.07.020.

Gaudin, D., Moroni, M., Taddeucci, J., Scarlato, P. and Shindler, L. (2014a). Pyroclast Tracking Velocimetry: A particle tracking velocimetry-based tool for the study of Strombolian explosive eruptions. J. Geophys. Res. Solid Earth 119, 2014JB011095. doi:10.1002/2014JB011095.

Gaudin, D., Taddeucci, J., Scarlato, P., Del Bello, E., Houghton, B., Orr, T., Andronico, D. and Kueppers, U., (2015). Game of thrown bombs in 3D: using high speed cameras and photogrammetry techniques to reconstruct bomb trajectories at Stromboli (Italy). Presented at the AGU Fall Meeting, San Francisco.

Gaudin, D., Taddeucci, J., Scarlato, P., Del Bello, E., Ricci, T., Orr, T., Houghton, B., Harris, A., Rao, S., and Bucci, A. (2017a). Integrating puffing and explosions in a general scheme of vent dynamics during Strombolian-style volcanic activity. Journal of Geophysical Research: Solid Earth, 122(3), 1860-1875, doi: 10.1002/2016JB013707.

Gaudin, D., Taddeucci, J., Scarlato, P., Harris, A.J.L., Bombrun, M., Del Bello, E. and Ricci, T., (2017b). Characteristics of puffing activity revealed by ground-based, thermal infrared imaging: the example of Stromboli volcano (Italy). Bulletin of Vulcanology, *79*(3), 24, doi:10.1007/s00445-017-1108-x.

Gaudin, D., Taddeucci, J., Scarlato, P., Moroni, M., Freda, C., Gaeta, M. and Palladino, D.M. (2014b). Pyroclast Tracking Velocimetry illuminates bomb ejection and explosion dynamics at Stromboli (Italy) and Yasur (Vanuatu) volcanoes. J. Geophys. Res. Solid Earth 119, 2014JB011096. doi:10.1002/2014JB011096.

Gaudin, D., Taddeucci, J., Scheu, B., Valentine, G., Capponi, A., Kueppers, U., Graettiger, A. and Sonder, I. (2014c). Pyroclast acceleration and energy partitioning in fake explosive eruptions. Presented at the EGU General Assembly Conference Abstracts, p. 12959.

Goto, A., Ripepe, M. and Lacanna, G. (2014). Wideband acoustic records of explosive volcanic eruptions at Stromboli: New insights on the explosive process and the acoustic source. Geophys. Res. Lett. 41, 2014GL060143. doi:10.1002/2014GL060143.

Harris, A. and Ripepe, M. (2007). Temperature and dynamics of degassing at Stromboli. J. Geophys. Res. Solid Earth 112, B03205. doi:10.1029/2006JB004393.

Houghton, B.F., Taddeucci, J., Andronico, D., Gonnermann, H.M., Pistolesi, M., Patrick, M.R., Orr, T.R., Swanson, D.A., Edmonds, M., Gaudin, D., Carey, R.J. and Scarlato, P. (2016). Stronger or longer: Discriminating between Hawaiian and Strombolian eruption styles. Geology G37423.1. doi:10.1130/G37423.1.

James, M.R., Lane, S.J., Chouet, B. and Gilbert, J.S. (2004). Pressure changes associated with the ascent and bursting of gas slugs in liquid-filled vertical and inclined conduits. J. Volcanol. Geotherm. Res., The role of laboratory experiments in volcanology 129, 61–82. doi:10.1016/S0377-0273(03)00232-4.

James, M.R., Lane, S.J., Wilson, L. and Corder, S.B. (2009). Degassing at low magma-viscosity volcanoes: Quantifying the transition between passive bubble-burst and Strombolian eruption. J. Volcanol. Geotherm. Res., Models and products of mafic explosive activity 180, 81–88. doi:10.1016/j.jvolgeores.2008.09.002.

Landi, P., Marchetti, E., La Felice, S., Ripepe, M. and Rosi, M. (2011). Integrated petrochemical and geophysical data reveals thermal distribution of the feeding conduits at Stromboli volcano, Italy. Geophys. Res. Lett. 38, L08305. doi:10.1029/2010GL046296.

Leduc, L., Gurioli, L., Harris, A., Colò, L. and Rose-Koga, E.F. (2015). Types and mechanisms of strombolian explosions: characterization of a gas-dominated explosion at Stromboli. Bull. Volcanol. 77, 1–15. doi:10.1007/s00445-014-0888-5.

Llewellin, E., Jones, T. and Jenkins, A. (2015). Formation and Maintenance of a Viscous Plug in a Strombolian Volcanic Conduit, in: 2015 AGU Fall Meeting. Agu.

Moroni, M. and Cenedese, A. (2005). Comparison among feature tracking and more consolidated velocimetry image analysis techniques in a fully developed turbulent channel flow. Meas. Sci. Technol. 16, 2307. doi:10.1088/0957-0233/16/11/025.

Oppenheimer, J., Rust, A.C., Cashman, K.V. and Sandnes, B. (2015). Gas migration regimes and outgassing in particle-rich suspensions. Interdiscip. Phys. 60. doi:10.3389/fphy.2015.00060.

Patrick, M.R., Harris, A., Ripepe, M., Dehn, J., Rothery, D.A. and Calvari, S. (2007). Strombolian explosive styles and source conditions: insights from thermal (FLIR) video. Bull. Volcanol. 69, 769–784.

Ripepe, M. and Gordeev, E., (1999). Gas bubble dynamics model for shallow volcanic tremor at Stromboli. J. Geophys. Res. Solid Earth 104, 10639–10654. doi:10.1029/98JB02734.

Ripepe, M. and Harris, A.J.L. (2008). Dynamics of the 5 April 2003 explosive paroxysm observed at Stromboli by a near-vent thermal, seismic and infrasonic array. Geophys. Res. Lett. 35, L07306. doi:10.1029/2007GL032533.

Ripepe, M., Harris, A.J.L. and Carniel, R. (2002). Thermal, seismic and infrasonic evidences of variable degassing rates at Stromboli volcano. J. Volcanol. Geotherm. Res. 118, 285–297. doi:10.1016/S0377-0273(02)00298-6.

Ripepe, M., Poggi, P., Braun, T. and Gordeev, E. (1996). Infrasonic waves and volcanic tremor at Stromboli. Geophys. Res. Lett. 23, 181–184. doi:10.1029/95GL03662.

Rosi, M., Bertagnini, A. and Landi, P. (2000). Onset of the persistent activity at Stromboli Volcano (Italy). Bull. Volcanol. 62, 294–300. doi:10.1007/s004450000098.

Rosi, M., Pistolesi, M., Bertagnini, A., Landi, P., Pompilio, M. and Roberto, A.D. (2013). Chapter 14 Stromboli volcano, Aeolian Islands (Italy): present eruptive activity and hazards. Geol. Soc. Lond. Mem. 37, 473–490. doi:10.1144/M37.14.

Spina, L., Taddeucci, J., Cannata, A., Gresta, S., Lodato, L., Privitera, E., Scarlato, P., Gaeta, M., Gaudin, D. and Palladino, D.M. (2015). Explosive volcanic activity at Mt. Yasur: A characterization of the acoustic events (9–12th July 2011). J. Volcanol. Geotherm. Res. 302, 24–32. doi:10.1016/j.jvolgeores.2015.07.027.

Taddeucci, J., Capponi, A., Scarlato, P., Palladino, D.M., Cocomello, S. and Gaudin, D. (2013). The slug buster: an analogue experiment for the study of Strombolian explosions. Presented at the IAVCEI General Assembly, Kagoshima, Japan.

Taddeucci, J., Edmonds, M., Houghton, B., James, M.R. and Vergniolle, S. (2015). Hawaiian and Strombolian Eruptions, in: The Encyclopedia of Volcanoes. pp. 485–503.

Taddeucci, J., Scarlato, P., Capponi, A., Del Bello, E., Cimarelli, C., Palladino, D.M. and Kueppers, U. (2012). High-speed imaging of Strombolian explosions: The ejection velocity of pyroclasts. Geophys. Res. Lett. 39, L02301. doi:10.1029/2011GL050404.

Taddeucci, J., Sesterhenn, J., Scarlato, P., Stampka, K., Del Bello, E., Pena Fernandez, J.J. and Gaudin, D. (2014). High-speed imaging, acoustic features, and aeroacoustic computations of jet noise from Strombolian (and Vulcanian) explosions. Geophys. Res. Lett. 41, 2014GL059925. doi:10.1002/2014GL059925.

Vergniolle, S. and Brandeis, G. (1996). Strombolian explosions: 1. A large bubble breaking at the surface of a lava column as a source of sound. J. Geophys. Res. Solid Earth 101, 20433–20447. doi:10.1029/96JB01178.

Washington, H.S. (1917). Persistence of vents at Stromboli and its bearing on volcanic mechanism. Geol. Soc. Am. Bull. 28, 249–278. doi:10.1130/GSAB-28-249.

Damien Gaudin, France
damgaudin@gmail.com

Affiliation under NEMOH
Istituto Nazionale di Geofisica e Vulcanologia, Sezione di Roma, Roma, Italy

Research theme under NEMOH
Observations and modelling of gas and pyroclast ejection in explosive volcanism

I started my PhD in 2008 in the Laboratoire Domaines Océaniques of the University of Brest in France, working on handheld thermal infrared cameras, and how high resolution can bring new information on planetary surfaces, beaches, rivers… and volcanoes!

My first encounter with a volcano took place in 2010 in Guadeloupe. After two years trying to track small thermal contrast in French Brittany, I fell in love with the sulphur smell of La Soufrière, and above all on a small area located at the base of the dome itself, where the surface temperature was really hot. I spent the two last years of my PhD studying this zone –the Ty fault fumarolic zone– with thermal cameras of course, but also using a permanent temperature monitoring station, modeling and trying to quantify the fluxes.

In 2012, I came to Roma, attracted by the high-speed thermal camera that was just bought to study explosions at Stromboli. I quickly understood that the keyword was not “thermal” but “high-speed”. I used my skills in computer programming, image processing and physics to adapt software with the permanent objective to quantify everything: velocities, masses, volumes, temperature.

Now, I just want to look at volcanoes. As many as possible, and to use my monitoring and processing techniques to compare them, trying to spot family traits and their differences. Since September 2016, my next step is Munich where I study lightning in ash plumes. Still in the scope of a Marie Curie project, but this one is named "Voltaic" (http://voltaic-eu.com/). Still with thermal infrared, but also with lab experiments. Still trying to quantify what I’m seeing. After La Soufrière and Stromboli, it is now time for a third volcano whose name starts with S: Sakurajima!

Chapter 12

Aquifers in volcanic regions: Monitoring capabilities and hazards

Karen Strehlow

School of Earth Sciences, University of Bristol, Bristol, United Kingdom

Tutorship: Joachim Gottsmann[1], Alison Rust[1], Laura Sandri[2], Magnús Tumi Guðmundsson[3]

[1] *School of Earth Sciences, University of Bristol, Bristol, United Kingdom*
[2] *Istituto Nazionale di Geofisica e Volcanologia, Sezione di Bologna, Bologna, Italy*
[3] *Institute of Earth Sciences, University of Iceland, Reykjavík, Iceland*

Abstract

Volcanic systems can significantly perturb the local hydrology, whose responses range from changes in aquifer pressures and temperatures to violent phreatic explosions. This NEMOH project addressed two manifestations of volcano-aquifer interactions, working towards a better understanding of monitoring signals and hazards associated with hydrological systems in volcanic regions.

The first part investigates poroelastic water level changes at volcanoes. We develop numerical models that simulate crustal deformation accompanying pressurization of magma reservoirs and the dynamic aquifer response. Simulated magma chamber inflation leads to observable hydraulic head transients and porous flow in overlying hydrological reservoirs that strongly depend on a complex interplay of aquifer and source parameters. The models are then applied to a case study, which concludes that pre-eruptive well level changes at Usu volcano (Japan) in 2000 were induced by the pressurization of both the magma chamber and a large, shallow hydrothermal system. The models are a significantly improved tool for the interpretation of well level signals in volcanic areas that can provide valuable constraints for volcanic strain sources.

The second part consists of a statistical approach to assess the often-underestimated hazard associated with phreatic explosions. Time-series analysis of the eruption catalogue of Ruapehu Volcano (New Zealand) suggests that phreatic eruptions at this crater lake volcano tend to cluster. Combining probabilistic clast ejection simulations with a Bayesian event tree tool, we generate hazard maps for ballistic ejecta on the summit of Ruapehu that contribute to local hazard assessment.

Keywords: poroelasticity, volcano deformation, finite element modelling, phreatic eruptions, probabilistic hazard assessment.

12. 1 **- Introduction**

It is well known that the presence of water can significantly affect the style of volcanic activity, and the resulting phreatomagmatic eruptions have been widely studied (e.g. Mastin et al., 2004; Gudmundsson et al., 2008; Lupi et al., 2011; Liu et al., 2015). But the interactions of hydrological and

magmatic systems are manifold and work two-ways (Newhall et al., 2001). Phenomena resulting from magmatic processes affecting the local hydrology have, however, been comparatively understudied. Observed volcanic unrest signals have often been interpreted as hydrological responses to changes in the state of the magmatic system. Variations in water levels, temperatures or composition, as well as hydrologically induced ground deformation and gravity transients, are typical examples of "wet unrest". There are reports of such signals at numerous volcanoes, including Usu, Japan (Matsumoto et al., 2002), Kilauea, Hawaii (Hurwitz and Johnston, 2003) and Mayon, Philippines (Tiampo et al., 2007). Commonly postulated triggers for wet unrest are magmatically induced variations in temperature, changes in local stress conditions, the opening of fractures or the injection of magmatic fluids into an aquifer (Newhall et al., 2001). Volcano-aquifer interactions can culminate in steam-driven explosions that often precede magmatic events, yet many crises have peaked at the phreatic stage (e.g. Le Guern et al., 1980; Kilgour et al., 2010). Changes in aquifer dynamics can hence be valuable indicators of volcanic unrest and contribute to volcanic hazards, but very few of the suggested mechanisms for hydrological unrest have been sufficiently quantitatively tested.

This NEMOH project focused on two volcano-hydrological phenomena: water level changes caused by magmatic stress changes and phreatic explosions. While the latter represents a volcanic hazard whose associated risk is often underestimated, induced water level changes can be used as windows into the magmatic system. Improving the knowledge base on either of the two currently poorly understood processes may support volcano monitoring and eruption forecasting.

12. 2 **- Monitoring capabilities: Poroelastic aquifer responses to volcanic strain**

12. 2.1 **- Generic models (reproduced from Strehlow et al., 2015)**

The compression or dilatation of an elastic porous medium leads to a decrease or an increase in pore space, respectively, which in turn influences the pore pressure and thereby the water level (Wang, 2000). Aquifers are so-called poroelastic media, and well water level changes associated with magmatic unrest can therefore be interpreted as a result of pore pressure changes in the aquifer due to crustal deformation. A dramatic example is the water level rise of more than 85 m in a geothermal well at Krafla volcano, Iceland, associated with a dyke intrusion in 1977 (Stefansson, 1981).

Information about the local strain field is valuable for volcano monitoring and eruption forecasting, as it can allow derivation of the strain-inducing subsurface processes (e.g. Linde et al., 2010; Bonaccorso et al., 2012). If we can translate water level changes to volcanic strain, wells can therefore be a useful addition to existing monitoring systems. Previous attempts to use aquifers as strainmeters relied on analytical deformation models in combination with the aquifer's strain sensitivity, a material property giving the hydraulic head change per unit applied strain (e.g. Matsumoto et al., 2002). However, these methods ignore crustal heterogeneities, complex source morphologies and fluid flow processes. Due to these shortcomings, the models do not always succeed in fully explaining observed well signals.

We developed numerical models to overcome these limitations and to assess to what extent confined aquifers can serve as indicators of strain partitioning in the shallow crust. They solve a series of partial differential equations that result from the full coupling of continuum mechanics equations for stress-strain relations of a linear elastic material with Darcy's law and mass conservation within the porous flow theory. Applying the software COMSOL Multiphysics, we used finite element analysis (FEA) to simulate the response of shallow aquifers to volumetric strain induced by pressurized magma reservoirs at depth. The time-dependent, fully coupled models simulate crustal deformation accompanying chamber pressurization and the resulting hydraulic head changes as well as flow through the porous aquifer. The flexibility of the FEA method allows testing of a variety of geometrical settings. Figure 1 shows the generic 2D-axisymmetric set-up used for parametric studies, input parameters for the reference simulation are given in Table 1.

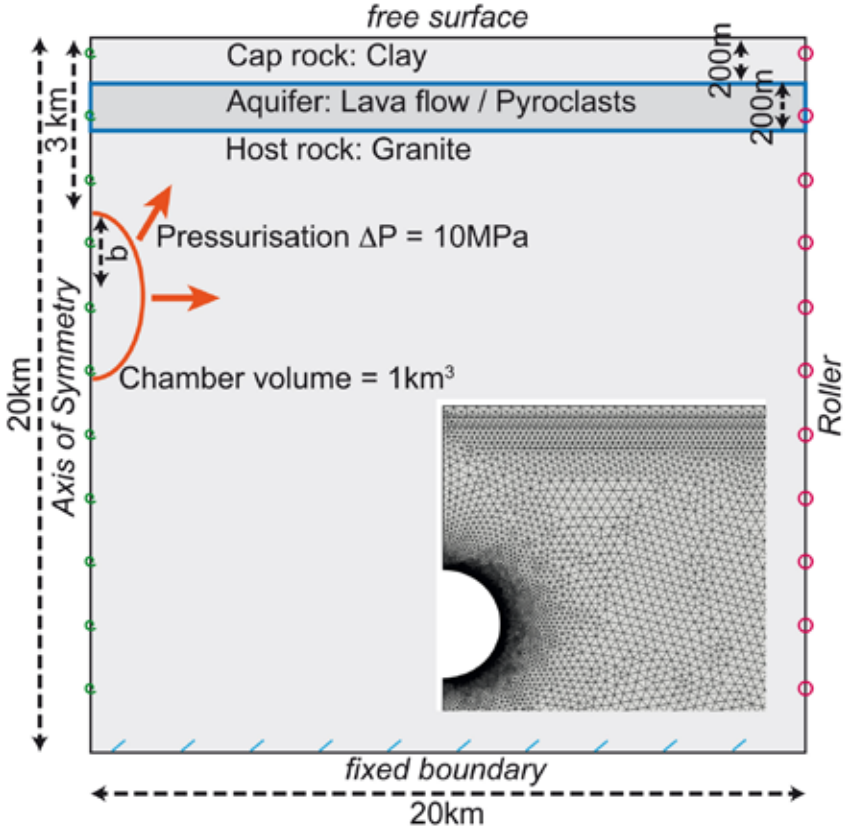

Figure 1. 2-D axisymmetric model set-up: a boundary load is applied on a cavity at depth, representing the magma chamber. This strains the surrounding linear elastic host rock, the poroelastic, water-saturated aquifer and the overlying linear elastic cap rock. The bottom boundary is fixed, the upper boundary is treated as a free surface, the lateral boundaries have a roller condition (free lateral, but no vertical displacement). There is no flow outside the aquifer; stress and displacement at the internal boundaries are continuous. Initial conditions are hydrostatic pressure and no flow in the aquifer. An extract of the finite element mesh is shown only for illustration. The mesh density is finer around the cavity, at aquifer boundaries and the free surface.

Parameter	Reference Value	Parameter	Reference Value
Aquifer depth z_{aq}	200 m	Cap rock density r_c	1800 kg m^{-3}
Aquifer thickness d_{aq}	200 m	Host rock density r_h	2600 kg m^{-3}
Chamber top depth z_{CH}	3 km	Aquifer density - pyroclastic r_{aq}	2000 kg m^{-3}
Chamber radius (spherical) r	1 km	Aquifer density - lava flow r_{aq}	2800 kg m^{-3}
Distance chamber – aquifer dist	2.6 km	Aquifer permeability - pyroclastic k	$5x10^{-11}$ m^2
Vertical semi-axis b	1 km	Aquifer permeability - lava flow k	$5x10^{-12}$ m^2
Cap rock Young's Modulus E_c	70 MPa	Aquifer porosity - pyroclastic f	0.35
Host rock Young's Modulus E_h	30 GPa	Aquifer porosity - lava flow f	0.1
Aquifer Young's Modulus - pyroclastic E_{aq}	10 MPa	Biot-Willis coefficient - pyroclastic a	0.7
Aquifer Young's Modulus - lava flow E_{aq}	50 GPa	Biot-Willis coefficient - lava flow a	0.2
Cap rock Poisson's ratio n_c	0.45	Water density r_f	1000 kg m^{-3}
Host rock Poisson's ratio n_h	0.25	Water viscosity m	10^{-3} Pa s
Aquifer Poisson's ratio – pyroclastic n_{aq}	0.275	Water compressibility c_f	$4x10^{-10}$ Pa^{-1}
Aquifer Poisson's ratio – lava flow n_{aq}	0.225	Pressurization values DP	10 MPa

Table 1. Input parameters of reference simulation

12. 2.1.1 **- Results of generic models**

Two different aquifers were invoked - an unconsolidated pyroclastic deposit and a vesicular lava flow - that differ in flow and elastic properties. They show significantly different poroelastic behaviour, which is mostly due to the difference in stiffness. The simulated strain due to an instantaneous magma chamber pressurization of 10 MPa leads to centimetres of hydraulic head change in the softer pyroclastic, but to meters of head change in the stiffer lava flow aquifer. The initial hydraulic head change profile perfectly mirrors the strain curves (Fig. 2). The dilation (positive strain) due to the ground uplift above the chamber leads to hydraulic head falls, while the compression (negative strain) at radial distance from the centre of the computational domain causes hydraulic head rises. Strain and hydraulic head change with time due to substantial porous flow in the hydrological system (Fig. 3).

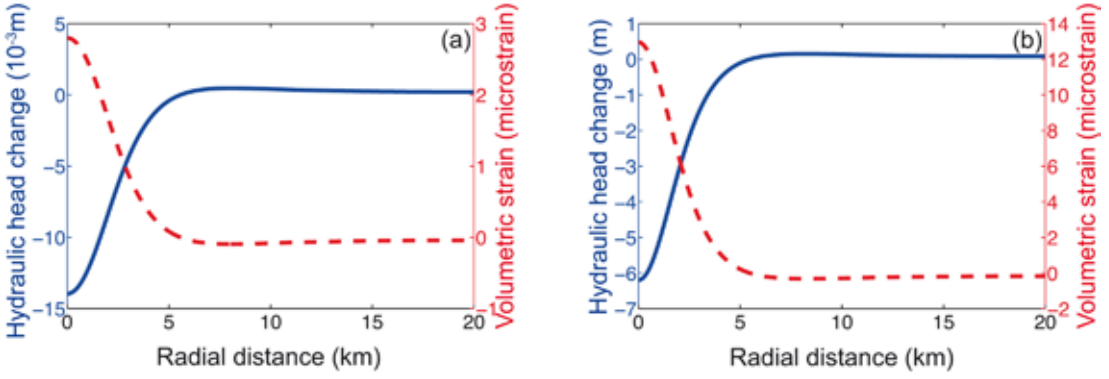

Figure 2. Results of the reference simulation, shown as the initial hydraulic head change (blue solid line) and volumetric strain (red dashed line) along profiles through the two aquifer types: (a) pyroclastic aquifer, (b) lava flow aquifer.

Both the strain-induced pressure gradient in the aquifers and the topographic gradient due to the ground uplift (about 4 cm directly above the chamber) induce porous flow, because groundwater flows from larger to smaller pressure and from higher to lower elevation. These gradients oppose each other: The topographic gradient points away from the centre of uplift, the pressure gradient points towards the centre. As the hydraulic head fall in the centre of the pyroclastic aquifer is smaller than the topographic uplift, gravitational flow dominates over strain-induced flow and hence fluid flow is away from the centre (Fig. 3a). In the lava flow aquifer, strain-induced hydraulic head changes are two orders of magnitude larger than the topographic change; therefore, flow in this aquifer is towards the centre, following the dominant pressure gradient (Fig. 3b). Despite its lower permeability, the lava flow aquifer shows higher flow velocities, as the strain-induced pressure gradient in this stiffer aquifer is large enough to overcome not only the topographic change but also the difference in permeability.

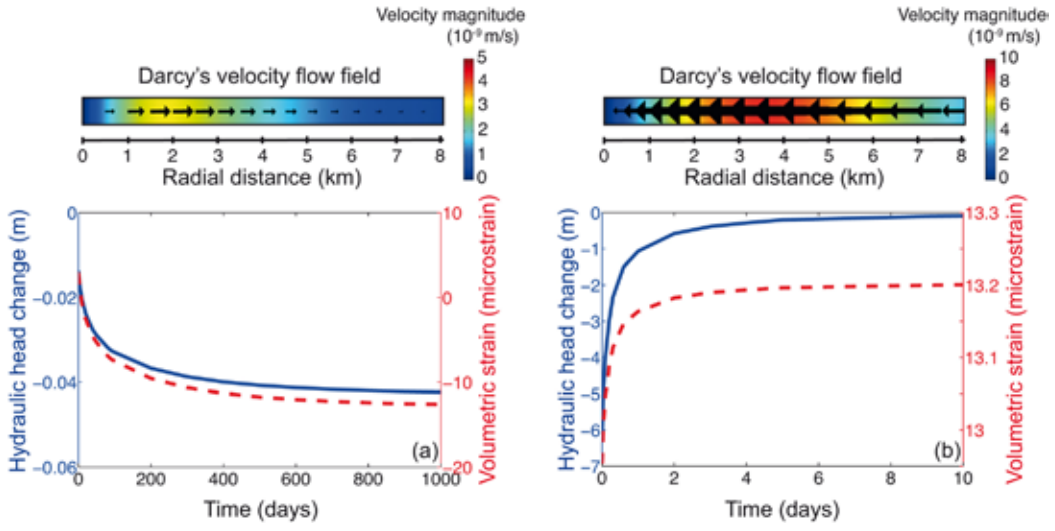

Figure 3. Upper graphs: porous flow pattern shown for the reference simulation at t=0.1 d: (a) pyroclastic aquifer, (b) lava flow aquifer. Arrows indicate flow direction at the point where the arrow is attached, their length is proportional to flow velocity (note: different scales for (a) and (b)), colours show velocity magnitude. Lower graphs show hydraulic head and strain development with time in the centre of the aquifers. Note the different time scale - flow processes are faster in the lava flow aquifer.

The hydraulic head continues to fall in the pyroclastic aquifer as water flows away from the centre of the computational domain, while the opposite flow direction in the lava flow aquifer leads to a decrease of the initial hydraulic head fall with time (i.e. head increases). Strain changes simultaneously with hydraulic head due to the poroelastic nature of the aquifers (Fig. 3): With lateral flow of water away from the centre, the pyroclastic aquifer responds to the removal of pore fluid with compaction - explaining the change of strain from dilation to compaction. Volumetric strain increases in the lava flow aquifer. When poroelastic media are subject to strain, some of it is absorbed by the pore fluid, which manifests as the initial pore pressure change. With equilibration of

the pressure in the lava flow aquifer due to the flow, this stress absorption effect vanishes and strain approximates an equilibrium value that represents the strain value in an elastically equivalent, but dry material.

The effect of the pore fluid and in particular its flow on the hydraulic head and strain signal underlines the importance of full coupling between solid mechanics and fluid flow processes when considering well level changes in order to monitor subsurface magmatic processes.

A sensitivity analysis of the tested parameter space revealed most important input parameters. Well level changes are particularly sensitive to chamber volume, shape and pressurization strength, followed by aquifer permeability and the phase of the pore fluid. The depths of chamber and aquifer, as well as the aquifer's Young's Modulus also have significant influence on the hydraulic head signal. While source characteristics, the distance between chamber and aquifer and the elastic stratigraphy determine the strain field and its partitioning, flow and coupling parameters define how the aquifer responds to this strain and how signals change with time. Here, we present those results from parametric studies that are most important for the comparison of traditional analytical (e.g. Mogi, 1985) with novel numerical deformation models - for full details please refer to Strehlow et al., (2015).

A significant simplification in analytical volcano deformation models is the inherent assumption of mechanical homogeneity of the crust. Our studies show that not only the aquifer's absolute stiffness, but also its stiffness relative to the surrounding crust is important. The ratios of elastic properties of the three rock layers are defined as $ER_h=E_h/E_{aq}$ and $ER_c=E_c/E_{aq}$, with E_{aq}, E_h and E_c being the Young's Modulus of the aquifer, the host rock and the cap rock, respectively. A larger ER_h for a fixed E_{aq} indicates a stiffer host rock and results in a smaller strain in the aquifer and hence smaller hydraulic head change (Fig. 4a-b). The relative cap rock stiffness ER_c has negligible influence when it is small (unless in cases with small ER_h), but becomes increasingly important when the cap rock stiffness is close to or larger than that of the aquifer (ER_c >1): A sufficiently stiff cap rock decreases the hydraulic head change and can even change its sign to a head rise. This "sign-flipped" signal increases with larger ER_c (Fig. 4a-b). The ER_c value at which the strain sign is flipped ("$ER_{c\text{-}flip}$") is determined by the geometry of the system, in particular by the distance between aquifer and magma chamber and the thickness of the cap rock (cap rock thickness: Fig. 4c).The shorter the chamber-aquifer distance and the thicker the cap rock layer, the smaller is $ER_{c\text{-}flip}$.

The elastic stratigraphy determines how strain is partitioned in the crust and how it changes at the boundaries between layers (Fig. 4d). A sufficiently stiff cap rock prevents the dilation of the aquifer and turns the dilatational strain into compression at the host rock - aquifer boundary, hence causing sign-flipped signals. In the reference set-up, the cap rock needs to be two orders of magnitude stiffer than the aquifer. In a different geometrical setting, however, a perhaps more likely geological situation can be imagined in which a sign-flipped response can be expected. For example, a cap rock that is only three times stiffer than the aquifer can already lead to a sign-flip, if the aquifer is about 1 km depth (Fig. 4c). Pyroclastic deposits show a range of stiffnesses due to different lithologies, rates of consolidation or grain size distributions and this situation is particularly feasible at stratovolcanoes.

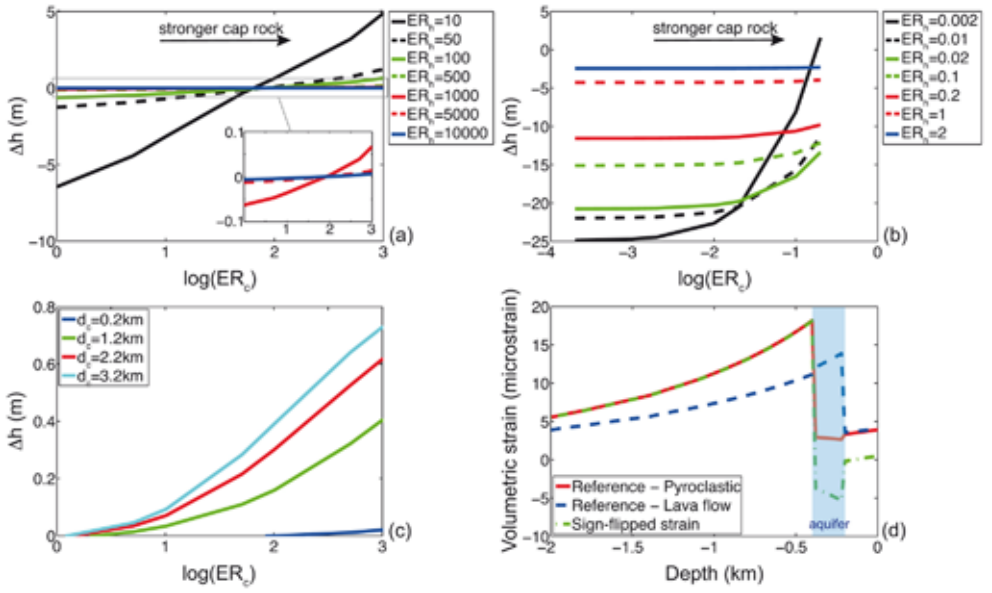

Figure 4. Influence of the elastic stratigraphy on the central, initial hydraulic head change Δh, shown using the ratios of Young's Moduli. (a) pyroclastic aquifer, (b) lava flow aquifer. (c) Behaviour of central initial head change in the pyroclastic aquifer with ER_c for different cap rock thicknesses d_c. (d) Vertical strain profiles through the centre of the domain from 2 km depth to the surface, for different elastic stratigraphies: the two reference simulations and a setting in which the sign of strain (and consequently hydraulic head) is flipped from dilation to compression due to a sufficiently stiff cap rock (ER_c=1000).

The subsurface stress and strain fields are also substantially dependent on the shape of the chamber. For oblate chambers, the aquifer area that is exposed to vertical stress is larger than for prolate chambers and it is therefore subject to stronger strain. Additionally, the centre of an oblate chamber is shallower than the centre of a prolate chamber (as the depth of the chamber top is fixed in the simulations). Chamber morphology can change the hydraulic head signal by an order of magnitude. The signal amplitude is highest for oblate chambers, intermediate for a sphere and smallest for prolate chambers (Fig. 5).

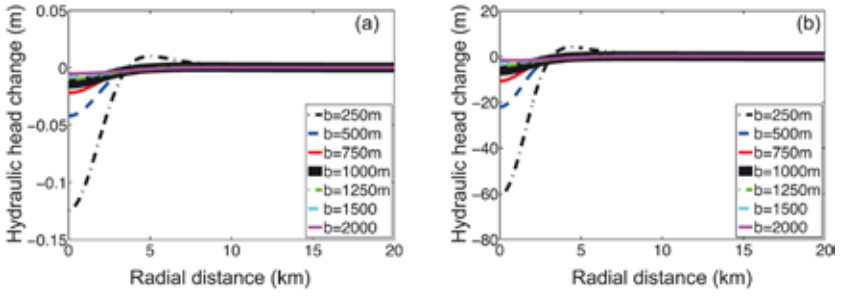

Figure 5. Influence of changing the aspect ratio of a spheroidal chamber (with constant chamber top depth and volume) on the initial hydraulic head change profile through the aquifer. Aspect ratio is changed by varying the vertical half radius b of an ellipsoid; oblate shapes have b < 1000 m, prolate chambers correspond to b > 1000 m. (a) pyroclastic aquifer, (b) lava flow aquifer.

12. 2.1.2 - Implications of generic model results

Our results show that well levels and the flow in aquifers can indeed reflect the deformation at volcanoes, suggesting that their implementation in volcano monitoring systems could provide insights into subsurface processes causing the strain. However, water levels are also influenced by a number of other processes (e.g. meteorological or hydrothermal), although these can often be excluded by means of information from other monitoring systems and knowledge of the local hydrology. Simulated initial hydraulic head change perfectly mirrors the strain, therefore - if the level changes are thought to be caused by strain - volumetric strain in the aquifer can be directly inferred from measured water level changes using strain sensitivity, the change of hydraulic head in the aquifer in meters per unit applied strain. This material property can be assessed by tracking water level changes as a result of predictable excitations (e.g. earth tides). However, the strain sensitivity value determined from aquifer responses to known strains only provides accurate strains when applied to the initial hydraulic head change, as it does not take flow and resulting poroelastic changes into account. Dense time series of well data are necessary to catch this initial response.

If strain sensitivity has been accurately used to infer volumetric strain, we still face the problem of interpretation of this signal. The source of volumetric strain can be inverted for with analytical volcano deformation models. However, these models commonly assume a source in a homogeneous half space and some only consider spherical or point-like chambers (e.g. Dzurisin, 2007, and references therein). Additionally, all previous approaches to model surface deformation induced by reservoir inflation assumed a concept of "dry deformation", i.e. they neglect the effect of pore fluids. Our results underline that any model using these simplifications will likely be inadequate for interpretation of poroelastic processes. Chamber shape is one of the two most important parameters influencing the hydraulic head signal up to an order of magnitude. The coupling between the solid matrix and its pore fluid - in particular its flow - alters the signal with time and can render strain sensitivity values useless. Furthermore, the assumption of a homogeneous half space is precarious as volcanoes are strongly heterogeneous - several previous studies have already shown that mechanical heterogeneities in the subsurface affect the ground deformation at volcanoes (e.g. Folch and Gottsmann, 2006; Manconi et al., 2007; Geyer and Gottsmann, 2010). We have shown that this also applies to hydraulic head change and consequently derived strain, which can significantly deviate from signals in a homogeneous crust. Especially in settings with a sign-flipped signal, this influence becomes crucial: The hydraulic head rises and hence interpretation of the hydraulic head data alone would suggest a deflating chamber, while in reality it would be inflating. We investigated the ground deformation signals to test whether tracking volcano deformation could aid with this interpretation problem. Indeed, surface deformation does not change sign and shows inflation of the ground also in the sign-flipped cases and can hence be used to indicate that the strain in the aquifer is sign-flipped. This underlines that well monitoring is possibly most valuable in conjunction with other geophysical and geochemical monitoring systems.

Our parametric studies show how poroelastic aquifer responses are influenced by a variety of source, geometric and aquifer parameters, which each have the potential to significantly alter the signal amplitude and development with time and space. Common analytical models do not

satisfactorily capture the complex subsurface mechanics leading to strain-induced well level changes, highlighting that their challenging interpretation requires sophisticated numerical models. Due to the ambiguities of stress and strain modelling and our insufficient knowledge of the subsurface, the inversions of water level signals will likely always remain non-unique; however, the simulated water table changes do mirror volumetric strain and are sensitive to source parameters. Therefore, the presented models provide a framework for interpreting well data to provide important insights into pre-eruptive dynamics.

12. 2.2 **- The 2000 Usu eruption**

Following a 4-day precursory phase of intense seismicity and increasing ground deformation, Usu volcano (Japan) erupted on 31 March 2000 after 22 years of quiescence (e.g. Jousset et al., 2003; Zobin et al., 2005). Activity consisted of phreatic and phreatomagmatic explosions (Yokoo et al., 2002) that produced 0.001 km^3 of tephra (Matsumoto and Nakagawa, 2010). Explosive activity was followed by a cryptodome formation leading to large ground deformation (Tobita et al., 2001). Several deformation sources were active prior to and during the eruption, suggesting a complex intrusion process. From deformation, seismic, petrological and gravity data, the following model - schematically shown in Fig. 6 - of pre-eruptive subsurface magma movement emerged (Yamamoto et al., 2002; Jousset et al., 2003; Matsubara and Yomogida, 2004; Yamagishi et al., 2004; Tomiya et al., 2010): Usu's deeper magma chamber at about 10 km depth was gradually inflating until 2 days before the eruption and deflated rapidly when magma migrated upwards. Magma was injected into the shallower chamber at 4-5 km depth beneath the Southwestern part of the summit, leading to inflation of this chamber. The simultaneous overpressurization of the chamber eventually triggered the eruption: magma moved towards the surface in a Northwestern direction through an inflating fissure zone. Shallower deformation sources (e.g. at 2-3 and 0.25-2 km depth) are interpreted as intrusions that formed during this magma ascent towards the eruption site.

Significant pre-eruptive water level changes were recorded at several monitoring wells around the volcano, as also reported for previous historic eruptions (Yokoyama and Seino, 2000). Matsumoto et al., (2002) describe data recorded at two wells 6.1 and 8.8 km from the summit, respectively (Fig. 7), where water levels increased simultaneously with seismic activity. Starting on 28 March, the more proximal well (DT1) showed a water level increase of 4.07 m, before it began to discharge water at 0.4 m^3/min on 30 March. The total rise is estimated as 9.7 m. The water level at the more distal well (DT2) started to rise on 29 March and increased by 0.95 m. Water levels started to decrease after the first eruption on 31 March.

Matsumoto et al., (2002) have interpreted these changes as poroelastic responses of aquifers to the inflation of a spherical deformation source at sea level, i.e. about 700 m depth beneath the central summit. They suggest a simple analytical deformation model (Mogi, 1958) to explain the observations, but agreement of model predictions and observations, especially at well DT1, is poor.

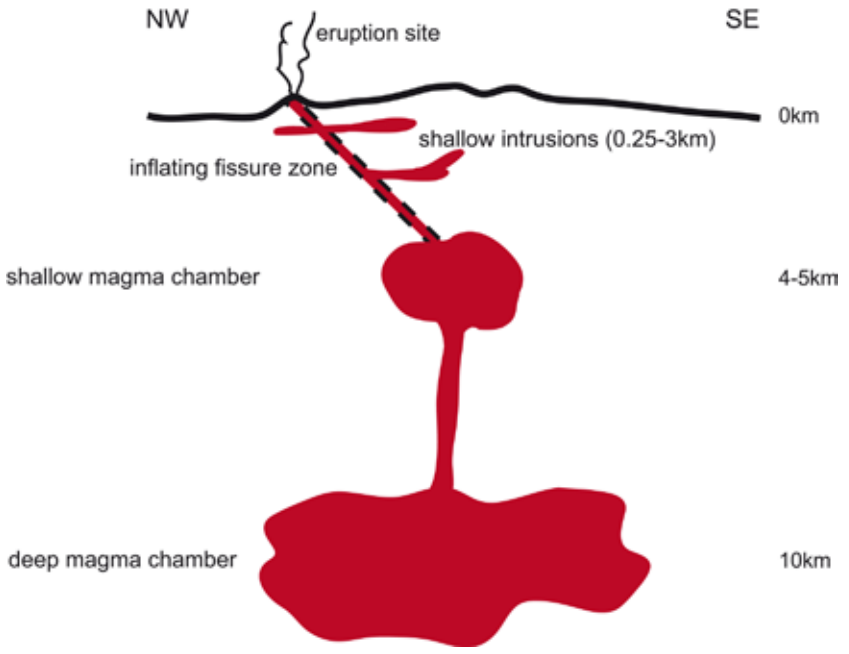

Figure 6. Conceptual model for the magma plumbing system and magma movement at Usu prior to the 2000 eruption, derived from seismic, geodetic and petrological data. Note that, while depths are fairly well constrained, chamber morphologies are not. Modified from Yamamoto et al., (2002).

Figure 7. Map of Usu volcano with locations of wells (DT1 and DT2) and GPS stations (DATE, OHD, UVO, KON). Also indicated are locations of eruption craters during the 2000 eruption.

12. 2.2.1 - Application of developed models to precursory water level changes at Usu volcano

We adapted the model from our generic studies to incorporate available information on aquifer properties, deformation sources and surrounding lithologies at Usu volcano. Starting from the simplest model set-up - a spherical deformation source and a homogeneous aquifer - we iteratively added complexities to fit observations, including varying chamber morphologies and aquifer heterogeneities. To test the applicability of each set-up, we systematically varied parameters and compared model results to the well level changes at DT1 and DT2, as well as displacement recorded at the GPS stations DATE and OHD (Fig. 7), which served as constraints for the desired model results. We focused on changing deformation source properties and flow properties (permeability) of the aquifers.

Our simulations showed that a single deformation source is not sufficient to explain observed aquifer pressure changes - and we tested for a variety of source depths, shapes and strengths. Only the inclusion of a secondary, more shallow-seated source led to the aspired steep lateral gradient in well level changes.

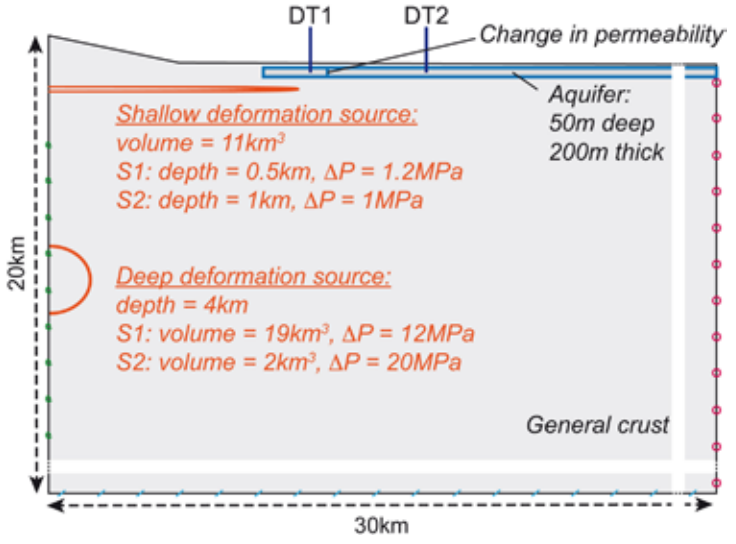

Figure 8. Suggested model set-up that provided simulated hydraulic head changes matching observations. Boundary conditions are as indicated in Fig. 1. A simplified topography of Usu is invoked in the form of a 6km diameter cone with a height of 735m. The shallow deformation source has an aspect ratio of 28, the deep deformation source has an aspect ratio of 2. Two set-ups are suggested as a possible solution, differing in deformation source depths and strengths: S1 stands for solution 1, S2 for solution 2.

We fixed the depth of the deeper deformation source at 4 km, representing the depth of Usu's shallower magma chamber, which is reasonably well constrained. Two preferred model set-ups emerged from parametric sweeps regarding the depth of the secondary, shallower source, source morphologies, volumes and pressurization strengths. Both suggested set-ups (illustrated in Fig. 8)

invoke a shallow-seated oblate deformation source and a deeper-seated almost spherical source (aspect ratio of 2). Additionally, a heterogeneity in aquifer permeability was necessary to satisfactorily fit the data. While both models reproduce observed well level changes prior to the eruption with an excellent fit (Fig. 9a), there is a trade-off between agreement of model results with recorded deformation data at DATE and the agreement with station OHD (Fig. 9b and c).

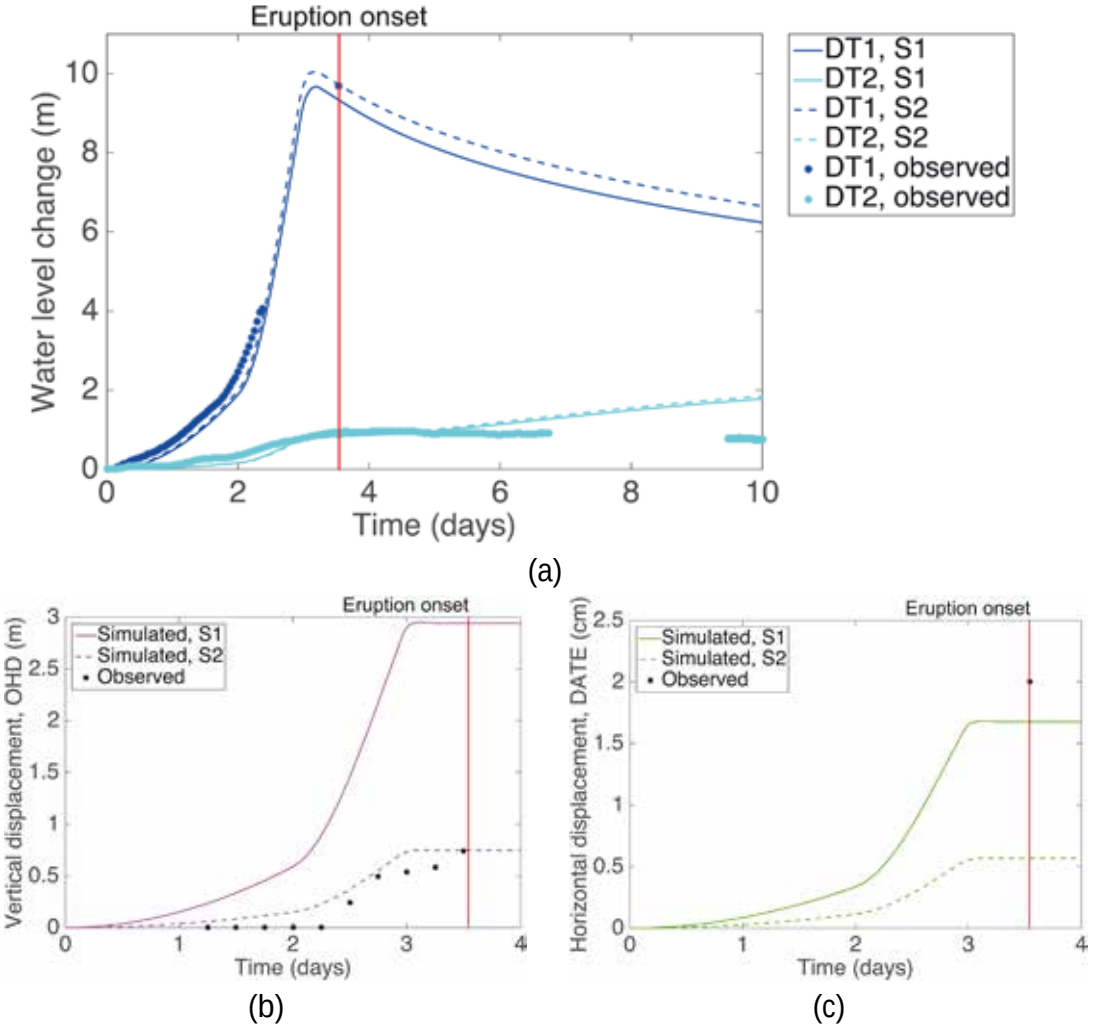

Figure 9. (a) Observed and simulated well level changes, S1 stands for solution 1, S2 for solution 2 (see Fig. 8). (b) Observed and simulated vertical displacement at GPS station OHD. (c) Observed and simulated horizontal displacement at GPS station DATE.

Due to the large number of parameters, this is clearly a non-unique solution, and several simplifying assumptions have been made. These include a simplified topography and an axisymmetric model set-up, which do not represent Usu's architecture accurately and can therefore

lead to errors in the simulated strain distribution. This is the most likely explanation for the apparent inadequacy of our models to explain both proximal and distal ground deformation. However, our results demonstrate that strain caused by inflation of the magma chamber at 4 km depth in combination with a shallow strain modulator can indeed explain the observed well level changes prior to the eruption. In line with results from other studies (Yamamoto et al., 2002; Jousset et al., 2003; Matsubara and Yomogida, 2004; Yamagishi et al., 2004; Tomiya et al., 2010), our simulations suggest that (at least) two deformation sources were active during the unrest just prior to the 2000 eruption. The 2 sources in our preferred model set-ups can be related to pre-eruptive magmatic processes at Usu: The deeper deformation source at 4km depth represents Usu's shallower magma chamber (Fig. 6) that inflated prior to and during the eruption due to an injection of magma from greater depths.

Interpretation of the shallower deformation source is less straightforward. Previous studies employing deformation and gravity data have suggested magmatic intrusions at shallow depths (0.25-2 km and 2-3 km, respectively) as origins for the observed deformation and gravity transients, formed during magma movement from the chamber towards the eruption site (Furuya et al., 2001; Okazaki et al., 2002). However, it has been pointed out by Tomiya et al., (2010) that these magma bodies cannot be large and long-lived but instead solidified quickly after emplacement. The sill suggested by our simulations on the other hand has a volume of 11 km^3 and a lateral extent of about 8 km. We therefore suggest the pressurization of a hydrothermal system as an alternative for a large shallow deformation source. The abundance of water and porous lithologies have favoured the development of hydrothermal systems at Usu volcano in association with its past eruptions (Symonds et al., 1996; Matsushima, 2003). The pressurization of hydrothermal reservoirs can cause significant unrest signals at the surface - including well level changes, changes in fumarolic flux and composition, and crustal deformation - and has been proposed for several volcanic systems (Dzurisin et al., 1994; Montalto, 1996; Gottsmann et al., 2007; Peltier et al., 2009; Chiodini et al., 2011; Capasso et al., 2014). The processes of fluid and heat flow have been extensively modelled in both generic and applied case studies (Delaney, 1982; Hayba and Ingebritsen, 1997; Chiodini et al., 2003; Todesco et al., 2003; Hutnak et al., 2009; Rinaldi et al., 2010; Chiodini et al., 2012; Fournier and Chardot, 2012; Coco et al., 2016). Three possible mechanisms for this hydrothermal pressurization can be envisaged: (i) the injection of magmatic fluids from depth (ii) the intrusion of magma directly into the reservoir and (iii) the perturbation of a hydrological system that is superheated, causing flashing of the pore water. Some supporting evidence can be found in observations during the eruption. A sudden water level increase of more than 100 m 3 days after the eruption at another well (Shibata and Akita, 2001) suggests the existence of highly pressurized water at depth, which was then suddenly released. Low frequency earthquakes have been interpreted as signals of ascending fluids through a crack (Matsubara et al., 2004; Matsubara and Yomogida, 2004). Finally, the intense interaction of ascending magma and water-bodies in the crust, entailing explosive vaporisation of pore water, manifested in phreatic eruptions.

The observed pre-eruptive water level changes at Usu volcano indicated shallow magma movement and possibly the pressurization of a large hydrological system prior to the eruption.

Previous studies on hydrothermal pressurization focused on non-eruptive unrest episodes, but the effects of pre-eruptive magma ascent and degassing on hydrological reservoirs are far from fully understood. Future research efforts invoking larger volumes of involved magmatic fluids, higher heat flow and the possibility of magmatic intrusions into hydrothermal reservoirs will improve our understanding of magma-water interactions and associated monitoring signals in the forerun of eruptions.

Knowledge on subsurface magmatic processes is important for eruption forecasting. Therefore, we propose that the monitoring of well water levels could provide valuable additional data for routine volcano monitoring. This case study underlines that overly simplified deformation models are inadequate to interpret water level changes, but shows that coupling of fluid and solid mechanics provides plausible explanations for the observed geodetic and hydrological time series at Usu volcano. The presented models are superior to models based on overly simplistic assumptions on reservoir shapes and crustal mechanics and represent the next step towards the interpretations of well data as part of volcano monitoring.

12. 3 **- Hazards: The statistics of phreatic eruptions at Ruapehu Crater Lake, New Zealand (reproduced from Strehlow et al., 2017)**

Phreatic eruptions are caused by the explosive expansion of water, steam and/or other gases and occur at many different volcanoes around the world. Overshadowed by larger magmatic events, they have been comparatively understudied, but recent tragic events at Mayon in 2013 (Philippines, 5 casualties) and Ontake in 2014 (Japan, 57 casualties) demonstrate that the impact of localised phreatic eruptions at frequently visited, apparently quiescent, volcanoes is not to be underestimated by the authorities. Despite their relatively small explosive magnitude, phreatic eruptions still pose a serious hazard, especially to people in the proximity of the crater. Hazards include ballistics, pressure waves, surges and lahars (e.g. Neri et al., 1999; Le Guern et al., 1980). A particular threat lies in the difficulty to identify the commonly very short-lived and highly localised precursors that makes forecasting steam-driven explosions very challenging.

The active stratovolcano Ruapehu in New Zealand hosts a hot acidic crater lake covering an active hydrothermal system that is origin of frequent phreatic explosions (Kilgour et al., 2014); 270 phreatic eruptions have been recorded since 1940. We investigated its detailed eruption catalogue (Scott, 2013), which offers an exceptional opportunity to study the statistics of recurring phreatic events. This can unravel possible statistical patterns in phreatic explosion occurrence and support the assessment of risk to people in the summit area, which is frequently visited by hikers.

12. 3.1 **- Results of the statistical analysis**

The phreatic explosions are not evenly distributed in time - there are periods of increased activity and periods of relative quiescence (Fig. 10a). The known magmatic phases are preceded by an increase in phreatic activity. Averaging eruption frequency over the whole time span from 1940 until January 2016, the overall probability for an eruption to occur within the next month is 10%. However, there are periods with a higher eruption frequency than others. Periods 2, 3 and 4 as

indicated in Fig. 10a precede magmatic phases and show a significantly higher relative occurrence of months with eruptions of 31, 32 and 17%, respectively. For comparison, period 1 - between July 1946 and March 1966 - has an eruption frequency of only 6%. In the time since the last magmatic phase in 1997, the average eruption occurrence has been even lower: 3%.

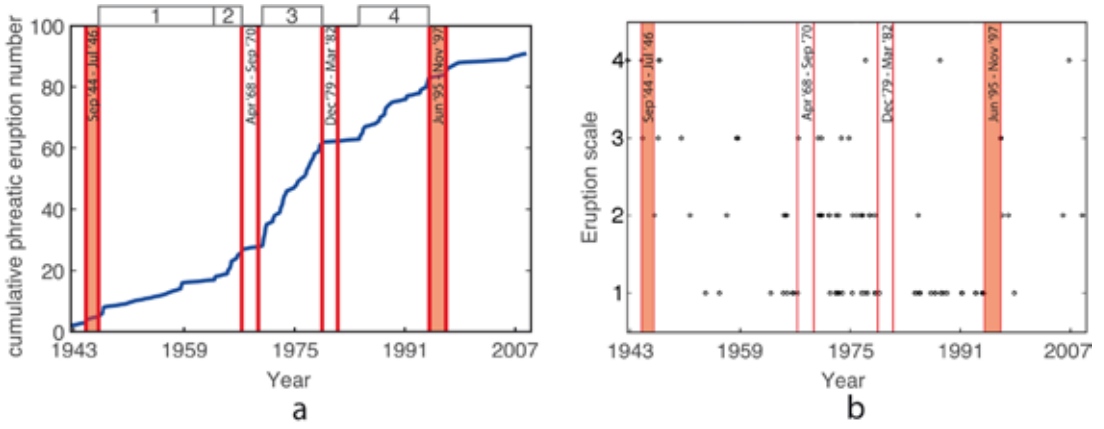

Figure 10. (a) Cumulative number of phreatic eruptions with time. Since we only considered the phreatic sub-dataset and magmatic eruptions could have occurred in gaps of phreatic activity, we cross-checked for magmatic eruptions in the original catalogue during longer periods of phreatic quiescence. Red vertical lines indicate periods of magmatic episodes during phreatic quiescence; red boxes indicate major magmatic episodes as identified by Scott (2013). Labelled grey boxes at the top indicate periods 1-4 with different explosion frequencies as discussed in the text. (b) Phreatic eruptions of different scales over time.

Phreatic eruptions at Ruapehu are classified into 4 scales, depending on the area covered by eruption deposits (Scott, 2013). Smaller-scale eruptions occur more frequently than larger ones (Fig. 10b). However, no statistical significant relationship between inter-eruption time (IET) and eruption size can be proven.

The average IET is 9 months, with a standard deviation σ of 14 months. Therefore, the coefficient of variation (Cox and Lewis, 1966) is CV = σ/IET = 1.6. This value is a good indicator of the statistical nature of processes: A Poisson process has a CV value close to one, while CV<<1 indicates that events occur regularly and a value >1 is typical for a clustering process. Therefore, it seems that phreatic eruptions at Ruapehu cluster. A χ^2-test confirms that the phreatic events do not follow a Poisson distribution (p-value of 0.0135).

It has previously been suggested that phreatic eruptions at Ruapehu correlate with lake temperatures: Ruapehu Crater Lake shows thermal cycling, with temperatures varying irregularly between 10 and 60° C, and increased phreatic and/or phreatomagmatic activity typically coincides with periods of higher lake temperatures (e.g. Christenson and Wood, 1993). The elevated heat flow through the hydrothermal system indicates a more shallow-seated magma source that could enhance eruptive activity. Since 1960, when regular monitoring began, only 3 eruptions have been observed during periods of decreased heat flow. These have been interpreted to result from pressure build up in a sealed hydrothermal system (e.g. Christenson et al., 2010).

To test whether there is a link between lake temperature and phreatic eruptions, we define temperature bins in 5° C intervals and compare the relative frequency of pre-phreatic eruption temperatures to a baseline dataset (Fig. 11). There is a wide range of pre-eruptive temperatures, but the mean pre-eruption temperature is significantly higher than the mean recorded lake temperature, and more than half of the eruptions follow lake temperatures higher than 40° C (Fig. 11b). This is in line with findings of previous studies (e.g. Hurst, 1981). While there might be some sampling bias, this supports the theory that phreatic explosions are more frequent during periods of a shallower seated magma - which is consistent with an increased frequency prior to (or indeed within) magmatic phases. The differing heat input from the magma column at depth is a possible reason for the clustering of phreatic explosions.

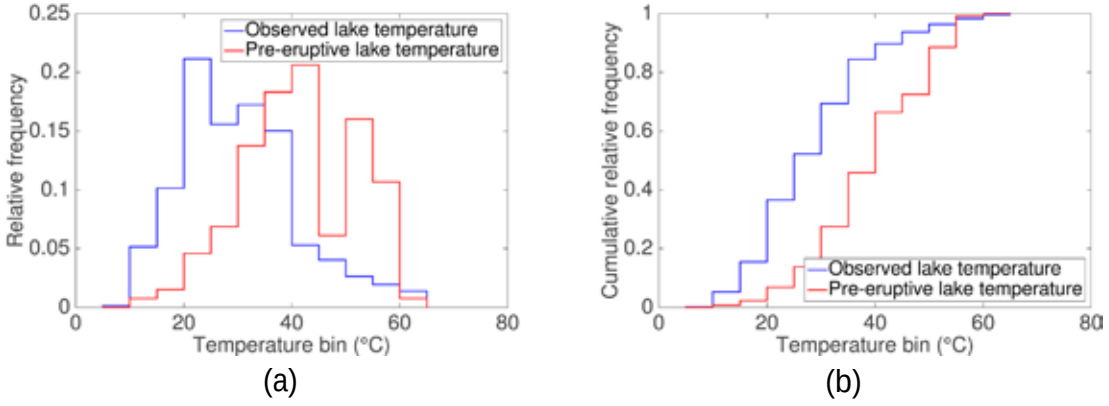

Figure 11. (a) Relative frequencies and (b) cumulative frequencies of observed lake temperature in comparison to pre-eruptive lake temperatures. Temperatures were measured irregularly. The baseline dataset includes a temperature for each day where data are available. The pre-eruption dataset includes the final temperature measured before each phreatic eruption as long as the measurement was less than 2 weeks before the eruption.

12. 3.2 - Probabilistic hazard assessment for phreatic eruptions at Ruapehu volcano

Following the statistical analysis, we performed a probabilistic assessment of the hazard due to ballistic ejecta (with a clast diameter >20 cm) in the summit area of Ruapehu using PyBetVH (Tonini et al., 2015), a Bayesian event tree model for long-term probabilistic volcanic hazard assessment. Prior knowledge (e.g. model results or a priori beliefs) are combined with frequencies from the catalogue and the procedure accounts for both the aleatoric and epistemic uncertainty. To gain prior knowledge on the ballistic hazard, we developed a MATLAB® procedure, which generates a large number of random input parameters for ballistic flightpaths, calculates the respective ballistic trajectories and thereby derives a probability density function for impact densities for the different areas on the summit. It takes into account Ruapehu's topography as well as the existence of 2 vents that show differing eruptive behaviour. The simulated mean impact densities vary with distance from the crater as well as the cardinal direction - being substantially greater on the northern side of

the lake - due to the varying topography of the summit and the influence of the northern vent that produces directed blasts.

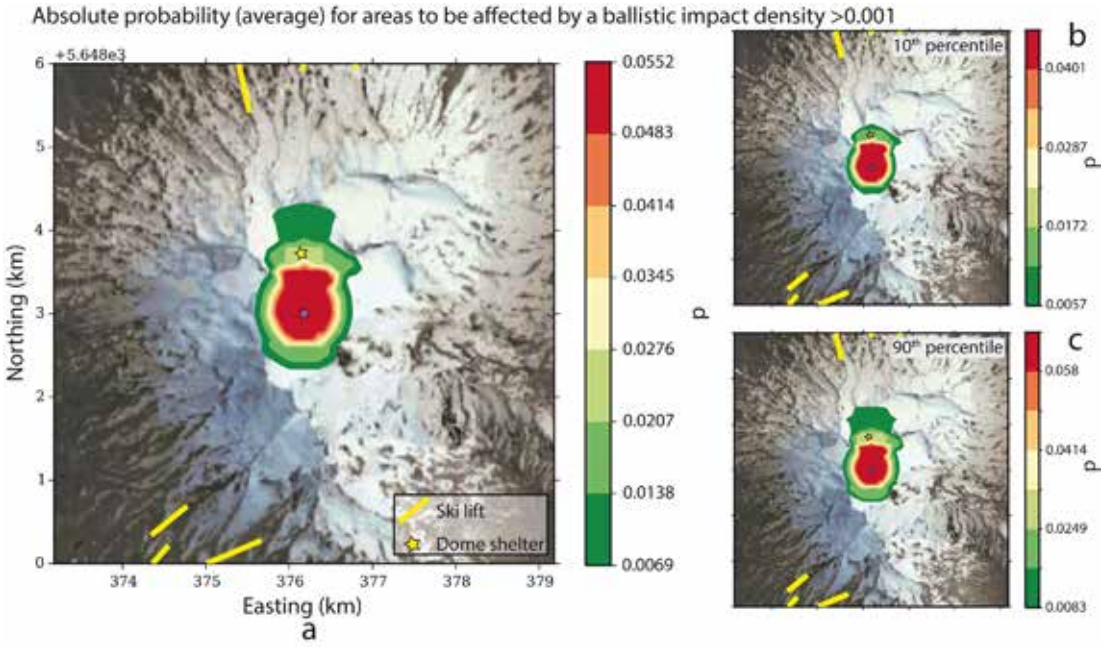

Figure 12. Absolute probability for areas to be affected by a ballistic impact density F > 0.001 within the next month, (a) average, (b), (c): 10th and 90th percentile, respectively.

The absolute probability for areas to be affected by ballistics (with an impact density >0.001 clasts per m^2) within the next month is larger than 1% up to 900 m away from the lake centre on the northern shore, and up to 500 m away on the other shores (Fig. 12). It increases to about 6% closer to the lake. Figure 13 shows hazard maps for the ballistic impact density conditional to the occurrence of an eruption of scale 2, 3 and 4, respectively (eruptions of scale 1 do not produce ballistics beyond the lake shore). These maps give the ballistic impact density expected to be exceeded during an eruption in 1% of the cases. Most significant is the extended hazardous area on the northern shore for eruptions of scale 4, where, in 1% of the cases, the impact density exceeds 0.01 clasts/m^2 up to 2 km away from the vent. This impact density roughly corresponds to a 10% chance of a person present on the summit being hit by a ballistic large enough to cause injury. The maps also indicate infrastructures on the summit, which are likely whereabouts of people and can be damaged by ballistics. The location of the dome shelter is within the most hazardous area for scale 3 and 4 eruptions; ballistics of a scale 4 eruption can even reach ski lifts on Ruapehu's northern flank.

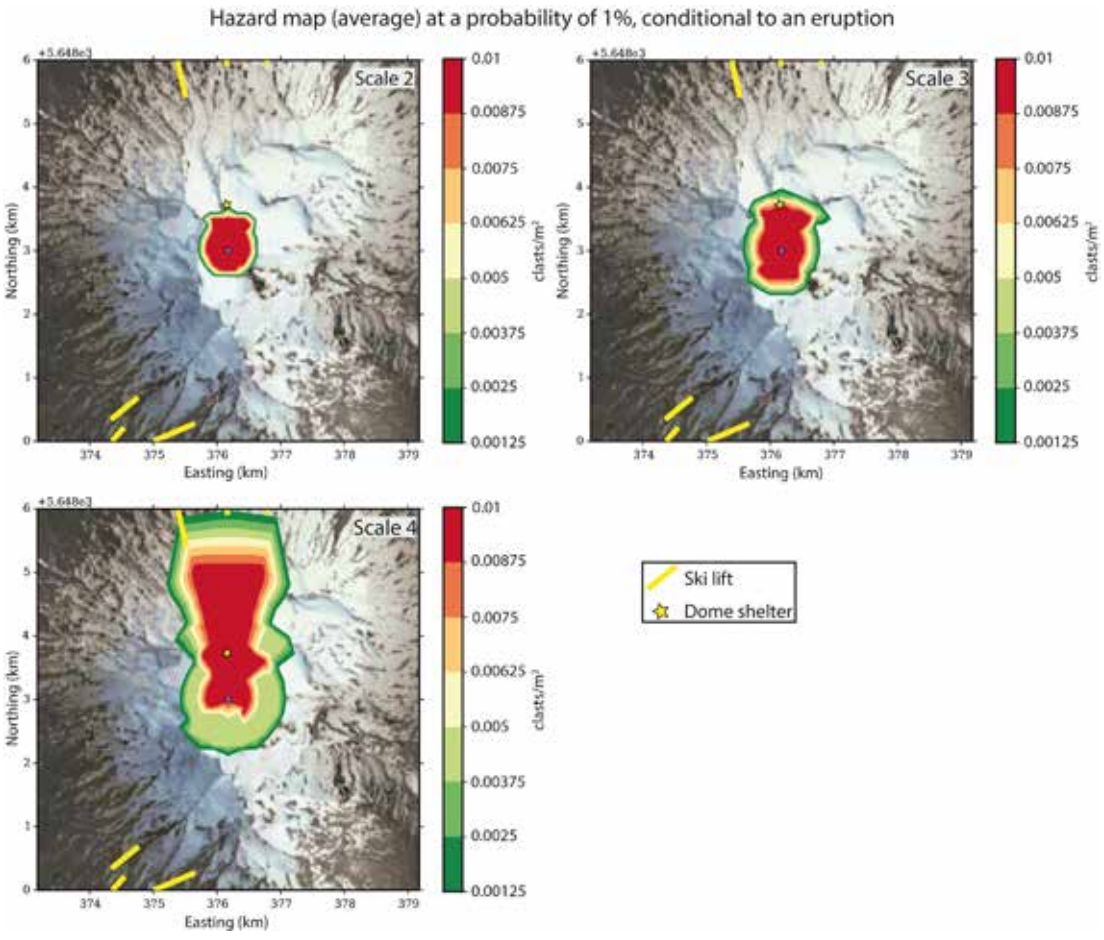

Figure 13. Hazard maps for the ballistic impact density at an exceedance probability of 1%, conditional to a phreatic eruption of scale 2, 3 or 4, respectively.

12. 3.3 **- Implications of the statistical study at Ruapehu volcano**

The presented insight into the statistics of phreatic events can raise awareness of the everyday threat posed by steam-driven explosions, which often occur without any precursors or warning time. In particular, they support the local hazard assessment at Ruapehu. Clustering of events implies that one can expect more phreatic explosions to follow once the system is reactivated. Since shorter IET are generally more likely than longer periods of quiescence, this also suggests that a bigger phreatic event is more likely within a few years after a phreatic explosion than during a prolonged quiet phase of the volcano. While Ruapehu currently seems to be in a quiet phase, a magmatic phase is likely to be preceded by an increase in phreatic activity - an up to 10-fold increase in explosion frequency has been recorded in the past.

At any time, there is a non-negligible probability for the summit area to be affected by ballistics. Conditional to a phreatic eruption, large areas are likely to experience an impact density sufficient to

threaten people present on the summit. Generally, there is a higher hazard on the northern shore of the lake - which is important, because the dome shelter on the summit is built there. While ski lifts are only mildly threatened by ballistics from a scale 4 eruption, the dome shelter lies within the most hazardous zone for scale 3 and 4 eruptions and there is an absolute probability of more than 2% that the shelter is affected by ballistics within the next month. However, our hazard and probability maps show that the hazard due to ballistic ejecta is mostly constrained to a ring of a few hundred metres around the crater lake - at least on the eastern and western lake shore. If a precursory signal for a phreatic explosion is identified, even a short warning time could therefore be sufficient to relocate to safer areas.

12. 4 - Overall conclusions and outlook

The manifold interactions of hydrological and magmatic systems result in a plethora of phenomena, most of which are still poorly understood. Some of these phenomena can be beneficial for society, because they produce observable hydrological signals that precede eruptions and can therefore serve as a warning. Aquifers modulate the signals of monitoring systems such as the recording of ground deformation, and also generate unrest on their own. The ultimate goal of volcano monitoring - to forecast volcanic eruptions - can only be achieved if we correctly interpret the recorded signals. To make accurate inferences about the state of the volcano we therefore need to improve our understanding of how volcanic unrest is generated - an inherently non-unique process - and how signals are altered on their way through the crust. This NEMOH project focused on one of these potentially beneficial hydrological signals: strain-induced water level changes. Our models explain recorded well level changes and can be used to infer underlying magmatic processes, as shown by the Usu case study. Many cases of reported or suggested water level changes remain to be investigated, for example at Hekla volcano (Stefanie Hautmann, pers. comm.), Krafla volcano (Stefansson, 1981) or Kilauea (Dvorak, 1992). But more importantly, our models can improve the inversion of future well level signals recorded at active volcanoes and thereby could assist in eruption forecasting. A challenge for future research will be to couple the poroelastic models with additional processes that affect the hydrology at volcanoes, such as hydrothermal fluid injections or increased conductive heat flow following dike intrusions. Furthermore, there are still a variety of hydrological unrest signals that require more in-depth investigation. These include water temperature and composition changes, hydrologically altered seismic and gas chemistry signals as well as hydrologically induced ground deformation and gravity transients.

The second focus of this NEMOH project was on phreatic eruptions, which have recently attracted attention through events at Mayon (2013) and Ontake (2014). In both cases, an unexpected phreatic explosion was fatal for hikers on the slopes of the volcano, leading to the death of 5 and 57 people, respectively. Especially Ontake is a popular tourist attraction and normally assumed to be safe. The results shed some light on the underlying statistics of recurring phreatic explosions at a hydrothermal system and our generated hazard maps contribute to local hazard assessment. Our statistical approach hopefully contributes to a change in the perception of risk due to steam-driven explosions and prompts similar studies for other volcanoes.

Acknowledgements

The research leading to these results has received funding from the European Union Seventh Framework Programme (FP7/2007-2013) under the project NEMOH, grant agreement n° 289976.

References

Bonaccorso, A., Calvari, S., Linde, A., Sacks, S. and Boschi, E. (2012). Dynamics of the shallow plumbing system investigated from borehole strainmeters and cameras during the 15 March, 2007 Vulcanian paroxysm at Stromboli volcano. Earth Planet Sc Lett, 357-358:249–256.

Capasso, G., Federico, C., Madonia, P. and Paonita, A. (2014). Response of the shallow aquifer of the volcano-hydrothermalsystem during therecent crises at Vulcano Island (Aeolian Archipelago, Italy). J Volcanol Geoth Res, 273:70–80.

Chiodini, G., Avino, R., Caliro, S. and Minopoli, C. (2011). Temperature and pressure gas geoindicators at the Solfatara fumaroles Campi Flegrei. Annals of Geophysics, 54(2):doi: 10.4401/ag– 5002.

Chiodini, G., Caliro, S., De Martino, P., Avino, R. and Gherardi, F. (2012). Early signals of new volcanic unrest at Campi Flegrei caldera? Insights from geochemical data and physical simulations. Geology, 40(10):943–946.

Chiodini, G., Todesco, M., Caliro, S., Del Gaudio, C., Macedonio, G. and Russo, M. (2003). Magma degassing as a trigger of bradyseismic events: The case of Phlegrean Fields, Italy. Geophys Res Lett, 30(8):doi:10.1029/2002GL016790.

Christenson, B., Reyes, A., Young, R., Moebis, A., Sherburn, S., Cole-Baker, J. and Britten, K. (2010). Cyclic processes and factors leading to phreatic eruption events: Insights from the 25 September 2007 eruption through Ruapehu Crater Lake, New Zealand. J Volcanol Geoth Res, 191:15–32.

Christenson, B and Wood, C. (1993). Evolution of a vent-hosted hydrothermal system beneath Ruapehu Crater Lake, New Zealand. B Volcanol, 55:547–565.

Coco, A., Gottsmann, J., Whitaker, F., Rust, A., Currenti, G., Jasim, A. and Bunney, S. (2016). Numerical models for ground deformatino and gravity changes during volcanic unrest: simulating the hydrothermal system dynamics of a restless caldera. Solid Earth, 7:557–577.

Cox, D. and Lewis, P. (1966). The Statistical Analysis of Series of Events. Methuen, New York.

Delaney, P. (1982). Rapid Intrusion of Magma Into Wet Rock: Groundwater Flow due to Pore Pressure Increases. J Geophys Res, 87(B9):7739–7756.

Dvorak, J. (1992). Mechanism of explosive eruptions of Kilauea Volcano, Hawaii. B Volcanol, 54:638–645.

Dzurisin, D. (2007). Volcano Deformation. Springer.

Dzurisin, D., Yamashita, K. and Kleinman, J. (1994). Mechanisms of crustal uplift and subsidence at the Yellowstone caldera, Wyoming. Bull Volcanol, 56:261–270.

Folch, A. and Gottsmann, J. (2006). Faults and ground uplift at active calderas. Geol Soc Lond Spec Publ, 269:109–120.

Fournier, N. and Chardot, L. (2012). Understanding volcano hydrothermal unrest from geodetic observations: Insights from numerical modeling and application to White Island Volcano, New Zealand. J Geophys Res -Solid Earth, 117(B11):doi: 10.1029/2012JB009469.

Furuya, M., Ohki, Y., Okubo, S., Maekawa, T., Oshima, H. and Shimizu, H. (2001). Urgent gravity measurements for the eruption of Usu volcano in 2000 -Construction of absolute gravity network and the co-eruptive and post-eruptive gravity changes. Bulletin of the Earthquake Research Institue, University of Tokyo, 76:237–246.

Geyer, A. and Gottsmann, J. (2010). The influence of mechanical stiffness on caldera deformation and implications for the 1971-1984 Rabaul uplift (Papua New Guinea). Tectonophysics, 483:399– 412.

Gottsmann, J., Carniel, R., Coppo, N., Wooller, L., Hautmann, S. and Rymer, H. (2007). Oscillations in hydrothermal systems as a source of periodic unrest at caldera volcanoes: Multiparameter insights from Nisyros, Greece. Geophys Res Lett, 34(L07307):10.1029/2007GL029594.

Gudmundsson, M., Larsen, G., Höskuldsson, Á. and Gylfason, Á. (2008). Volcanic hazards in Iceland. Jökull, 58:251–268.

Hayba, D. and Ingebritsen, S. (1997). Multiphase groundwater flow near cooling plutons. J Geophys Res, 102(B6):12,235–12,252.

Hurst, A. (1981). Pattern recognition applied to temperature and chemical measurements of Crater Lake, Ruapehu. Technical Report 181, Wellington, Geophysics Division, Dept. of Scientific and Industrial Research.

Hurwitz, S. and Johnston, M. J. (2003). Groundwater level changes in a deep well in response to a magma intrusion event on Kilauea Volcano, Hawai'i. Geophys Res Lett, 30(22):2173.

Hutnak, M., Hurwitz, S., Ingebritsen, S. and Hsieh, P. (2009). Numerical models of caldera deformation: Effects of multiphase and multicomponent hydrothermal fluid flow. J. Geophys. Res. Sol. Ea., 114(B04411).

Jousset, P., Mori, H. and Okada, H. (2003). Elastic models for the magma intrusion associated with the 2000 eruption of Usu Volcano, Hokkaido, Japan. J Volcanol Geoth Res, 125:81–106.

Kilgour, G., Manville, V., Della Pasqua, F., Graettinger, A., Hodgson, K. and Jolly, G. (2010). The 25 September 2007 eruption of Mount Ruapehu, New Zealand: Directed ballistic surtseyan jets, and ice-slurry lahars. J. Volcanol. Geoth. Res., 191:1–14.

Kilgour, G., Saunders, K., Blundy, J., Cashman, K., Scott, B. and Miller, C. (2014). Timescales of magmatic processes at Ruapehu volcano from diffusion chronometry and their comparison to monitoring data. J Volcanol Geoth Res, 288:62–75.

Le Guern, F., Bernard, A. and Chevrier, R. M. (1980). Soufriere of Guadeloupe 1976–1977 eruption—Mass and energy transfer and volcanic health hazards. Bulletin Volcanologique, 43(3):577–593.

Linde, A. T., Sacks, S., Hidayat, D., Voight, B., Clarke, A., Elsworth, D., Mattioli, G., Malin, P., Shalev, E., Sparks, S. and Widiwijayanti, C. (2010). Vulcanian explosion at Soufrière Hills Volcano, Montserrat on March 2004 as revealed by strain data. Geophys Res Lett, 37(L00E07).

Liu, E., Cashman, K., Rust, A. and Gislason, S. (2015). The role of bubbles in generating fine ash during hydromagmatic eruptions. Geology, 43(3):239–242.

Lupi, M., Geiger, S., Carey, R., Thordarson, T. and Houghton, B. (2011). A model for syneruptive groundwater flow during the phreatoplinian phase of the 28–29 March 1875 Askja volcano eruption, Iceland. J Volcanol Geoth Res, 203(3):146–157.

Manconi, A., Walter, T. R. and Amelung, F. (2007). Effects of mechanical layering on volcano deformation. Geophys J Int, 170(2):952–958.

Mastin, L., Christiansen, R., Thornber, C., Lowenstern, J. and Beeson, M. (2004). What makes hydromagmatic eruptions violent? Some insights from the Keanak¯ako'i Ash, K¯ılauea Volcano, Hawai'i. J Volcanol Geoth Res, 137(1):15–31.

Matsubara, W. and Yomogida, K. (2004). Source process of low-frequency earthquakes associated with the 2000 eruption of Mt. Usu. J Volcanol Geoth Res, 134:223–240.

Matsubara, W., Yomogida, K., Koyama, J., Kasahara, M., Ichiyanagi, M., Kawakatsu, H. and Yamamoto, M. (2004). Distribution and characteristics in waveform and spectrum of seismic events associated with the 2000 eruption of Mt. Usu. J Volcanol Geoth Res, 136:141–158.

Matsumoto, A. and Nakagawa, M. (2010). Formation and evolution of silicic magma plumbing system: Petrology of the volcanic rocks of Usu volcano, Hokkaido, Japan. J Volcanol Geoth Res, 196:185–207.

Matsumoto, N., Sato, T., Matsushima, N., Akita, F., Shibata, T. and Suzuki, A. (2002). Hydrological anomalies associated with crustal deformation before the 2000 eruption of Usu volcano, Japan. Geophys Res Lett, 29(5, 1057).

Matsushima, N. (2003). Mathematical simulation of magma-hydrothermal activity associated with the 1977 eruption of Usu volcano. Earth Planets Space, 55:559–568.

Mogi, K. (1958). Relations between the eruptions of various volcanoes and the deformations of the ground surfaces around them. B Earthq Res I Tokyo, 36:99–134.

Montalto, A. (1996). Signs of potential renewal of eruptive activity at La Fossa (Vulcano, Aeolian Islands). Bull Volcanol, 57:483–492.

Neri, A., Macedonio, G. and Gidaspow, D. (1999). Phreatic explosion hazard assessment by numerical simulation. Phys Chem Earth Pt A, 24(11):989–995.

Newhall, C., Albano, S., Matsumoto, N. and Sandoval, T. (2001). Roles of groundwater in volcanic unrest. Journal of the Geological Society of the Philippines, 56:69–84.

Okazaki, N., Takahashi, H., Kasahara, M., Ishimaru, S., Mori, H., Kitagawa, S., Fujiwara, K. and Churei, M. (2002). Crustal deformation associated with the 2000 eruption of Usu volcano as observed by a dense GPS array. Bulletin of the Volcanological Society of Japan, 47:547–557.

Peltier,A., Hurst, T., Scott, B. and Cayol,V.(2009). Structuresinvolvedintheverticaldeformation at Lake Taupo (New Zealand) between 1997 and 2007: New insights from numerical modelling. J Volcanol Geoth Res, 181:173–184.

Rinaldi, A., Todesco, M. and Bonafede, M. (2010). Hydrothermal instability and ground displacement at the Campi Flegrei caldera. Phys. Earth Planet. In., 178:155–161.

Scott, B. (2013). A revised catalogue of Ruapehu volcano eruptive activity: 1830-2012. GNS Science Report 2013/45.

Shibata, T. and Akita, F. (2001). Precursory changes in well water level prior to the March, 2000 eruption of Usu volcano, Japan. Geophys Res Lett, 28(9):1799–1802.

Stefansson, V. (1981). The Krafla geothermal field, in: Geothermal Systems: Principles and Case Histories, pages 273–294. Wiley, New York.

Strehlow, K., Gottsmann, J. and Rust, A. (2015). Poroelastic responses of confined aquifers to subsurface strain and their use for volcano monitoring. Solid Earth, 6:1207–1229.

Strehlow, K., Sandri, L., Gottsmann, J. H., Kilgour, G., Rust, A.C., and Tonini, R. (2017). Phreatic eruptions at crater lakes: Occurrence statistics and probabilistic hazard forecast. Journal of Applied Volcanology, 6:4.

Symonds, R., Mizutani, Y. and Briggs, P. (1996). Long-term geochemical surveillance of fumaroles at Showa-Shinzan dome, Usu volcano, Japan. J Volcanol Geoth Res, 73:177–211.

Tiampo, K. F., Fernández, J., Hayes, T. and Jentzsch, G. (2007). Modeling of Stress Changes at Mayon Volcano, Philippines. Pure and Applied Geophysics, 164(4):819–835.

Tobita, M., Murakami, M., Nakagawa, H., Yarai, H., Fujiwara, S. and Rosen, P. (2001). 3-D surface deformation of the 2000 Usu eruption measured by matching of SAR images. Geophys Res Lett, 28(22):4291–4294.

Todesco, M., Chiodini, G. and Macedonio, G. (2003). Monitoring and modelling hydrothermal fluid emission at La Solfatara (Phlegrean Fields, Italy). An interdisciplinary approach to the study of diffuse degassing. J Volcanol Geoth Res, 125:57–59.

Tomiya, A., Takahashi, E., Furukawa, N. and Toshihiro, S. (2010). Depth and Evolution of a Silicic Magma Chamber: Melting Experiments on a Low-K Rhyolite from Usu Volcano, Japan. J Petrol, 51(6):1333–1354.

Tonini, R., Sandri, L. and Thompson, M. (2015). PyBetVH: A Python tool for probabilistic volcanic hazard assessment and for generation of Bayesian hazard curves and maps. Computers and Geosciences, 79:38–46.

Wang, H. F. (2000). Theory of Poroelasticity with Applications to Geomechanics and Hydrogeology. Princeton University Press.

Yamagishi, H., Watanabe, T. and Yamazaki, F. (2004). Sequence of faulting and deformation during the 2000 eruptions of the Usu Volcano, Hokkaido, Japan -interpretations and image analyses of aerial photographs. Geomorphology, 57:353–365.

Yamamoto, M., Kawakatsu, H., Yomogida, K. and Koyama, J.(2002). Long-period (12sec) volcanic tremor observed at Usu 2000 eruption: Seismological detection of a deep magma plumbing system. Geophys Res Lett, 29(9, 1329):doi: 10.1029/2001GL013996.

Yokoo, A., Taniguchi, H., Goto, A. and Oshima, H. (2002). Energy and depth of Usu 2000 phreatic explosions. Geophys Res Lett, 29(24):doi:10.1029/2002GL015928.

Yokoyama, I. and Seino, M. (2000). Geophysical comparison of the three eruptions in the 20th century of Usu volcano, Japan. Earth Planets Space, 52(2):73–90.

Zobin, V., Nishimura, Y. and Miyamura, J. (2005). The nature of of volcanic earthquake swarm preceding the 2000 flank eruptions at Usu, Hokkaido, Japan. Geophys J Int, 163:265–275.

Karen Strehlow, Germany

kstrehlow@geomar.de

Affiliation under NEMOH
School of Earth Sciences, University of Bristol, Bristol, United Kingdom

Research theme under NEMOH
Aquifers in volcanic regions: Monitoring capabilities and hazards

Through my undergraduate studies at the University of Kiel (Germany), I have a background in mathematics and geology and enjoy combining the two subjects in quantitative volcanology. My motivations to work in volcanological research include the diversity of this fascinating field, and the hope that, eventually, my investigations will be useful for populations in regions exposed to volcanic risk. My research interests are volcanic hazard and risk assessment, volcano monitoring, eruption forecasting and the numerical modelling of volcanic processes.

Prior to NEMOH, I performed research for my diploma thesis at the GEOMAR Helmholtz Centre for Ocean Research Kiel. This provided me with experience in volcanological fieldwork, as well as granulometric and petrological methods for the study of eruptions. Thanks to NEMOH, I was able to join one of Europe's most accomplished research groups in quantitative volcanology to do my PhD and widen my skill set significantly. In Bristol, I performed extensive generic as well as volcano-specific studies on pre- and syneruptive water level changes. These studies were done with numerical models that simulate volcanic strain changes and resulting hydrological responses.

One of the best aspects of being a NEMOH fellow is the possibility for international collaboration and I highly benefited from the local expertise at my secondment institutions. I had the opportunity to investigate hydrothermal systems and phreatic eruption deposits on-site during my secondment in Iceland. A different approach to study phreatic explosions was applied for my research at INGV Bologna, where I studied the occurrence statistics of these events at volcanic crater lakes and performed a probabilistic hazard assessment for Ruapehu Volcano (New Zealand).

NEMOH has provided me with a well-rounded skill set, helped me to become an independent researcher and has smoothed my way into academics. In 2016 I started my first postdoctoral position at GEOMAR, where I am doing both research and public relations work in the field of volcanic hazards. Using the network that I was able to build through NEMOH, I am now collaborating on both current and possible future projects with researchers around the world.

Chapter 13

Numerical model for the dynamics of a fluid in deformable domains, with application to magma chamber dynamics

Deepak Garg

Istituto Nazionale di Geo isica e Vulcanologia, Sezione di Pisa, Pisa, Italy

Tutorship: Antonella Longo, Paolo Papale

Istituto Nazionale di Geofisica e Vulcanologia, Sezione di Pisa, Pisa, Italy

Abstract

This paper presents the space-time finite element formulation of the Navier-Stokes equations for 2D deforming domain problems. The governing fluid equations are transformed in pressure primitive variables which are valid to compute both compressible and incompressible flows. In order to compute the deformation of internal mesh nodes subject to given boundary conditions, elastic deformation technique is incorporated. Both systems of equations are solved separately and the algorithm employed to couple the two systems is reported. Flow around a moving cylinder at Re 40 and a broken dam are chosen as test cases for comparison and validation of the deforming domain flow model. Afterwards, the proposed numerical model is applied to a volcanic application to obtain the preliminary results of magma chamber dynamics when the chamber is shaken by a near-field earthquake.

Keywords: Finite element method, numerical modelling, volcano, magma dynamics, earthquake

13. 1 - Introduction

Flows with free surfaces and moving interfaces find a wide range of applications in many interdisciplinary fields. Fluid dynamics in deforming domains allows the computation of several complex problems. In particular, it allows the application to the natural case of a magma chamber shaken by a near-field seismic wave. This is a relevant issue in volcanology since the relation between the impinging of an earthquake on a magma chamber and the induced magma dynamics that can trigger an eruption is still an open problem. Earthquakes and volcanic eruptions are two phenomena which usually occur at the meeting boundary of converging and diverging tectonic plates. Seismic swarms are often observed in proximity to active volcanoes. This indicates that the seismic signals observed by monitoring networks at the surface of volcanoes can be directly related to the motion of magma taking place somewhere underneath. Several models have been developed in the recent past to study the deformation induced by the magma dynamics (Battaglia et al., 2013, Currenti et al., 2010). Mogi's magma intrusion model is one of the most widely used to predict the observed deformation of active volcanoes (Bonafede et al., 2009). The model simulates a small

spherical expansion source embedded in a homogeneous, isotropic, solid half-space. Further studies and the development of new models aimed at depicting the accurate deformation and strain as a result of applied magmatic forces are still an active area of research. Conversely, the impact of near-field earthquakes on the magma dynamics has not been explored in detail. It is thought that there is not much impact of the former event on the latter. Nevertheless, there have been a few studies in which a large-scale change in magma dynamics induced by seismic waves, even triggering an eruption in some cases, has been proposed. During his journey in Chile when an 8.5 magnitude earthquake struck in 1835, Charles Darwin reported that at least three volcanoes erupted there in the aftermath of the quake (Lomnitz 2004). The most unambiguous case of triggering is the November 29, 1975, magnitude 7.2 Kalapana, Hawai earthquake, which was immediately followed by a small and short-lived eruption at Kilauea volcano, Hawaii (Jachens et al., 1980). Another example of possible triggering occurred after the 9.5 magnitude earthquake on May 22, 1960, in Chile. Puyehue-Cordn Caulle in Central Chile, an inactive volcano for more than 25 years, erupted violently about 38 hours after the main shock (Lara et al., 2004). On the contrary, there are also a number of cases where no eruption was recorded after a proximal earthquake. Chile 2010 is one among these examples in which no activity was observed after a magnitude of 8.8 earthquake struck (Lay et al., 2010). Another case occurred in Japan where a magnitude 9.0 earthquake struck in 2011, resulting in no eruption (Shinji et al., 2011).

Although no eruption occurred in these cases, understanding the internal dynamics is crucial from a possible hazard point of view. High amplitude seismic waves passing through a magma reservoir may destabilise the system which was in a state of a semi-equilibrium prior to the arrival of seismic wave. The destabilisation can help the mingling/mixing of stable layers of magmas, with different composition, and can result in giving momentum to the dynamics. The objective of this work is to study this phenomenon by means of numerical modelling as well as to examine the scenario of development of magma dynamics. The article is structured as follows. We begin with the description of the physical model followed by the details of the numerical method used to solve the mathematical equations. The numerical model and the associated code are validated on selected benchmark cases and are applied on a volcanic test case. We present and discuss the preliminary results obtained from the simulation and finally draw the conclusions.

13. 2 - **Physical model**

Magma is a complex chemical fluid mixture of oxides and volatiles. Depending on the gas content and local velocity, magma can be compressible or incompressible at the same time, in different parts of the domain. In order to depict this variable behaviour, physical and mathematical models should be able to work for both compressible and incompressible regimes. For this purpose, the compressible Navier-Stokes equations are considered which also work in the incompressibility limit.

The governing equations for compressible fluid flow, along with specified Dirichlet and Newmann boundary conditions, can be written in the compact form as follows:

$$\boldsymbol{U}_{,t} + \boldsymbol{F}^a_{i,i} = \boldsymbol{F}^d_{i,i} + \boldsymbol{S} \qquad \text{on } \ \Omega \subset \mathbb{R}^n,\ t > 0 \qquad \text{(Equation 13.1)}$$

$$\boldsymbol{U} = \boldsymbol{U}_g \qquad \text{on } \ \Gamma^g,\ t > 0$$

$$(\boldsymbol{F}^a_i + \boldsymbol{F}^d_i) \cdot \boldsymbol{n}_i = \boldsymbol{h} \qquad \text{on } \ \Gamma^h,\ t > 0$$

where $()_{,t}$ denotes the Eulerian time derivative, Ω is the spatial domain in n dimensions and $\boldsymbol{U} = \rho[y_k, \boldsymbol{v}, E]$ is the vector of conservation variables. Γ_g is the Dirichlet boundary and $\boldsymbol{U}_g$ is the vector of Dirichlet boundary conditions. $\boldsymbol{F}^a_i$ and $\boldsymbol{F}^d_i$ are respectively the advective and diffusive flux vectors in i^{th} direction and are given by

$$\boldsymbol{F}^a_i = \begin{bmatrix} \rho v_i y_k \\ \rho v_i \boldsymbol{v} + \boldsymbol{\delta_i} p \\ \rho v_i E + v_i p \end{bmatrix} \qquad \boldsymbol{F}^d_i = \begin{bmatrix} J^k_i \\ \boldsymbol{\tau_i} \\ \tau_{ij} v_j - q_i \end{bmatrix}$$

Γ_h is the Neumann boundary and $\boldsymbol{h}$ is the vector of Neumann boundary conditions. $\boldsymbol{n}_i$ is the unit outward normal vector in i^{th} direction. $\boldsymbol{S} = [0, \boldsymbol{b}, b_i v_i + r]$ is the source vector.

The compact form equation 13.1 represent the conservation of mass for each component (two components are considered in this study) and conservation of momentum and energy for the mixture. In the relations ρ is the density; y_k is the weight fraction of k^{th} component; $\boldsymbol{v} = \{v_i\}$is the velocity vector; E is the total energy density; p is the pressure; $\boldsymbol{\delta} = \{\delta_{ij}\}$ is the Kronecker delta; $\boldsymbol{\tau} = \{\tau_{ij}\}$ is the viscous-stress tensor; $\boldsymbol{\delta}_i = \boldsymbol{\delta} \boldsymbol{e}_i$ and $\boldsymbol{\tau}_i = \boldsymbol{\tau} \boldsymbol{e}_i$ where $\boldsymbol{e}_i$ is the unit basis vector in the i^{th} direction; J^k_i is the mass diffusion flux of component k in the i^{th} direction; $\boldsymbol{q} = \{q_i\}$ is the heat-flux vector; $\boldsymbol{b} = \{b_i\}$ is the body force vector per unit mass; r is the heat supply per unit mass; and the summation convention is assumed throughout. The total energy density is the sum of the internal energy e, and the kinetic energy $\boldsymbol{v}^2/2$. The equation of state and relevant constitutive relations between all the thermodynamic quantities such as pressure, Gibbs free energy, chemical potential, enthalpy, temperature, density etc. can be found in appendix A of (Longo et al., 2012).

13. 3 - **Numerical method**

In deforming domain problems, the computational difficulty arises from the changing boundary part. The motion of fluid mechanics domain needs to be accounted for in the differential equations and boundary conditions. This makes our problem two-way, where the second unknown is the motion of fluid domain. A space-time finite element method (ST-FEM) is used to solve the fluid flow equations and in order to move the computational mesh, we use the elastic deformation technique. Both problems are solved iteratively and coupled for each time step with applied boundary conditions. The following algorithm is implemented to couple the systems.

Step 1. Solve the Navier-Stokes equations 13.1 by ST-FEM on a given domain $\Omega(t_n)$ at time t_n. Compute fluid variables pressure, velocities and temperature.

Step 2. Compute the fluid deformation from fluid velocities at moving boundaries. Solve the elastostatic equations passing fluid deformation as boundary conditions and compute the deformation **u** of internal nodes of the mesh.

Step 3. Obtain the new domain $\Omega(t_{n+1}) = \Omega(t_n) + \boldsymbol{u}$.

Step 4. Make the space-time slab (Figure 1) and go to Step 1 with domain $\Omega(t_{n+1})$.

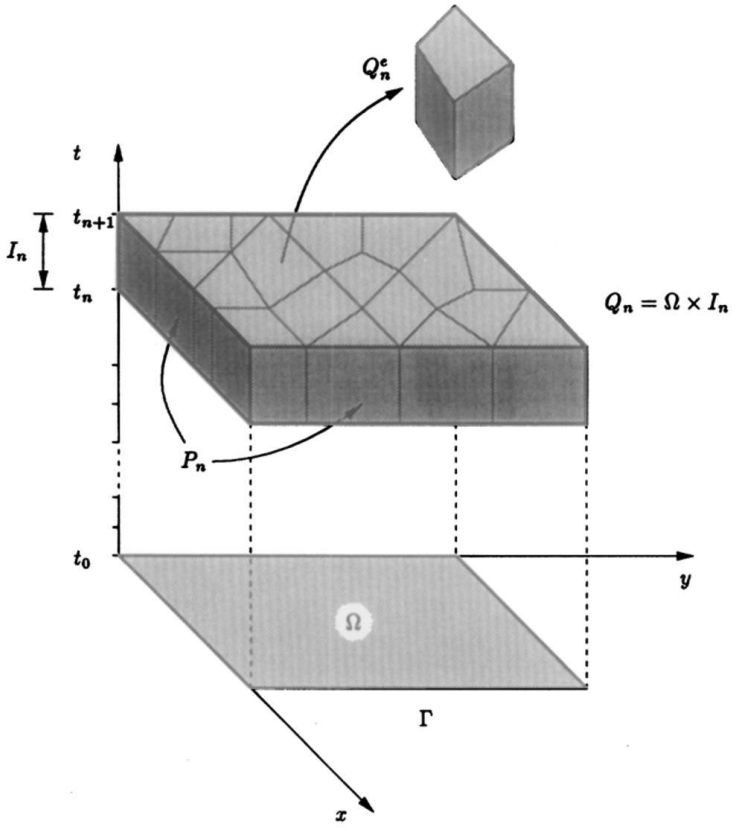

Figure 1. Illustration of space-time domain, slab and an element.

The details of the techniques to solve the fluid and elastostatic equations are given as follows. For the fluid, we start by writing the quasi-linear form of Text in any independent set of variables $\boldsymbol{Y}$. The equations can be written as

$$\boldsymbol{A}_0\boldsymbol{Y}_{,t} + \boldsymbol{A}_i\boldsymbol{Y}_{,i} = (\boldsymbol{K}_{ij}\boldsymbol{Y}_{,j})_{,i} + \boldsymbol{S} \qquad \text{(Equation 13.2)}$$

where $\boldsymbol{A}_0 = \boldsymbol{U}_{,\boldsymbol{Y}}$, $\boldsymbol{A}_i = \boldsymbol{F}^a_{i,\boldsymbol{Y}}$ is the i^{th} Euler Jacobian matrix and $\boldsymbol{K} = [\boldsymbol{K}_{ij}]$ is the diffusivity matrix with $\boldsymbol{K}_{ij}\boldsymbol{Y}_{,j} = \boldsymbol{F}^d_i$. Next step is to formulate the weighted residual formulation of Equation 13.2. For this, we consider a space-time domain $Q = \Omega \times (0, t_{tot})$ with boundary $P = \Gamma \times (0, t_{tot})$, where Ω is the spatial domain with boundary Γ. The time interval $(0, t_{tot})$ is subdivided into N intervals (t_n, t_{n+1}) with $t_0 = 0$ and $n = 0, 1 \cdots, N-1$. For each time interval a space-time slab is defined as $Q_n = \Omega \times (t_n, t_{n+1})$ with boundary $P_n = \Gamma \times (t_n, t_{n+1})$. As displayed in Figure 1, each space-time slab is divided into $(n_{el})_n$ elements Q^e_n with discontinuous basis functions across the slab boundaries in time-direction. The space-time finite element weak formulation of equation equation 13.2 is written as follows: given a trial function space $\boldsymbol{T}^h$ and weighting function space $\boldsymbol{V}^h$, within each Q_n, $\quad n = 0, 1, \cdots N-1$, find $\boldsymbol{Y}^h \in \boldsymbol{T}^h$ such that $\forall\ \boldsymbol{W}^h \in \boldsymbol{V}^h$:

$$\int_{Q_n} \left(-\boldsymbol{W}^h_{,t} \cdot \boldsymbol{U}(\boldsymbol{Y}^h) - \boldsymbol{W}^h_{,i} \cdot \boldsymbol{F}^a_i(\boldsymbol{Y}^h) + \boldsymbol{W}^h_{,i} \cdot \boldsymbol{F}^d_i(\boldsymbol{Y}^h) - \boldsymbol{W}^h \cdot \boldsymbol{S} \right) dQ$$

$$+ \int_{\Omega} \left(\boldsymbol{W}^h(t^-_{n+1}) \cdot \boldsymbol{U}(\boldsymbol{Y}^h(t^-_{n+1})) - \boldsymbol{W}^h(t^+_n) \cdot \boldsymbol{U}(\boldsymbol{Y}^h(t^-_n)) \right) d\Omega$$

$$+ \sum_{e=1}^{(n_{el})_n} \int_{Q^e_n} \boldsymbol{L}^{'} \boldsymbol{W}^h \cdot \boldsymbol{\tau} \left(\boldsymbol{L}\boldsymbol{Y}^h - \boldsymbol{S} \right) dQ + \sum_{e=1}^{(n_{el})_n} \int_{Q^e_n} \nu g^{ij} \boldsymbol{W}^h_{,i} \cdot \boldsymbol{A}_0 \boldsymbol{Y}^h_{,j} dQ$$

$$- \int_{P_n} \boldsymbol{W}^h \cdot \left(-\boldsymbol{F}^a_i(\boldsymbol{Y}^h) + \boldsymbol{F}^d_i(\boldsymbol{Y}^h) \right) \boldsymbol{n}_i \ dP = 0 \qquad \text{(Equation 13.3)}$$

In the above formulation the first and the last integrals are the Galerkin terms obtained by integration of parts and are written as a function of $\boldsymbol{Y}^h$. The second integral is the jump term to enforce continuity of the solution between consecutive slabs wit$t^+ = \lim_{\epsilon \to 0}(t + \epsilon)$h and $t^- = \lim_{\epsilon \to 0}(t - \epsilon)$. The third integral is the least-square stabilisation operator with $\boldsymbol{L} = \boldsymbol{A}_0 \dfrac{\partial}{\partial t} + \boldsymbol{A}_i \dfrac{\partial}{\partial x_i}$ and $\boldsymbol{L}^{'} = \boldsymbol{A}^{'}_0 \dfrac{\partial}{\partial t} + \boldsymbol{A}^{'}_i \dfrac{\partial}{\partial x_i}$, where $\boldsymbol{\tau}$ is the stabilisation matrix. The fourth integral is the discontinuity capturing operator. For compressible flows in the presence of shock waves, it is necessary to add a discontinuity capturing operator as a dissipation mechanism to remove the oscillations present near the sharp boundary layers or internal interfaces.

For the discretization of solution variables the space-time shape functions are assumed constant in time. The trial solution and weighting function are defined as

$$\boldsymbol{Y}^e = \sum_{i=1}^{n_{elnodes}} N_i(x) \boldsymbol{Y}_i(t_n) \qquad\qquad \boldsymbol{W}^e = \sum_{i=1}^{n_{elnodes}} N_i(x) \boldsymbol{W}_i(t_n)$$

where $N_i(x)$, $\boldsymbol{Y}_i$ and $\boldsymbol{W}_i$ are the spatial shape functions, vector of unknowns and weighting functions at node i for space-time element Q_n^e. In case of constant in time, we use the following two identities for each space-time element

$$\int_{Q_n} [..]\ dQ = \Delta t \int_{\Omega} [..]\ d\Omega \qquad\qquad \int_{P_n} [..]\ dP = \Delta t \int_{\Gamma} [..]\ d\Gamma$$

Discretization of model equations results in a system of non-linear equations, which are solved iteratively. For this purpose, a predictor/corrector method of first order is incorporated (Shakib et al., 1991). The non-linear system of equations is linearised by using Taylor series. In the predictor phase, for each time step the unknowns are initialized with the solution obtained at the previous time slab. In the corrector phase, the solution is updated with correction factor computed implicitly. To solve the deformation of interior nodes of the fluid mesh we solve the elastostatic equations of motion. The strong form of boundary value problem is given by

$$\begin{aligned} \boldsymbol{\nabla} \cdot \boldsymbol{\sigma} &= 0 \quad \text{on} \quad \Omega \subset \mathbb{R}^n \\ \boldsymbol{u} &= \boldsymbol{u}_g \quad \text{on} \quad \Gamma_g \\ \boldsymbol{\sigma} \cdot \boldsymbol{n} &= \boldsymbol{h} \quad \text{on} \quad \Gamma_h \end{aligned} \qquad \text{(Equation 13.4)}$$

where $\boldsymbol{\sigma} = \{\sigma_{ij}\} = \lambda u_{k,k} + 2\mu(u_{i,j} + u_{j,i})$ is the stress tensor. λ and μ are the Lamé coefficients. We denote $\boldsymbol{T}^h$ and $\boldsymbol{V}^h$ as trial and weighting function spaces. For a given trial function $\boldsymbol{u}^h \in \boldsymbol{T}^h$ and weighting function $\boldsymbol{w}^h \in \boldsymbol{V}^h$, the weighted residual formulation of equation 13.4 is written as:

$$\int_{\Omega} \boldsymbol{\epsilon}(\boldsymbol{w}) : \boldsymbol{\sigma}(\boldsymbol{u})\ d\Omega = \int_{\Gamma_h} \boldsymbol{w} \cdot \boldsymbol{h}\ d\Gamma \qquad \text{(Equation 13.5)}$$

In the above equation, $\boldsymbol{\epsilon}$ represents the strain, which depends on the gradient of deformation. Discretization of the variables by standard interpolation functions results in a set of linear equations. In order to solve the large sparse systems of linearised equations, a preconditioned block generalised minimal residual (GMRES) solver is applied (Saad et al., 1986). The solution is approximated by building a Krylov search space of 200 basis functions with 5 restarts. The total number of iterations is set to maximum, which is one less than the degrees of freedom. An appropriate preconditioner for the linear system of equations is necessary to accelerate the convergence of the solver. Consequently, incomplete lower and upper triangulation decomposition (ILU) preconditioner is employed, leading to an efficient solution technique for a variety of flow problems.

13. 4 - **Benchmarks**

To show the accuracy and efficiency of the space-time finite element method for deforming domain, we present two model problems here. For the finite element basis functions, we use bilinear functions in space and the linear function in time. The spatial mesh is made from unstructured quadrilateral elements and time slabs are formed simply by moving the spatial mesh in time. As pointed out earlier, to obtain the domain velocity we solve equation Text and compute the velocity at each vertex of the mesh. The velocity of the moving boundary part will be fixed according to the problem of interest. The problems are given below in detail.

13. 4.1 - **Horizontal moving cylinder**

In this problem, the algorithm is tested on a rigidly moving mesh and compared with the problem in which the mesh is stationary but subjected to a uniform flow In this test case a circular cylinder moving at dimensionless Mach number, M = 0.01 and Reynolds number 40 is introduced in a stationary fluid domain at time t = 0. The problem is displayed in Figure 2. The Reynolds number is based on the mean stream density of the fluid and the velocity and diameter of the cylinder. The computational domain covers an area (m^2) $-4.5 \leq x \leq 15.5$ and $-4.5 \leq y \leq 4.5$, with a unit diameter cylinder centred at x = 0 and y = 0. An unstructured mesh comprising 5353 elements is generated. At the right wall, zero pressure is imposed.

We compare the steady-state solution with the steady-state solution of flow past a fixed cylinder at Reynolds number 40. Figure 3 displays the temporal evolution of mesh deformation and streamlines. The pressure and its contours computed at time t = 1 sec are presented in figure 4. It is evident that both solutions are similar.

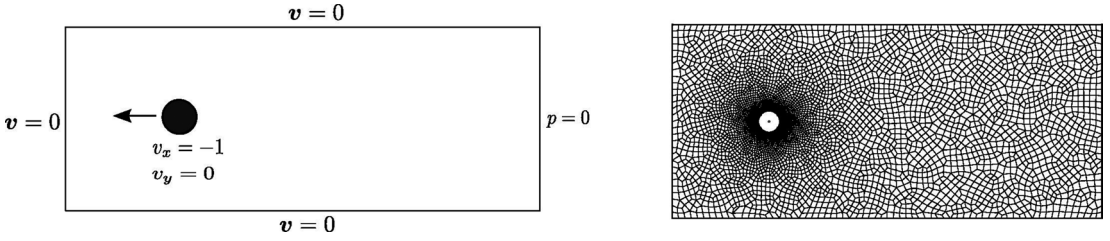

Figure 2. Horizontal moving cylinder: Problem illustration, boundary conditions and the computational mesh.

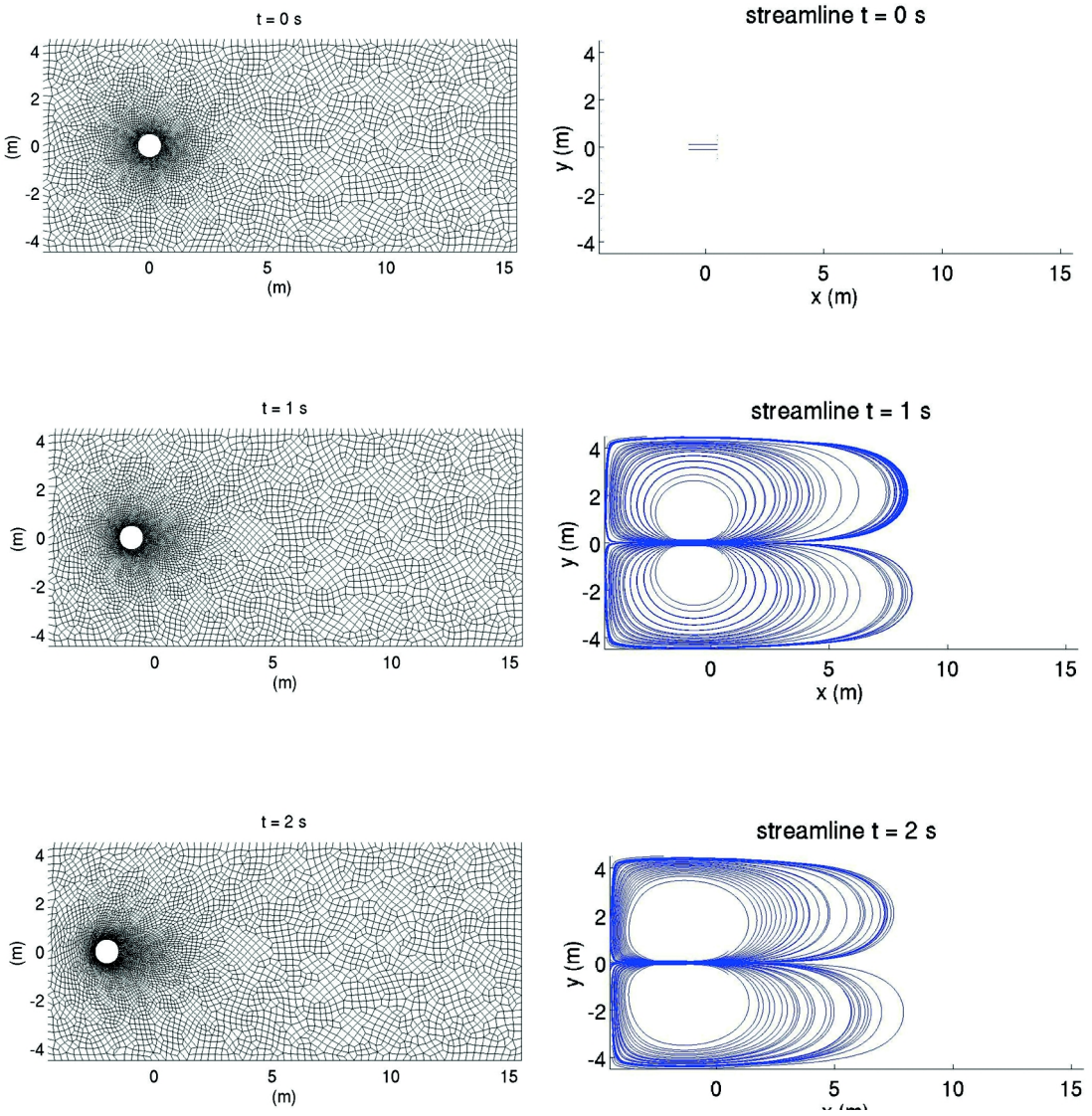

Figure 3. Horizontal moving cylinder: Mesh and streamlines at various times.

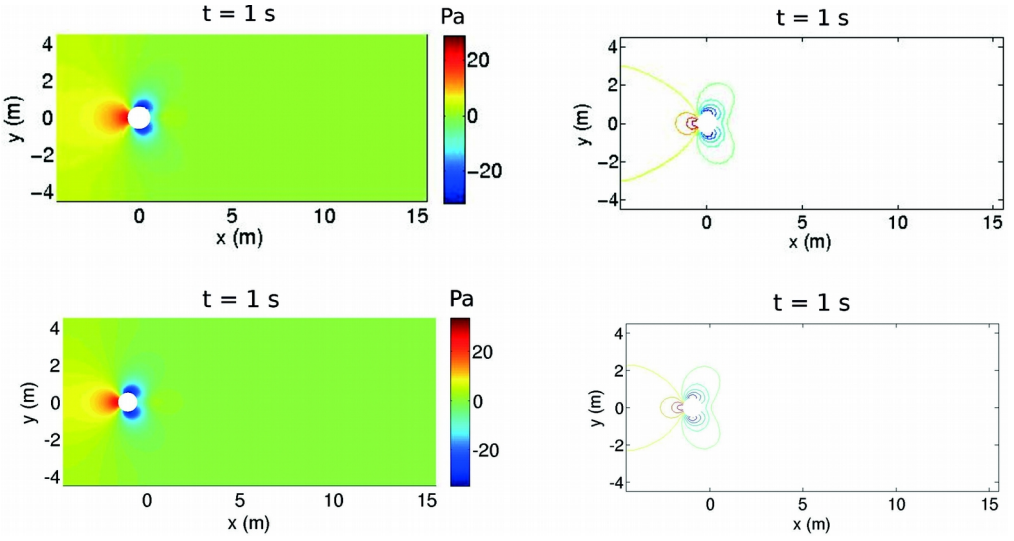

Figure 4. Pressure and pressure-contours at t=1s. The top panel displays the results of the fixed cylinder case and the bottom panel displays the results obtained from the current simulation with moving cylinder case.

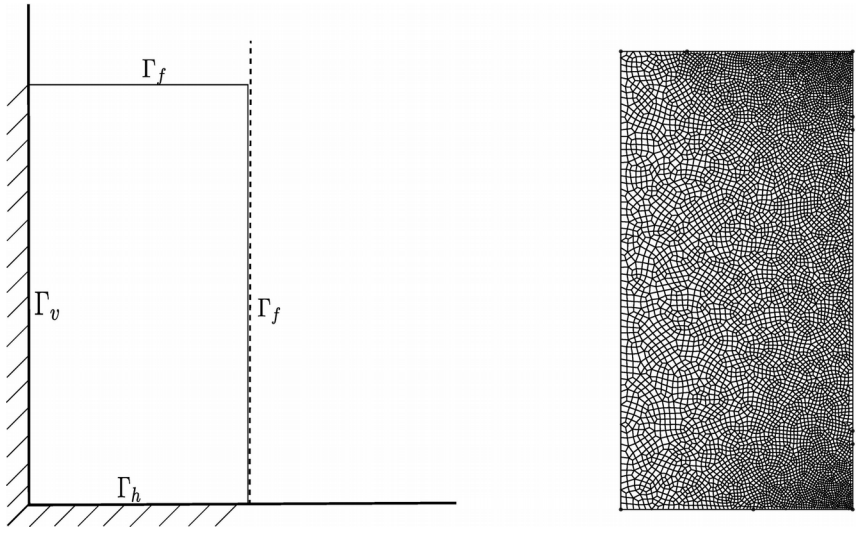

Figure 5. Broken dam: Domain geometry and the computational mesh

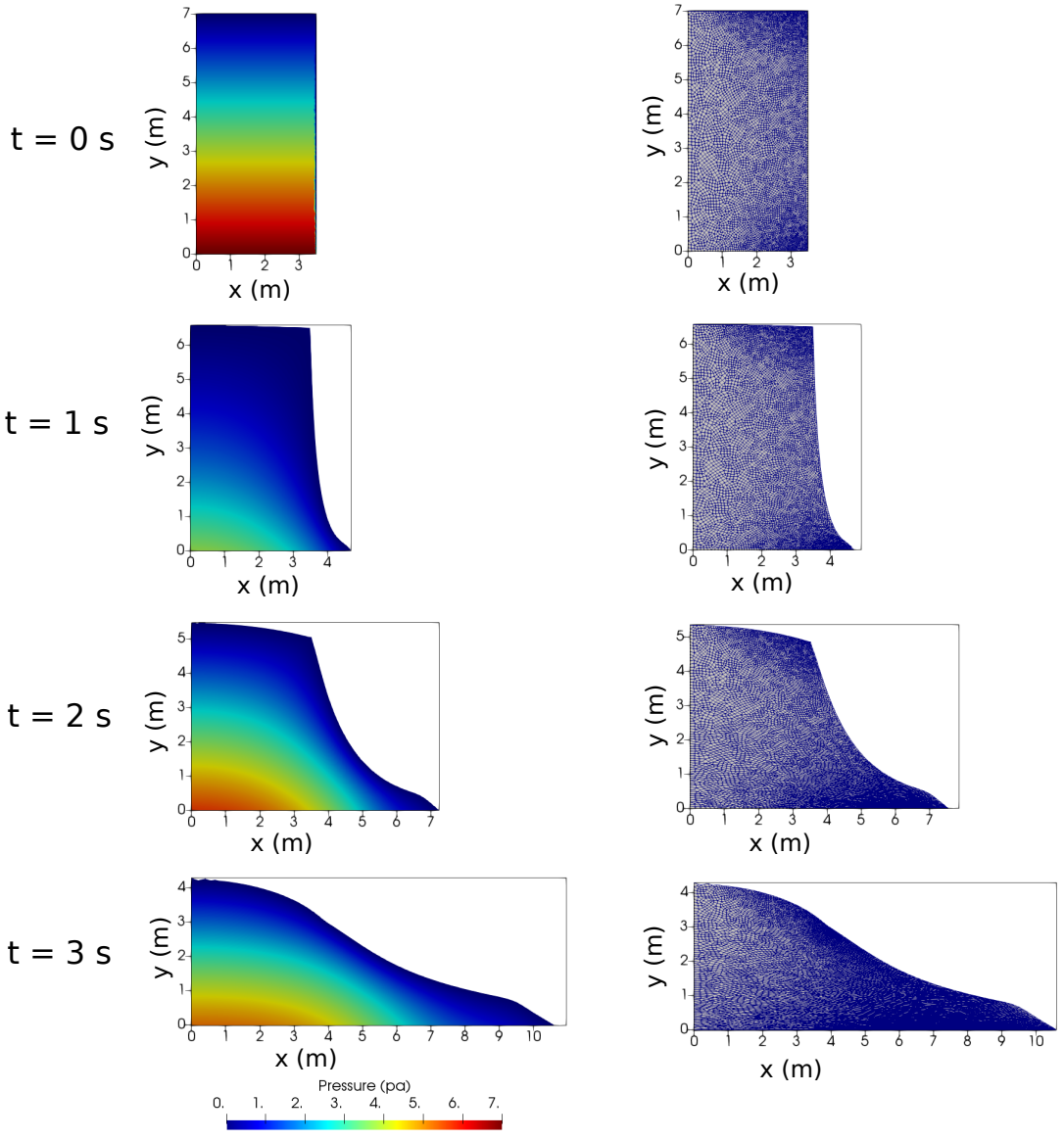

Figure 6. Broken dam: Mesh and pressure (Pa) at the various times.

13. 4.2 **-Broken dam**

Dam break flow problem has been the subject of extensive research for a long time and has direct application in the industrial areas of fluid mechanics and environment protection. In this problem, a block of water is kept at rest in a container in the initial stage using a thin paper film. Instantaneously, at time t = 0, the paper film is removed and the water spreads out under the influence of gravity. The geometry of solution domain is shown in Figure 5. In the Figure, Γ_h and Γ_v represent the horizontal and vertical walls of the container, where the fluid is allowed to slip. Whereas Γ_f represents the free surface boundary of the water column. The base length and height of the block of water are set to 3.5 m and 7 m respectively. The computational mesh used to solve this problem consist 7004 elements and is display in Figure 5. The top-right and bottom-right corners are critical regions where the mesh deforms very rapidly. To keep the mesh in reasonable shape for later time steps and to avoid re-meshing, the initial mesh is constructed by refining both right corners.

The density of water is taken to be ρ = 1 kg/m^3, and the dynamic viscosity is = 0.01 kg/(ms). Gravity is set to 1m/s^2. For the fluid at $\mathbf{\Gamma}_h$ and $\mathbf{\Gamma}_v$ the slip boundary conditions were applied and at free surface $\mathbf{\Gamma}_f$ traction free conditions were prescribed. The latter may be changed to fixed pressure and zero normal gradients of the velocities. For the elastostatic problem, at $\mathbf{\Gamma}_f$ the domain velocity is set equal to fluid velocity. At $\mathbf{\Gamma}_h$ the vertical displacement and at $\mathbf{\Gamma}_v$ the horizontal displacement is set to zero.

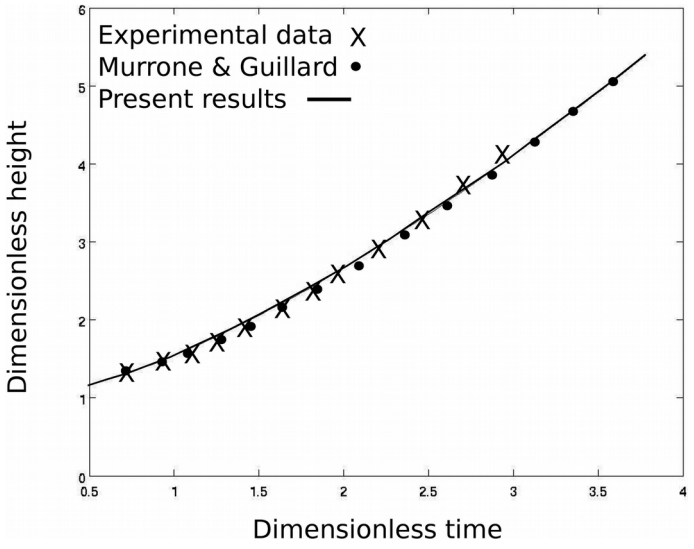

Figure 7. Broken dam: Plot of dimensionless height versus dimensionless time. The comparison of results is done with (Martin et al., 1952) and (Murrone et al., 2005)

The Gravity causes the water column to the left of the reservoir to seek the lowest possible level of potential energy. Thus, the column will collapse and eventually come to rest. The initial stages of the flow are dominated by inertia forces with viscous effects increasing as the water comes to rest. On such a large scale, the effect of surface tension forces is unimportant and therefore not considered in the model. Mesh deformation and pressure obtained at various simulation times are shown in Figure 6. The numerical results were validated by the quantitative comparison with experimental measurements obtained for the early stages of this experiment. The dimensionless position x/L (where L is the initial length of the dam) of the liquid front along the bottom of the cavity, versus the dimensionless time $t\sqrt{2g/L}$ is plotted in Figure 7. The predicted height of water column corresponds very well with experimental measurements (Martin et al., 1952) and numerical results (Murrone et al., 2005).

13. 5 - **Application**

Understanding the current dynamics of magma inside reservoirs is crucial to predicting the future events which can be extremely hazardous in several cases. Even a small eruption can be a potential threat for the people residing in the local area. An earthquake might add significant effect on the evolution of magma dynamics and hence contributes to its state of unrest. In this section, we are presenting a numerical study on the evolution of the magma dynamics when the seismic wave impinges on a magma chamber and compare the results to the case when there is no external disturbance.

13. 5.1 - **Simulation set up**

For this study, we constructed a magmatic system consists of two elliptical shaped magma chambers connected by a straight dike. The magmatic system resembles the magmatic subsurface reservoir at Campi Flegrei. The upper chamber is placed at 3 km depth with the length of major axis 800 m in horizontal direction and length of minor axis 400 m in the vertical direction. The lower chamber is considered much larger than the shallow chamber which is situated at 8 km depth from the surface. The length of the major and minor axis are 8 km and 1 km respectively. The width of the dike joining the shallow and deeper chamber is 20 m. Two different compositions of magma are used to perform the simulation. Magma is considered as a homogeneous multicomponent multiphase Newtonian mixture with exsolution and dissolution of volatiles (H_2O + CO_2). The shallow chamber is filled with degassed phonolite with 1 wt% of H_2O and 0.1 wt% of CO_2. The total gas content present is 1 vol%. The deeper chamber and dike are filled with gas-rich shoshonite with 2 wt% of H_2O and 1 wt % of CO_2, containing total gas content of 4 vol%. A Gravitationally unstable interface between the two magmas is set at 20 m depth in the dike, below the shallow chamber. Domain geometry, computational mesh and employed initial physical characteristics of magmas are displayed in Figure 8.

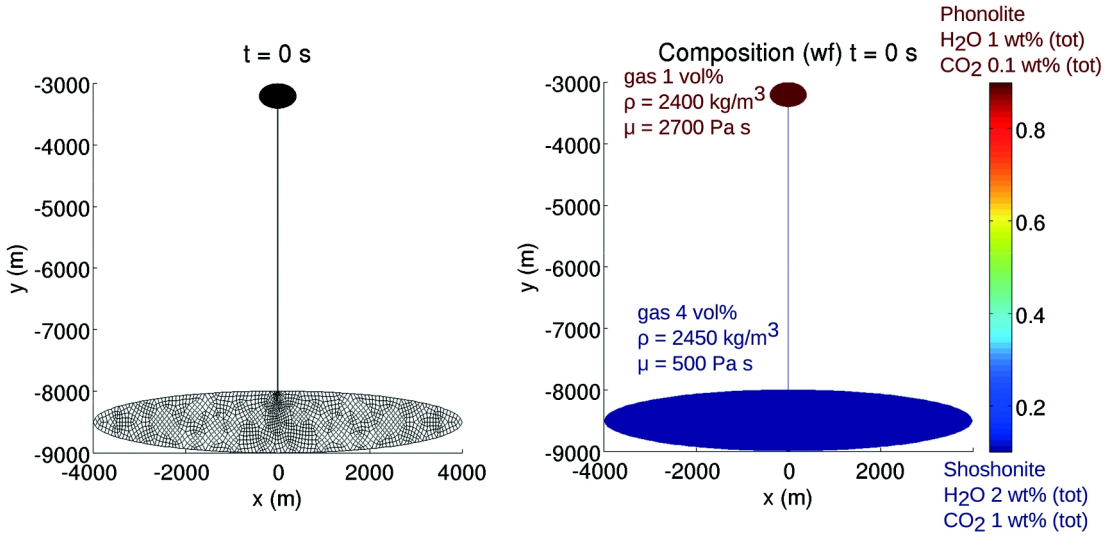

Figure 8. Volcanic system configuration: Domain geometry, computation mesh and the physical properties of magma.

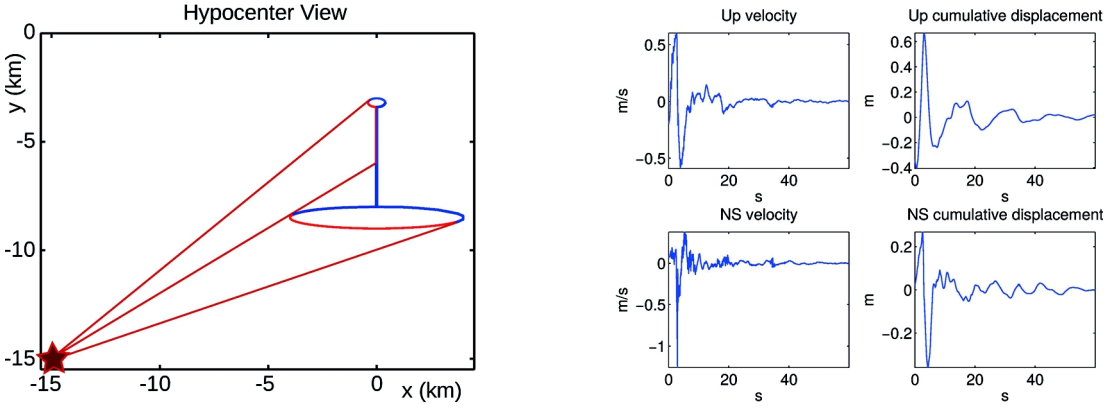

Figure 9. Hypocenter view and seismic wave.

Since the aim of this study is to investigate the magma dynamics induced by a near-field seismic wave, we assume that the distance between the source of the earthquake and the magmatic system is 15.5 km. The seismic wave data is taken from Petrolia/Cape Mendocino earthquake, 25-26 April 1992, of 7.2 magnitude Richter scale (Velasco et al., 1994). Figure 9 displays the hypocenter view of the system and the seismic wave data. For the simulation case, we assume the magma chamber is surrounded by an elastic thin (1m) layer of rocks. The absorption of the seismic wave by the rocks between the source and the magmatic system is not considered in the model.

For the exsolution and dissolution of volatile contents in magma, dependent upon local pressure and temperature model given by Papale et al., 2006 is used. The density of magmatic oxides is computed with the model given by Lange et al., 1994. For the density of dissolved H_2O and CO_2 model of Burnham et al., 1969 is employed. The density of H_2O and CO_2 gas are computed by using the ideal gas equation. The viscosity of the liquid mixture is modelled as in Giordano et al., 2008. Mixture viscosity (under the assumption of Newtonian rheology) is computed through the standard rule of mixing as in Reid et al., 1977 for one-phase mixture, and with a semi-empirical relationship as in Ishii and Zuber 1979 in order to account for the effect of non-deformable gas bubbles. Mixture density is modelled with the standard rule of mixing following Reid et al., 1977. For computational ease, the temperature of magmas is kept constant. The initial conditions for magma are composed of hydrostatic pressure and zero velocities everywhere. The hydrostatic pressure is assumed to be in meta stable equilibrium state with the lithostatic pressure of rocks. The initial conditions for the elastostatic mesh problem are set as zero deformation. The boundary conditions for the magma problem are set in the following way. Along the domain boundary where seismic wave strikes (boundary in red colour in Figure 9), the fluid velocity is set equal to the velocity of the seismic wave. On the remaining part of the domain boundary (boundary in blue colour in Figure 9), the fluid velocity is set equal to the velocity of deforming rock layer which is evaluated from the solution of the elastostatic problem. For the elastostatic problem, the boundary conditions are the seismic deformation on the boundary where seismic wave strikes (boundary in red colour in Figure 9) and the magma traction forces on the remaining part (boundary in blue colour in Figure 9).

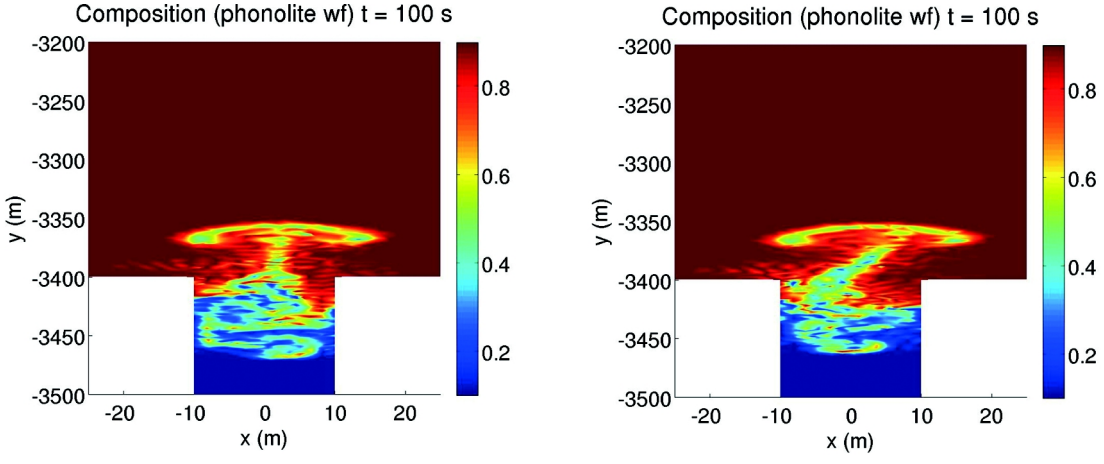

Figure 10. The inclination of the plume at time t = 100 s, the left image is of no seismic wave case and the right image is with seismic wave. The colorbar shows the weight fraction of phonolite magma.

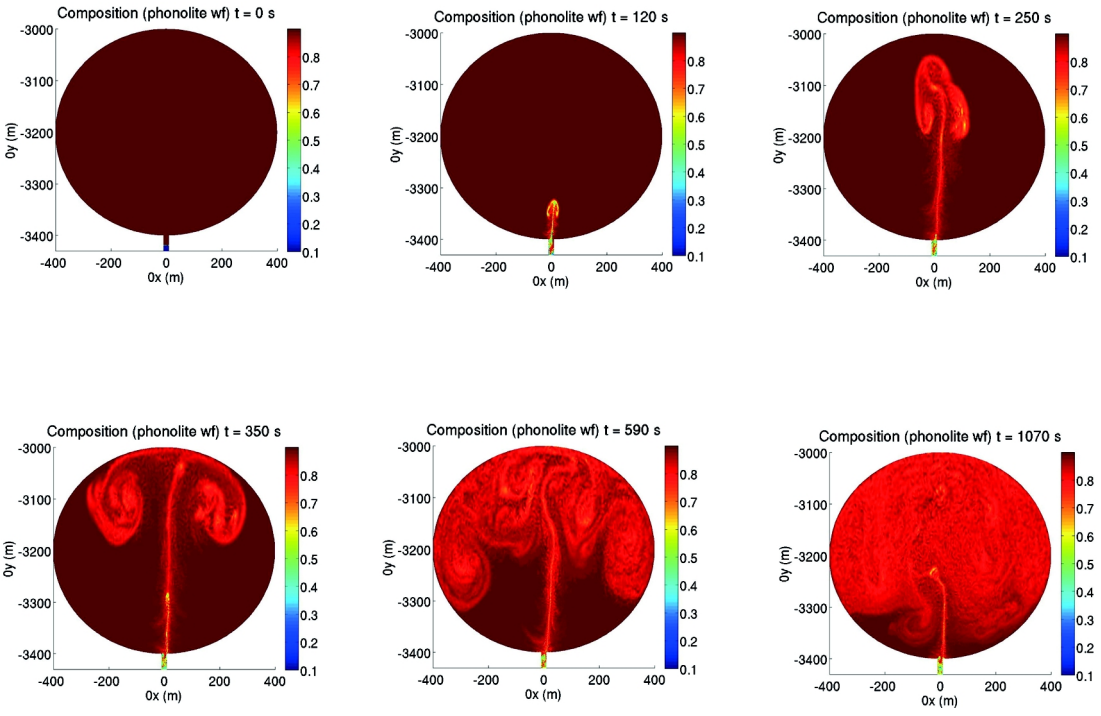

Figure 11. Temporal evolution of magma mingling. The colorbar shows the weight fraction of phonolite magma.

13. 5.2 - **Results and discussion**

At time t = 0 s, the seismic wave strikes on the magmatic system boundary shown in red colour in Figure. The seismic wave interacts with the system for 60 s. The sudden arrival of wave generates a longitudinal pressure wave which travels through the system from left to right and top to bottom. The speed of the generated wave is observed in the range of 750-1000 m/s. The interface starts getting perturbed around at 12 s and at 50 s a plume of buoyant shoshonite reaches at the top of dike and enters inside the upper chamber. Simultaneously phonolite makes a passage in the dike and starts diffusing with the surrounding magma and moving downwards.

The vertical motion of the rising and sinking magma is accompanied by the formation of a number of vortices which contribute in further magma diffusion. From the top of the dike to top of upper chamber plume covers 70 m between 50-110 s, 110 m between 110-170 s, 120 m between 170-230 s and 100 m between 230-270 s. Thus it takes approximately 220 s to reach from bottom of the upper chamber to top, covering a total distance of 400 m. We run the same simulation without an external disturbance and compared the results between the two simulations. In both cases, the mingling of magma is similar. The only minor difference between the two cases is the inclination of the rising plume. In the case of seismic wave, the rising plume is more inclined. Figure 10 shows a zoom view of rising plumes near the interface of two magmas for both cases at time t = 100 s. Figure 11 shows the temporal evolution of the mingling at various times.

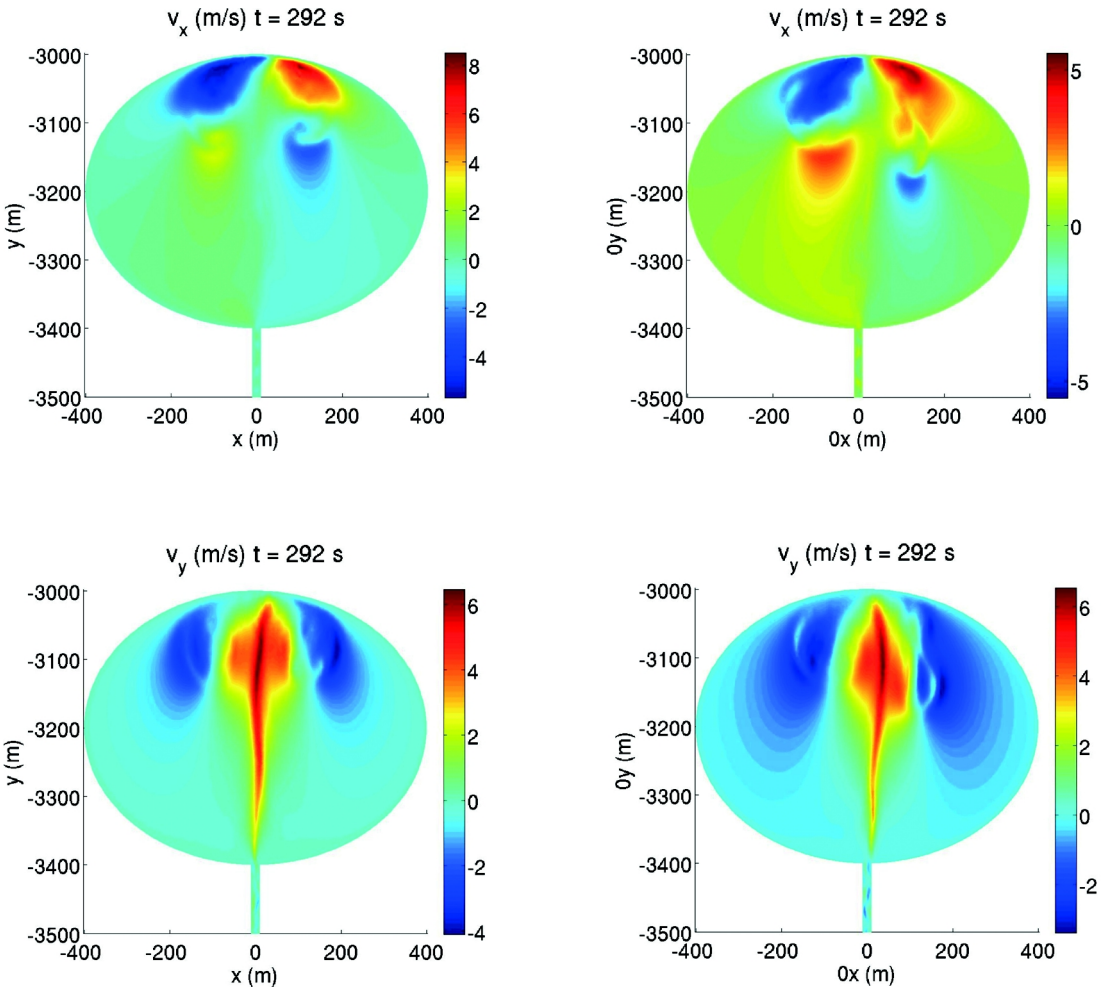

Figure 12. Velocities (m/s) comparison at time t = 292 s, the left panel is of no external disturbance case and the right panel is with seismic wave.

In the case of no seismic wave, the magnitude of velocity reaches up to 10 m/s, while in another case the magnitude is a little lower than 6 m/s. In the earlier phase of development of the flow, due to the seismic disturbance velocity shows oscillatory behaviour through the domain, in particular in the vicinity of the boundary. In the upper chamber at end of seismic wave t > 60 s the velocity follows the same pattern as without seismic wave. The comparison of velocity in both cases is shown in Figure 12. It is clear from the figure that y-component of velocity is almost similar while the x-component is greater in the case of no external disturbance.

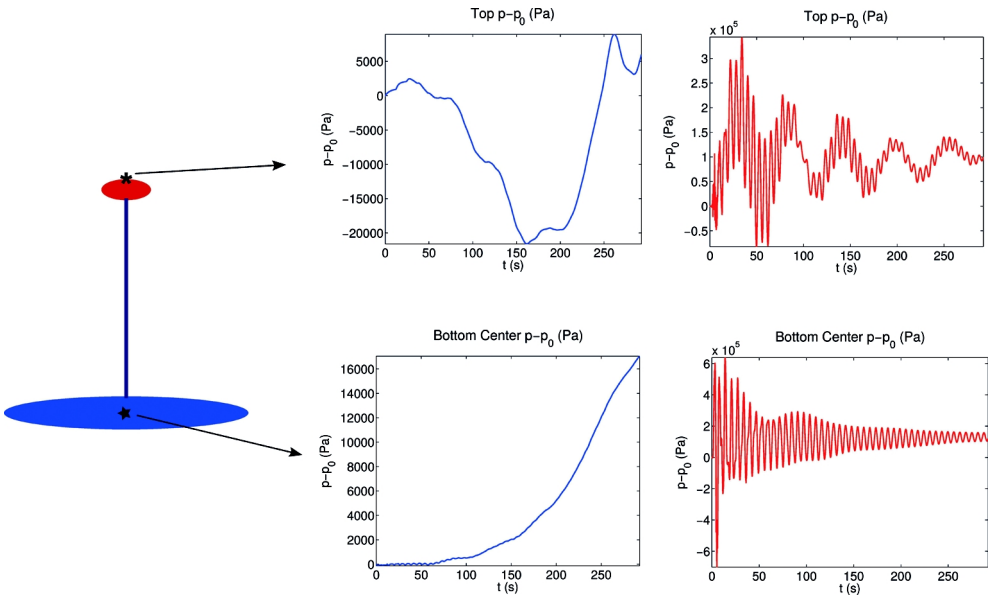

Figure 13. Overpressure (Pa) at top node of upper chamber and central node of lower chamber. Left side and right side correspond to no seismic wave case and seismic excitation case respectively.

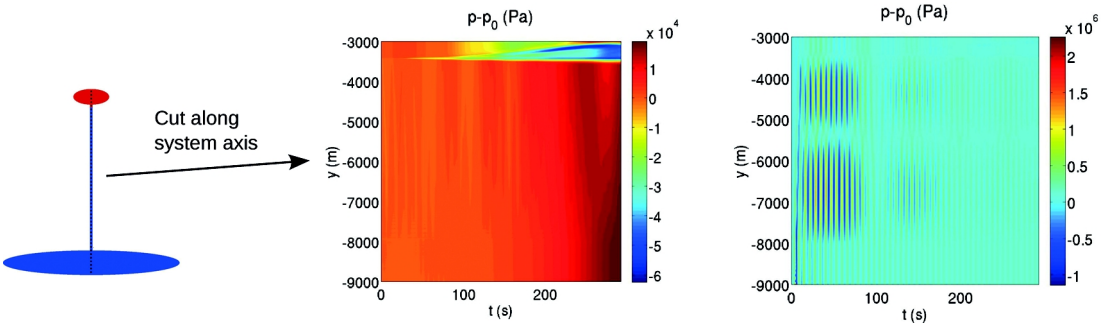

Figure 14. Overpressure (Pa) at vertical cut along the system axis. Left side and right side correspond to no seismic wave case and seismic excitation case respectively.

The natural convection case shows the dynamic evolution of pressure due to the advection of rising and sinking plumes, inflow/outflow of gas-rich/degassed magma from the upper chamber. We choose three locations in the system to represent the pressure variation; a point at top of upper chamber, the central point in the lower chamber and a vertical cut along the system axis. In the case of natural convection, at the top point, for first t<30 s pressure change increases up to its maximum value of 2500 Pa and then shows a decreasing trend for 30<t<160 s reaching -22 kPa. For 160<t<300 s pressure shows increasing and decreasing trend, reaching its maximum value of 8 kPa. At the bottom centre node pressure shows an increasing trend and crosses 16 kPa in 270 s. The maximum

value of overpressure inside the dike along the vertical cut reaches 18 kPa at t = 300 s. In the presence of seismic wave, a significant hike in over pressure is observed. Within first 60 s maximum overpressure is noticed to reach up to 2.2 MPa along the vertical cut in the dike (see Figure 13), 0.35 MPa at top point in the upper chamber and 0.62 MPa at the centre of the lower chamber (see Figure 14). Hence in case of seismic wave, the observed pressure is 2 order of magnitude greater. We observed that for later times the amplitude of the pressure wave continues to decrease and eventually attains the similar profile of natural convection case.

13. 6 - **Concluding Remarks**

We presented a space-time finite element model for deforming domains. A general formulation derived from the conceptual idea of a space-time finite element method has been established for the compressible Navier-Stokes equations. A detailed explanation of the numerical technique for fluid flow, mesh deformation and coupling algorithm has been provided. The incompressibility limit of the applied method has been verified on the standard benchmark problems for the moving domain. Finally, the model is used to study of magma dynamics in presence of an earthquake. In our simulation, we used real seismic wave data of M = 7.2 impinging on a magmatic system filled with phonolite and shoshonite magmas. Mixture characteristics dependent upon the local pressure and temperature have been computed with the advanced laws available in the literature. Our results showed that mingling between two different magmas is not affected in the presence of the earthquake. Velocities showed an oscillatory behaviour only whilst the seismic wave interacted with the system, for later times the pattern became similar to the natural convection case. The observed magnitude of velocity was a little lower in the case of seismic waves. Our results indicated that arrival of seismic waves generated an over imposed pressure wave which travelled through the whole system. Maximum overpressure was noticed to reach up to 0.35 MPa in the upper chamber, 0.62 MPa in the lower chamber and 2.2 MPa in the dike.

Acknowledgements

The research leading to these results has received funding from the European Union Seventh Framework Programme (FP7/2007-2013) under the project NEMOH, grant agreement n° 289976.

References

Battaglia, M., Cervelli, P. F. and Murray, J. R. (2013). A MATLAB software package for modeling crustal deformation near active faults and volcanic centers. J. Volcanol. Geotherm. Res., 254: 1-4.

Currenti G., Bonaccorso A., Del Negro, C., Scandura, D. and Boschi, E. (2010). Elastoplastic modeling of volcano ground deformation. Earth Planet. Sci. Lett., 296: 311-318.

Bonafede, M. and Ferrari, C. (2009). Analytical models of deformation and residual gravity changes due to a Mogi source in a viscoelastic medium. Tectonophysics, 471: 4-13.

Lomnitz, C. (2004). Major Earthquakes of Chile: A Historical Survey, 1535-1960: Seism. Res. Lett., 75: 368-378.

Jachens, R. C. and Eaton, G.P. (1980). Geophysical observations of Kilauea volcano, Hawaii, 1. temporal gravity variations related to the 29 November, 1975, M= 7.2 earthquake and associated summit collapse. J. Volcanol. Geotherm. Res., 7: 225-240.

Lara, L. E., Naranjo, J. A. and Moreno, H. (2004). Rhyodacitic fissure eruption in Southern Andes (Cordn Caulle; 40.5S) after the 1960 (Mw: 9.5) Chilean earthquake: a structural interpretation. J. Volcanol. Geotherm. Res., 138: 127-138.

Lay, T., Ammon, C. J., Kanamori, H., Koper, K. D., Sufri, O. and Hutko, A. R. (2010). Teleseismic inversion for rupture process of the 27 February 2010 Chile (Mw 8.8) earthquake. Geophys. Res. Lett., 37: L13301, 1-5.

Toda, S., Stein, R. S. and Lin J. (2011). Widespread seismicity excitation throughout central Japan following the 2011 M=9.0 Tohoku earthquake and its interpretation by Coulomb stress transfer. Geophy. Res Lett., 38: L00G03, 1-5.

Longo, A., Barsanti, M., Cassioli, A. and Papale, P. (2012). A finite element Galerkin/least-squares method for computation of multicomponent compressible-incompressible flows. Computer & Fluids, 67: 57-71.

Shakib, F., Hughes, T. J. R. and Johan, Z. (1991). A new finite element formulation for computational fluid dynamics: X. The compressible Euler and Navier-Stokes equations. CMAME, 89: 141-219.

Saad, Y. and Schultz, M. H. (1986). GMRES: A Generalized Minimal Residual Algorithm for Solving Non-symmetric Linear Systems. SIAM J. Sci. Stat. Comput., 7: 856-869.

Martin, J.C. and Moyce, W.J. (1952). Part IV. An experimental study of the collapse of liquid columns on a rigid horizontal plane, Philosophical Transactions of the Royal Society of London. Series A, Mathematical and Physical Sciences, 244: 312-324.

Murrone, A. and Guillard, H. (2005). A five equation reduced model for compressible two-phase flow problems. J. comp. Physics, 202: 664-698.

Velasco, A. A. et al. (1994). Recent large earthquakes near Cape Mendocino and in the Gorda plate: Broadband source time functions, fault orientations, and rupture complexities. Journal of Geophysical Research, 99: 711-728.

Papale, P., Moretti, R. and Barbato, D. (2006). The compositional dependence of the saturation surface of H_2O + CO_2 fluids in silicate melts. Chemical Geology, 229: 78-85.

Lange, R. A. (1994). The effects of H_2O, CO_2 and F on the density and viscosity of silicate melts. Reviews of Mineralogy, 30: 331-369.

Burnham, C. W., Holloway, J. R. and Davis, N. F. (1969). Thermodynamic Properties of Water to 1,000 °C and 10,000 Bars. Geological Society of America Special Papers, 132: 1-96.

Giordano, D., Russel, J. K. and Dingwell, D. B. (2008). Viscosity of magmatic liquids: a model. Earth and Planetary Sci. Lett., 271: 123-134.

Reid, R. C., Prausnitz, J. and Sherwood, T. (1977). The properties of Gases and Liquids. 3rd edn. McGraw Hill. New York.

Ishii, M. and Zuber, N. (1979). Drag coefficient and relative velocity in bubbly, droplet or particulate flows. AIChE Journal, 25: 843-855.

Deepak Garg, India
deepak.garg@ingv.it

Affiliation under NEMOH
Istituto Nazionale di Geofisica e Vulcanologia, Sezione di Pisa, Pisa, Italy

Research theme under NEMOH
Model and code for magma dynamics in deforming reservoirs

My background is in mathematics. I completed my Master's degree at the Panjab University (PU) Chandigarh, India in 2009. During my graduation, I studied both pure and applied mathematical subjects. Shortly after graduating my master's degree, I appeared for the national entrance exam conducted by the Council of Scientific and Industrial Research (CSIR-INDIA) and won a junior research fellowship to do research. Under the frame of the junior research fellowship, I worked for two years on operations research at mathematics department of PU. During this period my research was focused on developing the optimised task allocation models for heterogeneous distributed computing systems.

In December 2012, under the frame of NEMOH, I won Marie Curie Fellowship at INGV, Pisa, Italy. The fellowship introduced me the field of Earth Sciences and allowed me to apply my mathematical skills in volcanology. My job was to extend the numerical magma dynamics code GALES, developed at INGV Pisa, by including the effects of deformable walls. The project helped me to gain in-depth knowledge of the methods of numerical modelling, in particular, the finite element method and simulations applied to geophysics. The prime focus was to understand the magma dynamics in volcanic environments. The regular discussions with my supervisor Dr Antonella Longo and Prof. Paolo Papale have been always fruitful and improved my understanding of the geophysical processes. During this time, I largely benefited from the participation to many international scientific appointments, including those organised by NEMOH as well as dedicated courses and relevant conferences in geophysics and volcanology. The interaction with other NEMOH fellows and senior researchers helped to strengthen the networking and communication skills. My job at INGV gave me an opportunity to become a frequent user of Linux and work on INGV and CINECA servers. I learnt how to use Open Mpi with C++ programming. I did my secondment at Barcelona supercomputing centre where I learnt about the debugging of a parallel code and the cmake compiling system.

In October 2013, I started my PhD on the same topic as of my project under NEMOH. Currently, I am continuing with my research activities as a research fellow at INGV, Pisa. After finishing PhD, I would love to continue doing research, by doing possible collaborations and actively participating in future research projects.

Chapter 14

A spectral-based numerical method for Kolmogorov equations associated with stochastic differential equations.

Francisco Javier Delgado-Vences

Istituto Nazionale di Geofisica e Vulcanologia, Sezione di Pisa, Pisa, Italy

Tutorship: Paolo Papale , Franco Flandoli

Istituto Nazionale di Geofisica e Vulcanologia, Sezione di Pisa, Pisa, Italy

Abstract

We review a numerical solution for the solution of the Fokker-Planck-Kolmogorov (FPK) equations associated with stochastic partial differential equations in Hilbert spaces proposed by Delgado and Flandoli. The method is based on the spectral decomposition of the Ornstein-Uhlenbeck semi-group associated to the Kolmogorov equation. This allows us to write the solution of the Kolmogorov equation as a deterministic version of the Wiener-Chaos Expansion. By using this expansion we reformulate the Kolmogorov equation as a infinite system of ordinary differential equations, and by truncation it we set a linear finite system of differential equations. The solution of such system allow us to build an approximation to the solution of the Kolmogorov equations. The main motivation to our research is the simulation of stochastic partial differential equations and its future application to fluid dynamics that could represent magma.

Keywords: Fokker-Planck-Kolmogorov Equations; SPDEs; spectral methods, numerical solution

14.1 - Introduction

14.1.1 - Motivation of the research

The processes involved in volcanic eruption, from magma generation at depth to eruption and emplacement of deposits at the surface, comprise a suite of interlinked physical phenomena. To fully understand volcanic behaviour, volcanologists must employ a range of physics sub-disciplines, including thermodynamics, fluid dynamics, solid mechanics, ballistics and wave theory (Fagents et al.).

This work is based on: A spectral-based numerical method for Kolmogorov equations in Hilbert spaces, Francisco Delgado-Vences and Franco Flandoli, published in *Infinite Dimensional Analysis, Quantum Probability and Related Topics*, Vol. 19, No. 03, 1650020 (2016), http://www.worldscientific.com/doi/abs/10.1142/S021902571650020X.

There exist crucial several elements in the volcanic process, among then one found the magma, which is a mixture of molten or semi-molten rock, volatiles and solids. The magma is a complex high-temperature fluid substance which could have strong variations in density, viscosity, composition, temperature, pressure, etc. All this changes could be in a small time step.

It is well-known that is very complicate to do direct observations of the volcanoes or real simulations. For this reason volcanologists increasingly use numerical simulations to better understand the dynamics of volcanoes. Mathematical models are often used to explain the geological processes responsible for volcanic process.

There exist in literature several authors that have simulated the magma phenomena inside the magma chamber, but also in the eruption process. This simulations usually rely on the use of fluid dynamics models along a numerical method to solve this equations, that are really difficult to solve analytically. Fluid dynamics models use mathematical equations, usually differential equation, which are a good approximations to "real problems", however one could have huge uncertainties by using this models. In this cases, physical system behaviour often can only be described in terms of probability and has to be described by means of a stochastic model, see for instance Le Matre et al., Mathelin et al., (2004), (2005), where they mostly use Stochastic partial differential equations (SPDEs) to deal with uncertainty quantification. SPDEs are a generalization of partial differential equations and in these models one use random force terms and coefficients. This kind of models are important because it naturally includes the natural uncertainties inherent in the natural phenomena.

The main motivation to our research is the simulation of stochastic partial differential equations and its future application to fluid dynamics that could represent magma. So far, we have proposed a novel numerical method in Delgado et al. to simulate SPDEs and we have validated this method.

14.1.2 - **Mathematical introduction**

Stochastic Partial Differential Equations (SPDE's) are important tools in modeling complex phenomena, they arise in many fields of knowledge like Physics, Biology, Economy, Finance, etc.. Development of efficient numerical methods for simulating SPDE's is very important but also very difficult and challenging.

There exists in literature several approaches in order to solve numerically an SPDE. Among them there exists Monte Carlo simulations, Karhunen-Loeve Expansion, Wiener Chaos expansion, stochastic Taylor approximations for SPDE's, etc.

The Fokker-Planck-Kolmogorov (FPK) equation is a partial differential equation that describes the time evolution of the probability density function of the velocity of a particle under the influence of drag forces and random forces; it is a kind of continuity equation for densities. Prato and Zabzcyk (2002) stated that "parabolic equations on Hilbert spaces appear in mathematical physics to model systems with infinitely many degrees of freedom. Typical examples are provided by spin configurations in statistical mechanics and by crystals in solid state theory. Infinite-dimensional parabolic equations provide an analytic description of infinite dimensional diffusion processes in such branches of applied mathematics as population biology, fluid dynamics, and mathematical finance".

This kind of equations have been deeply studied in the last years, see for instance Bogachev et al., Da Prato et al., (2013), Da Prato (2004) and the references therein.

Numerical methods for FPK equations associated with SPDEs have been studied, up to our knowledge, just in a few articles, here we will mention just one. Schwab and Suli have formulated a space-time variational method to approximate solution of Kolmogorov-type equations in infinite dimensions. They consider an infinite-dimensional Hilbert space $\mathcal{H}$, a Gaussian measure μ with trace class covariance operator Q on $\mathcal{H}$ and the space $L^2(H,\mu)$ of functions on $\mathcal{H}$ which are square-integrable with respect to the measure μ. They showed the well-posedness of Fokker-Plank equations and Ornstein-Uhlenbeck equations on $L^2(H,\mu)$. Moreover, they constructed sequences of finite-dimensional approximations that attain the best possible convergence rates afforded by best N-terms approximations of the solution. They used an spectral method based on Wiener-Hermite polynomial chaos expansions in terms of a sequence of independent Gaussian random variables on $\mathcal{H}$ and a Wavelet type Riesz basis with respect to the time variable. The use of the spectral basis of Wiener-Hermite polynomial chaos allow them to avoid meshing the infinite-dimensional "domain" $\mathcal{H}$ of solutions of the Kolmogorov-type equations. However they do not present numerical examples and the questions about the feasibility of their method are still open.

In this paper, we review the numerical method proposed by Delgado-Vences and Flandoli. The method can have some similarity with the one proposed by Schwab and Suli but also have substantial differences. Indeed, our method is also based on spectral methods for the variable on $\mathcal{H}$, but we use a deterministic version of the Wiener-Chaos Expansion on the infinite-dimensional "domain" $\mathcal{H}$ instead the classical Wiener-Chaos Expansion with the use of a sequence of Gaussian random variables. This allows us to avoid meshing the space $\mathcal{H}$ but we also avoid the so-called curse of dimensionality: the associated computational cost grows exponentially as a function of the number of random variables defining the underlying probability space of the problem (see Doostan et al., (2009) for instance).

The second difference is with respect to the time variable, where, instead of using Wavelet type Riesz basis we set up a finite system of coupled ordinary differential equations and by solving it we fix the coefficients as a time functions. In Delgado and Flandoli the method has been applied to three SPDE's: a stochastic diffusion, a stochastic Fisher-KPP equation and a stochastic Burgers equation and the results show that the method is well-behaved. However, since the method is analogue to the classical deterministic spectral method, it can be extended to improve its performance. This is the subject of a future research.

This paper is organized as follows: in section (14.2) we review the Fokker-Plank-Kolmogorov equation associated with SPDE's in a separable Hilbert space. In section (14.3) we study the spectral decomposition of the Ornstein-Uhlenbeck semi-group associated to the Kolmogorov equation which will be used to do the numerical approximation to the solution of the FPK equation, which is done in section (14.4). In section (14.5) we prove a theorem on the well posedness and convergence of the numerical approximation. Results on the application of the proposed method are presented in section (14.6), where we have applied the method to a stochastic Burgers equation in one dimension.

14.2 - Fokker-Plank-Kolmogorov equation

In a separable infinite-dimensional Hilbert space $\mathcal{H}$ with inner product $\langle , \rangle_{\mathcal{H}}$ we define a Gaussian measure μ with mean zero and nuclear covariance operator Λ with $Tr(\Lambda) < +\infty$.

We focus on the stochastic differential equation in $\mathcal{H}$

$$dX_t = AX_t dt + B(X_t)dt + \sqrt{Q}dW_t, \qquad \text{(Equation 14.1)}$$

where the operator $A : \mathcal{D}(A) \subset \mathcal{H} \to \mathcal{H}$ is the infinitesimal generator of a strongly continuous semi-group e^{tA} in $\mathcal{H}$, Q is a bounded operator from another Hilbert space $\mathcal{U}$ to $\mathcal{H}$ and $B : \mathcal{D}(B) \subset \mathcal{H} \to \mathcal{H}$ is a non-linear mapping.

The equation (14.1) can be associated to a Kolmogorov equation in the following way. We define:

$$u(t, x) = \mathbb{E}[u_0(X_t^x)] \qquad \text{(Equation 14.2)}$$

where $u_0 : \mathcal{H} \to \mathbb{R}$ and X_t^x is the solution to (14.1) with the initial conditions $X_0 = x$ where $x \in \mathcal{H}$. Then u satisfies the Kolmogorov equation

$$\frac{\partial u}{\partial t} = \frac{1}{2} Tr(QD^2 u) + \langle Ax, Du\rangle_{\mathcal{H}} + \langle B(x), Du\rangle_{\mathcal{H}}, \qquad x \in D(A) \qquad \text{(Equation 14.3)}$$

Several authors have proved results on the existence and uniqueness of the solution of the Kolmogorov equations, see for instance Da Prato (2004) for a survey, Da Prato-Debussche (2007) for the Burgers equation, Barbu-Da Prato (2008) for the 2D Navier-Stokes stochastic flow in a channel.

14.3 - On the Ornstein-Uhlenbeck semigroup

Following Chow (2009) section 9.3, in $\mathcal{H}$ we define a Gaussian measure μ with mean zero and nuclear covariance operator Λ with $Tr(\Lambda) < +\infty$ and since $\Lambda : \mathcal{H} \mapsto \mathcal{H}$ is a positive definite, self-adjoint operator, then its square-root operator $\Lambda^{1/2}$ is a positive definite, self-adjoint Hilbert-Schmidt operator on $\mathcal{H}$. Define the inner product

$$\langle g, h\rangle_0 := \langle \Lambda^{-1/2} g, \Lambda^{-1/2} h\rangle_{\mathcal{H}}, \quad \text{for} \quad g, h \in \Lambda^{1/2}\mathcal{H}$$

Let $\mathcal{H}_0$ denote the Hilbert subspace of $\mathcal{H}$, which is the completion of $\Lambda^{1/2}\mathcal{H}$ with respect to the norm $\|g\|_0 := \langle g, g\rangle_0^{1/2}$. Then $\mathcal{H}_0$ is dense in $\mathcal{H}$ and the inclusion map $i : \mathcal{H}_0 \hookrightarrow \mathcal{H}$ is compact. The triple $(i, \mathcal{H}_0, \mathcal{H})$ forms an abstract Wiener space.

Let $\mathbb{H} = L^2(\mathcal{H}, \mu)$ denote the Hilbert space of Borel measurable functionals on the probability space with inner product

$$\langle \Phi, \Psi\rangle_{\mathbb{H}} := \int_{\mathcal{H}} \Phi(v)\Psi(v)\mu(dv), \quad \text{for} \quad \Phi, \Psi \in \mathbb{H},$$

and norm $\|\Phi\|_{\mathbb{H}} := \langle \Phi, \Phi\rangle_{\mathbb{H}}^{1/2}$. In $\mathcal{H}$ we choose a basis system $\{\varphi_k\}$ such that $\varphi_k \in \mathcal{H}$.

A functional $\Phi : \mathcal{H} \mapsto \mathbb{R}$, is said to be a smooth simple functional (or a cylinder functional) if there exists a C^∞-function ϕ on $\mathbb{R}^n$ and n-continuous linear functional $l_1, \ldots, l_n$ on $\mathcal{H}$ such that for $h \in \mathcal{H}$

$$\Phi(h) = \phi(h_1, \ldots, h_n) \quad \text{where} \qquad h_i = l_i(h), \quad i = 1, \ldots, n.$$

The set of all such functionals will be denoted by $\mathcal{S}(\mathbb{H})$.

Denote by $P_k(x)$ the Hermite polynomial of degree k taking values in $\mathbb{R}$. Then, $P_k(x)$ is given by the following formula

$$P_k(x) = \frac{(-1)^k}{(k!)^{1/2}} e^{\frac{x^2}{2}} \frac{d^k}{dx^k} e^{-\frac{x^2}{2}}$$

with $P_0 = 1$. It is well-known that $\{P_k(\cdot)\}_{k \in \mathbb{N}}$ is a complete orthonormal system for $L^2(\mathbb{R}, \mu_1(dx))$ with $\mu_1(dx) = \frac{1}{\sqrt{2\pi}} e^{-\frac{x^2}{2}} dx$.

Define the set of infinite multi-index as

$$\mathcal{J} = \left\{ \bar{\alpha} = (\alpha_i, i \geq 1) \quad \middle| \quad \alpha_i \in \mathbb{N} \cup \{0\}, \quad |\bar{\alpha}| := \sum_{i=1}^{\infty} \alpha_i < +\infty \right\}$$

For $\bar{n} \in \mathcal{J}$ define the *Hermite polynomial functionals* on $\mathcal{H}$ by

$$H_{\bar{n}}(h) = \prod_{i=1}^{\infty} P_{n_i}(l_i(h)), \quad h \in \mathcal{H}_0, \quad \bar{n} \in \mathcal{J}, \qquad \text{(Equation 14.4)}$$

and where

$$l_i(h) = \langle h, \Lambda^{-1/2} \varphi_i \rangle_{\mathcal{H}}, \quad i = 1, 2, \ldots$$

where $P_n(\xi)$ is the usual Hermite polynomial for $\xi \in \mathbb{R}$ and $n \in \mathbb{N}$.

Remark 14.1 *Notice that $l_i(h)$ is defined only for $h \in \mathcal{H}_0$. However, regarding h as a μ-random variable in $\mathcal{H}$, we have $\mathbb{E}\big(l_i(h)\big) = \|\varphi_i\|^2 = 1$ and then $l_k(h)$ can be defined μ-a.e. $h \in \mathcal{H}$, similar to defining a stochastic integral.*

It is possible to identify the Hermite polynomial functionals defined in (14.4), for $h \in \mathcal{H}_0$, as a deterministic version of the Wick polynomials defined on the canonical Wiener space. It is known as a numerical model in Malliavin calculus (for further details see Huang et al., (2000) for instance).

We have the following result (See Theorems 9.1.5 and 9.1.7 in Da Prato-Zabczyk (2002) or Lemma 3.1 in chapter 9 from Chow (2007).

Lemma 14.2 *For $h \in \mathcal{H}$ let $l_i(h) = \langle h, \Lambda^{-1/2} \varphi_i \rangle_{\mathcal{H}}$, $i = 1, 2, \ldots$. Then the set $\{H_{\bar{n}}\}$ of all Hermite polynomials on $\mathcal{H}$ forms a complete orthonormal system for $\mathbb{H}$. Hence the set of all functionals are dense in $\mathbb{H}$. Moreover, we have the direct sum decomposition:*

$$\mathbb{H} = \bigoplus_{j=0}^{\infty} K_j,$$

where K_j is the subspace of $\mathbb{H}$ spanned by $\{H_{\bar{n}} : |\bar{n}| = j\}$.

Spectral decomposition of the Ornstein-Uhlenbeck semigroup

Consider the linear stochastic equation

$$\begin{aligned} du_t &= Au_t dt + dW_t, \\ u_0 &= h \in \mathcal{H} \end{aligned} \qquad \text{(Equation 14.5)}$$

Here, as before $A : \mathcal{D}(A) \subset \mathcal{H} \to \mathcal{H}$ is the infinitesimal generator of a strongly continuous semigroup e^{tA} in $\mathcal{H}$. W_t is a Q-Wiener process in $\mathcal{H}$. Chow (2007) in Lemma 9.4.1 has shown the following lemma.

Lemma 14.3 *Suppose that* A *and* Q *satisfy the following:*

1. $A : \mathcal{D}(A) \subset \mathcal{H} \to \mathcal{H}$ *is self-adjoint and there is* $\beta > 0$ *such that*

$$\langle Av, v\rangle_{\mathcal{H}} \leq -\beta \|v\|_{\mathcal{H}} \quad \forall v \in \mathcal{H}.$$

2. A *commutes with* Q *in* $\mathcal{D}(A) \subset \mathcal{H}$.

Then (14.5) has a unique invariant measure μ which is a Gaussian measure on $\mathcal{H}$ with zero mean and covariance operator $\Lambda = \frac{1}{2}Q(-A)^{-1} = \frac{1}{2}(-A)^{-1}Q$.

We define the operator

$$\mathcal{A}_0 u = \frac{1}{2} Tr(QD^2 u) + \langle Ax, Du\rangle_{\mathcal{H}}, \qquad x \in \mathcal{H} \qquad \text{(Equation 14.6)}$$

and suppose that -A and Q have the same eigenfunctions e_k with eigenvalues λ_k y ρ_k respectively. Then the operator $\mathcal{A}_0$ satisfies the Lemma (14.4).

Lemma 14.4 *Let $H_{\bar{n}}(h)$ be a Hermite polynomial functional given by (14.4). Then the following holds*

$$\mathcal{A}_0 H_{\bar{n}}(h) = -\lambda_{\bar{n}} H_{\bar{n}}(h), \qquad \text{(Equation 14.7)}$$

for any $\bar{n} \in \mathcal{J}$ and $h \in \mathcal{H}$ and where

$$\lambda_{\bar{n}} := \sum_{k=1}^{\infty} n_k \lambda_k.$$

The proof can be found in Chow (2007) Lemma 9.4.3. Using lemmas (14.4) and (14.2), ($\{H_{\bar{n}}\}$ forms a complete orthonormal system for $L^2(\mathcal{H}, \mu)$) we can write

$$u(t,x) = \sum_{\bar{n} \in \mathcal{J}} u_{\bar{n}}(t) H_{\bar{n}}(x), \qquad x \in \mathcal{H}, \quad t \in [0,T], \qquad \text{(Equation 14.8)}$$

where $u_{\bar{n}} : [0,T] \mapsto \mathbb{R}$ and $H_{\bar{n}}(x)$ are the Hermite functionals.

Remark 14.5 *The decomposition given in (14.8) is a deterministic version to the Wiener Chaos expansion (WCe), also known as a Fourier-Hermite series. The WCe has been used to prove several results in stochastic analysis and also it has been applied to solve numerically stochastic partial differential equations (see for instance Lototsky and Rozovskii (2006), Lototsky (2011), Hou et. al. (2006). Notice that the Kolmogorov equation can be writen as*

$$\begin{aligned}\frac{\partial u}{\partial t} &= \frac{1}{2}Tr(QD^2u) + \langle Ax, Du\rangle_{\mathcal{H}} + \langle B(x), Du\rangle_{\mathcal{H}} \\ &= \mathcal{A}_0 u + \langle B(x), Du\rangle_{\mathcal{H}} \end{aligned} \qquad \text{(Equation 14.9)}$$

Using (14.8), we calculate

$$\frac{\partial u}{\partial t} = \sum_{\bar{n}\in\mathcal{J}} \dot{u}_{\bar{n}}(t) H_{\bar{n}}(x)$$

$$\begin{aligned}\mathcal{A}_0 u = \mathcal{A}_0 \sum_{\bar{n}\in\mathcal{J}} u_{\bar{n}}(t) H_{\bar{n}}(x) &= \sum_{\bar{n}\in\mathcal{J}} u_{\bar{n}}(t)\mathcal{A}_0 H_{\bar{n}}(x) \\ &= -\sum_{\bar{n}\in\mathcal{J}} u_{\bar{n}}(t)\lambda_{\bar{n}} H_{\bar{n}}(x),\end{aligned}$$

where in the last equality we have used the Lemma (14.4).
For the last term in (14.9) we have

$$\begin{aligned}\langle B(x), Du\rangle_{\mathcal{H}} &= \Big\langle B(x), D_x \sum_{\bar{n}\in\mathcal{J}} u_{\bar{n}}(t) H_{\bar{n}}(x)\Big\rangle_{\mathcal{H}} \\ &= \sum_{\bar{n}\in\mathcal{J}} u_{\bar{n}}(t)\big\langle B(x), D_x H_{\bar{n}}(x)\big\rangle_{\mathcal{H}},\end{aligned}$$

where D_x is the Fr$\acute{e}$chet derivative. Therefore the Kolmogorov equation becomes

$$\sum_{\bar{n}\in\mathcal{J}} \dot{u}_{\bar{n}}(t) H_{\bar{n}}(x) = -\sum_{\bar{n}\in\mathcal{J}} u_{\bar{n}}(t)\lambda_{\bar{n}} H_{\bar{n}}(x) + \sum_{\bar{n}\in\mathcal{J}} u_{\bar{n}}(t)\big\langle B(x), D_x H_{\bar{n}}(x)\big\rangle_{\mathcal{H}}.$$

Multiplying by $H_{\bar{m}}(x)$, $\bar{m} \in \mathcal{J}$ and integrating in $\mathcal{H}$ w.r.t $\mu(dx)$ we have

$$\begin{aligned}\sum_{\bar{n}\in\mathcal{J}} \dot{u}_{\bar{n}}(t) \int_{\mathcal{H}} H_{\bar{m}}(x) H_{\bar{n}}(x)\mu(dx) &= -\sum_{\bar{n}\in\mathcal{J}} u_{\bar{n}}(t)\lambda_{\bar{n}} \int_{\mathcal{H}} H_{\bar{m}}(x) H_{\bar{n}}(x)\mu(dx) \\ &\quad + \sum_{\bar{n}\in\mathcal{J}} u_{\bar{n}}(t) \int_{\mathcal{H}} H_{\bar{m}}(x)\big\langle B(x), D_x H_{\bar{n}}(x)\big\rangle_{\mathcal{H}}\mu(dx)\end{aligned}$$

.

From this, and using the orthogonality of the system $\{H_{\bar{m}}(x)\}$ we get the infinite system of coupled ordinary differential equations

$$\dot{u}_{\bar{m}}(t) = -u_{\bar{m}}(t)\lambda_{\bar{m}} + \sum_{\bar{n}\in\mathcal{J}} u_{\bar{n}}(t)C_{\bar{n},\bar{m}}, \qquad \bar{n},\bar{m}\in\mathcal{J} \tag{Equation 14.10}$$

where $C_{\bar{n},\bar{m}}$ is given by

$$C_{\bar{n},\bar{m}} := \int_{\mathcal{H}} \left\langle B(x), D_x H_{\bar{n}}(x)\right\rangle_{\mathcal{H}} H_{\bar{m}}(x)\mu(dx). \tag{Equation 14.11}$$

We focus on $C_{\bar{n},\bar{m}}$. Since $H_{\bar{n}}(x) = \prod_{i=1}^{\infty} P_{n_i}\left(\langle x, \Lambda^{-\frac{1}{2}} e_i\rangle_{\mathcal{H}}\right)$ we get

$$D_x H_{\bar{n}}(x) = \sum_{k=1}^{\infty}\prod_{\substack{i=1\\ i\neq k}}^{\infty} P_{n_i}\left(\langle x, \Lambda^{-\frac{1}{2}} e_i\rangle_{\mathcal{H}}\right) P_{n_k}^{'}\left(\langle x, \Lambda^{-\frac{1}{2}} e_k\rangle_{\mathcal{H}}\right)\Lambda^{-\frac{1}{2}} e_k,$$

then

$$\left\langle B(x), D_x H_{\bar{n}}(x)\right\rangle_{\mathcal{H}} = \sum_{k=1}^{\infty}\left\langle B(x), \Lambda^{-\frac{1}{2}} e_k\right\rangle_{\mathcal{H}} \prod_{\substack{i=1\\ i\neq k}}^{\infty} P_{n_i}\left(\langle x, \Lambda^{-\frac{1}{2}} e_i\rangle_{\mathcal{H}}\right) P_{n_k}^{'}\left(\langle x, \Lambda^{-\frac{1}{2}} e_k\rangle_{\mathcal{H}}\right)$$

Thus,

$$C_{\bar{n},\bar{m}} = \int_{\mathcal{H}} \sum_{k=1}^{\infty}\left\langle B(x), \Lambda^{-\frac{1}{2}} e_k\right\rangle_{\mathcal{H}} \prod_{\substack{i=1\\ i\neq k}}^{\infty} P_{n_i}\left(\langle x, \Lambda^{-\frac{1}{2}} e_i\rangle_{\mathcal{H}}\right) P_{n_k}^{'}\left(\langle x, \Lambda^{-\frac{1}{2}} e_k\rangle_{\mathcal{H}}\right) H_{\bar{m}}(x)\mu(dx).$$

A technical result

The following lemma is important for the numerical simulation since it will allow us to use the evaluation functional on the Hilbert space $\mathcal{H}$.

Lemma 14.6

i) *The Gaussian measure μ on $\mathcal{H} = L^2(0,1)$ with covariance $\Lambda = \frac{1}{2}(-A)^{-1}$ is supported on $C([0,1])$.*
ii) Let $\xi_0 \in [0,1]$ be given. Let $u_0 : C([0,1]) \to \mathbb{R}$ be defined as $u_0(x) = x(\xi_0)$. Then

$$\int_{\mathcal{H}} u_0^2(x)\,\mu(dx) < \infty$$

(and therefore $\sum_m \left(u_m^0\right)^2 < \infty$).

A concise proof of the claim $\int_{\mathcal{H}} u_0^2(x)\,\mu(dx) < \infty$ is

$$\int_{\mathcal{H}} u_0^2(x)\,\mu(dx) = \int_{\mathcal{H}} \langle x, \delta_{\xi_0}\rangle_{\mathcal{H}}^2\,\mu(dx) = \langle \Lambda\delta_{\xi_0}, \delta_{\xi_0}\rangle_{\mathcal{H}} = \frac{1}{2}\left\|(-A)^{-1/2}\delta_{\xi_0}\right\|_{\mathcal{H}}^2 < \infty$$

because $(-A)^{-1/2}\,\delta_{\xi_0} \in L^2\,(0,1)$, since by duality

$$\begin{aligned}\left\langle (-A)^{-1/2}\,\delta_{\xi_0}, f\right\rangle_{\mathcal{H}} &= \left\langle \delta_{\xi_0}, (-A)^{-1/2}\,f\right\rangle_{\mathcal{H}} = \left((-A)^{-1/2}\,f\right)(\xi_0)\\ &\leq \left\|(-A)^{-1/2}\,f\right\|_{L^\infty} \leq C\left\|(-A)^{-1/2}\,f\right\|_{H^1} \leq C\,\|f\|_{L^2}\end{aligned}$$

where we have used Sobolev embedding $H^1 \subset L^\infty$ and the fact that $(-A)^{-1/2}$ maps L^2 into H^1.

14.4 - Numerical approximation

Define the set of *finite* multi-index $\mathcal{J}^{M,N}$ as

$$\mathcal{J}^{M,N} = \left\{\bar{\alpha} = (\alpha_i, 1 \leq i \leq M) \quad \middle| \quad \alpha_i \in \{0,1,2,\ldots,N\}\right\}.$$

This is the set of M-tuple wich can take values in the set $\{0,1,2,\ldots,N\}$. We approximate the solutions of the Kolmogorov equation by the following expression

$$\hat{u}_N(t,x) = \sum_{\bar{n}\in\mathcal{J}^{M,N}} u_{\bar{n}}(t)H_{\bar{n}}(x), \qquad x \in \mathcal{H}, \quad t \in [0,T]. \tag{Equation 14.12}$$

Notice the use of the finite M-tuple in opposition to the infinite multi-index $\mathcal{J}$ as in (14.8). We truncate the infinite system (14.10) in the following sense: consider the same value M as in $\mathcal{J}^{M,N}$ and $\bar{m}_1,\ldots,\bar{m}_M \in \mathcal{J}^{M,N}$ and define the finite system of equations

$$\dot{u}_{\bar{m}_i}(t) = -u_{\bar{m}_i}(t)\lambda_{\bar{m}_i} + \sum_{j=1}^{M} u_{\bar{n}_j}(t)C_{\bar{n}_j,\bar{m}_i}. \qquad 1 \leq i \leq M. \tag{Equation 14.13}$$

Set the vectors

$$\begin{aligned}U^M(t) &= \left(u_{\bar{m}_1}(t), u_{\bar{m}_2}(t), \ldots, u_{\bar{m}_M}(t)\right)^T\\ \dot{U}^M(t) &= \left(\dot{u}_{\bar{m}_1}(t), \dot{u}_{\bar{m}_2}(t), \ldots, \dot{u}_{\bar{m}_M}(t)\right)^T\end{aligned}$$

and the matrix

$$A = \begin{pmatrix} -\lambda_1 + C_{1,1} & C_{2,1} & \cdots & C_{M-1,1} & C_{M,1}\\ C_{1,2} & -\lambda_2 + C_{2,2} & \cdots & C_{M-1,2} & C_{M,2}\\ \vdots & \vdots & \ddots & \vdots & \vdots\\ C_{1,M-1} & C_{2,M-1} & \cdots & -\lambda_{M-1} + C_{M-1,M-1} & C_{M,M-1}\\ C_{1,M} & C_{2,M} & \cdots & C_{M-1,M} & -\lambda_M + C_{M,M}\end{pmatrix}$$

where $\lambda_i = \lambda_{\bar{m}_i}$ and $C_{i,j} = C_{\bar{n}_i,\bar{m}_j}$ for $1 \leq i,j \leq M$. Notice that, given the expression (14.11), in general the matrix A is not symmetric. We now can write the system (14.13) as a matrix differential equation:

$$\dot{U}^M(t) = AU^M(t). \qquad \text{(Equation 14.14)}$$

If A has M real and distinct eigenvalues η_i and M eigenvectors $\vec{V}_i$ then the solution to the (14.14) is given by

$$U^M(t) = \sum_{i=1}^{M} c_i \vec{V}_i e^{\eta_i t}. \qquad \text{(Equation 14.15)}$$

In the case when some of the eigenvalues and eigenvectors, or at least one of them, take values in the complex field we still can have real solutions. Indeed, suppose that we have the case with one complex eigenvalue and eigenvector; then it is know that we will have M-2 real eigenvalues but we can obtain two real solutions from the complex eigenvalue, see Goldberg and Schwartz (1972) for instance. Let us write one of the complex eigenvalue and eigenvector as

$$\vec{V} = \vec{a} + i\vec{b},$$
$$\eta = \gamma + i\mu,$$

then we can write two *real* solutions as follows:

$$e^{\gamma t}\big(\vec{a}cos(\mu t) - \vec{b}sin(\mu t)\big), \qquad e^{\gamma t}\big(\vec{a}sin(\mu t) + \vec{b}cos(\mu t)\big).$$

14.4.1 - Initial conditions

In contrast to several types of differential equations, whether ordinary or partial, deterministic or stochastic, for FPK equations there is no standard way to determine the initial conditions. This is because in this type of equations we must choose a functional that acts on the initial condition. This implies that depending on the functional chosen we must adapt the method. Here we present the method for two examples of functionals.

We will consider two cases :

$$u_0^{z_0}(g) := g(z_0). \qquad \text{for fixed } z_0 \in [0,1]$$

and

$$u_0(g) := \int_0^1 g(z)dz.$$

For the first functional, define the set points in the set [a,b] as $\{z_i\}$, $i = 0, \ldots, P$, such that $z_0 = a$ and $z_P = b$. Then for each point z_i we have that $X_0(z_i) = X(0, z_i)$, and for each z_i set $u_0(x)$ as the evaluation functional $z_i \mapsto X_t^x(z_i)$ then from $u(t,x) = \mathbb{E}(u_0(X_t^x))$ we obtain

$$u(0,x) = \mathbb{E}\big(u_0^{z_i}(X_0^x)\big) = X^x(0, z_i) = x(z_i),$$

and at other hand

$$u(0,x) = \sum_{\bar{n}\in\mathcal{J}^{M,N}} u_{\bar{n}}(0)H_{\bar{n}}(x),$$

then for each z_i

$$x(z_i) = u(0,x) = \sum_{\bar{n}\in\mathcal{J}^{M,N}} u_{\bar{n}}(0)H_{\bar{n}}(x)$$

Then, multiplying by $H_{\bar{m}}(x)$ and integrating in the Hilbert space $L^2(\mathcal{H},\mu)$ we have

$$u_{\bar{m}}(0) = \int_{\mathcal{H}} x(z_i)H_{\bar{m}}(x)\mu(dx).$$

Here the value of the initial condition $u_{\bar{m}}(0)$ depends on z_i, i.e. $u_{\bar{m}}(0) = u_{\bar{m}}^{z_i}(0)$.

Notice that in the direction of the eigenfunction e_k the expression x can be writen as $\langle x, e_k\rangle_{\mathcal{H}} e_k$ and then we can write $H_{\bar{m}}(x)x(z_i)$in the direction e_k as $P_{m_k}(\xi_k)\langle x, e_k\rangle_{\mathcal{H}} e_k(z_i)$ with $\xi_k = \langle x, \Lambda^{-1/2}e_k\rangle_{\mathcal{H}}$. Furthermore, $\xi_k = \langle x, \Lambda^{-1/2}e_k\rangle_{\mathcal{H}} = |\lambda_k|\langle x, e_k\rangle_{\mathcal{H}}$ then we have

$$\begin{aligned}
u_{\bar{m}}^{z_i}(0) &= \int_{\mathcal{H}} x(z_i)H_{\bar{m}}(x)\mu(dx) \\
&= \int_{\mathbb{R}^{\mathbb{N}}} \sum_{k=1}^{\infty} e_k(z_i)\langle x, e_k\rangle_{\mathcal{H}} P_{m_k}(\xi_k)\mu(d\xi_1, d\xi_2, \cdots)e_k \\
&= \int_{\mathbb{R}^{\mathbb{N}}} \sum_{k=1}^{\infty} e_k(z_i)\frac{\xi_k}{\lambda_k} P_{m_k}(\xi_k)\mu(d\xi_1, d\xi_2, \cdots)e_k \\
&= \sum_{k=1}^{\infty} \frac{e_k(z_i)}{\lambda_k} \int_{\mathbb{R}} P_{m_k}(\xi_k)\xi_k\mu(d\xi_k) \\
&\approx \sum_{k=1}^{M} \frac{e_k(z_i)}{\lambda_k} \int_{\mathbb{R}} P_{m_k}(\xi_k)\xi_k\mu(d\xi_k). \qquad \text{(Equation 14.16)}
\end{aligned}$$

Notice that the general solution to each $u_{\bar{m}}^{z_i}(0)$ is given by the expression

$$\begin{pmatrix} u_1(t) \\ u_2(t) \\ \vdots \\ u_{M-1}(t) \\ u_M(t) \end{pmatrix} = (\mathbf{V}_1 \quad \mathbf{V}_2 \quad \cdots \quad \mathbf{V}_{M-1} \quad \mathbf{V}_M) \begin{pmatrix} c_1 e^{\lambda_1 t} \\ c_2 e^{\lambda_2 t} \\ \vdots \\ c_{M-1} e^{\lambda_{M-1} t} \\ c_M e^{\lambda_M t} \end{pmatrix}$$

where $\mathbf{V}_j$ and λ_j are the eigenvector and eigenvalue of the matrix A and we are denoting $u_j(t) = u^{z_i}_{\bar{m}_j}(t)$, $1 \leq j \leq M$. Evaluating in $t = 0$ we have

$$\begin{pmatrix} u_1(0) \\ u_2(0) \\ \vdots \\ u_{M-1}(0) \\ u_M(0) \end{pmatrix} = \begin{pmatrix} \mathbf{V}_1 & \mathbf{V}_2 & \cdots & \mathbf{V}_{M-1} & \mathbf{V}_M \end{pmatrix} \begin{pmatrix} c_1 \\ c_2 \\ \vdots \\ c_{M-1} \\ c_M \end{pmatrix},$$

and therefore

$$\begin{pmatrix} c_1 \\ c_2 \\ \vdots \\ c_{M-1} \\ c_M \end{pmatrix} = \begin{pmatrix} \mathbf{V}_1 & \mathbf{V}_2 & \cdots & \mathbf{V}_{M-1} & \mathbf{V}_M \end{pmatrix}^{-1} \begin{pmatrix} u_1(0) \\ u_2(0) \\ \vdots \\ u_{M-1}(0) \\ u_M(0) \end{pmatrix},$$

with $u_j(t) = u^{z_i}_{\bar{m}_j}(t)$ given by the expression (14.16). Now we are able to fix the value of the initial conditions for the first case. Notice that also the constants c_j depend on the value z_i, i.e. $c_j = c_j^{z_i}$. For the second functional, from $u(t,x) = \mathbb{E}(u_0(X_t^x))$ we obtain

$$u(0,x) = \mathbb{E}(u_0(X_0^x)) = \int_0^1 x(z)dz.$$

Since on the other hand

$$u(0,x) = \sum_{\bar{n} \in \mathcal{J}^{M,N}} u_{\bar{n}}(0) H_{\bar{n}}(x),$$

then

$$\int_0^1 x(z)dz = \sum_{\bar{n} \in \mathcal{J}^{M,N}} u_{\bar{n}}(0) H_{\bar{n}}(x).$$

Multiplying by $H_{\bar{m}}(x)$and integrating in the Hilbert space $L^2(\mathcal{H}, \mu)$ and by using Fubini we have

$$u_{\bar{m}}(0) = \int_{\mathcal{H}} \int_0^1 x(z)dz H_{\bar{m}}(x)\mu(dx) = \int_0^1 \left(\int_{\mathcal{H}} x(z) H_{\bar{m}}(x)\mu(dx) \right) dz$$

We focus on the integral on $\mathcal{H}$. By following the steps given for the first functional (just replacing z_i by z) we can arrive to the following expression

$$\int_{\mathcal{H}} x(z) H_{\bar{m}}(x)\mu(dx) \approx \prod_{k=1}^{M} \frac{e_k(z)}{\lambda_k} \int_{\mathbb{R}} P_{m_k}(\xi_k)\xi_k \mu(d\xi_k),$$

thus

$$u_{\bar{m}}(0) \approx \int_0^1 \prod_{k=1}^{M} \frac{e_k(z)}{\lambda_k} \left(\int_{\mathbb{R}} P_{m_k}(\xi_k) \xi_k \mu(d\xi_k) \right) dz$$

$$= \prod_{k=1}^{M} \int_{\mathbb{R}} P_{m_k}(\xi_k) \xi_k \mu(d\xi_k) \int_0^1 \frac{e_k(z)}{\lambda_k} dz \qquad \text{(Equation 14.17)}$$

Using this result and following the procedure for the first functional we are able to fix the initial conditions.

14.5 - Well posedness and convergence

Let $\mathcal{J}$ be a countable set, $\{\lambda_m; m \in \mathcal{J}\}$ a sequence of positive real numbers diverging to infinity $\{C_{nm}; n, m \in \mathcal{J}\}$and a sequence of real numbers. Consider the infinite system of equations

$$u'_m(t) = -\lambda_m u_m(t) + \sum_{n \in \mathcal{J}} C_{nm} u_n(t), \qquad t \geq 0$$

$$u_m(0) = u_m^0, \qquad m \in \mathcal{J}$$

with given initial condition $\left\{u_m^0; m \in \mathcal{J}\right\}$. We always assume

$$\sum_{m \in \mathcal{J}} \left(u_m^0\right)^2 < \infty.$$

Definition 14.7 *A solution is a sequence* $\{u_m(\cdot); m \in \mathcal{J}\}$ *of continuous functions on* $[0,T]$*such that:*

I) $$\sup_{t \in [0,T]} \sum_{m \in \mathcal{J}} u_m^2(t) + \int_0^T \sum_{m \in \mathcal{J}} \lambda_m u_m^2(s)\, ds < \infty$$

ii) The series $\sum_{n \in \mathcal{J}} C_{nm} u_n(t)$*converges, for a.e. t, to an integrable functions on* $[0,T]$*and*

iii) $$u_m(t) = u_m^0 - \int_0^t \lambda_m u_m(s)\, ds + \int_0^t \sum_{n \in \mathcal{J}} C_{nm} u_n(s)\, ds$$

for all $m \in \mathcal{J}$ *and* $t \in [0,T]$.

Consider also, for any finite subset $\widetilde{\mathcal{J}} \subset \mathcal{J}$, the finite system

$$\widetilde{u}'_m(t) = -\lambda_m \widetilde{u}_m(t) + \sum_{n \in \widetilde{\mathcal{J}}} C_{nm} \widetilde{u}_n(t), \qquad t \geq 0$$

$$\widetilde{u}_m(0) = u_m^0, \qquad m \in \widetilde{\mathcal{J}}$$

The definition of solution for this finite system is obvious and existence and uniqueness is well known.

Theorem 14.8

Assume that the family $\{C_{nm}; n, m \in \mathcal{J}\}$ *satisfies, for some constant* $C > 0$,

$$\sum_{n,m\in\mathcal{J}} C_{nm}\alpha_n\beta_m \leq C\left(\sum_{n\in\mathcal{J}} \lambda_n\alpha_n^2\right)^{1/2}\left(\sum_{m\in\mathcal{J}} \beta_m^2\right)^{1/2} \qquad \text{for all sequences } \{\alpha_n, \beta_n; n \in \mathcal{J}\}$$

(Equation 14.18)

Then there exists a unique solution. Moreover,

$$\sup_{t\in[0,T]} \sum_{m\in\widetilde{\mathcal{J}}} \left(u_m(t) - \widetilde{u}_m(t)\right)^2 + \int_0^T \sum_{m\in\widetilde{\mathcal{J}}} \lambda_m \left(u_m(s) - \widetilde{u}_m(s)\right)^2 ds \leq C_1 \int_0^T \sum_{m\in\widetilde{\mathcal{J}}^c} \lambda_m u_m^2(s)\, ds$$

for some $C_1 > 0$ *independent of* $\widetilde{\mathcal{J}}$*; where the term* $\int_0^T \sum_{m\in\widetilde{\mathcal{J}}^c} \lambda_m u_m^2(s)\, ds$ *converges to zero as* $\widetilde{\mathcal{J}}$ *converges to* $\mathcal{J}$. For a proof see Delgado and Flandoli.

14.6 - Numerical Results

14.6.1 - Algorithm description

In this subsection we describe the algorithm for simulating the Kolmogorov equations associated with stochastic partial differential equations whose results we show in Subsection (14.7).

1. Choose the algorithm's parameters:

   a) The space $\mathcal{H}$ where the SPDE will be defined.

   b) The operator A and its eigenfunctions λ_k and eigenvalues $\mathrm{e}_k(\cdot)$.

   c) The functional $u_0 : \mathcal{H} \to \mathbb{R}$.

   d) N, M and then fix the set $J^{N,M}$.

   e) The time step Δt and Δx in the physical space.

2. Compute the quantities $\bar{C}_{\bar{n},\bar{m}}$, for each $\bar{n}, \bar{m} \in J^{N,M}$, to approximate (14.11).

3. Set the finite system of coupled ordinary differential equation (14.13).

4. Rewriting the system (14.13) as a matrix differential equations and by solving it numerically we obtain, up to a set of constants, the time-functions $u_{\bar{n}}(t)$, for each $\bar{n} \in J^{N,M}$.

5. By using the functional u_0 the constants in the last step are fixed.

6. We then define the space-time approximation for the Kolmogorov equation as

$$u_N(t,x) = \sum_{j=1}^{N} u_j(t) H_j(x) \approx \sum_{j\geq 1} u_j(t) H_j(x) = u(t,x)$$

Remark 14.9

- *Given the operator* A*, we choose its eigenvalues as the basis for the Hilbert space* $\mathcal{H}$ *and we have to find its eigenvalues* λ_k*.*
- *The choice of the functional* u_0 *will change the way we determine the initial condition of the Kolmogorov equation, then it will necessary to adapt the method for each* u_0*.*
- *The quantities* $\bar{C}_{\bar{n},\bar{m}}$ *are those that require more computing resources because we have to compute and approximate several integrals for each* $\bar{n}, \bar{m} \in J^{N,M}$*. In our example these quantities are given by the expressions (14.23).*

14.7 - Stochastic Burgers Equation on an interval

Set $\mathcal{H} = L^2(0,1)$. We consider the stochastic Burgers equation in the interval $[0,1]$:

$$dX(t,\xi) = \Big[\nu \partial_\xi^2 X(t,\xi) + \frac{1}{2}\partial_\xi (X^2(t,\xi))\Big]dt + dW_t(t,\xi), \quad t > 0, \quad \xi \in (0,1)$$

(Equation 14.19)

$$X(t,0) = X(t,1) = 0, \quad t > 0,$$

$$X(0,\xi) = x(\xi), \quad x \in \mathcal{H}$$ (Equation 14.20)

W is a cylindrical Wiener process on $\mathcal{H}$, associated to a stochastic basis $(\Omega, \mathcal{F}, , (\mathcal{F}_t)_{t\geq 0})$. ν is the viscosity coefficient.

We rewrite the Burgers equation as an abstract differential equation in $\mathcal{H}$. Set $A = \nu\partial_\xi^2$ and $B(x) = \frac{1}{2}\partial_\xi(x^2)$, $x \in \mathcal{H}$, with domains $D(A) = H^2(0,1) \cap H_0^1(0,1)$ and $D(B) = H_0^1(0,1)$, respectively. Then, (14.19) can be rewritten as

$$dX = [AX + B(X)]dt + dW_t$$ (Equation 14.21)

$$X(0) = x \quad x \in \mathcal{H}.$$

The operator A is selfadjoint with a complete orthonormal system of eigenfunctions in $\mathcal{H}$ given by

$$e_k(\xi) = \sqrt{2}\sin(k\pi\xi), \qquad \xi \in [0,1], k \in \mathbb{N}.$$

Moreover, Asatisfies $Ae_k = -\nu\pi^2 k^2 e_k$, for $k \in \mathbb{N}$.

As before, we define $u(t,x) = \left[u_0(X_t^x)\right]$ and then $u(t,x)$ satisfies the Kolmogorov equation

$$\frac{\partial u}{\partial t} = \frac{1}{2}Tr(QD^2u) + \langle Ax, Du\rangle_{\mathcal{H}} + \langle B(x), Du\rangle_{\mathcal{H}}, \qquad x \in D(A).$$

Results on the existence and uniqueness of the solution to the Kolmogorov equation can be found, for instance, in Da Prato (2004), Chapter 5.

We will consider again two types of functionals :

$$u_0^{\xi_0}(g) := g(\xi_0). \qquad \text{for fixed } \xi_0 \in (0,1)$$

and

$$u_0(g) := \int_0^1 g(\xi)d\xi.$$

We now apply the numerical method. We write the solution u as

$$u(t,x) = \sum_{\bar{n}} u_{\bar{n}}(t)H_{\bar{n}}(x).$$

and by following the procedure before we arrive to an infinite system of ordinary differential equations:

$$\dot{u}_{\bar{m}}(t) = -u_{\bar{m}}(t)\lambda_{\bar{m}} + \sum_{\bar{n}\in\mathcal{J}} u_{\bar{n}}(t)C_{\bar{n},\bar{m}}, \qquad \bar{n},\bar{m} \in \mathcal{J} \qquad \text{(Equation 14.22)}$$

where $C_{\bar{n},\bar{m}}$ is given by

$$C_{\bar{n},\bar{m}} = \int_{\mathcal{H}} \left\langle B(x), D_x H_{\bar{n}}(x)\right\rangle_{\mathcal{H}} H_{\bar{m}}(x)\mu(dx).$$

First we need to calculate the value of the constants $C_{\bar{n},\bar{m}}$, then we need to calculate expressions such as $B(x), D_x H_{\bar{n}}(x)$. Focus on the term $B(x) = \frac{1}{2}\partial_\xi(x^2)$. By writing $x = \sum_k \beta_k e_k$, with $\beta_k := \langle x, e_k\rangle_{\mathcal{H}}$ we have

$$B(x) = \frac{1}{2}\partial_\xi\Big(\sum_k \beta_k e_k\Big)^2 = \frac{1}{2}\partial_\xi\Big[\sum_l\sum_k \beta_l\beta_k e_l e_k\Big] = \frac{1}{2}\sum_l\sum_k \beta_l\beta_k\big(e_l e_k' + e_l' e_k\big).$$

For the expression $D_x H_{\bar{n}}(x)$we have

$$D_x H_{\bar{n}}(x) = \sum_{j=1}^{\infty} \prod_{\substack{i=1 \\ i\neq j}}^{\infty} P_{n_i}\big(\langle x, \Lambda^{-1/2} e_i\rangle_{\mathcal{H}}\big) P'_{n_j}\big(\langle x, \Lambda^{-1/2} e_j\rangle_{\mathcal{H}}\big) \Lambda^{-1/2} e_j$$

Setting $\Lambda = (-A)^{-1}$ and by recalling that $Ae_j = -\nu\pi^2 j^2 e_j$ we have $\Lambda^{-1/2} e_j = \sqrt{2\nu}\pi|j| e_j$, and by using the last expression we have,

$$C_{\bar{n},\bar{m}} = \frac{1}{2}\int_{\mathcal{H}} H_{\bar{m}}(x)\mu(dx) \sum_{j=1}^{\infty} \prod_{\substack{i=1 \\ i\neq j}}^{\infty} P_{n_i}\big(\langle x, \Lambda^{-1/2} e_i\rangle_{\mathcal{H}}\big) P'_{n_j}\big(\langle x, \Lambda^{-1/2} e_j\rangle_{\mathcal{H}}\big) \sqrt{2\nu}\pi|j|$$

$$\times \sum_{l}\sum_{k} \beta_l\beta_k \big\langle e_l e'_k + e'_l e_k, e_j\big\rangle_{\mathcal{H}}$$

$$= \frac{1}{2}\int_{\mathcal{H}} \mu(dx) \sum_{j=1}^{\infty} \sqrt{2\nu}\pi|j| P_{m_j}\big(\langle x, \Lambda^{-1/2} e_j\rangle_{\mathcal{H}}\big) P'_{n_j}\big(\langle x, \Lambda^{-1/2} e_j\rangle_{\mathcal{H}}\big)$$

$$\times \prod_{\substack{i=1 \\ i\neq j}}^{\infty} P_{n_i}\big(\langle x, \Lambda^{-1/2} e_i\rangle_{\mathcal{H}}\big) P_{m_i}\big(\langle x, \Lambda^{-1/2} e_i\rangle_{\mathcal{H}}\big) \sum_{l}\sum_{k} \beta_l\beta_k \big\langle e_l e'_k + e'_l e_k, e_j\big\rangle_{\mathcal{H}}.$$

For $N_1 \in \mathbb{N}$ define as before the set$S_{N_1} = \{\bar{n}_1, \bar{n}_2, \ldots, \bar{n}_{N_1} : \bar{n}_i \in J^{M,N}, i = 1, \ldots, N_1\}$. Moreover, for $\bar{n}, \bar{m} \in S_M$ define

$$\bar{C}_{\bar{n},\bar{m}} := \frac{1}{2}\sum_{j=1}^{M} \sqrt{2\nu}\pi|j| \int_M P_{m_j}(\xi_j) P'_{n_j}(\xi_j)\mu(d\xi_j)$$

$$\times \prod_{\substack{i=1 \\ i\neq j}}^{M} P_{m_i}(\xi_i) P_{n_i}(\xi_i)\mu(d\xi_i) \sum_{l=1}^{M}\sum_{k=1}^{M} \beta_l\beta_k \big\langle e_l e'_k + e'_l e_k, e_j\big\rangle_{\mathcal{H}}. \qquad \text{(Equation 14.23)}$$

and the finite system of ordinary differential equations:

$$\dot{u}_{\bar{m}}(t) = -u_{\bar{m}}(t)\lambda_{\bar{m}} + \sum_{\bar{n}\in S_M} u_{\bar{n}}(t)\bar{C}_{\bar{n},\bar{m}}, \qquad \text{for each } \bar{m} \in S_M \text{ and } \bar{n} \in S_M.$$

(Equation 14.24)

Then (14.24) approximates to the infinite system of ordinary differential equations (14.22) when $N, M \to \infty$. We use the system (14.24) to approximate the solution of the FPK equation associated with the Burgers equation.

Deterministic equation associated with the stochastic Burgers Equation.

Set

$$y(t,\xi) = \mathbb{E}\big[X_t(\xi)\big]$$

then, $y(t,\xi)$ solves the differential equation

$$\frac{\partial y}{\partial t} = \nu \frac{\partial^2 y}{\partial \xi^2} + + \frac{1}{2}\partial_\xi (y^2(t,\xi)) \qquad \text{(Equation 14.25)}$$

$$y\big|_{t=0} = \mathbb{E}(X_0).$$

We solve numerically this equation by using the Matlab library *pdepe* and we compare our results by using the spectral method with the one obtained with the pdepe Matlab library.

Results of the simulation

The following graphs show simulations by using the proposed method with different values of $J^{N,M}$, $\mathrm{N}{=}4{,}5$. We make a comparison with the solution of the deterministic equation, as was described in subsection (14.7) by using the matlab library *pdepe*.

The results of the simulation for the evaluation functional are in the first group of graphs. The second graph shows the simulation for the second functional. The results were obtained with the coefficient $\nu = 0.2, 0.1, 0.01$.

The first graph (from the left to the right) in each group is the one obtained by using the Matlab library PDEPE. The other two graph are obtained with the use of the numerical method reviewed on this paper.

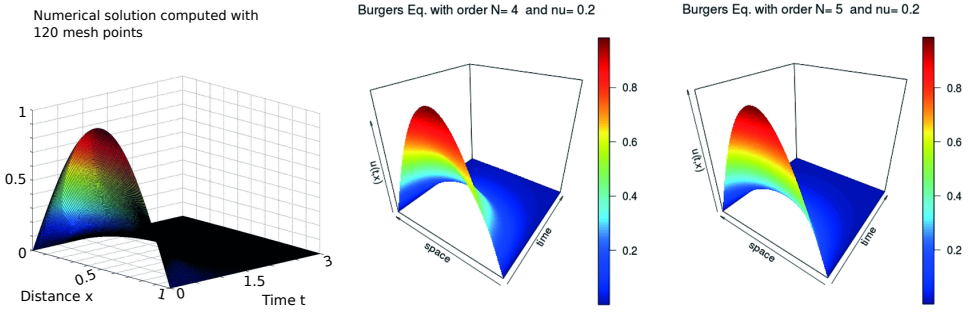

Figure 1: Simulations for the Burgers equation with the Matlab library pdepe and with the spectral method for , . $\mathrm{N}{=}4{,}5$, $u_0^{\xi_0}(g)$.

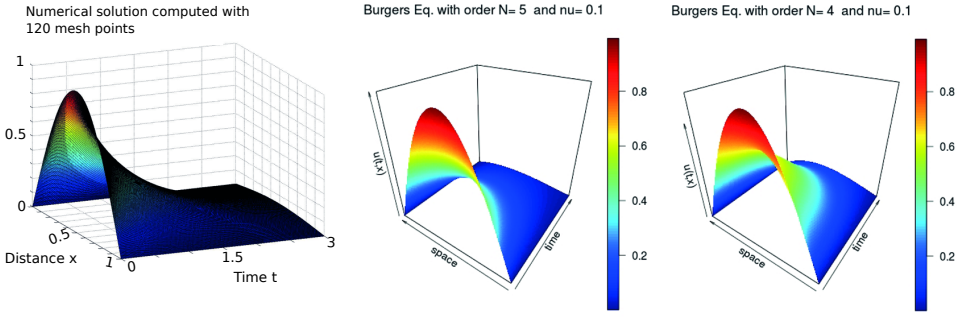

Figure 2: Simulations for the Burgers equation with the Matlab library pdepe and with the spectral method for $\mathrm{N}=4,5$, $u_0^{\xi_0}(g)$.

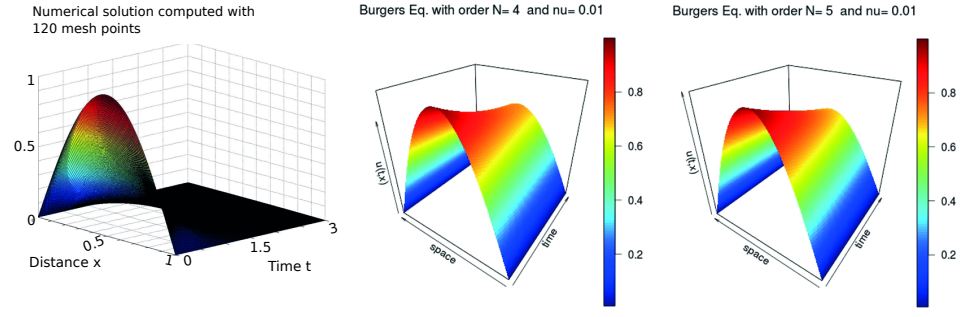

Figure 3: Simulations for the Burgers equation with the Matlab library pdepe and with the spectral method for $\mathrm{N}=4,5$, $u_0^{\xi_0}(g)$.

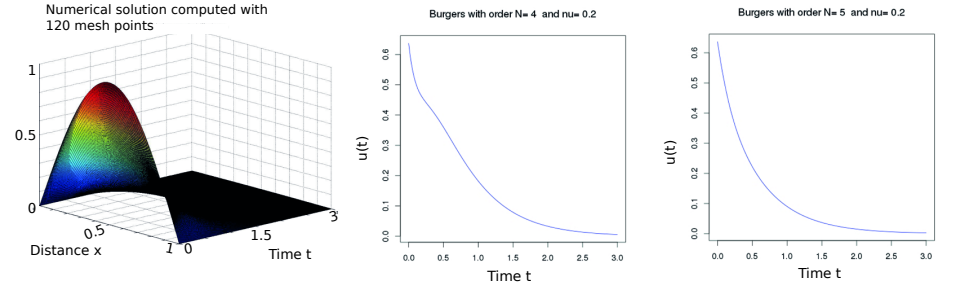

Figure 4: Simulations for the Burgers equation with the Matlab library pdepe and with the spectral method for $\mathrm{N}=4,5$, $u_0(g)$.

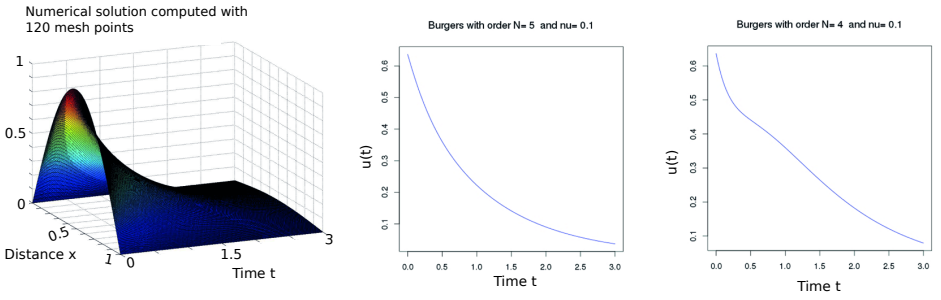

Figure 5: Simulations for the Burgers equation with the Matlab library pdepe and with the spectral method for $\mathrm{N}=4,5$, $u_0(g)$.

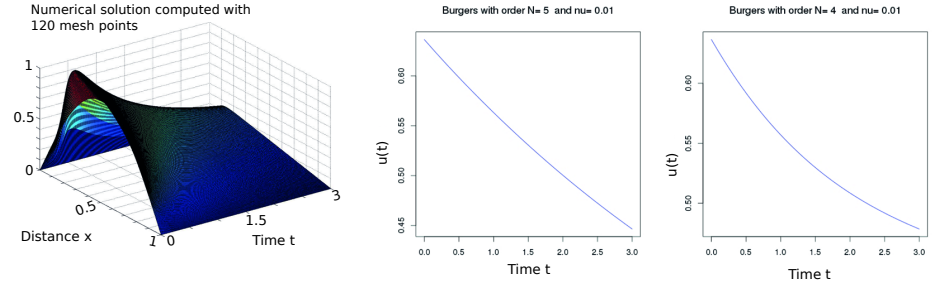

Figure 6: Simulations for the Burgers equation with the Matlab library pdepe and with the spectral method for $\mathrm{N}=4,5$, $u_0(g)$.

14.8 - Conclusions

In this paper we reviewed a numerical method to solve Fokker-Plank-Kolmogorov equations and we tested this method by applying it to the Kolmogorov equations associated to a stochastic Burgers equation in 1D, in a simple domain. The results obtained are really promising. However, there are a few limitations. The first is that the noise in the SPDE is restricted to the additive case and to cover the multiplicative case seems infeasible at this moment. Indeed, even if one is able to prove existence and uniqueness of an invariant measure ν for the Ornstein-Uhlenbeck semigroup associated with the SPDE, there would remain the fully characterization of the measure and to find a complete basis for the Hilbert Space $L^2(\mathcal{H},\nu)$. Another issue is that we have applied the method to very simple domains, However, to cover the cases with complex domains one can use ideas of domain decomposition techniques similar to those used in spectral element methods. This is part of a forthcoming paper.

The method can be adapted to cover the Fokker-Plank equations associated with SPDE's, this will be studied in a subsequent work.

An application to fluid dynamics is expected to be completed in the following years. The mentioned application will be completed by applying the method to the stochastic Navier-Stokes equations in physical dimension two and three. A future application to vulcanology is planned by using the experienced with the application to the stochastic Navier-Stokes equations.

Acknowledgements

The research leading to these results has received funding from the People Programme (Marie Curie Actions) of the European Union's Seventh Framework Programme (FP7/2007-2013) under the project NEMOH, REA grant agreement n. 289976. The author would like to express my special thanks of gratitude to the INGV sezione di Pisa for the great opportunity to do this project, which also helped me in learn several topics in Geophysics and its relationship with Mathematics. I want to thanks, in particular, to Paolo Papale for his big patience with me.

References

Barbu, V. and Da Prato, G. (2008). The Kolmogorov equation for a 2D Navier-Stokes stochastic flow in a channel, nonlinear Analysis. 69, pp. 940-949.

Bogachev, V., Da Prato, G. and R$\ddot{o}$eckner, M. (2010). Existence results for Fokker-Planck equations in Hilbert space, Seminar on Stochastic Analysis, Random Fields and Applications VI. Progress in Probability Volume 63, 2011, pp 23-35.

Cameron, R.H. and Martin W. T. (1947). The orthogonal development of non-linear functionals in series of Fourier- Hermite functionals, Annals of Mathematics 48 (2): 385-392.

Chow, P.L. (1996). Infinte-dimensional Kolmogorov equations in Gauss-Sobolev spaces, Stoch. Analy. Applic. 14, 257-282.

Chow, P.L. (2007). Stochastic partial differential equations, Chapman and Hall/CRC.

Da Prato, G. (2004). Kolmogorov equations for stochastic partial differential equations, Advanced Courses in Mathematics - CRM Barcelona. Birkh$\ddot{a}$user.

Da Prato, G. and Debussche A. (2007). m-Dissipativity of Kolmogorov Operators Corresponding to Burgers Equations with Space-time White Noise, Potential Analysis. Volume 26, Issue 1 , pp 31-55.

Da Prato, G. and Zabczyk J. (2002). Second order partial differential equations in Hilbert spaces, Cambridge University Press.

Da Prato, G. and Zabczyk J. (1992). Stochastic equations in infinite dimensions, Cambridge University Press.

Da Prato, G., Flandoli, F. and R$\ddot{o}$ckner, M. (2013). Fokker-Planck Equations for SPDE with Non-trace-class Noise, Communications in Mathematics and Statistics. Volume 1, Issue 3, pp 281-304.

Delgado-Vences, F. and Flandoli, F. (2016). A spectral-based numerical method for Kolmogorov equations in Hilbert spaces, http://arxiv.org/abs/1601.01503, Infinite Dimension analysis and Quantum Probability. 37 pages.

Doostan, A. and Iaccarino, G. (2009). A least-squares approximation of partial differential equations with high dimensional random inputs, Journal of Computational Physics, Vol. 228, No. 12, pp. 4332– 4345.

Fagents, S.A., Gregg, T.K.P., Lopes, R. M. C. Eds. (2012). Modeling Volcanic Processes, The Physics and Mathematics of Volcanism. Cambridge University Press.

Goldberg, A.J. and Schwartz, J.L. (1972). Systems of Ordinary Differential Equations : An Introduction, Published by Joanna Cotler Books.

Hou, T. Y., Luo, W., Rozovskii, B. and Zhou, H.M. (2006). Wiener Chaos Expansions and Numerical Solutions of Randomly Forced Equations of Fluid Mechanics, J. Comput. Phys. , 216 , 687-706.

Huang, Z. and Yan, J. (2000). Introduction to infinite dimensional stochastic analysis, Kluwer academics.

Le Matre, O. P. and Knio, O.M. (2010). Spectral methods for uncertainty quantification. With applications to computational fluid dynamics, Scientific Computation. Springer, New York.

Lototsky, S. V. (2011). Chaos Approach to Nonlinear Filtering. In: D. Crisan and B. L. Rozovskii (editors), The Oxford Handbook of Nonlinear Filtering, pp. 231-264, Oxford University Press.

Lototsky, S. V. and Rozovskii, B. L. (2006). Wiener Chaos Solutions of Linear Stochastic Evolution Equations, Annals of Probability, Vol. 34, No. 2, pp. 638-662.

Luo, W. (2006). Wiener Chaos expansion and numerical solutions for stochastic partial differential equations, PhD thesis. California Institute of Technology.

Mathelin, L., Hussaini, Y. and Zang, T. A (2005). Stochastic approaches to uncertainty quantification in CFD simulations, Numerical Algorithms 38.1-3, 209-236.

Mathelin, L., Hussaini, M. Y., Zang, T. A. and Bataille F. (2004). Uncertainty propagation for a turbulent, compressible nozzle flow using stochastic methods, AIAA journal, 42(8), 1669-1676.

Schwab, C. and S$\ddot{u}$li, E. (2013). Adaptive Galerkin approximation algorithms for Kolmogorov equations in infinite dimensions, Stochastic Partial Differential Equations: Analysis and Computations. 1:204-239.

Francisco Javier Delgado-Vences, Mexico
delgado@im.unam.mx

Affiliation under NEMOH
Istituto Nazionale di Geofisica e Vulcanologia, Sezione di Pisa, Pisa, Italy

Research theme under NEMOH
Development of a mixed deterministic/stochastic approach to the solution of the transport equations describing volcanic processes

I'm a mathematician interested in applications of stochastic and statistics models to business, finance, economy, engineering, physics, chemistry, psychology, biology, medicine, Computer science, etc.

I have a degree in actuarial sciences and a master degree in Mathematical sciences. I completed my PhD on Mathematics under the supervision of Dra. Marta Sanz-Solé working on Stochastic Partial Differential Equations (SPDE's). During my PhD I worked on theoretical aspects of the SPDE's and I wrote two research papers that were published in a high rank journal of mathematics.

After my PhD, under the Nemoh research position I started the study of numerical methods for Partial Diferential Equatons (PDE's) and Stochastis PDE's. The latter is a very new and complex research line that can play a central role in uncertainty quantification and risk assessment, for instance. In collaboration with prof. Franco Flandoli, we have proposed a new numerical method for the kolmogorov equations associated with SPDE's in Hilbert spaces. The proposed method allow us to simulate "directly" functionals of the solutions of SPDE's. We wrote a paper which has been accepted for publication in a high level peer-reviewed mathematical journal.

In October 2016 I get a professorship position called "Catedra Conacyt" in Oaxaca de Juarez, Mexico at the Instituto de Matematicas from the Universidad Nacional Autonoma de Mexico, Where I'm having the opportunity to continue working on the research lines I started during my Nemoh position.

Nemoh has given me the opportunity to learn several real problems that appears in Geophysics and in Volcanology in particular, such problems, I strongly believed, could be solved by using several mathematical tools, so in the future I will come back to think on all this problems to motivate my research on mathematics.

Chapter 15

Application of one-dimensional numerical models for investigation of coignimbrite plume formation

Samantha Engwell

Istituto Nazionale di Geofisica e Vulcanologia, Sezione di Pisa, Pisa, Italy

Tutorship: Mattia de' Michieli Vitturi, Tomaso Esposti Ongaro, and Augusto Neri

Istituto Nazionale di Geofisica e Vulcanologia, Sezione di Pisa, Pisa, Italy

Abstract

Coignimbrite plumes provide a common and effective mechanism by which large volumes of fine-grained ash are injected into the atmosphere. Such plumes form in association with the propagation of pyroclastic density currents, and therefore are common phenomena on active volcanoes. Herein, two one-dimensional axisymmetric steady state models were applied. The first describes the parent pyroclastic density current, specifically an ash flow, and is used to provide information on controls, location and characteristics of the ash flow as it lofts to form the coignimbrite plume. The second model describes plume rise, with a key output being the maximum plume height. The two models were coupled such that outputs from the ash flow model directly fed into the plume model to enable investigation of the effect of vent source conditions on modelled coignimbrite plume characteristics. Formal global sensitivity analysis was applied to statistically investigate these controls, describe the coignimbrite source and the maximum plume height attained. The results highlight the role of gas mass fraction and temperature, together describing the mixture buoyancy, of the propagating ash flow in controlling plume lift off, and the mass flux of material into the plume on controlling plume height. Finally, the study highlight inadequacies in describing the plume source condition, and in particular the transition from horizontal to vertical momentum.

Keywords: pyroclastic density currents, coignimbrite plumes, numerical modelling, sensitivity analysis

15. 1 **- Introduction**

During explosive volcanic eruptions, plumes are formed which transport ash high into the atmosphere above the volcano, from where it can be dispersed great distances downwind. Such plumes not only form directly above the vent, but can also form in association with the emplacement of pyroclastic density currents (PDCs, Figure 1). These plumes, commonly labelled coignimbrite plumes (Woods and Wohletz 1991), can rise to great altitudes and thus provide an extremely effective mechanism of ash injection into the atmosphere (e.g. Sparks et al., 1986).

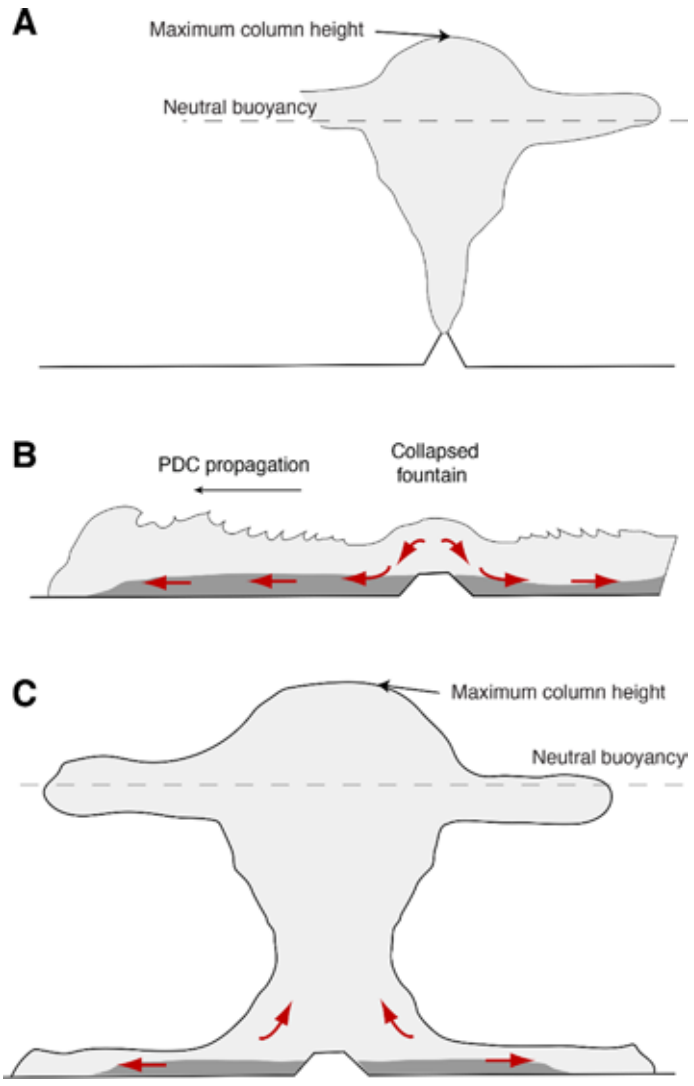

Figure 1. Schematic of vent derived compared to coignimbrite plumes. Vent-derived plumes (A) form as a mixture of hot gas and ash is ejected from the vent at high velocity during an explosive eruption. However, coignimbrite plumes (C) form in association with pyroclastic density currents (B), whereby the upper portion of the mixture entrains sufficient ambient air to result in buoyancy reversal, and lofting.

While a great deal is known regarding plumes originating directly from the vent, relatively little research has been conducted on the formation and rise of coignimbrite plumes. This is partly due to a comparative lack of recorded observations describing plume characteristics, with most focusing on the very largest events (e.g. Mount St. Helens 1980, Sparks et al., 1986; Pinatubo 1991, Holasek et al., 1996). As a consequence, controls on formation of these plumes as a function of eruptive conditions are still poorly constrained. Analysis of deposits imply that the material transported by coignimbrite plumes is very different to that for vent-derived plumes. Coignimbrite deposits are very

fine grained, and deposits from a number of different examples show remarkably similar characteristics implying very similar mechanisms regardless of scale (Engwell & Eychenne, 2016). In this study, we implement simple 1D numerical models to investigate the factors important for the formation of coignimbrite plumes, and those that control the height to which these plumes reach in the atmosphere, a key consideration when assessing risk to aviation. Sensitivity analysis techniques are applied to investigate the control of variance and uncertainty of model inputs on model outputs, to identify controlling model inputs for targeted further research.

15. 2 **- Application of one-dimensional models**

Two numerical models were applied to investigate the controls on coignimbrite plume formation, and their rise through the atmosphere. The first, a modified version of the Bursik and Woods (1996) ash flow model simulates the horizontal motion of a hot dilute PDC. The second model, a modified version of the Bursik (2001) plume model is used to simulate the vertical motion of the rising coignimbrite plume and enables investigation of the controls on plume height.

15. 2.1 **- Ash flow model**

The steady state ash flow model of Bursik and Woods (1996) was employed to simulate PDC propagation solving equations for conservation of mass (for both mixture and particles of different sizes), momentum and energy. Bursik and Woods (1996) describe two flow end member types, defined by their Richardson number; supercritical (Ri < 1) and subcritical flow (Ri > 1), however only the supercritical case was examined in detail in this study. For this purpose, the terms of the equations presented in Bursik and Woods (1996) were rearranged such that momentum is calculated as a function of the input Richardson number ($Ri = (gh(\beta-\alpha))/\beta u^2$, where g is gravitational acceleration, h is flow thickness, β is flow density, α ambient density and u flow velocity). The constitutive equations are presented in full in Engwell et al. (2016). These equations were solved using a FORTRAN90 code, with flow parameters calculated by integration with distance. The final flow runout is defined as the distance at which the flow density reaches ambient, and was assumed to be the point at which coignimbrite plume formation occurs.

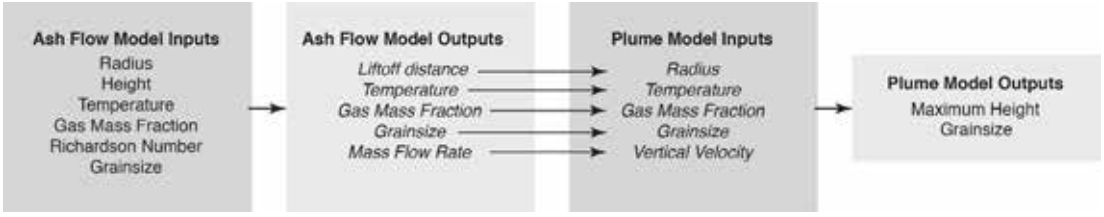

Figure 2. Flow diagram illustrating the key inputs and outputs from the ash flow and plume models.

15. 2.2 **- Plume rise model**

A modified version of the Bursik (2001) plume model was applied to study the relation between plume height and source conditions. The model (Barsotti et al., 2008) is written in FORTRAN90 and

solves equations for conservation of mass, momentum and thermal energy of bulk mixture with height. Required input parameters for the plume model are the mixture gas mass fraction and temperature and the velocity and radius of the lofting plume. A further required parameter is the entrainment coefficient, which describes the rate at which ambient air is entrained into the plume. In this study, two entrainment assumptions were used. The first assuming constant entrainment with height following Morton et al., (1956). The second assumptoin is based on the studies of Carazzo et al. (2008, 2012), whereby entrainment is variable dependent on the Richardson number of the plume, such that the entrainment rate is greater when the density of the plume is lower than ambient, but lower when the reverse is true.

15. 2.3 **- Coupled Model**

The ash flow model was coupled with the plume model to investigate the effect of varying ash flow model input parameters on simulated plume height (Figure 2). As mentioned above, herein only the supercritical ash flow model was applied. The required inputs for the ash flow model are: initial flow thickness and flow radius, Richardson number, temperature, gas mass fraction and a description of the characteristics of particles within the flow. In Table 1, parameter bounds for each of these inputs are provided, resulting in a range of mass flow rates between 10^8 to 10^{10} kg/s. We assume that the flows are propagating across a flat plane, a valid assumption given modelled runouts are on the order of many kilometres.

Input parameter	Minimum	Maximum	Sensitivity Indices			
			Liftoff distance		Plume height	
			Main	*Total*	*Main*	*Total*
Flow thickness (km)	0.25	2	0.170	0.236	0.353	0.416
Flow radius (km)	0.25	2	0.315	0.389	0.176	0.177
Richardson Number[a]	0.1	0.99	-0.00035	0.0047	0.07	0.08
Gas mass fraction	0.1	0.3	0.253	0.365	0.14	0.17
Temperature (K)[b]	800	1100	0.144	0.141	0.042	0.08
Friction[c,d]	0.001	0.02	0.003	0.003	0.0002	0.00008
Median (phi)	-3.0	3.0	0.005	0.01	-0.0009	0.0002

Table 1. Parameter bounds for initial conditions used for application of the coupled model, relating to mass flow rates of between 10^8 and 10^{10} kg/s. Variable grain size is only applied in estimation of sensitivity indices, in all other examples initial grainsize distribution has a median of 0 phi (1 mm) and a standard deviation of 2 phi. Initial magmatic gas mass fraction 0.03 throughout. Main and total sensitivity indices for liftoff distance and plume height as discussed in Section 2.4. [a]Bursik and Woods (1996);[b]Sparks et al., (1997); [c]Schlicting (1969), [d]Sparks et al., (1978).

The coupled model was run 2000 times, with each simulation sampling different input parameters from the ranges provided in Table 1. From the results, a number of flow characteristics are extracted at the ash flow model final integration step to provide insight into the process of coignimbrite plume formation, and constrain characteristics of the mixture at this point. In particular, the initial radius, velocity and temperature inputs for the modelled plume were defined by the 5th to 95th percentiles of the values at the final runout from the ash flow model, with a

uniform distribution assumed. The initial plume radius was assumed to be equal to the final flow runout. The initial vertical velocity of the lofting plume (u_p) was calculated using the flow mass flux (M) at the final runout (r), and the final flow density (ρ_m; corresponding to the condition of neutral buoyancy), whereby:

$$u_p = \frac{M}{\rho_m \pi r^2}$$

This simplified assumption is based on observation of the Mount St. Helens 1980 eruption, which indicated that the coignimbrite plume lofted from the entire inundation extent of the blast (Sparks et al., 1986), and assumes that transition from horizontal to vertical flow is instantaneous. In all examples, the starting density of the mixture was assumed to be neutral, i.e. equal to ambient, controlled by mixture temperature and gas mass fraction.

15. 2.4 **- Sensitivity Analysis**

Global sensitivity analysis was performed using the software DAKOTA (Adams et al., 2009), whereby input parameter space is explored such that input-output parameter interactions and model non-linearity are quantified using a variance-based Monte Carlo method. Application of sensitivity analysis requires identification of a valid distribution (in the examples a uniform distribution is assumed) of values for each input parameter (Figure 3). The numerical model is applied a number of times, while varying input parameters by sampling the ascribed distribution for each parameter. The sensitivity of model results to model inputs is depicted by Sobol Indices, which describe the fraction of the variation in model output that can be attributed to each input. Two measures are presented here, main and total sensitivity indices. The main sensitivity index quantifies the expected reduction in variance in the model output that would be achieved if a given input was fixed (Saltelli et al., 2008). The total sensitivity indices describe both the relation of the final model output to the input but also the interaction of the parameter of interest with other input parameters. In both cases, a larger index implies a greater reliance of the output on the input parameter.

15. 3 **- Results**

15. 3.1 **- Ash flow model results**

Prior to application of sensitivity analysis, each of the models (the ash flow and plume rise model) were run to investigate modelled behaviour. Figure 4 illustrates the radial behaviour of a few key ash flow variables - flow thickness, velocity, temperature, density - for three selected simulations where only the initial Richardson number is varied. Varying the initial Richardson number results in different initial flow velocities, and consequently entrainment efficiency. All simulations initiate with a thickness of 2 km. In each example, the model predicts an immediate reduction in thickness, followed by a relatively constant thickness until the final liftoff distance is reached (Figure 4A). The

flow with the lowest initial Richardson number is thickest, related to greater entrainment of air as evidenced by lower flow density than the other examples (Figure 4D).

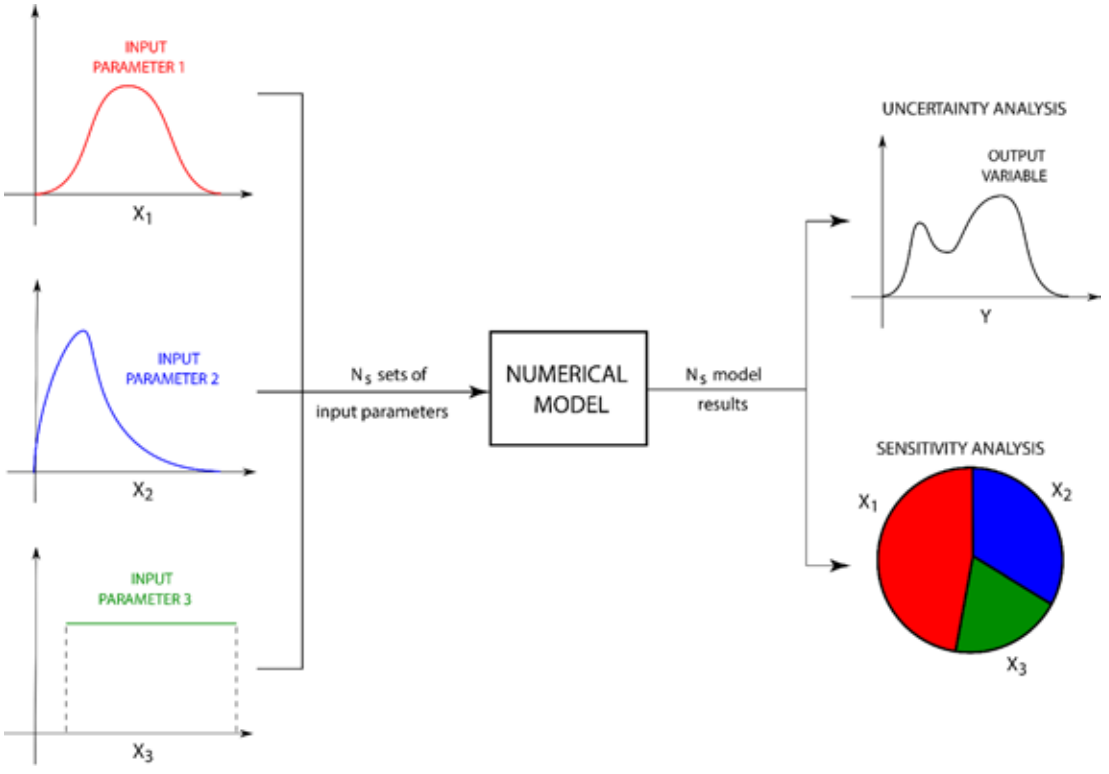

Figure 3. Schematic to illustrate how model uncertainty and sensitivity analysis are defined starting from uncertain input parameters. Please note that Ns refers to the number of simulations performed (i.e. the different sets of input parameters) and not the number of input parameters (from de' Michieli Vitturi et al., 2016).

The velocity profiles (Figure 4B) vary significantly for each modelled flow example, as initial velocity is controlled by the input Richardson number. In all of the examples, there is an initial increase in flow velocity related to the sudden reduction in flow thickness, followed by a small decrease as the density difference between the propagating current and ambient reduces. The final velocity for each of the modelled flows is greater than 100 m/s at the point at which flow density becomes equal to atmospheric (1.21 kg/m^3). Such high final velocities describe a significant mass flux, which were used to infer initial plume velocities that in some examples are many tens of metres per second (Engwell et al., 2016), comparable to Plinian events. Such high velocities are capable of carrying particles many cm's in diameter into the atmosphere, yet analysis of coignimbrite plume deposits suggest that they are universally composed of fine-grained ash (< 100 microns; Engwell and Eychenne 2016), indicating that large particles are not available for inclusion into the plume. In combination with the initial radius and liftoff mixture temperature, this initial velocity significantly impacts the final plume height attained.

Each flow simulation initiates with an eruption temperature of 1000 K, approximately equating to an initial flow temperature of 900 K once entrainment during column collapse is accounted for. Over the length of propagation, flow temperature decreases by 100 K in all examples, but at different rates associated with varying entrainment efficiencies (Figure 4C). Similar patterns are seen in flow density profiles (Figure 4D). Despite the same initial and final densities, density profiles vary as a function of Richardson number, with the mid Richardson number simulation density decreasing at a slower rate compared with the other simulations, due to reduced entrainment and therefore decreased sedimentation of particles.

While the other flow parameters vary at the liftoff distance, the final temperature and density are the same for each of the simulations, relating to the liftoff condition, whereby flow propagation ceases once the flow density reduces to that of the ambient. Despite different initial Richardson numbers, and consequently initial velocities and mass flow rates (between 4 x 10^9 and 10^{10} kg/s), the liftoff distance for each example is similar, between 7 and 8 km. For further results describing flow characteristics and behaviour, see Engwell et al., (2016).

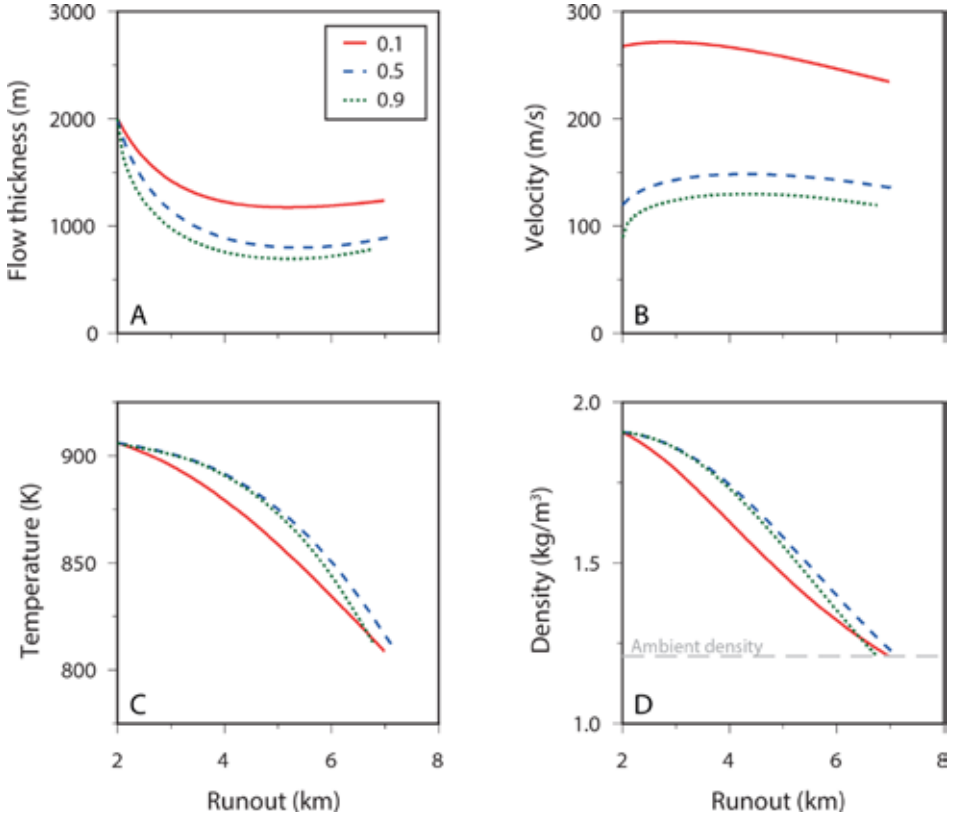

Figure 4. Profiles of selected pyroclastic flow characteristics with distance from source for three simulations with different Richardson numbers (0.1, 0.5, and 0.9) spanning the supercritical flow regime. Initial flow thickness and radius of 2 km, initial gas mass fraction is 0.2, initial temperature of 900 K, a friction coefficient of 0.001.

15. 3.2 - Plume rise model results

A number of differences exist between vent-derived and coignimbrite plume source conditions. In vent-derived plumes, the source area is small, the density of the mixture is considerably greater than the ambient, and the initial vertical velocity is on the order of hundreds of m/s (without considering the likely over-pressurised condition of the eruptive mixture at the vent). In comparison, coignimbrite plumes loft from a much larger area, have a similar density to the ambient, and have smaller vertical velocities. In order to highlight the differences, we conducted two sets of simulations (one for the vent-derived plume example and one for the coignimbrite) using the plume rise model, to compare plume characteristics with height given the different source characteristics, assuming an initial flow rate of 10^7 kg/s in both cases. To achieve the initial flow rate, the initial radius of the coignimbrite plume was an order of magnitude greater than that of the vent-derived plume, while both the density and the initial velocity were an order of magnitude less. For both plume types, simulations with two entrainment coefficient assumptions were conducted, the first using a constant entrainment coefficient (0.09 following Morton et al., (1956)) with height, and the second with a variable coefficient, as described above. Comparison of modelled plume radius, velocity and density with height for coignimbrite and vent-derived plumes (Figure 5) shows a number of differences both in profiles with height and also the maximum plume height. Specifically, the radius of the vent-derived plume increases with height, while the radius of the coignimbrite plume initially decreases, before following similar trends to the vent-derived plume and increasing with height (Figure 5A). The density of the vent-derived plume is initially much greater than ambient, but the plume becomes buoyant within the first few kilometres (Figure 5C). The vent-derived example with variable entrainment attains buoyancy at greater altitudes than the constant entrainment example (Figure 5C2). The starting condition of coignimbrite plume simulations is neutral buoyancy, and in comparison to the vent-derived results, there is very little difference in density trends with height for the two entrainment assumptions. The variable entrainment coefficient simulation results are density dependent, with reduced entrainment when the plume density is greater than ambient. In all cases, the plume density becomes equal to and then larger than ambient density at height in the atmosphere, but before the maximum plume height (determined as the point at which the vertical velocity is zero) is reached. This transition represents the neutral buoyancy level, and is assumed to be the height at which lateral intrusion of the plume occurs.

In comparison to plume radius and density, there are significant differences between velocity profiles both with plume type and entrainment assumption (Figure 5B). The initial vertical velocity of the vent-derived plume is large, and reduces drastically in the first few kilometres. Application of the two entrainment conditions results in different plume profiles for the vent-derived plume example. Where the constant entrainment coefficient is used, the plume velocity shows a decrease with altitude (simple buoyant), while when the variable entrainment coefficient is used the plume is super-buoyant (whereby the plume velocity decreases and then increases with height; Bursik and Woods (1991)). The velocity of the coignimbrite plumes increases more gradually with height, with significant deviation between the simulations with different entrainment assumptions occurring above an altitude of approximately 5 km. For both plume types, the plume height attained using the

constant entrainment coefficient assumption is considerably greater than that for the variable entrainment coefficient. The modelled results show that maximum plume height is not simply a function of initial mass flux. Here, where the variable entrainment coefficient is used, the coignimbrite plume is modelled to reach a greater height than that of the vent-derived plume, despite the same initial mass flux because the entrainment coefficient is larger for centrally buoyant plumes.

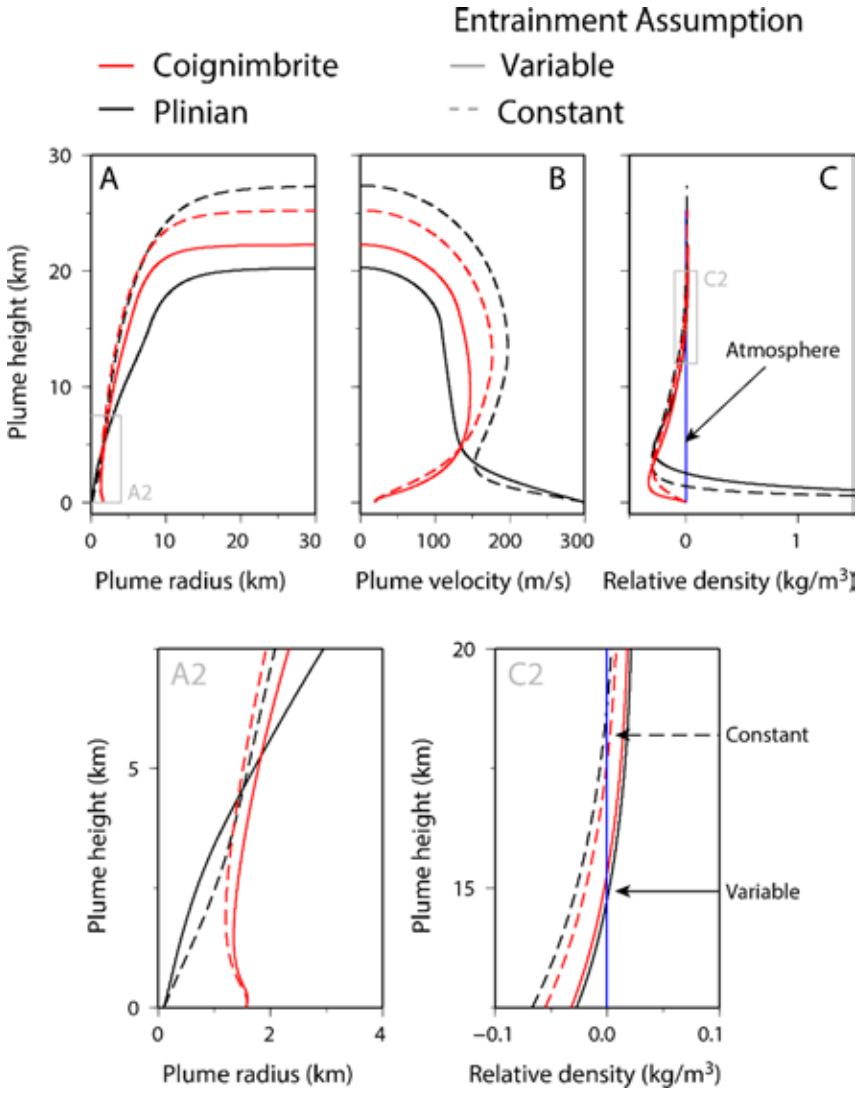

Figure 5. Typical plume profiles for a vent derived and co-PDC plume example with the same initial mass flow rate (10^7 kg/s), and for two different entrainment assumptions; constant with height following Morton et al. (1956), and variable with height following Carazzo and Jellinek (2012). A: plume radius with height with A2 showing variation in plume radius close to source. B: Plume velocity with height. C: Plume density with height. Standard atmospheric density profile also shown for comparison.

15. 3.3 - Coupled model results

The ash flow and plume models were coupled to investigate controls of initial PDC characteristics on those of the coignimbrite plume. A variable entrainment coefficient was assumed for the plume model, and output parameters from the ash flow model were either used directly, or to infer inputs for the plume model (Figure 2). Multiparameter sensitivity analysis results indicate the controlling parameters on modelled plume height are the initial flow height, radius, and gas mass fraction, in decreasing order of importance, with temperature and Richardson number having a minor effect (Figure 6A). This result is unsurprising given the initial plume velocity is calculated from the final mass flow rate of the flow, a function of the flow density (controlled by mixture gas mass fraction and temperature), flow velocity (determined by input Richardson number) and final flow runout. Further analysis of the simulation results (Figure 6B) shows a positive correlation between maximum plume height and initial flow radius, but a negative correlation with initial Richardson number and gas mass fraction.

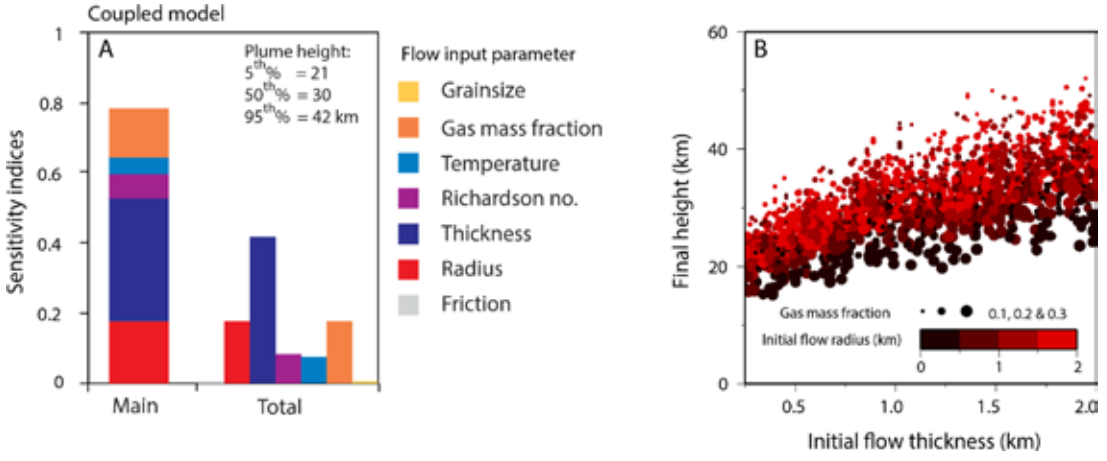

Figure 6. Sensitivity analysis for the coupled model (A) and model results (B) showing sensitivity of coignimbrite plume height on flow input. A. The dominant controls on coignimbrite plume as a function of flow thickness. B. The marker size relates to flow initial gas mass fraction, while colour relates to initial flow radius. Range of input parameters for the coupled model shown in Table 1.

15. 4 - Discussion and Conclusions

Application of the Bursik and Woods (1996) ash flow model in combination with formal sensitivity analysis highlights the role of flow temperature and gas mass fraction in the formation of coignimbrite plumes. Application of the ash flow model highlights some of the limitations associated with the use of one-dimensional models to simulate complex processes. Due to the simplicity of the model, it is unable to take into account a number of processes or interactions that would affect plume formation. For example, multiple observations of coignimbrite plume forming events, in addition to observations from laboratory experiments and outcomes from numerical simulations, highlight the importance of topography, specifically topographic barriers on plume formation

(Andrews and Manga 2011, 2012, Esposti Ongaro et al., 2012). Observations indicate that as the turbulent portion of the flow is forced over a barrier, entrainment and enhanced mixing of ambient air occurs. In addition, the sudden decrease in flow velocity results in mass sedimentation of particles, with both processes resulting in an almost instantaneous decrease in flow density, favouring formation of coignimbrite plumes. Such processes would result in much reduced runout than those predicted here, however, the effect of topography on coignimbrite plume formation is dependent on the relative scale of the current to the topographic barrier (Andrews and Manga 2011, 2012). Given the type (dilute and turbulent) and scale (initial thickness on the order of hundreds of metres to kilometres) of the flows simulated using the ash flow model, it is likely that topography has a secondary effect on coignimbrite plume formation. Instead we assume that plume formation occurs as the upper portions of the entire flow detach as neutral buoyancy is attained as modelled herein. However, such assumptions require further observations, and validation by the application of three-dimensional numerical models that are capable of capturing such complex interactions.

The plume rise results show that for a given mass flow rate, coignimbrite plumes have similar rise heights and characteristics to Plinian plumes, with neutral buoyancy levels often many kilometres lower than maximum heights. The dominant control on the height of these plumes is the initial mass flux, however choice of entrainment assumption can have significant implications, both for the plume height, and plume velocity profiles (Figure 5). The coupled plume model results correlate first order initial ash flow conditions to the final plume height, but are not sufficient for accurately describing the processes that occur during transition from horizontal to vertical momentum, and also require further investigation using analogue experiments and 2D/3D numerical models.

Acknowledgements

The research leading to these results has received funding from the European Union Seventh Framework Programme (FP7/2007-2013) under the project NEMOH, grant agreement n° 289976.

References

Adams, B.M., Bauman, L.E., Bohnhoff, W.J., Dalbey, K.R., Ebeida, M.S., Eddy, J.P., Eldred, M.S., Hough, P.D., Hu, K.T., Jakeman, J.D., Swiler, L.P. and Vigil, D.M. (2009). DAKOTA, A multilevel parallel object-oriented framework for design optimization, parameter estimation, uncertainty quantification, and sensitivity analysis: Version 6.2 user's manual, Sandia Technical Report SAND2014-4633, Updated May 2015, p. 337.

Andrews, B.J. and Manga, M. (2011). Effects of topography on pyroclastic density current runout and formation of coignimbrites, Geology, 39(12), 1099–1102, doi: 10.1130/G32226.1.

Andrews, B.J. and Manga, M. (2012). Experimental study of turbulence, sedimentation, and coignimbrite mass partitioning in dilute pyroclastic density cur- rents, Journal of Volcanology and Geothermal Research, 225-226, 30–44, doi: 10.1016/j.jvolgeores.2012.02.011.

Barsotti, S., Neri, A. and Scire J.S. (2008). The VOL-CALPUFF model for atmospheric ash dispersal: 1. Approach and physical formulation, Journal of Geophysical Research, 113 (B3), B03,208, doi:10.1029/2006JB004623.

Bursik, M.I. and Woods, A.W. (1991). Buoyant, superbuoyant and collapsing eruption columns, Journal of Volcanology and Geothermal Research, 45 (3-4), 347–350, doi: 10.1016/0377-0273(91)90069-C.

Bursik, M.I. and Woods, A.W. (1996). The dynamics and thermodynamics of large ash flows, Bulletin of Volcanology, 58 (2-3), 175{193, doi:10.1007/s004450050134.

Bursik, M.I. (2001). Effect of Wind on the Rise Height of Volcanic Plumes, Geophysical Research Letters, 28 (18), 3621-3624.

Carazzo, G., Kaminski, E. and Tait, S. (2008). On the dynamics of volcanic columns: A comparison of field data with a new model of negatively buoyant jets, Journal of Volcanology and Geothermal Research, 178 (1), 94:103.

Carazzo, G. and Jellinek, A. M. (2012). A new view of the dynamics, stability and longevity of volcanic clouds, Earth and Planetary Science Letters, 325-326, 39–51, doi: 10.1016/j.epsl.2012.01.025.

de' Michieli Vitturi, M., Engwell, S., Neri, A. and Barsotti, S. (2016). Uncertainty quantification and sensitivity analysis of volcanic columns models: results from the integral model PLUME-MoM, Journal of Volcanology and Geothermal Research.

Engwell, S. and Eychenne J., In press. Contribution of fine ash to the atmosphere from plumes associated with pyroclastic density currents. In: Volcanic Ash: Hazard Observation, edited by Mackie S, Ricketts H, Watson M, Cashman K, Rust A.

Engwell, S.L., de Michieli Vitturi, M., Esposti Ongaro, T., Neri, A., Accepted. Insights into the formation and dynamics of coignimbrite plumes from one-dimensional models. Journal of Geophysical Research: Solid Earth

Esposti Ongaro, T., Widiwijayanti, C., Clarke, A.B., Voight, B. and Neri, A. (2012). Multiphase-flow numerical modeling of the 18 may 1980 lateral blast at Mount St. Helens, USA, Geology, 39(6), 535–538.

Holasek, R.E., Self, S. and Woods, A.W. (1996). Satellite observations and interpretation of the 1991 Mount Pinatubo eruption plumes, Journal of Geophysical Research, 101 (B12), 27,635, doi:10.1029/96JB01179.

Morton, B., Taylor, G., Turner, J., (1956). Turbulent gravitational convection from maintained and instantaneous sources. In: Proceedings of the Royal Society of London A: Mathematical, Physical and Engineering Sciences. Vol. 234. The Royal Society, pp. 1:23.

Saltelli, A., Ratto, M., Andres, T., Campolongo, F., Cariboni, J., Gatelli, D., Saisana, M., and Tarantola, S. (2008). Global sensitivity analysis: the primer, John Wiley & Sons.

Schlicting, H. (1969). Boundary Layer Theory, McGraw Hill, New York.

Sparks, R.S.J., Wilson, L. and Hulme, G. (1978). Theoretical modeling of the generation, movement, and emplacement of pyroclastic flows by column collapse, Journal of Geophysical Research, 83(B4), 1727, doi:10.1029/JB083iB04p01727.

Sparks, R.S.J., Moore, J.G. and Rice, C.J. (1986). The inital giant umbrella cloud of the May 18th 1980 explosive eruption of Mount St. Helens, Journal of Volcanology and Geothermal Research, 28, 257-274.

Sparks, R.S.J., Bursik, M.I., Carey, S.N., Gilbert, J., Glaze, L.S., Sigurdsson, H. and Woods, A.W. (1997). Volcanic Plumes, Wiley.

Woods, A.W. and Wohletz, K.H. (1991). Dimensions and dynamics of co-ignimbrite eruption columns, Nature, 350, 225-227.

Woods, A.W. and Kienle, J. (1994). The dynamics and thermodynamics of volcanic clouds: Theory and observations from the April 15 and April 21, 1990 eruptions of Redoubt volcano, Alaska, Journal of Volcanology and Geothermal Research, 62, 273-299.

Samantha Engwell, United Kingdom
sameng@bgs.ac.uk

Affiliation under NEMOH
Istituto Nazionale di Geofisica e Vulcanologia, Sezione di Pisa, Pisa, Italy

Research theme under NEMOH
A numerical investigation into the formation of coignimbrite plumes

I graduated from the University of Edinburgh with a degree in Geology in 2008, and then moved to the University of Bristol to conduct a Masters in Natural Hazards, and it was there that I started to focus on volcanic environments and eruptive behaviour. Since then, my research has focused on developing and utilising techniques, for example numerical models, to interpret signatures from volcanic eruptions preserved within resultant deposits.

Prior to conducting my NEMOH fellowship, my experience of applying numerical models to investigate physical processes associated with explosive eruptions was limited to using 'black box' models, whereby inputs are chosen, the model is run, and the results analysed. The fellowship at INGV, Sezione di Pisa gave me the opportunity to build on the extensive experience and knowledge regarding eruption processes and deposits I gained while studying at the University of Bristol. During my PhD, I became increasingly interested in the formation and dispersion of coignimbrite plumes - plumes that form in association with propagating pyroclastic density currents - capable of lofting significant volumes of fine grained ash high into the atmosphere. Despite associated hazards, for example to aviation, relatively little research has been conducted on the conditions required for coignimbrite plume formation, and those that control the rise height of these plumes in the atmosphere. The fellowship allowed me to bring together data that I had collected during my PhD with numerical modelling techniques to better understand these processes.

While at Pisa, under the dedicated supervision of Dr. M. de Michieli Vitturi, I learnt how to develop and apply my own numerical models (specifically for ash-flow emplacement), from underlying physical assumptions in the literature. I also learnt how to statistically evaluate these models using sensitivity analysis techniques. My first secondment was conducted at the University of Bristol, where I was able to continue collaboration and further characterize coignimbrite plume deposits. My second secondment was with the University and Meteorological Office of Iceland where I learnt how to apply ash dispersion models.

My experience as part of the NEMOH network, and at INGV Pisa, showed me the advantages of application of a wide variety of techniques to truly learn about a process. The experience was not only beneficial in terms of my research interests, but also in terms of the great relationships that I formed, both at INGV Pisa, and within the NEMOH group.

Chapter 16

Field and theoretical investigations of volcanic ash aggregation: the case of the eruption of 3rd of August 2013 at Sakurajima Volcano (Japan)

Eduardo Rossi

University of Geneva, Geneva, Switzerland

Tutorship: Costanza Bonadonna

University of Geneva, Geneva, Switzerland

Abstract

Particle aggregation is considered as a key process that may affect dispersal and sedimentation of volcanic ash, with significant implications for the associated hazards. It is well known that aggregation has a major role in particle sedimentation affecting the residence time of volcanic ash in the atmosphere, but an exhaustive description of the phenomenon is still missing. In this report new techniques for field and theoretical investigations of volcanic ash aggregation are reported. The structure of the paper is conceived to be split in two different parts: in the first we will focus on observations of aggregates at Sakurajima Volcano (Japan) during the field campaign of August 2013. In the second, we propose the combination of a 1-D thermal plume model with sectional methods in order to provide a general description of the observed eruption. The basic idea of the whole paper is to show a multidisciplinary approach to the study of ash aggregation, that merges together new field techniques and new theoretical scenarios.

Keywords: ash aggregation, modelling, field investigation, Sakurajima

16. 1 **- Introduction**

Volcanoes are a source of multiple hazards, e.g. lava flows, pyroclastic density currents, tephra fallout and lahars. Among all the possible hazards, tephra fallout has the peculiarity to potentially affect the surrounding environment from short to very large distances, with disruptive consequences on local communities and both land and aviation transport. The spatial and temporal scales of tephra fallout strongly depend on how single particles interact among them and with all the gas phases involved in the eruption. Here we will focus on a particular aspect that has large consequences on tephra fallout: volcanic ash aggregation. In particular, field evidences from the Sakurajima campaign of August 2013 are discussed from a theoretical point of view. These results are presented exhaustively in the work of (Bagheri et al., 2016) and more details can be found there. The main

purpose of this work is to show how these two different and independent approaches, theoretical and field-based, may be connected together to complete our understanding of the problem.

Aggregation processes are well known to affect sedimentation of fine ash (< 63 μm) by considerably reducing its residence time in the atmosphere (Lane et al., 1993; Rose and Durant, 2011; Brown et al., 2012). If particle aggregation is not taken into account, volcanic ash transport and dispersal models fail to accurately describe both particle deposition in proximal areas and atmospheric concentrations in the far field, with important implications for hazard assessment and real-time ash forecasting (Folch et al., 2010; Rose and Durant, 2011; Brown et al., 2012). From a physical perspective, aggregation is essentially the interaction of single particles, or clusters, to generate larger agglomerates. It can be seen as a process where two main and distinct conditions must occur: collision and sticking. Volcanic particles mainly collide due to their different dynamics within the fluid. In fact, the degree of coupling of a particle with the flow inside a volcanic environment (Stokes number) may cover a wide number of ranges. This practically means that some particles will follow instantaneously the fluid changes and some others not. As a consequence, particles will experience different relative velocities and so they will collide if their cross sections are large enough. A collision is effective for aggregation if the relative kinetic energies of colliding particles are depleted by some dissipative mechanisms. The final clustering depends on complex interactions of surface liquid layers, electrostatic forces or shape factors. Depending on the water content, particle aggregation results in the formation of particle clusters if the presence of water is poor and accretionary pellets in all the other cases (including poorly-structured pellets AP1, pellets with concentric structures AP2, and liquid pellets AP3 in the nomenclature of Brown et al., 2012).

During the last two decades several experimental, numerical and field investigations have been carried out to describe aggregation processes in terms of particle grain-size distribution, terminal velocity, structure, density and porosity (e.g. (Lane et al., 1993; Gilbert and Lane, 1994; Schumacher, 1994; Schumacher and Schmincke, 1995; James et al., 2002; Bonadonna et al., 2011a; Taddeucci et al., 2011; Telling et al., 2013; Van Eaton, Harper, & Wilson, 2013)). However, due to the low preservation potential of particle clusters in the deposits, most studies focused on the characterization of the more resistant well-structured pellets (i.e. AP2 most commonly known as accretionary lapilli; (Gilbert and Lane, 1994; James et al., 2003)). In the first part of this paper we will introduce new field techniques especially designed for the study of particles clusters (also known as dry aggregates), which include ash clusters (PC1) and coated particles (PC2) according to the classification of (Brown et al., (2011). Ash clusters, PC1, are defined as fragile irregular shaped aggregates composed of particles < 1-40 μm, whereas coated particles, PC2, are defined as fragile aggregates comprised of a crystal, crystal fragment, pumice or lithic clast partially covered in fine ash particles. The traditional terminology "dry aggregates" can be somehow misleading. In fact, dry aggregation implies an aggregation process where there is no evidence of a macroscopic liquid layer inside the clusters. This does not exclude the presence of water vapour in the mixture or even condensed humidity upon particle surfaces. In this case the layer of water on the surfaces, if present, is much thinner than the size of the particles involved. Field investigations of real-time volcanic ash aggregation may count on studies that cover several decades: the 1980 eruption of Mount St.

Helens, USA (Sorem, 1982), 1990-1994 eruptions of Sakurajima volcano, Japan ([Gilbert et al., 1991; Sparks et al., 1997]), the 1997 eruption phase of Soufrière Hills volcano, Montserrat (Bonadonna, et al., 2002) and the 2010 eruption of Eyjafjallajökull volcano, Iceland (Bonadonna et al., 2011; Taddeucci et al., 2011). (Sorem, (1982) observed ash clusters with diameters between 250-500 μm about 390 km from the vent that were composed of particles <40 μm. (Gilbert et al., 1991) and (Sparks et al., 1997) reported ash clusters at Sakurajima volcano with diameters <3 mm, which consisted of particles <200 μm, whereas coated particles had diameters >200 μm and were covered with particles <20 μm. (Bonadonna, et al., 2002) observed both types of particle clusters resulting from either dome collapse or Vulcanian explosions at Soufrière Hills volcano. Finally, Bonadonna et al. (2011) observed both types of particle clusters between 10 and 55 km from vent. Ash clusters had diameters up to 600 μm and consisted of particles < 90 μm, while coated particles were composed of large particles up to 760 μm that were coated with particles < 100 μm. For the same eruption, High-Speed (HS) videos recorded by Taddeucci et al., (2011) show how most particle clusters fell with terminal velocities between 1 - 4 m/s m/s at ground level. In this work we have introduced a multi-technique approach for field investigations applied to a specific volcanic explosion of Sakurajima volcano (Japan), which includes field High-Speed-High-Resolution (HS-HR) imaging and analyses of in-situ collected particle clusters. The advantage of this technique relies on its capability to describe completely aggregates as they form and fall in a real environment, without any a priori assumption or bias. Aggregates are so described in terms of their terminal velocity, density, population and structure. This work represents the first step done under my fellowship within the NEMOH ITN to go towards a more detailed and physical-based approach to the unsolved problem of ash aggregation.

The novel contribution of this work is twofold: first, we provide strong field constrains on timescales and shapes of dry aggregates before their impact on the ground; second, discrete methods to the numerical solution of aggregation equations are introduced. The main objective of this study is to underline how modern observations can be linked to a general theoretical description, which can start from the physics of the processes to retrieve some measured evidences from the field, like sizes or timescales for observed aggregates. In order to do this, the second part of this work will be dedicated to the development of a volcanic plume theory which may take into account the aggregation of volcanic particles.

16. 2 **- Field observations: methods**

Dry aggregation of volcanic particles is frequently observed in those eruptions where fine ash is present (<63 μm) and meteorological conditions are favourable (high relative humidity). Direct observations of falling aggregates are not rare: some well-studied examples are the eruptions of Sakurajima Volcano in Japan (Gilbert et al., 1991) and Eyjafjallajökull eruption of 2011 in Iceland (Bonadonna et al., 2011; Taddeucci et al., 2011). Despite their importance, an exhaustive description of particle clusters not always easy due to their fragile structure leading to poor preservation in the deposits. For this reason, field techniques mainly involve the collection of tephra samples directly during fallout using sticky papers to collect falling aggregates (e.g. Bonadonna et al., 2011). This simple technique permits to analyse the population of each single aggregate with a Scanning

Electron Microscope (SEM). Recently, more sophisticated tools based on the use of high speed cameras have been applied to go deeper into the analysis of some major properties of aggregates, like its settling velocity (Taddeucci et al., 2011). Both techniques have advantages and disadvantages: direct collection of samples permits to reconstruct a posteriori the grain-size of aggregates and characterize the internal structure but it fails to capture the associated sedimentation dynamic. On the other hand, HS movies allow for fundamental details cluster sedimentation and impact with the ground to be described, but the information on the single components of aggregates is mostly missing. Only their combination can give a complete overview on dynamical and morphological properties of particle clusters without a-priori assumptions. Therefore, in order to fully characterize particle aggregation, we developed a multi-technique approach. Each aggregate is recorded during its falling and impact on the sticky paper. The part that sticks to the paper – which, in our experience, is rarely the entire aggregate - is further analyzed at the SEM.

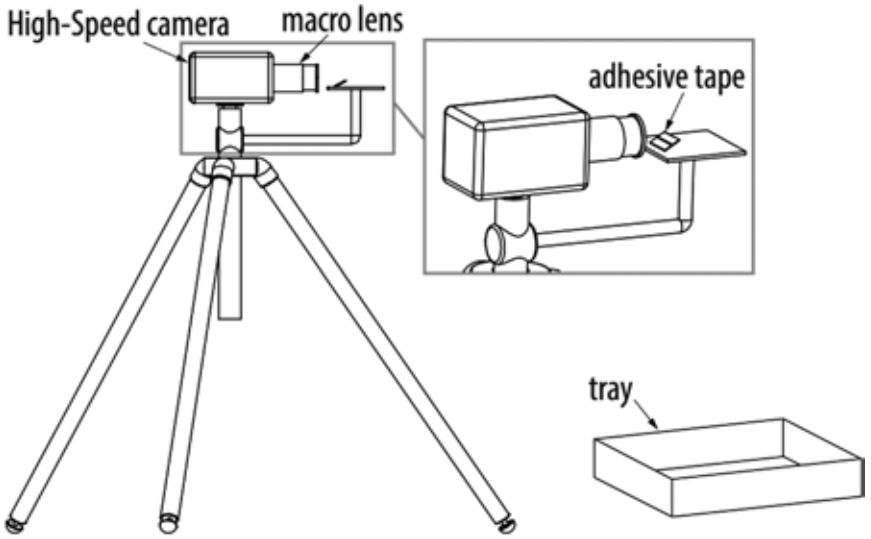

Figure 1. Setup optimized for field recording of falling aggregates. Particles that impact on the adhesive tape are filmed throughout the macro-lens of the High-Speed camera. The adhesive tape is usually strong enough to stick the coating part of the falling aggregates but not the internal core. Meanwhile a tray placed next to the tripod of the camera collects the falling tephra at that position.

In Figure 1 a schematic diagram of the field setup is reported: a High-Speed (HS) camera on a tripod focused on a thin-glass support covered with a specific double-sided tape allowing for further analyses with a Scanning Electron Microscope (SEM). The HS camera with a resolution of 1200×800 pixels at 800 fps mounted with a Nikon 60 mm f/2.8D AF Micro-Nikkor lens was used at the ground-based observation site in order to capture HS-HR movies with a pixel size of 40 µm. In addition, tephra samples are collected in dedicated trays at sequential time steps in order to monitor time variations in grain-size distribution. Associated samples were analyzed for grain-size using a Laser Diffraction (LD) particle-size analyzer (CILAS 1180). This technique allows measuring, directly or

indirectly, the following quantities: i) settling velocity; ii) aggregate population; iii) density; and iv) internal structure. This multi-approach was applied during the field campaign at Sakurajima Volcano (Japan) of July-August 2013. Detailed measurements were acquired for one particular eruption that occurred at 17:47 Japanese Standard Time (JST) on the 3rd of August 2013, which reached a maximum plume height of 2.8 km a.s.l. The eruption consisted of three major single explosions that produced an ash cloud that reached the complete development after about 240 seconds after the onset. The ash cloud spread toward south-east with a velocity of ~5.5 m/s as inferred from large angle HD movies. Our ground-observation site was located about 3.7 km downwind from the vent along the dispersal axis. Ash fallout was sampled at two time intervals in order to characterize sedimentation in time: i) between 18:00 and 18:07 JST, associated with individual particles followed by sub-spherical aggregates (Phase I), and ii) between 18:07 and 18:12 JST mostly associated with sub-spherical aggregates (Phase II). Individual particles were recognized as non-vesiculated fragments with diameters between ~300-1200 μm and density of ~2500 kg/m^3 (measured by water pycnometer).

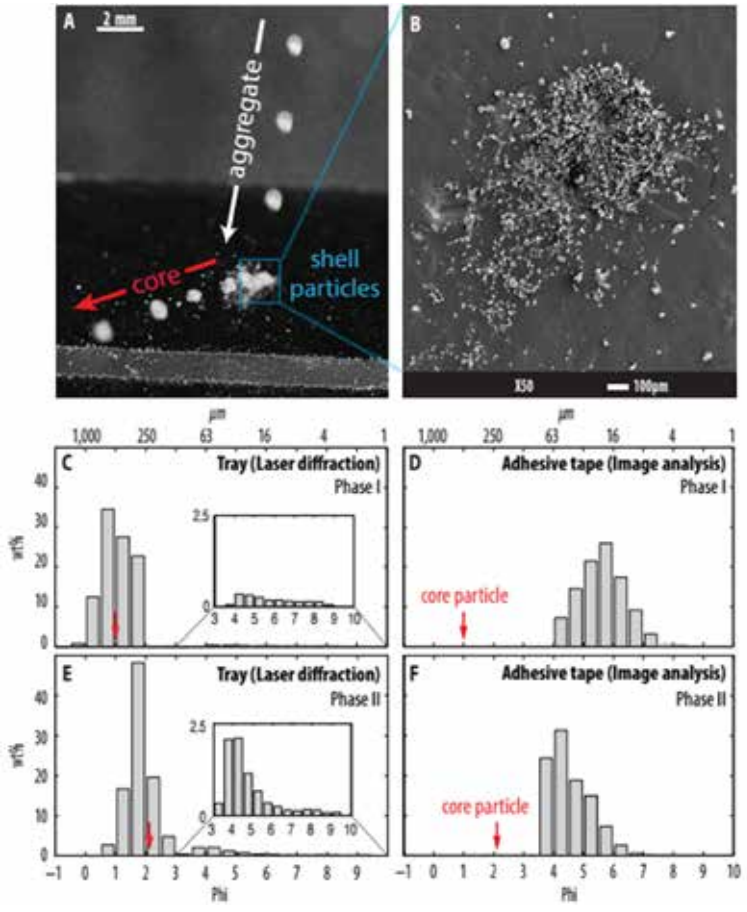

Figure 2. (a) Recorded image of a falling aggregate that shows the escape of a larger particle inside the whole cluster. (b) Scanning Electron Microscope image of particles of the shell. These small particles represent all what remains on the adhesive tape of the original aggregate. Without the recorded image, the shell particles could be erroneously misinterpreted as the whole aggregate (i.e. PC1). (c-e) Grain size analyses of ash collected in the tray during the first (18.00-18.07 JLT) and the second fallout phase (18.07-18.12 JLT). (d-f) Grain size analyses of particles contained inside two different aggregates sedimented respectively in the first (d) and second fallout phase (f).

16. 3 - **Field observations: results and discussion**

16. 3.1 - **Aggregate cores**

As shown in Fig 2., all aggregates broke at impact with the adhesive tapes, leaving behind an ensemble of fine ash and a significantly larger particle (from now on defined as *core*), which in most of the cases bounced off from the sticky paper. Sizes of cores (~ 200-500 μm) are comparable with the sizes of the entire aggregates before the impact (~ 400-800 μm) and correspond well to the mode of the coarse population of ground deposit for aggregates sedimented during both fallout phases (i.e. 500 μm and 250 μm, respectively; red arrows in Fig. 2). Ash coating mostly consists of particles < 90 μm and it is clear from Fig. 2b that this image on the sticky paper recalls the idea of what we typically interpreted as a fragile particle cluster in Brown et al. (2012) (i.e. PC1). The whole aggregate - core plus coating - is more similar to a coated particle (i.e. PC2). However, Bagheri et al. (2016) introduced a new category of particle clusters (PC3; *cored clusters*) to better describe these aggregates that have a larger coating than PC2. In fact, cored clusters (PC3) are mostly sub-spherical fragile aggregates that have never been observed in the deposits nor on adhesive tape as they typically break at impact with the ground. They consist of a core particle (coarse ash to fine lapilli size) fully covered by a thick shell of particles < 90 microns. The difference is not just a matter of nomenclature, but it has deep consequences on the dynamics of sedimentation and modelling in general. First, if aggregates are thought to be created from fine ash only, as previously thought based on SEM analysis alone (Sorem, 1982; Lane et al., 1993; Brown et al., 2012), they should be categorized as ash clusters, for which the main collision mechanisms are very weak. However, we suspect that most PC1 described in literature originally deposited as cored aggregates (i.e. PC3), as it can also be seen in the HS videos recorded during the Eyjafjallajökull 2010 eruption (e.g. VIDEO #2 of Taddeucci et al., (2011). Cored aggregates can form much faster and at much lower particle concentrations than PC1 because their collision mechanisms, i.e. differential settling, are several orders of magnitude more efficient than Brownian motion and turbulence (Elimelech et al., 1998), (Pruppacher & Klett, 2004), (Costa et al., 2010). Additionally, it is widely accepted that the grain-size of fallout deposits affected by particle aggregation are bimodal because they consist of simultaneous sedimentation of individual lapilli and/or coarse ash particles together with fine ash particles aggregated in clusters (Carey and Sigurdsson, 1982; Brazier et al., 1983). Although this theory can account for the deposition distance of individual particles, which in some cases matches the deposition distance of aggregate cores, it fails to explain the proximal deposition of aggregates only composed of fine ash unless unrealistic aggregate densities are considered (Carey and Sigurdsson, 1982). In fact, premature fallout of fine ash can be more easily explained if most aggregates are considered to consist of coarse-ash particles coated a thick layer of particles <100 μm (PC3) instead of consisting of only particles <100 μm (PC1).

16. 3.2 **- Aggregate dynamical features**

The measured quantities from our HS videos are basically the terminal velocities and sizes of falling aggregates and internal cores (Table 1). The densities of the whole aggregates are evaluated

inverting the formula for the terminal velocity. On the other side densities of central cores are estimated under the hypothesis that these particles are part of the population of those collected in the trays. A first interesting point is the clear variation in the characteristics of aggregates deposited during Phase I and Phase II, being aggregates of Phase I characterized by larger cores than aggregates of Phase II. Second, the ash coating of Phase I is thinner than the ash coating of Phase II aggregates compared to their core diameter. The ash fraction involved in the coating of individual aggregates, f_agg, for Phase I is about 10% whereas for Phase II it is 17% (Bagheri et al., 2016). This indicates that Phase I aggregates were associated with thinner ash coating than Phase II aggregates compared to their core diameter.

		Aggregates			***Core particles***		
Fallout phase	**Sed. Time**	**Diameter [μm]**	**Density [$kg\ m^{-3}$]**	**Velocity [ms^{-1}]**	**Porosity [%]**	**Diameter [μm]**	**Density [$kg\ m^{-3}$]**
I	18:02-18:07	718 – 807	806 – 1009	2.7 – 2.9	60 – 68	500 – 525	2500-2700
II	18:07-18:12	440 – 630	357 – 864	1.2 – 1.8	67 – 83	200 – 330	2500-2700

Table 1. Physical and cinematic properties of the observed aggregates at Sakurajima Volcano during the eruption of 3rd of August 2013.

16. 3.3 **- Timing of aggregation**

Given that Phase II clusters are characterized by thicker shells and most likely needed more time to form than Phase I clusters, it can be concluded from numerical inversions (Bagheri et al., 2016) that particle clusters can be formed within 180 seconds after the onset of the eruption. As a comparison, accretionary lapilli and frozen accretionary pellets were reported to be formed within 300 and 600 seconds after the onset of 1990 eruption of Sakurajima volcano (Japan) and the March 2009 eruption of Redoubt volcano (Alaska), respectively (Gilbert and Lane, 1994; Brown et al., 2012). It cannot be excluded that in our case aggregation continued to occur beyond 175 s simply because our observation is just based on a single proximal location in the field.

16. 4 **- Theoretical investigations**

One of the main challenges in the characterization of particle aggregation includes the capability to describe field observations from a theoretical point of view. In this section a mathematical model for ash aggregation is introduced. As outlined in the introduction, aggregation is the result of the sticking of single particles (or agglomerates) once they have collided together. It is evident that a theoretical description of aggregation processes should be dependent on, at least, three main quantities: i) concentration of particles; ii) collision rate and; iii) sticking efficiency. If at least one of these quantities is zero, aggregation can simply not occur. The equation that relates these three quantities is the so-called "Smoluchowski Coagulation Equation" (SCE) (Jacobson, 2005), which

describes the evolution in time of a population of particles of mass m in a control volume where no other physical processes occur (diffusion, advection, etc.):

$$\frac{dn(t,m)}{dt} = \frac{1}{2}\int_0^m K(t, m-\varepsilon, \varepsilon)\ n(t, m-\varepsilon)\, n(t,\varepsilon)\, d\varepsilon\ - n(t,m)\int_0^\infty K(t,m,\varepsilon)\, n(t,\varepsilon)\, d\varepsilon \tag{1}$$

Key quantities that appear inside the equation are:

- $n(t,m)$: distribution function of the number of particles per unit volume with a mass equal to m at a certain time t (units: $[\frac{\#}{m^3}]$)
- $K(t,m,\varepsilon)$: Aggregation kernel, which contains all the information about collision rates and sticking efficiencies of particles of mass m and ε (units: $[\frac{m^3}{s}]$). For clarity, this term is usually split in two different contributions to enhance the different roles of sticking and collision: $K(t,m,\varepsilon) = \alpha(t,m,\varepsilon) \cdot \beta(t,m,\varepsilon)$, where $\alpha(t,m,\varepsilon)$ is the sticking efficiency (units: [#]) and $\beta(t,m,\varepsilon)$ is the collision rate (units: $[\frac{m^3}{s}]$).

The Smoluchowski coagulation equation is a particular case of a more general and comprehensive theory which is called "Population Balance Equations" (PBE) (Ramkrishna, 2000). The underlying assumption in this theory is that there is a density function that describes the number of elements (particles) inside a population with a given selected property, such as "mass" in this case. This density function is described by the quantity $n(t,m)$, which represents the number of particles with a mass inside the interval $[m, m+dm]$. For clarity, it must be outlined that the aggregation equation is just a part of the General Dynamic Equation (GDE), which studies how the distribution function $n(t,m)$ evolves in presence of other physical processes, like for instance advection and diffusion, just to mention the more common ones in volcanology. The complete transport equation for an "advection-diffusion-aggregation" process is (Gelbard & Seinfeld, 1979):

$$\frac{\partial n(t,m)}{\partial t} + \nabla\cdot(n(t,m)\,\vec{\boldsymbol{v}}) - \nabla\cdot(D\,\nabla n(t,m)) = \frac{1}{2}\int_0^m K(t,m-\varepsilon,\varepsilon)\ n(t,m-\varepsilon)\, n(t,\varepsilon)\, d\varepsilon\ - n(t,m)\int_0^\infty K(t,m,\varepsilon)\, n(t,\varepsilon)\, d\varepsilon \tag{2}$$

The solution of the aggregation equations is not trivial and analytical solutions exist only for simple cases. There are several methods for the numerical solution of Eq. (1), but generally they can be grouped in three major families (Vanni, 2000): method of moments (Standard Moment Method, Quadrature Method of Moments), stochastic methods (Monte-Carlo) and sectional methods (Fixed-

Pivot, Cell-Average, Finite-Volume). Each of these approaches has different pros and cons: moment methods are usually faster than others, since they focus on some integrals quantities of interest – i.e. moments. Sectional methods - also called "discrete methods" - are computationally more expensive, but they provide a direct description of the evolution of populations (Kumar & Ramkrishna, 1996). In the following, we will focus on sectional methods with a specific attention to the fixed-pivot technique and how it can be applied inside a thermal plume model. The purpose is to see how far is this theoretical approach from the main features observed during the Sakurajima campaign of July 2013.

16. 5 - Sectional methods: the fixed-pivot technique

In the sectional methods the continuous density function $n(t, m)$ is discretized and each bin (section) evolves in time. The discretization is done substituting the density function $n(t, m)$ with the so-called "Dirac-comb", which samples the continuous function at fixed positions m_k, as shown in Fig. 3 (Kumar & Ramkrishna, 1996):

$$n(t, m) = \sum_{k=1}^{I} N_k(t)\, \delta(m - m_k) \tag{3}$$

The quantities N_k are the number of particles per unit volume with mass inside each interval $[m_{k-1/2}, m_{k+1/2}]$:

$$N_k = \int_{m_{k-1/2}}^{m_{k+1/2}} n(m)dm = \int_{m_{k-1/2}}^{m_{k+1/2}} \left(\frac{dN}{dm}\right) dm \tag{4}$$

A common problem to all the sectional methods arises when the fixed positions m_k are not aligned on a linear grid. In fact, for arbitrary grids, the collision of two different particles of masses m_k and m_j rarely correspond to an existent mass m_i. For linear grids this problem is implicitly avoided since it is always true that $m_k + m_j = m_i$. Unfortunately the use of a linear gridding does not permit to investigate a large number of diameters, due to the mathematical relation between mass, density and diameter. This is clear looking at the following relations:

$$d_1 \approx (m_1)^{1/3}\ ;\ d_{100} \approx (100\, m_1)^{1/3} \rightarrow \frac{d_{100}}{d_1} = (100)^{1/3} \approx 4.6 \tag{5}$$

That is, assuming spherical particles with the same density, one hundred linear bins in mass would cover just a factor 4.6 in diameter. This suggests to replace a linear gridding with a logarithmic one, capable to cover the larger interval of particle diameters. For this, one needs to re-distribute mass between the available grid points (bins) in order to conserve the total mass. All the different sectional methods differ basically in the way they establish this rule to redistribute the mass. Among all the different sectional methods we discuss here the so-called "fixed-pivot" technique. The fixed-pivot technique is described exhaustively in (Kumar & Ramkrishna, 1996) and (Jacobson, 2005) and

for a given bin labelled as m_i it redistributes the mass between the two closer bins $m_{i-1}$and m_{i+1} conserving the zeroth and first moment of the distribution, i.e. the number of particles and the total mass. If we refer to the scheme of Fig 3b this implies the following systems of equations:

$$\begin{cases} w_1(m, m_i)\ 1 + w_3(m, m_{i+1})\ 1 = 1 \\ w_1(m, m_i)\ m_i + w_3(m, m_{i+1})\ m_{i+1} = m \end{cases} \tag{6}$$

$$\begin{cases} w_2(m, m_i)\ 1 + w_4(m, m_{i-1})\ 1 = 1 \\ w_2(m, m_i)\ m_i + w_4(m, m_{i-1})\ m_{i-1} = m \end{cases} \tag{7}$$

For a given bin m_i the mass conservation is assured by the two quantities of interest $w_1$and w_2:

$$S = \begin{cases} w_1(m, m_i) = \dfrac{m_{i+1} - m}{m_{i+1} - m_i} \\ w_2(m, m_i) = \dfrac{m_{i-1} - m}{m_{i-1} - m_i} \end{cases} \tag{8}$$

The integration of Eq. (1) over the interval $[m_{i-1/2}, m_{i+1/2}]$, combined with the mass conservation assured by Eq. (8), leads to the fixed-pivot equations that rule the change in time of particles per unit volume of mass *i* due to aggregation (Kumar et al., 2006)

$$\frac{d\ N_i}{dt} = B_i - D_i \tag{9}$$

Where:

$$B_i = \sum_{m_i \le (m_k + m_j) < m_{i+1}} \left(1 - \frac{1}{2}\ \delta_{kj}\right) \left(\frac{m_{i+1} - m}{m_{i+1} - m_i}\right) K(m_k, m_j)\ N_k\ N_j + \sum_{m_{i-1} \le (m_k + m_j) < m_i} \left(1 - \frac{1}{2}\ \delta_{kj}\right) \left(\frac{m - m_{i-1}}{m_i - m_{i-1}}\right) K(m_k, m_j)\ N_k\ N_j \tag{10}$$

$$D_i = \sum_{j=1} K(m_i, m_j)\ N_i\ N_j \tag{11}$$

δ_{kj} is the so-called "Kronecker delta function" :

$$\delta_{kj} = \begin{cases} 0\ if\ k \neq j \\ 1\ if\ k = j \end{cases} \tag{12}$$

Equations (9), (10) and (11) represent the fixed pivot equivalent to (Eq.1). This means that the initial continuous problem has been transformed into a set of Ordinary Differential Equations (ODEs), one for each bin representing the *i*-th mass.

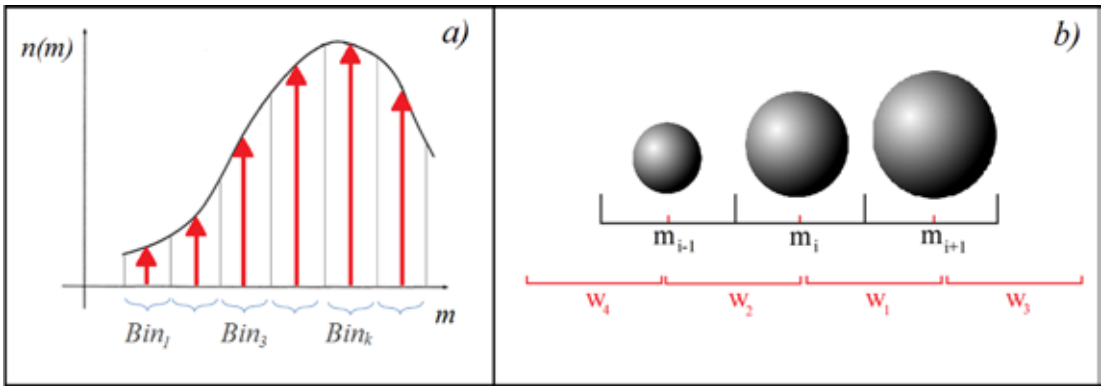

Figure 3. (a) Discretization of a continuous curve n(m) using a sum of Dirac deltas. (b) Notation used in the fixed pivot technique, defined in order to conserve the first two moments of the distribution (number of particles and mass).

16. 6 **- Aggregation kernels**

Next step is to clarify the importance and meaning of quantities $K(m_i, m_j)$, which basically contain all the physics of the process. Aggregation kernels are basic quantities to study the evolution in time of populations since they describe the collision rate of particles of mass m_i and m_j that give birth to a new aggregate. This implicitly means that $K(m_i, m_j)$ contains the information about "successful" collisions, i.e. collisions that bring two particles to be stuck together. If, for example, the collision rate inside a volume is really high (e.g. billions of collisions per second), but no sticking processes have been occurring, $K(m_i, m_j)$ will be zero. This suggests to split the kernel matrix $K(m_i, m_j)$ in two different parts: a dimensionless coefficient $\alpha(m_i, m_j)$, which describes the probability of sticking, and a dimensional parameter $\beta(m_i, m_j)$, which contains all the information about the collision rates (Jacobson, 2005).

$$K(m_i, m_j) = \alpha(m_i, m_j) \cdot \beta(m_i, m_j)$$

The dimensions of $\beta(m_i, m_j)$ are similar to a volumetric flow rate $[\frac{m^3}{s}]$. A complete discussion about collisional kernels and their derivation can be found in (Jacobson, 2005). In volcanology (e.g. Costa et al., 2010), the main different processes taken into account for collision rates are turbulent-related kernels (turbulent-inertial (TI) and turbulent shear (TS)), laminar shear (LS), differential sedimentation (DS) and the Brownian motion (BM), which is negligible for the sizes involved.

$$\beta_{ij}^{TI} = \left(\frac{\epsilon^{3/4}}{g\nu^{1/4}}\right)\frac{\pi}{4}(d_i + d_j)^2\left|u_{ti} - u_{tj}\right| \tag{13}$$

$$\beta_{ij}^{TS} = \left(\frac{\pi\epsilon}{15\,\nu}\right)^{1/2}(d_i + d_j)^3 \tag{14}$$

$$\beta_{ij}^{LS} = \frac{\Gamma_L}{6}(d_i + d_j)^3 \tag{15}$$

$$\beta_{ij}^{DS} = \frac{\pi}{4}(d_i + d_j)^2 |u_{si} - u_{sj}| \tag{16}$$

$$\beta_{ij}^{BM} = \frac{2\,K_B T}{3\mu} \cdot \frac{(d_i + d_j)^2}{d_i d_j} \tag{17}$$

Where ϵ is the dissipation rate of turbulent kinetic energy, g is the gravitational acceleration, μ and ν are the fluid dynamic and kinematic viscosities, Γ_L is the laminar shear coefficient, u_s is the sedimentation velocity and u_t is velocity provided to particles trapped inside turbulent eddies. Some of these expressions depend on quantities difficult to quantify, especially for turbulent flows, like ϵ, Γ_L or u_t. Some approximations or assumptions must be taken in these cases. For example, according to (Textor & Ernst, 2004), the value of ϵ is related to the plume velocity u_p and the sizes of the largest eddies inside the plume (which we consider equivalent to the plume radius):

$$\epsilon \approx 0.1\,\frac{{u_p}^3}{L} \tag{18}$$

The laminar shear coefficient is theoretically given by:

$$\Gamma_L = \left|\frac{du_p}{dr}\right| \tag{19}$$

A key point is which kernels are relevant inside the volcanic environment. Here some basic concepts contained in (Textor & Ernst, 2004) and (Marshall & Li, 2014) are summarized:

1) The turbulent kernels β_{ij}^{TI} and β_{ij}^{TS} are valid within the Saffman-Turner limit, that is, for particles smaller than a characteristic spatial scale (called the "Kolmogorov length") and with Stokes numbers $St < 1$. In order to be inside the Saffman-Turner limit, particles have to be smaller than the turbulent eddies, which implies having well correlated velocities between them. The Kolmogorov micro-scale is proportional to $\gamma_K \approx (\frac{{\nu_a}^3}{\epsilon})^{1/4}$, where ν_a is the air kinematic viscosity and ϵ is the dissipation rate of turbulent kinetic energy. For a plausible range of ϵ between $0.1 - 100\frac{m^2}{s^3}$, and for $\nu_a \approx 10^{-5} - 10^{-4}\frac{m^2}{s}$ we get $\gamma_K \approx 10^{-3} - 10^{-4} m$. This means that particles larger than some hundred microns will not be in the Saffman-Turner limit. In addition, as outlined by (Textor & Ernst, 2004) , the Stokes number of volcanic particles spans a huge number or values, roughly from 10^3 for bigger particles to 10^{-3} for the smaller ones. Also in this case is not easy to establish if the Saffman-Turner condition is valid.

2) Particles laying outside the Saffman-Turner limit show uncorrelated velocities among them, which basically means that are not trapped inside the fluid turbulent eddies. This extreme is often called "the accelerative-independent regime" and it has been treated by Abrahamson (Marshall & Li, 2014), who led to the following expression for collisions among two particles with Stokes number $St > 1$:

$$\beta_{ij}^{AI} = \left(\frac{\pi}{6}\right)^{\frac{1}{2}} (d_1 + d_2)^2 \sqrt{\langle u_{mi}^2 \rangle + \langle u_{mj}^2 \rangle} \tag{20}$$

In this expression $\langle u_{mi}^2 \rangle$ stands for the mean-square velocity magnitude for a *i*-th particle due to an isotropic turbulence. It is worth-mentioning that u_{mi} is obviously different from u_{ti} used in [Eq. 13] since u_{ti} contains info related to the small eddies above the Kolmogorov scale. u_{mi} is a mean velocity given by the bulk turbulence which of course depends also on the particles involved, how they interact with different eddies and how they keep their inertia passing through them. Abrahamson kernel [Eq. 20] remains undefined so far for a volcanic plume, due to its dependency from the unknown quantities u_{mi}. Complete CFD simulations of turbulent plumes coupled with particles could provide a better understanding of this collisional kernel in future.

3) Sedimentation kernel β_{ij}^{DS} is due to differences in particle terminal velocity because of size, density, and shape. (Textor & Ernst, 2004) suggest to compare gravitational and turbulent effects using their respective accelerations as a term for comparison. (Pruppacher & Klett, 2004) provide an expression for turbulent acceleration for particles with $St < 1$: $a_T = \frac{\epsilon^{3/4}}{\nu^{1/4}}$. In this case $g < a_T$ for $\geq 0.1 \frac{m^2}{s^3}$. For larger particles with $St \gg 1$ the acceleration due to turbulent eddies with size γ_m between the largest one ($\approx$ plume radius) and the smallest one before viscosity terms become dominant (i.e. the Kolmogorov micro-scale γ_K) is: $a_m = \frac{(\epsilon\, \gamma_m)^{2/3}}{\gamma_m}$. Textor shows that using reasonable numbers for γ_m of 10, 100 and 1000 meters, $g > a_m$ for a wide range of values of the dissipation rate of turbulent kinetic energy ($\epsilon < 100 \frac{m^2}{s^3}$). In practice this means that gravitational collection should be the dominant process for larger sizes in most of the volcanic plume and cloud. Nevertheless this comparison is true under the assumption that particles are under sedimentation: but volcanic particles are dragged upwards by the rising plume and as a rule of thumb sedimentation does not occur until upward velocity is higher than particles terminal velocities. From the comparison of Gaussian profiles of plume velocity and terminal velocities (Carey & Sparks, 1986) derive that relevant parts of the volcanic plume are not affected by sedimentation for particles with sizes less than 1 mm. This suggests that the role of the sedimentation kernel β_{ij}^{DS} inside a volcanic plume may be over-estimated if the role of the drag due to the upward velocity is neglected.

To sum up the previous analyses, the common leading parameters among all the different kernels concern the relative velocities and projected areas of two colliding particles. The source of uncertainty is the knowledge of the velocities assumed by different sizes in different fluid-dynamical conditions. In this report the collisional kernels of (Folch et al., 2016) will be used. They represent a good compromise between general features of particles inside the volcanic plume and simplicity. Once clarified the collisional part, we focus on the sticking efficiency $\alpha(m_i, m_j)$. This parameter is a dimensionless number that expresses the probability to have a given number N_s of stuck particles over the total number of collisions N_T for each couple of particles with mass m_i and m_j. The implicit assumption here is that the sticking efficiency is an ensemble average $\langle\alpha(m_i, m_j)\rangle$ over different collisions, involving couples of particles with the same physical and chemical features. In order to have the sticking, the relative kinetic energies of the two colliding particles must be depleted by dissipative mechanisms. Several processes are responsible for this, including viscous dissipation due to the presence of liquid layers upon the surfaces, presence of adhesion forces (electrostatic, chemical, etc.), work spent to rearrange the internal structure of aggregates, etc. A complete and exhaustive experimental investigation of all these processes is still far to be achieved, but theoretical expressions for specific cases are reported in literature. In this work the formulation of (Costa et al., 2010) for wet sticking is applied. This model is a recalibration for the volcanic environments of what contained in the work of (Liu & Litster, 2002). The expression used for the sticking efficiency is a function of the viscous Stokes number St_{ij}:

$$\alpha_{ij} = c_1 \frac{1}{(St_{ij}/St_{cr})^q + 1} \tag{21}$$

Where $St_{cr} = 1.3$, $q = 0.8$, $St_{ij} = \frac{8\,\rho_p|v_i - v_j|}{9\mu_l} \cdot \frac{d_i d_j}{d_i + d_j}$ and c_1 is a multiplicative constant ($c_1 = 1$ in the original work). It is important to note that the sticking efficiency depends on the relative velocities of particles, which is one of the major sources of uncertainties affecting the collisional kernels. Here we follow the simplified approach of (Costa et al., 2010) and set the relative velocities equal to the terminal velocities $|v_i - v_j| \approx |v_{si} - v_{sj}|$. The formulation of (Eq.21) should be used in all the situations where the pressure of water vapor inside the plume overcomes the saturation pressure of humid air respect to a liquid surface. In fact, in this condition the vapor contained inside the plume can condense and deposit upon the surfaces of interacting particles. One dimensional plume models can provide general indications about this condition, but on the other hand they may neglect important details due to turbulence and humid air entrainment that can lead to a local overcome of the saturation pressure. In this work we make the assumption that the shape of the sticking matrix is given by (Eq.21) throughout the rising plume, but different values will be investigated both for the parameters q and c_1. The idea is that, in general, the mathematical form of any sticking process should describe the tendency to have a decrease in the efficiency as the sizes of the particles involved increase, as shown from the plot of (Eq. 21) in fig.7.

16. 7 **- Thermal model**

Explosions at Sakurajima Volcano are very similar to an instantaneous release of ash. This observation justifies the idea of coupling the fixed-pivot equations with a non-sustained plume model, like the thermal-co-ignimbrite model of (Woods & Kienle, 1994). To do that, the mass conservation equation is split into the mass fraction n_d of the dry gas phase, the mass fraction n_v of the humid gas phase (vapor), the mass fraction n_w of the liquid water and, finally, the mass fraction n_s of the solid phase, introducing the equivalence for the bulk density $\rho_B = \rho_B n_d + \rho_B n_v + \rho_B n_w + \rho_B n_s$. In turn, the solid phase is divided among each *bin* according to the mass fractions x_i in order to assure $\sum_{i=1}^{N_{bin}} x_i = 1$. We introduce some basic definitions to describe the contributions of dry air and vapor from the atmosphere to the model. Defining the atmospheric mixing ratio q_x as the ratio of the mass fraction of vapor n_{av} relative to the mass fraction of dry air n_{ad}, the following relations hold for atmospheric values (Degruyter & Bonadonna, 2012):

$$\rho_a = \rho_a n_{ad} + \rho_a n_{av} \tag{22}$$

$$\rho_a n_{ad} = \frac{P}{R_v T_a} \cdot \frac{(1 + q_x)}{q_x + \frac{R_d}{R_v}} \cdot \left(\frac{1}{1 + q_x}\right) \tag{23}$$

$$\rho_a n_{av} = \frac{P}{R_v T_a} \cdot \frac{(1 + q_x)}{q_x + \frac{R_d}{R_v}} \cdot \left(\frac{q_x}{1 + q_x}\right) \tag{24}$$

The expressions above are all function of known environmental quantities except for the mixing ratio q_x. This quantity can be expressed in terms of the saturation vapor pressure e_s and the relative humidity r_h:

$$q_x = r_h \cdot \frac{R_v}{R_d} \cdot \frac{e_s}{P - e_s} \tag{25}$$

The modified conservation equations for mass yield to a new set of relations describing the thermal model in terms of a dry air gas phase, a vapor gas phase and, more important, a set of equations equal to the number of size bins available for the solid phase:

Dry air phase: $$\frac{d}{dt}\left[\frac{4}{3}\pi r^3 \rho_B n_d\right] = 4\pi\, r^2 k_\varepsilon u_p \rho_a n_{ad} \tag{26}$$

Vapor: $$\frac{d}{dt}\left[\frac{4}{3}\pi r^3 \rho_B n_v\right] = 4\pi\, r^2 k_\varepsilon u_p \rho_a n_{av} - \frac{4}{3}\pi r^3 \rho_B n_v \lambda \tag{27}$$

Liquid water: $$\frac{d}{dt}\left[\frac{4}{3}\pi r^3 \rho_B n_w\right] = \frac{4}{3}\pi r^3 \rho_B n_v \lambda \tag{28}$$

Solid phase (size *i*):
$$\frac{d}{dt}\left[\frac{4}{3}\pi r^3 \rho_B n_s x_i\right] = \frac{4}{3}\pi\, r^3 m_i (B_i - D_i) \tag{29}$$

Momentum:
$$\frac{d}{dt}\left[\frac{4}{3}\pi r^3 \rho_B u_p\right] = g\,(\rho_a - \rho_B)\,\frac{4}{3}\pi r^3 \tag{30}$$

Enthalpy:
$$\frac{d}{dt}\left[\frac{4}{3}\pi r^3 \rho_B \left(C_p T_p + gh + \frac{u_p^2}{2}\right)\right] = 4\pi r^2 \rho_a k_\varepsilon u_p (C_a T_e + gh) + L\frac{d}{dt}\left[\frac{4}{3}\pi r^3 \rho_B n_w\right] \tag{31}$$

Z-coordinate:
$$\frac{d}{dt} z = u_p \tag{32}$$

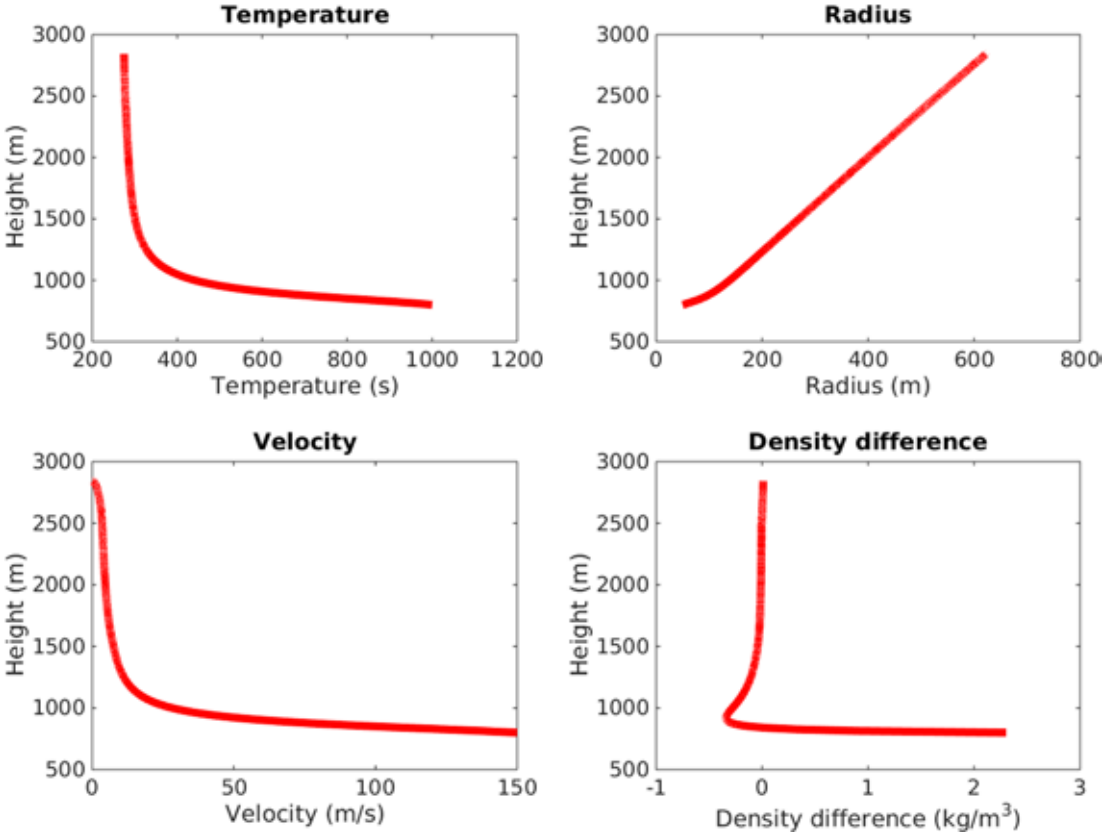

Figure 4. Outputs from the thermal model for an eruption with v_p0=150 m/s, r_0=50 m, n_d0=0.02, n_v0=0.02, n_s0=0.96, n_w0=0. Basic plume quantities such as temperature, radius, velocity and density differences displayed as a function of the height of the thermal.

The fixed-pivot equations (Eq.10-11) enter on the right-hand side of (Eq.29). This implementation represents a simplified description of the problem from several points of view, but it shows clearly how the discrete equations for aggregation can be embedded inside a more complete transport model for plume dynamics. This set of ODEs is solved explicitly with the ODE45 Runge-Kutta solver of Matlab. The typical outputs from the thermal model are shown in (fig. 4).

16. 8 **- Results and discussion**

16. 8.1 **- Sensitivity investigations**

Despite its simplifications, equations (26)-(32) represent a good testbed to analyze the dependence of the Smoluchowski equations on some key parameters implicit in the theoretical formulation. Three fundamental aspects of the thermal model are briefly analyzed here: i) the role of particle breaking (disaggregation) and its importance to not overestimate particle aggregation; ii) the importance of the initial conditions on the gas mixture; iii) how sensitive are the outputs to changes in the sticking efficiencies. For all the simulations shown in this section an initial distribution of particles equal to a Gaussian with mean of 5 ϕ and variance of 2 ϕ is used. It is sampled every 0.5 ϕ.

1) A complete approach describing collisions between particles and aggregates should also describe their tendency to break if their relative kinetic energies are high enough to destroy their bonds or internal structures. Disaggregation somehow compensates the amount of aggregates and keeps the grain size distribution similar to the initial one, or even finer. Progressively, as the relative kinetic energies decrease, aggregation prevails on breakings and equations (26)-(32) become reasonable to describe the population balance inside the thermal plume. We assume different initial areas above the vent where aggregation is forbidden in order to test the final TGSD (Fig.5): these areas are parameterized respect to the vent, from a null region (red bars) to 10 times the initial radius (blue bars). Results of Fig.5 show that neglecting the effect of particle disaggregation near the vent has severe consequences on the final distribution. Unfortunately, it is not easy to define quantitatively the region where aggregation can be considered as the leading process, since it depends on the relative velocities of particles and on the strength of the bonds. This deserves further investigation in a future.
2) Fig.5 shows that small changes in the initial conditions of mass fractions for the four different phases may lead to significant differences in the final grain size distribution. In fact, these parameters directly affect the concentration of solid fraction inside the plume and, consequently, the number of particles per unit volume. Fig.6 reports different runs with different initial conditions for phases in the dusty gas mixture.

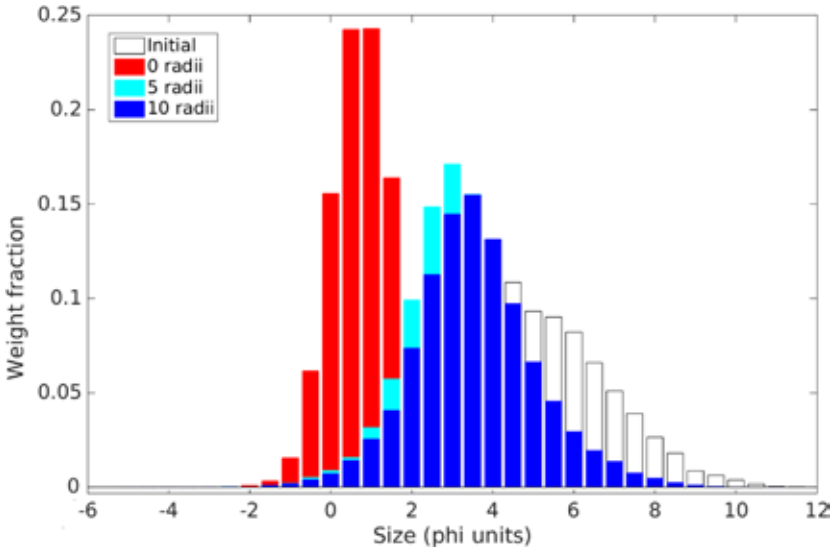

Figure 5. Sensitivity test to investigate the effects of a "no aggregation zone" close to the vent, in order to account for the effects of disaggregation on the final distribution. The width of this region is parameterized with respect to the vent radius (equal to 50 meters). Colored bars are relative to the final grainsize distribution at the top of the plume. Red bars show a plume model where aggregation is considered from the beginning of the eruption. The initial grain-size distribution (Gaussian with mean = 5, variance = 2) is shown inside the small box.

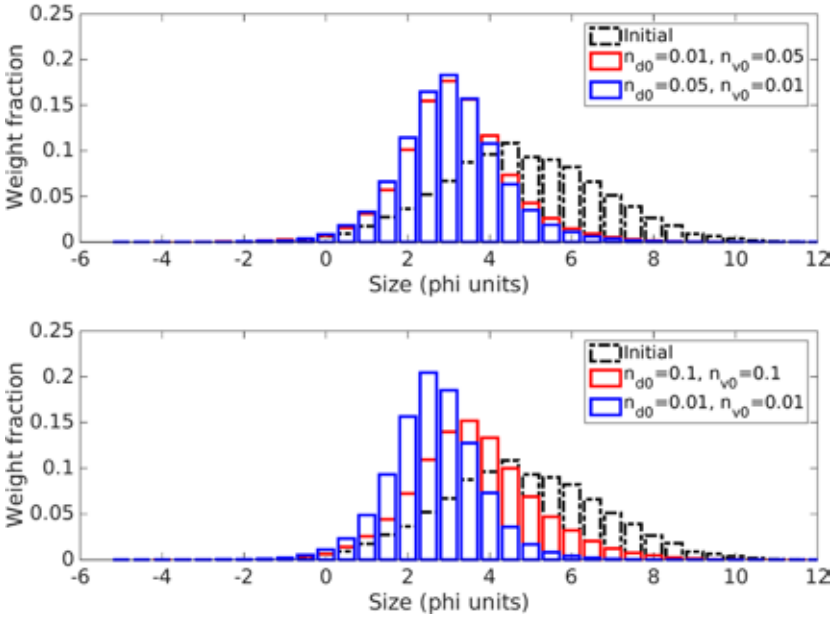

Figure 6. Sensitivity test to investigate how different initial gas fractions in the mixture can affect particle aggregation. n_d0 indicates the amount of initial dry air in the mixture, and n_v0 indicates the amount of vapor.

3) The role of modifications in the sticking efficiency is studied. This is particularly relevant since the sticking efficiency is a quantity poorly constrained, especially in volcanology. We focused on two different aspects of (Eq. 21): the role of two parameters $c_1$and q. c_1 is simply a multiplicative constant, on the other side q alters the global shape of (Eq.21) as shown in Fig. 7.

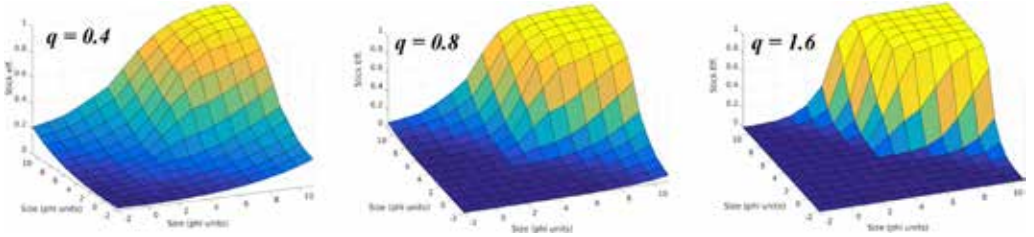

Figure 7. Effect of the q parameter on the sticking efficiency (Eq. 21). Smaller values of q involve larger sizes in aggregation processes.

In fig.8a it is interesting to notice that if we consider correct the original value of $c_1 = 1$, a difference in 10% in c_1 (red line) produces negligible differences among the particles classes. Instead a difference in 50% in c_1(blue line) can produce in this case a difference for a single class up to 30%. Deeper consequences on aggregation are related to the parameter q, that basically alters the shape of the sticking matrix and modifies the threshold where the sticking is zero between different particle sizes. The higher the values of q the slower will be the efficiency among larger sizes. In fig.8b it is evident how q really influences the final outputs, since it basically modifies the role of different collisional mechanisms inside the equations. In fact the sticking efficiency can be seen as a weight applied to the collisional kernel that can inhibit some sizes to be aggregated. This short analysis shows how dramatically important is a good knowledge of the sticking processes, since small changes in the parameters can affect deeply the aggregation. Future laboratory experiments, specifically designed for volcanic ash and aggregates, could fill the gap between quantities required by the theory and our present knowledge.

16. 8.2 **- Application to the Sakurajima eruption of the 3rd of August 2013**

In this work the main goal is to capture general aspects of ash aggregation in a real context avoiding complexity. As already mentioned, some basic information is missing for the eruption of 3rd of August at Sakurajima volcano (Japan), like the Total Grain Size Distribution (TGSD) and details on the initial conditions for the gas-solid mixture at the vent. Nevertheless field observations for this particular eruption provide alternative ways of comparison with models, such as the timescales of aggregation. As mentioned in the previous paragraphs, numerical inversions and direct observations at Sakurajima Volcano indicate that the observed aggregates formed within a time-window of 180 seconds after the eruption (Bagheri et al., 2016). This time threshold is used here as a term of *comparison.*

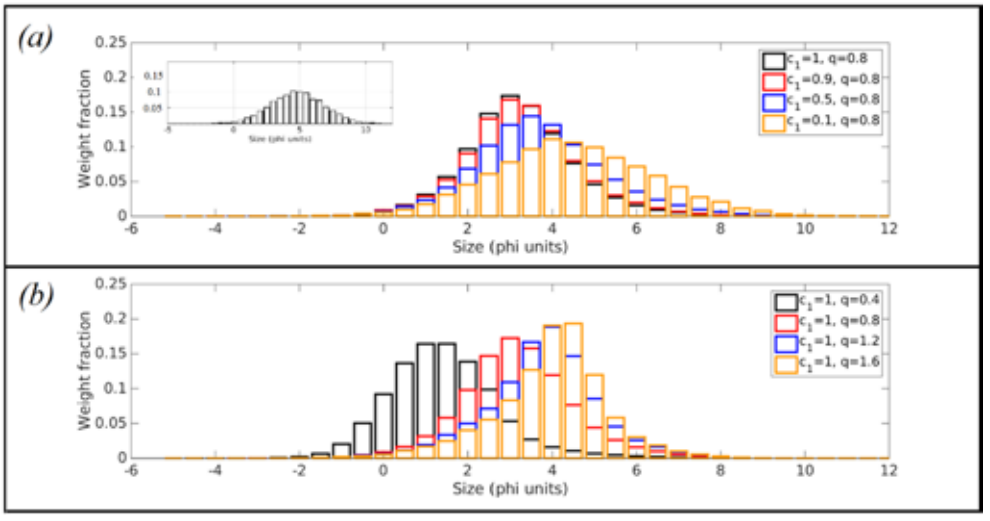

Figure 8. Sensitivity investigations on the sticking efficiency. (a) The parameterization of Costa et al., (2010) is reduced to 90%, 50% and 10%. The small box describes the initial grainsize distribution. The q parameter is kept equal to the original (i.e. q = 0.8). (b) Effects of the influence of a modified parameter q. The higher the value of q the less is the sticking for

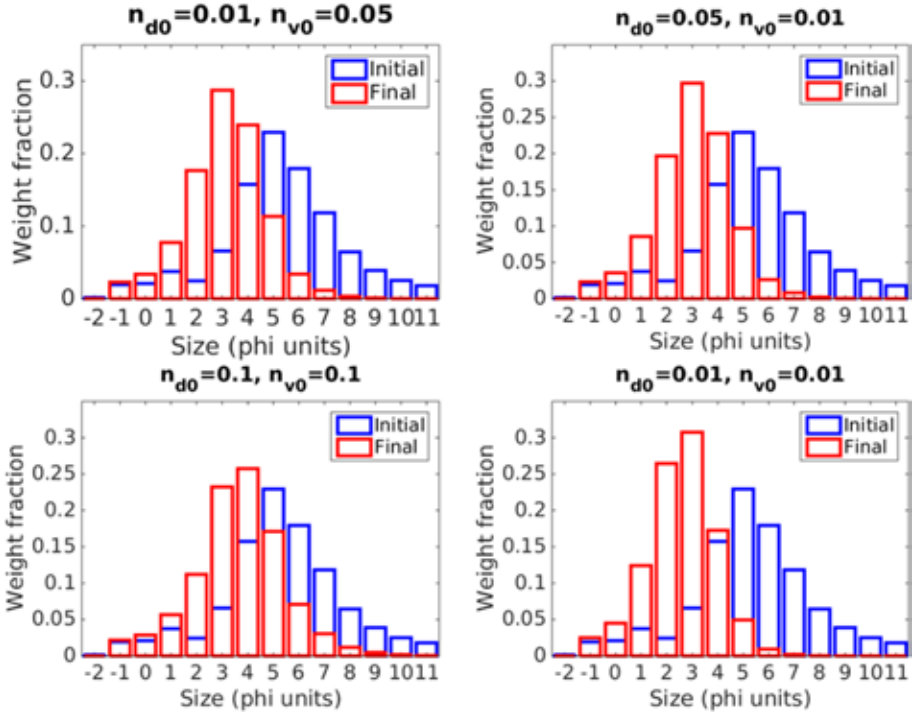

Figure 9. Final TGSD for a Vulcanian-type eruption. The initial grainsize distribution is taken from the eruption of 18 July 2005 at Montserrat Volcano (Cole et al., 2014). Different gas fractions are evaluated as initial conditions for the thermal.

The initial TGSD of a weak Vulcanian eruption occurred at Monserrat on the 18 of July 2005 (fig.9 – blue lines) is considered as initial condition. From direct observations we know that the eruption consisted of at least three main explosions, where the second and the third happened around 20 seconds and 50 seconds after the first one. The three thermals merged in a single large cloud which reached the maximum height of $\approx 2800\ m$ a.s.l. after 240 seconds. In Fig.9 the expected TGSD at the top of the plume is reported for four different initial scenarios (details in tab.2). In all these four scenarios aggregation is not allowed within 5 initial radii above the vent, which correspond to 35 s in time after the eruption. Final TGSD show how the expected maxima of weight fractions are around 3 ϕ. All the four scenarios produce plume heights that are in good agreement with ground observations, but the third scenario ($n_{d0} = n_{v0} = 0.1$) seems to be quite unrealistic for the rising time of the thermal. Ash aggregation is expected to reduce the total number of particles inside the volume, conserving the mass.

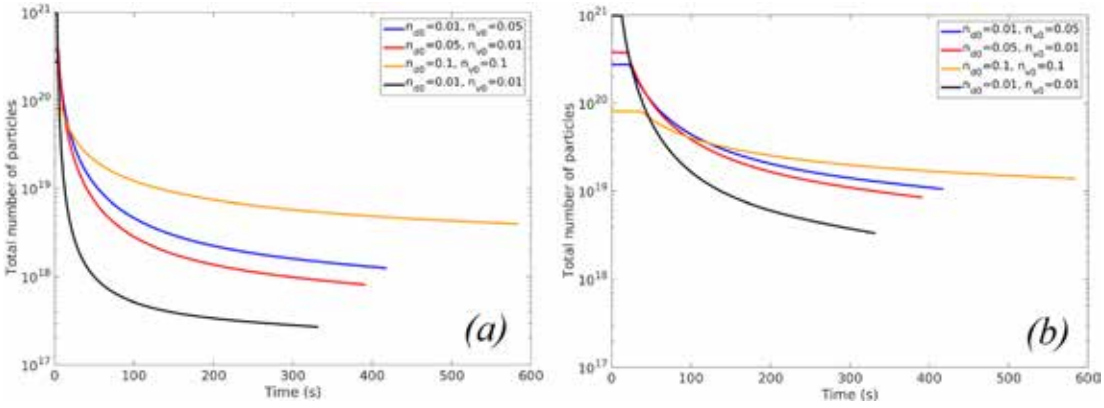

Figure 10. Total number of particles inside the thermal volume as a function of time. Time stops when the plume velocity approaches zero. In a pure aggregation model, the total number of particles is expected to decrease continuously until the plateau, where aggregation is no more effective due to the reduced concentration of particles. Two initial conditions for the forbidden zone for aggregation are analysed: five times the initial radius, i.e. 250 m (a) ten times the initial radius, i.e. 500 m (b).

The rate at which this happens is a function of the particle concentration inside the plume. At a specific time t_s aggregation will be not more effective and the total number of particles will converge to a plateau. A good indication about t_s is given from the analysis of the decay curve shown in fig.10a. Fig.10a shows that aggregation never stops completely but that its efficiency drops dramatically as the concentration reduces: we can define t_s as the time where the drop happens. This reveals that $150\ s < t_s < 380\ s$ for all the different scenarios under analysis (see tab.2 for details). The theoretical time window is thus in good agreement with the observed value of 200 s. However the sensitivity test on the region above the vent with no aggregation (see previous section) suggests investigating how the timescales change if we modify the extension of this region. Running aggregation immediately after the eruption leads to extremely short timescales which are quite unrealistic if compared with what we observed in the field. An increase of the no-aggregation region

up to ten initial radii (which corresponds to a maximum time of 35 s after the eruption, depending on different mass fractions concentrations – see fig.10) leads to a time window of high efficiency for aggregation comprised between $220\ s < t_s < 450\ s$. This confirms that pure aggregation models, i.e. without breaking of particles, tend to seriously overestimate the effects of particles aggregation if run immediately above the vent.

	n_{d0}	n_{v0}	$r_0\ (m)$	$v_0\ (m/s)$	k_ε	$t_s(s)$
Scenario 1	0.01	0.05	50	150	0.25	250
Scenario 2	0.05	0.01	50	150	0.25	230
Scenario 3	0.1	0.1	50	150	0.25	400
Scenario 4	0.01	0.01	50	150	0.25	150

Table 2. Initial conditions used for all the different simulated scenarios

16. 9 **- Conclusions**

In this work we have combined two different aspects of volcanic ash aggregation: field observations and theoretical description. Field data presented in this paper come from the eruption of 3rd of August at Sakurajima Volcano and they are based on combination of High-Speed movies and particle collection on sticky papers. Observations show the presence of large particles ($\approx 300 - 700\ \mu m$) inside the aggregates and a maximum time of formation of $180\ s$. This means that ash aggregation is a fast process, at least within the observed conditions. The theoretical perspective starts from the so-called Smoluchowski Coagulation Equation, which describes the change in mass of a population of particles interacting with given collision frequencies and sticking efficiencies. Several quantities and initial conditions are not easy to constrain and this represents a weak point for predictions. Nevertheless we showed that the way we combined aggregation and volcanic plume theory produces scenarios that are comparable to the observations. The main outcome of this work is the application of the Smoluchowski theory and the validation with field data that was never attempted before. Regardless of the many main assumptions used in the theory, the main aspects of collisions between particles are considered : the death and birth term for a pure aggregative process, the most important collisional kernels and the size dependent sticking efficiency . The combination of transport processes inside volcanic plumes and aggregation equations produces timescales that are reasonable with the observed data. This is a key result that should not be taken for granted a priori. Our promising outcomes confirm that the Smoluchowski Coagulation Equation and our theoretical approach are appropriate and relevant to the description of particle aggregation in volcanic plumes and clouds.

Acknowledgements

The research leading to these results has received funding from the European Union Seventh Framework Programme (FP7/2007-2013) under the project NEMOH, grant agreement n° 289976.

References

Bagheri, G.H., Rossi, E., Biass, S. and Bonadonna, C., (2016). Timing and Nature of Volcanic Particle Clusters Based on State-of-the-Art Field and Numerical Investigations. Journal of Volcanology and Geothermal Reasearch.

Bonadonna, C., Genco, R., Gouhier, M., Pistolesi, M., Cioni, R., Alfano, F., Hoskuldsson, A. and Ripepe, M., (2011). Tephra sedimentation during the 2010 Eyjafjallajökull eruption (Iceland) from deposit , radar , and satellite observations. Journal of Geophysical Research, Solid Earth, v. 116, no. B12, p. 1–20, doi: 10.1029/2011JB008462.

Bonadonna, C., Mayberry, G. C., Calder, E. S., Sparks, R. S., Choux, C., Jackson, P., et al. (2002). Tephra fallout in the eruption of Soufriere Hills Volcano, Montserrat. London: Geological Society.

Brazier, S., Sparks, R., Carey, S., Sigurdsson, H. and Westgate, J., (1983). Bimodal grain size distribution and secondary thickening in air-fall ash layers. Nature, v. 301, p. 115–119.

Brown, R.J.J., Bonadonna, C. and Durant, a. J.J., (2012). A review of volcanic ash aggregation. Physics and Chemistry of the Earth, v. 45, no. 0, p. 65–78, doi: 10.1016/j.pce.2011.11.001.

Carey, S.N. and Sigurdsson, H., (1982). Influence of particle aggregation on deposition of distal tephra from the May 18, 1980, eruption of Mount St. Helens volcano. Journal of geophysical research, v. 87, no. B8, p. 7061–7072.

Cole, P.D., Smith, P., Komorowski, J.C., Alfano, F., Bonadonna, C., Stinton, A., Christopher, T., Odbert, H. and Loughlin, S. (2014). Ash venting occurring both prior to and during lava extrusion at Soufrière Hills volcano, Montserrat, from 2005 to 2010. In: Wadge et al. (eds) The eruption of the Soufriere Hills Volcano, Montserrat, 2000-2010, Geological Society Memoir, Geological Society, London.

Costa, A., Folch, A. and Macedonio, G., (2010). A model for wet aggregation of ash particles in volcanic plumes and clouds: 1. Theoretical formulation. Journal of Geophysical Research, v. 115, no. B9, p. 1–14, doi: 10.1029/2009JB007175.

Folch, A., Costa, A., Durant, A. and Macedonio, G., (2010). A model for wet aggregation of ash particles in volcanic plumes and clouds: 2. Model application. Journal of Geophysical Research, v. 115, no. B9, p. 1–16, doi: 10.1029/2009JB007176.

Folch, A., Costa, A. and Macedonio, G. (2016). FPLUME-1.0: An integral volcanic plume model accounting for ash aggregation. Geoscientific Model Development, 431-450.

Elimelech, M., Gregory, J., Jia, X. and Williams, R., (1998). Particle deposition and aggregation: measurement, modelling and simulation. Butterworth-Heinemann.

Gilbert, J.S. and Lane, S.J., (1994). The origin of accretionary lapilli. Bulletin of Volcanology, v. 56, no. 5, p. 398–411, doi: 10.1007/s004450050048.

Gilbert, J., Lane, S., Sparks, R. and Koyaguchi, T., (1991). Charge measurements on particle fallout from a volcanic plume. Nature, v. 349, p. 598 – 600.

Jacobson, M. Z. (2005). Fundamentals of atmospheric modeling. Cambridge University Press.

James, M.R., Gilbert, J.S. and Lane, S.J., (2002). Experimental investigation of volcanic particle aggregation in the absence of a liquid phase. Journal of Geophysical Research, v. 107, no. B9, p. 1–13, doi: 10.1029/2001JB000950.

Kumar, S. and Ramkrishna, D. (1996). On the solution of population balance equations by discretisation. I: A fixed pivot technique. Chemical Engineering Science, 1311 – 1332.

Kumar, J., Peglow, M., Warnecke, G. and Morl, L. (2006). Improved accuracy and convergence of discretized population balance for aggregation: The cell average technique. Chemical Engineering Science , 3327-3342.

Lane, S., Gilbert, J. and Hilton, M., (1993). The aerodynamic behaviour of volcanic aggregates. Bulletin of volcanology, v. 55, no. 1993, p. 481–483.

Liu, L. X. and Litster, J. D. (2002). Population balance modelling of granulation with physically based coalescence kernel. Chem. Eng. Sci., 2183-2191.

Pruppacher, H.R. and Klett, J.D. (2004). Microphysics of Clouds and Precipitation. Springer Netherlands.

Ramkrishna, D. (2000). Population balances. Elsevier Inc.

Rose, W.I. and Durant, a. J., (2011). Fate of volcanic ash: Aggregation and fallout. Geology, v. 39, no. 9, p. 895–896, doi: 10.1130/focus092011.1.

Schumacher, R. and Schmincke, H.-U., (1995). Models for the origin of accretionary lapilli. Bulletin of Volcanology, v. 56, no. 8, p. 626–639, doi: 10.1007/s004450050069.

Sorem, R., (1982). Volcanic ash clusters: tephra rafts and scavengers. Journal of Volcanology and Geothermal Research, v. 13, p. 63–71.

Sparks, R.S.J., Burski, M.I., Carey, S.N., Gilbert, J.S., Glaze, L.S., Sigurdsson, H. and Woods, A.W., (1997). Volcanic plumes, John Wiley & Sons.

Taddeucci, J., Scarlato, P., Montanaro, C., Cimarelli, C., Del Bello, E., Freda, C., Andronico, D., Gudmundsson, M.T. and Dingwell, D.B., (2011). Aggregation-dominated ash settling from the Eyjafjallajokull volcanic cloud illuminated by field and laboratory high-speed imaging. Geology, v. 39, no. 9, p. 891–894, doi: 10.1130/G32016.1.

Telling, J. and Dufek, J., (2012). An experimental evaluation of ash aggregation in explosive volcanic eruptions. Journal of Volcanology and Geothermal Research, v. 209-210, p. 1–8, doi: 10.1016/j.jvolgeores.2011.09.008.

Vanni, M. (2000). Approximate Population Balance Equations for Aggregation-Breakage Processes. Journal of Colloid and Interface Science, 143-160.

Woods, A. W. and Kienle, J. (1994). The dynamics and thermodynamics of volcanic clouds: Theory and observations from the April 15 and April 21, 1990 eruptions of Redoubt Volcano, Alaska. Journal of Volcanology and Geothermal Research, 273-299.

Eduardo Rossi, Italy

Eduardo.Rossi@unige.ch

Affiliation under NEMOH
University of Geneva, Geneva, Switzerland

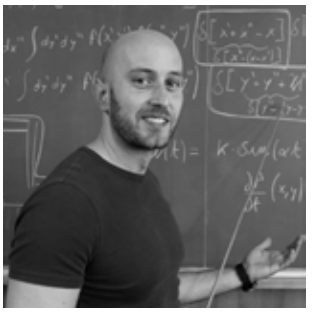

Research theme under NEMOH
Volcanic ash aggregation

During all my life I have been always fascinated by nature and its beauty: with the image of the Sombrero Galaxy (M104) in my mind I started my academic career in Physics, at the University of Pisa (Italy). My first turning point was to deviate from astronomy to focus on something closer here on the Earth. I did my master thesis in underwater acoustics and naval noise pollution, dividing my time in recording underwater noise with hydrophones and making ray-tracing models to describe it. But the second turning point of my career was even greater. Fascinated by a Jules Verne's book (it is easy to guess which one…), I became more and more curious in volcanoes and their hidden mechanisms. The ITN NEMOH project was exactly open at that time and it seemed a perfect occasion offered by fate to develop my curiosity. In November 2012 I joined the physical volcanology group at University of Geneva (Switzerland) under the supervision of prof. Costanza Bonadonna. The topic of my PhD is volcanic ash aggregation and sedimentation, a very interesting and complex subject since it has deep consequences on civil aviation and hazard in general. The strategy of investigation of ash aggregation was immediately clear: to develop a theoretical description in parallel with laboratory experiments at the vertical wind tunnel in Geneva. But as commonly happens in science, the observation of nature always stimulates new ideas and reveals new challenges. During a field campaign at Sakurajima Volcano (Japan), the observation of falling aggregates with high-speed cameras suggested that the theoretical description should have been more complete and complex. I spent almost all my PhD working on this, with promising results that I believe could be the ground for future innovative experimental investigations. One of the main advantages as a Marie-Curie fellow has been the possibility to spend several periods abroad for my scientific training. The most important ones have been at the INGV section of Bologna with Dr. Antonio Costa and at the UK MetOffice in Exeter, always working on ash aggregation.

As a scientist I have clear in mind that one of the most important attitudes in modern research is to make connections. This means to be capable to see the common features that mysteriously relate different fields. I have been lucky in this. Aggregation and its theoretical description seem to be the mathematical key to open several and, up to now, closed doors. Volcanic ash, food industry, planetary formation, social studies: they all show common theoretical features. My wish for the future is to prove to my-self that these connections really exist. That there is a common language in what seems to be far in space, time and mind.

Chapter 17

Volcanic ash modeling with the on-line NMMB-MONARCH-ASH model: model description, applications, and quantification of off-line modeling errors.

Alejandro Marti

Barcelona Supercomputing Center – Centro de Supercomputación Nacional (BSC-CNS), Barcelona, Spain

Tutorship: Arnau Folch

Barcelona Supercomputing Center – Centro de Supercomputación Nacional (BSC-CNS), Barcelona, Spain

---

Abstract

Volcanic ash modeling systems are used to simulate the atmospheric dispersion of volcanic ash and to generate forecasts that quantify the impacts from volcanic eruptions on infrastructures, air quality, aviation, and climate. The efficiency of response and mitigation actions is directly associated to the accuracy of the volcanic ash cloud detection and modeling systems. Operational forecasts build on off-line coupled modeling systems where meteorological variables are updated at the specified coupling intervals. Despite the concerns of other communities regarding the accuracy of this strategy, to date, no operational on-line dispersal model is available to forecast volcanic ash and the quantification of the systematic errors and shortcomings associated to the off-line modeling systems has received no attention. This work presents a comprehensive view of several papers that describe, validate and quantify off-line modeling errors with NMMB-MONARCH-ASH, a pioneering model to predict ash cloud trajectories, concentration of ash at relevant flight levels, and the expected ground deposit for both regional and global domains. The on-line coupled version of the model has been demonstrated to remove most inconsistencies found in traditional off-line modeling systems, offering high performance capabilities in terms of computational efficiency and modeling accuracy. The model has been successfully validated against several well-characterized eruptive events, and it has outperformed other traditional off-line dispersal models (i.e. FALL3D). The outcome of this paper encourages operational groups responsible for real-time advisories for aviation to consider employing computationally efficient on-line dispersal models.

Keywords: NMMB-MONARCH-ASH, volcanic ash transport, numerical modeling, operational forecast, natural hazards, error quantification.

17. 1 - Introduction

Volcanic ash modeling systems are used to simulate the atmospheric dispersion of volcanic ash and to generate operational short-term forecasts to support civil aviation and emergency management. These systems are vital in efforts to prevent aircraft flying into ash clouds, which could result in catastrophic impacts (e.g. Miller and Casadevall, 2000). The aviation community is concerned about the detection and tracking of volcanic ash clouds to provide timely warnings to aircrafts and airports. In the event of an eruption, the individual Volcanic Ash Advisory Center (VAAC) responsible for the affected region combines ash cloud satellite observations and dispersal simulations to issue periodic Volcanic Ash Advisories (VAAs). These are text and graphical products informing on the extent of the ash clouds at relevant flight levels and their forecasted trajectories at 6, 12 and 18 hours ahead that are updated periodically or whenever significant changes occur in the eruption source term. All this information is used to ensure flight safety by supporting critical decisions such as closure of ash-contaminated air space and airports or diversion of aircraft flight paths to prevent encounters. The noteworthy economic impact and social disruption of these air traffic restrictions are, therefore, directly associated to the accuracy of the volcanic ash cloud detection and modeling systems.

Volcanic ash modeling systems require of: i) a source term model to characterize the emission of ash depending on the so-called Eruption Source Parameters (ESPs); ii) a meteorological model (MetM) for the description of the atmospheric conditions, and; iii) a Volcanic Ash Transport and Dispersal Model (VATDM) to forecast the particle transport and deposition mechanisms (Fig. 1).

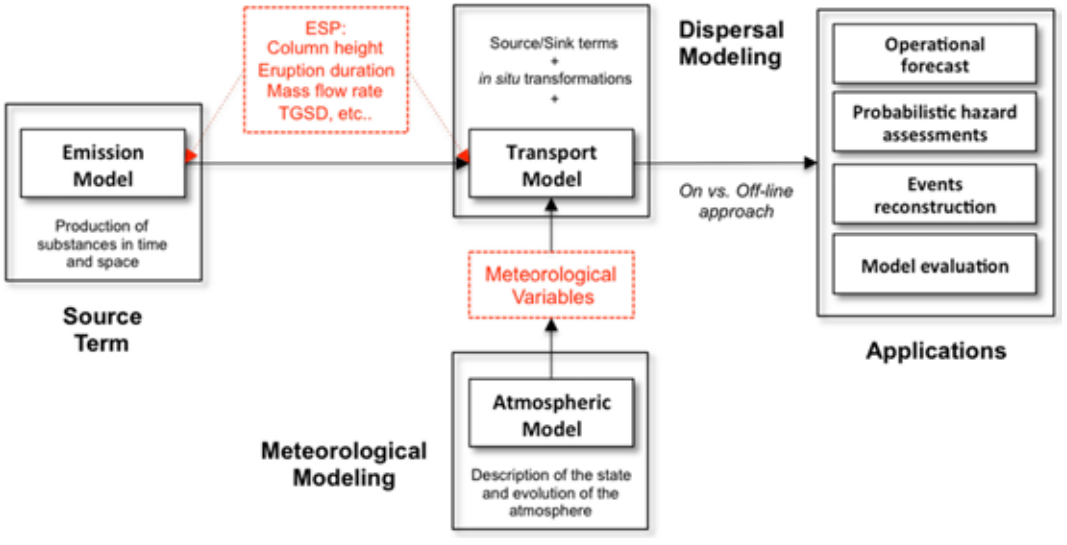

Figure 1. Schematic representation of the main components of an Atmospheric Transport Model. Red text shows model specifications for the transport of volcanic ash (Marti et al., 2017).

The MetM and the VATDM can be coupled either "on-line" or "off-line". In an off-line modeling system, the MetM runs *a priori* and independently from the VATDM to produce the required meteorological fields at regular time intervals, e.g. every 1 or 6 hours for typical mesoscale and global operational MetM outputs respectively. Meteorological fields are then furnished to the VATDM, which commonly assumes constant values for these fields during each time coupling interval or, at most, performs a linear interpolation in time. In contrast, in an on-line modeling system, the MetM and the VATDM run concurrently and consistently and the particle transport is automatically tied to the model resolution time and space scales, resulting in a more realistic representation (Fig.2).

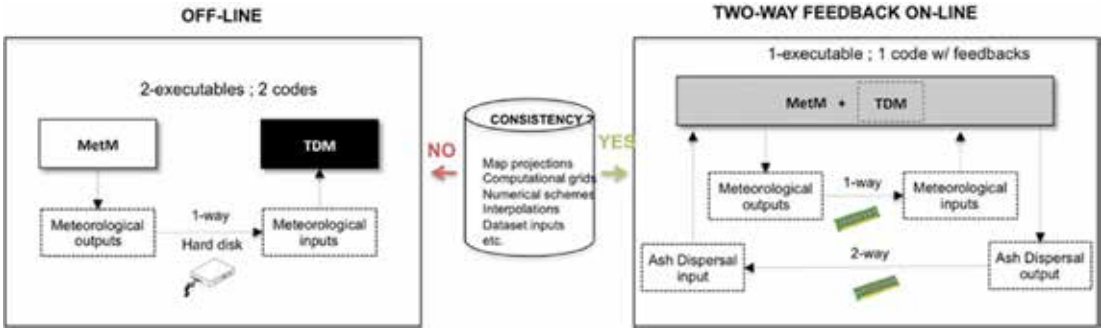

Figure 2. Schematic representation of the different coupling approaches for the meteorological (MetM) and transport and dispersal (TDM) models. Green and red arrows describe whether data consistency is preserved or not, respectively.

The off-line approach is convenient in terms of computing time because different VATDM model executions are possible without re-running the meteorological component, e.g. to update the source term whenever the eruption conditions vary, for inverse modeling of ash emissions (e.g. Marti et al., 2016), or to perform an ensemble forecast (e.g. Galmarini et al., 2010) in which all the ensemble members share the same meteorological conditions. However, notwithstanding the increase of computational power in recent years and the fact that the total computing time required to run an on-line coupled model is actually not substantially larger (e.g. Grell and Baklanov, 2011; Marti et al., 2017), the benefits of the traditional off-line systems are at question. In addition, there is a concern that off-line systems can lead to a number of accuracy issues (e.g., inaccurate handling of atmospheric processes) and limitations (e.g., neglect of feedback effects) that can be corrected by online approaches (Grell et al., 2004). These inconsistencies are especially important when meteorological conditions change rapidly in time or for long-range transport.

Despite these concerns and experience from other communities involved in the atmospheric dispersion of pollutants (e.g. air quality; Zhang, 2008; Baklanov et al., 2011), which have highlighted the importance of the on-line coupling strategy and its competence to solve these inconsistencies (Forkel et al., 2016), to date, no operational on-line dispersal model is available to forecast volcanic ash. Seemly, it is also surprising that the quantification of modeling errors and shortcomings associated to the off-line coupling strategy has received no attention despite the lessons learned

from other communities. Considering this framework, the focus on developing a fast and reliable on-line meteorological and atmospheric transport model to pioneer research and operational forecast for volcanic ash, and quantifying the model shortcomings and systematic errors associated with traditional off-line forecasts is timely. In this context, this paper has four objectives:

1) Introduce NMMB-MONARCH-ASH, a new multiscale meteorological and atmospheric transport model which aims at pioneering the forecast of volcanic ash and aerosols;
2) Present several applications of the NMMB-MONARCH-ASH on-line modeling system that properly illustrate the severe disruptive effects of tephra dispersal from volcanic eruptions;
3) Quantify the model shortcomings and systematic errors associated to traditional off-line forecasts employed in operational set-ups;
4) Present an application where employing traditional off-line modeling systems such as FALL3D is convenient in terms of computing time.

17. 2 **- NMMB-MONARCH-ASH: model description**

NMMB-MONARCH-ASH (Marti et al., 2017) is a novel on-line meteorological and atmospheric transport model to simulate the emission, transport and deposition of volcanic ash and aerosol particles released during a volcanic eruption. The model predicts ash cloud trajectories, concentration of ash at relevant flight levels, and the expected ground deposit for both regional and global domains. The on-line coupling in NMMB-MONARCH-ASH allows for solving both meteorology and tephra/aerosol transport concurrently and interactively at every time-step. The model attempts to pioneer the forecast of volcanic ash and aerosols by embedding a series of new modules on the Barcelona Supercomputing Center (BSC) operational system for short/mid-term chemical weather forecasts (NMMB-MONARCH, formerly known as NMMB/BSC-CTM; Badia et al., 2017; Jorba et al., 2012), developed at the BSC in collaboration with the U.S National Centers for Environmental Prediction (NCEP) and the NASA Goddard Institute for Space Studies. A comprehensive description of NMMB-MONARCH-ASH is presented in Marti et al., (2017). The following sections present a brief summary of the main components of the model.

17. 2.1 **- Meteorological core**

The meteorological core, the Non-hydrostatic Multiscale Model on a B grid (NMMB - Janjic and Gall, 2012), is a fully compressible meteorological model with a non-hydrostatic option that allows for nested global-regional atmospheric simulations by using consistent physics and dynamics formulations. The non-hydrostatic dynamics were designed to avoid over-specification. The cost of the extra non-hydrostatic dynamics is about 20% of the cost of the hydrostatic part, both in terms of computer time and memory. The Arakawa B-grid horizontal staggering is applied in the horizontal coordinate employing a rotated latitude-longitude coordinate for regional domains and latitude-longitude coordinate (Janjic, 2003) with polar filtering for global domains. Rotated latitude-longitude grids are utilized for regional simulations in order to obtain more uniform grid distances. In the

vertical, the Lorenz staggering vertical grid is used with a hybrid sigma-pressure coordinate. The general time integration philosophy in NMMB uses explicit schemes when possible for accuracy, computational efficiency and coding transparency (e.g., horizontal advection), and implicit for very fast processes that would otherwise require a restrictively short time-step for numerical stability with explicit differencing (e.g., vertical advection and diffusion, vertically propagating sound waves). The NMMB model became the North American Mesoscale (NAM) operational meteorological model in October of 2011, and it has been computationally robust, efficient and reliable in operational applications and pre-operational tests since then. In high-resolution numerical weather prediction applications, the efficiency of the model significantly exceeds those of several established state-of-the-art non-hydrostatic models (e.g. Janjic and Gall, 2012). The computational efficiency of its meteorological core suggests that NMMB-MONARCH-ASH could be used in an operational setting to forecast volcanic ash (Marti et al., 2017).

17. 2.2 **- The volcanic ash module**

The volcanic module is embedded within the NMMB meteorological core to solve the mass balance equation for volcanic ash, taking into account: i) the characterization of the source term (emissions); ii) the transport of volcanic particles (advection/diffusion); and iii) the particle removal mechanisms (sedimentation/deposition). A schematic representation of the ash module in NMMB-MONARCH-ASH is presented in Figure 3. The options implemented in the model to represent the different ash-related processes are described in detail in Martí´s et al. (2017) section 3.

The coupling strategy of NMMB-MONARCH-ASH can be turned on or off, depending on the solution required (on-line vs. off-line). The on-line version of the model solves both the meteorological and aerosol transport concurrently and consistently. This strategy allows the particle transport to be automatically tied to the model resolution time and space scales, resulting in a more realistic representation of the meteorological conditions. In contrast, the off-line approach uses an “effective wind field” in which, meteorological conditions (e.g. wind velocity, mid-layer pressure, etc.) are set to constant, and are only updated at specific coupling intervals (i.e. time for which meteorological fluctuations are not explicitly resolved). This strategy replicates the off-line coupling effect of traditional dispersal models used at operational levels (e.g. every 1 or 6 hours for typical mesoscale and global operational MetM outputs respectively).

To assure the conservativeness of the model, the model includes a conservative, positive definite and monotone Eulerian scheme for advection. The positive definiteness is guaranteed by advecting the square root of the tracer using a modified Adams-Bashforth scheme for the horizontal direction and a Crank-Nicolson scheme for the vertical direction. The conservation of the tracer is achieved due to conservation of quadratic quantities by the advection scheme. Monotonization is applied *a posteriori* to eliminate new extrema (Janjic et al., 2009).

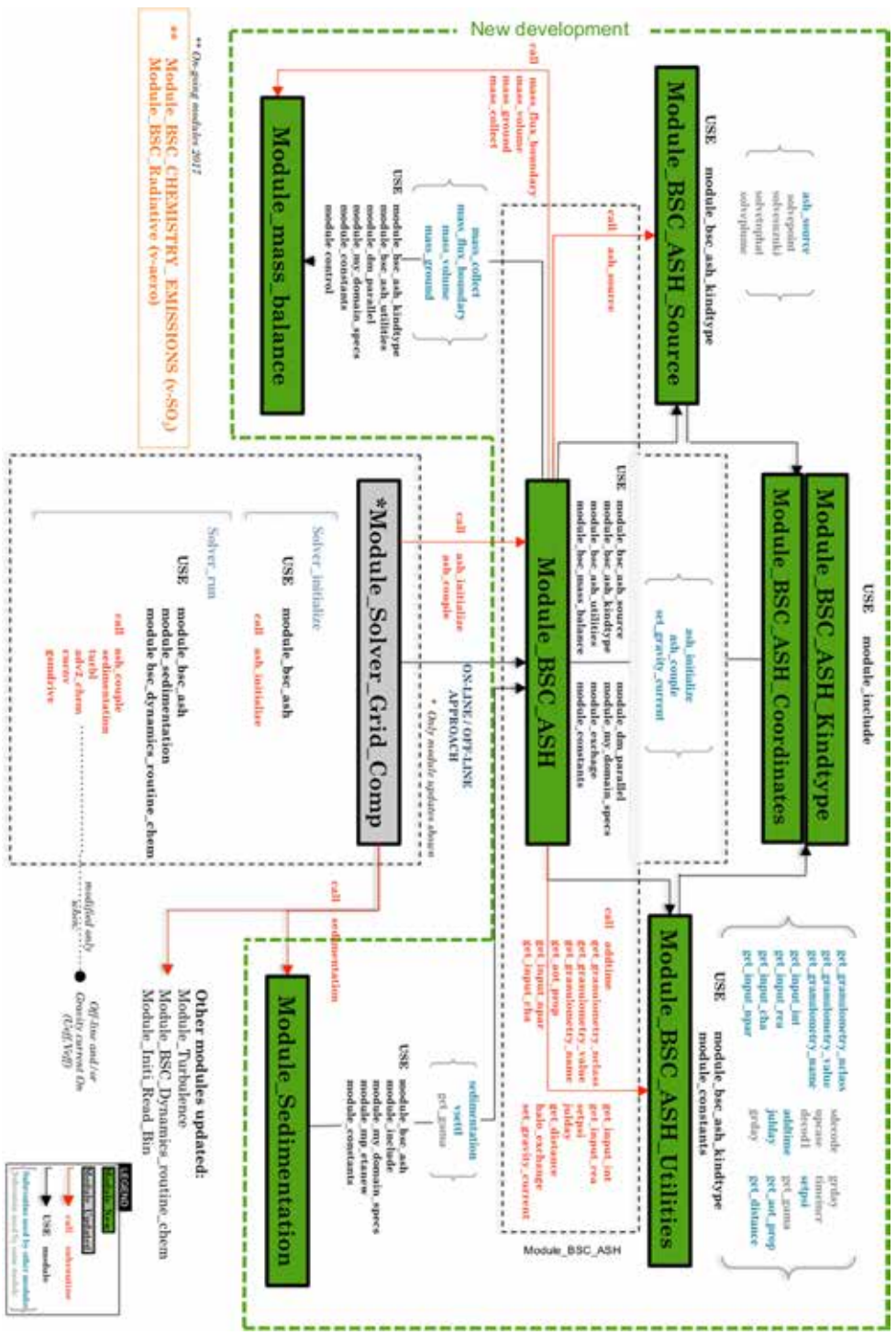

Figure 3. Schematic representation of the ash module in NMMB-MONARCH-ASH (green dashed lines).

17. 2.3 - Operational set-up and numerical performance

The Barcelona Supercomputing Center is currently working on a modeling integrated system to provide operational forecast of volcanic ash with NMMB-MONARCH-ASH. Details about the preliminary implementation of the system are presented in (Marti et al., 2017). The system includes a preprocessing tool, an executable file to run the model, and a user-based postprocessing utility tool. In addition, the system takes a series of input files to define the computational, meteorological and volcanological parameters of the model. Figure 4 shows a simple schematic representation of the operational implementation of NMMB-MONARCH-ASH.

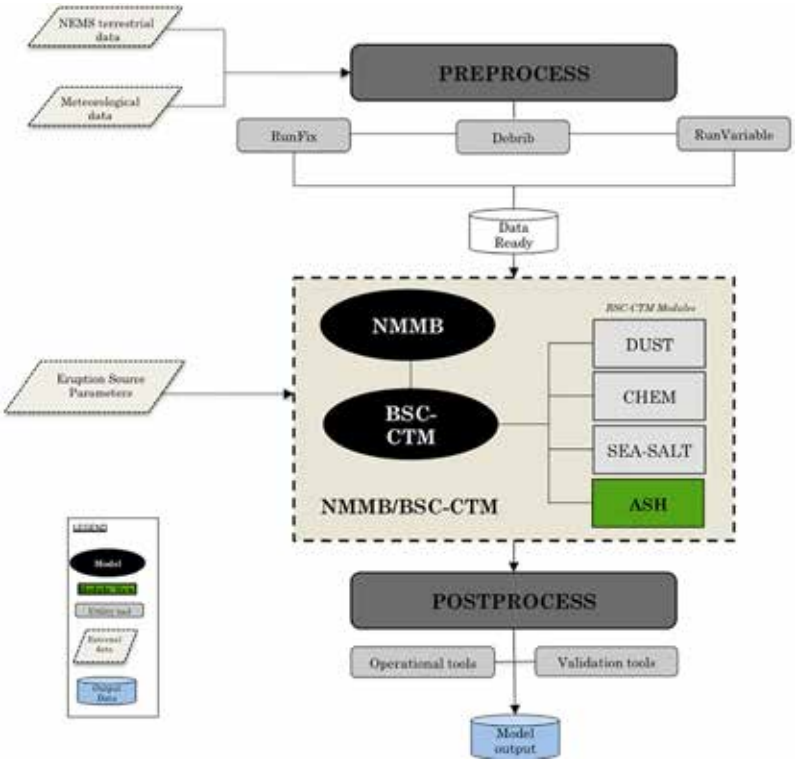

Figure 4. Schematic representation for the operational implementation of NMMB-MONARCH-ASH (Marti et al., 2017).

The preprocessing utility system consists of a set of programs whose collective role is to prepare the model for real-data simulations. Programs are grouped to preprocess geographical, meteorological and climatological inputs and interpolate them to the model grid(s). The postprocess utility tools are designed to interpolate outputs from the NMMB-MONARCH-ASH native grid(s) to National Weather Service (NWS) standard levels (pressure, height, etc.) and standard output grids (Lambert Conformal, polar-stereographic, etc.) in NetCDF format. The system also includes specific programs to produce similar plots to the Volcanic Ash Graphics (VAG) used by Volcanic Ash Advisory Centers in operational forecasts.

The high computational efficiency of the NMMB meteorological driver allows for the application of nonhydrostatic dynamics at a global scale (Janjic et al., 2009), and supports that the NMMB-MONARCH-ASH could be used in an operational forecast of volcanic ash clouds (Marti et al., 2017). Model parallelization is based on the well-established Message Passing Interface (MPI) library. The computational domain is decomposed into sub-domains of nearly equal size in order to balance the computational load, where each processor is in charge to solve the model equations in one sub-domain. The Eulerian schemes in the model require relatively narrow and constant width halos (i.e. data points from the computational domain of neighboring sub-domains that are replicated locally for computational convenience), which simplify and reduce communications.

For operational purposes, the computational time employed to provide ash dispersal forecast using NMMB-MONARCH-ASH was evaluated in Marti et al., (2017) for the global simulation of the 2011 Caulle eruption (see Table 1) but with only 1 bin of ash. The maximum time required by the model to perform a 24 h forecast, running all the available processes (e.g., advection, diffusion, sedimentation, etc.) every time-step (180 seconds) is less than 3 minutes when using the best domain decomposition presented above. This time can be further optimized for operational purposes, i.e., calling the model physics less frequently in order to save computational time. In terms of computational cost, the computational efficiency of the NMMB-MONARCH-ASH meteorological core allows for on-line integrated operational forecasts employing between 2 and 3 times less than the Weather Research and Forecasting Model (ARW-WRF; Skamarock et al., 2008), and an equivalent computational time than FALL3D for the same computational domain and number of processing cores.

	NMMB-MONARCH-ASH				**FALL3D**
	2011 Cordón Caulle	**1970 Deception Island**	**2010 Eyjafjallajökull**	**2001 Mt. Etna**	**39 ka Campanian Ignimbrite**
Source Term (emissions) Duration Vertical distribution MER formulation	20 days Suzuki distribution Mastin et al. (2009)	12h Point source Degruyter and Bonadonna (2012)	96h Suzuki distribution Degruyter and Bonadonna (2012)	3 days Suzuki distribution Mastin et al. (2009)	23h Suzuki distribution ~ 2.08 × 10^{14}kg/s
Ash bins	11 bins	5 bins	5 bins	8 bins	14 bins
Aggregation model	Percentage	None	None	Cornell et al. (1983)	Cornell et al. (1983)
Sedimentation model	Ganser (1993)	Ganser (1993)	Ganser (1993)	Ganser (1993)	Ganser (1993)
Run Set-up Number of processors Domain Vertical layers Top of the atm.	512 Regional / Global 0.15ºx0.15º /1ºx 0.75 60 21 hPa	256 Global 1º x 0.75º 60 21 hPa	256 Global 0.15º x 0.15º 60 21 hPa	256 Regional 0.05º x 0.05º 60 21 hPa	64 Regional 0.25º x 0.25º 60 0.1 hPa

Table 1. Model configuration for several NMMB-MONARCH-ASH and FALL3D runs. Meteorology boundary conditions from the ECMWF EraInterim Reanalysis were reinitialized every 6h with a spatial resolution of 0.75º x 0.75º.

17. 3 **- On-line applications with NMMB-MONARCH-ASH**

17. 3.1 **- Volcanic ash forecast**

NMMB-MONARCH-ASH has been validated against several well-characterized events including, the Mt. Pinatubo 1991 (Philippines), Mt. Etna 2001 (Italy), Chaitén 2008 (Chile), Eyjafjallajökull 2010, (Iceland) or Cordón Caulle 2011 (Chile) eruptions (e.g Marti et al., 2013, 2014, 2017). Here we summarize the ash dispersal results for the regional and global configurations of the model for the 2011 Cordón Caulle eruption. This event represents a typical mid-latitude Central and South Andean eruption, where dominating winds carried ash clouds over the Andes causing abundant ash fallout across the Argentine Patagonia. A detailed chronology of the eruption can be found in Collini et al., (2013) and Elissondo et al., (2016), the stratigraphy and characteristics of the resulting fallout deposit are described in and Bonadonna et al., (2015b), and a summary of the environmental impacts of the eruption is discussed in Raga et al., (2013). This event is evidence of the global nature of the volcanic ash dispersion phenomena and highlights the need for accurate real-time forecasts of ash clouds. The model domain and ESP characteristics for this case are presented in Table 1.

17. 3.1.1 **- Regional configuration**

The regional computational domain spans in longitude from 41º W to 81º W and in latitude from 18º S to 58º S. Runs were performed with the on-line version of NMMB-MONARCH-ASH from 3 June 2011 at 00:00 UTC to 21 June 2011 at 00:00 UTC. Daily eruption source parameters and grain size distributions were obtained from Osores et al., (2014) and Collini et al., (2013), respectively. Model results for the airborne mass concentration of ash were validated using qualitative and quantitative comparisons with data obtained using two different techniques. Here we present the qualitative comparison between the simulated column mass (g m^{-2}) from the model and the NOAA-AVHRR satellite imagery provided by the high-resolution picture transmission (HRPT) division of the Argentinian National Meteorological Service. Figure 5 shows how NMMB-MONARCH-ASH predictions for cloud trajectory and arrival times are in agreement with the NOAA-AVHRR satellite imagery observations, capturing the major dispersion episodes.

A quantitative comparison between the model results and the airborne ash mass loadings described above can be found in Marti et al., (2017). Results from the NMMB-MONARCH-ASH forecast for ash deposition were validated against an isopach map derived from measurements taken for the period beginning on 4 June until 30 June. Figure 6 illustrates the model results at the end of the simulation (30 June) against the measure ground deposit presented by Collini et al., (2013). Deposit load variations produced by remobilization were not considered in this analysis. Results shows good agreement between the modeled deposit load (kg m^{-2}) at the end of the simulation and the measured ground deposit isopachs (kg m^{-2}) at 30 June from. Finally, the model resulted in a cumulative mass of $\sim 4.2 \times 10^{11}$ kg. This value is in agreement with previous works, where total mass was either modeled (Collini et al., 2013) or estimated by empirical fits (Bonadonna et al., 2015b).

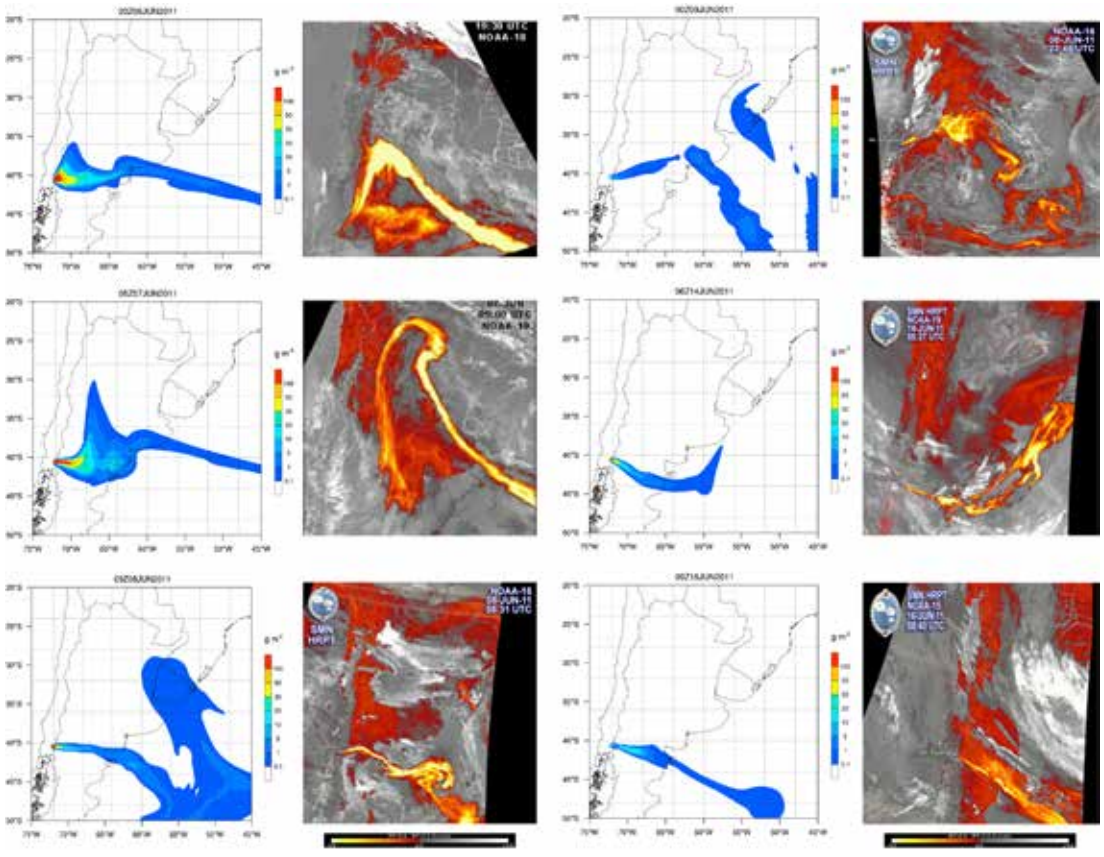

Figure 5. Composite image of NMMB-MONARCH-ASH results for dispersion of ash for the 2011 Caulle eruption at different time slices. Simulation results are compared against split windows algorithm NOAA-AVHRR satellite images (bands 11-12 microns). Contours indicate ash column load (g m^2) resulting from integrating the mass of the ash cloud along the atmospheric vertical levels. (Marti et al., 2017).

17. 3.1.2 **- Global configuration**

The model domain for the global configuration is presented in Table 1. Figure 7 shows the global dispersal of ash for the 2011 Cordón Caulle eruption after different times of the simulation. As it can be inferred from this figure, by 10 June, the plume entered the Australian and New Zealand airspace (Fig 7b) covering more than half of the southern hemisphere. At that point, the Civil Aviation Authority of New Zealand warned pilots that the ash cloud was between 20,000 and 35,000 feet (6 to 11 kilometers), the average cruising level for many aircraft. Before the end of our simulation, on 13 June the ash cloud had completed its first circle around the globe. This is in agreement to satellite images reported by the Darwin Volcanic Ash Advisory Centre (Darwin VAAC, 2011). Finally, results from the global simulation are also in agreement with those from our regional run.

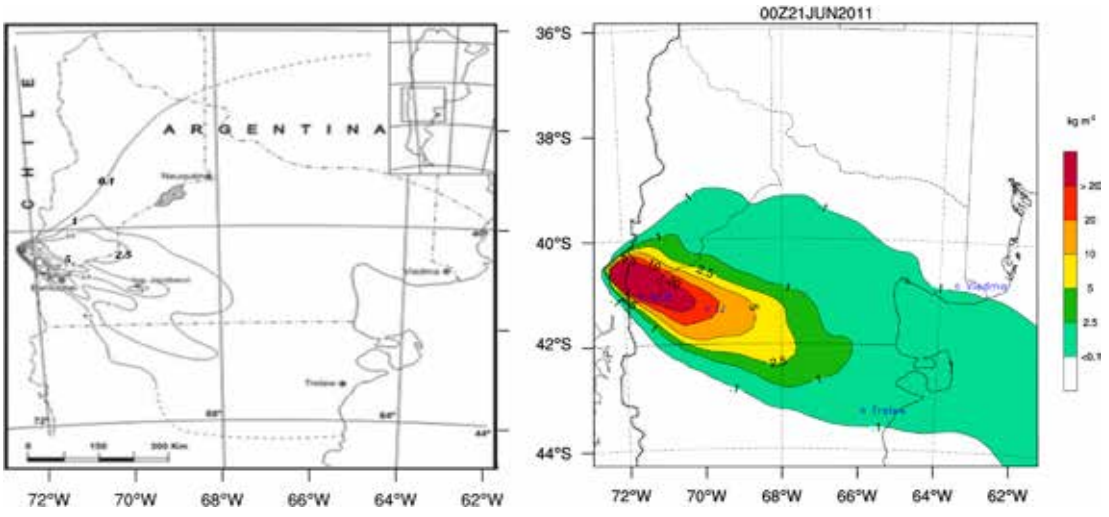

Figure 6. Left: measured ground deposit isopachs (kg m^{-2}) for the period beginning on 4 until 30 June. Dashed lines infer the limit of the deposits (modified from Collini et al., 2013). Right: Predicted deposit load (kg m^{-2}) with NMMB-MONARCH-ASH at the end of the simulation. Key locations in blue include San Carlos de Bariloche (SCB; 90 km from the vent), Ingeniero Jacobacci (IJ; 240 km), and Trelew and Viedma (~ 600 km SE and NE of the vent, respectively) - (Marti et al., 2017).

17. 3.2 **- Forecasting impacts on air traffic**

Explosive volcanic eruptions pose proximal hazards by tephra fallout and can disperse fine ash and volcanic aerosols over vast areas of the globe thereby causing long-range air traffic disruptions. Several disrupting events occurred in recent years, including the 2010 Eyjafjallajökull, 2011 Grímsvötn, and 2011 Cordón Caulle eruptions, led to large economic losses to the aviation industry and its' stakeholders, and demonstrated the global impact of the phenomenon.

NMMB-MONARCH-ASH can furnish values of airborne concentration at relevant flight levels (FL), defined as the vertical altitude (expressed in hundred of feet) at standard pressure at which the ash concentration is measured. This information is particularly important for air traffic management and can be used to decide alternative routes to avoid an encounter with a volcanic cloud. Airborne concentration at FL050 (5,000 feet on nominal pressure) is relevant for the determination of flight cancellations and airports closures, while concentrations at FL300 (30,000 feet) are critical to assist flight dispatchers while planning flight paths and designing alternative routes in the presence of a volcanic eruption. The model runs as if responding to an eruptive event, i.e. we only used the semi-quantitative data available at that time as volcanological inputs.

17. 3.2.1 **- Regional application**

Here we employ the regional configuration of NMMB-MONARCH-ASH presented in the previous section to forecast the airspace contamination caused by the 2011 Caulle eruption during the 6-7 June at flight levels FL050 and FL300, within a latitude band between 20º S and 55º S. Figure 8 shows the volcanic cloud twisting in different directions during that period of time, achieving critical concentration values within a wide area east of the Andes range.

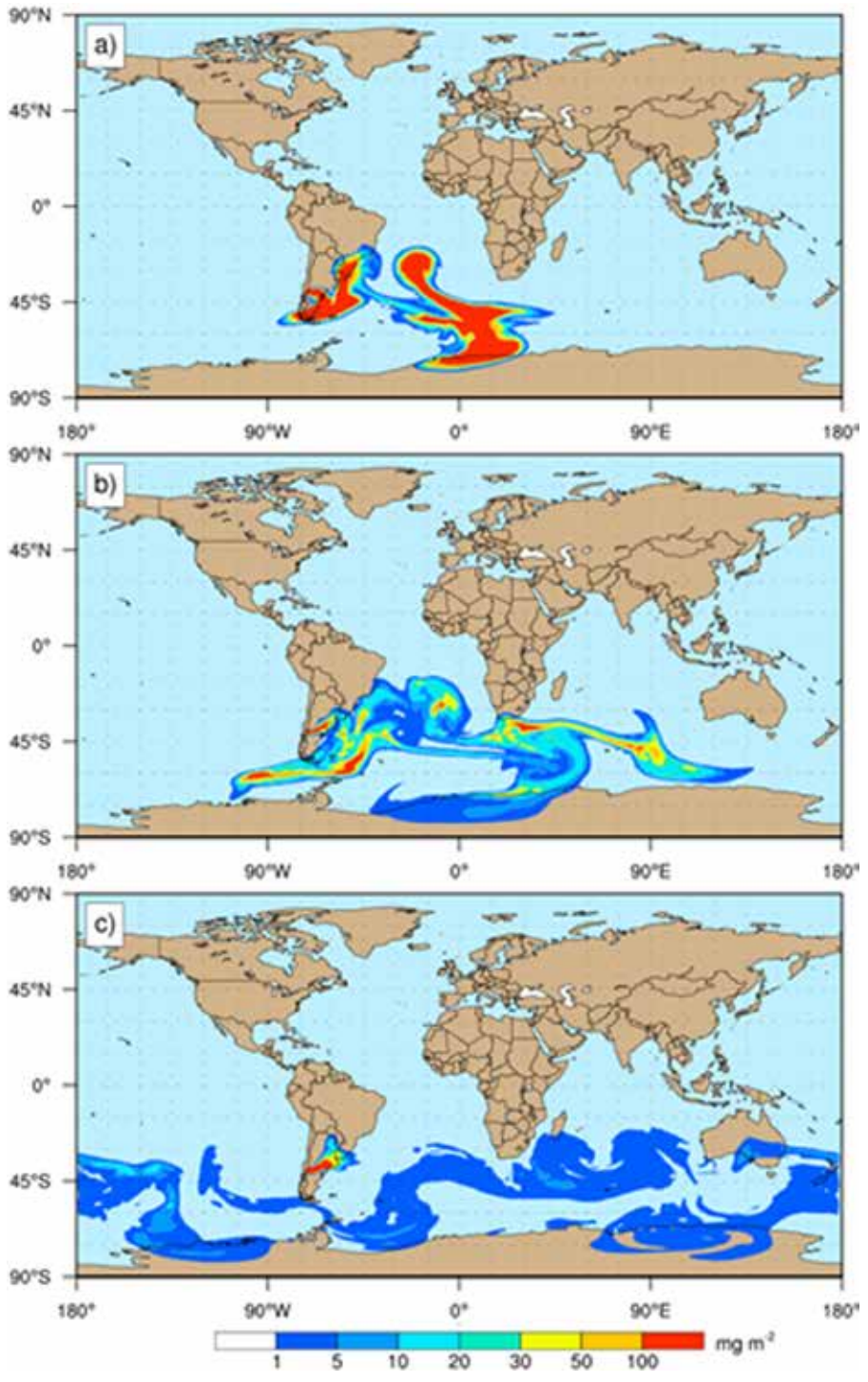

Figure 7. NMMB-MONARCH-ASH total column concentration (mass loading; mg m^{-2}) from global simulations. Results for a) 8 June at 09:00 UTC, b) 10 June at 04:00 UTC, and c) 14 June at 06:00 UTC. Modified from Marti et al., (2017).

On 6 June, simulation results show the volcanic cloud at high atmospheric pressure (~ 30,000 feet or 300 hPa) moving northwards, and the one at lower atmospheric pressure (~ 5,000 ft or 50 hPa) threatening the main international airports that service the region of Buenos Aires (Fig. 8a). In the morning of 7 June, the ash cloud present at lower atmospheric pressure (~ 5,000 ft or 50 hPa) changed its direction towards the SW, ultimately affecting part of the Patagonia and Chile (Fig. 8b), while higher ash clouds started their course around the globe (Fig. 8c). These results suggest that the cancellation of multiple flights in several Argentinean airports during this time was justified.

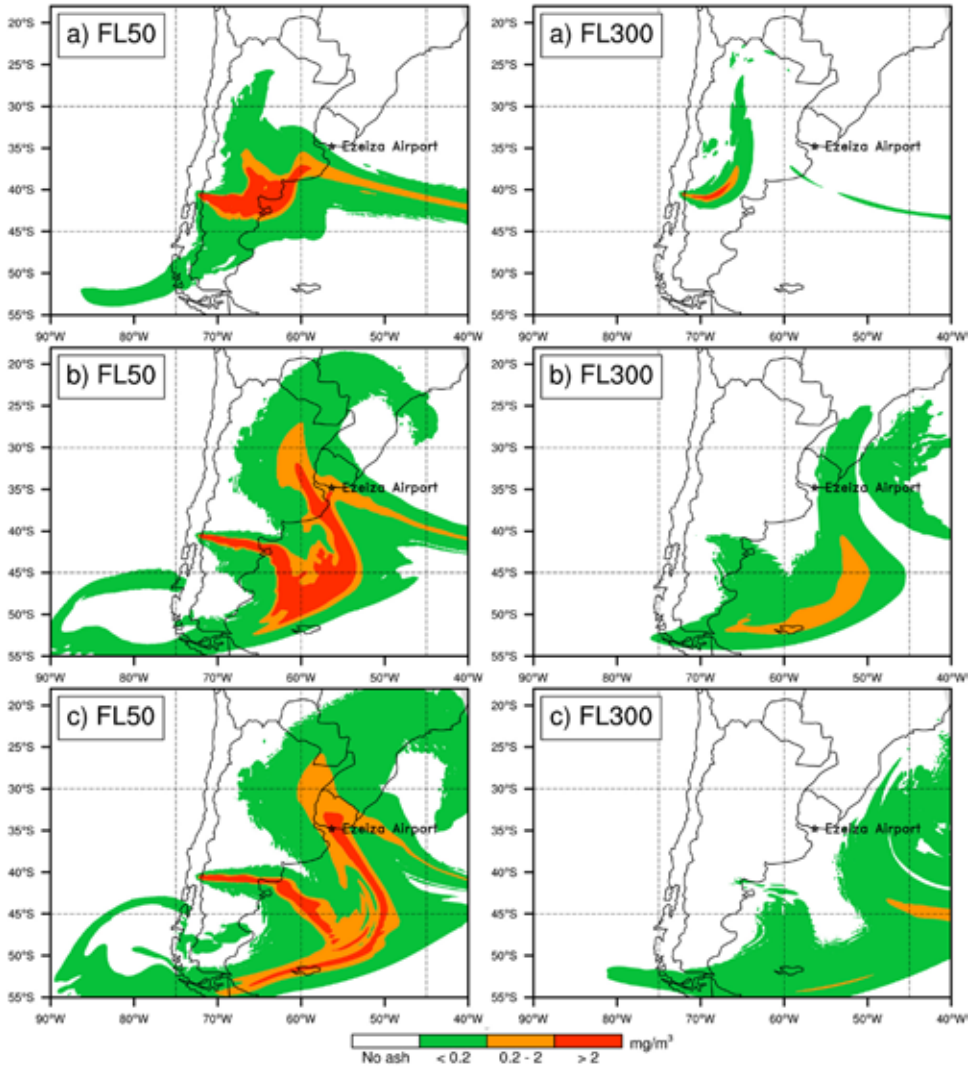

Figure 8. NMMB-MONARCH-ASH Flight level ash concentrations (mass loading; mg m^{-3}) before and after closure of the Buenos Aires (Ezeiza) airport and air space. Results for FL50 (left) and FL300 (right) for a) 6 June at 11:00 UTC, b) 7 June at 04:00 UTC, and c) 7 June at 12:00 UTC. Safe ash concentration thresholds are shown (red contours illustrate "No Flying" zones) (Marti et al., 2017)**.**

17. 3.2.2 **- Global application - Deception Island (Geyer et. al., 2017, NSR)**

Here we evaluate the potential impacts of ash of a 1970-like eruption scenario from one of the most active volcanoes in Antarctica, Deception Island (Martí et al., 2013). The Eruption source parameters for this scenario (Table 1) were obtained from Pedrazzi et al. (2014), who inferred a column height 10 km and a volume of 0.1 km^3 using field data from Geyer et al. (2008) and Pallàs et al., (2001). The particle Total Grain Size Distribution (TGSD) was reconstructed from tephra deposits measured at Livingstone island (Geyer et al., 2008; Pallàs et al., 2001).

The seasonal climate variability of Antarctica is mainly triggered by the Southern Annular Mode (SAM). Changes in this mode explain up to 30% of the deseasonalized variability in both geopotential and winds. For this reason, we considered employing typical meteorological situations for the Antarctic summer (1982) and winter periods (1995). These two meteorological situations were selected randomly in order to avoid possible subjective bias in the date selection. For each of these two periods (S-82/W-95), the specific days with season-mean upper-level winds were selected for simulations.

Figure 9 shows the model meteorological results over the South Pole during the two selected seasons (S-82/W-95). A persistent large-scale clock-wise circulation around an upper-level low-pressure zone located close to the Pole is clearly visible at any time. The polar vortex extends up to the stratosphere, with a global-scale circulation covering latitudes from 70º up to 50º depending on the period. At these stratospheric levels (15km height plots), the resulting polar jet stream is very intense (wind speeds over 60 m/s), widening notably during the winter (Fig. 9b) and narrowing during the summer (Fig. 9a). This is also true close at the tropopause (10km height plots), where Rossby waves start to form and large-scale wind meandering appears. Finally, at mid-tropospheric levels (5 km height plots), the meteorological situations show lesser seasonal dependency and are characterized by a breaking of the jet stream and a pronunciation of the meanders reaching much lower latitudes. These well-known synoptic situations have implications on tephra dispersal patterns and anticipate distinct behaviors depending on the volcano location and eruption column height. On the one hand, low plumes (<10 km) from high-latitude (>70º) volcanoes are likely to be confined within the less-intense-winds zone encircled by the jet stream, i.e. displaying no transcontinental dispersal. However, this may not be the case for higher plumes, which could be advected towards the continental periphery and then entrapped by the jet stream before ash settles on the ground.

Figure 10 shows global-scale air traffic impacts for the summer seasons. At global scale, moderate to high values of ash column load (>1 g m^{-2}) are found up to 4 days (96 h) after the eruption. The highest cloud column mass load values (>100 g m^{-2}) are limited to the first 48 h after the eruption start and are mainly found over the Atlantic Ocean, the Scotia and the Weddell Seas.

However, a residual amount of ash (0.1-1 g m^{-2}) is still present in the atmosphere up to 8 days after the eruption onset. Ash concentrations above the flight safety thresholds (0.2-2 mg m^{-3}, orange and red contours) can be observed over South Africa and, in some cases, over southern Australia or even over austral Patagonia, confirming the potential threat of this DI eruptive scenario to aviation activity.

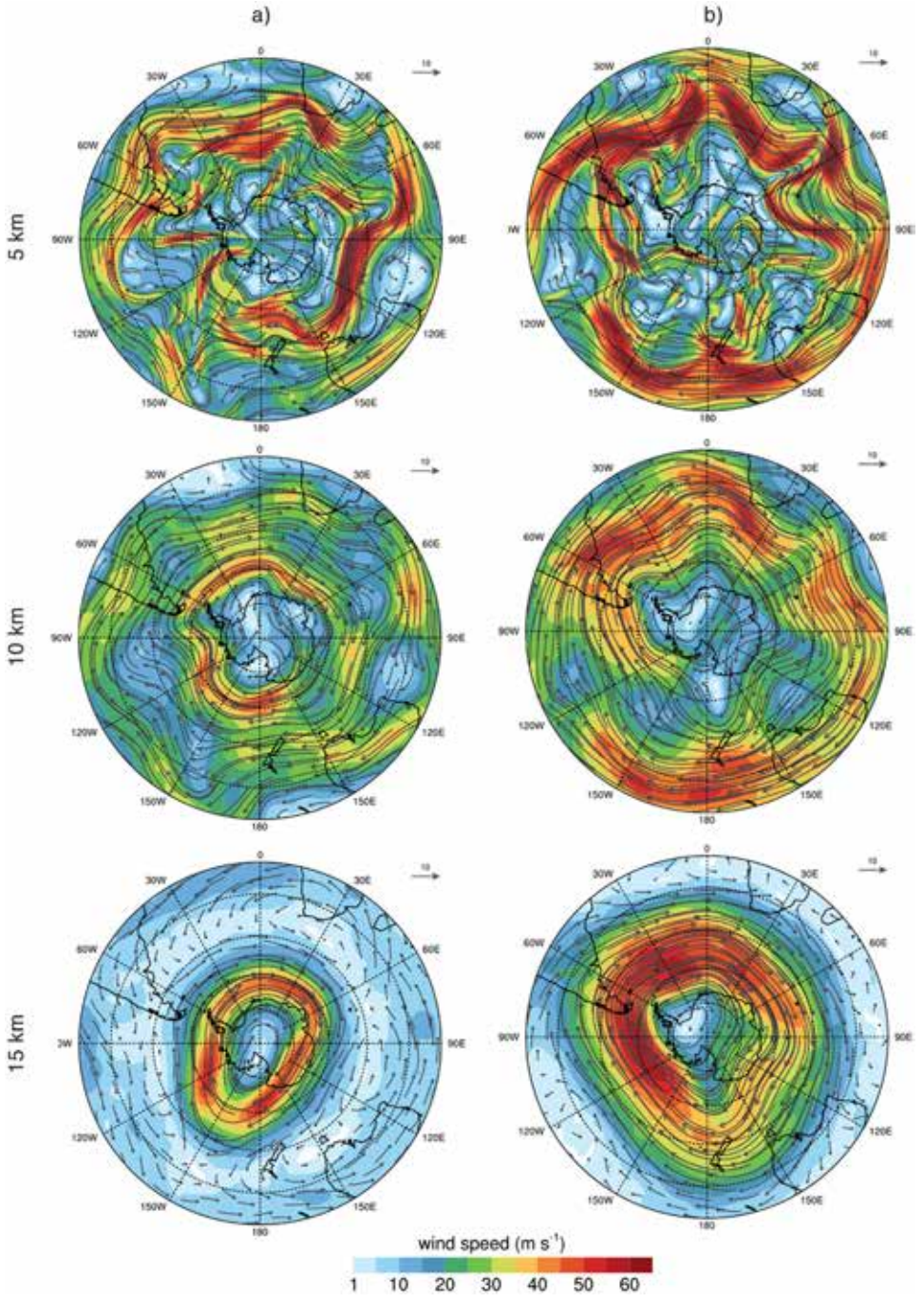

Figure 9. NMMB-MONARCH-ASH meteorological results over the South Pole during the summer (a), and winter (b) seasons. Plots show wind vectors and velocity contours (in ms^{-1}) at 5 (top), 10 (middle) and 15 (bottom) km a.sl., roughly corresponding to mid-troposphere, tropopause and stratosphere respectively.

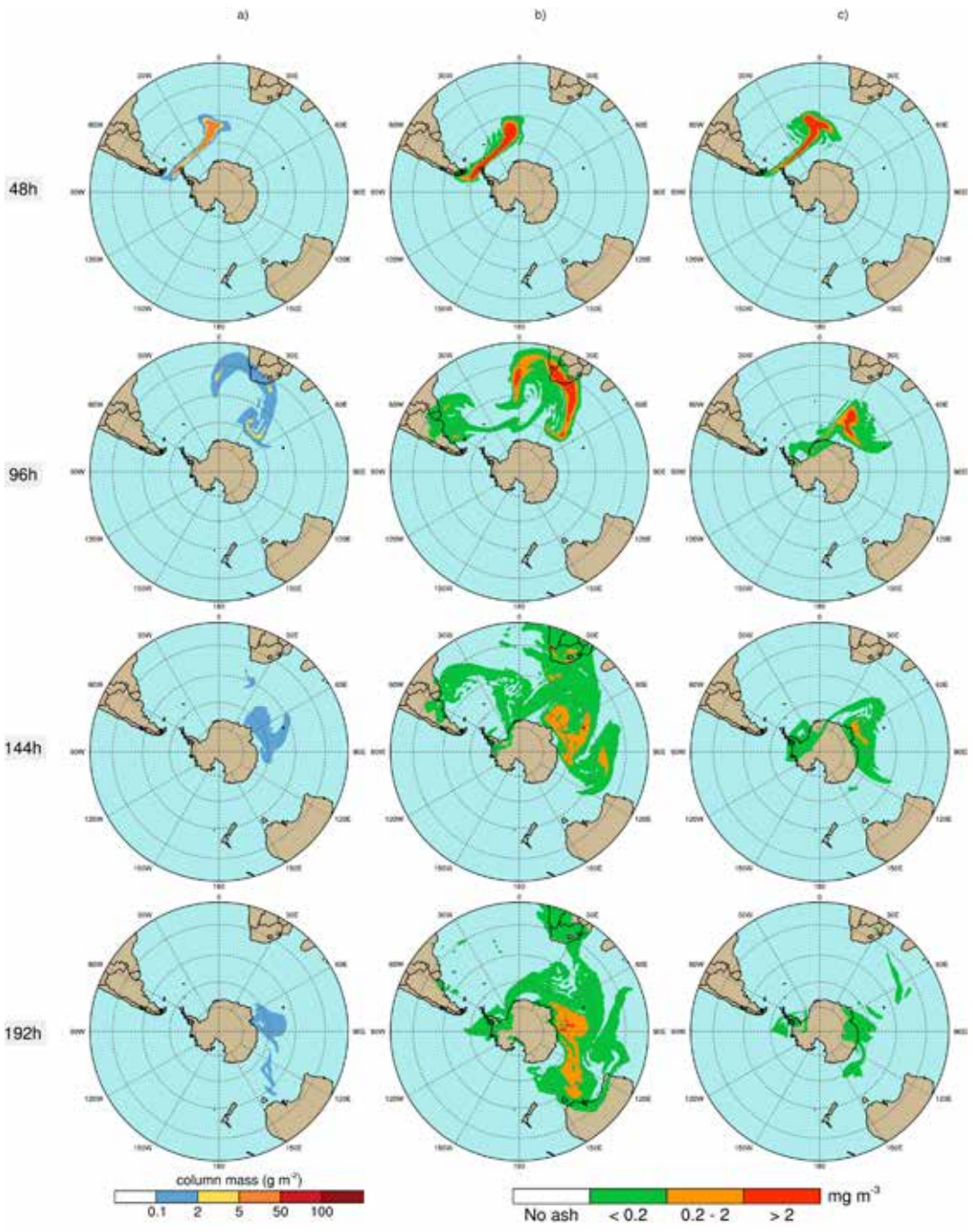

Figure 10. Global-scale NMMB-MONARCH-ASH model results for the summer period at different time instants (2, 4, 6, and 8 days after the eruption). An eruptive column of 10 km height was considered for the 1970-like scenario to simulate: a) the total column mass loading (in g m^{-2}), b) the concentration of ash at Flight Level FL050 (in mg m^{-3}), and c) the concentration at FL250. Safe ash concentration thresholds are shown (red concentration contours illustrate "No Flying" zones).

17. 4 **- Quantification of off-line modeling errors (Marti, 2017b, ACP)**

Since the 2010 Eyjafjallajökull eruption in Iceland, considerable effort and progress has been made to quantify and reduce ash cloud modeling and forecasting errors associated with a number of critical aspects (e.g. Bonadonna et al., 2012, 2015) including, among others, characterization of the source term and related uncertainties in model inputs (e.g. Costa et al., 2016) model parameterization of relevant physical phenomena (e.g. aggregation, particle settling velocities, deposition mechanisms, etc.), propagation of errors in the driving MetM forecast, or satellite detection and retrieval algorithms. However and surprisingly, the quantification of shortcomings associated to the off-line coupling strategy has received no attention despite the fact that lessons from other communities show that these can be substantial (e.g. Baklanov et al., 2014).

Marti et. al. 2017b quantifies the model shortcomings and systematic errors associated with traditional off-line forecasts. NMMB-MONARCH-ASH simulations were performed to account for the sensibility of the off-line modeling option towards the coupling interval and the dispersal distance of the forecast. Case studies were considered for a synthetic eruption with constant eruption source parameters and for two historical events, which suitably illustrate the severe disruptive effects on the aviation industry of European (2010 Eyjafjallajökull) and South-American (2011 Cordón Caulle) volcanic eruptions. Finally, the magnitude of the model forecast errors implicit in the off-line approach was evaluated by comparing it with other better-constrained sources of forecast error, e.g. uncertainties in eruption source parameters.

On-line forecasts were evaluated against simulations from four different off-line coupling intervals (i.e. 1, 3, 6 and 12h) to compare the skills of each off-line coupling approach in terms of their ash column loading (ACL). We used different quantitative and categorical evaluation scores to do so, including: i) basic continuous evaluation scores (e.g. RMSE, bias, Pearson's correlation coefficient); ii) the SAL score, a three-dimensional quantitative object-based measure (Wernli et al., 2008); iii) and a set of categorical score values (i.e. POD: probability of detection, FAR: false alarm ratio, FBI: frequency bias index, and the FMS: Figure of Merit in Space score employed for operational forecast in meteorology (e.g. Shrestha et al., 2013). These scores were grid-point-based comparing observations and predictions per grid cell and computing various metrics for the entire set or subset of grid-points. Ash-contaminated grid cells are selected based on an ash cloud loading threshold value of ~ 0.2 g m^{-2} (Prata and Prata, 2012). For the purpose of this study, forecasts predict ash cloud trajectories and concentration of ash at relevant flight levels for a period up to 48 hours. This approach is consistent with most volcanic ash forecasts operational systems.

Figure 11 shows a qualitative comparison between the on-line and the different off-line coupled forecasts (i.e. 1, 3, 6 and 12h) corresponding to the first explosive phase (14–18 April) of the 2010 Eyjafjallajökull eruption. Qualitative comparisons are presented for each coupling interval in different rows (i.e. 1st row = 1h; 2nd row = 3h; 3rd row = 6h; 4th row= 12h coupling). Areas in grey ("Hits") represent grid points for which both forecasts (off-line and on-line) exceed the established threshold. Red areas ("Misses") indicate those regions where the off-line forecast fails to predict existing ash (underprediction). Finally, blue areas ("False Alarms") illustrate those domain areas for which only off-line forecasts exceed the threshold, implying a false prediction of ash

(overprediction). In general terms, off-line forecasts for the Eyjafjallajökull event tend to overpredict towards the north of the plume and to underpredict towards the south. While results of the 1h off-line forecast indicate mostly Hits (H), Fig. 11 clearly suggests that the number of Missed (M) and False Alarm (FA) points increase with the coupling frequency and the length of the forecast.

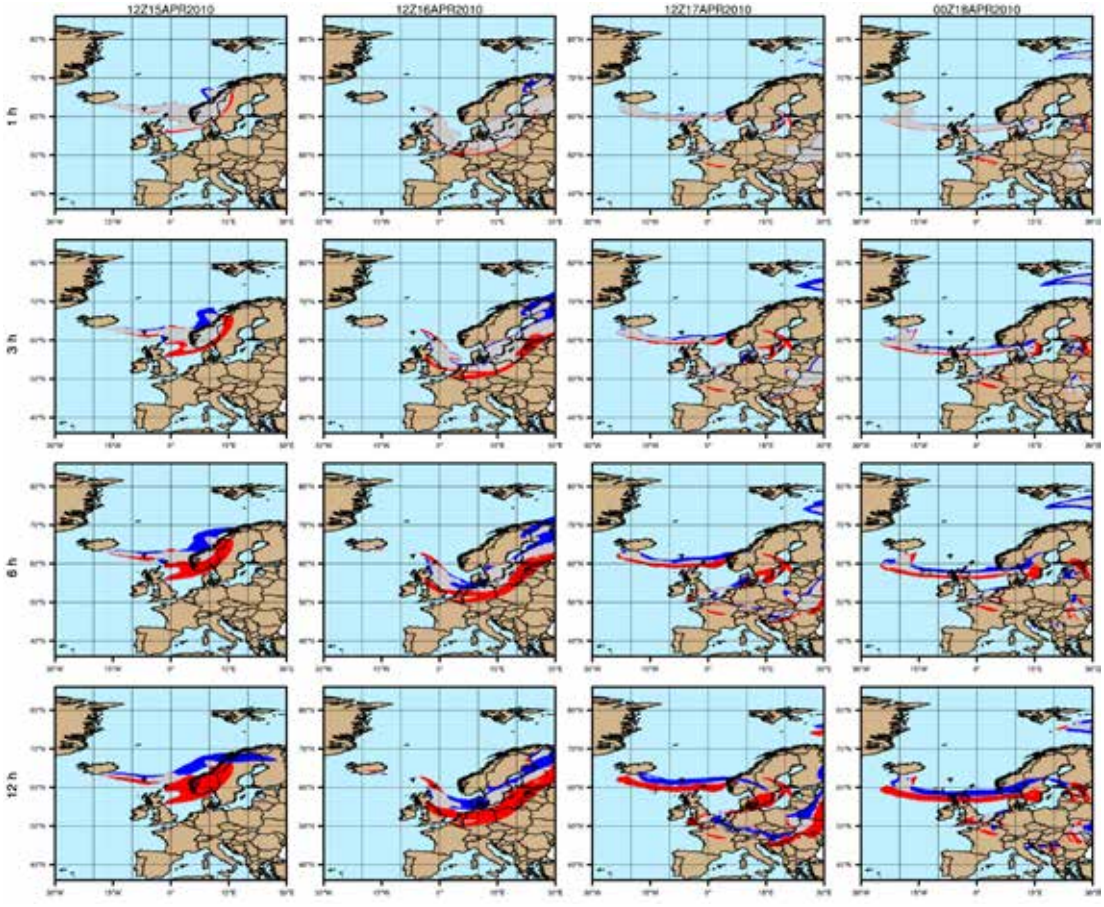

Figure 11. Qualitative comparison between the on-line and off-line forecasts with 1h (row 1), 3h (row 2), 6h (row 3) and 12h (row 4) coupling intervals. Hit (grey), Missed (red) and False Alarm (blue) predictions are shown for the 2010 Eyjafjallajökull case over time.

As a consequence, these forecasts would miss, for example, the arrival of volcanic ash over northern Germany in the late afternoon of 16 April as indicated by the DWD ceilometer network at the time of the eruption (Flentje et al., 2010). As a general rule, Fig. 12 suggests that for the Eyjafjallajökull eruption, off-line forecasts with coupling intervals of 3h and above could result in significant inconsistent predictions (M + FA areas). Figure 12 shows the results of the quantitative and categorical metrics for the forecast ACL evaluation as a function of the length for each coupling frequency of the forecast for the 2010 Eyjafjallajökull application. In general terms, metrics lessen

their scores for longer coupling intervals and forecast lengths. For the purpose of summarizing the results of these evaluation scores, we focus on describing those scores from the 6h-coupled forecast. After 48h of simulation, the 6h-coupled forecast scores show barely any correlation with the on-line forecast and a RMSE of 0.149 g m^{-2}. Bias scores suggest that all off-line forecasts tend to underestimate ACL between -0.33 and -2.5 g m^2 at the end of the forecast. SAL scores indicate that both structure and amplitude from the off-line forecasts explain most of the discrepancy with the on-line forecast. Particularly, amplitude scores indicate that off-line forecasts tend to underestimate the total concentration of ash in the domain by a factor of 1.5 with. Location scores suggest a comparable mass distribution of the ACL fields for the on-line and off-line forecast. Categorical metrics indicate that POD scores are below 50% (i.e. 0.46) at the end of the simulation with FAR scores suggesting a misrepresentation of near 45% objects in the domain. Results from the Frequency Bias metric indicate that all off-line forecasts tend to overestimate the ACL. Finally, FMS scores suggest that the spatial overlap between the on-line and the offline forecasts after 48h of simulation is below 50% for those simulations with coupling intervals of 3h or more.

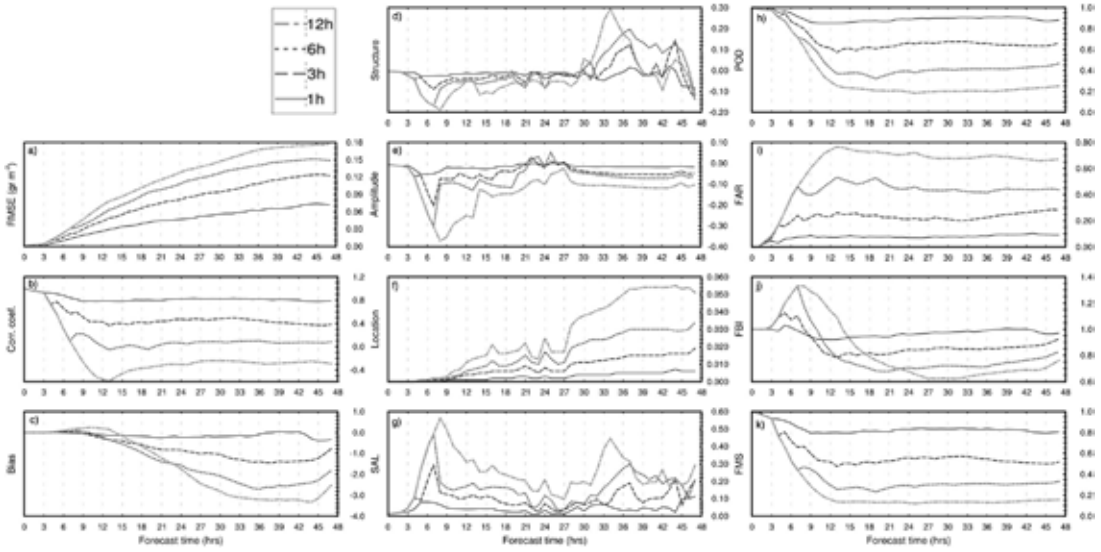

Figure 12. On-line vs. off-line evaluation scores for the 2010 Eyjafjallajökull case.

17. 4.1 **- Model intercomparison NMMB-MONARH-ASH vs. FALL3D**

In order to further evaluate the operational forecast capabilities of NMMB-MONARCH-ASH, a model intercomparison study is performed against the FALL3D model operational at the Buenos Aires VAAC. Simulations with the same spatial resolutions and model inputs were conducted to evaluate the performance of the models for the reconstruction of the 2001 Etna (Italy) eruption (see Table 1). The 2001 Etna eruption represents a good test to study short events where tephra deposits are well represented. For this particular case, simulation results are compared against tephra observations reported in Scollo et al., (2007). Figure 13 suggests an improvement on modeled tephra

distribution across the dispersal area by NMMB-MONARCH-ASH if compared with FALL3D simulations for the same event (R^2; 0.80/0.64), reducing the RMSE (0.014/0.24) and bias (0.02/0.6) by an order of magnitude.

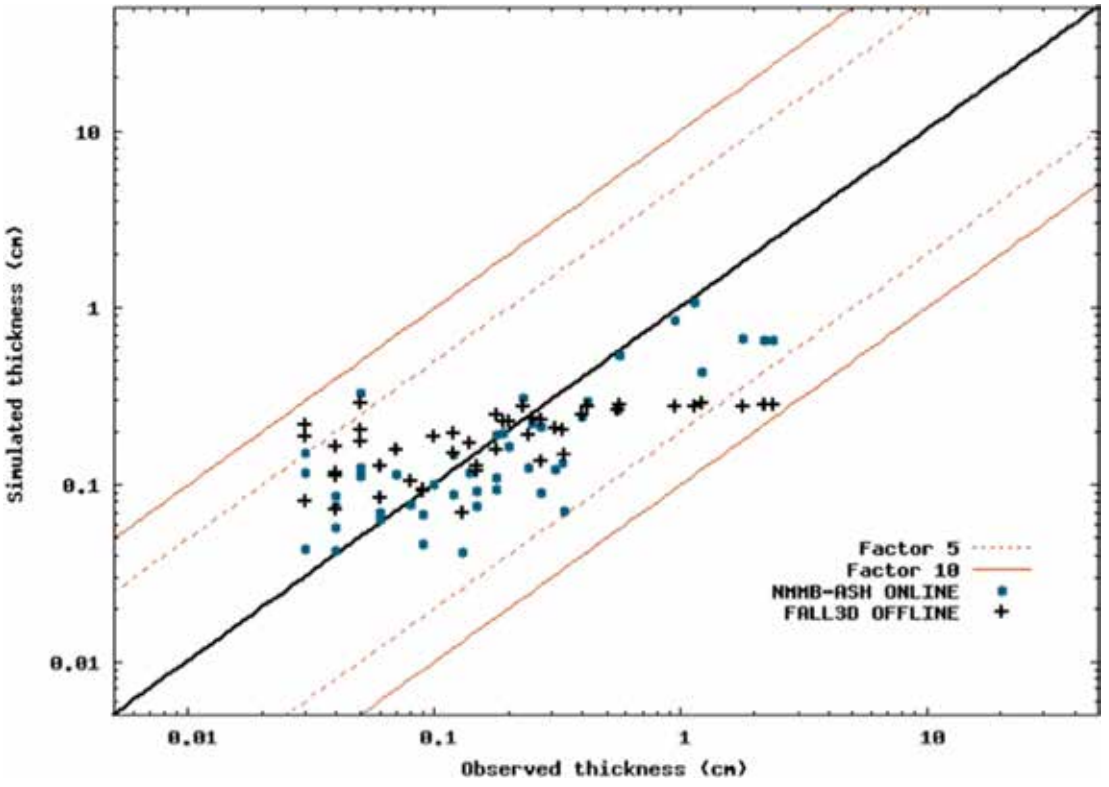

Figure 13. Simulated versus observed thicknesses for the reconstruction of the 2011 Etna eruption with NMMB-MONARCH-ASH (circles) and FALL3D (crosses). The solid bold line represents a perfect agreement, while the dashed and solid thin black lines mark the region that is different from observed thicknesses by a factor 5 (1/5) and 10 (1/10), respectively.

17. 5 - Reconstruction of historical eruptive events with off-line modeling systems

Reconstructing the volume and tephra dispersal from volcanic super-eruptions is necessary to gain further insight into these catastrophic events and assess their widespread impact on humans, ecosystems and climate. Many aspects of volcanic super-eruptions are not fully understood due to a lack of historical precedents, and such eruptions must be reconstructed from their geological deposits employing inversion modeling. For scenarios where ensembles activities or inversion modeling is required, the use of off-line modeling systems is preferred over more complex on-line systems. In this context, a novel computational approach is applied to infer the eruption source parameters for each phase of the Campanian Ignimbrite (CI) eruption accounting for the gravitational spreading of the umbrella cloud (Fig. 14).

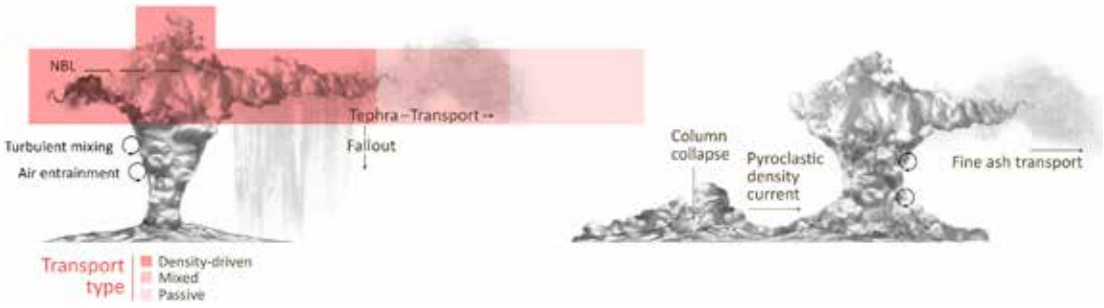

Figure 14. Schematic diagram (not to scale) of a super-eruption event with an initial (left) sustained Plinian phase followed by a column-collapse and large pyroclastic density currents eventually leading to co- ignimbrite plumes offset from the vent (right).

Our methodology uses the FALL3D tephra dispersion model in conjunction with a downhill simplex inversion method (Connor and Connor, 2006) that selects a solution that best represents each phase of the eruption. Two independent datasets (Engwell et al., 2014) containing deposit thickness were used for inversion and validation. This novel approach improves modeled tephra distribution across the dispersal area when compared with the traditional single-phase approach from Costa et al. (2012) (R^2; 0.81/0.77), and reduces the RMSE by ~33% (0.18/0.27) and bias by ~52% (0.21/0.47). The inclusion of the gravity-driven transport improves tephra distribution in proximal areas reducing the overall RMSE by ~20% and the bias by ~20% (0.28 to 0.21). The full description of this work can be found in (Marti et al., 2016). Additionally, an interactive website providing a layman explanation of this methodology and its results is available to the general public at: (http://www.bsc.es/viz/campanian_ignimbrite).

From a climactic perspective, the amount of sulfur dioxide (SO_2) released by the eruption was estimated to be 168–178 Tg of SO_2 (84-89 Tg S), most of which reached the stratosphere, assuming negligible release in the troposphere (Self, 2004). These values represent a 10–15% decrease compared to previous CI reconstructions as a single-phase event (Costa et al., 2012) and are three times higher than those estimated for the largest historic eruption, the 1815 Tambora event (Self, 2004). Finally, tephra fallout from the eruption would have reduced the area available for human settlement in Europe by up to 30% (Fig. 15) causing a halt in the westward dispersal of modern human groups and leading to a significant “genetic bottleneck” (Zilhão, 2006). This being considered, it is possible that modern humans would have gravitated towards repopulating these recovered areas rather than resuming their westward dispersal, permitting prolonged Neanderthal survival in South-Western Europe.

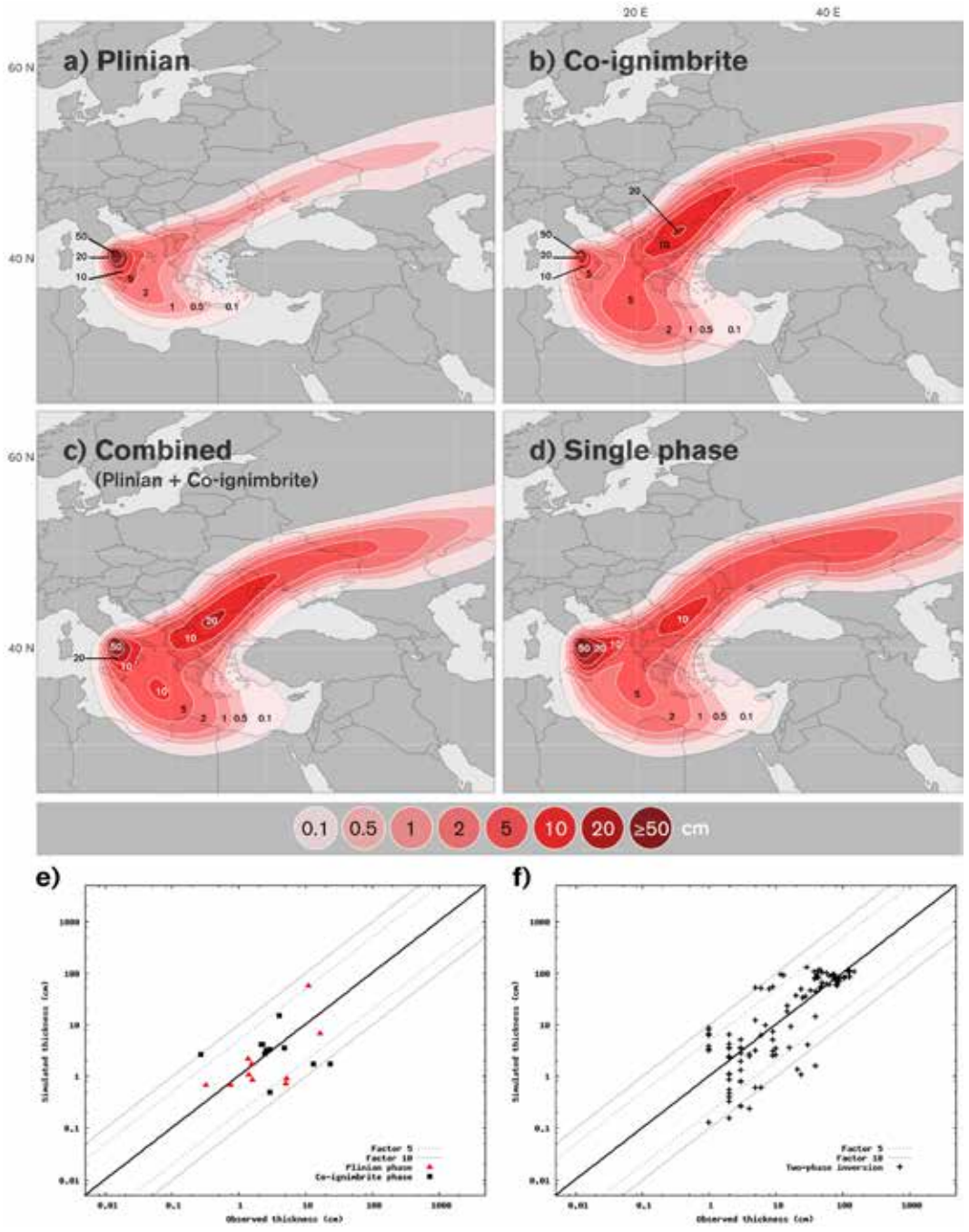

Figure 15. Isopach maps (cm) from inversion. (a) Plinian phase, (b) co-ignimbrite phase, (c) combined two-phase and, (d) single-phase. Bottom plots show simulated versus observed thicknesses for (e) Plinian and co-ignimbrite phases and (f) two-phase approach. The solid bold line represents a perfect agreement, while the dashed and solid thin black lines mark the region that is different from observed thicknesses by a factor 5 (1/5) and 10 (1/10), respectively.

17. 6 **- Discussion and conclusive remarks**

Employing on-line models for operational dispersal forecast requires larger computational resources and is not always feasible at all operational institutes. Nevertheless, due to the increase in computing power of modern systems, one can argue that such gradual migration towards stronger on-line coupling of MetM with VADTM poses a challenging but attractive perspective from the scientific point of view for the sake of both high-quality meteorological and volcanic ash forecast. This paper demonstrates that traditional off-line forecasts employed in operational model setups can result in significant uncertainties, failing to reproduce, in the worst cases, up to 45-70% of the ash cloud of an on-line forecast. These inconsistencies are anticipated to be even more relevant in scenarios where the meteorological conditions change rapidly in time.

This work discusses the modeling advantages of NMMB-MONARCH-ASH, a pioneering model to predict ash cloud trajectories, concentration of ash at relevant flight levels, and the expected ground deposit for both regional and global domains. The on-line coupled version of the model has demonstrated to eliminate most typical inconsistencies found in traditional off-line modeling systems, offering high performance capabilities in terms of computational efficiency and modeling accuracy. The model has been successfully validated against several well-characterized eruptive events, and it has outperformed other traditional off-line dispersal models (i.e. FALL3D). The outcome of this paper encourages operational groups responsible for real-time advisories for the aviation sector to consider employing computationally efficient on-line dispersal models.

Acknowledgements

The research leading to these results has received funding from the European Union Seventh Framework Programme (FP7/2007-2013) under the project NEMOH, grant agreement n° 289976. The author would like to thank Arnau Folch and Oriol Jorba (Barcelona Supercomputing Center) for their co-authorship and mentorship in developing NMMB-MONARCH-ASH. Distinctive acknowledgement is credited to Zavisa Janjic (NCEP) and Carlos Perez (NASA-GISS) for their technical assistance in implementing the model. The author would also like to thank Arnau Folch, Antonio Costa, Sam Engwell, Adelina Geyer and Santiago Pallàs for their contribution in some of the applications presented here. Last but not least, the author would like to express his deepest appreciation to all the NEMOH researchers for this exceptional experience. A special gratitude is given to Paolo Papale, Raffaela Pignolo and Alessandro Fornaciai, for their stimulation, encouragement and mentorship.

References

Badia, A., Jorba, O., Voulgarakis, A., Dabdub, D., Pérez García-Pando, C., Hilboll, A., Gonçalves, M. and Janjic, Z. (2017). Description and evaluation of the Multiscale Online Nonhydrostatic AtmospheRe CHemistry model (NMMB-MONARCH) version 1.0: gas-phase chemistry at global scale. Geosci. Model Dev., 10(2), 609–638, doi:10.5194/gmd-10-609-2017.

Baklanov, A., Mahura, A. and Sokhi, R. (2011). Integrated Systems of Meso-Meteorological and Chemical Transport Models. Springer Berlin Heidelberg. [online] Available from: https://books.google.es/books?id=hseg5tsp-qAC.

Baklanov, A., Schlünzen, K., Suppan, P., Baldasano, J. M., Brunner, D., Aksoyoglu, S., Carmichael, G., Douros, J., Flemming, J., Forkel, R., Galmarini, S., Gauss, M., Grell, G., Hirtl, M., Joffre, S., Jorba, O., Kaas, E., Kaasik, M., Kallos, G., Kong, X., Korsholm, U., Kurganskiy, A., Kushta, J., Lohmann, U., Mahura, A., Manders-Groot, A., Maurizi, A., Moussiopoulos, N., Rao, S. T., Savage, N., Seigneur, C., Sokhi, R. S., Solazzo, E., Solomos, S., Sørensen, B., Tsegas, G., Vignati, E., Vogel, B. and Zhang, Y. (2014). Online coupled regional meteorology chemistry models in Europe: Current status and prospects. Atmos. Chem. Phys., 14(November 2013), 317–398, doi:10.5194/acp-14-317-2014.

Bonadonna, C., Folch, A., Loughlin, S. and Puempel, H. (2012). Future developments in modelling and monitoring of volcanic ash clouds: Outcomes from the first IAVCEI-WMO workshop on Ash Dispersal Forecast and Civil Aviation. Bull. Volcanol., 74(1), 1–10, doi:10.1007/s00445-011-0508-6.

Bonadonna, C., Biass, S. and Costa, A. (2015a). Physical characterization of explosive volcanic eruptions based on tephra deposits: Propagation of uncertainties and sensitivity analysis. J. Volcanol. Geotherm. Res., doi:10.1016/j.jvolgeores.2015.03.009.

Bonadonna, C., Cioni, R. and Pistolesi, M. (2015b). Sedimentation of long-lasting wind-affected volcanic plumes : the example of the 2011 rhyolitic Cordón Caulle eruption, Chile. Bull. Volcanol., doi:10.1007/s00445-015-0900-8, 2015b.

Collini, E., Osores, M. S., Folch, A., Viramonte, J., Villarosa, G. and Salmuni, G. (2013). Volcanic ash forecast during the June 2011 Cordón Caulle eruption. Nat. Hazards, 66, 389–412, doi:10.1007/s11069-012-0492-y.

Connor, L. and Connor, C.: Inversion is the Key to Dispersion (2006). Understanding Eruption Dynamics by Inverting Tephra Fallout. Special Publications of IAVCEI, 1. Geological Society, London, pp. 231–242.

Costa, A., Folch, A., Macedonio, G., Giaccio, B., Isaia, R. and Smith, V. C. (2012). Quantifying volcanic ash dispersal and impact of the Campanian Ignimbrite super-eruption. Geophys. Res. Lett., 39(10), L10310, doi:10.1029/2012GL051605.

Costa, A., Suzuki, Y., Cerminara, M., Devenish, B. J., Esposti Ongaro, T., Herzog, M., Van Eaton, A., Denby, L., Bursik, M., De' Michieli Vitturi, M., Engwell, S., Neri, A., Barsotti, S., Folch, A., Macedonio, G., Girault, F., Carazzo, G., Tait, S., Kaminski, É., Mastin, L., Woodhouse, M., Phillips, J., Hogg, A., Degruyter, W. and Bonadonna, C. (2016). Overview of the Results of the Eruption Column Model Intercomparison Exercise. J. Volcanol. Geotherm. Res., doi:10.1016/j.jvolgeores.2016.01.017.

Darwin VAAC (2011). Satellite image of path of the Cordon Caulle ash cloud around the southern hemisphere from 5-12 June 2011. Bur. Meteorol. [online] Available from: http://www.bom.gov.au/info/vaac/cordon_caulle.shtml, 2011.

Elissondo, M., Baumann, V., Bonadonna, C., Pistolesi, M., Cioni, R., Bertagnini, A., Biass, S., Herrero, J. C. and Gonzalez, R. (2016). Chronology and impact of the 2011 Cordon Caulle eruption, Chile. Nat. Hazards Earth Syst. Sci., 16(3), 675–704, doi:10.5194/nhess-16-675-2016.

Engwell, S. L., Sparks, R. S. J. and Carey, S. (2014). Physical characteristics of tephra layers in the deep sea realm: the Campanian Ignimbrite eruption. Geol. Soc. London, Spec. Publ., 398(1), 47–64, doi:10.1144/SP398.7.

Flentje, H., Claude, H., Elste, T., Gilge, S., Köhler, U., Plass-Dülmer, C., Steinbrecht, W., Thomas, W., Werner, A. and Fricke, W. (2010). The Eyjafjallajökull eruption in April 2010 - Detection of volcanic plume using in-situ measurements, ozone sondes and lidar-ceilometer profiles. Atmos. Chem. Phys., 10(20), 10085–10092, doi:10.5194/acp-10-10085-2010.

Forkel, R., Brunner, D., Baklanov, A., Balzarini, A., Hirtl, M., Honzak, L., Jiménez-Guerrero, P., Jorba, O., Pérez, J. L., San José, R., Schröder, W., Tsegas, G., Werhahn, J., Wolke, R. and Žabkar, R. (2016). A Multi-model Case Study on Aerosol Feedbacks in Online Coupled Chemistry-Meteorology Models Within the COST Action ES1004 EuMetChem, in Air Pollution Modeling and its Application XXIV, edited by D. G. Steyn and N. Chaumerliac, pp. 23–28, Springer International Publishing, Cham.

Galmarini, S., Bonnardot, F., Jones, A., Potempski, S., Robertson, L. and Martet, M. (2010). Multi-model vs. EPS-based ensemble atmospheric dispersion simulations: A quantitative assessment on the ETEX-1 tracer experiment case. Atmos. Environ., 44(29), 3558–3567, doi:10.1016/j.atmosenv.2010.06.003.

Geyer, A., Casas, J. M., Pallàs, R. and Gimeno, D. (2008). Chemical and physical characterization of tephra layers from Livingston Island (Antarctica): ice drill data. Geotemas, 10, 216.

Geyer, A., Marti A., Giralt S., and Folch A. (2017), Potential ash impact from Antarctic volcanoes: Insights from Deception Island's most recent eruption, Scientific Reports, 7(1), 16534, DOI: 10.1038/s41598-017-16630-9

Grell, G. and Baklanov, A. (2011). Integrated modeling for forecasting weather and air quality: A call for fully coupled approaches. Atmos. Environ., 45(38), 6845–6851, doi:10.1016/j.atmosenv.2011.01.017.

Grell, G. a., Knoche, R., Peckham, S. E. and McKeen, S. a. (2004). Online versus offline air quality modeling on cloud-resolving scales. Geophys. Res. Lett., 31(April), 6–9, doi:10.1029/2004GL020175.

Janjic, Z. (2003). A nonhydrostatic model based on a new approach. Meteorol. Atmos. Phys., 82, 271–285, doi:10.1007/s00703-001-0587-6.

Janjic, Z. and Gall, R. (2012). Scientific documentation of the NCEP nonhydrostatic multiscale model on the B grid (NMMB). Part 1 Dynamics., (April), 72, doi:10.5065/D6WH2MZX.

Janjic, Z., Huang, H. and Lu, S. (2009). A unified atmospheric model suitable for studying transport of mineral aerosols from meso to global scales. IOP Conf. Ser. Earth Environ. Sci., 7, 12011, doi:10.1088/1755-1307/7/1/012011.

Jorba, O., Dabdub, D., Blaszczak-Boxe, C., Pérez, C., Janjic, Z., Baldasano, J. M., Spada, M., Badia, A. and Gonçalves, M. (2012). Potential significance of photoexcited NO2 on global air quality with the NMMB/BSC chemical transport model. J. Geophys. Res., 117(August), doi:10.1029/2012JD017730.

Marti, A. and Folch, A. Volcanic ash modeling with the NMMB-MONARCH-ASH model: quantification of off-line modeling errors, Atmos. Chem. Phys. Discuss., https://doi.org/10.5194/acp-2017-354, in review, 2017

Marti, A., Folch, A. and Jorba, O. (2013). On-line coupling of volcanic ash with multiscale meteorological models: a case for 1991 Mt. Pinatubo, in IAVCEI 2013 Scientific Assembly, Kagoshima, Japan.

Marti, A., Folch, A. and Jorba, O. (2014). On-line coupling of volcanic ash and aerosols transport with multi-scale meteorological models: a case for 2008 Chaitén eruption, in Cities on Volcanoes 8, Jakarta, Indonesia.

Marti, A., Folch, A., Costa, A. and Engwell, S. (2016). Reconstructing the plinian and co-ignimbrite sources of large volcanic eruptions: A novel approach for the Campanian Ignimbrite, Sci. Rep., 6, 21220, doi:10.1038/srep21220.

Marti, A., Folch, A., Jorba, O. and Janjic, Z. (2017a). Volcanic ash modeling with the online NMMB-MONARCH-ASH v1.0 model: model description, case simulation, and evaluation. Atmos. Chem. Phys., 17(6), 4005–4030, doi:10.5194/acp-17-4005-2017.

Marti, A., Folch, A., Jorba, O. and Janjic, Z. (2017b). Volcanic ash modeling with the NMMB-MONARCH-ASH model: quantification of off-line modeling errors. Atmos. Chem. Phys. Discuss., doi:10.5194/acp-2017-354, 2017.

Martí, J., Geyer, A. and Aguirre-Diaz, G. (2013). Origin and evolution of the Deception Island caldera (South Shetland Islands, Antarctica). Bull. Volcanol., 75(6), 1–18, doi:10.1007/s00445-013-0732-3.

Miller, T. P., Casadevall, T. J. (2000). Volcanic ash hazards to aviation in: Encyclopedia of Volcanoes, edited by H. Sigurdsson, Academic Press, Cambridge.

Osores, M. S., Folch, A., Ruiz, J. and Collini, E. (2014). Estimación de alturas de columna eruptiva a partir de imáges captadas por el sensor IMAGER del GOES-13, y su empleo para el pronóstico de dispersión y depóstio de cenizas volcánicas sobre Argentina, in XIX Congreso Geologico Argentino.

Pallàs, R., Smellie, J. L., Casas, J. M. and Calvet, J. (2001). Using tephrochronology to date temperate ice: correlation between ice tephras on Livingston Island and eruptive units on Deception Island volcano (South Shetland Islands, Antarctica). The Holocene, 11(2), 149–160, doi:10.1191/095968301669281809.

Pedrazzi, D., Aguirre-Díaz, G., Bartolini, S., Martí, J. and Geyer, A. (2014). The 1970 eruption on Deception Island (Antarctica): eruptive dynamics and implications for volcanic hazards. J. Geol. Soc. , 171(6), 765–778, doi:10.1144/jgs2014-015.

Prata, A. J. and Prata, A. T. (2012). Eyjafjallajökull volcanic ash concentrations determined using Spin Enhanced Visible and Infrared Imager measurements. J. Geophys. Res. Atmos., 117(6), 1–24, doi:10.1029/2011JD016800.

Raga, G. B., Baumgardner, D., Ulke, a. G., Torres Brizuela, M. and Kucienska, B. (2013). The environmental impact of the Puyehue-Cordon Caulle 2011 volcanic eruption on Buenos Aires. Nat. Hazards Earth Syst. Sci., 13, 2319–2330, doi:10.5194/nhess-13-2319-2013.

Scollo, S., Del Carlo, P. and Coltelli, M. (2007). Tephra fallout of 2001 Etna flank eruption: Analysis of the deposit and plume dispersion, J. Volcanol. Geotherm. Res., 160(1–2), 147–164, doi:10.1016/j.jvolgeores.2006.09.007.

Self, S. (2004). Magma volume, volatile emissions, and stratospheric aerosols from the 1815 eruption of Tambora. Geophys. Res. Lett., 31(20), L20608, doi:10.1029/2004GL020925.

Shrestha, D. L., Robertson, D. E., Wang, Q. J., Pagano, T. C. and Hapuarachchi, H. a P. (2008). Evaluation of numerical weather prediction model precipitation forecasts for short-term streamflow forecasting purpose. Hydrol. Earth Syst. Sci., 17, 1913–1931, doi:10.5194/hess-17-1913-2013.

Skamarock, W. C., Klemp, J. B., Dudhi, J., Gill, D. O., Barker, D. M., Duda, M. G., Huang, X.-Y., Wang, W. and Powers, J. G. (2008). A Description of the Advanced Research WRF Version 3. Tech. Rep., (June), 113, doi:10.5065/D6DZ069T.

Wernli, H., Paulat, M., Hagen, M. and Frei, C. (2008). SAL—A Novel Quality Measure for the Verification of Quantitative Precipitation Forecasts. Mon. Weather Rev., 136(11), 4470–4487, doi:10.1175/2008MWR2415.1.

Zhang, Y. (2008). Online-coupled meteorology and chemistry models: history, current status, and outlook. Atmos. Chem. Phys., 8, 2895–2932, doi:10.5194/acp-8-2895-2008.

Zilhão, J. (2006). Neandertals and moderns mixed, and it matters. Evol. Anthropol., 15, 183–195, doi:10.1002/evan.20110.

Alejandro Marti, Spain

Alejandro.Marti@bsc.es

Affiliation under NEMOH
Barcelona Supercompting Center
Centro Nacional de Supercomputación, Barcelona, Spain

Research theme under NEMOH
On-line coupling of volcanic ash and aerosols transport with global and regional meteorological models

I am a self-motivated and dedicated professional with 15 years of cross-disciplinary experience managing projects and developing business within matrix organizations. I have extensive experience in developing and maintaining key relationships with industry, academics and public sector. My academic background encompasses a transversal scientific, innovative and business education in volcanology, atmospheric sciences, environmental engineering, and geospatial technology. I am committed to attaining project goals, with a keen eye for details and a strong focus on continuous improvement. I feel comfortable working independently and as part of a team to provide everyday solutions to problems. I have strong verbal and written communication skills with the ability to establish rapport with audiences and convey information with clarity.

Currently, I am a researcher and a business developer at the Computer Applications in Science and Engineering (CASE) group within the Barcelona Supercomputing Center - Centro Nacional de Supercomputación (BSC-CNS), where I lead the business development of a spin-off aimed to provide atmospheric impact services (e.g. from volcanic ash) to different industries. During my time as a NEMOH fellow I developed and implemented a novel on-line multiscale meteorological and atmospheric transport model (NMMBMONARCH-ASH) for the dispersion and deposition of volcanic aerosols particles. The model attempts to pioneer the forecasting of volcanic aerosols both at research and operational level. My NEMOH research has been published in Nature Scientific Reports and Atmospheric Chemistry and Physics (ACP).

Before joining the BSC-CNS, I held a researcher position at the University of Exeter under the Climate Dynamics group, where he worked as a climate modeler in collaboration with the U.K Met Office Hadley Centre. Prior to my time in England, I worked for 10 years, as a Senior Researcher and Project Manager at the Meadowlands Environmental Research Institute (MERI), the scientific arm of a U.S governmental agency in New Jersey. During this time, I managed a range of interdisciplinary science projects mainly focused on hydrology, land use management, GIS, and climate sciences.

Finally, I have served as an Assistant Professor at different American universities teaching courses in GIS and Remote Sensing. I hold a PhD in Environmental Engineering from the Polytechnic University of Catalonia (UPC); a business postgraduate from the UPC focused to commercialize scientific outcomes; a Masters Degree in Environmental Engineering from Rutgers and the New Jersey Institute of Technology; a Masters Degree in Geographic Information Systems and Remote Sensing from Rutgers; and a Bachelor degree in Environmental Engineering from Fairleigh Dickinson University.

Chapter 18

Energy Cone to simulate Pyroclastic Density Currents for probabilistic volcanic hazard: model validation and uncertainty quantification at Somma-Vesuvius (Italy)

Pablo Tierz

Istituto Nazionale di Geofisica e Vulcanologia (INGV), Sezione di Bologna, Bologna, Italy

Tutorship: Laura Sandri[1], Warner Marzocchi[2]

[1]*Istituto Nazionale di Geofisica e Vulcanologia (INGV), Sezione di Bologna, Bologna, Italy*
[2]*Istituto Nazionale di Geofisica e Vulcanologia (INGV), Sezione di Roma1, Roma, Italy*

Abstract

Pyroclastic Density Currents (PDCs) are hot gravity-driven mixtures of gas and volcanic particles which travel at high speed over the surroundings of the erupting volcano and can potentially cause massive life losses and structural damage along their path. Volcanic hazard assessments of PDCs need to be as robust and accurate as possible and should incorporate a quantification of the large uncertainties which are related to this volcanic hazard. This is especially true for densely populated areas located in the vicinity of explosive volcanoes where such a probabilistic hazard assessment is required well in advance of the onset of the eruption. One of the greatest challenges in probabilistic hazard of PDCs is to find the optimal combination of the PDC physical model and the uncertainty quantification technique which permits calculation of the probabilistic hazard at a reasonable computational cost.

In this paper, we couple the Energy Cone model with Monte Carlo sampling techniques to explore two crucial aspects of PDC hazard at Somma-Vesuvius (Italy), located barely 15 km away from the downtown of Napoli (~ 1M population). Firstly, we quantitatively check the performance of Energy Cone against past PDC deposits at Somma-Vesuvius. Jaccard similarity coefficients between 0.47 and 0.83 are higher than those obtained for other volcanic mass flows models in the literature. The probability of simulating areas of PDC invasion and maximum runouts equal or greater than those preserved from past eruptions ranges between 3% and 60%. Moreover, the spatial distribution of the probability of PDC invasion is similar between simulations and PDC deposits. Secondly, we quantify the impact of diverse sources of epistemic uncertainty on the Energy Cone outputs. In particular, we address uncertainties arising from the Digital Elevation Model (DEM) resolution, the parameterization of aleatory uncertainty, theoretical assumptions adopted in the modeling framework and limitations in the physical model itself. Theoretical uncertainty is the largest source of epistemic uncertainty, up to 100 times bigger than DEM uncertainty. Incorporating epistemic uncertainty in the hazard analysis allows us to compute ranges of probability of PDC invasion (instead of single values) across the hazard domain. For instance, these probabilities are found to be [1-15]% and [50-60]% beyond the topographic barrier of Mt Somma, while they are [0-1]% and [0-15]% at the Napoli-Capodichino airport, for simulated eruptions in the

order of magnitude of the 1631AD and Pompeii eruptions, respectively. All this information can be very valuable in the light of improving probabilistic hazard assessment of PDCs at Somma-Vesuvius and the city of Napoli.

Keywords: probabilistic volcanic hazard, Pyroclastic Density Currents, epistemic uncertainty, Energy Cone, Somma-Vesuvius

18. 1 **- Introduction**

Pyroclastic Density Currents (PDCs) are among the most dangerous physical processes that occur during volcanic eruptions. They are hot gravity-driven complex mixtures of gas and volcanic particles that travel at high speed over the surroundings of the erupting volcano (Cas and Wright, 1987; Druitt, 1998; Branney and Kokelaar, 2002; Sulpizio et al., 2014). The extreme complexity of PDC generation, transport, and deposition processes gives rise to large aleatory (inherent to PDC natural variability) and epistemic (linked to different sources of incomplete knowledge) uncertainties. Commonly, volcanic hazard associated with PDCs has been assessed through the extent of past PDC deposits (Hall et al., 1999; Orsi et al., 2004; Gurioli et al., 2010) or has focused on single scenarios (Esposti Ongaro et al., 2008; Sulpizio et al., 2010b; Procter et al., 2010), hence overlooking the whole impact of the aforementioned uncertainties. Only recently, Probabilistic Volcanic Hazard Assessment, PVHA (Newhall and Hoblitt, 2002; Aspinall et al., 2003; Marzocchi et al., 2004), which provides a complete probabilistic description of the uncertainties associated with the volcanic hazard, has become the pursued target. PVHA has been implemented for different volcanic hazards: tephra fallout (Bonadonna et al., 2005), lava flows (Del Negro et al., 2013) or lahars (Sandri et al., 2014); but it has not been applied yet extensively to PDCs (Dalbey, 2009; Spiller et al., 2014; Neri et al., 2015). This is mainly due to the difficulty to simulate PDCs both in terms of numerical algorithms and computational resources. PDC models that aim to reproduce the most detailed physics of the process are computationally expensive (e.g. PDAC, Esposti Ongaro et al., 2008) and, therefore, not suitable for the exploration of the large uncertainties involved in the hazard assessment. On the other hand, simple models (e.g. Energy Cone, Malin and Sheridan, 1982) describing a few crucial variables such as maximum runout or area of PDC invasion have been criticized because of their physical oversimplifications which supposedly make them insufficient to capture the intrinsic complexity of PDC transport. Nonetheless, a robust and structured validation of such models using actual data from past PDC deposits has not been developed yet.

In this paper, we implement this kind of validation procedure for the Energy Cone model applied to Somma-Vesuvius (Italy), a stratovolcano with the potential to produce large explosive eruptions (Cioni et al., 2008) and located in a very highly-populated area which includes the city of Napoli. The validation is set up in a completely blind manner, that is: (1) the data used to configure the Energy Cone simulations are fully independent of the data utilized to validate them; and (2) the simulations are set up to capture the natural variability (aleatory uncertainty) attainable during an eruption of a given size. This setup is by no means restricted to the typology of past events at the volcanic system under study. The major goal of our validation is to unravel whether the Energy Cone is able to produce hazard footprints that are statistically reliable when compared to real data of PDCs, in terms of maximum runout and area of PDC invasion. In other words: can a statistical sample (and/or all

samples as a whole) of Energy Cone simulations capture the values and variability of some parameters measured from the PDC deposits? Should the validation identify that the model is able to capture such footprints, it would justify its application for a preliminary PVHA of PDCs over the surroundings of Somma-Vesuvius.

Moreover, we provide a quantification of not only aleatory uncertainty but also four different sources of epistemic uncertainty, utilizing a classification modified after Rougier and Beven (2013). Input uncertainty refers to the lack of knowledge about boundary conditions, for instance the real terrain over which PDCs propagate; here we quantify input uncertainty by running equivalent sets of simulations over Digital Elevation Models (DEMs) with different horizontal spatial resolutions. Parametric uncertainty stems from the fact that we do not know exactly the PDFs for sampling the eruptive parameters describing the aleatory uncertainty; here we describe the effects of using different kinds of PDFs on model output. Theoretical uncertainty is linked to the assumptions adopted in the simulation strategy, for example, whether considering the model parameters as independent or not; this source of epistemic uncertainty is addressed by testing several possible relationships between the Energy Cone parameters. Finally, structural uncertainty derives from all the simplifications of the model itself; in other words, it is the uncertainty that remains after having run the model using perfect-known boundary conditions and the 'best' parameter values (Rougier and Beven, 2013). We evaluate structural uncertainty by using computed values of misfit between the 'best' set of Energy Cone simulations and past PDC deposits at Somma-Vesuvius. Exploring all these sources of uncertainty allows us to quantify their specific contribution as recorded in the model outputs. We express such a quantification through: (1) Empirical Cumulative Distribution Functions (ECDFs) of the area of PDC invasion and the maximum runout; and (2) probability maps of PDC arrival around Somma-Vesuvius (conditional on the occurrence of an eruption of a specific size). The implications of this analysis are twofold: on the one hand, the method presented allows one to rank the different types of uncertainty and check, quantitatively, their effect on the model outputs. On the other hand, it provides a detailed and structured quantification of epistemic uncertainty associated to modeling PDCs through the Energy Cone. This can be further applied to assess epistemic uncertainty within PVHA tools and, in the end, may help to improve quantitative volcanic risk assessments.

18. 2 **– Geological setting and methodology**

18. 2.1 **- Somma-Vesuvius**

Somma-Vesuvius is a nested caldera system with a main stratocone (Gran Cono) located about 15 km from the city of Napoli, in southern Italy (Fig. 1). Its present-day edifice shows a complex morphology shaped during the last 40 ka and highlighted by the presence of Mount Somma, a topographic remnant of several volcanic-edifice collapses that occurred during the last 20 ka (Cioni et al., 1999). For hazard purposes, Cioni et al., (2008) proposed these last 20 ka of eruptive history as a reasonable proxy for what to expect during future eruptions at Somma-Vesuvius. The authors defined four main eruptive scenarios: Plinian, sub-Plinian I, sub-Plinian II, violent Strombolian eruptions and ash emission events. The first two classes would represent eruptions with Volcanic

Explosivity Index, VEI (Newhall and Self, 1982), of VEI≥5 and VEI4, respectively; while the last three classes could be related to VEI3 eruptions (Cioni et al., 2008). These VEI classes were proposed by Marzocchi et al., (2004) as an exhaustive set of the possible sizes in case of renewal of explosive activity at Somma-Vesuvius, given the minimum energy required to re-open the conduit after the current repose time of about 70 years. In terms of PDCs, Plinian and sub-Plinian eruptions tend to generate more or less radial PDCs produced by partial and total column collapses and pyroclastic fountaining, with different degrees of phreatomagmatic fragmentation involved in the process (Cioni et al., 2008). In the case of sub-Plinian II and violent Strombolian eruptions (approximately equivalent to VEI3 and VEI2-3 eruptions, respectively, Cioni et al., 2008), PDC events can vary from small-volume PDCs formed by column collapse to low-mobility hot avalanches (Hazlett et al., 1991). In this study, we follow the assumption of Marzocchi et al., (2004) and the classification of eruption sizes by Tierz et al., (2016a,b) and model PDCs attainable during small (violent Strombolian/sub-Plinian II/VEI3), medium (sub-Plinian I/VEI4) and large (Plinian/VEI≥5) eruptions at Somma-Vesuvius.

Figure 1. Geographical setting of the study area. Top left: map of South-Central Europe with Italy featured in the middle of the map. The yellow square denotes the boundaries of the main image where different key locations are identified. The city of Napoli stands on or is surrounded by 2 principal volcanic systems: Campi Flegrei to the west, and Somma-Vesuvius, our target volcano, to the east. The Campanian Plain is the tectonic basin where the two volcanic systems originated. Some geomorphological highs which limit the Campanian Plain are the Nola-Sarno Mountains (on the top-right of the map) and the Sorrento Peninsula (on the bottom-right of the map). Northwards from Somma-Vesuvius, a remnant from a previous edifice collapse is present: Mt Somma. A 3D view from the southwest (Torre del Greco is in the bottom-center of the sub-image) of Somma-Vesuvius Gran Cono and Mt Somma caldera rim is displayed on the bottom left of the figure. Modified after Tierz et al., (2016a).

18. 2.2 - Energy Cone

The Energy Cone (EC) is an analytical model proposed by Malin and Sheridan (1982) to simulate PDC propagation through a simplified formulation of the principle of the conservation of energy (the Energy Line concept, Heim, 1932). The model assumes that potential energy (of the pyroclastic mixture at the point of generation) is transformed into kinetic energy as the PDCs move away from the volcanic source. The pyroclastic current behaves as a gravity-driven, cohesionless suspension of particles and gas with mass remaining constant (Sheridan, 1979) and loses its energy, due to effective friction, linearly with distance:

$$[(H_v + H_0) - h(x)] \cdot g = 1/2 \cdot v^2(x) + gx \cdot \tan\varphi \quad (1)$$

where H_v is the height of the volcanic vent (a.s.l.), H_0 is the height of column collapse (above H_v), $h(x)$ is the topographic height at distance x from the vent, g is the acceleration of gravity, $v(x)$ is the velocity of the PDC at distance x, and $\tan\varphi$ denotes the equivalent coefficient of friction, in other words, the PDC mobility (the smaller φ, the more mobile the PDCs). PDCs stop where the Energy Line intersects the topographic surface (i.e. all energy has been dissipated):

$$v^2(x_{stop}) = 0 \rightarrow (H_v + H_0) - H_{stop} = L \cdot \tan\varphi \quad (2)$$

where x_{stop} is the point where PDCs stop, H_{stop} is the topographic height (a.s.l.) of the point, and L is the PDC runout (for a given EC simulation: max(L) = MR, the maximum runout of PDCs). Note that $\tan\varphi = \Delta H/L$ (with ΔH being the total vertical drop or the difference in height between PDC initiation and stopping).

Therefore, the main model parameters are the collapse height (H_0) and the PDC mobility (φ). Other parameters are the DEM over which the simulation is run, the number of Energy Lines simulated, and the x-y coordinates for PDC initiation. Regarding the latter, we choose the current central crater of Somma-Vesuvius given that the vent-opening probability over the crater area is considerably higher than outside it (Sandri et al., 2009). For the number of Energy Lines, we use 7200 lines, one per each 0.05° of azimuth around the volcano.

18. 2.3 - Aleatory uncertainty description

We model aleatory uncertainty (i.e. the natural variability in PDC generation and propagation that can occur during an eruption of a given size at Somma-Vesuvius) through the following steps: (1) define a closed set of collapse height and PDC mobility values per each eruption size; (2) within each set, parameterize a Probability Density Function (PDF) which describes the relative likelihood of each value; (3) draw a representative sample (10,000 realizations) of each PDF through Monte Carlo sampling schemes; (4) run the Energy Cone 10,000 times (one per each H_0-φ couple) for each eruption size.

Steps (1) and (2) are constrained according to the PDC phenomenology expected during eruptions of different magnitude, as explained before. Collapse heights are modeled through

Truncated Exponential PDFs bounded between 20 m and 0.1H_T m (Tierz et al., 2016a,b), where H_T represents total eruption column heights (per eruption size) simulated by Sandri et al. (2016) at Somma-Vesuvius. PDC mobility is modeled through Truncated Gaussian PDFs (Sheridan and Macías, 1995; Tierz et al., 2016a,b) which are parameterized using data from a worldwide database of PDC mobility for volcanic systems similar to Somma-Vesuvius (Ogburn, 2012). Consequently, we assume that the φ values in the database are a good proxy for the mobility of PDCs at Somma-Vesuvius. Table I shows the PDF parameterizations for each model parameter (H_0, φ) and each eruption size. Finally, steps (3) and (4) above allow us to propagate aleatory uncertainty into the Energy Cone outputs. The effect and impact of aleatory and epistemic uncertainties can then be displayed through Empirical Cumulative Distribution Functions (ECDFs) or through maps of frequency of PDC arrival over the hazard domain (Tierz et al., 2016a; see next subsection).

EC param.	***Collapse Height (H_0) [meters]***					***PDC mobility (φ = atan(ΔH/L)) [degrees]***							
PDF	Trunc. Exp.			Linear Decay		Trunc. Gaussian				Asymm. Tukey Window			
PDF param.	λ^{-1}*	min	max	min	max	μ	σ	min	max	a	b	min	max
Small	173	20	1000	20	1000	22	6	15	36	18	28	15	36
Medium	441	20	2000	20	2000	17	8	8	28	10	25	8	28
Large	807	20	3498	20	3498	12	4	2	20	10	15	2	20

Table I. Summary of the shape parameters for Probability Density Functions (PDFs) of H_0 and φ (before truncation) utilized to quantify aleatory and parametric uncertainties in PDC modeling at Somma-Vesuvius (Italy), considering three eruption sizes: small, medium and large. EC: Energy Cone; param.: parameters; Trunc.: Truncated; Exp.: Exponential; Asymm.: Asymmetric; λ^{-1}: mean of the Exponential PDF; μ and σ: mean and standard deviation of the Gaussian PDF a and b: lower and upper boundaries, respectively, of the equal-probability plateau of the Asymmetric Tukey PDF; min: minimum value; max: maximum value. N.B. λ^{-1} is indicated as the average value from all λ^{-1} calculated from the eruption column heights simulated by Sandri et al., (2016).

18. 2.4 - Epistemic uncertainty description

The epistemic uncertainty associated with modeling of PDCs via the Energy Cone can be disassembled into different contributions. Here we follow a classification modified after Rougier and Beven (2013) and quantify four sources of epistemic uncertainty, namely: input, parametric, theoretical and structural (Tierz et al., 2016a). Input uncertainty is linked to boundary conditions such as the DEM over which the Energy Cone simulations are run. We assess input uncertainty by running the same set of simulations over DEMs with different spatial resolutions from 10 m up to 80 m. Parametric uncertainty derives from the fact that the 'proper' PDFs to model the aleatory uncertainty are unknown, that is: there is not enough knowledge or data to perfectly constrain them. We assess parametric uncertainty by repeating steps (2) to (4) in the previous sub-section using

alternative PDFs: Linear-Decay PDF for H_0 and Asymmetric Tukey Window PDF for φ (Fig. 2). We finally compare the Energy Cone outputs (area of PDC invasion and maximum runout) coming from different PDF combinations (Tierz et al., 2016a). Theoretical uncertainty stems from incomplete knowledge about the possible relationships between collapse height and PDC mobility. While recent papers have proposed somewhat opposite relationships between the parameters (Esposti Ongaro et al., 2008; Doyle et al., 2010), ΔH vs φ data from many volcanoes do not show any specific pattern (Ogburn, 2012; Tierz et al., 2016b). We assess theoretical uncertainty by splitting our simulations into three different H_0-mobility patterns (direct, inverse and independent) and comparing the Energy Cone outputs derived from each of them. Lastly, structural uncertainty arises from all the limitations of the PDC model or, in other words, it would be the epistemic uncertainty that remains when all other sources of epistemic uncertainty vanish (Rougier and Beven, 2013). We assess structural uncertainty (as a first-order approach) by computing the misfit between the 'best' set of simulations and the observed/actual values of area of PDC invasion and maximum runout, and then using these misfit values to modify the outputs computed when just the aleatory uncertainty is accounted for. By 'best' set of simulations we consider those which have areas and runouts the closest to the observed ones.

There are two main ways in which we present our uncertainty quantification. The first is based upon ECDFs, that is: functions which display $p(X \leq x)$ according to a given vector of empirical data, in our case the Energy Cone outputs (X is an output random variable and x is a particular value of the variable). Aleatory uncertainty is denoted by a single ECDF (Exponential-Gaussian outputs). Epistemic uncertainty materializes as the dispersion of this ECDF and is quantified by the area between alternative ECDFs (Tierz et al., 2016a). The second way of expressing uncertainty is by mapping it into the hazard domain. Aleatory uncertainty is the probability (here approximated as the frequency based on the Energy Cone simulations) of PDCs arriving at each grid point of the domain. Epistemic uncertainty is represented by the dispersion around this probability (Marzocchi et al., 2004, 2008). This dispersion can be shown through frequency-difference maps where the differences in frequency (probability) of PDC arrival, depending on the source of epistemic uncertainty considered, are mapped into the hazard domain (Tierz et al., 2016a; see section *Frequency maps*).

18. 2.5 **- Validation procedure**

We evaluate the ability of EC to reproduce some features of PDC propagation and emplacement by comparing the aleatory-uncertainty outputs for each eruption size with PDC deposits preserved from eruptions of equivalent size (Gurioli et al., 2010; Hazlett et al., 1991). We develop three approaches to check the EC performance (Tierz et al., 2016b): (a) compute and analyze the values of some validation metrics defined ad-hoc; (b) assess the likelihood of simulating areas of PDC invasion and maximum runouts similar to the ones measured from the deposits (through the use of p-values); (c) qualitatively compare the spatial distribution of the probability of PDC arrival as obtained with EC and the PDC deposits.

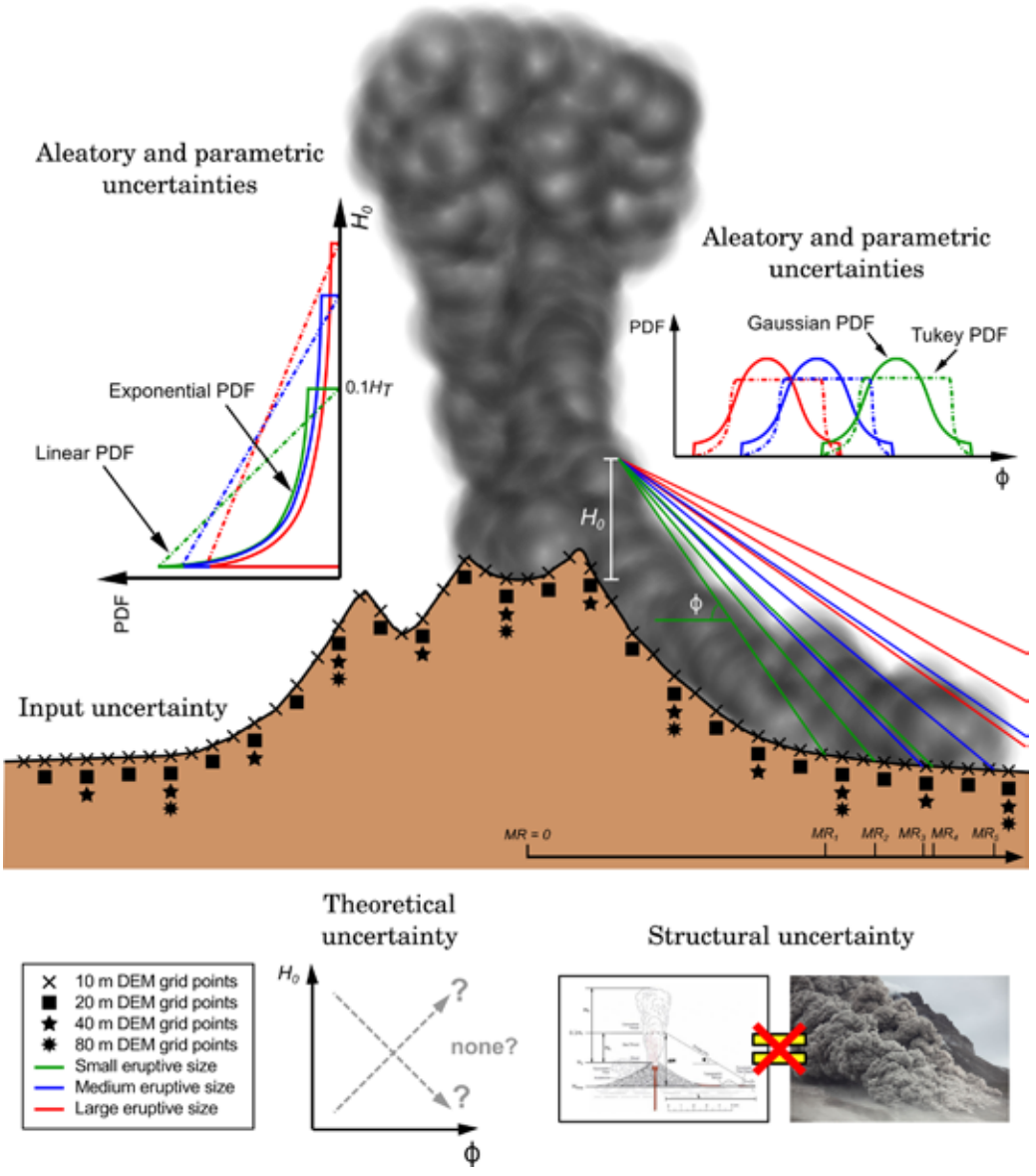

Figure 2. Schematic representation of the origin and way of addressing the different types of uncertainty (aleatory and epistemic) presented in this paper. Aleatory uncertainty (solid lines) is described through Probability Density Functions (PDFs) of the Energy Cone (EC) model parameters: collapse height, H_0, and PDC mobility, φ (note that H_0 values are not to scale and φ values might seem greater than the actual values used in the paper). Every simulation provides a value of area of PDC invasion (not shown) and maximum runout (*MR*; bottom right of the cartoon). Input uncertainty is explored by running the EC over Digital Elevation Models (DEMs) with diverse spatial resolutions (also notice that only the horizontal position of the 20, 40 and 80 m DEM grid points has to be considered). Parametric uncertainty is characterized by means of alternative choices for the PDFs (e.g. Tukey or Linear PDFs; dotted-dashed lines). Theoretical uncertainty arises from the fact that possible relationships between H_0 and φ are not known. Finally, structural uncertainty derives from all the simplifications adopted by simulating the real phenomenon, PDCs, using EC. Modified after Tierz et al., (2016a).

The quantitative validation metrics created are the following:

- *Areal Fit (AF):* is the ratio between the intersection area, $A_{INT} = A_{OBS} \cap A_{SIM}$, (where A_{OBS} is the area of invasion measured in past PDC deposits and A_{SIM} is the area of invasion simulated through the EC), and the union of areas, $A_U = A_{OBS} + A_{SIM} - A_{INT}$, a measure commonly known as the Jaccard similarity coefficient (Jaccard, 1926). Hence: $AF = A_{INT} / A_U$. This metric is dimensionless and can range from 0 to 1. $AF = 1$ only in the case that the simulated area is exactly equal to the preserved PDC area. Whenever A_{SIM} is bigger, smaller or does not coincide in space with A_{OBS}, the fit is penalized and $AF < 1$, reaching zero in the case that no overlapping occurs between both areas.
- *Areal Overestimation (AO):* is a measure of the over- or under-estimation of A_{SIM} with respect to A_{OBS}: $AO = A_{OVER} - A_{UND}$, where A_{OVER} is the simulated area that exceeds the area covered by deposits and A_{UND} is the area of the deposits which is not covered by the simulation. That is, if $AO > 0$, the simulation overestimates the PDC deposit area; if $AO < 0$, then the simulation underestimates the PDC deposit area. The units of the metric are km^2.
- *Areal Misfit (AM):* is a measure of the overall bias between the simulated and the observed area of PDC invasion, expressed as the total area that lies outside A_{INT}, i.e. $AM = A_{OVER} + A_{UND}$. The units of the metric are km^2.

18. 3 – Results

18. 3.1 - Empirical Cumulative Distribution Functions (ECDFs)

ECDFs are a graphical expression of aleatory and epistemic uncertainties once these are propagated into the Energy Cone outputs: area of PDC invasion and maximum runout. Crucial questions in terms of hazard assessment can be addressed through the use of ECDFs. For instance: are the PDC invasion areas or the maximum runouts very widespread? Are they dominated by small or large values? Which output variable is most influenced by considering diverse sources of epistemic uncertainty? Does epistemic uncertainty have a greater impact on the outputs of a specific eruption size? Some of these questions will be discussed in the next section. Here we describe the general patterns and most meaningful quantities found in our data.

As a reminder, aleatory uncertainty is described by the outputs coming from the following configuration (Tierz et al., 2016a): Truncated Exponential PDF (for H_0), Truncated Gaussian PDF (for φ), independent pattern between H_0 and φ, all simulations run over the 40m-resolution DEM. Alternative configurations, which lead to alternative ECDFs, are a description of epistemic uncertainty. In particular, and this applies to every source of epistemic uncertainty, the area between ECDFs represents the extent of each source. Therefore, the following example illustrates the extent of aleatory and theoretical uncertainties for area of PDC invasion in large-size eruptions (Fig. 5 in Tierz et al., 2016a): to say that the 80th percentile of area of PDC invasion is equal to 450 km^2 is a measure of aleatory uncertainty; to say that the 80th percentile of area of PDC invasion falls within the range [250, 450] km^2 is a measure of theoretical uncertainty. Table II collects the median

and 90th percentile values of area of PDC invasion and maximum runout for the three eruption sizes analyzed. A general feature observed in the whole output dataset is the positively-skewed ECDFs, indicated by systematically higher means than medians. This may be caused by the use of the Truncated Exponential PDF for H_0. In the following, we detail more specific findings per each type of uncertainty (Fig. 3).

ECDFs are commonly characterized by a high percentage of simulations with very low values of area of PDC invasion and maximum runout due to the blocking of the Energy Lines by the most proximal topography of the volcano (Tierz et al., 2016a). All ECDFs do also show a wide range of output values with considerably rare but very high values located in the tail of the distributions. For instance, the maximum values of area of PDC invasion reach about 100, 1000 and 3700 km² for small, medium and large eruptions, respectively. Concerning the maximum runouts, the highest values occur around 6, 19 and 47 km, respectively. Moreover, the ECDFs display a horizontal segment from 0.3 km to 1-3 km (depending on the eruption size) which means the virtual absence of maximum runouts in between those two values. This is again a result of individual Energy Lines interacting with the crater topography (Tierz et al., 2016a). For both output variables, extreme values are restricted to very high percentiles (i.e. they are very rare events). Taking into account only large eruptions, areas of PDC invasion equal or greater than 1000 km² represent about the 5% of the cases, while maximum runouts equal or greater than 30 km occur approximately in 1% of the simulations.

Alternative ECDFs describing input uncertainty are really similar to the ECDF obtained from the aleatory uncertainty quantification. This is true for both area of PDC invasion and maximum runout. The highest absolute values of input uncertainty, for small, medium and large eruptions respectively, are around 3, 7 and 25 km² for area of PDC invasion and 1, 1.5, 3.5 km for maximum runout. Fig. 3 shows that the extent of input uncertainty is low for maximum runout and almost indistinguishable for area of PDC invasion, especially in the case of medium and large eruptions.

ECDFs exhibit a larger impact of parametric uncertainty, with respect to input uncertainty, on both area of PDC invasion and maximum runout and, mostly, in medium and large eruptions (Fig. 3). Small eruptions are featured by similar values of input and parametric uncertainties. Maximum absolute values of parametric uncertainty are found to be about 20, 300 and 700 km² for area of PDC invasion and 1, 4 and 8 km for maximum runout, regarding small, medium and large eruptions, respectively.

Theoretical uncertainty shows the largest contribution to total epistemic uncertainty. Its highest absolute values, for small, medium and large eruptions respectively, are as big as 90, 850 and 3000 km² for area of PDC invasion and 3, 11 and 33 km for maximum runout. These values are the response to two main facts which maximize them: (a) the inverse-pattern output distribution (the larger H_0, the more reduced the PDC mobility) has a much tighter range of output values which, besides, are smaller than the outputs in the aleatory uncertainty ECDF; and (b) the direct-pattern output distribution (the larger H_0, the higher the PDC mobility) has a moderately heavier tail than the aleatory uncertainty ECDF.

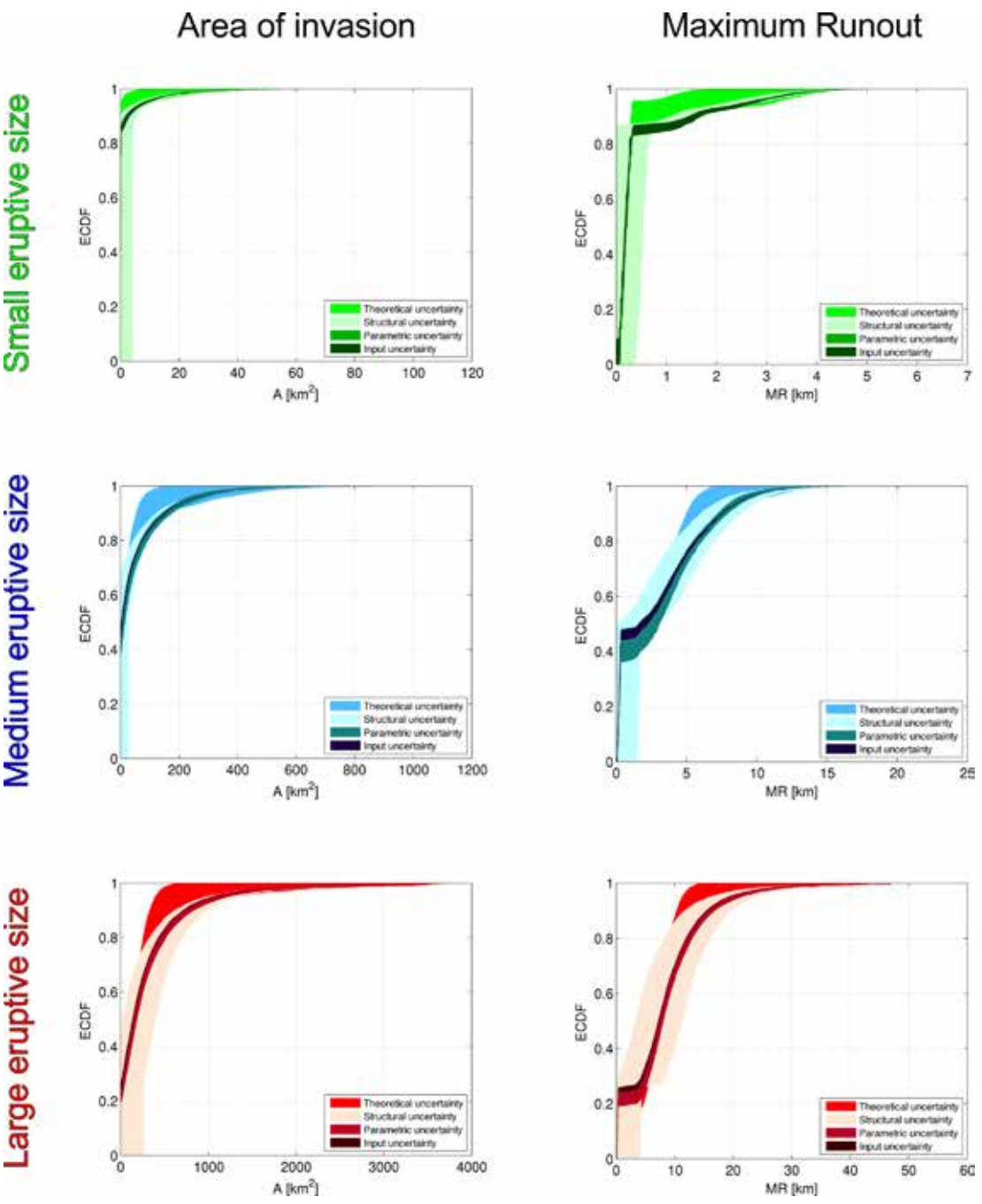

Figure 3. Aleatory and epistemic uncertainty description of the area of PDC invasion (*A*) and maximum runout (*MR*) of PDCs at Somma-Vesuvius (Italy) for three different eruption sizes: small (green), medium (blue) and large (red). The aleatory-uncertainty output ECDF lies within the band of input uncertainty. Note how the contribution of each type of epistemic uncertainty to the total uncertainty changes along the graphs. Modified after Tierz et al., (2016a).

Structural uncertainty is the most uniform source of epistemic uncertainty (Fig. 3). The maximum absolute values are found at approximately 6, 50 and 380 km² for area of PDC invasion, and about 0.7, 3 and 8 km for maximum runout, when investigating small, medium and large eruptions, respectively. It is important to note that more refined characterizations of structural uncertainty (i.e. spatially-varying quantifications according to the main flow behavior expected from PDCs at a given distance from the vent) would be quite worth implementing.

Output var.	***Area of PDC invasion [km²]***						***Maximum Runout [km]***					
Erup. size	Small		Medium		Large		Small		Medium		Large	
Percentile	50th	90th	50th	90th	50th	90th	50th	90th	50th	90th	50th	90th
AU	0.075	1.61	2.15	149	138	725	0.183	1.41	1.58	7.43	7.26	15.6
IU	[0,0]	[2,3]	[2,6]	[149,155]	[138,145]	[725,734]	[0,0]	[1,2]	[2,2]	[7,8]	[7,7]	[16,16]
PU	[0,0]	[2,3]	[2,15]	[139,177]	[134,186]	[703,834]	[0,0]	[1,2]	[2,3]	[7,8]	[7,8]	[15,17]
TU	[0,0]	[0,2]	[2,3]	[52,149]	[138,144]	[329,725]	[0,0]	[0,1]	[2,2]	[5,7]	[7,7]	[10,16]
SU	[0,4]	[0,6]	[0,28]	[121,174]	[21,397]	[609,985]	[0,1]	[1,2]	[0,3]	[6,9]	[3,11]	[12,20]

Table II. Summary of 50th and 90th-percentile statistics computed from the Energy Cone simulations at Somma-Vesuvius (Italy) for two output variables (area of PDC invasion and maximum runout), three eruption sizes (small, medium and large) and different types of uncertainty. AU: aleatory uncertainty; IU: input uncertainty; PU: parametric uncertainty; TU: theoretical uncertainty; SU: structural uncertainty. N.B. All numbers are rounded to the nearest integer apart from the AU values which display three significant figures (including leading zeros).

18. 3.2 **- Conditional-probability maps**

A second way of quantifying and displaying aleatory and epistemic uncertainties propagated into the Energy Cone outputs is by means of the spatial conditional probability of PDC arrival (*CP*), in this case approximated as the frequency of PDC arrival calculated from the 10,000 simulations per each eruption size analyzed. Hence, at each grid point over the hazard domain, this conditional probability (*CP*) is:

$$CP = \Sigma^{N}_{i=1} r_i / N \qquad (3)$$

where r_i is a variable which takes the value 1 if the grid point has been inundated by PDCs according to the *i*-th simulation and 0 otherwise, and *N* is the total number of simulations (10,000 per each size, 30,000 considering all eruption sizes). As introduced before, aleatory uncertainty is assessed by a single value of probability, obtained from the configuration indicated in the previous subsection. Epistemic uncertainty is defined as the dispersion in this single value of probability (Marzocchi et al., 2004) and it is assessed through computing the probability of PDC arrival taking into account alternative configurations (Table III).

In particular, the impact of specific sources of epistemic uncertainty can be displayed spatially as the differences (ΔCP) between their probability (frequency) of PDC arrival and the probability of PDC arrival when accounting only for aleatory uncertainty. That is, a positive value of ΔCP indicates that the probability of PDC arrival for that specific configuration is greater than the probability of PDC arrival when accounting only for aleatory uncertainty (and vice versa for negative ΔCP values). In the following, we explain the most interesting insights extracted from this analysis.

The differences in the spatial distribution of the (aleatory) probability of PDC arrival for the three eruption sizes studied are noteworthy. The main similarity among eruption sizes is the fact that Mount Somma does act as a topographic barrier for PDC propagation towards the north. This effect is recognizable for all sizes, although the extent to which the barrier is able to block the simulated PDCs obviously varies (Fig. 4).

For small-size simulations, probabilities equal or greater than 5% are confined to the south flank of the volcano as a result of the relatively small areas of PDC invasion associated with this size. In the case of medium eruptions, probabilities equal or greater than 40% are still limited to medial sectors over the west, east and south flanks of Somma-Vesuvius. Grid points with probability of PDC arrival equal or greater than 5% draw a circle of approximately 9 km around the volcano (Fig. 4). Finally, large-size simulations result in probabilities equal or greater than 40% over a similar 9km-radius area surrounding the vent. Grid points with probabilities equal or greater than 5% are located as far as about 22 km from the volcano. Notwithstanding this, the distal topographic highs, like the Sorrento Peninsula and the Nola-Sarno Mountains, are still able to block the majority of long-runout simulated PDCs. According to the Energy Cone simulations, nearly the whole city of Napoli is located inside the 5%-probability envelope.

The contribution of input uncertainty to changes in probability of PDC arrival over the surroundings of Somma-Vesuvius is extremely reduced. Accordingly, Fig. 4 does not show any map for input uncertainty since they would be very similar to the maps showing aleatory uncertainty. In other words, $\Delta CP \sim 0$ in the case of input uncertainty.

The spatial distribution of the probability of PDC arrival when we consider parametric uncertainty, in particular the Gaussian-Linear configuration, is clearly different from the one obtained when analyzing aleatory uncertainty only (second column, Fig. 4). The main feature evidenced in these maps is that $\Delta CP \geq 0$ over the whole hazard domain and for all three eruption sizes. This may be explained in terms of the greater density of probability across moderate values of H_0 in the Linear-Decay PDF with respect to the Truncated Exponential PDF (Fig. 2; note that the maximum limits are equal for the two types of PDF, Table I). On the whole, the positive differences in probability of PDC arrival are greater in the proximal sectors of the volcano and decrease with distance from the vent. In the case of large-size simulations, the positive differences are greater in the proximal NE sector (reaching around $\Delta CP = 0.1$) than over the proximal SW sector (Fig. 4). This means that the probability of PDC arrival, when using the Gaussian-Linear configuration, is more homogeneous around the whole volcanic edifice and that the efficiency of Mount Somma in preventing PDC propagation towards the north is rather low in this case.

Regarding the frequency maps, theoretical uncertainty is again the source of epistemic uncertainty that shows the most evident impact on the Energy Cone simulations. Both the direct (higher H_0 implies more mobile PDCs) and inverse (higher H_0 implies less mobile PDCs) patterns are presented in Fig. 4 (third and fourth columns). The direct-pattern difference maps are characterized by having: (a) positive differences over proximal sectors; (b) a ring of negative differences over medial sectors; and (c) again positive differences, albeit small, over the distal sectors of the volcano.

This holds for all three eruption sizes although the extent of each area defined in (a)-(c) varies according to size. Hence, the ring with $\Delta CP < 0$ values described in (b) occurs at around 4 and 7 km from the vent for medium and large eruptions, respectively. It is worth noting that the differences in probability of PDC arrival beyond Mount Somma are slightly positive (large size), zero (small size) or even negative (medium size). Therefore, in direct-pattern simulations, Mount Somma seems to be more effective in hindering PDC northwards propagation. Concerning the inverse-pattern simulations, the maps are simpler. Firstly, positive differences are common over the proximal-medial sectors of the volcano. Again, the extent of this area with positive differences in probability of PDC arrival is size-dependent, and larger for higher eruption sizes (Fig. 4). Beyond this area, all the ΔCP values are negative and can be as low as $\Delta CP < -0.15$, that is, the probabilities of PDC arrival decrease more than 15% in absolute value. These negative differences get smaller with distance from the vent. All these data point to one fact: no inverse-pattern simulation reaches medial and distal areas.

In this study, structural uncertainty is not mapped into probabilities of PDC arrival. The goal we pursue is to obtain a characterization of the misfit between the 'best' set of Energy Cone simulations and past PDC deposits preserved at Somma-Vesuvius (Tierz et al., 2016a; see previous section *Epistemic uncertainty description*) and use distributions of misfit to modify the output ECDFs and, hence, preliminarily quantify structural uncertainty. Mapping the impact of this source of epistemic uncertainty into probabilities of PDC arrival would be a successive step which could be attained, for instance, by using an asymmetric buffer (e.g. Widiwijayanti et al., 2009) coupled to each simulation of the Energy Cone. Plausible values for the buffer might be obtained by applying the data collected from our structural uncertainty quantification.

18. 3.3 **- Energy Cone performance**

As introduced before, the performance of the Energy Cone model is checked through three strands of evidence: (i) validation metrics focused on the areal similarity between the simulations and the PDC deposits; (ii) likelihood indices (p-values) which assess how likely is to simulate an area of PDC invasion or a maximum runout equal or greater than the observed one, given the use of Energy Cone and our defined PDFs; and (iii) qualitative comparison of the probability of PDC arrival at each grid point of the hazard domain when using the simulations and the PDC deposits.

In our study, the most informative indicator of the resemblance between the Energy Cone simulations and the PDC deposits at Somma-Vesuvius is the Areal Fit (*AF*) metric. Besides, the same type of metric has been used for other volcanic mass flow physical models (e.g. Procter et al., 2010; Tarquini and Favalli, 2011) which will aid us in comparing our findings with other cases (see

Discussion). Fig. 5 displays the areal fit values computed for all the six eruptions analyzed in our study: 1944 AD (small size), Pollena and 1631 AD (medium size), and Mercato, Pompeii and Avellino (large size). Across the parameter space (H_0, φ), different values of areal fit are observed. For all the cases, one region of moderate to quite high areal fits is surrounded by low to very low values of areal fit. The former is an elongated area with positive slope, H_0/φ, that probably reflects the linear nature of the Energy Cone, that is, similar areas of PDC invasion result from whether energy cones with low values of both H_0 and φ or energy cones with high values of both H_0 and φ. Nevertheless, different ranges of φ can be individuated in the high-*AF* sectors belonging to different eruption sizes: the larger the size, the smaller the φ values (i.e. the more mobile the PDCs) linked to high areal fits (Fig. 5). Moreover, if we look at the minimum values of areal misfit (*AM*, white stars in Fig. 5), they tend to be related to higher values of H_0 in larger eruption sizes. The 1631 AD and Mercato eruptions are exceptions in this tendency. The former shows H_0 ~ 0.4 km for the simulation with the minimum areal misfit. The 1631 AD eruption was characterized by extensive propagation of PDCs over the southern flank of the volcano (Rosi et al., 1993) but hardly any trace of PDC deposit beyond Mount Somma (Gurioli et al., 2010). This makes the minimum areal misfit to be associated with a H_0 that precludes the overcoming of Mount Somma. In the case of the Mercato eruption, the minimum areal misfit is found for H_0 ~ 1.3 km, which is lower than for the Pollena eruption (medium size, H_0 ~ 1.6 km) and the Pompeii and Avellino eruptions (both large size, H_0 ~ 1.5 km and 2 km, respectively). However, even though the Mercato eruption is classified as large-size eruption according to its total volume (Cioni et al., 2008), the peak in Mass Eruption Rate (Cioni et al., 2008), PDC volume, area of PDC invasion and maximum runout (Gurioli et al., 2010) are closer to those reported for medium-size eruptions than for large-size eruptions.

Eruption size		***Small***			***Medium***			***Large***		
Location	d [km]	min	AU	max	min	AU	max	min	AU	max
SoVe	5.8	0.000	0.000	0.000	1.35	12.8	15.5	50.9	51.3	60.4
TdG	4.8	0.000	0.110	0.251	12.0	24.8	30.6	66.1	66.5	77.3
Scf	12	0.000	0.000	0.000	0.000	1.22	2.77	2.94	20.5	24.7
MdSH	5.2	0.000	0.020	0.046	4.07	18.8	23.1	60.4	60.8	69.6
NCA	14	0.000	0.000	0.000	0.000	0.300	0.691	0.022	12.4	15.5

Table III. Conditional probabilities of PDC arrival (in percentage) at five selected locations on the surroundings of Somma-Vesuvius (Italy) computed from Energy Cone simulations and taking into account aleatory and epistemic uncertainties and three different eruption sizes (small, medium and large). d: distance from the vent; AU: aleatory uncertainty; SoVe: Somma Vesuviana; TdG: Torre del Greco; Scf: Scafati; MdSH: Massa di Somma Hospital; NCA: Napoli-Capodichino Airport.

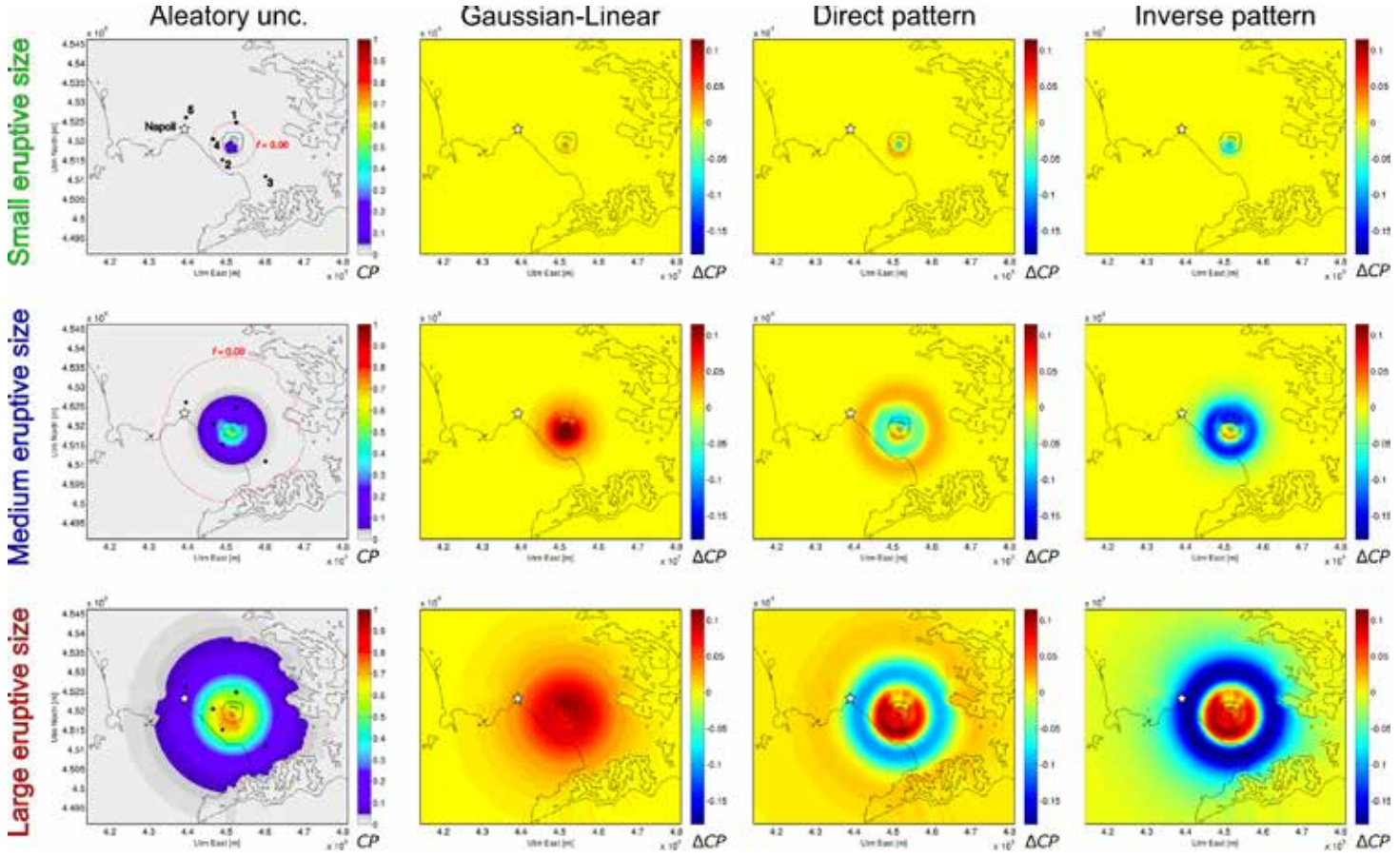

Figure 4. Conditional-probability (CP) maps of PDC arrival (given the occurrence of an eruption of a specific size) computed by the Energy Cone model at Somma-Vesuvius (Italy) for three different eruption sizes: small (green text), medium (blue text) and large (red text). Leftmost columns are actual CP (between 0 and 1) while the other three columns show the differences in conditional-probability (ΔCP), at each grid point, between alternate configurations (Gaussian-Linear, 40 m DEM, independent pattern -2nd column-; Gaussian-Exponential, 40 m, direct pattern -3rd column-; and Gaussian-Exponential, 40 m, inverse pattern -4th column-) and the aleatory-uncertainty configuration (see text for more details). Colored zones in aleatory-uncertainty maps indicate conditional-probabilities greater than 0.05 and the solid red line displays the limit of CP > 0 (notice there is no red line in the large-size aleatory-uncertainty map). The white star indicates the location of the city of Napoli. 1: Somma Vesuviana; 2: Torre del Greco; 3: Scafati; 4: hospital in Massa di Somma; 5: Napoli-Capodichino airport. Modified after Tierz et al., (2016a).

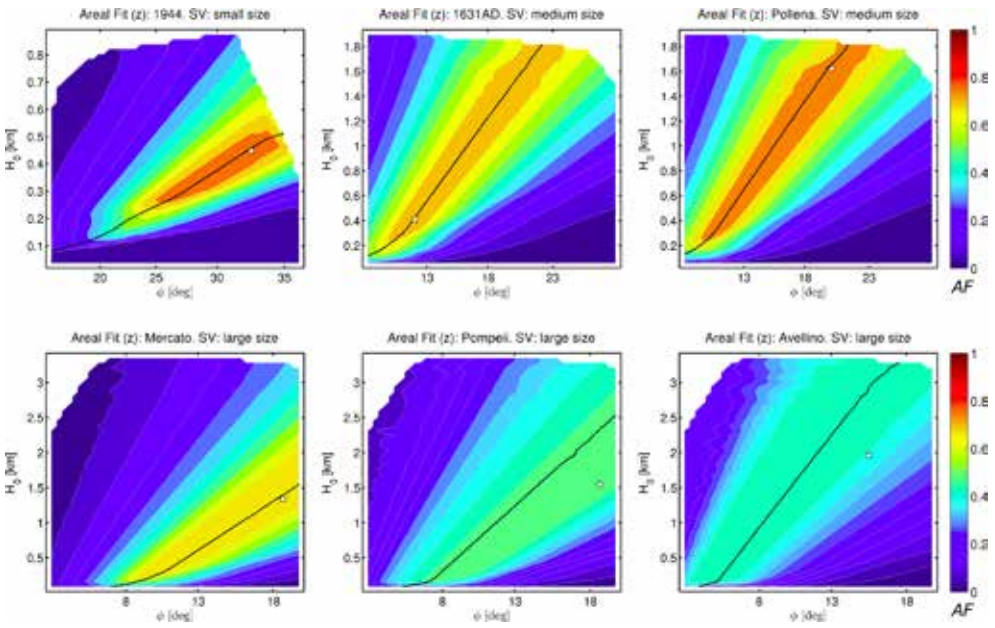

Figure 5. Areal Fit (*AF*) values calculated by comparing the areas of PDCs simulated via EC to the actual areas of PDC deposits preserved at Somma-Vesuvius (SV). Black dashed lines indicate sectors where *AO* = 0. White stars locate the minimum values of areal misfit.

In terms of Areal Overestimation (*AO*), we check for the location, within the parameter space, of the simulations for which *AO* = 0, i.e. $A_{OVER} = A_{UND}$ (Fig. 5, black dashed line). The *AO* = 0 line separates the parameter space into two regions: to the left and up from the line, the simulations overestimate the deposit ($A_{OVER} > A_{UND}$) due to higher H_0 and smaller φ values; to the right and down from the line, the simulations underestimate the deposit ($A_{OVER} < A_{UND}$) due to smaller H_0 and bigger φ values. In a relatively unbiased PDC model, *AO* = 0 would coincide with high values of areal fit. In systematically-biased PDC models, we could find that high areal fits always occur in the underestimation (or overestimation) region or, even, there is no *AO* = 0 line along the parameter space (i.e. all the simulations do either underestimate or overestimate). In our set of Energy Cone simulations, we notice that the *AO* = 0 lines are always inside the high-*AF* region of the parameter space. In most of the cases, the minimum areal misfit is coincident with both *AO* = 0 and the highest areal fits. For the Pompeii and Avellino eruptions, however, the minimum areal misfit is located in the underestimation region (Fig. 5). These two cases are also the ones with the lowest best-*AF* among the six eruptions studied. All this is due to the strong asymmetry of their PDC deposits (Tierz et al., 2016b).

The use of *p*-values in this work is not to be related to statistical-hypothesis testing (e.g. Fisher, 1925) but to a Bayesian use of the *p*-values as a proxy for the likelihood function (e.g. Gelman, 1995): $p(y \mid \vartheta)$, where y is a set of observations and ϑ are parameters of a model, a set of assumptions, etc.

In our particular case, y is represented by the values of area of PDC invasion and maximum runout measured on the PDC deposits from six eruptions at Somma-Vesuvius, and ϑ denotes the use

of Energy Cone as the PDC model and our selected PDFs as the description of aleatory uncertainty. The quantity that we actually calculate is: $p(Y > y \mid \vartheta) = 1 - F(Y)$, where Y is the random variable area of PDC invasion (or maximum runout), y is A_{OBS} (or MR_{OBS}), that is, the observed area of PDC invasion or maximum runout on the deposit, and $F(Y)$ is the ECDF for the area of PDC invasion (or maximum runout) based on the Energy Cone simulated values (A_{SIM} or MR_{SIM}). In this way, the smaller our calculated *p*-value, the more unlikely it is to simulate a value of area of PDC invasion or maximum runout which is greater than the observed/measured one. In other words, if the *p*-value is (very) small: (a) our physical model and/or aleatory uncertainty description are not reliable; or (b) the considered eruption is actually quite an extreme event within the eruptive phenomenology expected for that particular size (that is, its probability of occurrence is low to very low).

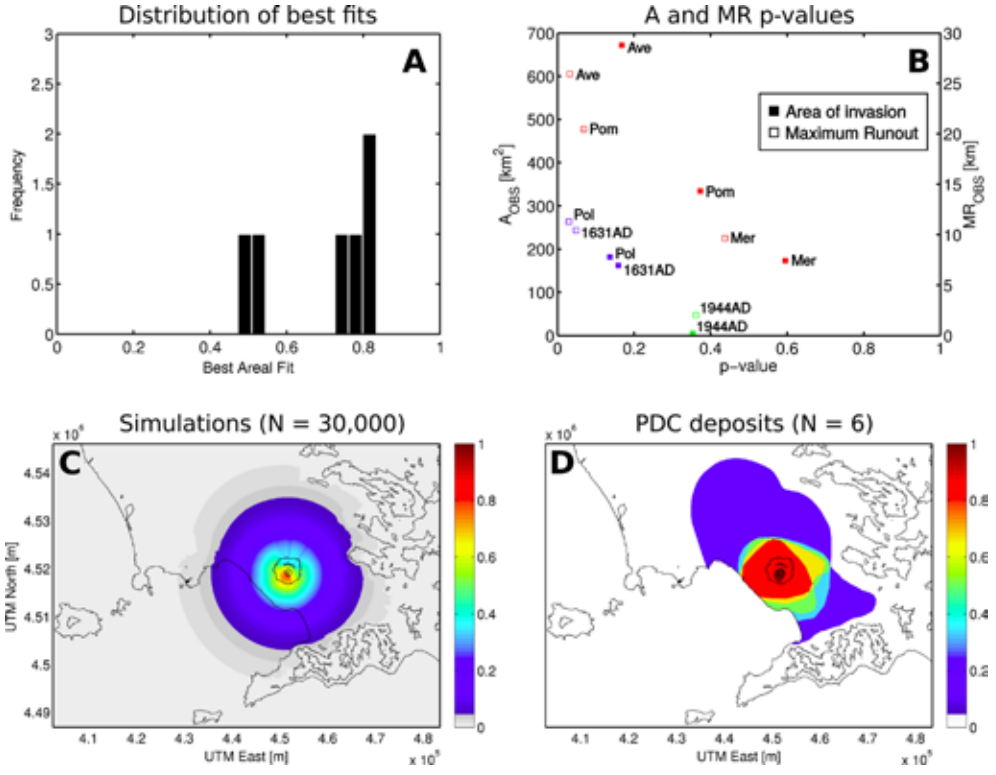

Figure 6. Summary of the Energy Cone performance in modeling PDC deposits at Somma-Vesuvius, Italy. A: histogram of best areal fits computed from the six eruptions analyzed; B: *p*-values associated with A_{OBS} and MR_{OBS} for the same six eruptions (1944 AD, small size -green-; 1631 AD and Pollena, medium size -blue-; Mercato, Pompeii and Avellino, large size -red-); C: probability map showing the frequency of PDC arrival to each point of the hazard grid according to the Energy Cone simulations. D: probability map built from the PDC deposits preserved from the aforementioned eruptions.

Fig. 6b displays the *p*-values for all six eruptions analyzed and both area of PDC invasion and maximum runout variables. Regarding the first variable, the *p*-values are always greater than 0.13 which indicates that it is not unlikely to simulate the observed values of area of PDC invasion. In

contrast, some *p*-values for maximum runout are smaller than 0.05, in particular: both medium-sized eruptions (Pollena and 1631 AD; *p*-values equal to 0.03 and 0.05, respectively), and the large-size Avellino eruption (*p*-value = 0.03). This may be partially due to some general underestimation in the maximum runout by the Energy Cone but there might be other causes as we will discuss in the following section.

Finally, we assess the similitude between Energy Cone simulations and PDC deposits at Somma-Vesuvius by mapping the probability of PDC arrival (using formula (3)) over the hazard domain (Fig. 6c, d). It is clear from the maps that the simulations give rise to a more homogeneous spatial distribution of these probabilities (Fig. 6c) in comparison to the map computed from the PDC deposits (Fig. 6d). The main similarities between the two maps are the following: (1) high-probability zones cover fairly equivalent areas, mainly proximal-medial sectors in a 7-8 km radius; (2) zones with low probability of PDC arrival (about 2-5%, gray coronae, Fig. 6c) in the simulations map also coincide quite well with the limit of the PDC deposits (colored area, Fig. 6d). In both cases, the main regional topographic highs (e.g. the Sorrento Peninsula to the south or the Nola-Sarno Mountains to the northeast) act as distal barriers for PDC propagation. Finally, the probability values obtained for grid points on the sea are not to be considered, since Energy Cone is too simple to capture PDC propagation over the sea surface (Córdoba, 2007). We do not close the simulated polygons (areas of PDC invasion) along the coastline (something that we do for the PDC deposits) to avoid that the areal fits artificially increase as a result (Tierz et al., 2016b).

18. 4 **– Discussion**

18. 4.1 **- Uncertainty ranking and topographic effects**

One relevant implication of our results is the possibility of ranking the different sources of epistemic uncertainty, both among each other and with respect to the aleatory uncertainty. To attain this, we calculate the relative maximum expected deviation as:

$$\delta_{ij} = \Delta_{ij} / x_{50i} \quad (4)$$

where, for a given eruption size *i* and a given source of epistemic uncertainty *j*, Δ_{ij} is the maximum horizontal distance between the aleatory-uncertainty output ECDF and the output ECDFs for the specific source, and x_{50i} is a reference value, in this case the median of the aleatory-uncertainty output ECDF. By definition, if $\delta_{ij} > 1$, then the maximum expected deviation is greater than this median, i.e. epistemic uncertainty is larger than a central measure of aleatory uncertainty. Moreover, all the sources of epistemic uncertainty are able to significantly modify the output ECDFs obtained from the Energy Cone simulations (Tierz et al., 2016a).

Values of δ_{ij} for area of PDC invasion range from 10^{-1} to 10^{3} considering all sources of epistemic uncertainty (Fig. 7), with the largest deviations occurring for parametric and theoretical uncertainties, and small and medium eruption sizes (Tierz et al., 2016a). Concerning maximum runout, the calculated δ_{ij} values are more clustered around 10^{-1} to 10^{1}, considering all sources of epistemic uncertainty. Theoretical uncertainty clearly is the source with the largest contribution to

total epistemic uncertainty. Structural and input uncertainties are linked to relatively minor deviations even though the latter can be relevant in the small eruption size, where the interaction between PDCs and the proximal topography (e.g. the crater and Mt Somma caldera rim) is expected to be stronger. Indeed, some interesting features arise when topographic altitude is plotted against the probability of PDC arrival, for different eruption sizes and taking into account both aleatory and epistemic uncertainties (Fig. 10 in Tierz et al., 2016a): (a) the smaller the eruption size, the greater the influence of Mt Somma; (b) all probability profiles greatly change from the south to the north flank (Mt Somma) of the volcano; and (c) the larger the eruption size, the more homogeneous the probability profile, which implies that large PDCs are less influenced by topography (e.g. Druitt, 1998).

On the other hand, the very small contribution of input uncertainty to the Energy Cone outputs may be related to two main aspects. Firstly, in the case of Somma-Vesuvius, a stratocone surrounded by a more or less extensive plain, input uncertainty may be less relevant than in other cases, such as Campi Flegrei (Italy), where caldera- and edifice-collapse structures are spatially combined with preserved eruptive cones (e.g. Di Vito et al., 1999; Orsi et al., 2004). Secondly, it should be emphasized that the topographic control on PDC propagation that can be modeled with Energy Cone is restricted, hence some physical processes are not captured, for instance: PDC channelization (Esposti Ongaro et al., 2008) or dense-dilute PDC decoupling (Fisher, 1995). Nonetheless, these processes can be vital for PVHA. Regarding surge-decoupling PDC processes (like one might expect to happen when PDCs hit Mt Somma), it is possible that structured stochastic analyses, as the one presented here, can somehow assess this hazard, since the many thousands of simulations run, which cover coherent ranges of H_0 and φ, serve to obtain probabilities of PDC arrival before and beyond Mt Somma (Fig. 4; Table III). As for PDC channelization (like one might expect to develop towards the western end of Mt Somma), it cannot be simulated with the Energy Cone and more complete simulators are necessary (e.g. Esposti Ongaro et al., 2008).

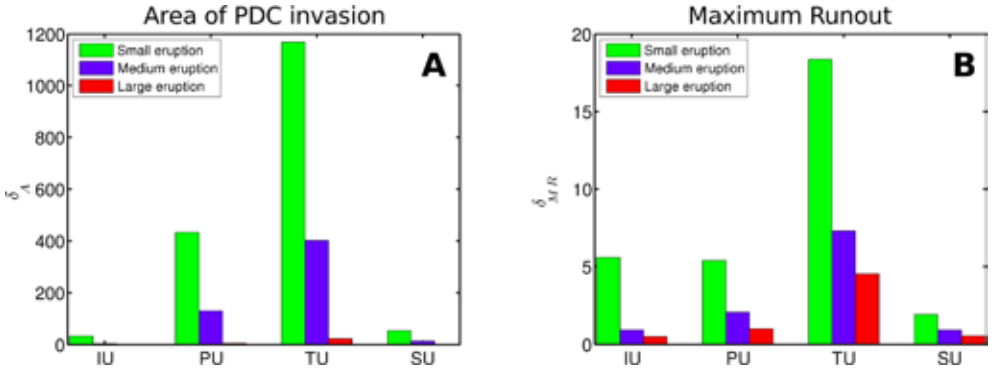

Figure 7. Color bars for the maximum deviations between the output Empirical Cumulative Distribution Functions (ECDFs) coming from alternative configurations (epistemic uncertainty quantification) and the aleatory-uncertainty configuration, divided by the median of the latter (see text for more details) for different eruption sizes and output variables. IU: input uncertainty; PU: parametric uncertainty; TU: theoretical uncertainty; SU: structural uncertainty.

Finally, we report the values of (conditional) probability of PDC arrival, accounting for aleatory and epistemic uncertainty and according to three different eruption sizes, over some locations of interest around Somma-Vesuvius (Table III): (1) beyond Mt Somma (e.g. Somma Vesuviana); (2) at Torre del Greco (Napoli-Reggio Calabria highway and train station); (3) at Scafati (E-SE from Mt Vesuvius); (4) at the hospital in Massa di Somma; and (5) at the Napoli-Capodichino airport. The values tend to be small to moderate apart from the case of a large-size eruption.

18. 4.2 **- Applicability of Energy Cone to PVHA**

Even though the Energy Cone model is simplified in terms of physical processes, our results at Somma-Vesuvius (Italy) indicate that it can be applied to quantify the possible extent of PDCs at a given volcanic system. Indeed, the use of Energy Cone coupled with Monte Carlo sampling permits exploration of both aleatory and epistemic uncertainties in a structured, but still computationally tractable, manner (Tierz et al., 2016a). Within the six eruptions analyzed in this paper, the best areal fit values are found between 0.47 and 0.83, with 5 out of 6 having $AF > 0.5$ (Fig. 6a). If we compare these values with areal fits calculated for other volcanic mass flow models (e.g. AF = 0.35-0.69 for lava flows at Mt. Etna, Italy: Tarquini and Favalli, 2011; or maximum areal fit around 0.6 for BAFs simulated via Titan2D at Mt. Taranaki, New Zealand: Procter et al., 2010), the performance of the Energy Cone seems reasonably good. Additionally, our set of simulations is not constructed with the goal of fitting the past events but it tries to describe the natural variability in PDC phenomenology that might unfold during an eruption of a specific size (Tierz et al., 2016b). Therefore, apart from simulations with high areal fits, there are simulations with lower areal fits, which intuitively denote areas of PDC invasion smaller or larger than the ones preserved from the past PDC deposits. This represents a crucial aspect of exploring aleatory uncertainty of geophysical processes with probabilistic hazard assessment purposes (Marzocchi et al., 2010; Selva et al., 2010; Sandri et al., 2016).

Looking at the link between areal overestimation and areal fit, we see that the best areal fit values tend to coincide with simulations for which $AO = 0$ (Fig. 5). It suggests that the Energy Cone is not particularly biased through a proclivity to overestimate (in such case, we would observe $AO > 0$ for high areal fits) or underestimate (conversely, we would observe $AO < 0$ for high areal fit values) the area of PDC invasion. Likewise, areal misfits are usually minimum when the areal fit is maximum, although some minimum areal misfits can be related to lower areal fits and $AO < 0$. These situations are highly dependent on the ratio of the maximum to the minimum runout (MR:mR ratio) of the specific PDC deposit and seem independent of the eruption size considered (Tierz et al., 2016b). Hence, the more asymmetric the PDC deposit with respect to the (inferred) vent location, the smaller the best areal fit. All this is in part associated with the symmetric nature of the Energy Cone which cannot reproduce PDC deposits that show a preferable direction of spreading, except if there is (or there was at the time of the eruption) a clear topographic control on the spatial distribution of the PDC deposit. For instance, the inferred vent for the Avellino eruption is located west from the Somma-Vesuvius edifice and caldera (Sulpizio et al., 2010a) which may have reduced Mt Somma's

capability to efficiently block PDC propagation towards the northwest. In fact, the maximum runout of the PDC deposit was measured in this very direction (Gurioli et al., 2010).

In terms of maximum runout, the Energy Cone looks able to replicate the observed value for every individual eruption. However, it is not obvious whether the whole set of simulations is consistent with the observed values. The cases in which *p*-value is relatively small may be clarified in terms of one (or a combination) of the following explanations: (1) the model fails in reproducing the observed values on past PDC deposits; (2) the model parameter space (joint distribution of H_0, φ) is not well-constrained to capture the PDC phenomenology for a given eruption size; and (3) the studied event is actually quite extreme (i.e. its theoretical probability is relatively small) considering the typical PDCs generated during an eruption of this eruption size. We argue that the first explanation is not the general case, considering all the presented results. However, the Energy Cone may struggle to produce accurate sets of outputs if the *MR*:*mR* ratio is high (see above). The second and third explanations can be plausible for most of the cases with small *p*-values. Hence, for medium-size eruptions, a lack of completeness in the dataset utilized to set up the PDF for φ (only 4 data are available to parameterize this PDF) can give rise to some irregularities in the consequent output ECDF. The minimum value of the PDF is $\varphi = 7.5°$ while the mean is placed at $\varphi \approx 17°$ (Table I). Given the PDC phenomenology reported for the 1631 AD (Rosi et al., 1993) and Pollena eruptions (Sulpizio et al., 2005) and their medium-long preserved maximum runouts (these being equal or greater than the one recorded during the large-size Mercato eruption, Gurioli et al., 2010), the cited φ values may be too big to capture the moderate to high-mobility PDCs generated during those medium-size eruptions. Finally, in the case of Avellino eruption, the observed maximum runout of about 25 km could represent a 'right-tail' event (i.e. low theoretical probability of occurrence) within the PDC phenomenology to unfold during large-size eruptions at Somma-Vesuvius.

18. 5 – Conclusions

The present study demonstrates that epistemic uncertainty, which represents an essential part of uncertainty assessment procedures (e.g. Rougier and Beven, 2013) can be quantified, at a reasonable computational cost, by coupling the Energy Cone model with Monte Carlo sampling. Our approach is ready to be applied to other volcanic systems of interest without needing to have: (a) a large dataset of past PDC deposits; or (b) a comprehensive pool of experts to elicit the epistemic uncertainty quantification from (e.g. Neri et al., 2015). On the other hand, our validation procedure indicates that a statistical sample of Energy Cone simulations seems able to capture the values and variability of hazard-related variables (area of invasion and maximum runout) measured from actual PDC deposits at Somma-Vesuvius (and also at Campi Flegrei, Italy: Tierz et al., 2016b).

This is a crucial finding for it may open the door to compute PVHA for dilute and dense PDCs using the Energy Cone. This type of hazard assessment has rarely been produced (e.g. Dalbey, 2009; Neri et al., 2015) owing to the dichotomy between the physical reliability of the PDC numerical model and the computational cost of quantifying aleatory and epistemic uncertainties (Neri et al., 2015; Tierz et al., 2016a). To date, a general solution for implementing PVHA of PDCs has not been reached.

Despite the strong physical limitations of Energy Cone as a PDC model, it still seems a possible answer to construct preliminary PVHA for PDCs, given the results detailed in this paper and the current lack of computationally-cheap but physically-robust simulators for dilute PDCs. Moreover, the use of Monte Carlo sampling as the Uncertainty Quantification Technique (UQT) frees the choice of the PDFs for the model parameters to even empirically-built distributions. This choice is much more limited when using other UQTs such as Polynomial Chaos Quadrature (e.g. Dalbey et al., 2008) because the efficiency of the method relies upon the use of specific types of PDFs and/or independence assumptions about the model parameters. Given the existence of established statistical models for PVHA (e.g. BET_VH/PyBetVH; Marzocchi et al., 2010, Tonini et al., 2015: vhub.org/resources/betvh; Bayesian Belief Networks, e.g. Aspinall et al., 2003), the application of the Energy Cone to compute comprehensive probabilistic hazard assessments (including the associated uncertainties) of PDCs at a specific volcanic system becomes a reachable target.

Acknowledgements

The research leading to these results has received funding from the European Union Seventh Framework Programme (FP7/2007-2013) under the project NEMOH, grant agreement n° 289976, and the project MED-SUV, grant agreement n° 308665; from the Futuro in Ricerca 2008 FIRB Project ByMur [RBFR0880SR] financed by MIUR, the Italian Ministry for Research and Education, and from the Italian project DPC-INGV V1: Probabilistic Volcanic Hazard Analysis, funded by Dipartimento della Protezione Civile. Some results shown here were obtained through computational resources provided by the Center for Computational Research (University at Buffalo, NY, USA). The 20 m and 40 m DEMs are courtesy of the Laboratory of Geomatics (INGV, Osservatorio Vesuviano). We are profoundly grateful to Antonio Costa, Roberto Sulpizio, Lucia Zaccarelli and Mauro Antonio Di Vito for their help and support. We warmly thank Jacopo Selva for valuable discussions, Giuseppe Vilardo for providing some DEM products, Fawzi Doumaz for gathering and making available the OpenMap cartographic data, and Andrea Di Vico for GIS assistance. We are extremely thankful to Alison Rust for her suggestions about how to improve the manuscript, and to Alessandro Fornaciai for his editorial help. The NEMOH family from *papà, mamma, zio* to all the amazing NEMOH fellows is thanked for all the hard work and fun times we shared.

References

Aspinall, W.P., Woo, G., Voight, B. and Baxter, P.J. (2003). Evidence-based volcanology: application to eruption crises. J Volcanol Geoth Res, 128, 273-285.

Bonadonna, C., Connor, C.B., Houghton, B.F., Connor, L., Byrne, M., Laing, A. and Hincks, T.K. (2005). Probabilistic modeling of tephra dispersal: Hazard assessment of a multiphase rhyolitic eruption at Tarawera, New Zealand. J Geophys Res: Solid Earth (1978–2012), 110(B3).

Branney, M.J. and Kokelaar, B.P. (2002). Pyroclastic density currents and the sedimentation of ignimbrites. Geological Society of London.

Cas, R.A. and Wright, J.V. (1987). Volcanic successions, modern and ancient: a geological approach to processes, products, and successions. Allen & Unwin.

Cioni, R., Bertagnini, A., Santacroce, R. and Andronico, D. (2008). Explosive activity and eruption scenarios at Somma-Vesuvius (Italy): Towards a new classification scheme. J Volcanol Geoth Res, 178, 331-346.

Cioni, R., Santacroce, R., and Sbrana, A. (1999). Pyroclastic deposits as a guide for reconstructing the multi-stage evolution of the Somma-Vesuvius Caldera. B Volcanol, 60, 207-222.

Córdoba, G. (2007). Dilute particle-laden currents: dynamics and deposit patterns. Dissertation. University of Bristol.

Dalbey, K., Patra, A.K., Pitman, E.B., Bursik, M.I. and Sheridan, M.F. (2008). Input uncertainty propagation methods and hazard mapping of geophysical mass flows. J Geophys Res: Solid Earth (1978–2012), 113(B5).

Dalbey, K.R. (2009). Predictive simulation and model based hazard maps of geophysical mass flows. State University of New York at Buffalo.

Del Negro, C., Cappello, A., Neri, M., Bilotta, G., Hérault, A. and Ganci, G. (2013), Lava flow hazards at Mount Etna: constraints imposed by eruptive history and numerical simulations. Scientific reports, 3.

Doyle, E.E., Hogg, A.J., Mader, H.M. and Sparks, R.S.J. (2010). A two-layer model for the evolution and propagation of dense and dilute regions of pyroclastic currents. J Volcanol Geoth Res, 190, 365-378.

Druitt, T.H. (1998). Pyroclastic density currents. Geological Society London, Special Publications, 145(1), 145-182.

Esposti Ongaro, T., Neri, A., Menconi, G., de'Michieli Vitturi, M., Marianelli, P., Cavazzoni, C., Erbacci, G. and Baxter, P.J. (2008). Transient 3D numerical simulations of column collapse and pyroclastic density current scenarios at Vesuvius. J Volcanol Geoth Res, 178, 378-396.

Fisher, R.A. (1925). Statistical methods for research workers. Genesis Publishing Pvt Ltd.

Fisher, R.V. (1995), Decoupling of pyroclastic currents: hazards assessments, J Volcanol Geoth Res, 66 (1), 257–263.

Gelman, A. (1995). Bayesian data analysis (No. 04; QA279. 5, B38.).

Gurioli, L., Sulpizio, R., Cioni, R., Sbrana, A., Santacroce, R., Luperini, W. and Andronico, D. (2010). Pyroclastic flow hazard assessment at Somma–Vesuvius based on the geological record. B Volcanol, 72, 1021-1038.

Hall, M.L., Robin, C., Beate, B., Mothes, P. and Monzier, M. (1999). Tungurahua Volcano, Ecuador: structure, eruptive history and hazards. J Volcanol Geoth Res, 91 (1), 1–21.

Hazlett, R.W., Buesch, D., Anderson, J.L., Elan, R. and Scandone, R. (1991). Geology, failure conditions, and implications of seismogenic avalanches of the 1944 eruption at Vesuvius, Italy. J Volcanol Geoth Res, 47, 249-264.

Heim, A. (1932). Bergsturz und menschenleben. Vol. 30, Fretz & Wasmuth.

Jaccard, P. (1926). Le coefficient generique et le coefficient de communaute dans la flore marocaine. Impr. Commerciale.

Malin, M.C. and Sheridan, M.F. (1982). Computer-Assisted Mapping of Pyroclastic Surges. Science, 217, 637-640.

Marzocchi, W., Sandri, L., Gasparini, P., Newhall, C. and Boschi, E. (2004). Quantifying probabilities of volcanic events: the example of volcanic hazard at Mount Vesuvius. J Geophys Res: Solid Earth (1978–2012), 109(B11).

Marzocchi, W., Sandri, L. and Selva, J. (2008). BET EF: a probabilistic tool for long-and short-term eruption forecasting. B Volcanol, 70 (5), 623–632.

Marzocchi W., Sandri L. and Selva J. (2010). BET_VH: a probabilistic tool for long-term volcanic hazard assessment. B Volcanol, 72, 705-716.

Neri, A., Bevilacqua, A., Esposti Ongaro, T., Isaia, R., Aspinall, W.P., Bisson, M., Flandoli, F., Baxter, P.J., Bertagnini, A., Ianuzzi, E., Orsucci, S., Pistolesi, M., Rosi, M. and Vitale, S. (2015). Quantifying volcanic

hazard at Campi Flegrei caldera (Italy) with uncertainty assessment: 2. Pyroclastic density current invasion maps. J Geophys Res: Solid Earth, 120(4).

Newhall, C.G. and Self, S. (1982). The volcanic explosivity index (VEI) an estimate of explosive magnitude for historical volcanism. J Geophys Res: Oceans (1978–2012), 87(C2).

Ogburn, S. E. (2012). FlowDat: VHub Mass Flow Database. https://vhub.org/resources/2076

Orsi, G., Di Vito, M.A., and Isaia, R. (2004). Volcanic hazard assessment at the restless Campi Flegrei caldera. B Volcanol, 66, 514-530.

Procter, J.N., Cronin, S.J., Platz, T., Patra, A., Dalbey, K., Sheridan, M. and Neall, V. (2010). Mapping block-and-ash flow hazards based on Titan 2D simulations: a case study from Mt. Taranaki, NZ. Nat Hazards, 53, 483-501.

Rosi, M., Principe, C. and Vecci, R. (1993). The 1631 Vesuvius eruption. A reconstruction based on historical and stratigraphical data. J Volcanol Geoth Res, 58, 151-182.

Rougier, J.C. and Beven, K.J. (2013). Model and data limitations: the sources and implications of epistemic uncertainty. In: Rougier, J.C., Sparks, R.S.J., Hill, L.J. (eds) Risk and uncertainty assessment for natural hazards. Cambridge University Press, Cambridge, pp 19-39.

Sandri, L., Guidoboni, E., Marzocchi, W. and Selva, J. (2009). Bayesian event tree for eruption forecasting (BET_EF) at Vesuvius, Italy: a retrospective forward application to the 1631 eruption. B Volcanol, 71(7), 729-745.

Sandri, L., Thouret, J-C., Constantinescu, R., Biass, S. and Tonini, R. (2014). Long-term multi-hazard assessment for El Misti volcano (Peru). B Volcanol, 76, 771-797.

Sandri, L., Costa, A., Selva, J., Tonini, R., Macedonio, G., Folch, A. and Sulpizio, R. (2016). Beyond eruptive scenarios: assessing tephra fallout hazard from Neapolitan volcanoes. Scientific Reports, 6.

Selva, J., Costa A., Marzocchi W. and Sandri L. (2010). BET_VH: exploring the influence of natural uncertainties on long-term hazard from tephra fallout at Campi Flegrei (Italy). B Volcanol, 72, 717-733.

Sheridan, M.F. (1979). Emplacement of pyroclastic flows: a review. Geological Society of America Special Papers, 180, 125–136.

Sheridan, M.F. and Macías, J.L. (1995). Estimation of risk probability for gravity-driven pyroclastic flows at Volcan Colima, Mexico. J Volcanol Geoth Res, 66, 251-266.

Sulpizio, R., Mele, D., Dellino, P. and La Volpe, L. (2005). A complex, Subplinian-type eruption from low-viscosity, phonolitic to tephri-phonolitic magma: the AD 472 (Pollena) eruption of Somma-Vesuvius, Italy. B Volcanol, 67, 743-767.

Sulpizio, R., Bonasia, R., Dellino, P., Mele, D., Di Vito, M.A. and La Volpe, L. (2010a). The Pomici di Avellino eruption of Somma–Vesuvius (3.9 ka BP). Part II: sedimentology and physical volcanology of pyroclastic density current deposits. B Volcanol, 72(5), 559-577.

Sulpizio, R., Capra, L., Sarocchi, D., Saucedo, R., Gavilanes-Ruiz, J.C. and Varley, N.R. (2010b). Predicting the block-and-ash flow inundation areas at Volcán de Colima (Colima, Mexico) based on the present day (February 2010) status. J Volcanol Geoth Res, 193, 49-66.

Sulpizio, R., Dellino, P., Doronzo, D.M. and Sarocchi, D. (2014). Pyroclastic density currents: state of the art and perspectives. J Volcanol Geoth Res, 283, 36-65.

Tarquini, S. and Favalli, M. (2011). Mapping and DOWNFLOW simulation of recent lava flow fields at Mount Etna. J Volcanol Geoth Res, 204, 27-39.

Tierz, P., Sandri, L., Costa, A., Sulpizio, R., Zaccarelli, L., Di Vito, M. A. and Marzocchi, W. (2016a) Uncertainty Assessment of Pyroclastic Density Currents at Mount Vesuvius (Italy) Simulated Through the Energy Cone Model, in Natural Hazard Uncertainty Assessment: Modeling and Decision Support (eds K. Riley, P. Webley and M. Thompson), John Wiley & Sons, Inc., Hoboken, NJ, USA, 125-145.

Tierz, P., Sandri, L., Costa, A., Zaccarelli, L., Di Vito, M.A., Sulpizio, R. and Marzocchi, W. (2016b). Suitability of energy cone for probabilistic volcanic hazard assessment: validation tests at Somma Vesuvius and Campi Flegrei (Italy). B Volcanol, 78:79.

Tonini, R., Sandri, L. and Thompson, M.A. (2015). PyBetVH: a Python tool for probabilistic volcanic hazard assessment and for generation of Bayesian hazard curves and maps. Comput Geosci, 79, 38-46.

Widiwijayanti, C., Voight, B., Hidayat, D., and Schilling, S. (2009), Objective rapid delineation of areas at risk from block-and-ash pyroclastic flows and surges, B Volcanol, 71 (6), 687–703.

Pablo Tierz, Spain

pablo@bgs.ac.uk

Affiliation under NEMOH
Istituto Nazionale di Geofisica e Vulcanologia, Sezione di Bologna, Bologna, Italy

Research theme under NEMOH
Bayesian Probabilistic Volcanic Hazard Assessment (PVHA)

Where I came from: I was born in Zaragoza (Spain) on the 24th of November 1986. Having been attracted to Earth Sciences since I was 15, I completed a BSc+MSc program in Geology at the Universidad de Zaragoza in 2011 with a Master's thesis about the petrological, geochemical and structural features of magmatic dike intrusions in the Central Pyrenees, Aragón (Spain). Due to cuts to funding for basic research in my country, I looked for opportunities further afield. This led me to Bologna (Italy) where I started working as a NEMOH fellow at INGV Bologna in January 2013, under the supervision of Dr. Laura Sandri and Dr. Warner Marzocchi.

Background developed under NEMOH: Being part of NEMOH gave a completely new dimension to my understanding of what scientific research means within an international multi-disciplinary consortium. I found the strategy of *training-through-research* very useful since it allowed me to carry out my research at INGV Bologna in close collaboration with my supervisors but, at the same time, it boosted my volcanological background and networking/communication skills through complementary activities: from 2013 to 2015, I attended 20 workshops, 5 international meetings and I was a visiting post-graduate at three different institutions (University at Buffalo, NY, USA; Dipartimento della Protezione Civile, Rome, Italy; and University of Bristol, UK).

Current scientific interests: I consider myself a geoscientist with a hybrid background (between Geology and Geophysics) and a strong passion for volcanology in particular, and magmatic systems in general. Therefore, my scientific interests range from uncertainty quantification and probabilistic volcanic (multi) hazard assessment to physical-chemical properties of magmas from mantle reservoir conditions to intrusion or eruption.

Future perspectives: I am now pursuing a PhD on probabilistic volcanic hazard assessment of Pyroclastic Density Currents at Somma-Vesuvius and Campi Flegrei (Italy). Afterwards, I would really love to continue my career in volcanology and, hopefully alongside some of my NEMOH fellows, become one of the members of the next generation of European volcanologists.

Finito di stampare nel mese di aprile 2018 presso le
Industrie Grafiche della Pacini Editore Srl Via A.
Gherardesca • 56121 Ospedaletto • Pisa
Tel. 050 313011 • Fax 050 3130300
www.pacinieditore.it

Numerical, Experimental and Stochastic Modelling of Volcanic Processes and Volcanic Hazards

NEMOH

a Marie-Curie Initial Training Network for the next generation of European volcanologists

Editors

Paolo Papale, Editor-in-Chief
Hideo Aochi
Christopher Bean
Costanza Bonadonna
Arnau Folch
Alessandro Fornaciai
Magnus Tumi Gudmundsson
Stephen Lane
Raffaela Pignolo
Alison Rust
Gilberto Saccorotti
Bettina Scheu

Pacini Editore

ISBN: 978-88-6995-428-3